



Dedicated to building research infrastructure and the promotion of Science, Technology, Engineering and Math (STEM) education in West Virginia

2014–2015 STUDENT RESEARCH REPORTS

Summer Internships

Undergraduate Research Fellowship Program

Graduate Research Fellowship Program

NASA West Virginia Space Grant Consortium
West Virginia University
PO Box 6070
Morgantown, WV 26506-6070
(304) 293-4099

www.wvspacegrant.org

Published July 2015



PREFACE

The National Space Grant College and Fellowship Program (also known as Space Grant) was first established under Title II of the National Aeronautics and Space Administration (NASA) Authorization Act of 1988 (P.L. 100-147). Space Grant is a unique national state-based network in 50 states, Puerto Rico and the District of Columbia. The program is a component of NASA's Education Directorate portfolio charged with carrying out effective education, research, and public outreach activities in science, technology, engineering and mathematics (STEM), particularly in fields most relevant to NASA's future workforce.

Currently, Space Grant is comprised of 52 consortia that engage over 1,000 affiliates nationally, including more than 600 colleges/universities, and state, industry, non-profit and federal partners, including NASA Centers. They work collectively to meet the nation's needs for developing and training a high-tech workforce to sustain a robust U.S. space science and space exploration program.

As one of the 52 university-based Space Grant consortia, the West Virginia Space Grant Consortium (WVSGC or Consortium) was established in August 1991. The Consortium is housed in the Benjamin M. Statler College of Engineering and Mineral Resources on the Evansdale Campus of West Virginia University in Morgantown, West Virginia. It is comprised of 12 West Virginia academic institutions and 8 corporate and scientific partners (a list of affiliates is listed on page 2). It is dedicated to building research infrastructure and promoting STEM education in West Virginia. The Consortium's programs focus on research, collaborations with high technology industries, student fellowships as well as K-12, and public outreach programs. This is consistent with the strategic vision for the state's participation in the nation's current and future endeavors in science and technology.

This publication is a compilation of student reports from summer internships, the NASA Undergraduate Research Fellowship Program and the NASA Graduate Research Fellowship Program for the 2014- 2015 fiscal year.

On behalf of the Board of Directors of NASA WVSGC, we would like to take this opportunity to express our appreciation to students who applied for these programs, the mentoring offered to West Virginia students by their faculty advisors in their research projects as well as the different internship locations that provided these opportunities. Without them, our internships and fellowship programs would not be where they are today: a crucial step in the workforce development pipeline for NASA and the high technology sector in the United States.

For additional information on our programs, please contact our office or visit wvspacegrant.org.

CONSORTIUM AFFILIATES

West Virginia University (Lead)

Bethany College

Bluefield State College

Fairmont State University

Glenville State College

Marshall University

NASA Independent Verification & Validation Facility

National Radio Astronomy Observatory

Polyhedron Learning Media, Inc.

Shepherd University

TechConnect WV

The Clay Center for the Arts and Sciences of West Virginia

TMC Technologies, Inc.

West Liberty University

WV High Technology Consortium Foundation

West Virginia State University

WVU Institute of Technology

West Virginia Wesleyan College

Wheeling Jesuit University

Table of Contents

LIST OF PROGRAMS	1
I. SUMMER INTERNSHIPS.....	1
II. NASA UNDERGRADUATE RESEARCH FELLOWSHIP PROGRAM	3
III. NASA GRADUATE RESEARCH FELLOWSHIP PROGRAM.....	4
I. Summer Internships Reports	6
Ball, Georgette. West Virginia University. <i>Space Telescopes: A Glimpse into the Unknown SPOT Presentation</i>	7
Bierhals, Melinda. Bethany College. <i>Historical Risk Data Collection and Analysis Effort</i>	12
Billian, Hannah. West Virginia University. <i>Prediction Framework for Mosquito Abundance Using Satellites</i>	18
Coleman, Jacob. West Virginia Wesleyan College. <i>Design A Remote-Sensing Rocket Payload for Sensing Radiation</i>	26
Cvetnick, Andrew. West Virginia Wesleyan College. <i>Supersonic Flight</i>	28
Davari, Denna. West Virginia University. <i>Hydration Study of Hand/Finger/Nail System to Understand Mechanism of Glove-Related Injuries</i>	36
Doss, Christopher. West Virginia University. <i>Asymmetric Reconnection with a Shear Flow and Application to X-Line Motion at the Polar Cusps</i>	45
Grant, Lynnora. West Virginia University. <i>A Look at Planetary Protection Implementation</i>	55
Krall, Joseph. West Virginia University. <i>Faster Evolutionary Multi-Objective Optimization via Gale: The Geometric Active Learner</i>	65
Mardmomen, Nadia. West Virginia University. <i>Alternative Vaccination Routes in Pediatrics Today</i> 74	
O’Meara, Cody. West Virginia Wesleyan College. <i>Implementation of a Rotating Diffusor in the NASA LARC Structural Acoustic Loads and Transmission (SALT) Facility</i>	79
Rhodes, Corey. West Virginia Wesleyan College. <i>Developing and Verifying a Computer Model to Predict the Flight Characteristics of a Water Rocket</i>	89
Siburt, Matthew. West Virginia University. <i>Design, Build and Fly a Dual Use UAS for Search and Rescue and Precision Agriculture</i>	99
Speelman, Justin. West Virginia University. <i>Summer Internship with TMC Technologies</i>	107
II. NASA Undergraduate Research Fellowship Reports	112
Billups, David. West Virginia University. Dr. Andrew Nix. <i>Quantifying Turbulence Intensity and Boundary Layer Thickness for Use in an Investigation of the Effect of Boundary Layer State and Thickness on Film Cooling Effectiveness</i>	113
Carte, Destiny. Marshall University. Dr. Brian Scott Day. <i>Effect of Linker Length on DNA Aptamer Performance</i>	123

Carter, Arrin. Marshall University. Dr. Elmer Price. <i>Modulating Neural Cell and Central Nervous System Biodegradation of Implantable Engineered Microenvironments using Aprotinin-Stabilized Fibrin</i>	134
Collins, Evan. Wheeling Jesuit University. Dr. James Coffield. <i>Standardization of E. coli Coliform Counting for the Determination of Stream Health from Combined Sewer Outflows along Wheeling Creek</i>	148
Gray, Miles. Marshall University. Dr. Marcos Serrat. <i>Temperature Effects on Limb Growth and IGF-I Delivery to Mouse Bones</i>	168
Kagen, Shane. Marshall University. Dr. Derrick Kolling. <i>Exploring the Temperature Dependence of Photoassembly</i>	176
Meyer, Elijah. West Virginia University. Dr. Avinash Unnikrishnan. <i>Assessing Reliance and Planning Expansions of Transportation Infrastructure While Accounting for Future Climate Scenarios</i>	191
Robinson, Emily. Wheeling Jesuit University. Dr. Raudenbush. <i>The Effects of Soccer Ball Heading on Scent Perception: Severity of Effects in Adolescence During High School Competition</i>	202
Strader, Jared. West Virginia University. Dr. Yu Gu. <i>Combined Methods for Object Recognition</i>	211
III. NASA Graduate Research Fellowship Reports	221
Cavender, Hannah. West Virginia State University. Dr. Barbara Liedl and Dr. Micheal Fultz. <i>Synthesizing and Trailing Triesterified Monosaccharides on the Biocontrol Generalist Predator, Green Lacewing, Chrysoperia Rufilabris</i>	222
Graves, Andrew. West Virginia University. Dr. Charter Stinespring. <i>Graphene-nanoparticle Composite Gas Sensors</i>	235
Hypes, Alexander. West Virginia University. Dr. Yu Gu. <i>Autonomous Minding of Loose Aggregate</i>	252
Komar, Colin. West Virginia University. Dr. Paul Cassak. <i>The Nature of Magnetic Reconnection at the Dayside Magnetopause</i>	265
Nande, Rounak. Marshall University. Dr. Pier Paolo Claudio. <i>Ultrasound Mediated Gene Delivery in Immune-Competent C57BL/6 Mice</i>	280
Tamski, Holly. Marshall University. Dr. Maria Serrat. <i>Unilateral Heating to Increase IGF1 Uptake and Bone Length in Mice</i>	296
Timm, Shelby. Marshall University. Dr. Jayme Waldron. <i>The Sublethal Effects of Stream Liming on Life History Shifts in Gyrinophilus Porphyriticus</i>	309

LIST OF PROGRAMS

I. SUMMER INTERNSHIPS

For the 2014–2015 fiscal year, we have sixteen undergraduate and graduate students who successfully received internship opportunities. Below is a list of their names, the university they attend, the internship facility as well as their research topic. A copy of their research reports is included under Section I.

Ball, Georgette

University: West Virginia University
Location: NASA IV&V Facility
Research: *Space Telescopes: A Glimpse into the Unknown SPOT Presentation*

Bierhals, Melinda

University: Bethany College
Location: NASA Goddard Space Flight Center
Research: *Historical Risk Data Collection and Analysis Effort*

Billian, Hannah

University: West Virginia University
Location: West Virginia University
Research: *Prediction Framework for Mosquito Abundance Using Satellites*

Coleman, Jacob

University: West Virginia Wesleyan College
Location: West Virginia Wesleyan College
Research: *Design A Remote-Sensing Rocket Payload for Sensing Radiation*

Cvetnick, Andrew

University: West Virginia Wesleyan College
Location: West Virginia Wesleyan College
Research: *Supersonic Flight*

Davari, Denna

University: West Virginia University Institute of Technology
Location: West Virginia University Institute of Technology
Research: *Hydration Study of Hand/Finger/Nail System to Understand Mechanism of Glove-Related Injuries*

Doss, Christopher

University: West Virginia University
Location: West Virginia University
Research: *Asymmetric Reconnection with a Shear Flow and Application to X-Line Motion at the Polar Cusps*

Grant, Lynnora

University: West Virginia University
Location: NASA Goddard Space Flight Facility
Research: *A Look at Planetary Protection Implementation*

Krall, Joseph

University: West Virginia University
Location: West Virginia University
Research: *Faster Evolutionary Multi-Objective Optimization via Gale: The Geometric Active Learner*

Mardmomen, Nadia

University: West Virginia University
Location: United Hospital Center
Research: *Alternative Vaccination Routes in Pediatrics Today*

O'Meara, Cody

University: West Virginia Wesleyan College
Location: NASA Langley Aerospace Research Summer Scholars
Research: *Implementation of a Rotating Diffusor in the NASA LARC Structural Acoustic Loads and Transmission (SALT) Facility*

Rhodes, Corey

University: West Virginia Wesleyan College
Location: NASA Langley Aerospace Research Summer Scholars
Research: *Developing and Verifying a Computer Model to Predict the Flight Characteristics of a Water Rocket*

Siburt, Matthew

University: West Virginia University
Location: NASA Langley Research Center: Aeronautics Academy
Research: *Design, Build and Fly a Dual Use UAS for Search and Rescue and Precision Agriculture*

Speelman, Justin

University: West Virginia University
Location: TMC Technologies in Fairmont, West Virginia
Research: *Summer Internship with TMC Technologies*

II. NASA UNDERGRADUATE RESEARCH FELLOWSHIP PROGRAM

The NASA WVSGC Undergraduate Research Fellowship Program provides support for undergraduate students under the supervision of their academic advisor. For the 2014-2015 fiscal year, we have thirteen undergraduate students who were awarded research fellowships. Below is a list of their names, the university they attend, their mentor as well as their research topic. A copy of their research reports is included under Section II.

Billups, David

University: West Virginia University

Mentor: Dr. Andrew Nix

Research: *Quantifying Turbulence Intensity and Boundary Layer Thickness for Use in an Investigation of the Effect of Boundary Layer State and Thickness on Film Cooling Effectiveness*

Carte, Destiny

University: Marshall University

Mentor: Dr. Brian Scott Day

Research: *Effect of Linker Length on DNA Aptamer Performance*

Carter, Arrin

University: Marshall University

Mentor: Dr. Elmer Price

Research: *Modulating Neural Cell and Central Nervous System Biodegradation of Implantable Engineered Microenvironments using Aprotinin-Stabilized Fibrin*

Collins, Evan

University: Wheeling Jesuit University

Mentor: Dr. Mary Railing

Research: *Standardization of E. Coli Coliform Counting for the Determination of Stream Health from Combined Sewer Outflows along Wheeling Creek*

Eisenhart, Andrew

University: Wheeling Jesuit University

Mentor: Dr. James Coffield

Research: *Synthesis of 1-butyl-3-methylimidazolium hexafluorophosphate: Investigation of its use as an electrochemical solvent for electroanalytical studies of metal dithiocarbamate complexes*

Gray, Miles

University: Wheeling Jesuit University

Mentor: Dr. Maria Serrat

Research: *Temperature Effect on Limb Growth and IGF-I Delivery to Mouse Bones*

Kagen, Shane

University: Wheeling Jesuit University

Mentor: Dr. Derrick Kolling

Research: *Exploring the Temperate Dependence of Photoassembly*

Meyer, Elijah

University: Wheeling Jesuit University

Mentor: Dr. Avinash Unnikrishnan

Research: *Assessing Reliance and Planning Expansions of Transportation Infrastructure While Accounting for Future Climate Scenarios*

Robinson, Emily

University: Wheeling Jesuit University

Mentor: Dr. Bryan Raudenbush

Research: *The Effects of Soccer Ball Heading on Scent Perception: Severity of Effects in Adolescence During High School Competition*

Strader, Jared

University: Wheeling Jesuit University

Mentor: Dr. Yu Gu

Research: *Combined Methods for Object Recognition*

III. NASA GRADUATE RESEARCH FELLOWSHIP PROGRAM

The NASA WVSGC Graduate Research Fellowship Program provides funding for graduate students working on a thesis or dissertation with faculty from member institutions. For the 2014-2015 fiscal year, we have six graduate students who were awarded research fellowships. Below is a list of their names, the university they attend, their mentor as well as their research topic. A copy of their research reports is included under Section III.

Cavender, Hannah

University: West Virginia University

Mentor: Dr. Barbara Liedl

Research: *Synthesizing and Trailing Triesterified Monosaccharides on the Biocontrol Generalist Predator, Green Lacewing, Chrysoperia Rufilabris*

Graves, Andrew

University: Marshall University

Mentor: Dr. Charter Stinespring

Research: *Graphene-nanoparticle Composite Gas Sensors*

Hypes, Alexander

University: Marshall University

Mentor: Dr. Yu Gu

Research: *Autonomous Minding of Loose Aggregate*

Komar, Colin

University: Marshall University

Mentor: Dr. Anne Axel

Research: *The Nature of Magnetic Reconnection at the Dayside Magnetopause*

Nande, Rounak

University: Marshall University

Mentor: Dr. Pier Paolo Claudio

Research: *Ultrasound Mediated Gene Delivery in Immune-Competent C57BL/6 Mice*

Tamski, Holly

University: Marshall University

Mentor: Dr. Anne Axel

Research: *Unilateral Heating to Increase IGF1 Uptake and Bone Length in Mice*

Timm, Shelby

University: Marshall University

Mentor: Dr. Anne Axel

Research: *The Sublethal Effects of Stream Liming on Life History Shifts in *Gyrinophilus Porphyriticus**

I. Summer Internships Reports

Space Telescopes: A Glimpse into the Unknown SPOT Presentation

Georgette Ball
Industrial and Management Systems Engineering
West Virginia University
Morgantown, WV, 26505

“To really address life beyond our solar system requires complex telescopes and instruments with truly unique capabilities. The technological breakthrough made possible by missions like the Hubble Space Telescope, Kepler and James Webb Space Telescope (JWST) are not only profoundly important for advancing discovery they show us what kind of innovation means for our leadership as a nation and international partner in exploration.”

– Ellen Stofan, Chief Scientist, NASA Headquarters

ABSTRACT

My project this summer focuses on a Space Telescope Presentation for the WV SPOT program. This presentation specifically is on the telescopes and satellites apart of NASA’s exoplanet missions; Hubble, Spitzer, Kepler, TESS and James Webb. I believe that this presentation will help enhance public awareness of, and appreciation for, space science. I hope to incorporate educational and public outreach activities along with the presentation.

INTRODUCTION

The West Virginia Space Public Outreach Team, WV SPOT, sole mission is to inspire an appreciation of STEM and STEM careers in K-12 students through the delivery of interactive presentations by undergraduate students that highlight cutting edge space science and engineering research in the Mountain State. Not only does SPOT influence the audiences of these presentations, it is also impactful on the students who present them. These presentations provide the audience the opportunity for increased awareness and appreciation for astronomy and other space related topics through Science, Engineering, Technology and Math (STEM). In addition, the students providing these presentations are attaining a wide range of skill sets such as science communication, public speaking, autonomy, and space science content knowledge.

These SPOT presentations utilize a variety of slides, videos, animations and have an inquisitive approach to relay the excitement of new discoveries in space science. NRAO and NASA research and careers here in West Virginia are highlighted in each show. Presentations are either presented in a classroom or assembly setting. After this summer concludes there will be four SPOT presentations readily available. These presentations include: Invisible Universe, Mars: Past, Present, Future, The International Space Station, and Space Telescopes: A Glimpse into the Unknown. Each show lasts approximately 30-45 minutes.

PROJECT

The presentation I decided to prepare this summer for WV SPOT is on space telescopes. More specifically space telescopes that have a focus on exoplanet missions. An exoplanet is a planet outside our solar system. I chose this because I firmly believe that in the next twenty years we will

know of life outside our solar system. And we're going to know this because of the space telescope technology that we currently are using and the technology that will be launched within the next decade. It was not too long ago that the human race knew of only nine planets, now eight, within our universe. In the past five years we've discovered thousands. Every star in the night sky is a sun, and each star has the possibility of hosting at least one planet, some even earth-like. I believe increasing awareness on this will greatly impact the future of STEM careers and hopefully will inspire future generations.

METHODS

My method for approach was to first do extensive research. I spent approximately one month researching space telescopes that specially focus on exoplanet research. I studied their technology, functions, locations etc. With the immense of research I found I narrowed down my presentation to five space telescopes; Hubble, Kepler, Spitzer, The Transiting Exoplanet Survey Satellite (TESS), and James Webb Space Telescope (JWST).

PRESENTATION

The Space Public Outreach Presentation, Space Telescopes: A Glimpse into the Unknown will introduce many science related topics. The beginning of the presentation introduces the student to the bigger picture of it all. By slowing and gradually showing them the perspective of Earth within our universe. It starts with a picture of a starry night and then goes to a picture of our solar system, all eight planets. By introducing the familiar, the students will be able to expand their learning. Next the galaxy is introduced, then finally an illustration of many galaxies. This is meant to familiarize to the students that our solar system is just one of many within our galaxy, and our galaxy is just one galaxy amongst hundreds of billions of galaxies within the universe.

Now that the students have a sense of perspective of our place within the universe the presentation goes right into the history of the telescope. By the use of the telescope we are able to know our place within our universe and know that there are many other planets out in the universe. The presentation hits on the history of Galileo Galilei and how he revolutionized the use of the telescope by using it to peer at the sky. Next, Isaac Newton is introduced. He modified Galileo's refracting telescope, which is a telescope that consists of two lenses, to a reflecting telescope, which consists of two mirrors. Also, light spectrums are introduced at this point of the presentation. Our modern understanding of the visible light spectrum comes from Isaac Newton's prism experiment. He refracted white light into a glass prism that resolved to the components of the rainbow. In addition to this experiment, other experiments were done with visible light such as the Hershel experiment where he took the temperature of each wavelength of visible light. In doing so, he discovered that the temperature increased as he went from the blue end of the spectrum to the red. In addition, an even greater temperature was recorded pass the red spectrum, making way to the discovery of infrared light.

A variety of ground telescopes are shown next. The present day telescopes are visible and radio telescopes found all over the world, this slide is used to show that in present day times ground telescopes are used all over the world and they range in size and shape depending on the type of telescope. Mention of the Greenbank Radio Telescope and the West Virginia University Observatory are also discussed at this point in the presentation as a way to linked to the state of

West Virginia to this topic which is crucial for the SPOT program because we want to make it a point that students don't need to leave the state to be a part of STEM careers.

During this point of the presentation is an opportunity for discussion. In the show, a gif of a starry night appears with the stars twinkling. This is where the presenter will incorporate the analogy of the nursery rhyme 'twinkle, twinkle little star.' Here on Earth, telescopes have a disadvantage. The students here have a chance to interact with the presenter by brainstorming some of these disadvantages. The four key disadvantages the presenter should make sure they get are clouds, city lights, the atmosphere, and pollution. Another analogy that is used is opening your eyes underwater. When one opens their eyes underwater they do not see clearly, this is an example of how the atmosphere distorts our views of space.

The beginning of the presentation introduced the visible and infrared spectrums. This is the point of the presentation where the presenter will introduce the entire electromagnetic spectrum. This is only meant to introduce to the students and familiarize them to the topic. Most students seeing this presentation may not have learned it yet (Most students are not introduced to this subject matter until the fifth or sixth grades.) The presentation shows a number of space telescopes that have been launched, and like ground telescopes they don't all look alike and are used for a variety of purposes. Then the electromagnetic spectrum is revealed and the different wavelengths are shown of each; radio, microwave, infrared, visible, ultraviolet, x-ray and gamma. The main thing to take away for the students at this point is that there are a variety of light spectrums and humans are only able to see the visible light spectrum, the rest are invisible and our eyes are not sensitive to their wavelengths.

Since this presentation focuses on exoplanet research, infrared and visible light space telescopes will be what the rest of the presentation focuses on. At this point, the students have the knowledge that there are many space telescopes in space, so how scientist get them in space is the next thing addressed. Space telescopes are sent into space by the shuttle program or by rockets. Since the retirement of the shuttle program, launches are primarily done now with rockets.

The first telescope discussed is Hubble. Hubble is the most well-known space telescope, so it only made sense to start off with it. The presentation hits on the orbit of Hubble, the year of launch, and type of telescope Hubble is. In addition, how scientist communicates with Hubble up in space is also addressed. It is understood that scientist use approximately the same method when communicating with other space telescopes. This is a method of using a network of satellites that relay information. An analogy used here is the analogy of satellite television. If you have dish TV the television provider sends a signal to your dish so that you receive cable. Much like how scientists send commands to Hubble to look at specific things out in space. Another reason I talk about Hubble is because we have used Hubble to monitor planets within our own solar system, like dust storms on mars or the progression of The Great Red Spot on Jupiter. By talking about how we use space telescope technology to observe planets in our solar system, the presentation is easing the students into the topic of observing planets outside our solar system.

The rest of Hubble's section of the presentation consists of the Hubble Ultra Deep Field View. This introduces to the students the fact that there are many other galaxies in the universe. There has been debate on whether this part of the presentation should stay or get cut. Since the focus is

on exoplanets some believe that by talking about the Ultra Deep Field View makes the presentation go off tangent.

The presentation continues with the Kepler Space telescope; which like Hubble is a visible space telescope. Unlike Hubble, Kepler has a very specific mission. The Hubble Space Telescope is used for many types of scientific studies such as monitoring planets, determining the age of the universe and observing nebulae or supernovas. Kepler's sole mission is to discover exoplanets, more specifically earth-like exoplanets. The presentation then explains where Kepler's field of view is. A video is then played on how Kepler finds these planets through the transit photometry method. Also, the video explains the Habitable Zone. This is a zone that is where liquid water can exist within a solar system. If a planet is in the Habitable Zone, or Goldilocks Zone, then it is possible that planet could be earthlike. The video does a fantastic job at comparing the Kepler Space Telescope to the explorers learned in history books. Like Lewis and Clark or Christopher Columbus, Kepler is exploring new lands and literally discovering new worlds.

After the video finishes, students see an example of the transit method. This slide is important because it introduces the use of graphs to determine patterns in data, a technique that these students will do themselves in future grades. Next, a planet that has been discovered using Kepler is talked about, Kepler- 22b. The presenter will also explain how scientist name the planets it finds. All the planets that are found using the Kepler Telescope are named Kepler. Each are also assigned a number and letter. The number stands for the order in which the star in that system was found and the letter stands for the order of that planet in the system. (Kepler 22-b; 22nd star found using Kepler, first planet in that system. Planets are never called 'a')

Kepler Telescope has its limitations; it can only inform scientists of the planets location in its system, the planets orbital system, and the planets size. Kepler cannot tell scientists the composition or atmosphere of the planet they are studying they can only speculate on that.

This is the point of the presentation that transitions from visible to an infrared space telescope, Spitzer. The beginning of the presentation explains infrared light but this is where the importance of an infrared telescope is explained in the presentation. An infrared telescope or camera can look right through objects that a visible telescope can't. For example, a garbage bag can hide a person's hand when the hand is placed within the bag, but when looking at the person with an infrared telescope or camera you can look right through the garbage bag and see the person's hand. That is how infrared telescopes work in space. They are able to see right through dust in space that can otherwise obstruct views for visible telescopes. In addition to this it was discovered that Spitzer is actually helpful in exoplanet missions. Spitzer can block out a stars brightness and pick up planets that Kepler can otherwise miss. This is a strategy that scientists use to discover exoplanets.

With the help of Hubble, Kepler, and Spitzer scientist have been able to study and learn so much through the years. It was not very long ago that scientist only knew of the eight planets in our solar system and now they know of thousands of planets within our galaxy. Essentially every time you look up at the night sky and see a star, that star has at least one planet that orbits it. This is the point of the presentation that addresses what's to come with space telescope technology. Many people think that since the retirement of the shuttle program NASA hasn't been doing much, but that is not the case. In the next four years two telescopes will be launched.

The first is an upgrade of Kepler, The Transiting Exoplanet Survey Satellite, TESS. Like Kepler, TESS will survey the sky for earthlike planets within our solar neighborhood. Instead of staring at a fixated region of the sky like Kepler, TESS will be an all sky surveyor and scan the entire sky in a two year mission. Also, TESS has four cameras that will be used to survey.

Next to be launched in 2018 is The James Webb Space Telescope, JWST. A video is played to explain what essentially JWST will do and its mission goals. JWST will be an infrared space telescope that can take in 60% more the infrared light Spitzer can and precisely pinpoint on what it's observing like Hubble can.

The presentation explains that these last two telescopes are in their developmental stages but will have a profound and unique role on furthering our understanding of our universe. This topic is extremely important because these telescopes are going to tell us how rare or how common earthlike worlds are within the universe.

The presentation ends with a few slides on NASA IV&V and its role in the space telescope missions discussed in the presentation and also on the software checking that is done there. In addition, the location and internship opportunities at IV&V are also mentioned.

HANDS-ON ACTIVITY

The SPOT presentations this summer have been decreased to thirty minutes so that there is time for a hands-on activity. The activity that will be given during this presentation is Seeing Through Alien Eyes, see attached for more details. This activity is meant to demonstrate to the students that scientist use a variety of different filters to sort out the details in the structures and compositions of the objects they are looking at in space.

RESULTS/OUTCOMES

The results of this presentation thus far have been positive. However, the expected outcomes and statistics for meeting the WV SPOT goals are yet to be determined. The presentation will need to be shown throughout the state of West Virginia through the 2014-2015 school term to have the data to make the evaluation of how impactful this presentation was to the targeted audiences. This presentation will be presented to children attending the Greenbank Camp in Greenbank, WV on Monday August 4th.

FUTURE PLANS

I plan to be heavily involved with WV SPOT throughout this school term and continue to help with this presentation's development. In addition to this, I am the SPOT officer for the Space Club of WVU and plan to incorporate and instill some interest to the members of the club and throughout the university. I think the WV SPOT presentation program is an excellent way to impact the younger generation of West Virginians and increase their awareness/interest in space science and I am optimistic that the program continues to have success and excel.

HISTORIC RISK DATA COLLECTION AND ANALYSIS EFFORT

Melinda Bierhals
Mathematics

Bethany College & Marshall University
1 Main Street, Bethany, WV 26032 & One John Marshall Drive, Huntington, WV 25755

ABSTRACT

The purpose of this project is to collect, consolidate, and analyze historical risk data from projects in the IT and Communications Directorate (ITCD) to find opportunities to improve the risk management process. A few subject matter experts were consulted to identify the key questions that needed to be answered, such as: Do project managers favor certain types of risks in ITCD? Is there a significant difference in risk levels from one project to another? Hypotheses were developed based on the questions and a preliminary look at the trends in certain data points. For example, the risk likelihood and consequence levels (extent of the impact) of each risk showed they had a tendency to decrease or stay the same over time, so this became one of the hypotheses. The hypotheses and questions led to the necessary data to gather. For example, it was necessary to gather information on the risk types, risk priority, and risk consequences to ascertain most common risk type, the frequency of changes in risk priority, and the most impactful types of risk, respectively. Another factor that informed the analysis was the amount of missing data among project risks, the percentage of required data the project managers omitted. In order to answer these questions a substantial amount of risk data needed to be collected. The data was retrieved from monthly Project Status Review (PSR) reports in PowerPoint from 2008 to the present. Once the data was collected and put into the risk list template in Excel, it was analyzed to test the hypotheses and answer the questions. After analyzing the information needed for the analysis it was determined that not all of the hypotheses were true. For example, a few projects had trends that increased in consequence and likelihood levels. It was found that the most common risk types were Technical, Schedule, and Management-Programmatic. These risks also had the highest priority level, meaning they are the riskiest types. Once the percentage of reported data was determined it showed that project managers should be more thorough and consistent in reporting risk data. The results of this project showed that project managers need to be more specific and consistent in reporting risks. At the conclusion of this project it was determined that there are now more questions to be answered, such as, why are the consequence and likelihood levels increasing over time? The results also show that there are concrete measures that can be taken to improve the amount and quality of risk data such as increasing the availability of risk training tailored to ITCD project managers and incentives for reporting quality risk data more frequently.

INTRODUCTION

This project contains many goals that lead to the purpose of helping the Information Technology and Communications Directorate improve their risk management process. The goals of this project are to determine how much required risk data had been recorded historically to date and to determine what portion of that data will be useful in the future. The hypotheses for this research include: The consequences of risk score should stay the same or decrease over time, as long as everything else remains the same; The likelihood risk score should stay the same or decrease over

time if the mitigation strategy is in place; Likelihood of risk should stay the same or increase over time if a “watch” or “accept” approach is in place. In order to help improve the risk management process certain questions needed to be answered as well. The questions were: What are the most common risk types? What insight can we derive from the frequency of changes in risk priority? Are there particularly successful mitigation strategies? What are the most risky types of risks? What percentage of required data has been captured? The answers to these questions will help ITCD improve their risk management process.

BACKGROUND

Risks are reported every day in the decision-making process of project managers in various corporations. The risks need to be carefully evaluated and assessed by the project teams to make sure that their project runs smoothly and successfully. Once a risk is realized it is then defined as being the combination of the likelihood that an undesired event will occur during a project and the consequences of this undesired event, if it were to take place. Likelihood is also referred to as the probability of an event actually happening. Consequence is the impact which describes the possible negative outcomes of conditions that create uncertainty and describes the severity of a risk if it is realized.

Reporting risks involves the use of the ITCD Standard Risk Scorecard. The scorecard separates the likelihood and consequence levels into five different levels each being evaluated quantitatively and qualitatively. The description of the individual risk levels are as follows:

Likelihood:

- 5 (Very High) – Probability > 75%; expected to happen
- 4 (High) – 50% < Probability ≤ 75%; likely to happen
- 3 (Medium) – 25% < Probability ≤ 50%; could happen.
- 2 (Low) – 10% < Probability ≤ 25%; not expected to happen.
- 1 (Very Low) – 2% < Probability ≤ 10%; remote possibility of occurrence

Consequence:

- 5 (Very High) –Minimum success criteria is not achievable; >10% increase over allocations and cannot be handled with reserves
- 4(High) – Major impact to success criteria; between 7%-10% increase over allocated, and/or exceeds proper reserves and/or exceeds proper reserves
- 3 (Medium) – Medium impact to success criteria, with minimum success criteria still achievable; between 5%-7% increase over allocated and cannot handle with reserves
- 2 (Low) – Minor impact to success criteria; between 2% - 5% increase over allocated and can handle with reserves
- 1 (Very Low) – No impact to success criteria; less than 2% increase over allocated and negligible impact on reserves

These likelihood and consequence values are used to map out the 5x5 matrix that indicates the criticality or exposure value of a risk. On the matrix the criticality level is indicated by the colors green (low), yellow (medium), and red (high). For example, in this risk chart (Figure 1) the risk has a likelihood level of 4 and a consequence level of 5, giving the risk a numeric value of 20 and placing it in the color red. This ranks the criticality level as high, which is indicated by the star.

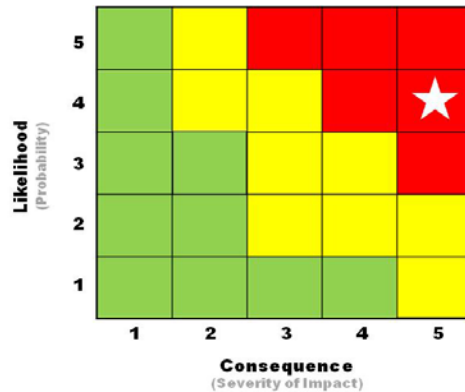


Figure 1: The 5x5 Risk Matrix

Most of the time, the criticality level of a risk coincides with the priority level of a risk. For example a high criticality level usually means the risk will be of high priority. In some cases this is not true due to certain resources or requirements.

When planning for each risk the project team must decide on an appropriate way to handle them and these, which are call Approaches. Risk approaches in ITCD include the following:

Mitigate - modification to a process, system, or activity to reduce a risk by reducing its likelihood and/or consequences

Watch - monitor a risk and its indications that might reveal a risk event is imminent.

Accept – accept the potential consequences because it’s been determined that further mitigation is not cost-effective

Research - investigation of a risk to acquire sufficient information to support another disposition of the risk (i.e., close, watch, mitigate, accept, or elevate)

Elevate - A process to increase the visibility of a risk, and to transfer the decision for the management of an identified source of risk to a higher organizational level

Once a risk has been identified it is then categorized for reporting and mitigation purposes. A mitigation plan is used to help lower the consequences of a risk or completely avoid it. The categorization of the risk also helps with future risk planning. Some examples of risk categories are: Cost, Schedule, Technical, and Management-Programmatic. For a risk to be considered into one of these types it must meet the requirements for each type. Each type has a description that the project manager can use to help categorize the type. For example, cost risks relate to the ability to execute within allocated costs or budget.

After the mitigation plans have been established it is then necessary to identify the risk triggers. Risk triggers act as warning signs that a risk may actually occur. The triggers help project teams identify when it is time to implement the mitigation plan for a risk, if it were to become an issue.

A very important aspect to this project lies in the tracking and reporting part of risk management. This step allows for the analysis of the risks. Risks are to be tracked, reported, and communicated every month. Project managers need to reevaluate every risk at least every month. The consequence and likelihood levels should be looked at to see if they are going to decrease or

increase. If the priority of a risk changes then the report given by the project team must reflect such actions.

Every project team is required to use the same template when they are communicating the risk statuses. The project managers report their top-three risks in the Project Status Review (PSR) reports. The PSR reports' are put together using Microsoft PowerPoint. There are required risk slides that must be included in the PowerPoint that give the highlights of the top-three risks. The first slide has a template showing the 5x5 matrix labeled with the risks and their ranks, the trends, risk ID, approach, and risk name. The slide which follow each contain a table with the risk rank number, risk ID, trend, risk IF-THEN statement, approach and plan, and the status or comments for each of the three risks. Every month the project managers must explain and defend their risk statuses (among other project attributes) to the Chief of the Project Management Office (PMO) in the PSR session.

The last part of risk management is deciding to close the risk. A risk may be closed when there is no more action required. This can occur when the risk is:

Rejected – the project manager decides to reject the proposed risk.

Accepted – the mitigation process has been determined to be not cost-effective and the remaining risk is at an acceptable level.

Realized – 100% likelihood has occurred.

Resolved (successfully) – the probability of the risk occurring is zero because; it has either been successfully avoided or mitigated.

METHODS

All of the work on the historical risk data took place in Microsoft Excel.

The first part of this project involved collecting historical risk data from Project Status Review (PSR) reports from the months of June 2013 to June 2014. Once the data was collected it was then put into a new risk list template. A risk list template was created for each individual project so that project managers can log them in a format that could be easily used to compile statistics. Two aggregated risk list templates were also made for the purpose of analyzing the data as a whole. The first of the two lists compiled the data from month to month; the second list only consisted of the unique risks over the years.

After the data was compiled it was then analyzed to find the frequency of changes in risk priority. To do this the only risk list template that could be looked at was the aggregated risk list that contained the month to month updates. Other data characteristics that were compiled included the most common type of risk, the most risky types of risks, and the trends in likelihood and consequence levels. The most common type of risk was found by using the unique aggregated risk list and filtering the data by risk type and then they were counted by Excel. Finding the most “risky” types of risks required the data to be filtered by consequence levels of four and five and then sorted by risk type. Riskiness was defined as a relative indicator of the negative impact of a risk as determined by a score of 4 or 5 on the consequences attribute. Looking at the trends in likelihood and consequence levels involved the use of the data recorded from month to month.

Along with these calculations it was necessary to determine the percentage of required data that was reported by project managers. This was done by taking all of the captured data and having Excel count the number of cells that had the appropriate data in it. The data was then compared to the amount of data that should have been in the cells and then a percentage was calculated. These calculations would be used to assess the effectiveness of the risk template itself. Low percentages could indicate where project managers had difficulty in understanding or assessing the required data.

Lastly, the mitigation plans were examined to determine which ones were successful and could be used in the future. If the risk was successfully avoided or resolved, then the mitigation plan can be called successful. Determining if a mitigation plan was successful required the risk to have a status of closed.

RESULTS

The top three most common risks types were found to be Technical at 25.23%, Schedule at 21.58%, and Management-Programmatic at 14.29%. These three types of risks were also calculated to be the most risky types of risks. The percentage of required data that was actually reported was found to be 66%. One of the major parts of the data that was not reported at all was the triggers for the risks.

The number of times a risk priority changed in a risks life was found to be between one and two. This result was based on an average of one risk or less per project per month.

It was found that more data needs to be reported in order to successfully analyze more of the risk lists. Since the closing dates were unknown at the time the data was collected successful mitigation plans could not be found. The percentage of risks realized were less than 5%, this could be low because of the amount of data.

While compiling the risk lists there were trending discrepancies found in some PSR reports. In some cases data in the detailed risk slide did not match the contents of the summary slide. Some of the narratives on the detailed slide did not match the trending arrows on the summary slide. For example, the narrative slide would suggest that the risk was trending upward, but the summary slide would suggest the risk was trending downward. Finding this discrepancy showed that more attention needs to pay to the results reported in the PSR reports.

During the process of collecting the data, files were made for each project so that each project manager can have the files to update on their own. The aggregated risk lists that were created will also be kept for more historical analysis.

CONCLUSION

Since the average trending change of a risk is between one and two within its life, it was concluded that risk scores are not showing a significant rate of change over time.

There is still more work that needs to be done with this project, but substantial progress was made. After collaborating with subject experts it was concluded that project management reports need to

be more specific. For example, some of the risk types need to be categorized better, according to their specific descriptions.

Being more precise when reporting data will help analysts discover where additional improvements can be made. One additive that would help substantially is the recording of the date of a risk being opened and closed. With the addition of this data, analysts might be able to decrease the likelihood and consequence level of a risk. Also, the mitigation plans will be able to be analyzed and used again, if they were successful.

Since data gaps exist within the risk lists, it was concluded that the gaps need to be filled so that more analysis can take place. One piece of information that was missing from the PSR reports was the triggers of each risk. The reporting of triggers would help other project managers in the future by giving them more knowledge that will allow them to identify possible risks in their projects. The number of discrepancies between trending data implies subjecting ranking and trending vs. the objective process that tie the data points together. By making improvements in the reporting process of risks the ITCD project managers will enable analysts to help improve risks in the future. These improvements could help lower either the likelihood or consequence level of a risk.

ACKNOWLEDGEMENTS

I would like to thank the NASA West Virginia Space Grant Consortium for the grant they gave me for this internship, and my mentor Timothy Dunfee for my internship opportunity. I would also like to thank Robert Spector and Koreen Waz for their help and guidance with the historical risk analysis project.

REFERENCES

Code 740 / Program Integration & Management Division. "Risk Management Procedures and Guidelines." 12 August 2013.

Project Management Office. "ITCD Risk Management Risk List Manual." February 2014.

PREDICTION FRAMEWORK FOR MOSQUITO ABUNDANCE USING SATELLITES

Hannah Billian
Civil Engineering
West Virginia University
Morgantown, WV 26506

ABSTRACT

West Nile virus (WNV) is the most widely dispersed arbovirus in mid-latitudes, having reached the Western Hemisphere in 1999. As a vector-borne disease, WNV is primarily spread by mosquitoes; the disease is predominantly found in tropical and temperate regions of the world, and is now considered an endemic pathogen in the United States, Africa, Asia, Australia, the Middle East, and Europe. Environmental circumstances play a vital role in transmission of WNV; as transmission of WNV is challenging to predict, this research quantifies the relationships between hydroclimatic processes and mosquito abundance for WNV in the continental United States of America using hydroclimatic information across spatial and temporal scales. It is shown that reported cases of this disease are more prevalent during spring and summer months in the United States of America, when there is more precipitation and higher surface air temperatures, on average. It has been found that the number of reported cases directly correlates with higher surface temperatures and higher precipitation rates from the years 2003-2013. The key impacts of this research are those related to the improvement of human health, and a means to predict mosquito breeding patterns long term as they relate to the prevalence of vector-borne illnesses.

INTRODUCTION

Vector-borne diseases, namely those transmitted by mosquitoes, continue to be a major concern globally (Chuang & Wimberly, 2011). West Nile Virus (WNV) is transmitted by female mosquitoes (Cooke, 2006); for optimal reproduction, mosquitoes require a temperature range of 20° C to 30° C, and a relatively high amount of rainfall since their eggs and larvae require standing water to survive (CDC, 2014). Figure 1 shows prevalence of mosquitoes that further equates to how the climate affects the breeding and life span of mosquitoes (Githeko et al., 2000). Figure 3 displays the cumulative number of mosquito infections reported from 2005-2013 (ArboNET). The growth and population of mosquitos in an area is dependent on macro-environmental dynamics such as climatic conditions (surface air temperature and precipitation rate), and micro-environmental influences which occur within the mosquito itself. As mosquito populations increase, it is hypothesized that the number of WNV cases will increase as well (Kilpatrick et al., 2012). Since eighty percent of the individuals who contract WNV display no symptoms of the disease, and the illness has an incubation period of three to fourteen days (CDC, 2014), it is important to be able to predict an outbreak in advance. Although micro- and macro-environmental factors are important in understanding WNV, only a macro-environmental understanding of a disease is useful for prediction because mosquitoes exist and adapt naturally in the environment. Remote sensing, such as satellite measurements, does not detect vectors such as mosquitoes, but in fact characterizes the environmental conditions (land/sea surface temperature, vegetation characteristics, precipitation rate, and humidity) in which these vectors survive and flourish

(Kalluri et al., 2007). This satellite data can identify the climatic conditions favorable to mosquito breeding habits, as well as aid in establishing associations between macro-environmental processes and disease occurrence at various temporal and spatial scales. Past research that has focused on examining micro- and macro-environmental factors has produced a broad range of information regarding vector-borne diseases, namely those transmitted by mosquitoes, but we still cannot effectively predict when a future disease epidemic will occur. This research models the prevalence of WNV with hydroclimatic factors such as surface air temperatures and precipitation rates in the United States of America for each state; correlating these variables gives insight to when a WNV outbreak may take place.

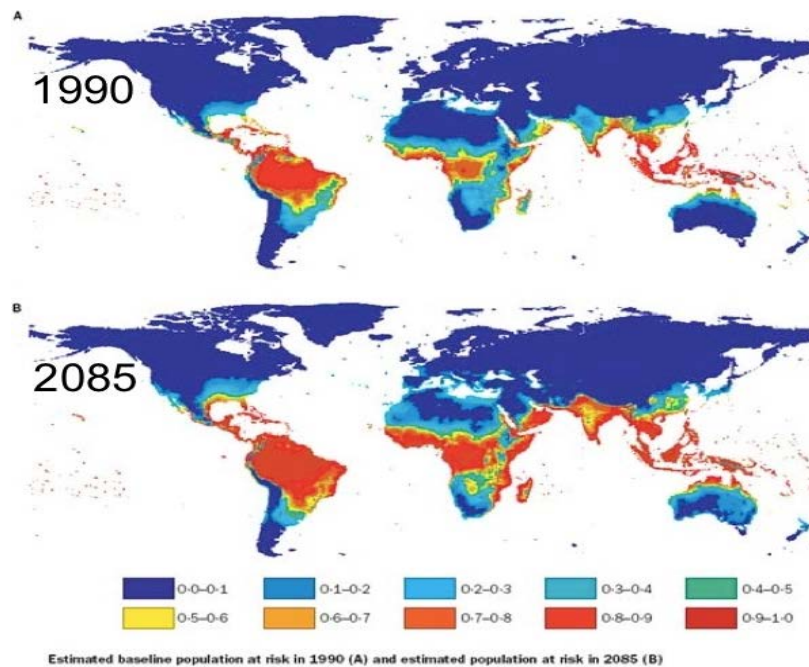


Figure 1: Human Risk of Mosquito Prevalence in 1990 and 2085 (USGS)

METHODS

Laboratory based hypothetical evidence is the framework for the methodology, where warm surface temperatures followed by rainfall increases water abundance, soil saturation, inundation, as well as vegetation cover resulting in conditions favorable for mosquito activity. Figure 2 displays the average annual incidence of WNV neuroinvasive disease reported to the United States Centers for Disease Control (CDC) by state throughout the years 1999-2013. To properly model the relationship between the prevalence of the disease, and the climate, it is a necessity to obtain a significant data set. In this research, monthly precipitation rates and temperature data were obtained from the National Oceanic and Atmospheric Administration by means of a time series of monthly/seasonal mean values based upon the latitude and longitude of each state. West Nile Virus prevalence data was obtained through the United States Geological Survey; this data represents a summary of total cases of the disease per month throughout the years 2003 – 2013. The disease

data was obtained as a discrete weekly summary of West Nile Virus cases each year, and it was then summed for each month to obtain monthly totals for each state.

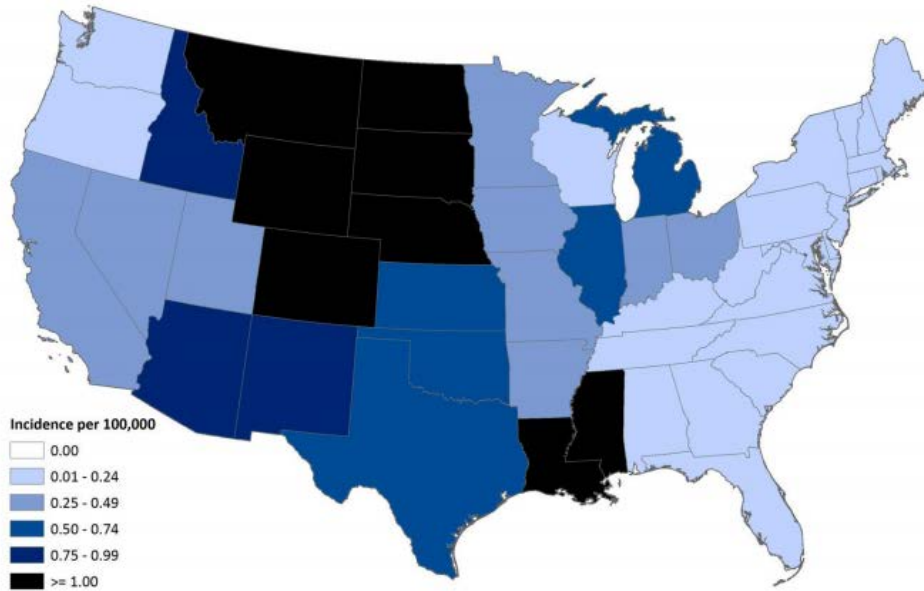


Figure 2: Average annual incidence of WNV neuroinvasive disease reported to CDC by state 1999-2013 (ArboNET)

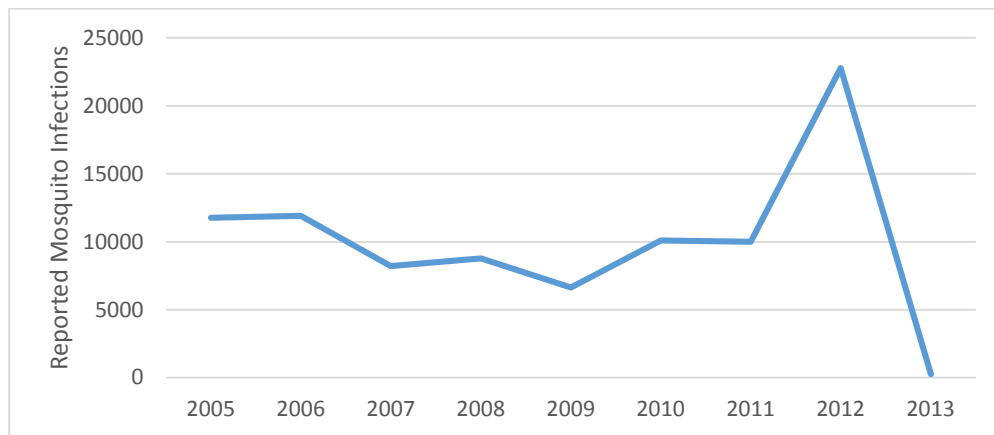


Figure 3: Cumulative number of mosquito infections reported 2005-2013 (ArboNET)

Using binary logistic regression analysis, the relationship between WNV prevalence and precipitation rate/temperature are measured by using probability scores as the predicted values of the disease prevalence, as described by the form of:

$$\ln\left(\frac{p_i}{1-p_i}\right) = \beta_0 + \beta_1 x_{1,i} + \dots + \beta_m x_{m,i}$$

where p_i represents the probabilities, the x-values represent the independent variables (precipitation rate and temperature), and the β -values represent the regression coefficients determined by the model. The final model was then constructed and is described by the form of:

$$P = \frac{1}{1 + e^{-(\beta_0 + \beta_1 x_{1,i} + \dots + \beta_m x_{m,i})}}$$

where P is the probability of WNV occurrence. This probability was then plotted against the actual reported mosquito infections of WNV to determine the simulated WNV prevalence versus the number of observed mosquito infections from 2003-2013 for any individual region. A distinct model was constructed that corresponds to every state in the continental United States. In cases where no WNV cases were reported (e.g., Alaska, Hawaii, Maine) a model could not be created. Kendall's Tau was also determined for each model, and was calculated as follows:

$$\tau = \frac{(\text{Number of Concordant Pairs}) - (\text{Number of Discordant Pairs})}{\frac{1}{2} n(n - 1)}$$

where n is the number of observations. In addition to Kendall's Tau, the Goodman-Kruskal Gamma and Somers' D correlation coefficients were also determined; the percentage of concordant pairs and discordant pairs were determined as well, along with the P-values and odds ratios for the independent variables of the model (surface air temperature and precipitation).

Once a model was developed for each state, a time series lag by one month was implemented for the surface air temperature, as well as the precipitation rate. This is enabled to determine if a WNV outbreak could be predicted by one month in advance. A new model was then developed for each state for both of these cases following the same procedure as was done with the original data.

RESULTS

Geographically, larger quantities of WNV positive mosquitoes were reported in the midwestern and southern regions of the United States (Figure 1). These regions, historically, also have higher surface air temperatures on average. The final models had rather high correlation between the variables, on average, with relatively low p-values (smaller than 0.05) which suggest some statistical significance to the correlation of the data. No outliers were removed since the data had a fairly strong positive correlation coefficient prior to identifying/removing outliers. The data also displayed 90.59 percent concordant pairs, on average, between the independent and dependent variables, with an average Goodman-Kruskal Gamma value of 0.82 over the entire United States; this parameter measures the strength of association of the data when both variables are measured at the ordinal level, where a value of zero would have indicated no correlation and a value of 1 would indicate a strong positive correlation. The average Somers' D value of 0.81 also indicates a strong positive association between the variables. Figure 4 displays the reported mosquito infections versus the simulated chance of a WNV infected mosquito (from the model) in Connecticut, United States, throughout 2003-2013, where 1 indicates an infected mosquito and a 0 indicates that there is not a WNV infected mosquito present. The models for each state exhibited an average Kendall's Tau coefficient of 0.31, indicating a positive correlation between WNV mosquito infections and the independent variables (surface air temperature and precipitation rate). Figure 5 displays the Kendall's Tau values over the entire continental United States. The average

odds ratio for precipitation rate was found to be 1.32 and 1.34 for the surface air temperature. This measure of association represents the odds that an outbreak of WNV would occur given a certain value of the independent variables; in this case, using binary logistic regression, the odds ratio is the estimated increase in the log odds of an outbreak per unit increase in temperature or precipitation rate. Since the odds ratio for each of the independent variables is greater than 1, there are higher odds of a WNV outbreak given the conditions of the independent variables.

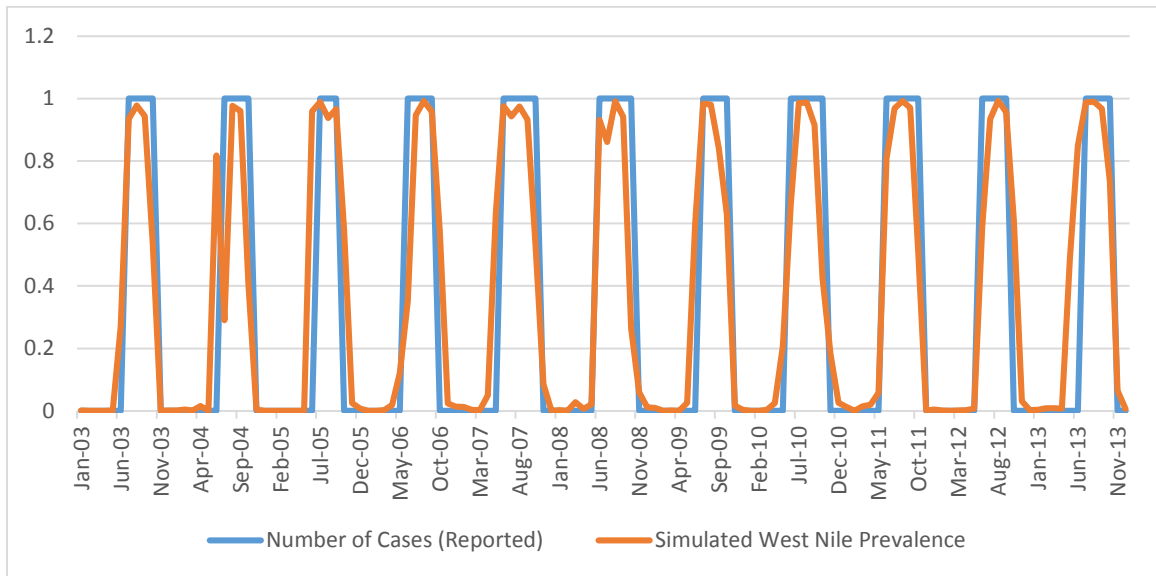


Figure 4: Simulated versus Observed WNV cases 2003-2013 in Connecticut, United States of America

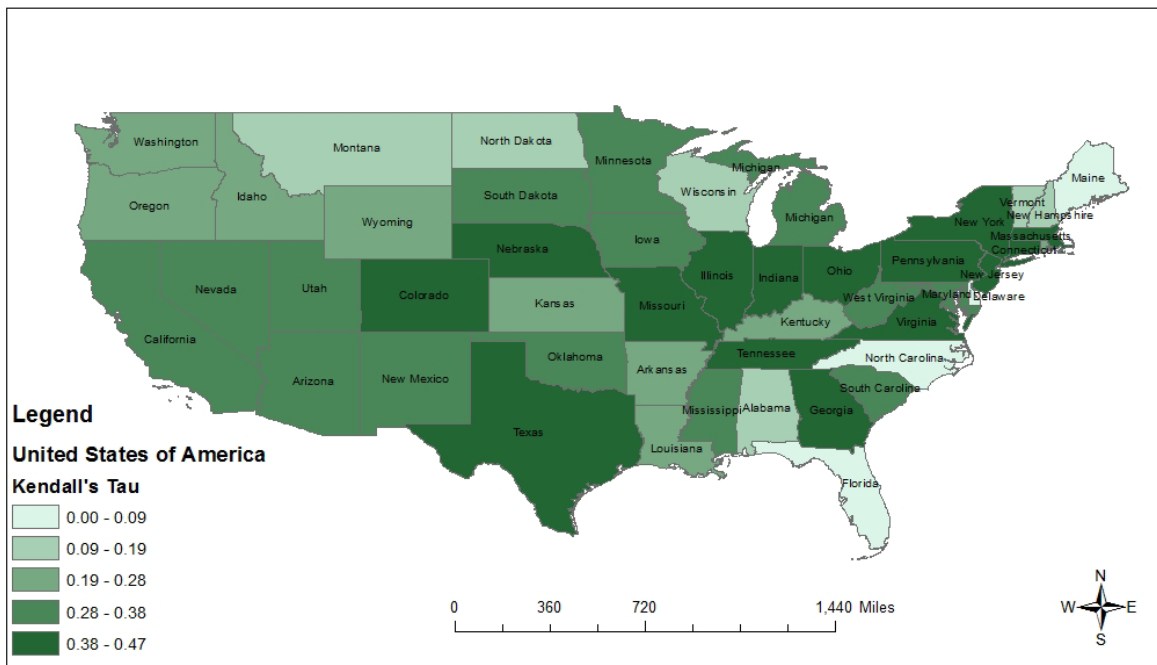


Figure 5: Correlation of WNV with Surface Temperature and Precipitation rate 2003-2013

For the second trial, a one month surface air temperature lag was implemented, while leaving precipitation rate unchanged. The final models in this case also exhibited a fairly significant correlation, on average, with an average p-value for the surface air temperature of 0.020, and 0.260 for the precipitation rate. This dataset also had 93.20 percent concordant pairs on average, with only 6.84 percent discordant pairs. An average Kendall's Tau coefficient of 0.32 was determined as well, indicating a positive correlation between WNV mosquito infections and the independent variables (surface air temperature and precipitation rate). Figure 6 demonstrates the correlation of WNV with surface temperature (one month time lag) and precipitation rate over the period of the study. The average odds ratio for precipitation rate was found to be 138.75 and was 1.52 for the surface air temperature; since both of these values are greater than one, there are theoretically greater odds of a WNV infected mosquito occurring given the conditions of the independent variables at that time.

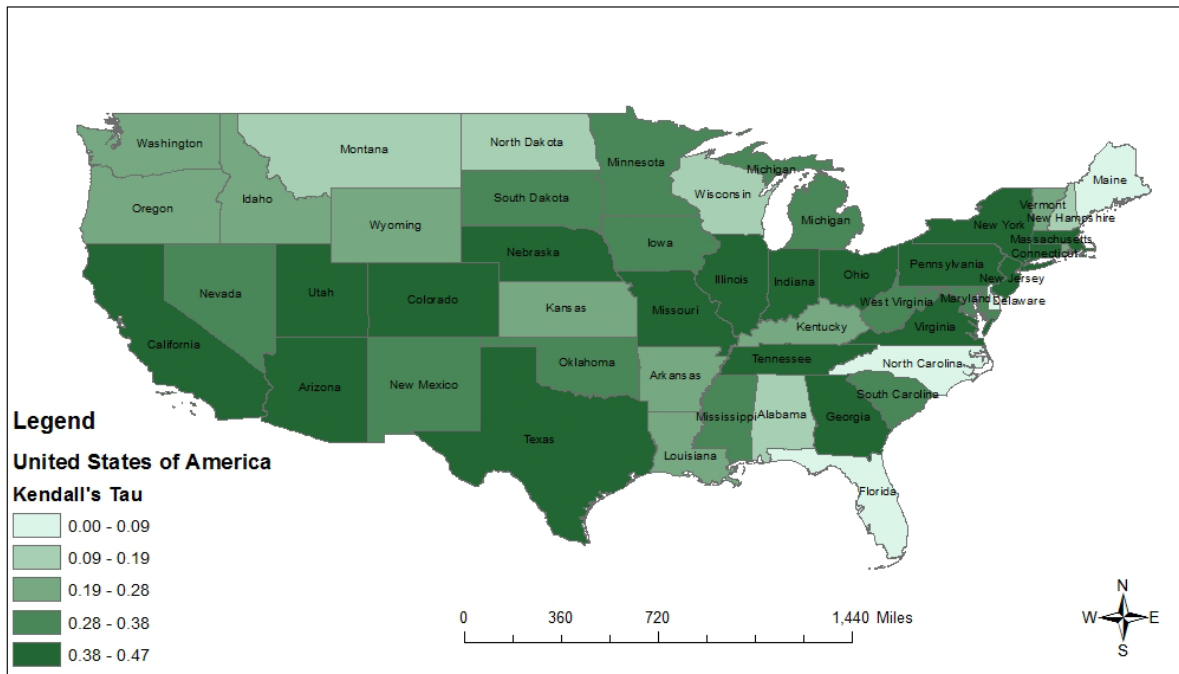


Figure 6: Correlation of WNV with Surface Temperature (One month time lag) and Precipitation rate 2003-2013

For the third trial, a one month surface air temperature lag and a one month precipitation rate lag were implemented. The final models in this case also displayed a legitimately strong correlation, on average, with an average p-value for the lagged variables surface air temperature of 0.020, and 0.220 for the precipitation rate. The independent variables exhibited 92.92 percent concordant pairs on average, having only 6.93 percent discordant pairs. An average Kendall's Tau coefficient of 0.32 was calculated as well, indicating a positive correlation between WNV mosquito infections and the independent variables (surface air temperature and precipitation rate). Figure 7 demonstrates the correlation of WNV with surface temperature (one month time lag) and precipitation rate (one month time lag) over the period of the study. The average odds ratio for

precipitation rate was found to be 255.58 and was 1.48 for the surface air temperature; since both of these values are greater than one, there are theoretically greater odds of a WNV infected mosquito occurring given the conditions of the independent variables at that time.

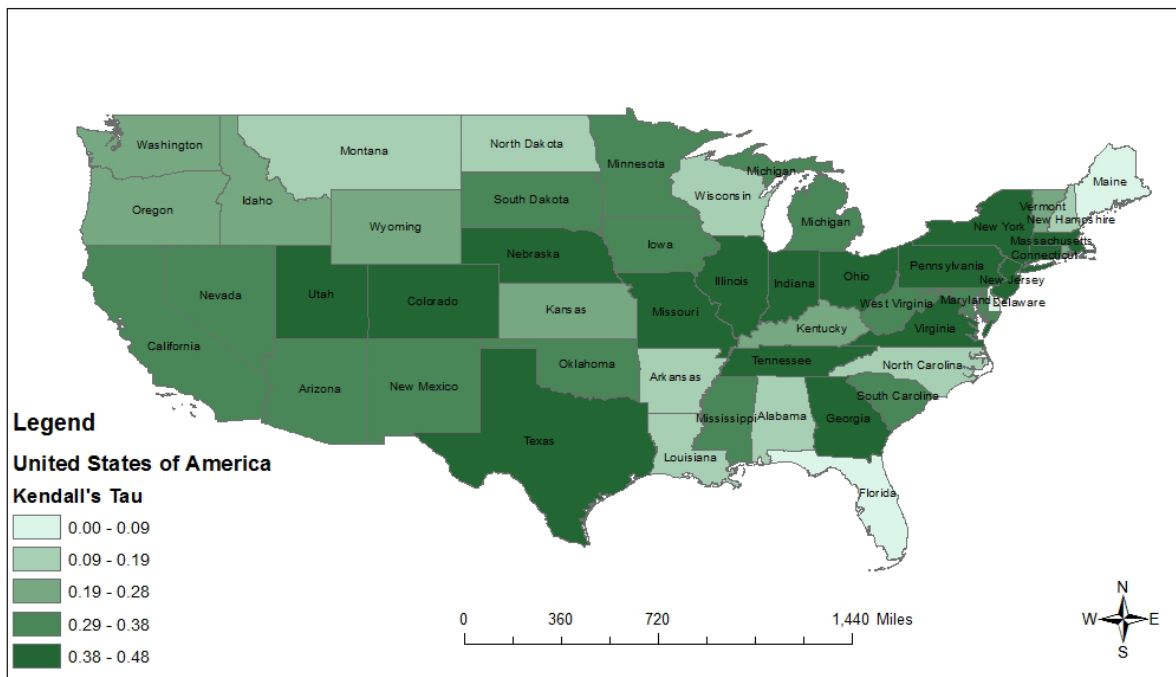


Figure 7: Correlation of WNV with Surface Temperature (One month time lag) and Precipitation rate (One month time lag) 2003-2013

CONCLUSION

Satellite remote sensing is a useful tool in characterizing the environmental conditions in which vectors, such as mosquitoes, survive and endure. By linking these environmental circumstances (precipitation rate and surface air temperature) in a given region with the prevalence of the mosquitoes over a given period of time, the climatic conditions that comprise the mosquitoes' niche or optimal breeding conditions can be determined. Although correlation does not imply causation, association between macro-environmental processes and WNV occurrence at numerous temporal and spatial scales can assist us in the determination of climatic conditions advantageous to mosquito abundance.

This research indicates that as temperature and precipitation increase, such as during the spring and summer seasons, there is a greater chance that a WNV infected mosquito will be found. The significance of the correlation of the original dataset indicates that mosquito abundance is directly associated with an increase in surface air temperature and precipitation rate.

This analysis will aid in determining the needs for developing collaboration with appropriate research teams in the future, and will assist in providing a means to predict mosquito breeding patterns long term as they relate to the prevalence of vector-borne illnesses, such as WNV.

ACKNOWLEDGMENT

The project described was supported by a grant from the National Aeronautics and Space Administration. The present work benefited from the input of Dr. Antar Jutla, who provided valuable comments/ideas/assistance to the undertaking of the research summarized here. Its contents are solely the responsibility of the authors and do not necessarily represent the official views of NASA.

REFERENCES

- Chuang, T. & Wimberly, M. C. (2012). Remote sensing of climatic anomalies and West Nile Virus incidence in the northern great plains of the United States. *PLoS ONE*, 7(10)
- Cooke, William H. "Avian GIS Models Signal Human Risk for West Nile Virus in Mississippi." *International Journal of Health Geographics* 5.36 (2006): n. pag. Print.
- Githeko, Andrew K.; Lindsay, Steve W.; Confalonieri, Ulisses E.; Patz, Jonathan A. Climate change and vector-borne diseases: a regional analysis *Bull World Health Organ* vol.78 n.9 Geneva Jan. 2000.<<http://dx.doi.org/10.1590/S0042-96862000000900009>>.
- Gubler, D., 2007: The continuing spread of West Nile Virus in the Western Hemisphere. *Clinical Infectious Diseases* 45(8), 1039-1046.
- Kalluri, Satya, Peter Gilruth, David Rogers, and Martha Szczur. "Surveillance of Arthropod Vector-Borne Infectious Diseases Using Remote Sensing Techniques: A Review." *PLoS Pathogens* 3.10 (2007): E116. Print.
- Kilpatrick, A. M., and S. E. Randolph. "Drivers, Dynamics, and Control of Emerging Vector-borne Zoonotic Diseases." *The Lancet* 380.9857 (2012): 1946-955. Print.
- "West Nile Virus." *Centers for Disease Control and Prevention*. Centers for Disease Control and Prevention, 01 July 2014. Web. 06 July 2014.
- "West Nile Virus Maps - Mosquito - USA." *West Nile Virus Maps - Human - USA*. U.S. Geological Survey, n.d. Web. 20 Nov. 2013.

DESIGN A REMOTE- SENSING ROCKET PAYLOAD FOR SENSING RADIATION

Jacob Coleman
Mathematics and Philosophy
West Virginia Wesleyan College
Buckhannon, West Virginia 26201

ABSTRACT

Radiation is all around us- in the sky above us, the ground below us, and even in the air we breathe. The sun sends radioactive waves through the atmosphere, causing reactions that release particles detectable by specialized sensors, the most common being Geiger Muller counter. By detecting energized particles being emitted by these radioisotopes, the Geiger counter can tell how many of those particles are being emitted over a period of time. Certain isotopes have specific count numbers per minute, so with this information and a Geiger counter, one could test to see if specific radioactive materials were present in an area.

INTRODUCTION

The intent of this project was to design and construct an apparatus to sense and store radiation, most specifically gamma radiation and beta particles. The intended payload was to be in two parts: an Arduino Uno microprocessor and a small Geiger counter kit. This payload would sense radiation in the atmosphere via high altitude balloon or small rocket, store the information on an SD card in an Openlog Storage device, and be retrieved from said SD card. From the counts recorded, we could see what radioisotopes were in the vicinity of the sensor by comparing to the known counts per time period of various radio isotopes. The project in its entirety was for the purposes of gathering information, possibly for future projects, and to serve as an introductory into research and experimentation for someone (me) who has never done something like this before.

PROJECT

The central piece to this project, obviously, was the Geiger counter that would be making the readings. We requested and received money to buy a small unit from Chaney Electronics, Inc. that was small enough to fit nicely into the payload, but gave out enough voltage on the output end to be detected by the Arduino's digital input pins. The link to the website where the kit was purchased can be found in the important links section of the report. Construction of the kit didn't take much time at all. Note that the LED was replaced with two output wires to be connected to the Arduino. The speaker was left as it was in the circuit for the purposes of having a way to make sure the unit was properly functioning. Also, the OpenLog data storage device was purchased from Sparkfun Electronics and connected to the Arduino; basic test codes, which can be found on the Sparkfun website, were used to make sure the Arduino and the OpenLog were communicating with one another. The link to the OpenLog page can be found in the important links section of the report.

The next step was to come up with code to get the Geiger unit and the Arduino to be able to communicate and count the number of times the Geiger unit sensed an energized particle. This proved difficult due to the short length of the pulses of voltage that the Geiger unit emitted; they

were either too short for the Arduino to detect at all or were so short that they were regarded as noise and disregarded. In any case, the rest of the project became trying to get the code to work correctly to get the data. Several suggestions from the internet were tried, mainly from research done on the Arduino website as well as separately, previously made libraries from independent sources, links to both of which can be found in the important links section of the report. Unfortunately, summer ran out before a successful code could be written, so the project remains incomplete, though much was learned about the more detailed workings of the Arduino Uno microprocessor's more specific workings in this area of pulse detection and recording.

IMPORTANT LINKS

Below is a list of links to websites that were important to the project.

<https://www.sparkfun.com/products/9530>

https://www.pjrc.com/teensy/td_libs_FreqCount.html

https://www.pjrc.com/teensy/td_libs_FreqMeasure.html

<http://www.electronickitsbychaneyelectronics.com/prodinfo.asp?number=C6986>

<http://forum.arduino.cc/index.php?topic=41729.0;wap2>

CONCLUSION

Unfortunately, there really is not much of a conclusion to give on this project, as it remains a work in progress.

AKNOWLEDEMENTS

At this time I would like to acknowledge the NASA WV Space Grant Consortium for their generous grant as well as Drs. Tracey DeLaney, G. Albert Popson, and Joseph Wiest for their time and effort helping me with this project, a new and foreign concept to me.

SUPERSONIC FLIGHT

Andrew Cvetnick
Applied Physics
West Virginia Wesleyan College
Buckhannon, WV 26201

ABSTRACT

The purpose of this experiment will be not only to construct a supersonic wind tunnel but also to see how vibrations caused by supersonic flight affect an aircraft. In order to perform this research I will have to construct a small scale blow down wind tunnel at my institution since the research facilities at this time do not include a supersonic wind tunnel. The wind tunnel will be built using materials that my institution already possesses in order to accommodate the air compressor and vacuum pumps available. The tunnel will also include a method of measuring the wind speed probably in the form of a pitot tube.

The wind tunnel will hopefully be able to achieve wind speeds in the range of high subsonic to about Mach 3. Subsonic air flow has a velocity less than the speed of sound at every point within the air wave. It is generally characterized by smooth stream lines and varying flow properties. There is a special case of subsonic flow known as transonic flow; it consists of regions of mixed air flow where there may be supersonic flow incident on a surface but then subsonic flow directly behind it.

Supersonic flow is classified as an air flow where the velocity exceeds the speed of sound at every point within the stream. When the air speed reaches supersonic it produces shock waves that are the result of highly compressed air around a surface.

INTRODUCTION

The goals of this project were to construct a small scale blowdown wind tunnel capable of supersonic speed and to investigate the vibrations caused by supersonic air flow on scale model aircrafts. The wind tunnel will be built so that it can be easily used with the compressors and vacuum pumps available at my institution. The supersonic speed in the wind tunnel is achieved by a very large pressure differential between the two ends of the wind tunnel.

The construction of the wind tunnel was the only part of the project that was completed due to the fact that it took longer to design and construct the wind tunnel than previously thought. The second part of the project can be completed later but it will not be approached before the deadline for the project. More than likely it will be turned into a senior research project and be completed in whole at that time.

In order to find the proper way to design the wind tunnel, a lot of research had to be done. A lot of this research was done through NASA websites. After researching the design for the wind tunnel, it became pretty simple to design a small scale version. There were two options to choose from to build the wind tunnel, PVC or aluminum. After discussing the options with my mentor it was

agreed upon that the easiest route would be aluminum because parts could be machined to the specifications needed and aluminum would be able to hold a much greater pressure.

Construction

At this point, drawings were made using Autodesk Inventor and the drawings that required machining were given to the machine shop. While waiting for the parts to be machined a method of sealing the wind tunnel to make it air tight had to be thought of. Since my institution does not have a welder available and due to the fact that thin aluminum is very easy to burn through, welding was out of the question. So a two stage process was thought of in order to seal the aluminum portions of the wind tunnel. First, the aluminum pieces would be adhered together simply using JB Weld and applying pressure to ensure a good seal. Secondly, pipe cement would be applied over top of the JB Weld to close up and completely seal each junction of the aluminum. The next issue that arose was trying to figure out a way to attach the test section to the rest of the wind tunnel. Since the test section is plastic it would have been impossible to attach it the same way the aluminum pieces were conjoined. It also could not be permanently attached because it is too small to make an airtight door. A rubber pipe coupler with a metal clamp around the outside would eventually be used to connect the test section and allow it to be removed while also creating an airtight seal. At this point the wind tunnel can be completely assembled and will be ready for testing.

BACKGROUND

Blowdown wind tunnels are normally used for high subsonic to high supersonic flow conditions. There are several possible configurations for these types of tunnels, but the one used for my research is a closed configuration, which means that the results are not subject to the outside atmosphere. Aerodynamicists most often use supersonic wind tunnels in order to study the air flow over supersonic aircraft models such as the Lockheed Martin F-35 Lightning II. The wind tunnel allows them to control many of the forces that will act on an aircraft during flight. This control allows the engineers to study how a new aircraft will react under different flight conditions.

Air Flow through the Wind Tunnel

As with anything, there are multiple parts that make up the wind tunnel. Here I will describe how the wind tunnel will be assembled as well as a brief description of the air flow within the tunnel. The test section sits between a high pressure chamber and a low pressure chamber. Air is brought into the high pressure chamber through a dryer bed, which is generally built in to most air compressors to prevent condensation, and is then pumped into the chamber by the compressor. At the same time, air is being sucked out of the low pressure chamber. As the air flows out of the high pressure chamber it enters a plenum, where a pressure regulator is installed to ensure consistent conditions in the test section. As the air continues to flow through the chamber it passes through a throat where the air will reach supersonic speed just before the test section. After passing through the test section the air will pass through a diffuser and another throat in order to decrease the air speed to subsonic before entering the low pressure chamber. The Mach number achieved within the tunnel is determined by the pressure and temperature in the plenum and the area ratio between the test section on the nozzle throat. Using the following equation, the theoretical velocity of the air just before the test section can be calculated:

$$v_2 = \sqrt{\frac{2(p_1 - p_2)}{\left(\frac{p_2}{T_2} - \frac{p_2^2 r^4 T_1}{p_1 R^4 T_2^2}\right)}}$$

Where v_2 is the theoretical velocity just before the test section, p_1 the pressure of the air supplied by the air compressor, p_2 is the pressure within the wind tunnel after it has been evacuated, T_1 is the temperature of the air being supplied by the air compressor, T_2 is the temperature of the air inside the wind tunnel after it is evacuated, r is the inner radius of the test section, and R is the radius of the air compressor.

Advantages and Disadvantages

There are some advantages as well as disadvantages with blowdown wind tunnels. Advantages that come with a blowdown wind tunnel are that they start up easily; they are generally cheaper to construct, and have a good design for implementing propulsion and smoke visualization. They also place less stress on the test model because of the faster start up time and the model is not subject to unnecessary stress. Disadvantages that blowdown wind tunnels have are that they have a limited test time and they can be somewhat noisy. The fact that this type of tunnel has a limited run time means that faster measuring equipment will be needed to collect accurate data.

Design

The tunnel being built will be made primarily of aluminum as to make it light weight and it will provide a minimal drag when the tunnel is in operation. A large air compressor will be used to provide the air pressure that will be necessary in order to achieve supersonic wind speed. The plenum will be made from a two inch outer diameter aluminum pipe. The plenum will flow in to a two inch long diffuser. The diffuser will be machined on a lathe out of a solid block of aluminum. It will have one end with a two inch outer diameter in order to match up with the outer diameter of the plenum and it will flow down to a one inch outer diameter. Here is where the most important part of the wind tunnel will be attached, the supersonic nozzle. The supersonic nozzle will be machined the same way as the diffuser just mentioned above. This nozzle is where the wind will reach the supersonic speed needed. It will flow from a one inch outer diameter that will match up with available diffuser end over six inches to the other end that will have a two inch outer diameter. The test section is where the supersonic wind will impact the test subject. This is where all the data will be taken during testing. It will simply be made of a clear plastic pipe. The test section will be able to be removed from the rest of the wind tunnel so that test subjects can be inserted and removed with ease. There will be a second diffuser downstream of the test section that will also be machined in the same manner as the first diffuser. It will flow from a two inch outer diameter at the test section to a one inch outer diameter over three and a half inches. The purpose of this second diffuser is to slow the wind speed well below supersonic speed before it enters the second plenum so that the wind tunnel is not torn apart by supersonic wind suddenly stopping. The wind tunnel will then flow into a second plenum that is identical to the one that is mentioned above. Ball valves will be fitted to both plenums to allow for the air compressor and vacuum to be properly attached and still maintain an air tight seal.

TESTING

The wind tunnel was completed and tested, but due to the time constraint on the project, that was all that was completed. Neither a pitot tube nor a method of visualization was able to be implemented into the wind tunnel due to running out of time, but the wind tunnel is operational.

The first test that was done with the wind tunnel was just a simple test to make sure that the wind tunnel was completely airtight. In order to due perform this test, one ball valve was closed and a vacuum pump was attached to the other valve. The wind tunnel was evacuated and then the valve that was connected to the vacuum pump was closed and the vacuum was shut off. The tunnel was then left to sit for ten minutes to see if it would remain evacuated. The tunnel did remain evacuated; this meant that the final testing of the wind tunnel could take place. The final test was to see if the wind would actually allow the air to flow and to see if would hold up under the pressure that would be flowing into it. In order to do this, the wind tunnel had to be taken to Bob Grose's house since he has an air compressor that supports the amount of pressure needed to reach supersonic speeds. Once the wind tunnel was where it needed to be for testing, the air compressor and vacuum pump were attached accordingly so that the flow of air was correct. The wind tunnel was then evacuated while the ball valve attached to the air compressor was closed. After the wind tunnel was evacuated, the valve connected to the vacuum pump was closed to prevent damage to the pump. The ball valve connected to the air compressor was then opened. The air rushed through the wind tunnel for a brief second before the pressure inside the wind tunnel became too great for the seal on the high pressure end of the test section and it failed, blowing the wind tunnel into two pieces.

CONCLUSION

This project was a very eye opening experience. It allowed me to experience first-hand what truly has to go into a project of this magnitude. It also opened me to listening to other people's opinions on how to approach certain parts of the project when I would get stuck on something for a few days. This is also how I realized how valuable having a team on this project such as this one that requires smaller multiple projects within to get complete the entirety of the project.

With the final testing of the wind tunnel turning out the way it did, it was determined that in order for it to work properly a lower pressure chamber will need to be built to allow for the high pressure air a place to go instead of building up in the wind tunnel. This will also allow for a longer run time. A better method of attaching the test section also needs to be thought of in order to keep the wind tunnel together so that accurate data can be gathered.

Later on to further the project, I would obviously like to finish what I originally set out to do and study the effects supersonic flight has on different scale models of current supersonic aircrafts. To do this I will need to construct the low pressure chamber mentioned above, equip the wind tunnel with a Pitot tube system in order to accurately measure the air speed in the wind tunnel, and I will also have to equip the wind tunnel with an imaging system. Ideally I would to use a Laser Doppler Anemometry system or Schlieren Imaging system because they would be the most accurate. But more realistically a smoke system will be incorporated into the wind tunnel because it is more cost effective. I will hopefully be able to use this as a senior research project and can begin to learn a lot about supersonic air travel and the different effects sonic boom can have on aircrafts.

ACKNOWLEDGMENTS

NASA WV Space Grant Consortium
Dr. Joseph Wiest
Dr. Albert Popson
Dr. Tracey Delaney
Mr. Bob Grose

REFERENCES

- Benson, Tom. "Blowdown Wind Tunnel." *Blowdown Wind Tunnel*. NASA, 12 June 2014. Web. 17 June 2014.
- Benson, Tom. "Wind Tunnel Design." *Wind Tunnel Design*. NASA, 12 June 2014. Web. 17 June 2014.
- Bradshaw, Peter, and Rabi Mehta. "Tunnel Configuration." *Wind Tunnel Design*. Tracey M. Duncan, 22 Nov. 2002. Web. 13 Aug. 2014.
- Bugden, William, and Others. *Design and Construction of a Supersonic Wind Tunnel with Diagnostics*. Worcester Polytechnic Institute. Worcester Polytechnic Institute Aerospace and Mechanical Engineering Departments, 17 Apr. 2013. Web. 27 May 2014.
- Jennings, Frank, Jr., and Karen L. Rugg. "NASA Centers Team Up to Tackle Sonic Boom." *NASA*. NASA, 17 Mar. 2014. Web. 13 June 2014.
- Ristic, Slavica. "Laser Doppler Anemometry and Its Application in Wind Tunnel Tests." *Scientific Technical Review* 57.3-4 (2007): n. pag. *Military Technical Institute*. Military Technical Institute, 12 July 2013. Web. 18 June 2014. <<http://www.vti.mod.gov.rs/ntp/rad2007/3-07/rist/rist.pdf>>.

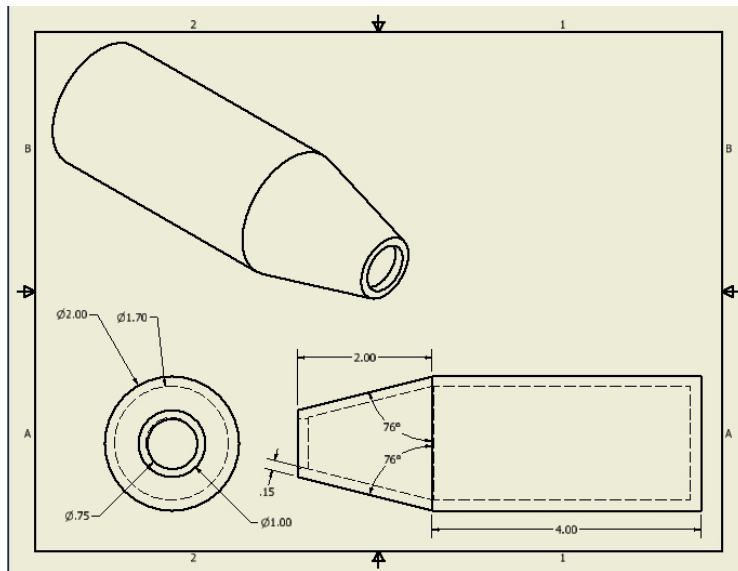


AIRTIGHT SEAL TESTING

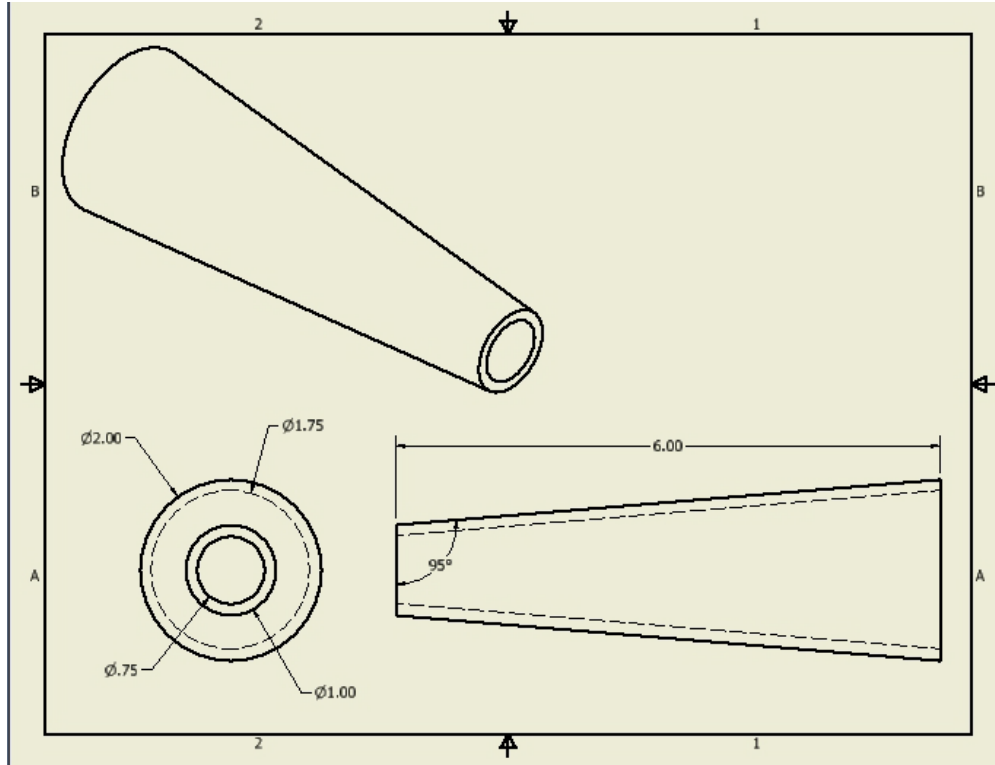


FINAL

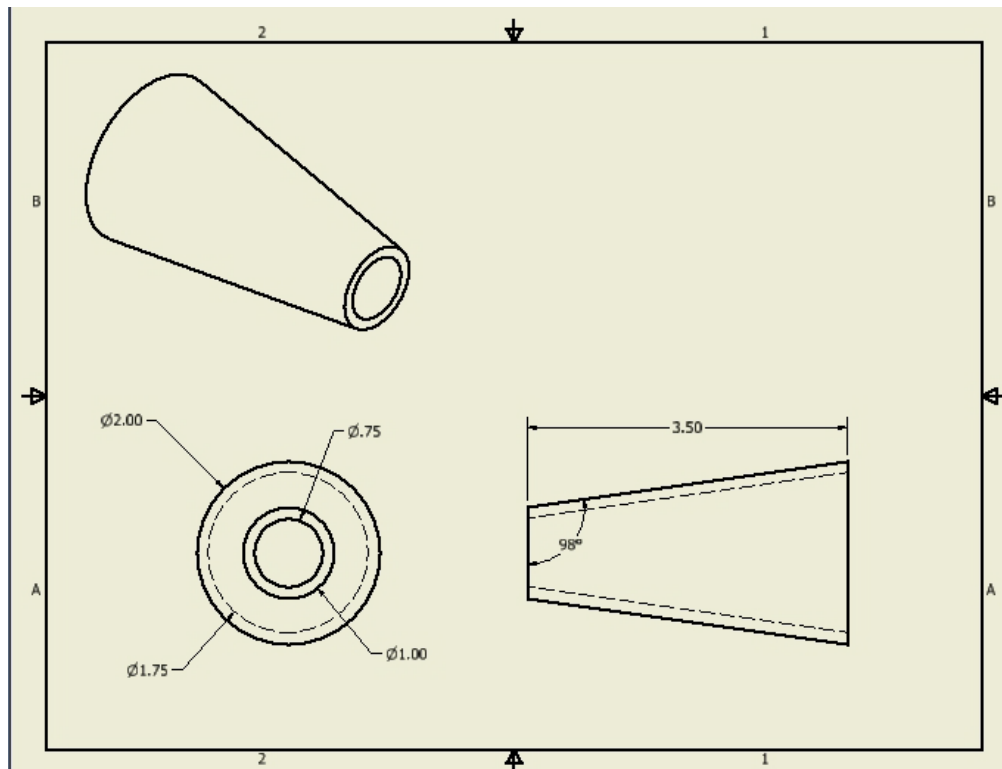
TESTING



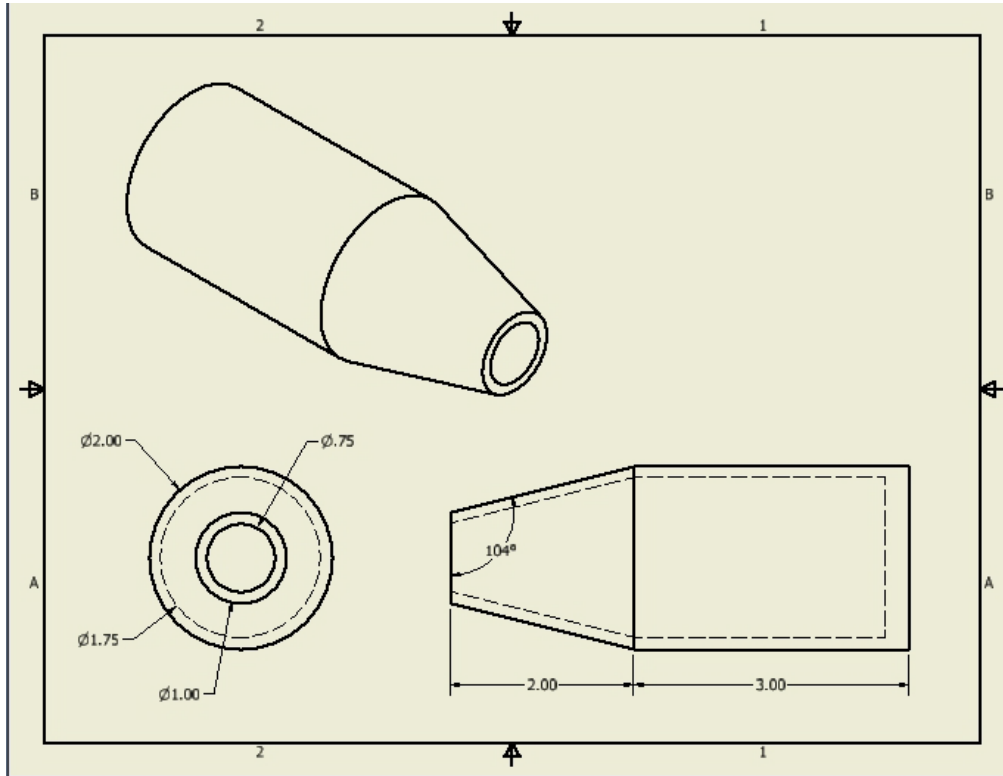
HIGH PRESSURE PLENUM



SUPERSONIC NOZZLE



DIFFUSER



LOW PRESSURE CHAMBER

HYDRATION STUDY OF HAND/FINGER/NAIL SYSTEM TO UNDERSTAND MECHANISM OF GLOVE-RELATED INJURIES

Denna Davari
Industrial and Management Systems Engineering
West Virginia University
Morgantown, West Virginia 26505

ABSTRACT

Hand injuries are common among astronauts. A causal relationship between the use of extra vehicular activity (EVA) gloves and hand/finger/nail trauma has been proposed in the literature. The atmosphere within the EVA glove is characterized by poor ventilation, moderate to high air temperature, and high relative humidity levels. The effect of such environmental factors specific to glove use on the physiological response of hand/finger/nail system is not well understood. In this study baseline data for the physiological response of the hand/finger system under different environmental conditions was studied. The data were recorded under different conditions of humidity, temperature and hand exertion levels. Physiological response of the hand/finger system was measured using hand hydration levels and perceived discomfort ratings. Hand hydration increased with the increase in the humidity and temperature while physical exertion further increased these moisture levels. Higher temperature had more pronounced effect on the moisture level than humidity. Similar trend was also observed for the perceived discomfort ratings.

INTRODUCTION

Throughout the U.S. space programs hand injuries, including fingernail trauma, have accounted for 75% of the total musculoskeletal injuries [1]. These injuries do not just occur in space, but have also been reported during pre-flight training programs [2]. In a recent 2014 study performed at Johnson Space Center NASA, it was discovered that the atmosphere within the Extra Vehicular Activity (EVA) gloves showed to have poor ventilation, moderate to high air temperature, high relative humidity, and high hand moisture levels [3]. Physical exertions performed by the hand/fingers under such conditions may lead to trauma such as fingernail delamination, a condition in which the fingernails start to detach from the nail beds as seen in Figure 1.

Currently, the effect of factors specific to glove use during hand/finger exertions on the physiological response of hand/finger/nail system is not well understood. Such knowledge would improve our understanding of the mechanism of pathogenesis of glove-related hand or finger injuries. Therefore, the objective in this study is to establish baseline data for the physiological response of the hand/finger/nail system to atmospheric exposures typical during exertions performed using EVA glove. A custom built temperature/relative humidity control chamber was used to simulated EVA glove environment.



Figure 1: The picture on the left is an image of NASA’s EVA gloves, while the picture on the right is displaying fingernail delamination.

Human participants performed two types of trials using this custom built temperature/relative humidity control chamber. During the trials the participants were asked to insert their dominant hand into the chamber and either perform pinching exertions or remain at rest. Skin moisture data were recorded at the beginning and the end of each trial. Also, blood perfusion data were collected continuously throughout the experiment. Once each trial was completed, the participant reported their perceived discomfort.

METHODOLOGY

Many factors were considered when designing and implementing the experiment. In the preliminary trials hand moisture buildup was observed preceding exertions performed at high relative humidity conditions. A new hand moisture normalization method was established to maintain consistent baseline hand moisture level. In order to get the hand moisture down to a baseline measurement, isopropyl alcohol was applied to the subject’s hand before each trial and the corresponding moisture level was recorded. The moisture levels were recorded thirty seconds after the application of isopropyl alcohol due to the sensitivity of the skin conductance sensors. If the rubbing alcohol was not allowed time to dry, the sensors would recognize the alcohol as moisture.

Another precaution that was taken when designing the experiment was that the humidity levels and the exertion condition during the trials were randomized. This was done by utilizing the RANDBETWEEN function on Excel and assigning numbers 1 through 4 for the different combinations of relative humidity range and exertion/no exertion. The chart is displayed below in Table 1.

Table 1: Chart used to assign variable combinations to trials

	No Exertion	Exertion
Lower Range of Relative Humidity	1	2
Higher Range of Relative Humidity	3	4

Procedures were put in place to minimize variability as well. For example the placement of probes and the order in which steps were taken throughout the experiment were kept very consistent for each subject. In addition, the instructions and information provided to the human subjects were consistent in content and order of presentation. Organization for data collection was also a very crucial part of this experiment in order to ensure consistency and accuracy. Data charts were created for each subject in order to be able to track their data throughout the experiment and compare pre/post moisture. The file names were kept uniform to prevent confusion when returning to analyze the data.

PARTICIPANTS AND EXPERIMENTAL CONDITIONS

Twenty one human participants (11 male and 10 female) were recruited for data collection. The average (SD) age, weight and height of the participants were 21.2 (2.8917) years, 72.0995 (18.2975) Kg, and 170.0784 (11.0127) cm, respectively. Each participant performed sixteen trials. There were two temperature conditions, two relative humidity conditions, and the trials were split evenly between exertion/no exertion conditions. The first eight trials were within the lower temperature range (65-75°F), and the last 8 trials were within the higher temperature range (85-95°F). As stated before humidity and exertion were randomized. Humidity was controlled at 35-45% and 55-65% Relative Humidity (RH). Although humidity and exertion/no exertion were randomized, they were still split evenly amongst the sixteen trials meaning there were eight trials in the higher humidity range and eight trials in the lower humidity range. Likewise, there were eight trials where the subject performed exertion and eight trials where the subject simply placed their hand in the chamber and did not perform any type of exertion. The trials in which the subject performed pinching exertions were performed at 50% of maximum voluntary contraction (MVC) shown in Figure 3.



Figure 2: Custom-made control chamber

EQUIPMENT

This experimental study was accomplished with the assistance of various types of equipment such as control devices, sensors, and laser probes. The control devices for the humidifier and heater were essential for maintaining the ranges needed for this experiment. They operated by having an outlet of their own, separate from the main power source. The desired ranges were selected on the control devices and the humidifier/heater were then plugged into the control devices. The control devices would supply power to the humidifier/heater until the desired range was accomplished and maintained.

Sensors were also incorporated with the skin conductance sensor and pinch meter. The pinch meter consisted of a metal disk with a sensor in the center of it. Subjects would place their thumb on the sensor and rest the disk on their other fingers shown in Figure 3. The skin conductance sensor recorded the subject's hand hydration in microsiemens (μS). The sensors were placed on the middle band of the subject's ring and index finger as shown in Figure 3. Subjects would hold their hands palm up when recording their skin moisture.



Figure 3: Skin conductance sensor (on left), Pinch meter (on right)

Blood perfusion was measured using the Periflux System 5000 Laser Doppling Blood Perfusion Monitoring system. The way this system operates is by transmitting a low power laser light to the tissue through a fiber optic probe. The light is then returned and processed. The relative number and velocity of the blood cells in the tissue are calculated and presented in units of blood perfusion. Blood perfusion is the process of the body delivering blood to a capillary bed in its tissue. This equipment was used to better understand what was happening during exertion/no exertion trials to the hand while being under these different temperature/humidity conditions. As seen in Figure 4, the probe was placed in such a way that wouldn't affect the subject's pinching abilities.



Figure 4: Blood perfusion probe

PREPARATION PRIOR TO EXPERIMENTAL DATA COLLECTION

The first step in setting up the experiment was to ensure that temperature of the room was within the lower temperature range of 65-75° of the experiment. After this initial step, the blood perfusion meter was powered on due to a 20 minute start up process. The humidifier was then filled with water and placed in the chamber along with the heater and power strip. The temperature control device was placed outside of the chamber in order to prevent possible moisture damage. A small hole was drilled into the side to allow the temperature control probe to be within the chamber without having to place the whole device inside. The humidity control device was hooked up to the power strip inside the chamber itself, since the equipment was made to be in humid circumstances. Then the laptop used for data collection of moisture and force was powered on and began startup. After completion of the laptop startup, the moisture meter and pinch meter were properly set up. The pinch meter was placed in the chamber, ready for the upcoming exertion trials. Once the other equipment was set up, the blood perfusion meter was then calibrated. This is done by submerging the probe in motility standard, pressing the calibrate button, and waiting for the blood perfusion meter to give readings that are within range. The motility standard included in the PF 1000 Calibration Device is a colloidal suspension of polystyrene particles and is shown in Figure 5. Motion of these particles provides a standardized perfusion value of $250 \text{ PU} \pm 15$. Calibration was done before each new subject to ensure accuracy.



Figure 5: PF 1000 Calibration Device

Data collection

Human participant's maximum voluntary contraction was measured as the first step of data collection. The participant pinched the pinch meter with maximum force for 10 seconds, and repeated this step for a total of three times. These three maximum pinching trials were then averaged. The participant would later maintain 50% of this calculated average of their maximum voluntary contraction during exertion trials. Before starting the actual trials, time was allotted for the participant to practice maintaining 50% of their maximum voluntary contraction with the pinch meter. Initial moisture was measured for 10 seconds and then rubbing alcohol was applied to the human subject's hand. The post alcohol moisture was recorded for 10 seconds similarly to the initial moisture by sliding on the skin conductance sensors on the inside of the subject's ring and index fingers. Once this was done, the blood perfusion probe was attached to the subject's palm. The probe was attached in such a way that refrained from restricting blood flow and the human participant's pinching abilities. The actual trials were then ready to begin.

If it was an exertion trial the participant placed their hand in the chamber, and held the pinch meter in preparation. The first 30 seconds of this trial would be without exertion, followed by 30 seconds of exertion. This same pattern continued for five minutes. If it is a no exertion trial then the participant would simply place their hand in the chamber for 5 min. The start and stop times of these trials were recorded in order to compare the pinching data to the blood perfusion data. After the trial, hand moisture was immediately recorded for 10 seconds with the skin conductance sensors. Once that was done, the rubbing alcohol could be applied. The subject's overall discomfort was also recorded on a scale of 1-10, 1 indicated "no discomfort" and 10 indicated "unbearable". Half way through the experiment the temperature was raised to the higher temperature range. The experiment took approximately 3 hours in total.

RESULTS AND CONCLUSION

Once the data collection was completed, the data was processed and analyzed. Figure 6 displays a graph showing the relationship between discomfort, humidity, temperature, and exertion.

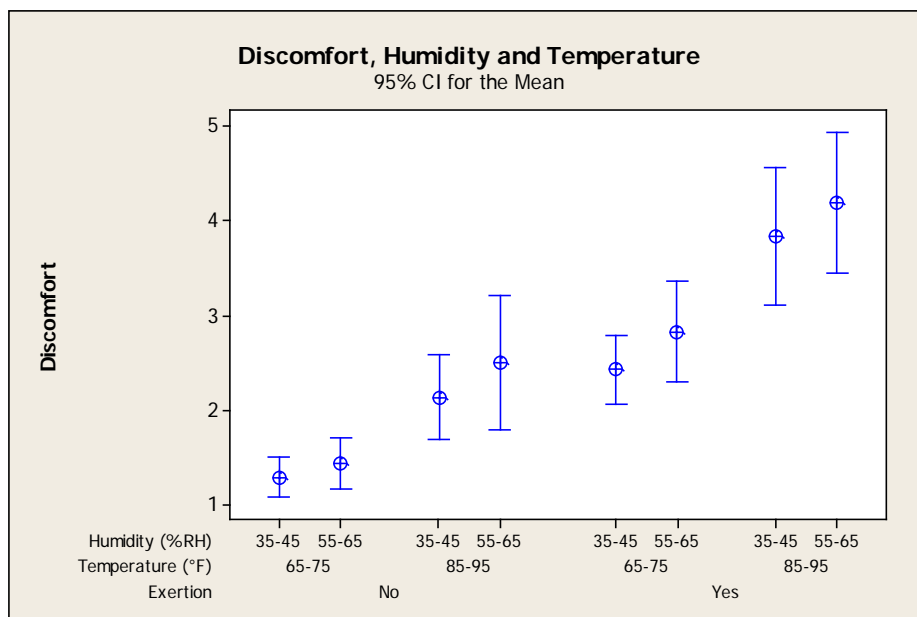


Figure 6: Graph displaying 95% CI for the mean of the discomfort and the contributing variables

From Figure 6, it can be seen that there is a strong correlation between discomfort, high humidity, high temperature, and exertion. In general higher perceived discomfort was observed for exertion trials with the increase in the temperature and humidity.

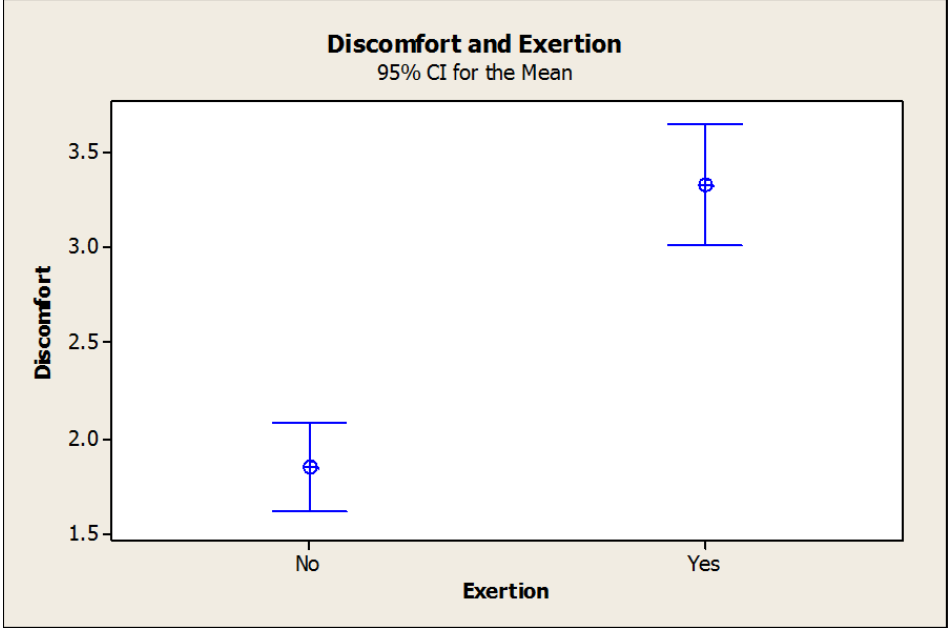


Figure 7: Graph comparing perceived discomfort and exertion

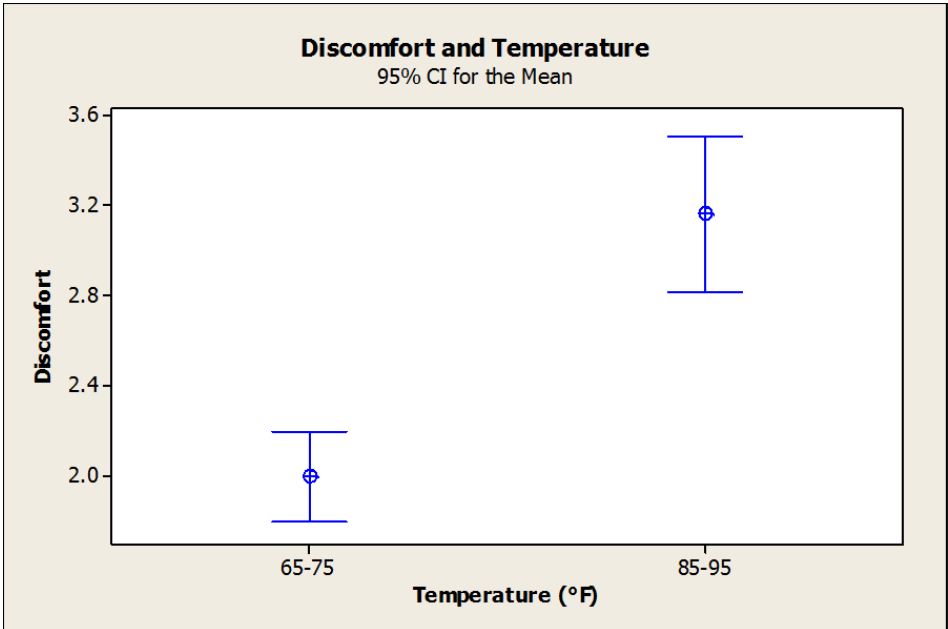


Figure 8: Graph comparing perceived discomfort and temperature

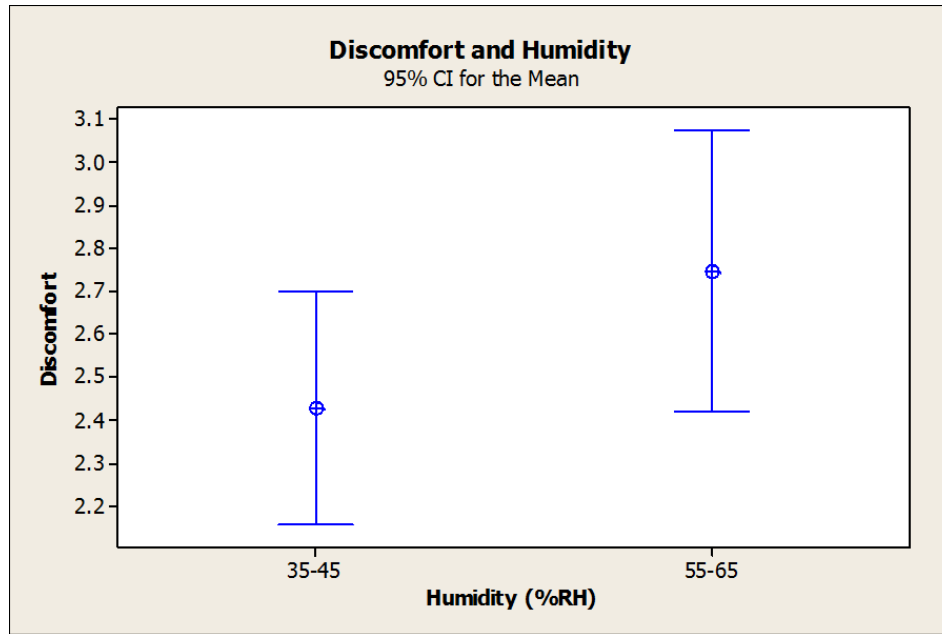


Figure 9: Graph comparing perceived discomfort and humidity

Trends in the individual variables provided some very valuable information. Based on graphs in figures 7 to 9, exertion caused the highest discomfort, followed by temperature, and lastly humidity. Another aspect that was analyzed was moisture due to these same variables with the inclusion of time due to the fact that moisture readings were recorded both pre and post trials. Figure 10 displays a graph of moisture levels compared to temperature, exertion, and time.

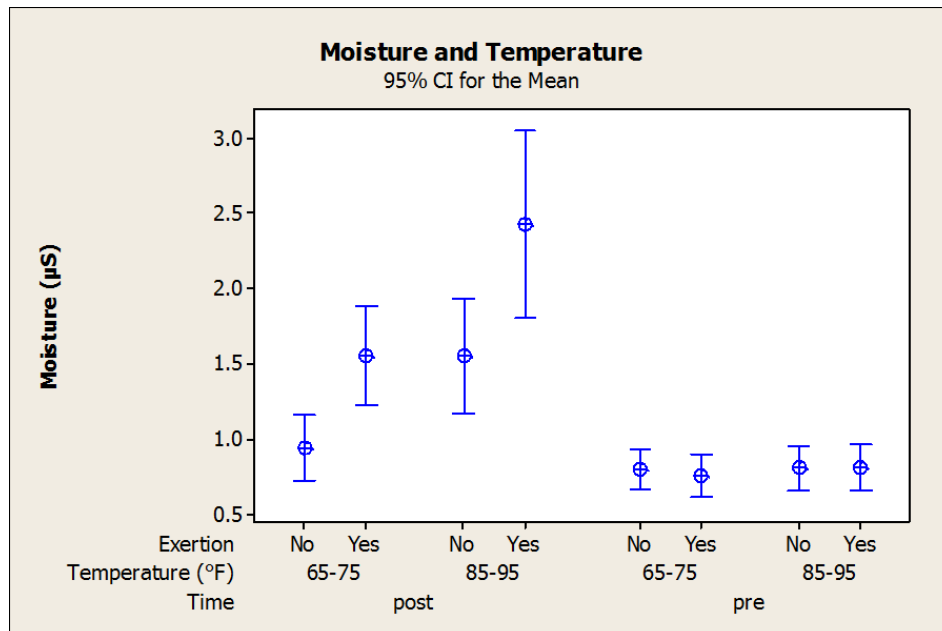


Figure 10: Graph comparing moisture, exertion, temperature, and time

Several understandings can be made by reviewing Figure 10. Upon examining the post/pre moisture levels, it is very apparent that the rubbing alcohol method used before each trial to bring subjects down to baseline moisture was successful. This was crucial in delivering necessary data. There's also a strong correlation between exertion and high skin moisture levels. This also suggests that moisture contributes to high levels of perceived discomfort since exertion has a strong correlation with perceived discomfort and moisture.

Overall, it was found that finger skin moisture increased with the increase in the humidity and temperature while physical exertion further increased these moisture levels. Higher temperature had more pronounced effect on the moisture level than humidity.

VALUABLE ASPECTS OF THE PROGRAM

This research internship was a very treasured experience that allowed me to broaden my knowledge, skill, and outlook on research. This opportunity has further fueled my drive for learning while also opening my mind to pursuing higher education. Not only did I get important research training, but I also learned a lot about time management which is a crucial skill in the real-world. Overall I believe the most valuable aspects of this program was the knowledge gained from taking part in this program, the financial support given for further education, and the ability to work on something you truly are excited about.

ACKNOWLEDGEMENTS

I'd like to thank the NASA WV Space Grant Consortium for funding this wonderful research opportunity as well as my research mentor, Dr. Ashish Nimbarte, for all the guidance and time he has provided throughout this process. I would also like to thank, John Kaiser, for all of his partnership and help throughout this entire project.

REFERENCES

- [1] Viegas, S.F., Williams, D., Jones, J., Strauss, S., and J. Clark, (2004), Physical demands and injuries to the upper extremity associated with the space program, *Journal of Hand Surgery [America]* 29 (3), 359–366.
- [2] Scheuring, R.A., Mathers, C.H., Jones, J.A., and M.L. Wear, (2009), Musculoskeletal injuries and minor trauma in space: incidence and injury mechanisms in US astronauts, *Aviation, Space, and Environmental Medicine*, 80(2), 117-124.
- [3] Jones, J.A., Hoffman, R.B., Buckland, D.A., Harvey, C.M., Bowen, C.K., Hudy, C.E., Strauss, S., Novak, J., and M.L. Gernhardt, (2008), The use of an extended ventilation tube as a countermeasure for EVA-associated upper extremity medical issues, *Acta Astronautica*, 63 (7), 763-768.

Asymmetric Reconnection With A Shear Flow and Applications to X-line Motion at the Polar Cusps

Christopher Doss
Physics / Computer Science
West Virginia University
Morgantown, WV 26506

ABSTRACT

Magnetic reconnection at the polar cusps of the magnetosphere is marked by strong asymmetries in plasma density and magnetic field strength in addition to a potentially strong bulk flow shear parallel to the reconnecting magnetic field caused by the solar wind. Much has been learned about the effect of either asymmetries or shear flow on reconnection, but only a handful of studies have addressed systems with both. We perform a careful theoretical, numerical, and observational study of such systems. It is known that an asymmetry in magnetic field offsets the X-line from the center of the diffusion region in the inflow direction toward the weaker magnetic field. A key finding is that this alters the flow profile seen at the X-line relative to expectations from symmetric reconnection results. This causes the X-line to drift in the outflow direction due to the shear flow. We calculate a prediction for the X-line drift speed for arbitrary asymmetric magnetic field strengths and show the result is consistent with two-fluid numerical simulations. These predictions are also shown to be consistent with recent observations of a tailward moving X-line in Cluster observations of reconnection at the polar cusp. The reconnection rate with a shear flow is observed to drop as in symmetric reconnection, and the behavior of the reconnection qualitatively changes when the shear flow speed exceeds the hybrid Alfvén speed of the outflow known from asymmetric reconnection theory.

INTRODUCTION

Processes in the solar corona send high energy particles through space towards Earth. These particles make up the solar wind, and this plasma brings with it a magnetic field known as the interplanetary magnetic field (IMF). If the interaction between the IMF and the Earth's magnetic field was ideal with no dissipation, then the magnetosphere (the region of influence of the Earth's magnetic field) would deflect the solar wind. Consequently spacecraft in orbit around Earth would not be in danger of these particles harming their circuits. However, through a process called "magnetic reconnection," some of the particles carried by the solar wind are able to infiltrate into the magnetosphere.

In the simplest form of magnetic reconnection, two anti-parallel magnetic fields break and cross-connect at a point where the magnetic field is zero, the X-line (Zweibel and Yamada, 2009). These cross-connected magnetic fields are bent when they are formed, converting magnetic energy into plasma energy by pulling in plasma from the anti-parallel magnetic field regions as they straighten out. This expels the plasma along with the newly formed cross-connected magnetic fields.

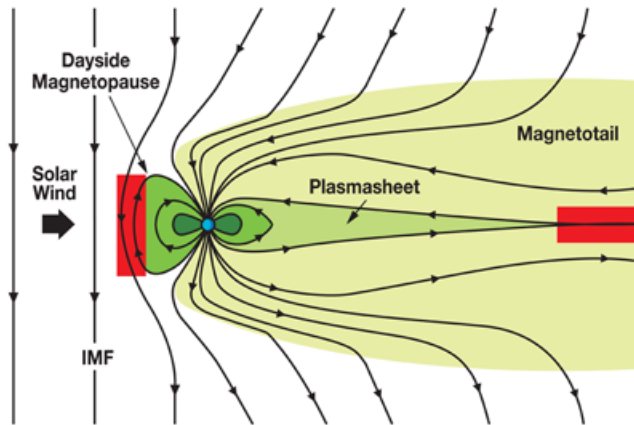


Figure 1: Reconnection locations (red box on the left) at the magnetopause for a due southward IMF. Reconnection during due northward IMF occurs at the polar cusps (leftmost edge of the yellow magnetotail region). Image courtesy of MMS (NASA/SWRI).

The classical models of Dungey [1961, 1963] first applied the idea of magnetic reconnection to Earth's magnetopause, the edge of the magnetosphere. Figure 1 shows the locations of magnetic reconnection when the IMF is pointing directly southward. However, when the IMF points southward, the locations where reconnection occur migrate to the polar cusps, closer to due north and south of Earth's poles.

The magnetospheric magnetic field is typically much stronger than the IMF at the Earth's magnetopause. This characteristic asymmetry can be observed all across the dayside magnetopause. Likewise, the plasma of the solar wind is also of a much higher density than that of the magnetosphere. Additionally, at all points on the dayside magnetopause other than the subsolar point, the closest point of the magnetopause to the solar wind, the plasma bulk flow along the edges of the magnetosphere creates a sheared flow parallel to the field lines undergoing magnetic reconnection.

While there have been magnetic reconnection studies in the past on configurations with asymmetric magnetic fields and plasma densities and similar studies with plasma bulk flows on a symmetric system, there has yet to be a systematic study of asymmetric magnetic reconnection along with a sheared flow. It is important to study this unique configuration of magnetic reconnection that occurs naturally at the magnetopause near the polar cusps in order to further understand how this type of magnetic reconnection will effect space weather (National Research Council, 2004).

This research seeks to systematically study magnetic reconnection in systems of asymmetric magnetic fields in the presence of a plasma sheared flow. Building off of previous studies, we arrive at an equation to predict the rate of reconnection in this configuration. We also predict a drifting of the reconnection site and confirm this using large-scale numeric simulations. We use a code that models the two-fluid equations and run several different setups to analyze reconnection with different magnetic asymmetries and sheared flows. By consistently choosing intervals over which to measure representative values, simulations and observations show good agreement with

the predicted reconnection rate and reconnection site drifting. We further confirm that reconnection changes completely when the sheared flow exceeds a threshold.

THEORY

To obtain the reconnection rate in systems with both asymmetric magnetic fields and a sheared flow, we first review asymmetric magnetic reconnection. Cassak and Shay [2007] developed a scaling for both reconnection rate E and outflow speed v_{out} in configurations of asymmetric magnetic fields and plasma densities. Using conservation of mass and energy, these quantities scale as

$$E \sim \left(\frac{B_1 B_2}{B_1 + B_2} \right) \frac{v_{out}}{c} \frac{2\delta}{L} \quad (1)$$

and

$$v_{out}^2 \sim \frac{B_1 B_2}{4\pi} \frac{B_1 + B_2}{\rho_1 B_2 + \rho_2 B_1}, \quad (2)$$

where B_1 and B_2 are magnetic field strengths on either side of the reconnection site, ρ_1 and ρ_2 are plasma densities, and δ and L are the dissipation region's width and length, respectively. Both of these equations were shown to be valid for representing magnetic reconnection with the Hall term (Cassak and Shay, 2008).

We next review scaling of reconnection rates in systems with a sheared flow and symmetric magnetic fields and plasma densities. Cassak and Otto [2011] found a scaling of the reconnection rate E_{shear} in symmetric reconnection with a sheared flow to be

$$E_{shear} = E \left(1 - \frac{v_{shear}^2}{c_A^2} \right), \quad (3)$$

where E is given by equation (1), v_{shear} is the velocity of the symmetric sheared flow, and $c_A = B/(4\pi\rho)^{1/2}$ is the Alfvén speed, or the outflow speed of symmetric reconnection, where B is the reconnecting magnetic field strength and ρ is the plasma mass density. It was shown that the reconnection rate decreases as the sheared flow increases, ultimately shutting off once the sheared flow surpasses the Alfvén speed. We expect E_{shear} to decrease as the sheared flow speed increases.

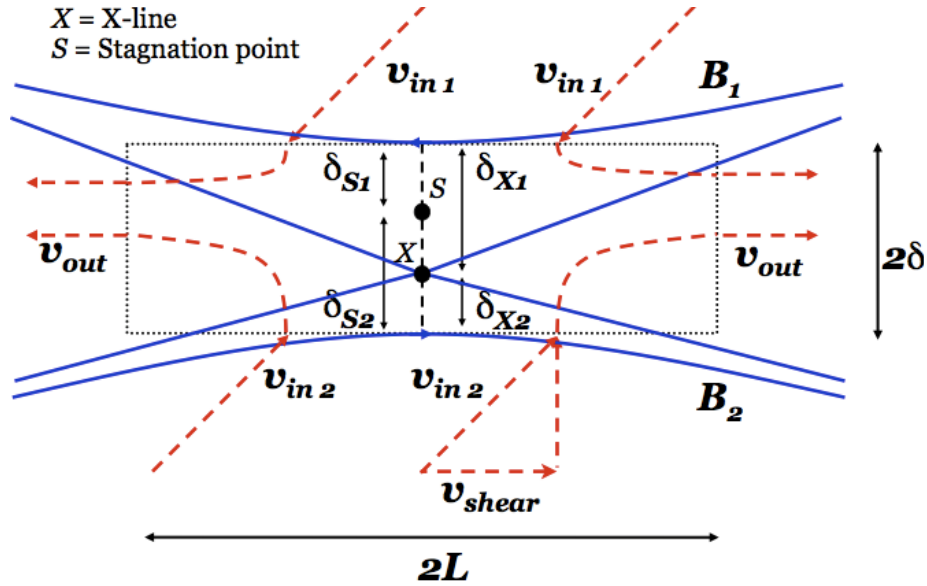


Figure 2: Diagram for Asymmetric Reconnection with Sheared Flow

Combining these effects leads to a reconnection looking like Figure 2. The sheared flow changes the direction of the inflowing plasma. In asymmetric reconnection, the Alfvénic outflow speed is given by equation 2. We hypothesize that the reconnection rate for asymmetric systems with a sheared flow will be consistent with equation 3 where E_0 is the reconnection rate with no shear. Consequently, we predict asymmetric reconnection shuts off if $v_{\text{shear}}^2 > v_{\text{out}}^2$. The magnetic asymmetries also shift the X-line and stagnation point (where the incoming flow velocity goes to zero) from the center of the dissipation region.

Another interesting effect can be predicted from this unique configuration. In these simulations, the sheared flows are equal in magnitude but opposite in direction on either side of the dissipation region. Assuming a linear ramp from v_{shear} to $-v_{\text{shear}}$ across the dissipation region, v_{shear} is equal to zero at the center, where the X-line is located in symmetric reconnection.

However, in asymmetric reconnection, the X-line and stagnation points are displaced from the center of the reconnection region (Cassak and Shay, 2007). They showed that

$$\frac{\delta_{X1}}{\delta_{X2}} \sim \frac{B_1}{B_2} \quad (4)$$

and

$$\frac{\delta_{S1}}{\delta_{S2}} \sim \frac{\rho_1 B_2}{\rho_2 B_1}, \quad (5)$$

where δ_{X1} and δ_{X2} are the distances from the X-line to the edge of the reconnection region on the first side and to the edge of the reconnection region on the second side, respectively, and δ_{S1} and δ_{S2} are the distances from the stagnation point to these respective edges. According to these, the

X-line shifts towards the side with the weaker field, and the stagnation point inversely shifts towards the side with the larger ratio of field over plasma density.

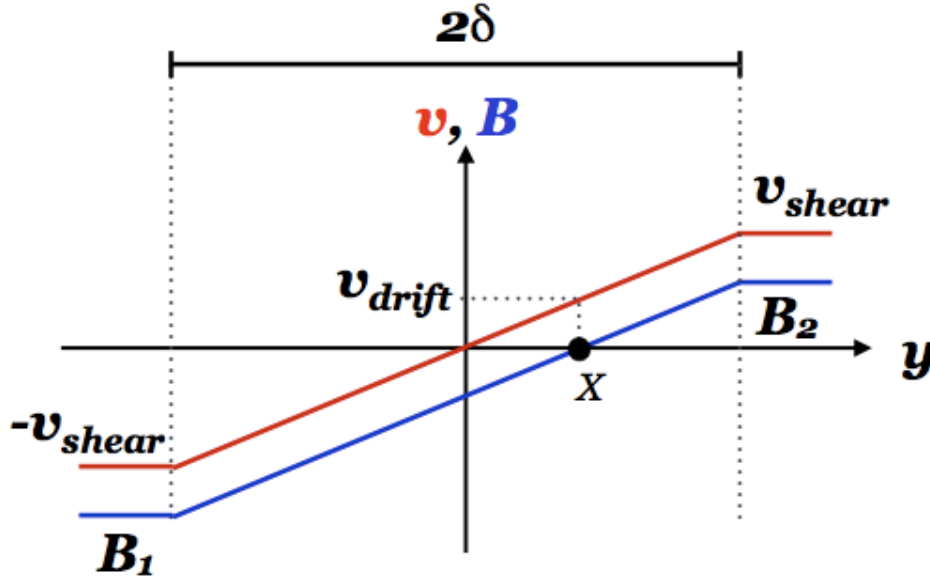


Figure 3: Diagram for linear profiles of v_{shear} and B .

Since the X-line is no longer at the center of the dissipation region, the X-line is immersed in some fraction of the sheared flow of the weaker magnetic field. This causes the X-line to drift at the velocity of the sheared flow experienced by the X-line. To motivate this idea, Figure 3 is a sketch of B and v_{shear} across the dissipation region. This drift speed of the reconnection site v_{drift} can be estimated by assuming a linear ramp in flow to be

$$v_{drift} = v_{shear} \left(\frac{B_1 - B_2}{B_1 + B_2} \right). \quad (4)$$

It is important to note that this equation assumes a symmetric sheared flow profile. To calculate drift speeds for X-lines between asymmetric sheared flows one must take into account a non-zero mean and a different slope through the dissipation region.

SIMULATIONS

We use the two-dimensional, two-fluid numerical F3D code (Shay et al. [2004]) to simulate asymmetric reconnection with a sheared flow. The initial profiles of the magnetic fields and the sheared flows are setup using a double tearing mode tanh configuration. There is no initial out-of-plane magnetic (guide) field. The plasma density is initially normalized to a value of 1 throughout the simulation domain. The temperature is non-uniform to ensure pressure equilibrium and the

asymptotic value of temperature is 1 far from the current sheet. Electrons are of a mass $m_e=m_i/25$, where m_i is the ion mass. The computational domain is of size 204.8×102.4 , with each cell of size 0.05×0.05 . Periodic boundary conditions are employed, so there are two opposite out-of-plane current sheets in the domain at a far distance from each other. Reconnection is initiated through a perturbation in the magnetic fields to break symmetry and equilibrium.

Simulations are performed on the Department of Energy’s (DOE) National Energy Research Scientific Computing Center’s (NERSC) “edison” supercomputer using 512 processors running in parallel. We perform numerous simulations with different magnetic asymmetries and sheared flows, which are summarized in Table 1. Simulations are performed for varying amounts of time, as each run has varying rates of reconnection

Table 1: List of runs and their initial conditions.

Run	B1	B2	v_shear	Run	B1	B2	v_shear
AB1a	3	1	0	AB1g	3	1	2.4
AB1b	3	1	0.4	AB1h	3	1	2.8
AB1c	3	1	0.8	AB1i	3	1	3.5
AB1d	3	1	1.2	AB2a	2	1	1.2
AB1e	3	1	1.6	AB2b	2	1	2.4
AB1f	3	1	2.0				

RESULTS

Simulation Results

For each simulation, we choose an interval over which the islands, bubbles of plasma created as a result of reconnection, are between two particular widths is chosen for finding representative values. These boundary widths are first chosen by watching animations and determining when the magnetic reconnection site appears to be in a steady state; the same widths are used in analyzing all runs. For these simulations, the intervals use initial and final island widths of 7 and 11 units. Within these intervals, we find representative values for the reconnection rate, average drift speed, plasma velocities, and dissipation region geometries. The position of the X-lines for each time step are tracked and we look at cuts through the X-line to quantitatively measure values for magnetic fields, plasma densities, plasma velocities, and determine the location of the stagnation point within the dissipation region.

We hold v_{shear} constant and compare the drifting of the X-line between two different magnetic asymmetries. Figure 4 shows the position of X-line with a consistent sheared flow speed of $v_{\text{shear}}=1.2$ in a system with $B_1=3$ and $B_2=1$ (blue) and $B_1=2$ and $B_2=1$ (red). The X-line drifts faster when the magnetic field asymmetry is $B_1=3$ and $B_2=1$ with a measured $v_{\text{drift}}=0.632$ than when $B_1=2$ and $B_2=1$ with $v_{\text{drift}}=0.366$. These values are consistent with our hypothesis, where a higher magnetic asymmetry leads to a larger displacement of the X-line resulting in a faster drift speed.

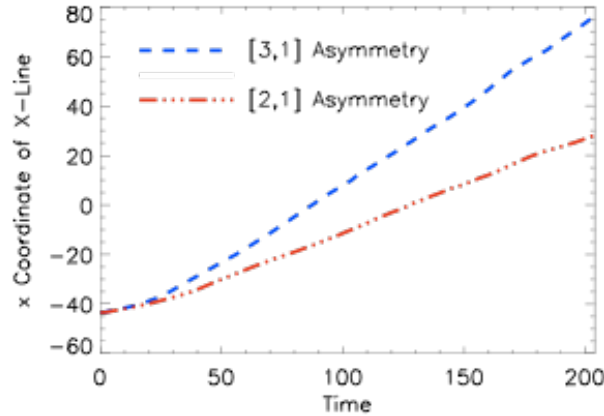


Figure 4: Measured X-Line position with a sheared flow of $v_{\text{shear}}=1.2$ in simulations with a magnetic asymmetry of [2,1] (red) and [3,1] (blue).

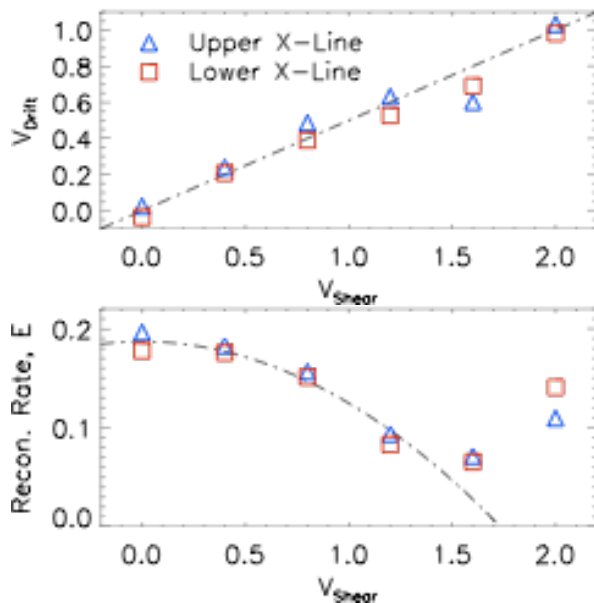


Figure 5: Average drift speed of X-line vs sheared flow speed for magnetic asymmetry of [3,1]. Dashed line is the prediction from equation 6.

Figure 6: Average reconnection rate vs sheared flow speed for magnetic asymmetry of [3,1]. Dashed line is prediction from equation 3.

We now hold $B_1=3$ and $B_2=1$ constant and measure the X-line drift speed as a function of sheared flow speed. Figure 5 shows the average drift speed across the aforementioned intervals for different sheared flow speeds. The upper (triangles) and lower (squares) X-lines drift in the same direction, consistent with the direction of the sheared flow on the side of the lower magnetic field. The dashed line is the predicted drift speed from equation 6, and agrees very well.

Figure 6 shows the expected reconnection rate (dashed line) from equation 3 as a function of increasing sheared flow speed, normalizing E as the average reconnection rate in the absence of sheared flow. The average reconnection rate during the aforementioned intervals is plotted for both the upper (triangles) and lower (squares) X-lines. The prediction closely matches the measured values obtained from our simulations, though sheared flow speeds higher than ~ 1.6 start

to drastically stray from the prediction. Reconnection for such speeds is qualitatively different; this agrees with the prediction that reconnection changes for sheared flow speeds exceeding v_{out} , which is ~ 1.73 for these parameters.

Using a moving reference frame v_{drift} of the X-line we see the sheared flow speeds on either side of reconnection region are no longer symmetric, with one side having $v_{shear} - v_{drift}$ and the other having $v_{shear} + v_{drift}$. At higher drift speeds this causes one field to possess a super-Alfvénic sheared flow speed while the other field still possesses a sub-Alfvénic sheared flow speed, and reconnection becomes increasingly chaotic and a steady state analysis is less reliable. The reconnection rate should ultimately shut off after both sheared flow speeds are relatively greater than the Alfvénic outflow speed with respect to the motion of the reconnection site.

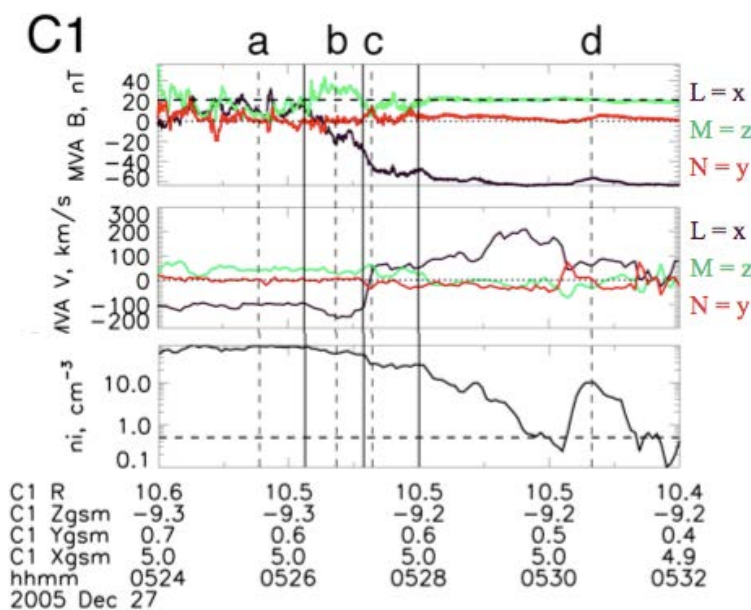


Figure 7: Magnetic field strength, plasma velocities and plasma density for a reconnection event measured by Cluster (Wilder et al., 2014).

Satellite Observations

The Cluster satellites measured a drifting X-line at the magnetopause's southern polar cusp on December 27, 2005. By using values obtained from these satellites, we are able to further test our hypothesis on the drifting of the X-line based on asymmetries and sheared flow conditions. Figure 7 displays magnetic field, velocity, and plasma density measured by Cluster 1 (C1). The interval that C1 encounters the reconnection site is between times 05:26 and 05:28. We use the following values obtained from the satellite measurements for the magnetic fields and sheared flow speeds inside (ms) and outside (sh) the magnetopause: $B_{ms}=60$ nT, $B_{sh}=10-15$ nT, $v_{ms}=0.0$ km/s, and $v_{sh}=100$ km/s. Using our hypothesis for a linear slope between sheared flow speeds and adapting equation 6 to account for asymmetric sheared flows, we predict a drift speed of 80-86 km/s. This

is in excellent agreement with the observed drift speed of 83 km/s (Wilder et al., 2014), providing further evidence of the validity of our predictions.

CONCLUSIONS

We have systematically studied magnetic reconnection with asymmetric magnetic fields and sheared flows, similar to the conditions observed naturally near the magnetopause's polar cusps. We predict the reconnection rate in this unique configuration, and our theoretical model suggests the reconnection site drifts in the direction of the sheared flow resulting from the X-line's displacement along the inflow direction in asymmetric reconnection.

We perform simulations with different magnetic field asymmetries and sheared flows to obtain measurements for the reconnection rate and X-line drift speed. The X-line drift speed agrees well with predictions from equation 6. Reconnection with a higher magnetic asymmetry causes a larger displacement of the X-line, and this causes the X-line to experience a greater sheared flow and a higher drift speed. Additionally, the X-line drift speed increases linearly as sheared flow speeds increase for fixed magnetic field strengths. We find the reconnection rate agrees with predictions up until the drifting of the reconnection site effectively renders one of the sheared flows super-Alfvénic. We further tested our X-line drift prediction with satellite observations and found excellent agreement.

FUTURE WORK

To more closely model the configuration observed at the magnetopause around Earth, we will perform simulations with density asymmetries. Previous research has shown that density asymmetries shift the location of the stagnation point (Cassak and Shay, 2007) and change the outflow speed. While the latter should have an effect on the reconnection rate in the absence of sheared flow, it is unclear whether the location of the stagnation point has any effect on the drift speed of the X-line.

Another topic of future study is the exploration of systems with super-Alfvénic and sub-Alfvénic sheared flow speeds on either side of the dissipation region. This effect completely changes the appearance of reconnection, and it may be applicable to the polar cusps of the magnetopause if the sheared flow speed of the solar wind reaches these high velocities.

ACKNOWLEDGEMENTS

I would like to acknowledge the NASA WV Space Grant Consortium for funding during the Summer of 2014. The stipend supported my salary as an undergraduate research assistant and this enabled me to pursue my interests in Physics research. As an undergraduate I was able to gain much experience doing scientific research that I could not have obtained in the classroom. Thanks to this program, I will soon work with my research professor and colleagues to produce a scientific paper documenting these findings. I presented my research at West Virginia University's Undergraduate Research Symposium for the Summer of 2014, and submitted an abstract to the 2014 Fall American Geophysical Union Meeting.

I thank my research professor, Paul Cassak, and my two colleagues, Colin Komar and Matthew Beidler, for their knowledge, support, and advice throughout my research experience. The value

of their help is beyond measure to me. Simulations were performed on NERSC's supercomputer, "edison." I would like to thank Rick Wilder for the Cluster data.

REFERENCES

Cassak, P. A. and M. A. Shay. "Scaling of asymmetric magnetic reconnection: General theory and collisional simulations." *Phys. Plasmas*, 14, 102114, (2007)

Cassak, P. A. and M. A. Shay. "Scaling of asymmetric Hall magnetic reconnection." *Geophysical Research Letters*, 35, L19102, (2008)

Cassak, P. A. and A. Otto. "Scaling of the magnetic reconnection rate with symmetric shear flow." *Phys. Plasmas*, 18, 074501, (2011)

Dungey, J. W. "Interplanetary magnetic field and the auroral zones", *Phys. Rev. Lett.*, 6, 47. (1961)

Dungey, J. W. "The structure of the exosphere, or adventures in velocity space, in Geophysics: The Earth's Environment", edited by C. De Witt, J. Hieblot, and A. Lebeau, p. 505, Gordon Breach, New York. (1963)

National Research Council. "Storms from the Sun: The Emerging Science of Space Weather." Washington, DC: The National Academies Press, (2002)

Shay, M. A., J. F. Drake, M. Swisdak and B. N. Rogers. "The scaling of embedded collisionless reconnection." *Phys. Plasmas*, 11, 2199, (2004)

Wilder, F. D., S. Eriksson, K. J. Trattner, P. A. Cassak, S. A. Fuselier and B. Lybakk. "Observation of a Retreating X-Line and Magnetic Islands Poleward of the Cusp During Northward Interplanetary Magnetic Field Conditions." submitted to *J. Geophys. Res.*, (2014)

Zweibel, Ellen G. and Masaaki Yamada. "Magnetic Reconnection in Astrophysical and Laboratory Plasmas." *Annu. Rev. Astron. Astrophys.*, 47, 291, (2009)

A LOOK AT PLANETARY PROTECTION IMPLEMENTATION

Lynnora Grant
Mechanical Engineering
West Virginia University
Morgantown, West Virginia 26506

ABSTRACT

Planetary Protection Engineering is a subset of Contamination Control Engineering that focuses on preventing biological contamination. Key concerns are to preserve the Earth's eco-system during sample return missions, preserve possible traces of life on other planets, and preserve the science of life-seeking missions. One component of a life-seeking mission being built at Goddard Space Flight Center is a mass spectrometer that will be part of the 2018 ExoMars rover. One method to decrease the level of biological contamination on spacecraft components during the integration and testing period, prior to launching them into space, is to introduce ultra violet C radiation in the construction environment. To test the effectiveness of this strategy, a foil was inoculated with local environmental bacteria and later exposed to ultra violet C lights for various time increments. After exposure, the bioburden was examined by transferring bacteria from the foil onto trypticase soy agar plates. The plates were observed for one week for growth of bacterial colonies, and it could be seen that there were differences in the amount of colony growth based on the times of UV-C exposure. By day 6, the samples that had not been exposed to UV-C radiation had too many colonies to count (over 200 colonies per plate), while samples from 60 minutes of exposure had a total colony count of four. In conclusion, the hypothesis that UV-C exposure would lead to a dramatic decrease in bioburden was supported. Further analysis and replication of the experiment will be necessary once Goddard's planetary protection lab is in commission in order to obtain more precise and accurate results. This research provides preliminary data justifying the use of UV-C radiation in clean-rooms housing hardware essential in life-seeking missions.

INTRODUCTION

The three major goals of the research internship were to experience various tasks of contamination engineers, aide in the construction of a lab, and examine the effects of UV-C on the bioburden in clean rooms.

Research on the bioburden found in clean rooms is becoming more and more essential as NASA develops more spacecraft that will be sent to extraterrestrial locations that could possibly harbor life. Goddard is in the process of procuring the equipment necessary to conduct bioburden assays, which will be used to determine whether the hardware meets the planetary protection requirements. To aid in gathering materials for the lab, the task of drafting a procurement request for an image analysis system was completed. Also, standard swab assays were conducted and a procedures report was drafted. The report noted the deviations from the standard protocol due to the absence of equipment. The report will be useful in the event that the assays would need to be conducted again under similar conditions.

Experiences with contamination engineers resulted in a better knowledge of the duties associated with preventing the buildup of contaminants on spacecraft. Experience in the pre-clean room led

to a better knowledge of processes used to prepare equipment for the clean room. These processes included autoclaving, sonicating, drying, and baking equipment. Contamination control continues in the clean room as well. Processes in the clean room such as white and UV light inspections, setting up foils, running air particle counters, and placing particle fall out wafers were also conducted. Once in the office, experience was gained with using Excel to monitor the pattern of air particle accumulation based on particle fall out wafers.

The number of particles in a clean room is normally kept low due to HEPA filters. Likewise, the amount of bacteria in a clean room can be decreased using UV-C radiation. A project was conducted to observe the effects of the UV-C lighting system currently in use in one of Goddard's clean room facilities.

BACKGROUND

Contamination Control & Planetary Protection

Contamination is any matter foreign to a project. The two types of contamination that contamination engineers at Goddard want to prevent are particulate and molecular. As can be deduced by the names, particulate contaminants are particles, such as fibers and dust, and molecular contaminants are molecules, like silicones from rubber materials, and plasticizers from plastics. Molecular and particulate contamination have the potential to cause an array of problems for missions, ranging from a decrease in scientific yield to a catastrophic failure. It is for this reason that contamination control is needed. Contamination control consists of preventing the buildup of contaminants during flight hardware assembly. This is done so that when the hardware is ready for flight, it will meet contamination requirements.

Planetary Protection (PP) is a subset of Contamination Control which focuses on decreasing the likelihood of spreading biological matter among the planets. The key concerns are to: preserve the eco-system of Earth during sample return missions, preserve possible signs of life on other planets, and preserve the science obtained in life-seeking missions. Planetary Protection requirements are implemented when the spacecraft is traveling to an extra-terrestrial body that has an environment that may be able to foster life as we know it. The requirements were first implemented with the Viking missions to Mars in 1975. Planetary Protection was originally called Planetary Quarantine in the 1970s. The PP requirements are dictated by the 1967 Outer Space Treaty signed by every space faring nation. This same treaty also prohibits the installation of objects of mass destruction in space, and also designates space as a peace zone.

To meet contamination and PP requirements, clean-rooms have to be monitored. Ways to monitor clean rooms include the use of particle fall out wafers, particle counters and non-volatile residue foils. The monitoring of the environment is significant because it indicates levels of contamination that hardware in the area is exposed to.

To prevent the buildup of particles and other contaminants in the clean rooms, workers must wear clean room suits and items entering clean rooms have to be pre-cleaned. Often, this process of pre-cleaning requires a wipe down with IPA, but when planetary protection precautions need to be taken, more steps are added. Hardware that is sensitive to biological containments is run through a process called Dry Heat Microbial Reduction in which it is exposed to 110-120° C. One example

of this type of hardware is the Mars Organic Molecule Analyzer-Mass Spectrometer, MOMA-MS.

MOMA & the MS

The Mars Organic Molecule Analyzer is an instrument suite on the 2018 ExoMars rover. It is composed of a gas chromatograph and a laser desorption mass spectrometer. The mass spectrometer is currently under construction at Goddard.

The ExoMars rover will collect Martian soil samples and then bake them at temperatures allowing for the volatile materials to evaporate. The vapors will travel to the gas chromatograph where they will be separated and identified. They then will move to the mass spectrometer where electrons will be used to ionize the particles. This process will cause the particles to break down and become charged ions. The masses of the ions will then be compared to the masses of known atoms and molecules for identification. The identification process will allow for the identification of organic molecules which will be paramount in the search for life.

UV-C FOR BIOBURDEN CONTROL

Ultra violet C is a form of radiation with a short wavelength of 100 to 280 nanometers. UV-C from the sun is normally absorbed by the Earth's atmosphere, but artificial forms are commonly used as a sterilization agent in hospitals and food processing locations. Wavelengths at 254 nanometers have germicidal effects, causing thymine in the DNA to bond to itself. When this occurs the bacteria is rendered unable to reproduce.

Currently, UV-C lights are being used in the MOMA clean room primarily to control the amount of bacteria in the environment. The intensity and time of exposure needed to damage spore forming bacteria has been calculated. The intensity at floor level is $\sim 30 \mu\text{W}/\text{cm}^2$. At this intensity, 15 minutes of exposure time should decrease colony growth by a two log reduction. An experiment was conducted to test the current UV-C lighting system on a local environmental bacteria.

EXPERIMENT

An experiment was conducted to study the germicidal effect of the lights in the MOMA clean room. Bacteria obtained from a water fountain was exposed to UV-C radiation for varying times and then was cultured on TSA and 2% blood TSA plates over a week.

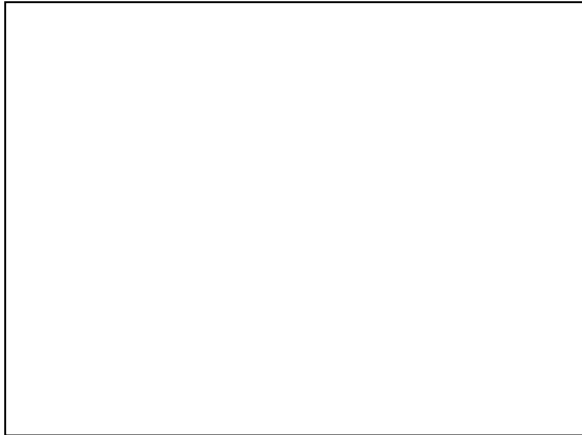
Hypothesis

It is hypothesized that the UV-C lights will decrease the level of bacteria growth. It is also expected that as the time of exposure increases, the amount of bacteria growth will decrease.

Preparation

- Obtain a sheet of foil at least 32x40 cm.
- Wipe the foil with 100% IPA and then with 70% IPA to clean and sanitize it
- Dry foil with nitrogen gas.
- Using a ruler and a permanent marker, mark off 20 5x5cm squares, 2.5cm away from adjacent squares.

- Below each square in the 2.5 cm boundary, label the graph as shown in Figure 1. The numbers stand for the amount of time the cells are anticipated to be exposed to the UV-C radiation. C stands for control, which will be a sample taken right before experimentation begins. -C is negative control, a sample taken at the same time as the control but the square has only sterile water.



A	-C ₁	-C ₂	60	30(1)	30(2)
B	-C	60	C	15	5
C	60	C	15	5	10
D	C	15	5	10	30
Table 1. Grid Layout					

- Place Kapton tape on the 2.5cm boundaries, (over the labels)
- Wipe the foil with 100% IPA and then with 70% IPA to clean and sanitize it
- Dry foil with nitrogen gas.
- Set the sheet of aluminum aside for later.
- Acquire a TSA plate with visible colony growth. In this case colonies grown from the water fountain were used.
- Perform modified standard swab assay procedure (found on page 5) using the plate as the surface to be analyzed.
- Vortex the tube for time intervals of 5 seconds. Do this three times all together.
- Transfer the 2.5 ml to a 50ml tube.
- Add 12.5ml of sterilized water to the 50ml tube.
- Vortex the tube again for 15 seconds
- Aliquot .5mL of the liquid on to each of the 20 squares.
- Allot time for the water to evaporate off of the foil (overnight)
- Complete the preparation procedure found in the Swab Assay Procedure as well as these.

Measure Bacterial Concentration

- Gather 4, 15ml tubes.
- Add 4.5 ml of sterilized water to each tube.
- Label the tubes as follows; 1:10, 1:100, 1:1000, 1:10000
- With the remaining 5ml of the undiluted liquid, prepare a series of dilutions to check the concentration of inoculated solution.
- Serial dilutions:
 - Start with 1.5ml of original (undiluted) inoculum
 - Take .5ml of the liquid, add it to the tube labeled 1:10. Vortex for 15 seconds.
 - Take .5ml of the 1:10 dilution, add it to the tube labeled 1:100. Vortex for 15 seconds.

- Take .5ml of the 1:100 dilution, add it to tube labeled 1:1000. Vortex for 15 seconds.
- Take .5ml of the 1:1000 dilution, add it to the tube labeled 1:10000. Vortex for 15 seconds.
- Plate .5ml of the undiluted solution onto a TSA plate, and swirl the plate around to spread the solution.
- Repeat the previous step with the other dilutions, using a new plate each time.
- Observe colonies every 24 hours

Collection

- Use the collection section of the standard swab assay procedure to take samples of the control squares on the foil.
- Read & follow the procedures for using the UV-C lights.
- Set up UV-C probe to measure the energy dosage.
- Turn on UV-C lights. After 5 minutes, turn lights off and repeat the collection procedure for the squares labeled 5.
- Turn on UV-C lights. After 5 minutes, turn lights off and repeat the collection procedure for the squares labeled 10.
- Turn on UV-C lights. After 5 minutes, turn lights off and repeat the collection procedure for the squares labeled 15.
- Turn on UV-C lights. After 15 minutes, turn lights off and repeat the collection procedure for the squares labeled 30.
- Turn on UV-C lights. After 30 minutes, turn lights off and repeat the collection procedure for the squares labeled 60.

Transfer to Plates

- Use the transfer section of the modified standard assay procedure to transfer .7mL of the liquid in the tube to one blood TSA and one TSA plate.

Modified Standard Swab Assay Procedure

Preparation- aseptic, flow bench

- Prior to using the flow hood, wipe down surfaces with 70% IPA
- Prepare/acquire TSA plates and TSA plates with 2% blood agar
- Aliquot 2.5 ml of sterilized water in 15mL falcon tubes using the pipette
 - Standard swab procedure instruct to autoclave tubes prior to experimentation. The tubes were not autoclaved prior to collection, but were trusted to be sterile
 - Standard swab procedure instructs to fill Eppendorf tubes with 1ml of sterile water. Eppendorf tubes were not available and so this step was not taken.
 - Standard procedure indicates to aliquot phosphate buffered saline (PBS) into the falcon tubes. The falcon tubes were filled with sterile water as opposed to the PBS.

Collection- collection room

- Designate a 25 cm² surface to be analyzed
- Pre-label all of the tubes with time and sample row letter (A-D)

- Remove a sterile swab from the wrapping and dip it into a tube with 2.5 ml of sterilized water, before removing the swab from the tube, use the interior wall to remove excess moisture.
- Position the head of the swab at a 30° angle with the collection surface. In a continuous motion, swipe the swab slowly and continuously in one direction while rolling, so that all parts of the head make contact with the surface. After covering the 25cm², rotate the swab 90° and repeat the collection and then do the same with a 135° rotation.
- Insert the swab back into the 15 ml falcon tube, break along perforation so that the swab falls in and is immersed in the water. Replace the cap on the tube.
 - Standard procedure instructs to have two separate tubes, one with sterile water to moisten the swab, and one with phosphate buffered saline (PBS) to store the swab after collection. In this procedure the tube used to moisten the swab was the same one used to store the swab post collection.
 - Standard procedure instructs to store samples in a temperature of 4°C if they will not be processed within 24 hours. Samples were not stored in 4°C as specified but were transferred within one hour, well under the 24 hour time frame.

Transfer to plates- aseptic, flow bench

- Prior to using the flow hood, wipe down surfaces (including exterior of collection tubes) with 70% IPA
- Bring the plates, samples in the tubes, and the pipette into the flow hood
- Vortex each sample for 15 seconds.
 - Standard procedure instructs to vortex for 5-6 seconds as opposed to the 15, the 15 seconds may have accounted for the sonication process that was not used.
 - Standard procedure instructs to put the samples through a heat shock. A heat shock was not conducted because this is not a test for heat resistant spores.
- Aliquot .7ml of the liquid in one tube onto a plate
 - Standard procedure specifies 0.5ml onto 4 TSA plates, in this experiment 0.7ml was spread on 1 TSA plate and 1 TSA + 2% sheep's blood plate.
- Tilt the plate to allow the liquid to evenly disperse
- Repeat previous two steps with remaining samples
- Secure the plates with parafilm
- Leave secured plates lid side down for storage at room temperature
- Observe the colonies every 24 hours
 - Standard procedure instructs to place the plates in an incubator. An incubator was not available, this may cause the colonies to take longer to grow. As a result a longer observation time of a week is advised as opposed to the stated 24, 48, 72 hour observations.

Equipment

- Sterilized water
- 15 ml falcon tubes
- Flocked nylon swabs
- Vortex mixer
- Micro liter pipette

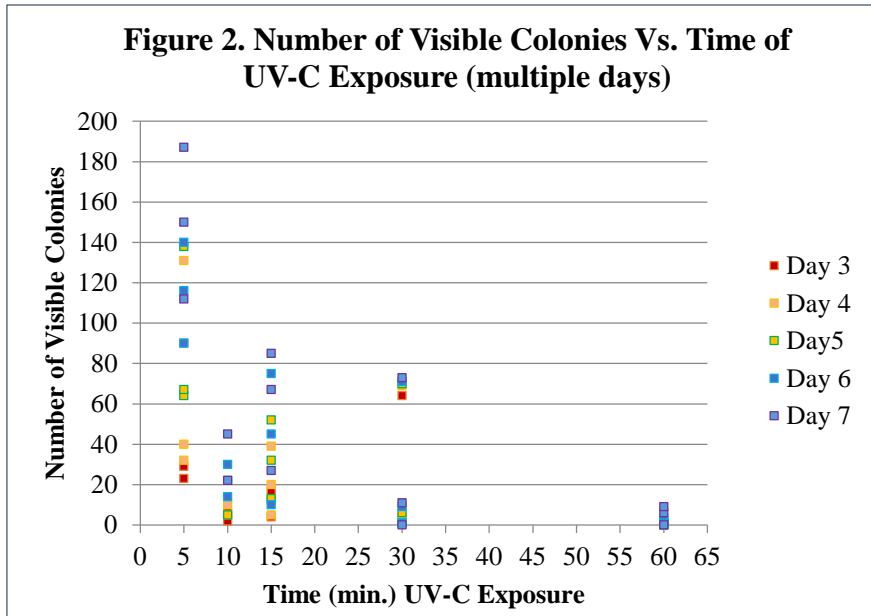
- Sterile, disposable 5ml pipettes
- Laminar flow bench
- Gloves
- 70% IPA wipes

RESULTS & CONCLUSIONS

Grid Location	Day 3	Day 4	Day 5	Day 6	Day 7
B5	29	40	64	116	150
C5	90	131	138	140	187
D5	23	32	67	90	112
C10	2	5	5	14	22
D10	6	10	22	30	45
B15	12	20	32	45	67
C15	17	39	52	75	85
D15	4	5	13	10*	27
A301	64	69	70	71	73
A302	3	4	6	9	11
D30	2	1*	1	1	0
A60	1	0*	1	3	6
B60	0	0	2	1*	9
C60	1	1	0*	0	0

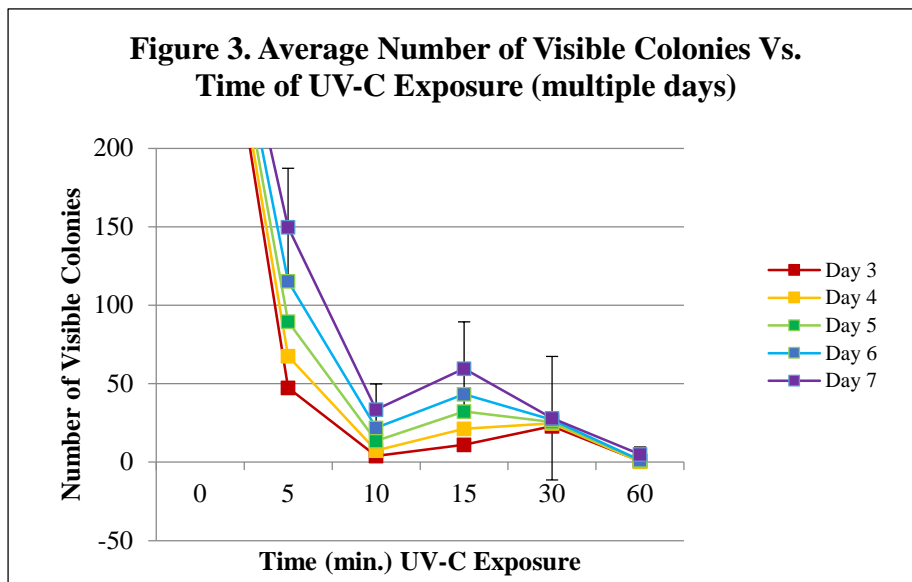
Table 2. Total Count for Each Sample

*The numbers on the table are a sum of all the colonies on a given day but some numbers are lower than the previous day. This is because a small spot that was assumed to be a colony one day, was determined the next day to be a particle because there was no further growth.



Time	Day 3	Day 4	Day 5	Day 6	Day 7
-C	0	0	0	0	0
C	400	400	400	400	400
5	38.33333	67.66667	107	115.33333	149.66667
10	9	27	56	22	33.5
15	28.33333	45	61.66667	43.33333	59.66667
30	2	2.666667	5.666667	27	28
60	0.5	1	4.5	1.333333	5

Table 3. Average Colony Count and time of Exposure



The table and figures on pages 7&8 show the average number of colonies verses the time of UV-C exposure. Average colonies were calculated by counting all colonies on both plates from each grid sample and averaging that by the number of samples per time point. Standard deviation is graphed only for the day 7 time points. The positive control locations (0 min) were all too numerous to count with more than 400 colonies.

On day 3, the sum of the colony growth for the positive control plates were too numerous to count, well over 200 colonies per plate. Even the lowest UVC exposure time (5 minutes) had a dramatic decrease in the number of colonies compared to the control as shown in Figure 2. In comparison, the longest exposure time (60 minutes) a dramatically low colony growth with only two visible colonies. Thus it can be concluded that the UV-C exposure had an effect on the colony growth.

From the data collected, there does appear to be a declining trend in bacteria count as the time of exposure increases, but more trials would need to be conducted for verification. It can be concluded that UV-C caused a dramatic decrease in the environment bioburden which may aid in meeting the planetary protection requirements in life-seeking missions.

Experimental Considerations

The plates are were analyzed over a period of seven days at room temperature as opposed to the standard procedure by NASA which is three days in an incubator. Because of this, there may have been a difference in the number of colonies grown. This will be solved once the incubator and other items arrive.

The UV-C light was turned off between exposures to take samples. Therefore the exposure times are total, but not continuous. These breaks could have allowed the bacteria to repair itself. To address this, different sheets of foil can be used then swapped out after the collection. This way the full exposure time will not be broken up/

The complete sample of 2.5 ml was not used on the plates because of the limited supply of plates. There is a possibility that the remaining solution in the tubes had a differing concentration of bacteria from the solution sampled. This can be solved with more plates.

Future Plans

The experiment was conducted during the process of procuring all of the items needed in standard bioburden assays such as an incubator, plate spinner, and an automated image analysis system. For this reason, the procedure was changed to fit with the resources available, possibly resulting in error. Once all of the materials are gathered, more accurate assays will be able to be conducted.

The UV-C light is run more than once a week. It may be interesting to use the radiation on the colonies over a number of days, to observe how effective this is.

It seemed like the process selected for one type of bacteria found on the water fountain. It may be interesting to look at other bacteria, especially spore forming bacteria because they may have more of a resistance to the UV-C exposure, and those are the ones that are most likely to survive in space conditions.

ACKNOWLEDGMENTS

Thank You to the West Virginia Space Grant Consortium for sponsoring the research internship. Thank you to my mentors: Nancy Carosso, Erin Lalime & Code 546 employees who made the summer enjoyable.

REFERENCES

- "ESA - Robotic Exploration of Mars: The ExoMars Rover Instrument Suite." *ESA - Robotic Exploration of Mars: The ExoMars Rover Instrument Suite*. N.p., n.d. Web. 24 July 2014
- Hogan, C. "Sunlight." *Sunlight*. EOEarth, 2012. Web. 24 July 2014.
- "NASA Office of Planetary Protection." *NASA Office of Planetary Protection*. N.p., n.d. Web. 24 July 2014.
- "OUTER SPACE TREATY." *U.S. Department of State*. U.S. Department of State, n.d. Web. 25 July 2014.
- "UV Irradiation Dosage Table." *Germicidal UV Dose*. American Air & Water®, Inc., n.d. Web. 01 Aug. 2014.
- "UV Water Disinfection - BersonUV." *Berson UV-technik*. N.p., 2013. Web. 24 July 2014.

Faster evolutionary Multi-objective Optimization via GALE: The Geometric Active Learner

Joseph Krall
Computer Science
West Virginia University
Morgantown, WV, 26506

ABSTRACT

Goal optimization has long been a topic of great interest in computer science. The literature contains many thousands of papers that discuss methods for the search of optimal solutions to complex problems. In the case of multi-objective optimization, such a search yields iteratively improved approximations to the Pareto frontier, i.e. the set of best solutions contained along a trade-off curve of competing objectives. Approximating that Pareto Frontier has been a challenge, but has led to the development of commonly used tools (e.g. NSGA-II, SPEA2, etc). Two problems that arise with efficiently approximating the Pareto Frontier is that sometimes too many solutions are generated. And secondly, it can be very inefficient if many solutions are being evaluated.

To solve these two problems, this thesis presents GALE (Geometric Active Learning). GALE is an active learner that finds approximations to the Pareto frontier by spectrally clustering candidates using a near-linear time recursive descent algorithm that iteratively divides candidates into halves (called leaves at the bottom level). Active learning in GALE selects a minimally most-informative subset of candidates by only evaluating the two-most different candidates during each descending split; hence, GALE only requires at most, $2\log_2(N)$ evaluations per generation.

The experiments of this thesis lead to the following conclusion: a near-linear time recursive binary division of the decision space of candidates in a multi-objective optimization algorithm can find useful directions to mutate instances and find quality solutions much faster than traditional randomization approaches. Specifically, in comparative studies with standard methods (NSGA-II and SPEA2) applied to a variety of models, GALE required orders of magnitude fewer evaluations to find solutions. As a result, GALE can perform dramatically faster than the other methods, especially for realistic models.

Forward

This work in part is based on a dissertation by the same author and title, submitted to the Electronic Library of WVU Dissertations. For more information, please refer to <http://wvusolar.wvu.edu/> or the slides which accompany that dissertation located at <http://www.slideshare.net/TanzaIratier/faster-evolutionary-multiobjective-optimization-via-gale-the-geometric-active-learner>.

Introduction

Goals are valued objectives; goal optimization then, is a search strategy that can be applied to identify optimal solutions that can attain such goals. Such search strategies are an everyday activity but these involve trivial decisions. Complex systems require a deeper analysis of possible decisions and goal optimization, or multi-objective optimization (MOO), is the key.

The study of such strategies has been a topic of increasing interest since the early 1950's [1] and [2]. Coello lists over 8,500 research papers that discuss and experiment with optimization methods since the 1970's, and continues to add resources to that list¹. One interesting field of interest is Search-based software engineering, in which search strategies for software engineering problems are studied. The chart in Figure 1 shows a rising interest in Search-based Software Engineering (SBSE) alongside MOO (data for SBSE comes from the Crest SBSE Repository²).

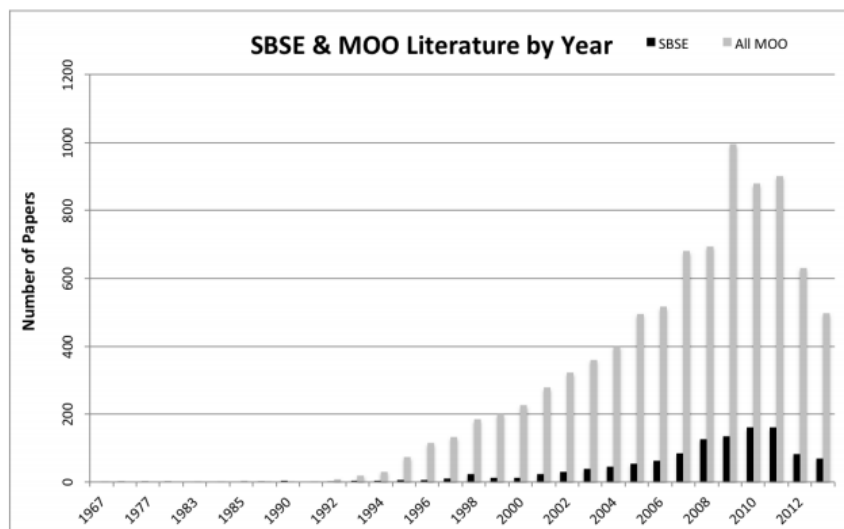


Figure 8

Software engineering comprises a lot of problems that are well-suited for search strategies because they apply designs that can be optimized to maximize some goals. In general, the idea is to generate software products that are of high quality but cost the least to build. Most of these kinds of software engineering problems are usually multi-objective (as opposed to single objective) with competing goals that define an expansive trade-off curve of optimal solutions, called a Pareto frontier [3]. There are thus, many optimal solutions and not just one single best design is most appropriate. Multi-objective strategies thereby generate approximations to the Pareto frontier. A decision maker must then choose one solution along that trade-off curve, and the purpose of multi-objective search strategies is to aid the decision maker by explaining the solutions that exist along that trade-off curve.

¹ <http://delta.cs.cinvestav.mx/~ccoello/EMOO/EMOObib.html>

² http://crestweb.cs.ucl.ac.uk/resources/sbse_repository/repository.html

One common multi-objective search strategy is the genetic algorithm, sometime called a stochastic search. Sayyad & Ammar have studied stochastic search tools and report that the NSGA-II [4] and the SPEA2 [5] are two of the most popular search tools in the current literature for software engineering [6]. Stochastic search tools such as these explore the solution space "blindly", with the goals of a) avoiding locally optimal solutions that may entrap the search and prevent discovery of better global optima; and b) diversifying the set of approximations to the Pareto frontier in hopes of revealing the entirety of the optimal trade-off curve.

Stochastic search has two problems. Firstly, the search can unnecessarily be computationally expensive due to the fact that many sub-optimal solutions are discarded in favor of better solutions, and thus an overwhelming number of evaluations are conducted.

Most realistic problems are usually cpu-intensive to evaluate [7]. Lohn et al. comment that the time and resources required for the evaluation of candidate solutions '*swamps out the running time*' of the underlying search methodology [8]. This condemns the runtime of any search strategy performed on complex systems where evaluations are expensive.

Secondly, stochastic search often produces too many solutions in its approximation-set of the Pareto frontier. Harman cautions that many frontiers are very *crowded*; i.e. contain thousands (or more) candidate solutions [9]. This makes the challenge of choosing just one solution among them much more difficult [10].

To solve these two problems, a more-directed, less-stochastic approach is necessary. This paper suggests Geometric Active Learning (GALE). GALE has previously been published in [11] and is described in an under-review article for the IEEE TSE journal of transactions on software engineering [12]. GALE is defined as a multi-objective evolutionary algorithm (MOEA) which manages populations of solutions and iteratively refines (each iterative pass is called a generation) them through a mutation policy to find approximations to the Pareto frontier.

GALE is an *active learner* (i.e. performs its inferences on a minimally most-informative subset of each population) that *spectrally clusters* its populations of candidate guesses (i.e. clustering on the spectral dimensions of greatest variance is better than clustering on the raw dimensions of the population) to identify a minimally most-informative subset to mutate. GALE employs the *WHERE* spectral clustering algorithm [13]. *WHERE* is a near-linear time recursive descent algorithm that iteratively divides the candidate population into halves (called leaves at the bottom level), evaluating only the two-most different candidates in each half. Thus, GALE requires at most, only $2\log_2(N)$ evaluations per generation. GALE then *directionally mutates* the members of most promising leaves towards the better end of each leaf in a non-stochastic manner. These leafs thereby become piece-wise approximations to the Pareto frontier (these terms in italics are all further explained in the expanded version of this paper).

To be formal, GALE is an approach to MOO and cannot solve *every* problem. Rather, the nature of the problem by which GALE is best suited should be such that following assumptions hold true:

1. More than one objective
2. Competing Objectives
3. Non-Categorical Objectives (numeric, continuous)
4. Piece-wise linear Pareto frontier

5. Spectral assumptions:
 - a. Spectral Dimensions must exist (i.e. real eigenvectors)
 - b. An accurate low-rank approximation for the candidate population must exist
6. Model Runtime:
 - a. GALE is most suitable when model runtime is high
 - b. That is, the runtime to evaluate a solution is high (and high is relative: 2ms or more)

In principle, GALE could be too naive and might fail because it utilizes so few evaluations to find approximations to the Pareto frontier. To test that, a refined experimental method was developed through a critique of various multi-objective optimization studies. That critique shows that many experimental methods lack the rigor to deliver powerful conclusions, and so several guiding principles are given by which to design rigorous experimental methodologies.

In this thesis, the results of that critique are applied to design rigorous experimental methods that perform numerous case studies on the effectiveness and utility of GALE when compared to the standard methods: NSGA-II and SPEA2. This way, a powerful conclusion regarding the results can be given. Those results show that GALE can find comparable solutions in vastly far fewer evaluations (20-50, not 1600-4000) of the solution space, enabling the potential to explore and study realistic problems (in 6-20 minutes, not 3-5 hours) that require expensive evaluation-runtimes.

The structure of this paper is as follows. In the next section, a summary of the critique and survey of MOO literature is given. From this survey, an experimental method is drafted to demonstrate the value of GALE compared to NSGA-II and SPEA2. In the “Experiments” section, some of the results are given and analyzed. Lastly, conclusions are given with some future work directions.

SURVEY CRITIQUE

The concepts behind GALE seem so simple that it is somewhat odd it has not be previously discovered. GALE requires orders of magnitude fewer evaluations and can dramatically reduce runtimes for realistic models. This level of improvement cannot be easily accepted without an extensive assessment on possible threats to the validity of the findings. Hence, rigorous experimental methods are constructed by examining and critiquing the literature of multi-objective optimization. The details and organization of the critique is given in the following section. The conclusions from that critique are a series of principles discussed in further detail in the subsequent sections. Those principles are:

1. Models: Study lots of both lab and realistic-setting models improve *External Validity*.
2. Repeats: Run the experiments many times to improve *Conclusion Validity*.
3. Statistics: Use appropriate statistics to improve *Conclusion Validity*.
4. Runtimes: Report raw runtimes to improve *Construct Validity*.
5. Evaluations: Report the number of evaluations to improve *Construct Validity*.
6. Parameters: Detail and defend parameters choices to improve *Internal Validity*.
7. Threats: Include a “threats to validity” section to assess *Conclusion Validity* of the results.

EXPERIMENTS

Among the experiments, the first performs a MOO search on the NASA CDA model of cockpit simulations for an aircraft approaching a runway. That CDA model is a very computationally expensive model, requiring 6-8 seconds per simulation. Hence, any MOO tool that would require running it thousands of times would suffer on runtime. GALE on the other hand only needs to run CDA just a few dozen times, and so hence its runtime is vastly superior to that of NSGA-II and SPEA2. The question that remains is whether or not GALE performs as well, in terms of finding quality solutions – and the answer is that they are all quite the same. Shown below are the total runtimes for brevity in Figure 2.

MOEA	Total Time (seconds)	Total Time (hours)
GALE	11,947	3.3
NSGA-II	280,367	77.9
SPEA2	251,630	69.9
TOTAL	543,943	151.0

Figure 9

The second experiment runs a MOO search on a software engineering model of requirements engineering. In essence, there are software projects with many subtasks each with varying priorities and costs, but the assignment of which tasks to do first has been a problem with much focus in search-based software engineering. Here, MOO is used to optimize the total cost and minimize idle rates spent while some developer teams are waiting on others to finish their tasks. This model, called POM, is not as computationally expensive as CDA but it is still a concern to run POM thousands of times. The results (shown in Figure 3) indicate what little increases in model runtime can lead to vast increases in MOO search times. POM3C is technically the hardest model at about 1/10th of a second of runtime. POM3B is the simplest, which runs in just above 2 milliseconds of runtime. Despite the fact that 2 milliseconds sounds very fast, there is still a visible improvement in total runtime through the use of GALE.

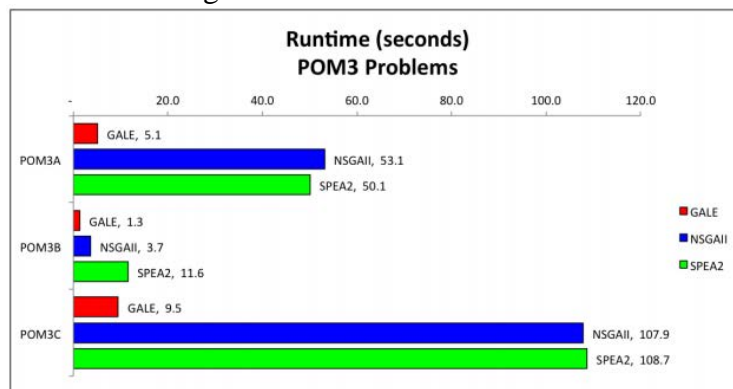


Figure 10

The third and fourth experiments involve the use of MOO on standard assessment models that are typically used in the literature as a means to test MOO methods (i.e. constrained and unconstrained models). Those models are very small and it is usually of no concern to run those millions of times

as they require less than a millisecond of runtime. Hence, the primary concern with experiments of this kind is to find good solutions. Hence, it is not important to report the number of evaluations or runtimes since they are all fairly similar. However, GALE improves much better on a majority of these models, as indicated in the following chart of Figure 4.

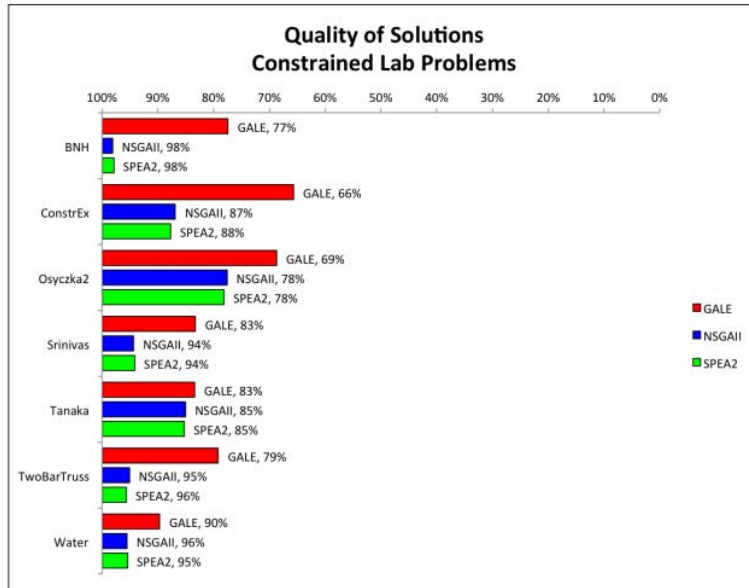


Figure 11

In summary, there were three research questions performed for each experiment, and there were four experiments:

- 1) Can GALE find solutions in fewer evaluations than NSGA-II and/or SPEA2?
- 2) Can GALE find solutions in less time than NSGA-II and/or SPEA2?
- 3) Can GALE find solutions of equivalent or better quality than NSGA-II and/or SPEA2?

The results for each experiment and research question are shown below. An “=” signifies that the algorithm was similar to another. A “-“ symbol indicates that the algorithm performed worse than another. A “+” symbol indicates that the algorithm did better, and “++” or “+++” is used to indicate orders of magnitude of improvement.

RQ#	Category	Experiment Area	GALE	NSGA-II	SPEA2
1	Evals	CDA	+++	=	=
2	Speed	CDA	+++	=	=
3	Quality	CDA	=	=	=
4	Evals	POM3	+++	=	=
5	Speed	POM3	++	=	=
6	Quality	POM3	=	=	=
7	Evals	Constrained	+++	=	=
8	Speed	Constrained	=	=	-
9	Quality	Constrained	+	=	=
10	Evals	Unconstrained	+++	=	=
11	Speed	Unconstrained	=	=	-
12	Quality	Unconstrained	+	=	=

Figure 12

The chart of Figure 5 indicates that GALE is a tool for MOO that performs vastly better than NSGA-II and SPEA2. In no case was there ever a time when GALE performed worse, and in nearly all the cases, GALE performed not just better, but two orders of magnitude better.

CONCLUSION

This thesis has shown that the popular methods in NSGA-II and SPEA2 for multi-objective optimization can be improved. In several sets of experiments, a consistent theme was shown: GALE is much faster (never much slower) and could always find solutions of equivalent quality (usually much better quality).

A core issue was identified in the standard stochastic processes of search methods like NSGA-II or SPEA2: random search can explore too much of the solution space and thus requires many evaluations. For real world models, this can incur huge computational costs and lead to complicated comprehension of the approximated Pareto frontier, due to the over-exploration of the solution space.

For example, the CDA problem is one such real world model with a high computational cost of evaluation. NSGA-II and SPEA2 were very slow (3-5 hours) whereas GALE could optimize CDA in 6-20 minutes. In a further, much larger study with CDA, NSGA-II and SPEA2 would have taken, combined, an entire year of runtime. Hence, only GALE could be used for that study. To further heighten the urgency of the problem, that larger study is just a mere subset of the total space of options to explore in CDA, and so incredible computational costs could be wasted by exploring the wrong options. This was cautioned even as GALE explored 16 modes of CDA and further work is necessary to explore other modes.

In general, these results comment on the value of directed, less-stochastic search. Whereas random search can spend too much time evaluating many thousands of solutions, directed-search can employ a decision-space clustering algorithm to assess the relative directions of more-promising solutions and then mutate old candidates in those directions.

Future work always exists to validate and reproduce findings. In this thesis, a strong effort was made to provide rigorous experimental methods with high reproducibility. For example, all of these experiments can be implemented with the JMOO Python software. Beyond reproducibility,

much other future work exists: for instance, improving the GALE algorithm and discovering other case studies to apply GALE to. Moreover, GALE is merely a search tool which is yet to be embedded in larger systems that automate the selection and employment of chosen solutions from a search.

AVAILABILITY

GALE is publicly available on the web along with all of the experiments in this thesis (except CDA, which is proprietary of NASA), for the purpose of reproducibility. GALE and all the other models and algorithms is implemented and included as part of JMOO. It is encouraged that researchers use JMOO to reproduce those results and perform experimentation of their own, and implement their own models and search tools for even broader experimentation.

The links to GALE and JMOO are given below:

- GALE is available as part of the JMOO package: <http://unbox.org/open/tags/JMOO/Gale>
- And JMOO is available at: <http://unbox.org/open/tags/JMOO>

ACKNOWLEDGEMENTS

I would like to thank the following sources:

The funding: this thesis was partially funded by several sources: the Lane Department of Computer Science and Software Engineering, the NSF grant CCF:1017330, the Qatar/West Virginia University research grant NPRP 09-12-5-2-470, as well as the NASA WVU Space Consortium.

The labs: much of the research in this thesis was conducted at the West Virginia University Modeling Intelligence Lab (the "MILL"). In addition, parts of this thesis correspond to research that was conducted at the NASA Ames Research Center. Note however, that any reference herein to any specific commercial product, process, or service by trade name, trademark, manufacturer, or otherwise, does not constitute nor imply its endorsement by the United States Government.

The people: Dr. Tim Menzies, Dr. Misty Davies, Dr. Majid Jaridi, and many more.

REFERENCES

- [1] H. Robbins and S. Monro, "A stochastic approximation method," *The Annals of Mathematical Statistics*, vol. 22, no. 3, pp. 400–407, 09 1951. [Online]. Available: <http://dx.doi.org/10.1214/aoms/1177729586>
- [2] J. Kiefer and J. Wolfowitz, "Stochastic estimation of the maximum of a regression function," *The Annals of Mathematical Statistics*, vol. 23, no. 3, pp. 462–466, 09 1952. [Online]. Available: <http://dx.doi.org/10.1214/aoms/1177729392>
- [3] A. S. Sayyad, T. Menzies, and H. Ammar, "On the value of user preferences in search-based software engineering: A case study in software product lines," in *ICSE'13*, 2013.
- [4] K. Deb, A. Pratap, S. Agarwal, and T. Meyarivan, "A fast elitist multi-objective genetic

algorithm: Nsga-ii,” IEEE Transactions on Evolutionary Computation, vol. 6, pp. 182–197, 2000.

[5] E. Zitzler, M. Laumanns, and L. Thiele, “Spea2: Improving the strength pareto evolutionary algorithm,” Swiss Federal Institute of Technology (ETH) Zurich, Tech. Rep., 2001.

[6] A. Sayyad and H. Ammar, “Pareto-optimal search-based software engineering (posbse): A literature survey,” in RAISE’13, San Fransisco, May 2013.

[7] W. Mkaouer, M. Kessentini, S. Bechikh, K. Deb, and C. M. O., “High dimensional search-based software engineering: Finding tradeoffs among 15 objectives for automating software refactoring using nsga-iii,” Aalto University School of Business, Tech. Rep., September 2013.

[8] J. D. Lohn, W. F. Kraus, and G. L. Haith, “Comparing a coevolutionary genetic algorithm for multiobjective optimization,” in Proceedings of the Evolutionary Computation on 2002. CEC ’02. Proceedings of the 2002 Congress - Volume 02, ser. CEC ’02. Washington, DC, USA: IEEE Computer Society, 2002, pp. 1157–1162. [Online]. Available: <http://dl.acm.org/citation.cfm?id=1251972.1252368>

[9] M. Harman, “Personal communication,” 2013.

[10] V. Veerappa and E. Letier, “Understanding clusters of optimal solutions in multi-objective decision problems,” in RE’ 2011, Trento, Italy, 2011, pp. 89–98.

[11] J. Krall, T. Menzies, and M. Davies, “Learning the task management space of an aircraft approach model,” in Proceedings of the 2014 AAAI Conference, ser. AAAI’14, 2014.

[12] ———, “Geometric active learning for software engineering,” Under-Review, IEEE TSE, 2014.

[13] T. Menzies, A. Butcher, D. Cok, A. Marcus, L. Layman, F. Shull, B. Turhan, and T. Zimmermann, “Local vs. global lessons for defect prediction and effort estimation,” IEEE Transactions on Software Engineering, p. 1, 2012.

Alternative Vaccination Routes in Pediatrics Today

Nadia Mardmomen
Biology
West Virginia University
Morgantown, WV 26505

ABSTRACT

More and more children today are not being fully vaccinated because of new theories stating that fully vaccinating, or strictly following the American Academy of Pediatrics vaccination schedule, is a health benefit for children. One of the largest influences to this theory is a pediatrician named Dr. Robert Sears whom wrote a book called “The Vaccine Book.” In this book he states that parents can take a different route to vaccinating their children. He has created an alternative vaccination schedule. Over the years the book, and overall idea, has picked up a lot of press from new parents. Many doctors have advised against it stating that children need all of the recommended vaccinations because the diseases are still present in today’s world. Since this new theory has picked up, more cases of these diseases are appearing in the United States such as the whopping cough and measles. Measles has seen an alarming rise in the United States since the “measles elimination” in 2000. It cannot be fully proven that it is caused solely from unvaccinated children, but according to the Centers for Disease Control and Prevention many individuals are catching the diseases because of not being vaccinated against it.

INTRODUCTION

One of the biggest mistakes made in pediatrics today is that parents are not fully vaccinating their children with the recommended vaccines. The recommended vaccine list may be lengthy, but is fully necessary to protect children from diseases that almost always lead to death. The diseases being prevented are chickenpox, diphtheria, Hib, Hepatitis A and B, Measles, Mumps, Pertussis, Polio, Pneumococcal, Rotavirus, Rubella, and Tetanus. These diseases in the past have heavily impacted society, in turn making the vaccines to prevent them very critical in a child’s life. Until recently, a large population of parents always followed the American Academy of Pediatrics’ guidelines to fully vaccinating their children. Recently more parents are opting out of vaccines or changing the timespan in which their children are receiving their vaccines because new trends are stating that these shots may not be necessary. A large influence contributing to parents opting out of the recommended vaccines is due to a doctor claiming the recommended vaccines from the American Association of Pediatrics are not fully necessary because the disease are not problems in the United States today. His claim states that now that the diseases are not such large issues in today’s societies, not all children need to be “fully” vaccinated. Dr. Sear’s has created an alternative vaccine schedule for parents that still want to vaccinate their children. The alternative schedule spreads out the vaccines much longer than the recommended list by extending it up to 5-6 years instead of 4-6 years, and by prioritizing the vaccines in order of importance. The most “important” vaccines will be given at the younger ages and then the less critical vaccines are saved for the later years of vaccinations. Also the alternative list doesn’t allow the child to receive more than two vaccines at a time. Other than the alternative schedule, there is a selective schedule parents can choose to follow. The selective schedule only includes the “bare minimum” which are

whooping cough (pertussis) and rotavirus. The selective schedule omits other important vaccines such as polio and MMR. (Feature 2012).

BACKGROUND

American Academy of Pediatrics Recommended Vaccine Schedule:

AGE	VACCINATIONS
BIRTH	Hep B
1-2 MONTHS	Hep B (2 nd dose)
2 MONTHS	Rotavirus, DTap, Hib, PCV, and Polio IPV
4 MONTHS	Rotavirus, DTap, Hib, PCV, and Polio IPV (2 nd dose of each)
6 MONTHS	Rotavirus, DTap, Hib, PCV (3 rd dose of each)
6- 18 MONTHS	Hep B and Polio IPV (3 rd dose)
6 MONTHS OR OLDER	Influenza (1 st and 2 nd dose)
12-15 MONTHS	Hib (4 th dose), PCV (4 th dose), MMR, Varicella
12-23 MONTHS	Hep A
15-18 MONTHS	DTaP (4 th dose)
18 MONTHS OR OLDER	Hep A (2 nd dose)
4-6 YEARS	DTaP (5 th dose), Polio IPV (4 th dose), MMR(2 nd dose), Varicella (2 nd dose)
11-12 YEARS	Tdap, MCV4, HPV

*CDC recommended immunization schedule for children birth to 12 years (“Choosing a Vaccination Schedule for Your Child” 2012).

Dr. Robert Sear’s Vaccine Schedule:

AGE	VACCINATION
2 MONTHS	Rotavirus, DTap

3 MONTHS	PCV, Hib
4 MONTHS	Rotavirus, DTaP (2 nd dose)
5 MONTHS	PCV, Hib (2 nd dose)
6 MONTHS	Rotavirus, DTaP (3 rd dose)
7 MONTHS	PCV, Hib (3 rd dose)
9 MONTHS	Polio, Influenza (given until 19 years old)
12 MONTHS	Polio (2 nd dose), Mumps (separated from MMR)
15 MONTHS	PCV, Hib (4 th dose)
18 MONTHS	DTaP (4 th dose), Varicella
2 YEARS	Rubella (separated from MMR), Polio (3 rd dose)
2.5 YEARS	Hep B, Hep A
3.5 YEARS	Hep B (2 nd dose), Measles(separated from MMR)
4 YEARS	DTaP (5 th dose), Polio (4 th dose)
5 YEARS	MMR (2 nd dose of each vaccine)
6 YEARS	Varicella (2 nd dose)
12 YEARS	HPV (1 st and 2 nd dose- 12 years and 2 months)
13 YEARS	HPV (3 rd dose) MCV4

* **Dr. Robert Sear’s Recommended Alternative Vaccine Schedule** (“Choosing a Vaccination Schedule for Your Child” 2012).

RESULTS

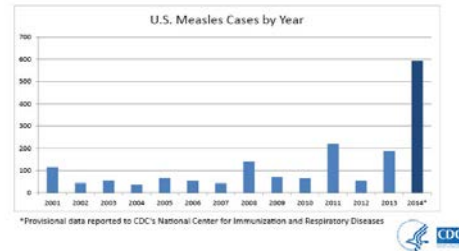
Resulting from these alternative and selective vaccine schedules are increases in diseases that their vaccines are taken later or not taken at all. Whooping cough and measles are two of the more common diseases out breaking in today’s world. One of the largest increases of cases and outbreaks is with the disease, Measles. According to the Centers for Disease Control and Prevention, the United States has had its largest outbreak of measles since 2000. In 2000 was the measles elimination, making this year since then the highest number of people developing the disease. Also, the CDC states that the reason for the outbreaks are people visiting areas where the disease it more common and developing the disease because of not being vaccinated “Measles Cases and Outbreaks” 2014).

Measles Cases and Outbreaks

January 1 to August 1, 2014*

593 Cases reported in 21 states: Alabama, California, Connecticut, Hawaii, Illinois, Indiana, Kansas, Massachusetts, Minnesota, Missouri, New Jersey, New York, Ohio, Oregon, Pennsylvania, Tennessee, Texas, Utah, Virginia, Washington, Wisconsin

18 Outbreaks representing 89% of reported cases this year



DISCUSSIONS

According to the American Academy of Pediatrics vaccines are scheduled based off of two things. The first factor is age and the second factor is the need to vaccinate a child as early as possible. When it comes to factoring in the child's age, the AAP wants to vaccinate a child when the body's immune system will work at its maximum efficiency. As the immune system advances in a child's life it is critical to vaccinate he or she when the body will respond the best. Next, the second factor is critical because a child needs to be vaccinated as soon as possible to avoid chances of coming in contact with the diseases (The Childhood Immunization Schedule: Why Is It Like That? 2008). The reason that Dr. Sear's vaccine schedule is dangerous is because he has scheduled vaccines at different times and has spaced them much further apart. It is critical that a child receives a vaccine when the body can handle it best. Dr. Sear's theory has not been scientifically tested, and should not be consider reliable until there is evidence supporting it.

FUTURE RESEARCH

Considering Dr. Robert Sear's theory has not been actually tested, parents should not trust the theory completely until scientific research is conducted. It could be concluded that more outbreaks in the recent years could be due to the number of children not being vaccinated. Future plans should involve studying children that are not being fully vaccinated compared to children being fully vaccinated in specific regions to see how the number of diseases outbreaks is being affected. The American Academy of Pediatrics have thoroughly studied vaccinations, but if parents are choosing to not use every vaccines they should test to see if there is a healthier vaccination alternative.

CONCLUSION

Parents should not assume that these new theories are accurate because more and more cases of diseases, that were once considered almost eliminated, are having a rise again in today's society. Dr. Robert Sears is depending on other children to be vaccinated when all children should worry about being individually vaccinated. These diseases are still present in other countries and could potentially harm children that seem to be protected in the United States. Until new theories about

vaccinating children are scientifically proven, one should not assume alternative routes are safe, or even healthy.

ACKNOWLEDGEMENTS

NASA West Virginia Undergraduate Space Grant Consortium West Virginia University Morgantown, WV.

Dr. Joseph Momen Pediatrics Associates 7 Chenoweth Drive Bridgeport, WV.

REFERENCES

"Choosing a Vaccination Schedule for Your Child." *Focus Autism Inc*, June 2012.: n. pag. Focus Autism Inc. Web. <http://focusautisminc.org/wp-content/uploads/2012/06/CDC-Alternative-Vaccine-Schedule.pdf>

Feature, Katherine KamWebMD. "Robert Sears' Alternative Vaccine Schedule for Babies." *WebMD*. WebMD, 2 July 2012. Web. 1 Aug. 2014. <<http://www.webmd.com/children/vaccines/features/robert-sears-alternative-vaccine-schedule>>.

"Measles Cases and Outbreaks." *Centers for Disease Control and Prevention*. Centers for Disease Control and Prevention, 18 Aug. 2014. Web. 1 Aug. 2014. <<http://www.cdc.gov/measles/cases-outbreaks.html>>.

"The Childhood Immunization Schedule: Why Is It Like That?" *The Childhood Immunization Schedule: Why Is It Like That?* (n.d.): n. pag. *American Academy of Pediatrics*. American Academy of Pediatrics, Oct. 2008. Web. 2 Aug. 2014. <<http://www.aap.org/en-us/advocacy-and-policy/Documents/Vaccineschedule.pdf>>.

IMPLEMENTATION OF A ROTATING DIFFUSOR IN THE NASA LARC STRUCTURAL ACOUSTIC LOADS AND TRANSMISSION (SALT) FACILITY

Cody O'Meara
Applied Physics
West Virginia Wesleyan College
Buckhannon, WV 26201

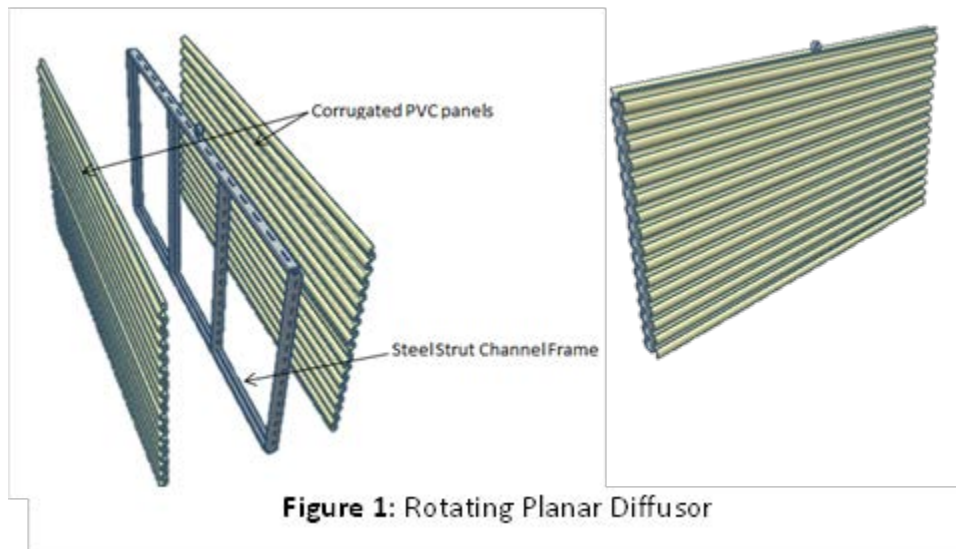
ABSTRACT

In order to reduce the effect of the strong modal characteristics at low frequencies present in the NASA LaRC SALT facility, a prototype rotating diffuser targeting frequency bands down to 80 Hz has been implemented. The purpose of the diffuser is to modulate the room modes during acquisition, which is expected to average out the effects of room modes and reduce variance in the ensemble averaged results. We evaluated a low frequency resonant absorber with and without a rotating diffuser. The rotating diffuser appeared to improve the quality of the test data by reducing the variance in the noise reduction spectrum attributed to introducing the resonator array to the room. Further analysis of the data is currently underway.

INTRODUCTION

Recently, experimental evaluation of resonant, narrowband noise control concepts have been performed in the 278 m³ reverberation room at the NASA LaRC SALT facility. The typical approach taken when evaluating noise control devices is to determine the absorption area of the device by measuring the band-limited reverberation time (i.e. T60) in the room with and without the device present or active. This results in fractional octave, e.g. 1/3 octave, band-limited data and often precludes the evaluation of narrowband performing resonant noise control devices, which are currently of interest [1]. Due to this limitation, a non-standard approach is taken, whereby the narrowband Noise Reduction (NR) attributed to the noise control device is measured directly. A NR test involves the measurement of the space averaged room level during steady state ensonification of the room with and without the noise control device present in a two-step process. The difference of the two resulting room level spectra provide the NR attributed to the concept. At low frequencies, the variance of the NR spectrum makes it difficult to evaluate the performance of a resonant noise control device, especially when the NR attributed to the device is particularly low or narrowband in character. In order to confidently evaluate a device such as this, the measurable performance can be increased by increasing the test article size, which can be costly, or the variance of the measurement can be reduced by introducing a rotating diffuser to increase the *effective* room diffusivity in a time averaged sense. The benefit of the rotating diffuser becomes particularly apparent during the direct measurement of NR due to a resonant noise control device. Specifically, introducing a strong, local impedance change in the room in the form of a resonant noise control device has been found to “shift” or “split” the otherwise fixed room modes. It is postulated that this increases the variance of the resulting NR spectrum and is an artifact of the room and not indicative of the performance of the noise control concept on average. While the diffuser panel rotates, it continuously warps the room shape in time, while also continually redirecting the energy flow in space. The combination of these two events helps to create a more

diffuse field by continuously shifting both modal frequencies and incidence angles during testing [2]. This effect has been found to average out the mode splitting effect produced by the resonator. A schematic of the rotating diffusor concept is shown in Figure 1.



The methodology of this project can be summarized in six steps. The first consisted of performing background research on diffusors used in reverberation rooms. Next, 10' x 6' diffusor dimensions were established based on practical limitations such as maintaining clearance with the microphone array in the reverberation room. This was followed by material ordering and fabrication of the diffusors. The diffusors were then evaluated in the reverberation room by conducting room level acquisitions at fixed diffusor positions and NR tests with and without the diffusor actively rotating during acquisition. A numerical model of the room was created in parallel using the Finite Element (FE) modeling software Cubit, and the Salinas FE solver was subsequently used to assess the ability of various diffusor configurations to effectively modulate room modes by viewing relative changes in the low frequency room modes during simulated diffusor rotation.

SUMMARY OF RESEARCH

Referring to the original project goals, the mission was to design, model, and implement a prototype rotating diffusor in the SALT facility's reverberation room in order to reduce the variance of measurements by modulating the room modes during data acquisition. Because of the complexity of this project, it was necessary to split the tasks into two different subsets: namely the design and fabrication of the diffusors, and the modeling. This report focuses on the design, fabrication, and experimental evaluation of the diffusors.

Several factors were involved when determining what type of diffusor to build. Two main constraints were immediately apparent when this project was assigned: time, and ease of fabrication. With only a ten week period to design, build, test, and analyze the effectiveness of the diffusors, it was necessary to choose a design that would allow for a quick and simple fabrication without taking away from its ability to modulate the room modes. Because of this, it was determined that a rotating planar diffusor panel would be built, as opposed to more complex conical shaped designs.

Next, the dimensions needed to be determined. The panel needed to be large enough to reflect low frequencies well, but also small enough to be able to be easily handled by two people during installation, while also maintaining a size that allows it to be rotated without rearranging the existing microphone array. Because of the restrictions provided by the microphone array in the room, it was determined that the width would be ten feet, as this was the maximum width that could be obtained without having to rearrange the microphones. A height of six feet was also determined, as anything taller would have been difficult to move in and out of the reverberation room's door.

Material choice was also researched, as the materials must be light enough to install and remove from the room, while also remaining acoustically solid in order to reflect the sound waves. Because of these factors, a steel strut channel frame was built for stability, while corrugated PVC panels were attached to both sides by punching holes around the perimeter of the PVC panels and attaching them to the steel frame with zip ties, as seen in Figure 1. No filler material was installed in the space between the panelings, however, it may be advantageous to do so in the future.

TESTS CONDUCTED

Once the diffusor panel was complete, it was then installed into the SALT facility's 278 m³ reverberation room as shown in Figure 3. In order to properly test the panels, the microphones in the room had to be calibrated using a Brüel & Kjær model 4134 piston phone microphone calibrator. This calibrator sends a pure tone to the microphone, which is then matched in the system to ensure an exact calibration. The equipment and instrumentation used for testing can be seen in Table 1 and is further described in [3]. Room sound pressure level (SPL) and noise reduction (NR) measurements were taken with the panel either stationary or rotating in order to determine its effectiveness at modulating the room modes, as well as its ability to average out the mode splitting effect produced by a resonant noise control device evaluated during NR measurements. Initially, the diffusor was rotated manually at approximately 5 RPM before the use of steady aerodynamic force via fixed fans was found to be more favorable. The diffusor panel was hoisted near the center of the room from a chain that is mounted to a swivel as shown in Figure 2. An arrangement of three or more box speakers, as shown in Figure 3, were used to excite the room with steady state noise while the sound pressure levels were measured with twelve microphones placed randomly throughout the room. Tables 2-4 show the types of tests that were run. When evaluating a resonant noise control device, such as the resonator array panel shown in Figure 4, room sound pressure levels were acquired with both open and closed inlets in order to determine the NR attributed to the resonator array.

Figure 2: Diffusor panel installed in center configuration, 0°, mounted on swivel



Figure 3: SALT facility with speaker box locations in reverberation room

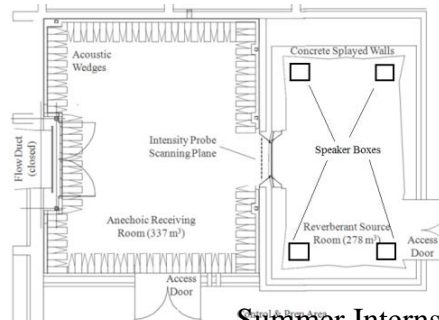


Figure 4: Resonator array panel with open (left) and closed (right) inlets.

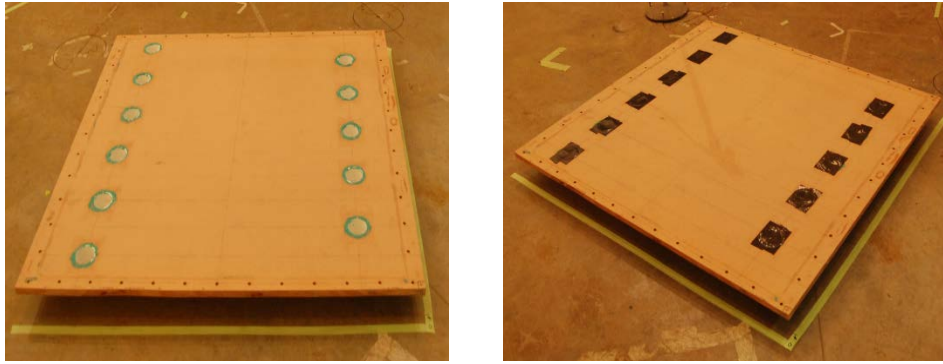


Table 1: Instrumentation and equipment used for testing.

Description	Manufacturer	Model/Type
½-inch Prepolarized Condenser Microphones	G.R.A.S.	40AO
½-inch Microphone Preamplifiers	G.R.A.S.	26CA
ICP Signal Conditioner	PCB Piezotronics	584A
Multi-Channel Amplifier	Rane	MA6S
Signal Switching System	Precision Filters	PF 464K
Chassis with Dynamic Signal Acquisition Modules	National Instruments	NI PXI-1045 NI PXI-4472B (3)
Acoustical Calibrator	Brüel & Kjær	4231
Two-way Speaker Box	JBL Professional	JBL JRX115

Table 2: Fixed diffusor angle tests.

Output File	Drive Signal	Diffusor Angle
roomSPL_10_Jul_2014_14_01_46	Uncorrelated Random	30°
roomSPL_10_Jul_2014_14_09_06	Uncorrelated Periodic Random	30°
roomSPL_10_Jul_2014_14_11_36	Correlated Periodic Random	30°
roomSPL_10_Jul_2014_14_41_57	Uncorrelated Random	60°
roomSPL_10_Jul_2014_14_48_33	Uncorrelated Periodic Random	60°
roomSPL_10_Jul_2014_14_54_09	Correlated Periodic Random	60°
roomSPL_10_Jul_2014_15_02_53	Uncorrelated Random	90°
roomSPL_10_Jul_2014_15_47_38	Uncorrelated Periodic Random	90°
roomSPL_10_Jul_2014_15_49_27	Correlated Periodic Random	90°
roomSPL_10_Jul_2014_16_00_30	Uncorrelated Random	120°
roomSPL_10_Jul_2014_16_07_43	Uncorrelated Periodic Random	120°
roomSPL_10_Jul_2014_16_09_57	Correlated Periodic Random	120°
roomSPL_10_Jul_2014_16_18_10	Uncorrelated Random	150°
roomSPL_10_Jul_2014_16_25_12	Uncorrelated Periodic Random	150°
roomSPL_10_Jul_2014_16_27_07	Correlated Periodic Random	150°

Table 3: Cases acquired during fixed or rotating diffusor, for placement of the resonator array test article during ensemble averaging procedure

Output File	Diffusor Angle	Resonator Location	Inlet Open/Closed
roomSPL_11_Jul_2014_10_49_59	0°	1	Closed
roomSPL_11_Jul_2014_11_08_43	Rotating	1	Closed
roomSPL_11_Jul_2014_11_19_36	0°	2	Closed
roomSPL_11_Jul_2014_14_23_39	Rotating	2	Closed
roomSPL_11_Jul_2014_14_54_05	0°	3	Closed
roomSPL_11_Jul_2014_15_10_03	Rotating	3	Closed

Table 4: Series of fixed vs. rotating NR tests with no resonant test article present.

Output File	Diffusor Angle
roomSPL_24_Jul_2014_09_51_22	0°
roomSPL_24_Jul_2014_09_51_22	0°
roomSPL_24_Jul_2014_10_04_52	0°
roomSPL_24_Jul_2014_10_13_19	0°
roomSPL_24_Jul_2014_10_19_11	0°
roomSPL_24_Jul_2014_10_25_02	0°
roomSPL_24_Jul_2014_10_30_54	0°
roomSPL_24_Jul_2014_10_36_46	0°
roomSPL_24_Jul_2014_10_42_38	0°
roomSPL_24_Jul_2014_10_49_13	0°
roomSPL_24_Jul_2014_11_10_15	Rotating
roomSPL_24_Jul_2014_11_16_07	Rotating
roomSPL_24_Jul_2014_11_22_00	Rotating
roomSPL_24_Jul_2014_11_27_52	Rotating
roomSPL_24_Jul_2014_11_33_45	Rotating
roomSPL_24_Jul_2014_11_39_38	Rotating
roomSPL_24_Jul_2014_11_45_30	Rotating
roomSPL_24_Jul_2014_11_51_23	Rotating
roomSPL_24_Jul_2014_11_57_18	Rotating
roomSPL_24_Jul_2014_12_03_14	Rotating

DATA REDUCTION AND RESULTS

In order to evaluate the effectiveness of the diffusor, the raw data had to be compiled into an interpretable format. The first data that is used relates to the space averaged room pressure power spectral density (PSD) measured when the PVC panel diffusor is mounted in the center of the room and fixed at different angles (refer to Table 2). The pressure PSD is determined by

$$PSD = \frac{\langle p^2 \rangle}{df}$$

where df is the spectral resolution, which is 0.1 Hz, and $\langle p^2 \rangle$ is the time and space averaged mean squared pressure acquired from 12 reverb room microphones during steady state random noise excitation, as seen in Figure 5. The modes begin to be effected at higher frequencies, typically above 200 Hz. However, the effects can still be seen at these lower frequencies.

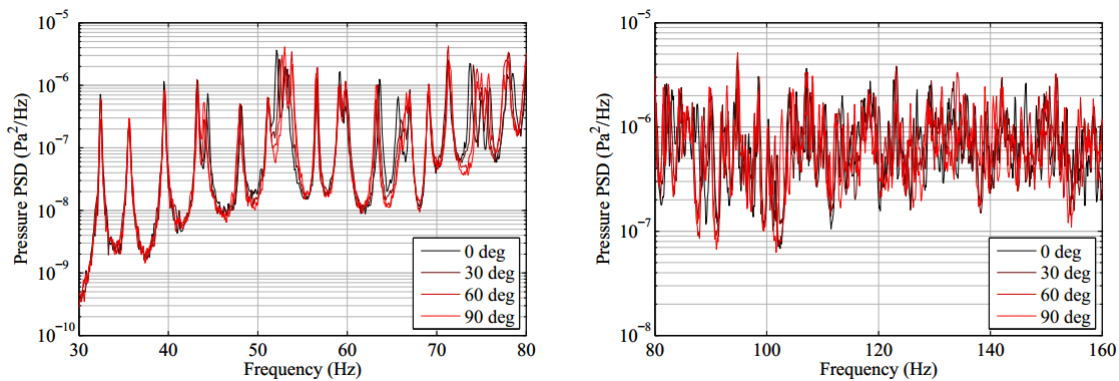


Figure 5: PSD spectrum for fixed diffusors ranging from 0°-90°, and 30-160 Hz.

When measuring the NR spectrum of the resonator array shown in Figure 2, the space and time averaged room sound pressure spectra are measured with and without the resonator inlets closed. The NR spectrum is the dB difference between these two measurements and shows the relative change in room level with the resonator array open and closed. The noise reduction is calculated using

$$NR = 10 \log_{10} \frac{\overline{\langle p^2 \rangle}_{closed}}{\overline{\langle p^2 \rangle}_{open}}$$

where $\overline{\langle p^2 \rangle}$ is the space and time averaged mean square pressure acquired from 12 reverb room microphones during steady state random noise excitation and averaged over 3 test article locations. Figure 6 and Figure 7 shows the results. The resonator array used in this example exhibits positive narrowband NR at the first and second “quarter wave” resonances near 95 Hz and 280 Hz respectively. The ability to perceive the resonator array NR is improved by the reduced variance, as shown in Figures 6 and 7, especially at higher frequencies.

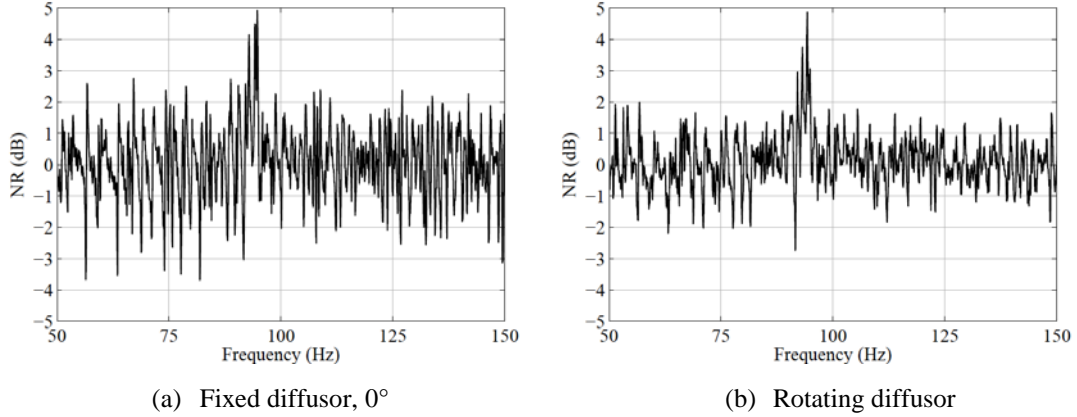


Figure 6: The NR spectrum for a fixed diffusor and a rotating diffusor, 50-150 Hz.

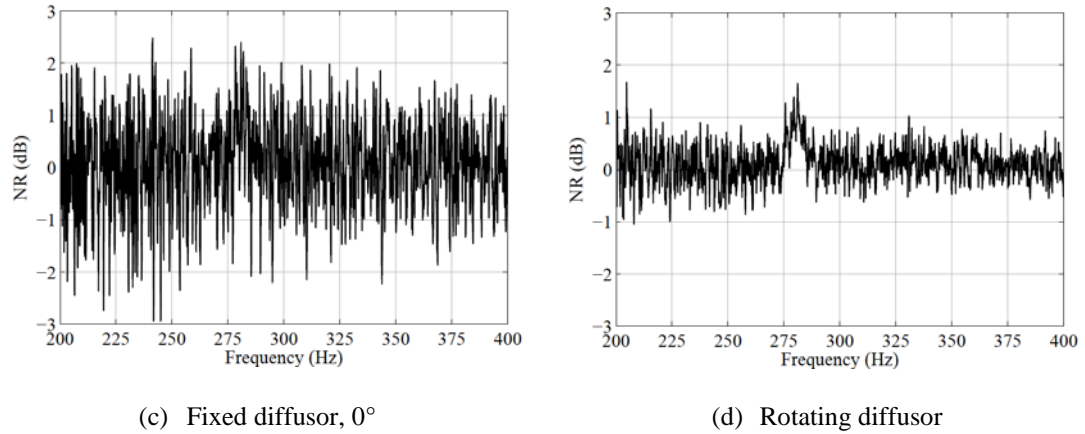


Figure 7: The NR spectrum for a fixed diffusor and a rotating diffusor, 200-400 Hz.

While the NR spectrum shows an apparent reduction in variance that increases with frequency, it can still be difficult to quantify the effect of the rotating diffusor. In an attempt to further characterize the frequency dependent effect that using the diffusor has on the variance of measured NR spectra, a series of additional tests were conducted (see Table 4) with no test article to the room to provide a set of many NR spectra with and without use of the rotating diffusor. These NR measurements are referred to as zero-NR measurements, because the expected NR from subtracting out two measurements of room level spectra with no test article in place during either measurement is zero. In order to have a better understanding of the variance in the NR spectra, it helps to make histograms of the narrowband NR values within specific frequency bands, namely 1/3 octave bands. Fixed and rotating diffusor histograms were calculated in this way from both the resonator array NR results and the zero-NR measurements and are shown in Figures 6-7. To more clearly view the relative difference in spread between the fixed and rotating diffusor NR values, vertical dashed lines are also shown in Figures 8-9 representing +/- one standard deviation, which can be found using

$$s = \left(\frac{1}{n-1} \sum (x_i - \bar{x})^2 \right)^{1/2}$$

Where n is the number of elements in the sample, x is the vector of all points in the NR spectrum within each 1/3 octave band with 0.1 Hz resolution, and $\bar{x} = \frac{1}{n} \sum_{i=1}^n x_i$. The y axes are normalized by dividing the bin counts by the total area under all the bins.

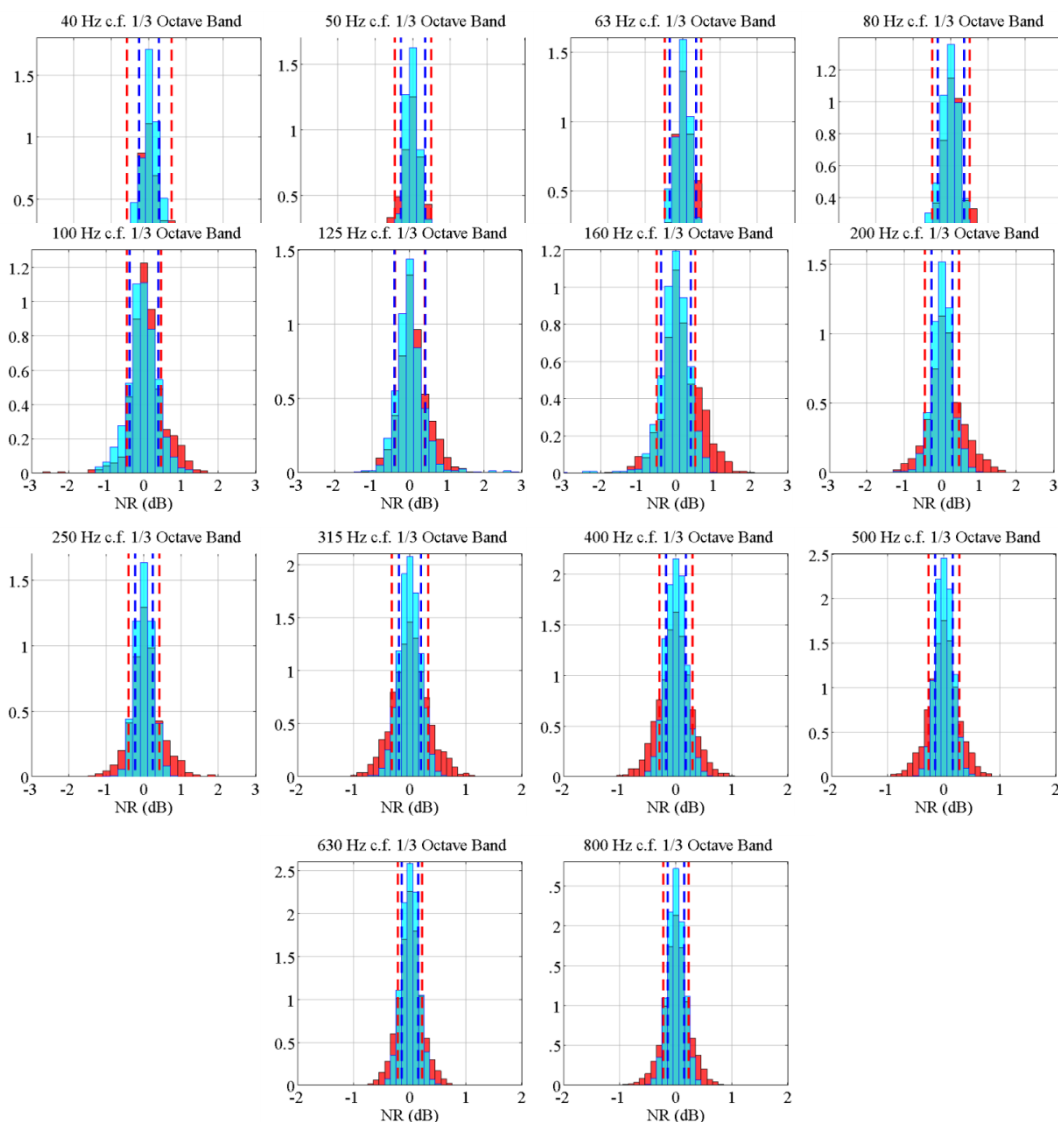


Figure 8: Histograms showing the NR in the room at specific frequencies with no resonator present, and when the resonator is present (right).

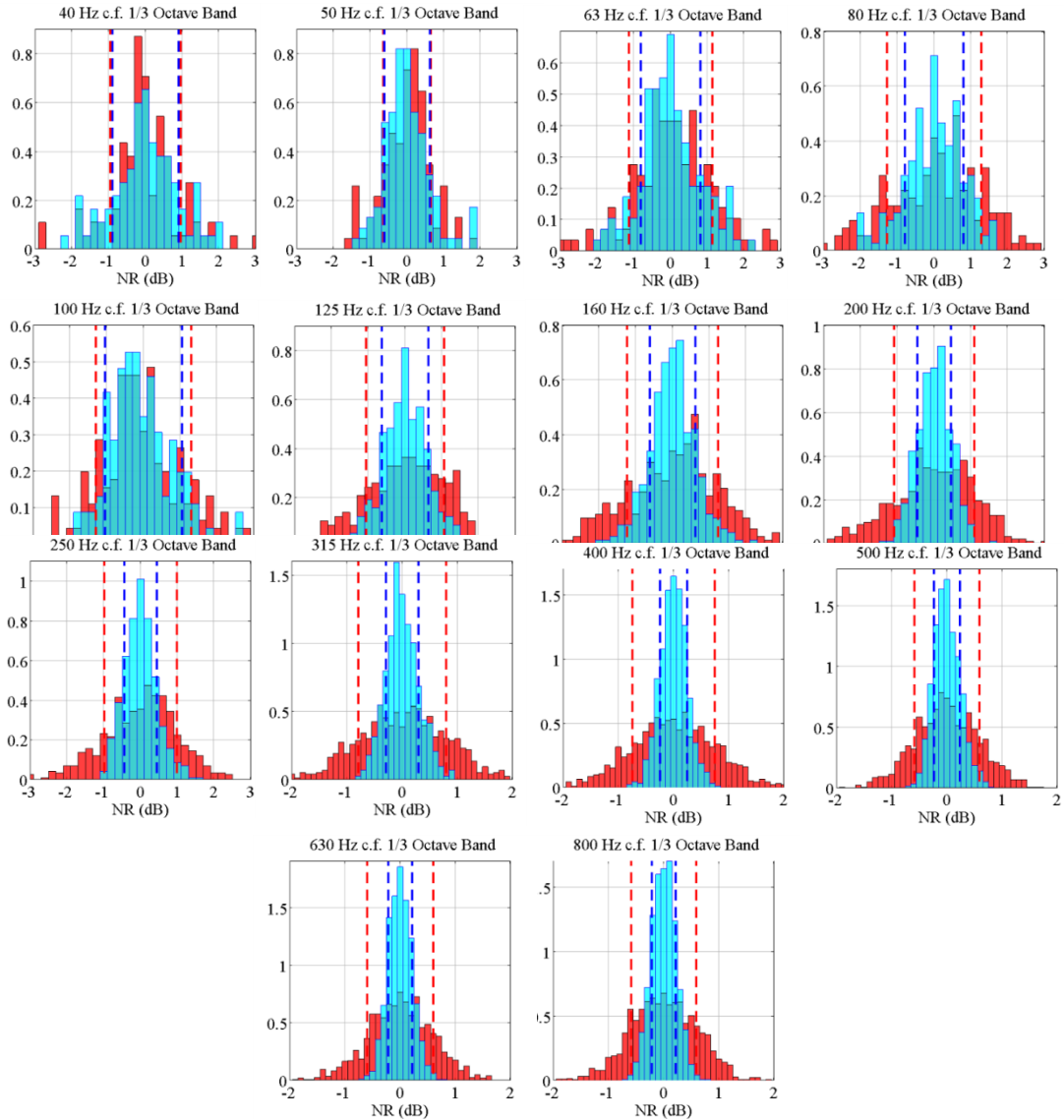


Figure 9: Histograms showing the NR in the room at specific frequencies with the resonator present.

Due the NR's being determined from acquisitions using no test article, the mode shifting due to the test article's effect on the room modes were not there, so the variance was relatively small, and the effect of the diffuser was not as significant.

CONCLUSION

An experimental assessment of the ability of a rotating diffuser to reduce the variance of reverberation room measurements by modulating the room modes during data acquisition has been carried out on a prototype diffuser panel that is either held stationary or rotated at approximately 3 RPM using a fan during data acquisition. Measurements of space and time averaged room sound pressure levels acquired during steady state noise excitation was used to analyze the effectiveness of the prototype diffuser panel when evaluating a candidate resonant noise control device. Diffuser

rotation appeared to improve the quality of the test data by reducing the variance in the noise reduction (NR) attributed to introducing a resonator array, especially at higher frequencies. Interestingly, the variance reduction when using the rotating diffusor was found to be much less significant when no test article was present, which suggests that the diffusor is most effective at reducing variance in the NR spectrum due to the mode shifting effect of local impedance boundary condition changes introduced by a resonant noise control device. Due to the promising initial results of the prototype diffusor panel and its ability to reduce variance in measurements, further investigation into a more permanent diffusor panel and rotational drive system seems advantageous.

ACKNOWLEDGEMENTS

The author gratefully acknowledges the West Virginia Space Grant Consortium, Albert Allen, NASA Langley Research Center, and the LARSS Program for their role in making this summer, as well as this project a success. None of this would be possible without their help.

REFERENCES

- [1] Allen, A. R., & Schiller, N. H. NASA LaRC, (2014). *Transmission loss and absorption of corrugated core sandwich panels with embedded resonators*. Fort Lauderdale, FL: Noise-Con.
- [2] Schultz, T. Diffusion in reverberation rooms. *Journal of Sound and Vibration*, 17-28.
- [3] Grosveld, F. W. (2013). *Characterization of the reverberation chamber at the NASA Langley structural acoustics loads and transmission (SALT) facility* (Report No. NASA/CR--2013-217968). Hampton, VA: NASA.

Developing and Verifying a Computer Model to Predict the Flight Characteristics of a Water Rocket

Corey Rhodes
Applied Physics
West Virginia Wesleyan College
Buckhannon, WV 26201

ABSTRACT

One of NASA's goals is to inspire and educate students in the science, technology, engineering, and mathematics (STEM) disciplines. To support this goal, a water rocket flight experiment is being designed with the intent of being demonstrated to high school students to increase their interest in STEM. More specifically, our goal with this experiment is to introduce students to computer modeling a physical system, as well as the basics of rocket flight and aerodynamics. Additionally, this experiment introduces the concepts of microcontroller programming and data acquisition techniques. Work for this summer focused on developing a computer-based simulation model to predict the flight trajectory performance in addition to developing, implementing, and testing a flight data measurement and parachute recovery system for the water rocket flight experiment.

The first step in this effort was to develop a computer model to predict the flight characteristics of the rocket. This task is complicated by the fact that water rockets have three different flight phases that are described by different sets of equations. Subsequently, the model had to be created by deconstructing the flight into its three main phases and entering the appropriate equations of flight into a computer program to describe the important variables of the flight. Once completed, the model could be used to predict the acceleration of the rocket over the entire flight time. A simple Euler integration was then performed to give velocity as a function of time. Performing the integration once more would then give the position as a function of time or trajectory of the rocket.

Water rockets are a type of model rocket constructed from a used plastic soda bottle that employs water as its propellant. Water rockets are built to be lightweight, in order to fully utilize the limited thrust available from them. The rocket also has to be reusable, necessitating the use of a parachute recovery system. In addition, the rocket needs to have data logging capabilities so that the predictions made by the computer model could be validated. This was accomplished by adding an onboard accelerometer and pressure altimeter, which were controlled by an Arduino microcontroller. For this experiment, a smaller version of the standard Arduino was used (Arduino mini pro) to reduce weight. The Arduino was programmed to read data from the accelerometer and pressure altimeter and then write this data to an onboard micro SD card in real-time. This data was then collected and compared to the output of the computer model to determine how close the correlation was between the predicted and measured rocket flight data. Early results show that the model is accurately predicting the overall trend of the rocket's acceleration throughout the flight, but there will need to be more testing conducted with a higher data sampling rate to confirm the maximum acceleration and altitude the rocket achieves during its flight.

INTRODUCTION

When I began my work on this project back in June, I was tasked with solving four outstanding problems that remained from preliminary work conducted in summers past. Once these problems are solved, this project will be available as a flight experiment to high school students in support of NASA's mission to educate and inspire young students in the STEM disciplines. The first of these problems was adjusting the existing computer simulation of the water rocket's flight so that the model more accurately depicted what was being observed in the field during actual test flights. The second of these problems was the reusability of the water rocket. In the past, the rockets would be launched and subsequently crash landed. This seriously reduced the longevity of any instrumentation that was flown on the rocket, as well as the structural integrity of the rocket itself. To rectify this problem, I was to implement a parachute recovery system into the rocket to diminish the amount of repairs that needed to be performed after each flight, as well as allow for more sensitive and expensive instrumentation to be flown without the risk of damage due to high g-forces experienced in a crash landing. The third problem was that more instrumentation needed to be implemented into the rocket so that a wider array of data from the flight could be logged. The addition of a parachute recovery system allowed for the rocket to have more data collection capabilities. The purpose of this was so that data could be collected on more aspects of the flight in order to truly analyze the accuracy of the refined computer model. The fourth problem was that a launch detection system needed to be developed. With the addition of data logging equipment, a system was required to reliably tell the onboard electronics when the rocket had left the launch pad so that data logging procedures could commence.

BACKGROUND

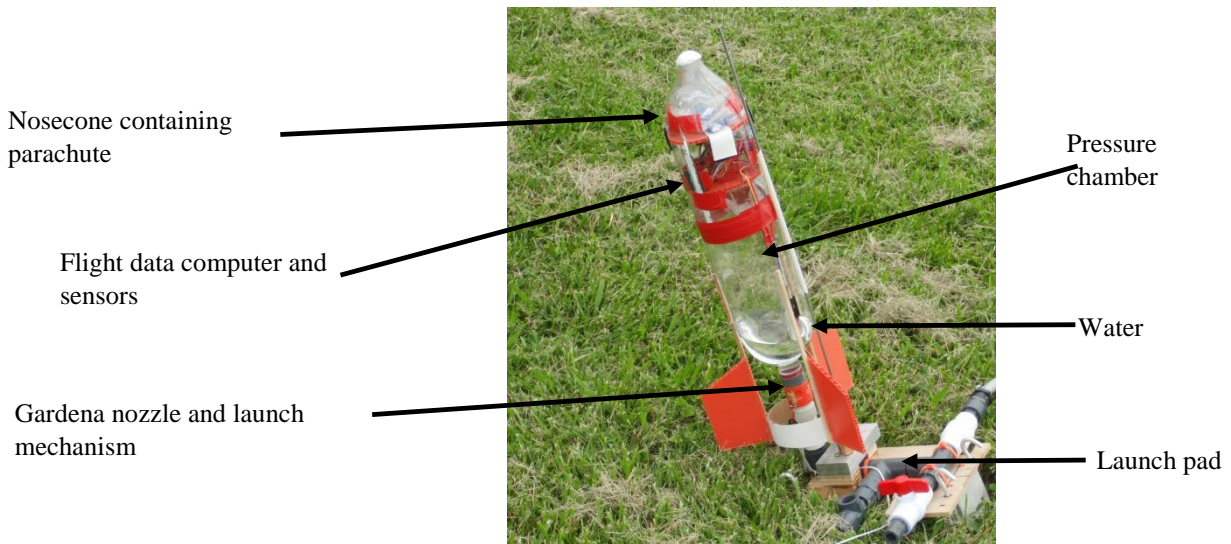


Fig. 1 First design of the water rocket on the launch pad

Work for this summer revolved around the use of water rockets. Water rockets function by adding water to a vessel and subsequently pressurizing it with air or another gas. Forward thrust is then achieved when water is expelled from one end of the rocket through a nozzle by the pressurized gas expanding. Surprisingly, using materials as commonplace as water and air, water rockets can achieve upward velocities of 70 m/s or 157 mph (Wheeler, 2002). Due to the manner in which the rocket produces thrust, there are actually multiple thrust phases as opposed to one continuous flight. The first of these phases occurs immediately after launch. During this phase, all of the thrust is produced by water being expelled from the pressure chamber through the nozzle. This phase occurs quite rapidly, usually on the order of between one and two-tenths of a second (Wheeler, 2002). Thrust produced in this phase accounts for the majority of the entire thrust produced by the rocket and can be calculated by multiplying the mass flow rate of the water by its exit velocity. After all of the water contained in the vessel has been exhausted, thrust will then be produced by the remaining air pressure. The remaining pressurized air in the tank will continue to expand out through the nozzle until the pressure inside the bottle normalizes back to atmospheric pressure. Though the time required for the pressure to equalize inside the bottle takes almost as long as the water thrust phase (Wheeler, 2002), the air produces significantly less thrust than the water due to water weighing significantly more than the air. Finally after the pressure inside the vessel has equalized, the rocket will no longer be generating any thrust and will begin quickly decelerating. This final phase is known as the coast phase, and will last until the rocket has completed its flight.

PROJECT

Improving the Computer Model

I first tackled the task of refining the water rocket computer model. Originally, the model treated thrust generated during the air impulse phase as negligible and based all of its calculations from the water thrust phase. Past observations had shown that this method was not accurate enough as the model would significantly under predict the altitude at apogee that the rocket would attain. Modeling the air thrust phase of a water rocket however, is slightly more challenging than the water phase due to air being a high speed compressible gas. The process for deriving the governing equations for these relationships tend to be more complex than those used to model the water phase. For example, the equation below is used to calculate the time-variant chamber pressure (Worcester & Frederick, 1992).

$$P_{t2} = \frac{P_{t1}}{\left(\frac{t}{\frac{2}{(\gamma - 1) * \sqrt{\gamma RT}} * \frac{V}{A} * \left(\frac{\gamma + 1}{2} \right)^{\frac{\gamma + 1}{2\gamma - 2}} + 1 \right)^{\frac{2\gamma}{\gamma - 1}}}$$

P_{t1} = current chamber pressure

t = time

γ = specific heat capacity ratio

V = chamber volume

R = ideal gas constant

Once the pressure inside the chamber has been calculated, the thrust generated by the expanding air can be seen below.

$$F_T = c_F * P_c * A_N$$

c_F = thrust coefficient
 P_c = chamber pressure

The thrust coefficient is a correction factor that is given by the equation below (Worcester & Frederick, 1992).

$$c_F = \sqrt{\gamma^2 * \left(\frac{2}{\gamma + 1}\right)^{\frac{2\gamma}{\gamma - 1}} + \left(\frac{2}{\gamma + 1}\right)^{\frac{\gamma}{\gamma - 1}} - \frac{P_a}{P}}$$

γ = specific heat capacity ratio

P_a = atmospheric pressure

Once the thrust generated by the air phase had been accounted for, testing could begin to examine if the computer model was now making more accurate predictions.

Data Logging with Arduino

With the computer model modified, work turned to the rocket itself. In order to validate the predictions made by the computer model, we would need to equip the rocket with data logging capabilities and determine if the flight data matched the model. Therefore, the rocket was equipped with an adafruit ADXL 345 Triple-axis accelerometer controlled by an Arduino microcontroller. It was decided to use an Arduino microcontroller due to the ease of its programming and low cost. Arduinos also come in many different form factors and sizes, which allows for an Arduino that is tailored to the needs of the experiment. In this case, something that was lightweight was needed in order to achieve the best thrust-to-weight ratio possible. An Arduino mini pro was chosen to fill this role as it is one of the lightest Arduino's available. Unfortunately, the minimal weight comes with a cost. The Arduino mini pro lacks the internal RAM necessary to log an entire flight worth of data. As a result, data must be transferred to an onboard SD card. One problem that results from this is, while data can be written from the accelerometer to the internal RAM at a rate of 500 Hz, data written in real-time to an SD card occurs at a much slower rate of 40 to 50 Hz. Considering the thrust phase of a water rocket is over within the first two-tenths of a second, a data rate of only 40 to 50 Hz could miss important events that would occur during the initial thrust phase. For this reason, later tests were conducted by writing as much data as possible during the initial thrust phase to the internal RAM. Then once the RAM was full, subsequent data would be written straight to the SD card when a higher data rate was not as crucial.

The Launch Detection System

Now that the rocket was equipped with data logging capabilities, the Arduino and accelerometer needed a way to know when the rocket has left the pad and to start recording data. For this purpose, it was decided that a US5881 Hall Effect sensor placed on a tail fin be used. These sensors work by outputting a voltage based on the presence or absence of a magnetic field. So by wiring the Hall Effect sensor to the Arduino and placing a magnet on the launch pad, the Arduino could determine when launch occurred. The Arduino was set to continuously read the Hall sensor once it is powered on. If the Hall sensor detected that it was in the presence of the south pole of the magnet, it would send a signal to the Arduino, which would subsequently power a LED light to inform that the sensor sees the magnet and to wait before proceeding with data collection. Once the rocket launches and leaves the launch pad, the Hall sensor would send the Arduino another signal to allow data collection procedures to commence.

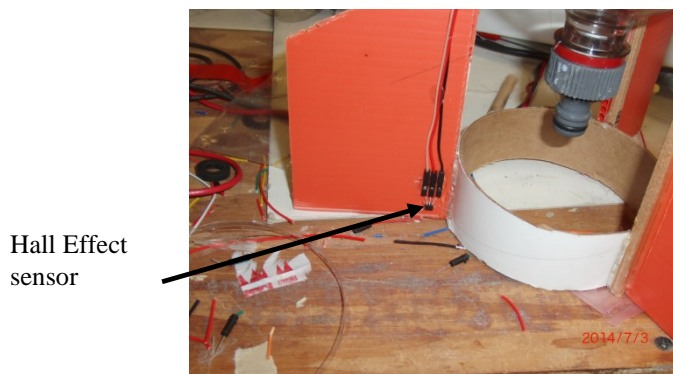


Fig. 2 Hall Effect sensor located on one of the rocket's three tail fins



Fig. 3 Overhead view of the onboard electronics

The Parachute Recovery System

The final problem that needed to be solved was the implementation of a parachute recovery system. The first design that was implemented involved using a mini servo motor to turn a metal rod, which would then release the rubber bands that held the nosecone on top of the rocket and release the parachute contained beneath it into the airflow. Though it cannot be seen in the picture below, the servo is tucked underneath the parachute. This design is based on a concept by <http://www.aircommandrockets.com>

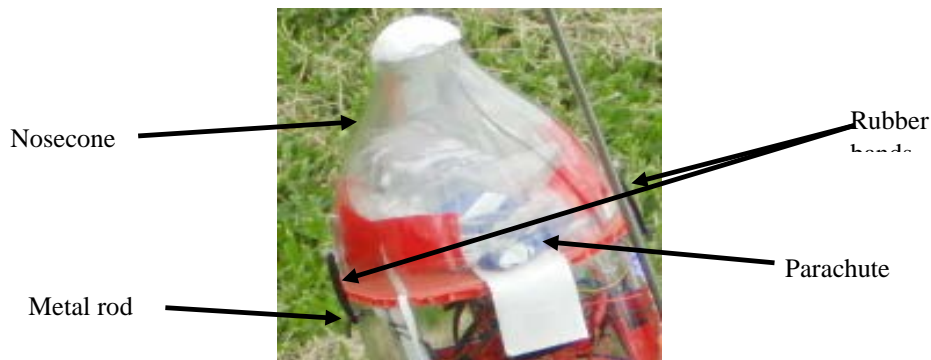


Fig. 4 First design of the parachute recovery system

Early testing with this system brought into question its reliability. Often, the rubber bands would not release from the metal rod. This would mean that in a launch scenario the nosecone would not separate and the parachute would not deploy. Despite the questionable reliability, the rocket was flown twice using this system of deployment. Unfortunately, in both attempts the parachute failed to open properly and the rocket crash landed. After these two failures, this system was abandoned and a new design was put in place.

The next design, albeit very similar to the first, proved in testing to be more reliable. It used rubber bands wrapped around a wooden dowel rod to secure the nosecone on one end, while the other end of the rubber bands was secured to a servo motor. When commanded by the Arduino, the servo would turn, releasing the rubber bands and removing the nosecone. See the picture below. This design is based on another concept shown at <http://www.aircommandrockets.com>.

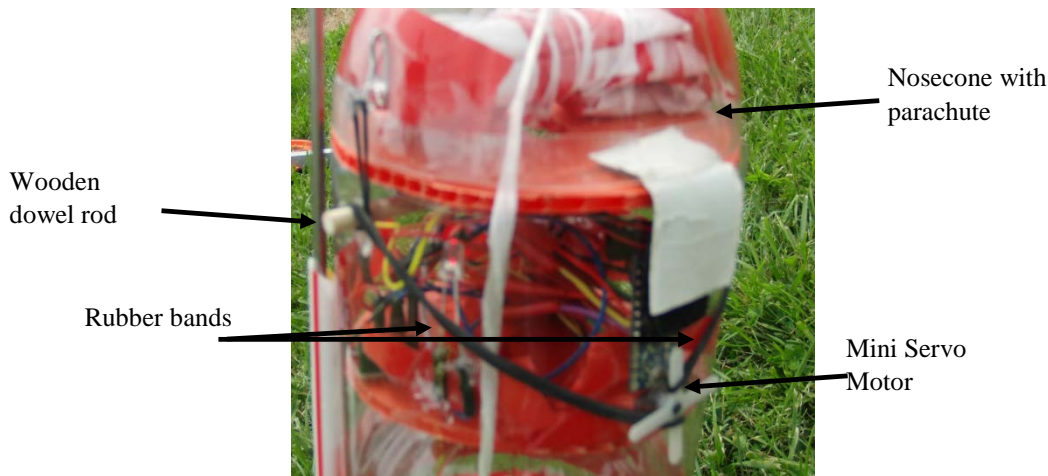


Fig. 5 Second design of the parachute recovery system

While testing showed that this was a more reliable system for releasing the nosecone, the one flight using this system resulted in an unsuccessful parachute opening and crash landing. With the failure of this system, the feasibility of a forward deploying parachute was brought into question, so this parachute deployment method was also abandoned in favor of a side deployment method.

The side deployment method works by securing the parachute to the side of the rocket with a bigger cylindrical piece of plastic that wraps around the entire bottle. A rubber band is wound tightly around the plastic to ensure that it holds its shape around the bottle. The end of this rubber band is then attached to a servo so that when the servo releases the rubber band, it will uncoil and pull the cover off along with the parachute. This system proved to be much more reliable, as every subsequent launch was a successful parachute deploy and landing. With the recovery problem solved, focus could be turned to validating the computer model. A picture of the side deployment system can be seen below. This design is based on a concept by <http://www.uswaterrockets.com>.

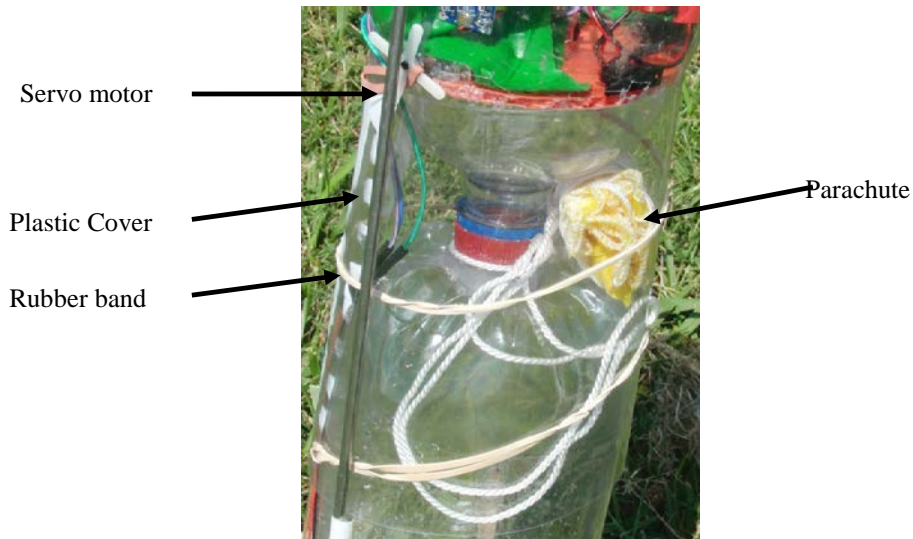


Fig. 5 Final design of the parachute recovery system

After collection of several flights worth of data, comparison of the data and computer model could commence. Acceleration data in both the z-direction (vertical) and y-direction (downrange) was plotted against the output of the computer simulation. Figures 6-11 below show the results of this comparison.

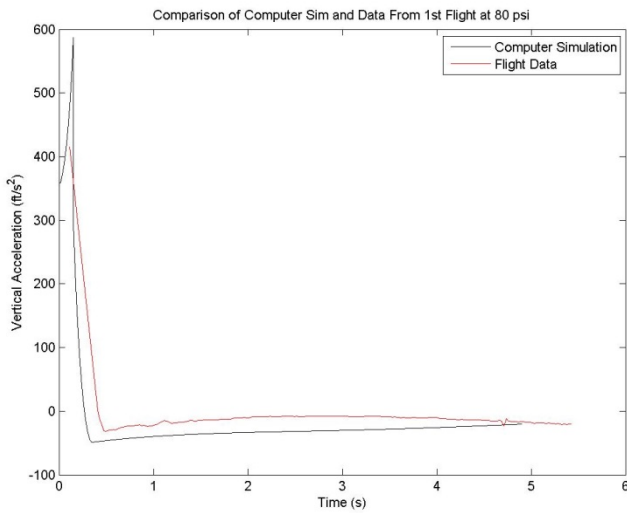


Fig. 6 Vertical acceleration data taken from first flight and overlaid with computer simulation. No parachute deployment

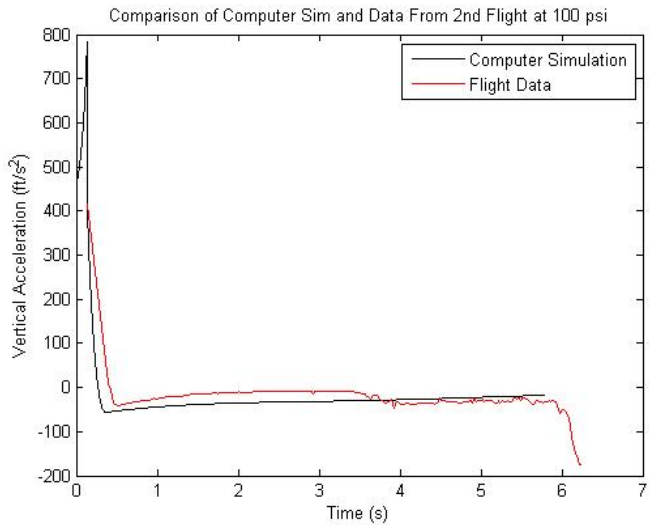


Fig. 7 Vertical acceleration data taken from second flight and overlaid with computer simulation. Spike in negative acceleration around the 6 second mark is due to a crash landing

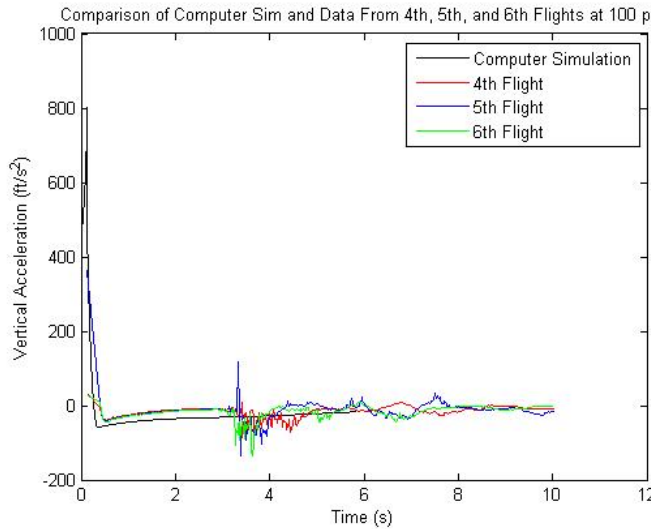


Fig. 8 Vertical acceleration data taken from multiple flights and overlaid with computer simulation. Noise after the 3 second mark is due to parachute deployment

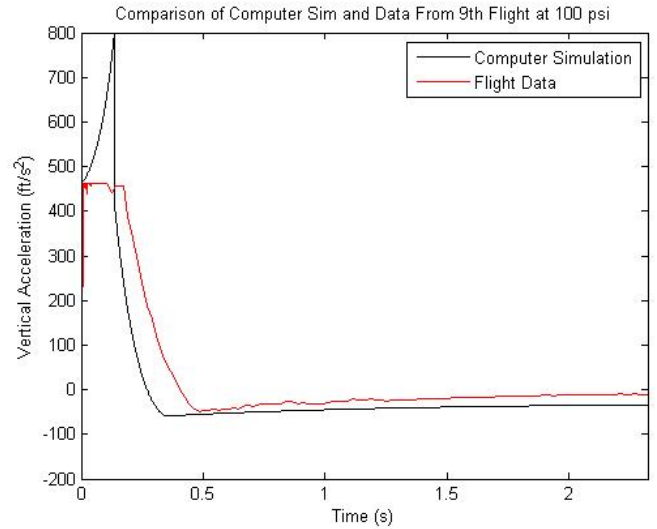


Fig. 9 Vertical acceleration data taken with increased data rate. The beginning of the flight has been zoomed in to give a better look at the peak acceleration. The acceleration peak was incorrectly measured due to sensor clipping

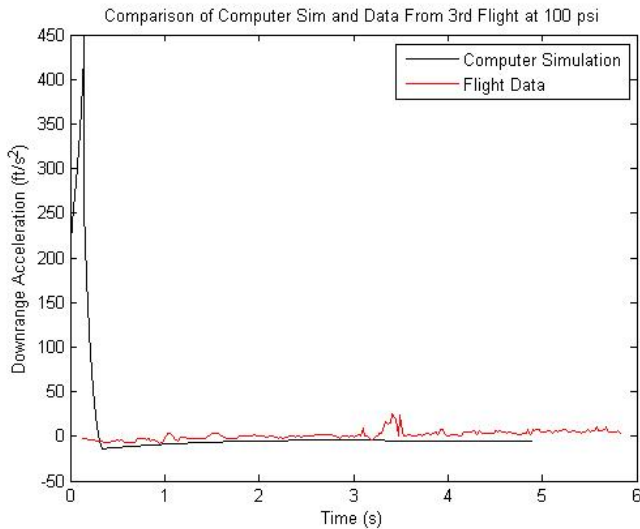


Fig. 10 Downrange acceleration data taken from third flight and overlaid with computer simulation. No parachute deployment.

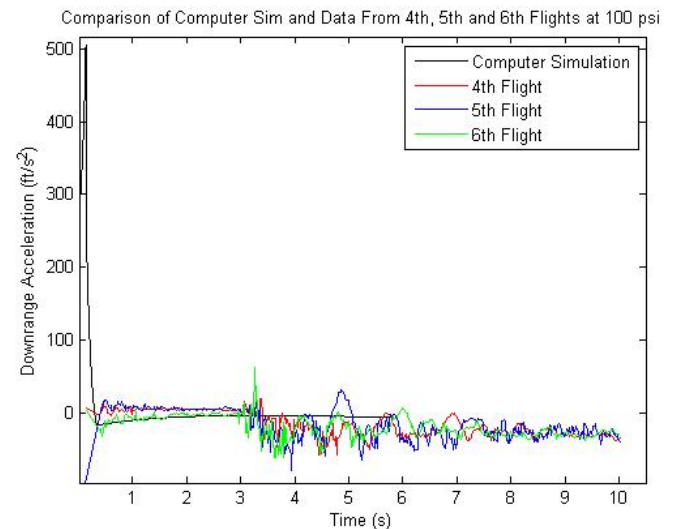


Fig. 11 Downrange acceleration data taken from multiple flights and overlaid with computer simulation. Noise after the 3 second mark is due to parachute deployment.

DISCUSSION / CONCLUSION

After performing multiple flight tests, it can be seen that our model is predicting the overall trend of the rocket's acceleration with some degree of accuracy. This also means that the velocity and position predictions made by the model should be accurate since they depend on the vehicle's acceleration. The reusability problem of the rocket has also been solved. With the implementation of the final parachute deployment design, the number of flights that can be performed by the rocket before significant damage occurs has increased greatly. Finally, the launch detection and data logging issues have also been solved. With the addition of the Arduino mini pro platform in the rocket, it is now fully capable of detecting launch with a Hall Effect sensor and logging data with an SD card reader and accelerometer. The data logging capabilities also have the possibility of being expanded in the future as more sensors can easily be integrated into the design.

During flight testing, it was noticed that the rocket is accelerating off the launch pad at a faster rate than the accelerometer can measure. The simulation predicts that the rocket is accelerating at 20 times the rate of gravity, whereas the accelerometer has a limit of a 16 g reading. On Fig. 9, this can be seen as the accelerometer effectively clipped off the peak of the acceleration curve. However, with the implementation of a parachute system and a data logging system, I would say the outcome of this experiment is a success and that if the peak acceleration the rocket achieves can be validated with another accelerometer, this project will be ready to be demonstrated to student audiences.

In the future, the use of an Arduino with enough internal RAM to record the entire flight would be beneficial to further verify the model. The process of writing data in real-time to an SD card is extremely slow compared to RAM, so by using RAM more data points could be logged and a better comparison would result. An accelerometer with a greater range of measureable g-forces would also be beneficial. It would be interesting to see how accurately the model is predicting the peak acceleration of the rocket, as the acceleration exceeds the capabilities of the current accelerometer. One final recommendation would be to use glue that bonds well to plastic in the future. Almost all of the parts of the rocket were held together by hot glue. However, hot glue does not bond well with the bottle plastic and pieces of the rocket tend to fall off and have to be replaced every few flights.

Overall, this was a great internship experience, and although this was the last year of the LARSS internship program, I would love to return to NASA's Langley Research Center in the future. Without question, the best part of this internship was the real life experience that was gained through it. Although the money was great, gaining technical knowledge that can't necessarily be learned in school from some of NASA's best scientists is what made the internship experience worthwhile.

ACKNOWLEDGEMENTS

First, I would like to thank the NASA WV Space Grant Consortium for the grant that allowed me to participate in this internship.

Next I would like to thank my research mentor John B. Davidson, for without his help and guidance I would not have made nearly as much progress in this research.

I would also like to acknowledge everyone else that works in the Orion Launch Abort System Office at Langley for all of their extra help and support with this project when necessary.

Finally, I would like to thank Debbie Murray and Sarah Pauls, along with the rest of the LARSS program staff, for making the final year of the LARSS internship program at NASA Langley so enjoyable for its participants.

REFERENCES

Wheeler, D. (2002). *Modeling the Thrust Phase*.

Worcester, R., & Frederick, R. (1992). *Bottle Rocket Analysis and Testing*.

In-line deployment mechanism. (n.d.). *Air Command Water Rockets Flight Log - Day 86 - In-line deployment mechanism*. Retrieved July 31, 2014, from <http://www.aircommandrockets.com/day86.htm>

G2 nosecone. (n.d.). *Air Command Water Rockets Flight Log - Day 98 - G2 nosecone*. Retrieved July 31, 2014, from <http://www.aircommandrockets.com/day98.htm>

Water Rocket Radial Parachute Deploy Mechanism. (n.d.). . Retrieved August 1, 2014, from http://www.uswaterrockets.com/construction_&_tutorials/Radial_Deploy/tutorial.htm

DESIGN, BUILD, AND FLY A DUAL USE UAS FOR SEARCH AND RESCUE AND PRECISION AGRICULTURE

Matthew Siburt
Aerospace and Mechanical Engineering
West Virginia University
Morgantown, WV 26506

ABSTRACT

This paper will give a brief overview of the process to design, build, and fly a dual purpose unmanned air system. This was completed in ten weeks at the NASA Langley Research Center as the 2014 Aeronautics Academy assignment. During that time a team of twelve students came together to successfully complete the assignment.

INTRODUCTION

The project given to the 2014 Langley Aeronautics Academy was to design, build, and fly an inexpensive, dual purpose, unmanned air system (UAS) in ten weeks. One use of the UAS was precision agriculture. For this the UAS had to take photos of crops and analyze them for stressed areas. The minimum goal was to create a Normalized Difference Vegetation Index (NDVI) map of the crop with the added goal of autonomously locating the stressed areas. The second purpose of the UAS was to act as a Search and Rescue (SAR) platform. Our minimum goal for this application was live video streaming from the UAS to a SAR ground station. The additional goal was to autonomously find the people for which the UAS was searching. Both of these missions were to be completed over an area of two square kilometers. The UAS also had to be fully autonomous from take-off to landing. This helps with farmers and search and rescue teams who do not want to go through training to fly a UAS.

BACKGROUND

Precision Agriculture

In modern agriculture NDVI mapping with UASs is becoming more common. This mapping can detect plant stress before it is noticeable with the human eye. It works off of the reflection of visible and infrared light. When plants are healthy they will absorb more visible light for their photosynthesis process. The light is absorbed by the chlorophyll in leaves of a healthy plant. The healthier the plant, the more chlorophyll it will have absorbing more light. When a plant comes under stress from pest invasion, lack of water, or lack of nutrients, it will have less chlorophyll. This will cause the plant to absorb less light when it is under stress. To the human eye the plant may look healthy because it is still green. However it could quickly die or an entire crop could be lost from an insect invasion that went unnoticed.

Search and Rescue

There are many limitations in the search and rescue field. Bad weather, harsh terrain, time, money, and man power are just a few to be named. These can be almost completely solved by using a UAS. It would only take a small crew to operate a UAS and it will not cost nearly as much as a helicopter or plane if it goes down in bad weather. Even Coastguard rescue missions cannot be flown in low cloud ceilings, thunder storms, and turbulence. Plus the thousands of dollars an hour the missions cost. There are also local sheriff's departments, park rangers, and search and rescue organizations that try to complete missions on almost no budget and very little man power. People these small organizations are looking for are usually lost in vast, remote areas with terrain that cannot be navigated on foot. The time it would take to search two square kilometers at a time on foot would be too long when someone's life is on the line.

METHODS

Autopilot and Mission Planning

To meet the goal of autonomous flight an autopilot had to be found that was easy to use and inexpensive. After searching and comparing various options the Pixhawk was chosen. This autopilot can be used for anything from rotorcraft to RC cars. It also had many accessories that were needed, like a pitot-static tube and GPS. The software the Pixhawk uses to plan the route of the UAS is also very easy to use. It is good for anyone who may not be computer savvy or just does not want to deal with a hard to use software.

The software used was Mission Planner. It uses Google Earth as the map and lets the user select an area to fly. Once the area is selected the user inputs speed, altitude, and various other parameters. Mission Planner then creates the path the aircraft will follow. The user can define the type of pattern they want the aircraft to fly if the default is not satisfactory. It also sends the Pixhawk triggers to take photos with the onboard camera. There are some cameras already in the software so it can tell you how often it will take a picture. The picture interval is based off of the specifications of the camera so the entire area will be photographed.

Sensor Selection

Sensor suites had to be chosen for each mission. This was done by breaking into two groups, one group for precision agriculture and the other for SAR. Each team member chose what group they wanted to be in based on personal preference.

The precision agriculture team only had to choose a camera to be used for the NDVI imaging. They chose the Canon SX260 for the ease of use with the Pixhawk and Mission Planner software. This was just one of the cameras that can be used with Mission Planner. It was the best choice because of the resolution and it has GPS built in. This helped with the image stitching and as a backup image locator if the UAS's GPS fails.

There were many sensor possibilities for the search and rescue team. Search and rescue organizations were contacted to find their opinions on what they would like to have on a UAS. Some commonly wanted sensors were thermal imaging, night vision, color video streaming, and real-time sensors. The initial thought was thermal had to be on the UAS because it is the best way to find people. After much debate and outside knowledge it was found that it was not the best way. For example on any day with a temperature of 74° F or higher a human body will not be visible on the ground. This would rule out many scenarios that this UAS would be used for. The size, weight, and cost of a thermal camera made it non-feasible also. Night vision cameras had a similar issue

to the thermal camera. Only very high end and expensive night vision cameras would have the resolution to differentiate a human on the ground from the air. Those cameras are also very expensive and not small enough to fit in a small UAS. It was decided that having a live video stream with automated image analysis was the best option for the UAS. The camera chosen was a Raspberry Pi camera that was only the size of a quarter and weighed ten grams. In comparison to a two pound thermal camera it was definitely the best option.

NDVI

The process of creating an NDVI map is as follows. First a camera is modified to take pictures that include the near infrared (NIR) spectrum. Any camera can be modified by removing the NIR filter from in front of the image sensor. This will allow the NIR and visible light spectrum to be recorded in photos. Once the pictures are taken they get processed through an image stitching software to create one large, map like photo of the crop. After that is created it processes that picture through software to create the NDVI map. This software works by using this equation:

$$NDVI = \frac{((NIR+G)-(2*B))}{((NIR+G)+(2*B))}$$

This equation uses the NIR, green (G), and blue (B) light spectrums to produce a number from -1 to 1. Numbers from -1 to 0 relate to non-plant life, as in water, pavement, or dirt. Numbers from 0 to 1 relate to plant life. Numbers closer to one mean the plant is healthy and as the numbers get closer to zero the plant is stressed or unhealthy. After the software is run a map with colors from red to green is produce as seen in Figure 1. Green relates to a healthy plant and dark red relates to non-plant life. Any color in between means an unhealthy or stressed plant.

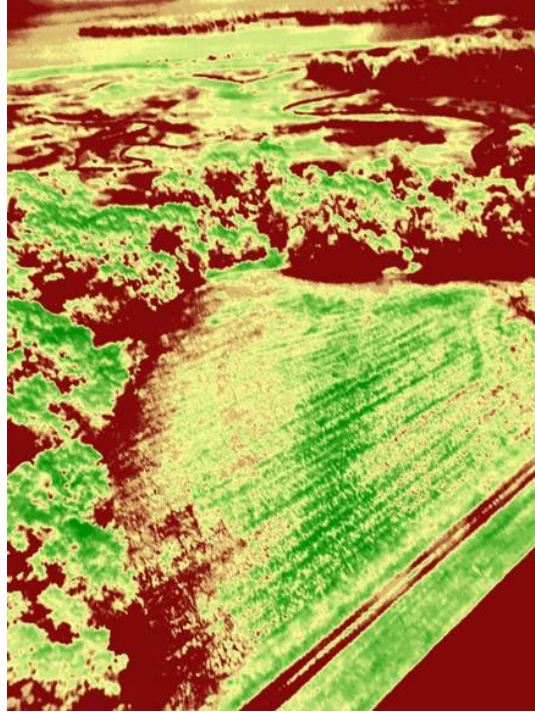


Figure 15: NDVI Picture

SAR

Live video streaming to a SAR ground station is vital for fast response in a life or death situation. During the video stream pictures are taken and analyzed with software. This software finds objects that differ from the collective background of the picture. It will first blur the picture to make everything less sharp. Then it finds large differences in the pixels next to each other to create an edge. These edges are then used to make curves in the picture. With the curves drawn the software produces a modified original image with boxes around anything that stands out from the background. Whether the object is the human they are looking for or not can be decided by the person analyzing the picture. This was done along with the video stream as a double check. A person watching a computer screen for an hour is bound to miss something coming from a moving aircraft. A sample of the detection image can be seen in Figure 2.

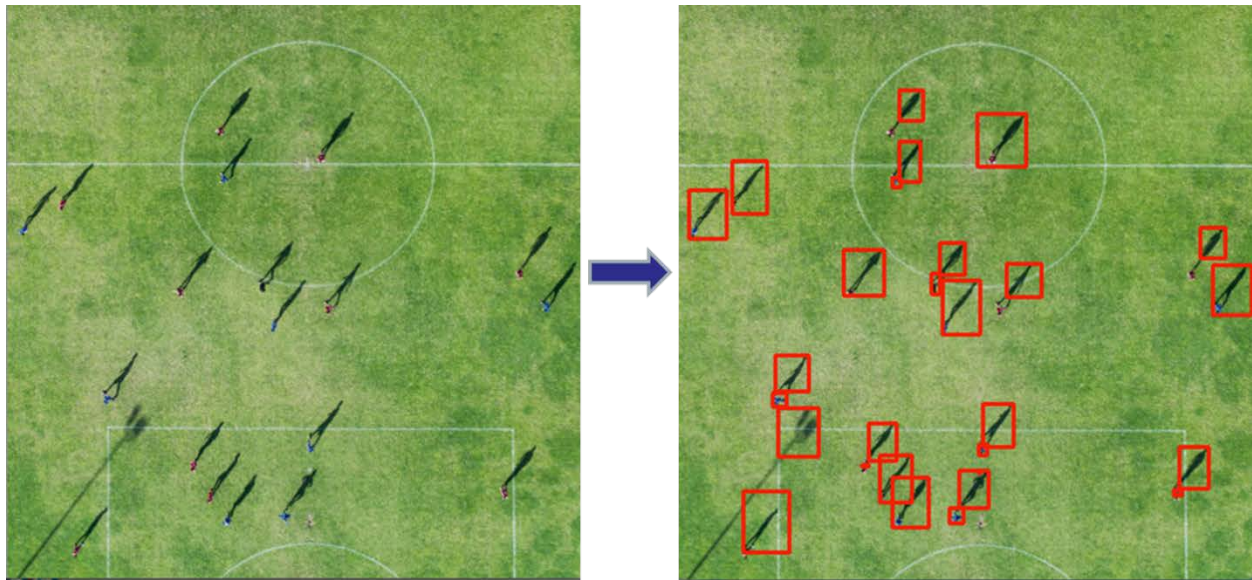


Figure 16: SAR Picture

The Raspberry Pi camera was attached to a Raspberry Pi board to take the video. The board was also the computer processing the images from the video and saving them on a memory card. After a flight the memory card can be pulled from the board and the images can be loaded onto a computer for further review.

UAS Design

With the sensor suite chosen and a weight estimate based off of those sensors, the design of the UAS began. First a type of aircraft needed to be selected. The two options were a traditional airplane and some type of rotorcraft, most likely a quadcopter. While they are very stable and take amazing photos with the ability to loiter, quadcopters and rotorcraft in general have endurance troubles. Since they have to lift their entire weight at take-off it will drain batteries very quickly. They also do not do well in high winds or storm conditions. Also the amount of payload that went along with this UAS would not be suitable for a small quadcopter. With a traditional airplane design it was more difficult to keep the cameras pointed straight down. It was overcome with adding an angle of incidence to the wings to generate enough lift during cruise and keep the fuselage level. With the traditional design the endurance can be increased by making the aircraft more like a glider. It can also carry more payload and take-off without draining the batteries too quickly. So a traditional fixed wing aircraft was chosen.

The first steps after deciding on the aircraft type were to find a motor with enough power and batteries that would give the endurance needed. A maximum total weight of the UAS was set at ten pounds. It was found that a vast majority of people can throw ten pounds from a position over their shoulder. Once the weight starts going over ten the amount of people drops off significantly. This UAS was meant for anyone to be able to use it so weight goal was ten pounds. A motor and battery combination was found and in calculations gave over enough endurance.

With the payload set and measurements of each component known the aircraft design began. The internal components were drawn in SolidWorks and assembled in the most compact and best arrangement. The center of gravity (CG) was also considered in the assembly process. It was kept far enough forward for aircraft stability. With the assembly of the internal components complete, the fuselage and wings were designed in Vehicle Sketch Pad (VSP). VSP is open source software that allows for rough sketches of aircraft to be created. These sketches can then be put into a program like SolidWorks to be fine-tuned. The main part created in VSP was the fuselage. While the wings and tail were drawn too, the airfoils were selected from an airfoil data base.

The selection of the airfoil was based off calculations. The Reynolds number of the UAS's flight regime was known to be low, in the hundreds of thousands. Another calculation was done to find the coefficient of lift needed at cruise to keep the UAS in the air. Therefore a search began for a low Reynolds number airfoil with the specific coefficient of lift. This coefficient also had to be at a low angle of attack so the wings could be mounted at that angle on the fuselage and not create too much drag. Finally an airfoil was found that meant all of the criteria needed.

Build Process

With the design complete the build of the UAS started. The first step taken was deciding on the building material. Foam insulation was used as the main structure of the UAS's wings and fuselage. The foam was coated in fiberglass for rigidity and protection. This combination of foam and fiberglass allowed for a strong yet light aircraft. The wings were the first parts created. They were cut using a computer controlled, hotwire foam cutter. Computer controlled cutting allowed for more accurate cuts compared to a handheld foam cutter. To give the wing extra strength a carbon tube was added to act as a spar. The tube was also used as the means of attachment to the fuselage. With the tube in the wing it was coated in fiberglass. The horizontal and vertical tail were then made with flat pieces of wood, cut to shape, then coated in carbon fiber.

The fuselage was the next step in the build process. It was drawn in VSP then transferred to SolidWorks. From there it was taken to the shop at Langley and cut on a CNC machine. The machine also cut the hole in the fuselage that housed the payload. Since the CNC has its limitations some of the opening had to be carved by hand. These sections were deeper into the fuselage where the machine could not reach. The completed fuselage was then coated in fiberglass. Once it hardened the motor mount was added to the front. The motor was mounted to a piece of thin plywood secured to the front of the fuselage.

To cover the payload compartment of the UAS a hatch was made that also acted as the attachment point of the wings. The hatch had to be sanded by hand to match the contours of the wings and fuselage. It was also modified to attach to the fuselage using wood inserts as hard points. A hole was drilled into the inserts for screws to go through and not tear the foam. The screws then go into hard points in the fuselage for secure attachment. For extra strength the hatch was not coated in fiberglass until the wood inserts were in place.

With everything assembled the servos were mounted on the wings and the tail of the UAS. They were mounted in the wing by carving out an area then bonding a piece of wood in to secure the servos to. These servos were connected to the ailerons which were attached to the wing with a

Kevlar strip acting as a hinge. Since the tail was made of wood the servos were just mounted right into them. Their control surfaces, the rudder and elevators, were made from the same material and used clear repair tape as the hinge. The last step was to sand and paint the UAS. The top was painted a bright orange for aerial visibility while the bottom was painted black for ground visibility. The completed UAS can be seen in Figure 3.



Figure 17: Finished UAS

OUTCOMES

With only one available flight day not every flight test was completed. However flight test for airworthiness and validation were completed. The first flight was an airworthiness test and for the pilot to get use to flying the UAS. It was a successful flight that verified the UAS flew and that the cameras were working in flight. This first test proved that the mission could be done on a small UAS. The next three flights were the initial flights for setting up the autopilot. All of which were successful but the full autopilot mode was never tested. The utmost confidence is had in the UAS and with additional testing it should fly completely autonomously.

CONCLUSION

There are many improvements that could be made in all aspects of the project. Most of the improvements lie within the build process. From the experience of making this UAS, the same one could be rebuilt in a shorter amount of time. The UAS could be lighter, stronger, and slightly better with more time spent working on it. Overall it was an amazing accomplishment for twelve complete strangers to finish the whole project in just ten weeks.

ACKNOWLEDGMENTS

I would like to thank the West Virginia Space Grant Consortium and Liz Ward for making it possible for me to have this amazing experience. I would also like to thank my team for making it as amazing as it was.

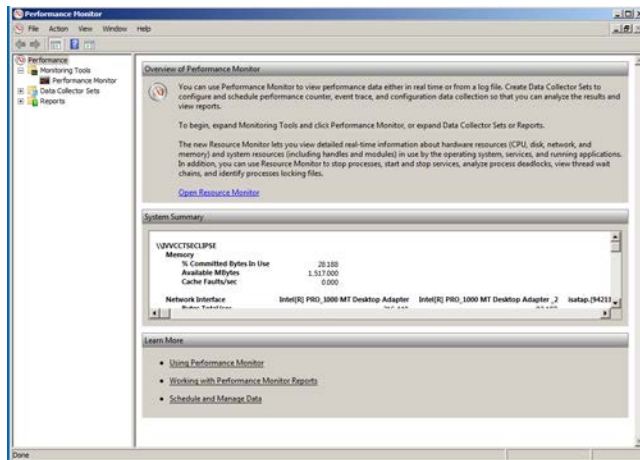
SUMMER INTERNSHIP WITH TMC TECHNOLOGIES

Justin Speelman
Electrical Engineering
West Virginia University
Morgantown, West Virginia 26506

ABSTRACT

At the beginning of my internship I was first tasked to find a profiling tool so that a ground support software could be tested for any performance errors. Alongside of that I was told that I would be improving network wiring in the JSTAR lab that TMC manages. A few weeks in to my internship I was asked to come up with software or a code that could pull text from a PDF and put the information into a spreadsheet like Excel. To give me a chance to learn a new skill I was given the chance to participate in NASA IV&V's Security Penetration Testing course. Nearing the end of my internship I was introduced to the concept of fault driven testing. I also had the ability to make videos using Adobe Captivate that can be used as guides to use the ground support software I was working with.

INTRODUCTION



Performance Monitor

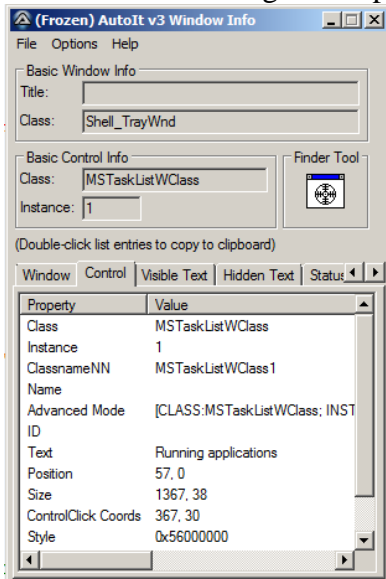
My first task as an intern for TMC Technologies was to read about what performance profiling entailed. I was told that I would be profiling some ground support software and that software would be running on a virtual machine and would be on Windows Server 2003. In my search I quickly saw that finding a reliable profiling tool that was supported on Windows server 2003 was just not an option. With a little explanation and a few phone calls the software was then going to be switched to Windows Server 2008. All of the profiling tools supported Windows Server 2008 and it gave more security. I was able to get free trials of the selection of profilers that I wanted to try. In the end the term “profile” was a term used for a developer that had the code available to them; we did not have the code so we were not able to actually profile the code.

Instead the term we should have been using was monitor. It turned out that Windows had a built in computer monitoring software called Performance Monitor. This tool gave me the ability to monitor individual processes and select how I wanted to look at the processes like memory use, or CPU usage. There were two functions that you could use the resource monitor which would show you the overall health of the computer and then there was the performance monitor that would

allow you to make what was called a data set where you could specify a single process and select how you want to monitor it.

I ran an initial test focusing on areas such as CPU usage, memory usage, and network usage. This test was run by repeatedly opening the ground support software running some of the software's functions then closing the software. This would have shown me if there were any aspects of the software that were not closing completely or if there was memory being stored. This test proved to be inconclusive due to the tests only being run for about ten minutes each. In those ten minutes seeing a tread, if one existed, would be very difficult.

The idea of automating the testing process was brought up and would allow for much longer and more accurate testing. I was pointed to a program called AutoIT. This tool uses a combination of code and its own information window to properly work.



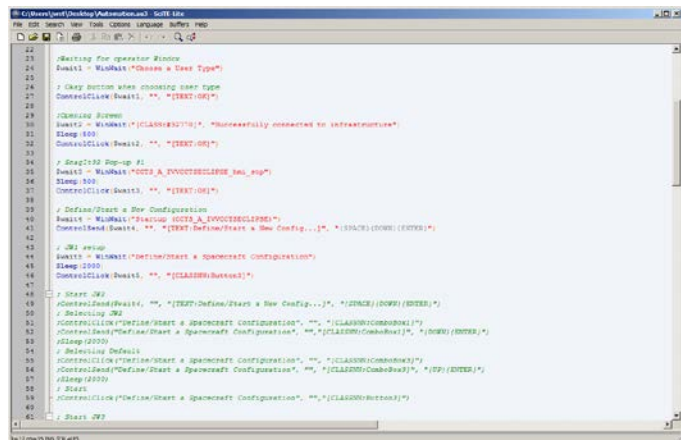
code and its own information window to properly work.

To do this effectively I was tasked to try and automate the testing cycles. To do this I was pointed to a program called AutoIT. This little macro was the perfect tool because it has a window that gives you information about each button or window so you can tell it where to click accurately. This window gives all the information that is needed to identify each individual button in windows.

The image on the left is an example of the information that is brought to you in the window. This information called in the code to properly position each click. Once I had the button information I was able to start writing the script itself.

AutoIT Information Window

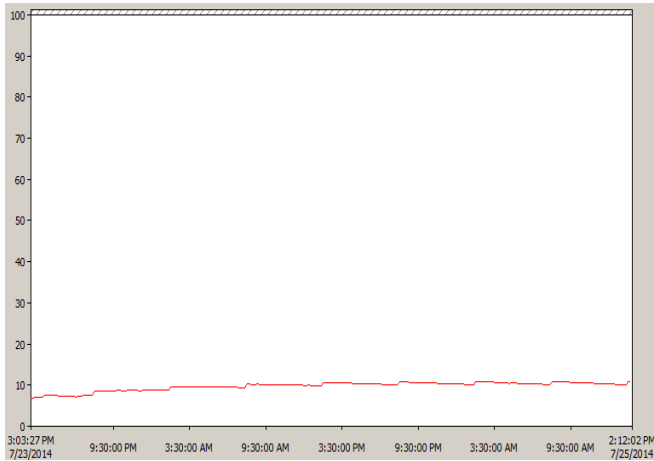
When it came to starting to write the scripts I asked a co-worker, Tim Riley, several questions about syntax and how the program actually worked. He then directed me toward the AutoIT help documentation. The help document has all the syntax for all the commands that you can implement with AutoIT. The three most used commands for me were ControlClick, Sleep, and Wait. The wait command could be used as a variable of sorts. It would pause the code until a certain window popped up then I was able to just put it into the ControlClick command to tell the script what window I wanted to click into. The Sleep command was simply a set delay that would give windows time to open.



Example AutoIT code

Once the code was constructed I could run continuous cycles of the ground software from the off

stage to the on stage. I also ran a long term run where I left the software running for 3 days and monitored its performance over that time period. Those tests did not reveal and major areas of concern. When I got tasked with the project they wanted me to find something that was wrong but having evidence that the software was sound in its resource use was just as important. I then wrote a report explaining my process and displaying my results in the form of graphs from the Performance Monitor. This process of getting to this point was conducted in pieces throughout my internship.



Example Performance Graph

One task that I worked on during the ground software testing was pulling text from a PDF file and putting it into a database such as excel. I ended up being more support on this task than anything.

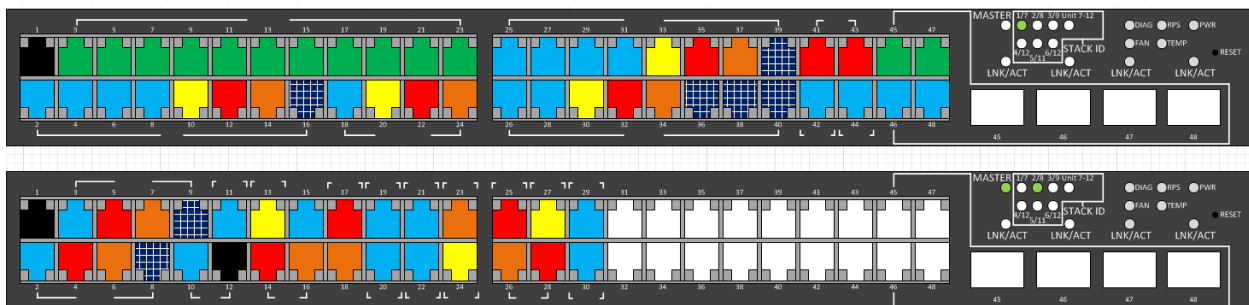
```
#!/usr/bin/env python
import subprocess
import argparse
import sqlite3
import os.path
import sys

class MEMFileProcessor:
    """MEM text file processor"""
    def __init__(self, ffile):
        self.fname = ffile
        self.remaining = ""
        self.line_num = 0
    def __next__(self):
        return self
    def next(self):
        if self.remaining:
            data = self.remaining
            self.remaining = ""
        else:
            data = self.fname.readline()
            self.line_num += 1
        return data
    def get_field(self, start_key, end_key):
        field = ""
        # find start key
        while True:
            data = self.next()
            if start_key in data:
                field += data.split(start_key)[-1].strip()
                break
        # check for end key on same line
        if end_key in field:
            field, self.remaining = field.split(end_key)
            return field
        # find end key
        while True:
            data = self.next()
            if end_key in data:
                field += data.split(end_key)[0]
                self.remaining = data
                break
            else:
                field += data
        return field.strip()
    def dump_mem_pdf(pdf_file, db_file):
        """Dump mem pdf files to database"""
        # dump mem pdf file to temporary text file
        tmp_file = temp
        subprocess.check_call(["pdftotext", pdf_file, tmp_file], stderr=subprocess.STDOUT)
        # open database
        connection = sqlite3.connect(db_file)
        connection.text_factory = str
        db = connection.cursor()
        # create MEM table
        fields = ["classification", "Resp Org", "SPM", "Subsystem", "NSL_ID", "Title", "Summary"]
```

Python Code

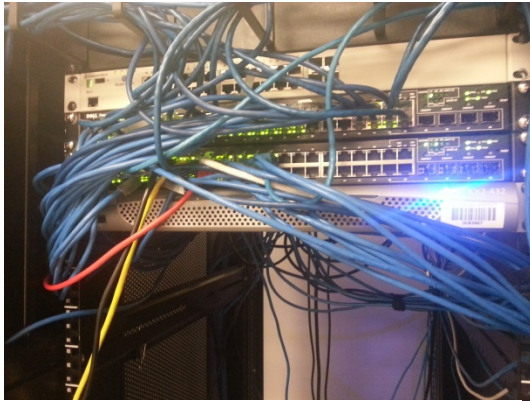
Another co-worker, Dustin Geletko, came in the day after I was tasked with this and told me that he had written the code in python last night because he got bored. This was an amazing help. His code pulled the text from the PDF into a SQLite database which I could then import into an excel spreadsheet. From there all that was left for me to do was go through the data and make sure it was all there and where it should have been.

Towards the middle of my internship TMC received their second Dell server. I was the tasked to help Brandon Bailey install this new server and to improve the wiring that was already there. The first step was to pull all the existing wires out of the server rack and then rerun them up to the



Dell Powerconnect models

front. This allowed me to group them a little tighter. Once we had the wires we needed a way to keep track of them so I constructed a Visio file to help do that.



Servers

Each color represents a different VLAN. The white lines represent that server they are allocated to I just have the names and the VLAN types removed for the purpose of this paper. We used Dell stacking modules to stack the two servers. This allowed them more basically act as a single unit. We did have some trouble with the old server rebooting constantly but simply unplugging it fixed the problem and then it was just a matter of putting everything into the ports they needed to be in. When finished the image to the left is what we had.

Shortly after that I was given the chance to take Brandon's Penetration Testing course. This course is used to train individuals in hacking techniques to help secure companies infrastructures. It was much different than anything I was used to due to me having to use Linux's command prompt for basically every aspect of the course which is a good skill to have.

In the last few weeks I was introduced to the concept of fault driven testing. This was something I had never really seen before. What this process does is it allows you to model hardware components with software and basically break different components and see how the system responds and if it responds properly. This concept could be used in almost any environment that uses hardware. It is the best way to test a network of hardware without potentially harming anything.

My final task as a TCM intern was to make some videos demonstrating different aspects of the ground support software. There were 5 videos in totally and I constructed them using Adobe's Captivate software. This software gave me the ability to add pop-up boxes to show/tell the user what was going on and I could easily highlight text that I wanted the viewer to know was there. These videos will be used to show interested parties how the software works without having to make sure that a computer that runs the software is available.

RESEARCH

I did very little research in my time at TMC, my time was mostly spend doing more hands on work. At the beginning of my internship I looked into tools for profiling an application but then shifted my search into monitoring tools. After that the only research that I did was reading user guides to get a better understanding of how to run the ground software, syntax for AutoIT, and how to stack the Dell powerconnect servers.

CONCLUSION

This internship was focused on giving me hands on work rather than research oriented work. This to me was more beneficial for me when I prepare to join the work force rather than having just done research the whole summer.

This internship was more of a software based internship which gave me the chance to learn more about using software instead of just looking at hardware. Having some knowledge of both hardware and software is a very valuable asset and being here with TMC has shown me that I still do need to learn much more about the software behind the hardware so I can be more well-rounded.

ACKNOWLEDGEMENTS

I would like to thank Candy Cordwell for finding this position for me and I would like to thank Scott Zemerick for mentoring me and allowing me the opportunity for further my education. I would also like to thank the other employees at TMC along with the civil servants that I work with at my time at NASA for helping me along the way.

REFERENCES

My resources I used were neither published papers nor published documents. They were user guides and help documentation. I used the ECLIPSE user guide, AutoIT help guide, and Dell Powerconnect user guide.

II. NASA Undergraduate Research Fellowship Reports

QUANTIFYING TURBULENCE INTENSITY AND BOUNDARY LAYER THICKNESS FOR USE IN AN INVESTIGATION OF THE EFFECT OF BOUNDARY LAYER STATE AND THICKNESS ON FILM COOLING EFFECTIVENESS

David Billups
Mechanical and Aerospace Engineering
West Virginia University
Morgantown, WV 26505

ABSTRACT

This study covers preliminary work in an investigation of boundary layer thickness and state on film cooling effectiveness. Film cooling is one solution to a common problem in gas turbine engine operation, specifically in aeronautic applications. This research looks to increase the efficiency of modern day gas turbine engines. At West Virginia University (WVU), a low speed wind tunnel that non-dimensionally imitates the conditions experienced by the turbine section of a gas turbine engine has been constructed to explore film cooling. An investigation of the effect of boundary layer state and thickness on film cooling effectiveness is currently being conducted. The turbulence intensity and length scale have been defined for two turbulence grid cases: ¼” grid and ½” grid. These grids passively disturb the flow, introducing turbulence ten hole diameters upstream of the film cooling holes. The boundary layer thickness has also been determined for the cases when the boundary layer suction motor is on and off. With these parameters quantified, a thermal imaging device and software were used to collect heat transfer data for each turbulence case when the boundary layer suction was on. From this data, heat transfer coefficient and film cooling effectiveness could be found for each case. It was determined that the film cooling effectiveness increases as turbulence increases.

INTRODUCTION

An important field in the advancement of aeronautics is gas turbine heat transfer. Gas turbine performance is limited mainly by the operating temperature of the blades in the high pressure turbine section of the engine and the compression ratio provided by the compressor section. To increase the potential operating temperature, many methods have been brought forth. The focus of this research is on one external cooling method known as film cooling. Film cooling involves redirecting relatively cooler air through the engine from the compressor exit to the turbine section, bypassing the combustion phase. This cooler air is then forced through channels within the turbine blades where it is injected into the hot, combusted flow via cooling holes aligned along the surface of the turbine blade. The goal is to blanket the turbine blade material in a cooler layer of air to protect the material from the extremely high mainstream flow temperatures. Many studies on film cooling have been done at various institutions. WVU recently built an open loop wind tunnel to non-dimensionally simulate the aerothermal environment experienced by the first stage vane of a gas turbine engine, represented by a flat plate geometry. The tunnel is capable of freestream velocities of 25 m/s. The most recent study that has been conducted at this facility involved comparing film cooling effectiveness and heat transfer coefficient at various turbulence intensity levels for multiple cooling hole geometries. A succeeding study involves comparing film cooling

effectiveness at various boundary layer thicknesses and turbulence intensities. The purpose of this research is to provide understanding of how each variable contributes to the overall impact of film cooling on engine efficiency. Previous research completed by Hayes [1] and Repko [2] found that film cooling effectiveness increases with turbulence intensity. In *Advances in Heat Transfer*, it is discussed that with larger boundary layers, heat transfer to the wall tends to decrease [3]. This leads to the hypothesis that the greatest film cooling effectiveness will be seen for the case of high turbulence intensity within a large boundary layer. To perform the previously mentioned succeeding study, multiple parameters need to be quantified: turbulence intensities due to various sized grids need to be defined, as do boundary layer thicknesses for the cases of no suction and full powered suction. To obtain these measured values, a straight wire hot wire, boundary layer hot wire, thermocouple, pitot static probe, and total pressure probe will be used in conjunction with a pressure transducer, mini constant temperature anemometer (CTA), National Instruments Data Acquisition (NiDAQ) system, MatLAB, LabView, and Microsoft Excel. Each hot wire probe was calibrated against the pitot static probe. The total pressure probe was used to provide confirmation on the accuracy of the boundary layer measurements found using the boundary layer hot wire probe. After calibration, the straight wire hot wire probe was used to quantify turbulence intensity and length scale. The boundary layer hot wire probe was used to measure velocity along the height of the test section to determine the boundary layer thickness. With the turbulence intensities and boundary layer thickness determined, the lab was set up for transient testing with a FLIR thermal imaging camera. The first set of data needed to analyze the impact of each variable on film cooling effectiveness was taken and reduced.

BACKGROUND

The birth of the gas turbine engine officially occurred in 1791, as John Barber filed a patent outlining the need for a compressor, combustor, and turbine section in an engine [4]. Due to technological restrictions, Barber's patent never came to fruition. It was not until the 1930's that gas turbine engines came to realization. Frank Whittle of the British Royal Air Force successfully tested a turbojet design in the late 1930's. Meanwhile, Hans von Ohain of Germany created his own turbojet design, which was successfully test flown on a Heinkel HE 178 aircraft in 1939 [5]. Interestingly enough, the two men were unaware of each other's achievements. Since the onset of the gas turbine engine, the machine has been subject to much advancement as the technology began to overtake other methods of propulsion in aircraft industry.

In more recent history, the focal point of advancements in gas turbine design is efficiency, rather than thrust. There are two primary ways to increase the efficiency of a gas turbine engine, namely, increasing the compressor pressure ratio and raising the combustor exit temperature. The first method is a matter of adding rotors and stators to the compressor section, adding weight. This is not a realistic method in the aerospace industry, as weight would require more lift, which inherently creates more drag and ultimately a need for more thrust, requiring more fuel burn. The later method, however, is a matter of shielding materials from the hot temperatures seen in the combustor exit region. It is this idea that provides the motivation for turbine cooling methods. Although there are many methods, both external and internal, to accomplish this task, turbine film cooling is the focus of the turbine heat transfer lab at West Virginia University. Film cooling is a process that redirects cooler air to the turbine section, bypassing the combustion section. The cooler air is directed through the turbine blades at which point it leaks out of small holes along the width of the blade to provide a thin layer of cool air over the metal, increasing the maximum

temperature that can be reached by the mainstream flow through the turbine section before the turbine blades begin to fail.

EXPERIMENT

HOT WIRE CALIBRATIONS

The pitot static probe and a hot wire probe were used simultaneously to measure velocity. Paired with a pressure transducer, the pitot static probe yielded voltage readings, corresponding to the difference between total pressure and static pressure in the flow. The hot wire probe, connected to a constant temperature anemometer (CTA), gave voltage outputs which were indicative of the free stream flow velocity. Using the ambient pressure reading from a reliable, online source and the temperature readings from the thermocouple along with the sensitivity of the transducer, velocity can be found for the pitot static probe measurements by the Bernoulli principle. King’s Law relates voltage and velocity for use in hot wire probe calibrations as demonstrated in equation 1.

$$U^n = m * V^2 + b \tag{1}$$

Typically, n varies between 0.4 and 0.5. In these cases, n was taken to be 0.45. With this relationship, the voltage outputs of the hot wire anemometer can be converted to a velocity by determining the linear relationship between the square of the hot wire voltage readings and the pitot static probe velocity measurements to the n th power. Figure 1 provides the relationship between velocity and voltage for the straight wire and boundary layer hot wire probes, where x is V^2 and y is U^n .

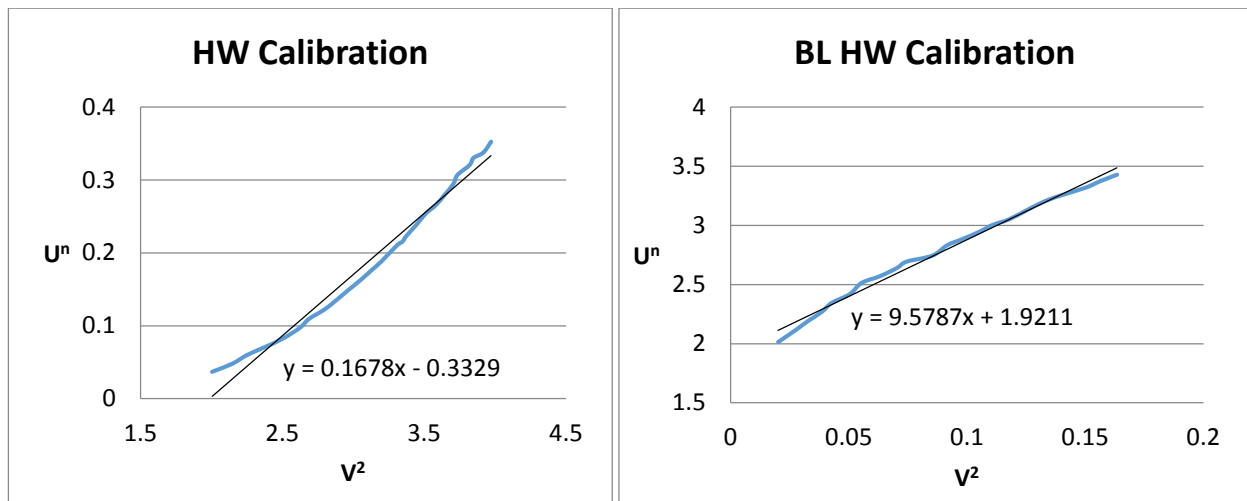


Figure 1: Calibration Curves for (Left) Straight Wire and (Right) Boundary Layer Hot Wire Probes

TURBULENCE MEASUREMENTS

Using the hot wire calibration curve to convert hot wire voltage readings to velocities (U), the hot wire probe was mounted in the freestream flow to measure turbulence intensity at three different streamwise locations. Turbulence measurements were made by taking velocity measurements at high frequency. The sampling frequency was determined to be 50 kHz, based on the capabilities of the data acquisition components and probes. The set of data collected has a mean velocity (\bar{U}). The deviations (u'_i) from the mean velocity at each sampling are used to calculate the turbulence intensity based on the following set of equations.

$$u'_{RMS} = \sqrt{\frac{1}{N} \sum_{i=1}^N u_i'^2}, \quad u'_i = U - \bar{U} \quad (2)$$

$$Tu = \frac{u'_{RMS}}{\bar{U}} \quad (3)$$

The turbulence length scale was also found during this process for use in comparing results to past measurements. The turbulence length scale can be found through an autocorrelation of the fluctuating velocities. The time scale (T) of the autocorrelation can be found using equation (4) where N_0 is the location where the autocorrelation curve first crosses the x-axis. An example of this is provided in figure 2.

$$T = \sum_{i=1}^{N_0} R_{11i} * \Delta\tau \quad (4)$$

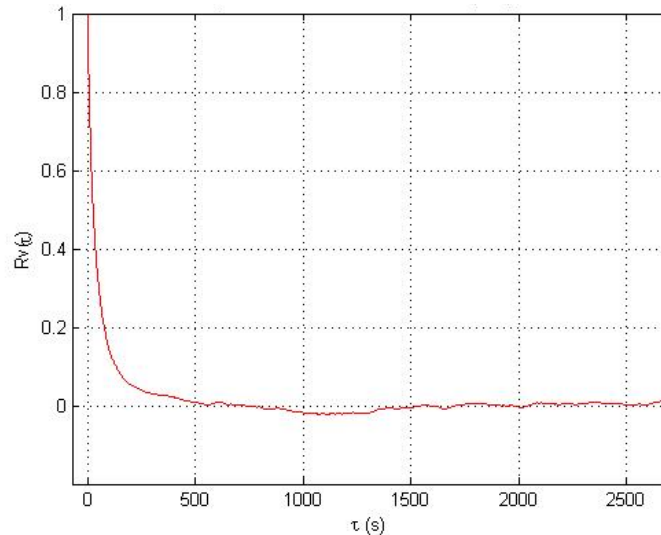


Figure 2: Zoomed in Autocorrelation of Velocity Signal

The turbulence length scale (Λ) can easily be found by multiplying the time scale by the freestream velocity (\bar{U}). Both the turbulence intensity and length scale were found using a MatLab code.

$$\Lambda = T * \bar{U} \quad (5)$$

BOUNDARY LAYER THICKNESS MEASUREMENTS

To alter the boundary layer thickness, the wind tunnel employs a 1/20 HP household radon fan mounted underneath two 1/2" slots near the inlet of the test section. The boundary layer thickness measurements required a boundary layer hot wire probe and a total pressure probe. The boundary layer hot wire probe is specifically designed for close proximity to objects, in this case, a wall. The probe was calibrated in the same way as the straight wire hot wire probe; however data was taken at a location closer to the wall because that is the region of interest. After calibration, a traverse along the height of the test section just in front of the cooling holes was performed using the total

pressure probe and the boundary layer hot wire probe. The resulting velocity profile plots were compared to ensure that the boundary layer hot wire probe was making accurate measurements.

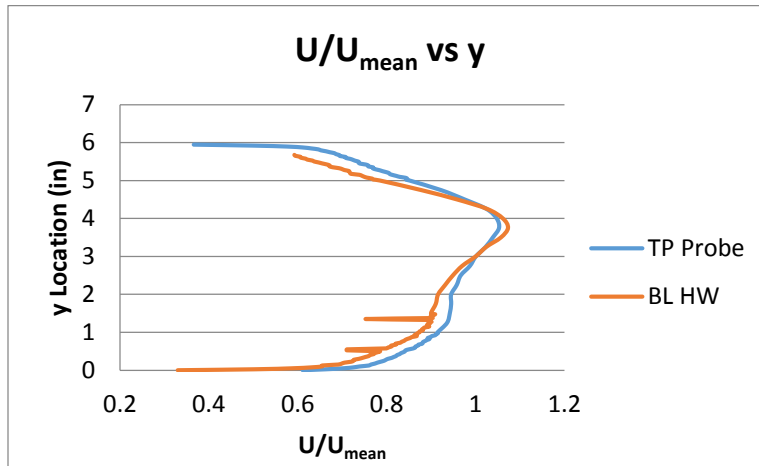


Figure 3: Total Pressure vs BL Hot Wire Velocity Profiles Non-Dimensionalized by Freestream Velocity.

Next, two more traverses were performed using the boundary layer hot wire that focused on the bottom half of the test section for the two cases of suction. These traverses were done with a step size of 0.005” to increase the accuracy of the boundary layer thickness measurement. This yielded two different cases for boundary layer thickness at the leading edge of the cooling holes. The thickness was determined from the data by the notion that the boundary layer height is the y-location associated with the location of 99% of the freestream velocity.

TRANSIENT THERMAL IMAGING MEASUREMENTS

The method of data collection that was implemented to obtain results for evaluation of film cooling effectiveness at various boundary layer conditions was to use a FLIR thermal imaging camera to capture transient heat transfer data. The tests were sixty seconds long and measured temperature across the flat plate, turbine blade representation. This data was extracted from the FLIR software and was written to a Microsoft Excel file. The data was then imported into a MatLab program that simultaneously solved for heat transfer coefficient and film cooling effectiveness. Of the two parameters, film cooling effectiveness will be the focus of this study. The results of the data reduction are quantitative results for the convective heat transfer coefficient and film cooling effectiveness as well as contour plots of each parameter over the surface of the flat plate. Typically, results are consolidated into span averaged and centerline averaged subsets. For this analysis, results will be limited to span averaged data because it is likely to give more insight into the effect of turbulence intensity.

RESULTS

TURBULENCE MEASUREMENTS

The results of the turbulence intensities and length scales are summarized in Table 1 for the streamwise location of $x/b = 10.25$, just upstream of the cooling holes. Note that b is the thickness of the turbulence grid. The previous measurements taken by an undergraduate researcher, Dustin Frohnappfel, are provided in the column labeled “previous” and are comparable to the measurements obtained in this work.

Table 1: Turbulence Intensity and Length Scale for Current Study and Previous Measurements

x = 10.25" - f = 50kHz		
b = 1/4"	Current	Previous
Tu (%)	8.7782	9.1182
Λ (in.)	0.4289	0.5718
b = 1/2"	Current	Previous
Tu (%)	14.721	15.0428
Λ (in.)	0.5282	0.5391

Similar measurements were taken at two additional locations along the length of the test section. This data is compared to Baines and Peterson's [6] theoretical decay of turbulence intensity and length scale.

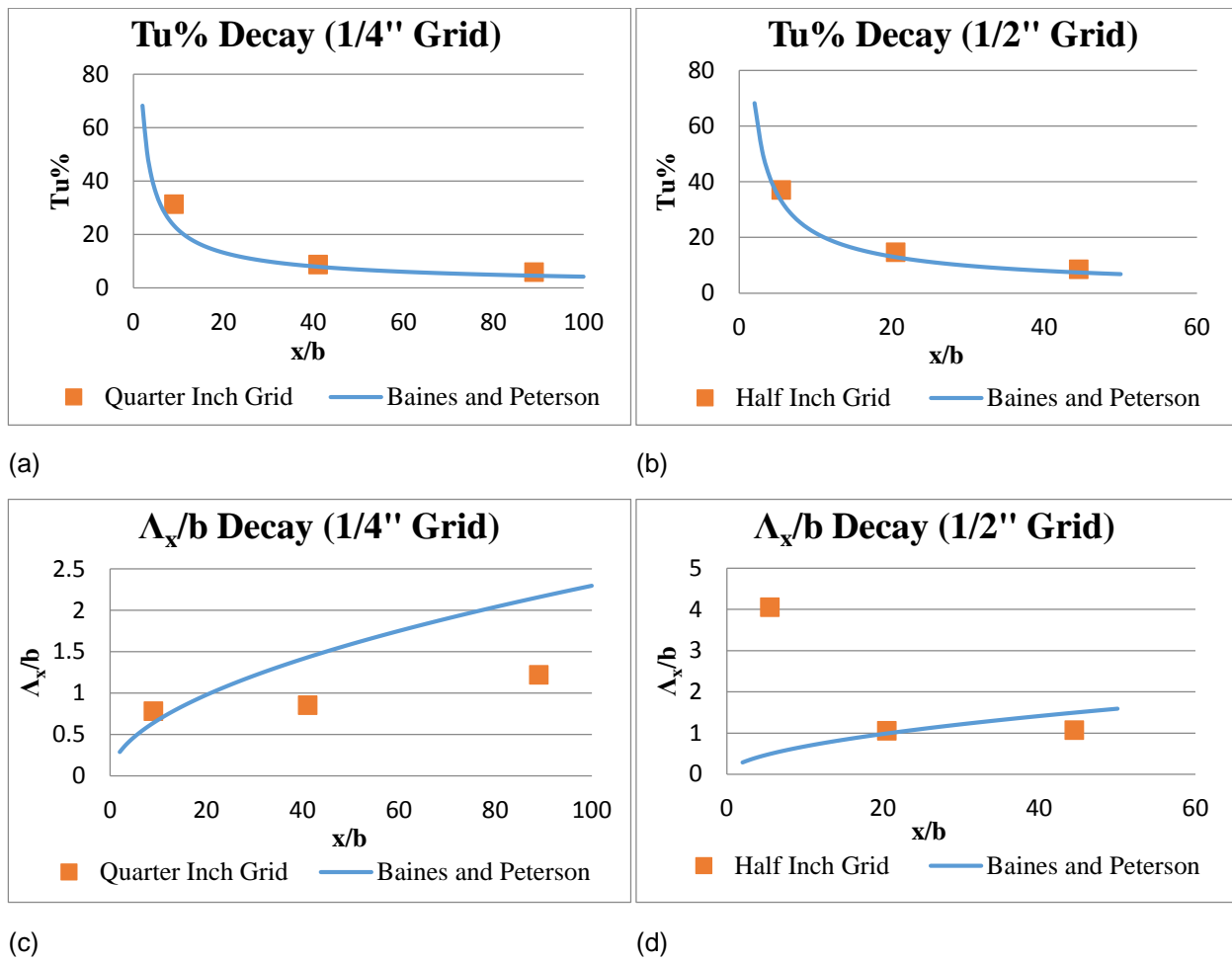


Figure 4: Turbulence Decay

As seen in Figure 4, the data closely follows the turbulence decay predicted by Baines and Peterson for turbulence intensity. The data does not as closely represent the trend for turbulence length scaled decay, however this is a much more difficult variable to predict.

Boundary Layer Thickness Measurements

The boundary layer thicknesses were found to be 1.06 inches when the suction motor was turned off and 0.605 inches when the motor was turned on. Thus, the suction motor provides a change of nearly one inch. Below are the curves that resulted from the hot wire traverses. The purpose of including a boundary layer suction mechanism and collecting this data has to do with real world application. To accurately study gas turbine heat transfer, the Reynolds and Mach numbers for the experimental facility should be similar to real world conditions. In the lab at WVU, it is possible to match Reynolds number, but not realistic to match Mach number. For this reason, when operated without the boundary layer suction, the tunnel produces a boundary layer that is not representative of what would occur in an engine during flight. To account for this, the ratio of boundary layer thickness to cooling hole diameter will be matched. This will give a more representative environment to study the effects of different variables on gas turbine heat transfer and is the reason that boundary layer thickness results are discussed here. This data will be used to find a suction motor setting that gives the desired boundary layer thickness to cooling hole diameter ratio.

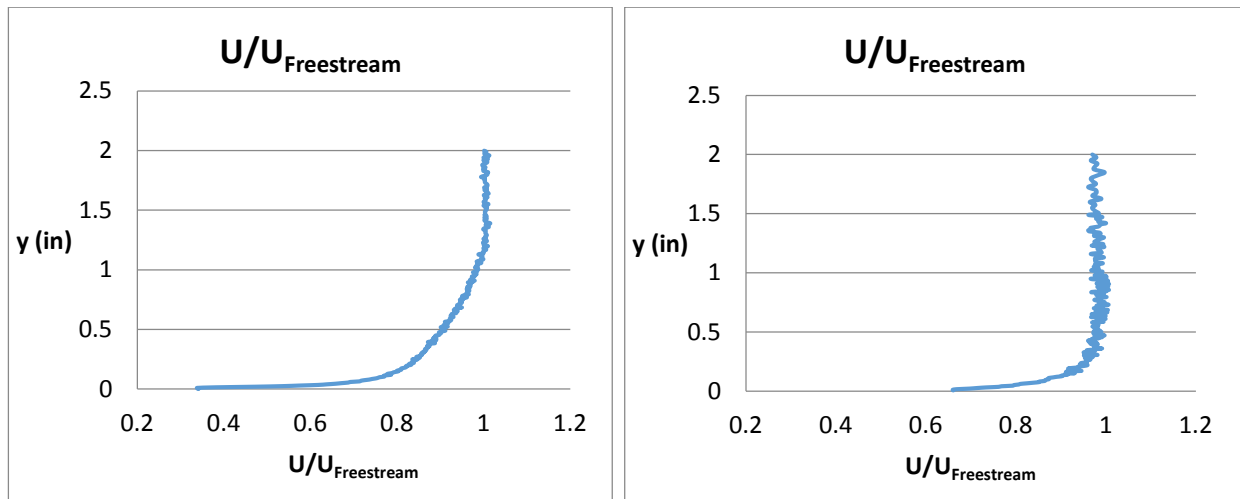
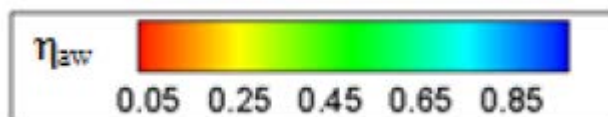


Figure 5: Non-Dimensionalized Velocity Profiles for the cases of (Left) Suction Off and (Right) Suction On

Film Cooling Effectiveness

The first set of thermal imaging data was collected in this study. A blowing ratio of 1.0 was chosen for the investigation. Repko [2] and Hunley [7], both of whom studied the effect of turbulence intensities of 5, 10, and 20% on film cooling effectiveness at a blowing ratio of 2.0, found that increasing turbulence intensity was indicative of higher span-averaged film cooling effectiveness. The experimental conditions for this data were turbulence intensities of 7.5% and 11.7% with boundary layer suction on. These turbulence intensities occur at the leading edge of the film cooling holes. The data collected for previous sections specified turbulence intensities at a different location.



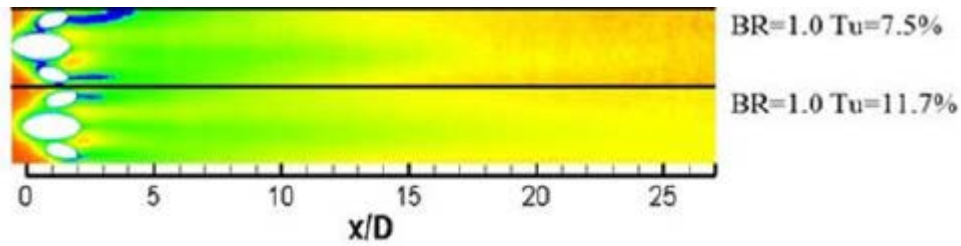


Figure 5: Contour Plot of Film Cooling Effectiveness at a Blowing Ratio of 1.0 and varying turbulence levels

From the contour plot in Figure 5, it appears that film cooling effectiveness increases as turbulence intensity increases. This observation is supported numerically by the span-averaged film cooling effectiveness data. A numerical comparison between the two cases is found below, in Table 2.

Table 2: Comparison of Film Cooling Effectiveness at Various Turbulence Intensities with Suction On.

	η_{aw}
Tu 7.5%	0.2943
Tu 11.7%	0.314

VALUABLE OUTCOMES

This experience provided many unexpected outcomes. Through working on this project, I have experienced how demanding this type of work is. In research, it is not enough to observe or quantify a phenomenon. You must have systems to back up the results obtained from the primary data collection system and investigate cases that have been done in previous works such that your facility is comparable to similar facilities and therefore your findings are valid. These additional tasks set the timeline for this work back, but they provided a valuable lesson in not expecting the work to go smoothly. On a different note, I enjoyed obtaining tangible data for physical phenomena that I have conceptually learned in class. It was rewarding and interesting to be able to prove topics like viscous boundary layers and turbulence through experimental data collection. I also valued the experience with the different systems employed in the lab. I have learned about pressure transducers, pitot static probes, hot wire anemometers, and thermocouples in class, but I have never needed to change the settings, calibrate, or use a multitude of these components in one system. Above all else, this opportunity provided me experience in useful critical thinking. Obtaining undesirable results and having to evaluate where the experiment went wrong is not a simple process, especially when the data collection incorporates multiple systems. The professional experience provided to me through this experience is invaluable and I hope that the lessons I have learned and knowledge that I have gained in the realm of research will open new opportunities such as this in the future.

FUTURE PLANS

I plan to take the experience I have gained and lessons I have learned to Orlando, FL this summer where I will be working with Siemens Power Generation on gas turbine research and development as an intern funded by the Southwest Research Institute's (SwRI) University Turbine System Research (UTSR) program. Upon returning for my final year at West Virginia University, I intend

to complete a full investigation on the effect of boundary layer thickness and state on film cooling effectiveness, using the findings outlined in this report. To accomplish this, more data needs to be taken for the other case of boundary layer thickness (with the suction off). This investigation will involve using thermal imaging equipment and software to collect transient data of a flow at varying turbulence intensities and boundary layer thicknesses over a flat plate representation of a turbine blade outfitted with AVH geometry for film cooling. The results of this study will be documented as a journal article and submitted to Scientific Research Publishing (SCIRP).

CONCLUSION

In conclusion, this project produced useful results to be used in a future study. The systems incorporated in the tunnel, such as the boundary layer suction motor and the turbulence grids, provide plenty of variation in key variables to be studied in terms of film cooling effectiveness. These cases will give clear conclusions on the impact of boundary layer thickness and turbulence intensity on film cooling effectiveness. The results compiled thus far suggest that higher turbulence intensities yield greater film cooling effectiveness. Physically, higher turbulence intensities provide better heat transfer because the randomness of the flow due to the turbulence distributes the coolant flow to a wider area. The trend observed is the desired outcome of this investigation, as high turbulence levels are more realistic to the first turbine stage of a gas turbine engine. The impact of boundary layer thickness will be determined in the coming months.

In retrospect, the systems used in this wind tunnel should have been better understood prior to beginning the work. There were numerous hold ups due to lack of knowledge and experience with the systems and components being used. It is also recommended that more time efficient methods of data acquisition be designed. One such suggestion would be to design a MatLab code for hot wire and total pressure probe traverses. Due to the manual input required to change the location of the probe, the code would be used to automate the saving process and data compilation and reduction processes, leaving the researcher with the simple obligations of starting the code and turning the knob on the traverse mechanism each time the code requests that a change be made.

ACKNOWLEDGEMENTS

I would like to thank West Virginia University and the Benjamin J. Statler College of Engineering and Mineral Resources for providing me with so many academic and professional opportunities. I would like to extend my gratitude to Dr. Andrew C. Nix, who brought this opportunity to my attention and assisted me throughout the process. Special thanks go out to Stephen A. Hayes, who mentored me along the way and helped me to gain experience and knowledge in the realm of gas turbine heat transfer through his graduate work. Thank you to Mr. Daniel Bartels who has inspired me to pursue research opportunities. Last but not least, thank you to my parents for providing all of the support and confidence I could ever need. Of course, none of this could be possible without the opportunity provided by the NASA WVSGC. The experience that I have gained from this opportunity is astounding. I am honored to have been selected to participate in such a generous program.

REFERENCES

- [1] Hayes, S., Nix, A. C. "An Experimental Investigation on the effects of Freestream Turbulence Intensity on Film Cooling Effectiveness and Heat Transfer Coefficient for an Anti-Vortex Hole."
- [2] Repko, T.W., Nix, A.C., and J. D. Heidmann, "A Parametric Numerical Study of the Effects of Freestream Turbulence Intensity and Length Scale on Anti-Vortex Film Cooling Design at High Blowing Ratio," in *ASME 2013 Summer Heat Transfer Conference*, Minneapolis, MN, USA, 2013.
- [3] Irvine Jr., Thomas F. *Advances in Heat Transfer, Volume 7. Film Cooling*. London. Academic Press, Inc. May 14th, 1971.
- [4] E. B. Inc. (2014, Sep. 29). *Gas-Turbine-Engine (Encyclopedia Britannica Online Academic Edition. ed.)*. Available: <http://www.britannica.com/EBchecked/topic/226481/gas-turbine-engine>
- [5] Hill, P. G. and Peterson, C. R., "Mechanics and Thermodynamics of Propulsion," *Reading, MA, Addison-Wesley Publishing Co., 1992, 764 p.*, vol. 1, 1992.
- [6] Baines, W.D. and Peterson, E.G., "An Investigation of Flow Through Screens," Iowa City: *ASME*, 1951. pp. 467-480.
- [7] Hunley, B. K., Nix, A.C., and Heidmann, J.D., "A Preliminary Numerical Study on the Effect of High Freestream Turbulence on Anti-Vortex Film Cooling Design at High Blowing Ratio," presented at the ASME Turbo Expo, Glasgow, Scotland, 2010.

EFFECT OF LINKER LENGTH AND STRUCTURE ON BIOSENSOR PERFORMANCE

Destiny Carte
Bachelor of Science in Chemistry
Marshall University
Huntington, West Virginia 25703

ABSTRACT

DNA monolayers on gold surfaces have numerous applications in the fields of chemistry, biology and biotechnology. Single-stranded DNA probe strands were bound to gold surfaces using thiol-modified dendrons to create DNA monolayers. The NHS-maleimide crosslinkers used to connect the ssDNA and dendrons were differed to determine how length and structure affect the hybridization of probe DNA to target strands, which was quantified using surface plasmon resonance reflectometry. Displaying similarly unhindered structures, the shortest linker, AMAS (4.4 Å) bound less efficiently to target DNA than the longer aliphatic linkers GMBS (7.3 Å) and sKMUS (16.3 Å), demonstrating that length and binding capacity are positively correlated. However, sKMUS, with its flexible aliphatic structure bound less efficiently than sSMCC (8.3 Å), suggesting that a hindered structure promotes better binding to target strands by minimizing probe entanglement. The lesser binding capacity of GMBS, an aliphatic linker of similar length to sSMCC further indicates that hindered structures promote better binding of conjugates to target analytes.

INTRODUCTION

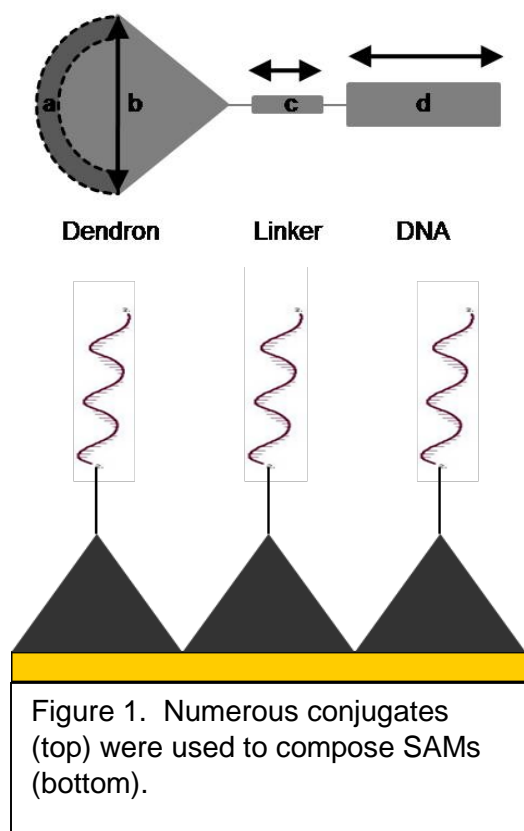
Biosensors, in which numerous samples are packed closely together on a surface typically the size of a 1" × 3" microscope slide, are renowned for their ability to rapidly analyze a large number of distinct substances.¹ Each biochip can contain up to tens of millions of probes designed to detect target analytes including DNA, proteins, antibodies, and other small biological molecules.²

SAMs composed of ssDNA probes on gold substrates have extensive applications in biosensor technology including DNA sequencing, genetic disease diagnostics^{3,4} and directed assembly of proteins.⁵ Most recently, research has explored the utilization of ssDNA aptamers probes, which are able to capture a large array of target analytes other than nucleic acids.⁶ Areas of biosensor research include⁷: allergies, Alzheimer's disease, apoptosis, autoimmunity, cancer, cardiovascular disease, connective tissue disorders, immunoglobulin isotyping, inflammation, infectious disease, metabolic diseases, oncology and sepsis. SAMs can also serve as diagnostic assays for medical conditions, such as allergies, autoimmune diseases, drug abuse, infectious diseases, heart failure and other coronary problems. In addition to diagnosing and researching disease, DNA aptamer monolayers have the potential to identify biological warfare agents.

Although biosensors that involve ssDNA probe strands are already widely used,¹ biochips utilizing protein-based capture molecules are less common due to the intricate structure-function relationships of proteins to their local environment. Protein-based capture molecules are more susceptible to denaturation than nucleic acid-capture molecules, as their stability and binding

capacity greatly depend upon conditions of the assay (pH, temperature, etc.).⁸⁻¹⁰ Further complications arise from the site-specific nature of some proteins, which dictate orientational control upon immobilization.¹¹ Antigens, for example, will not bind to the antigen-binding sites of antibodies if the antigen binding-sites are inaccessible. SAMs utilizing DNA aptamer probes may function as a more stable alternative to antibody biochips. Because the affinity of DNA aptamers to target analytes depends on their folded three dimensional structures, they simultaneously demonstrate the specificity of an antibody molecule and the stability of a nucleic acid.¹²

BACKGROUND



Traditionally, ssDNA probes have been bound to gold surfaces by a single thiol group. However, single point attachments can lead to heterogeneous surface coatings and desorption. Heterogeneous surface coatings can complicate both quantitative interpretation and DNA binding efficiency. DNA probes may be so crowded that their complementary strands do not sufficient space to hybridize with them. Conversely, DNA probes in sparsely covered areas may easily hybridize, but are inefficient due to their low surface density. Numerous studies have demonstrated that multi-thiol functionalized dendrons, or cleaved dendrimers, provide greater stability for DNA binding and signaling compared to DNA probe strands adsorbed to gold substrates through linear linkers, as dendrons promote surface homogeneity, allow greater control of probe packing density and provide a more robust attachment to the surface.¹³⁻¹⁷

Figure 1. Numerous conjugates (top) were used to compose SAMs (bottom).

illustration of the conjugates used to study binding capacity. Conjugates were composed of multi-thiol (“a”) functionalized dendrons (“b”), which were linked via an NHS-ester maleimide linker (“c”) to ssDNA probes (“d”) and immobilized to a gold substrate.

Dendrons were utilized as spacer molecules to create a more homogenous monolayer in which spacing can be controlled according to headgroup size based on dendrimer generations 1-5. Figure 2 portrays an

Although SAMs composed of generation 5 dendrons have demonstrated greater binding capacities than SAMs composed of dendron generations 1-4 (Figure 2)¹⁸, generation 4 dendrons instead were used to study the effect of linker length (Figure 1, “c”) and structure on the binding capacity of SAMs because of their relative ease of synthesis compared to generation 5 dendrons.

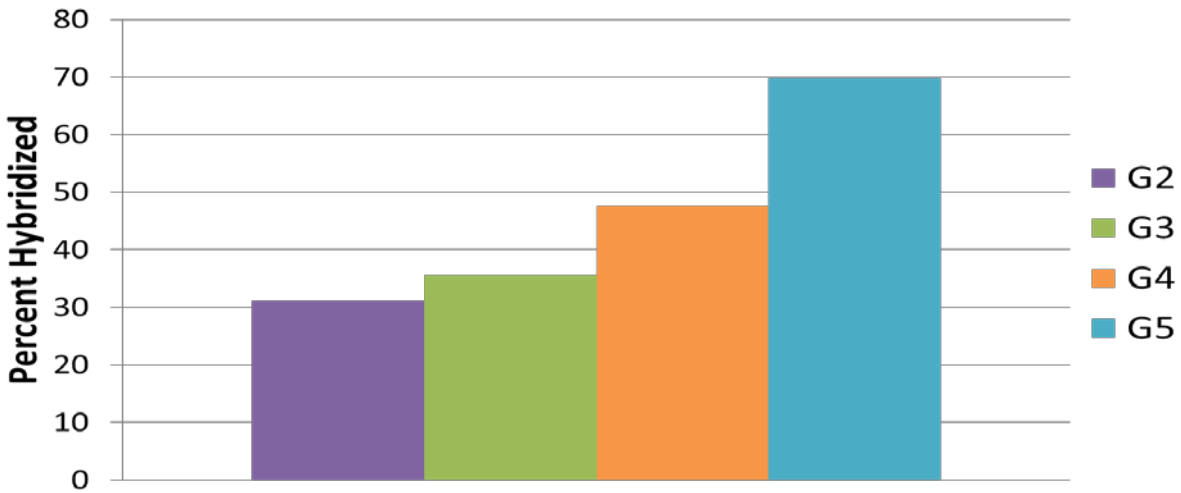


Figure 2. Hybridization efficiency for conjugate monolayers G2-G5 as determined by SPR.¹⁸

EXPERIMENTAL MATERIALS

Materials	Source
Probe DNA	Integrated DNA Technologies
Complementary DNA	Integrated DNA Technologies
Generation 4 cystamine-core dendrimers	Sigma – Aldrich Inc.
SATP	Pierce Thermoscientific
NHS – Maleimide Linkers (see Table 2)	Pierce Thermoscientific
BupH phosphate buffered saline packs	Pierce Thermoscientific
BI – 200 Surface plasmon resonance reflectometry system	Biosensing Instrument Inc.
Plasma Cleaner PDC – 32G	Harrick Plasma

Table 1. List of materials and the companies from which they came.

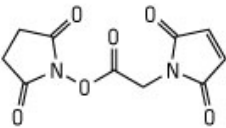
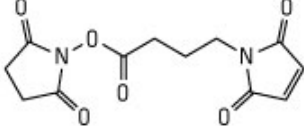
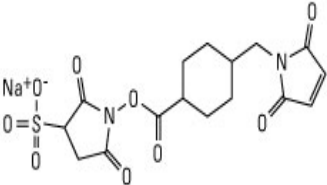
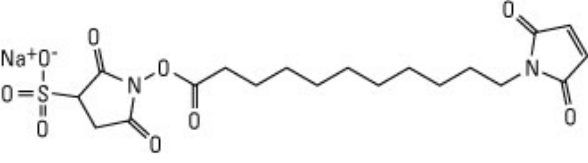
 <p style="text-align: center;">AMAS <i>N</i>-(α-Maleimidoacetoxy) succinimide ester MW 252.18 Spacer Arm 4.4 Å</p>	 <p style="text-align: center;">GMBS <i>N</i>-(γ-Maleimidobutyryloxy)succinimide ester MW 280.23 Spacer Arm 7.3 Å</p>
 <p style="text-align: center;">Sulfo-SMCC Sulfosuccinimidyl 4-(<i>N</i>-maleimidomethyl)cyclohexane-1-carboxylate MW 436.37 Spacer Arm 8.3 Å</p>	 <p style="text-align: center;">Sulfo-KMUS <i>N</i>-(κ-Maleimidoundecanoyloxy) sulfosuccinimide ester MW 480.46 Spacer Arm 16.3 Å</p>

Table 2. NHS – ester maleimide linkers used to synthesize conjugates.

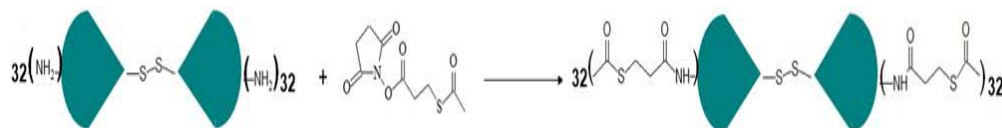
Conjugate Synthesis

For a schematic representation of the conjugate preparation reaction, refer to Figure 3.

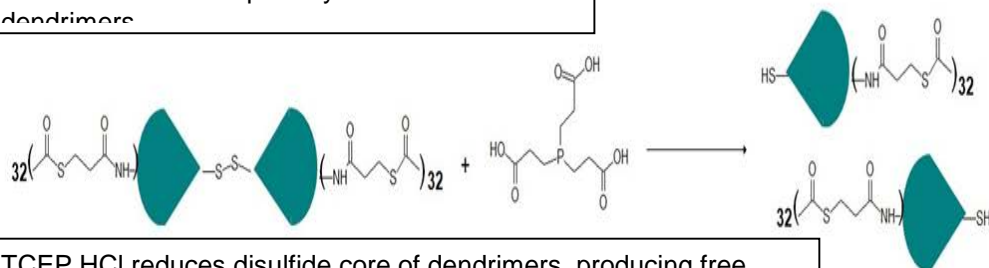
Generation 4 cystamine-core polyamidoamine (PAMAM) dendrimers were used as head groups for immobilizing the DNA probes to gold substrates. Via a nucleophilic substitution reaction, the primary amines of the dendrimers were reacted for 45 minutes with *N*-succinimidyl-*S*-acetylthiopropionate (SATP) in 0.1 M phosphate buffer solution, pH 7.2, in order to temporarily place protecting thioacetate groups on the periphery of dendrimers until immobilization to the substrate. After the functionalization of the terminal amines with SATP, the disulfide bond at the dendrimer core was cleaved via a 45 minute reaction with the reducing agent, Tris (2-carboxyethyl) phosphine Hydrochloride (TCEP HCl), creating two dendrons with free thiol groups necessary for later reaction with the maleimide groups on the DNA sequences.

While the dendrimers were functionalized, a 45 minute reaction took place between the NHS-ester group of the selected NHS-maleimide linker (Table 2) and the terminal amine of each ssDNA in a 0.1 M phosphate buffer solution, pH 7.2, forming a DNA-linker complex. Linkers that had not been modified with a sulfo group first had to be dissolved in dimethyl sulfoxide (DMSO) before being dissolved in phosphate buffer.¹⁹ Via an overnight Michael addition at 25 °C in 0.1 M

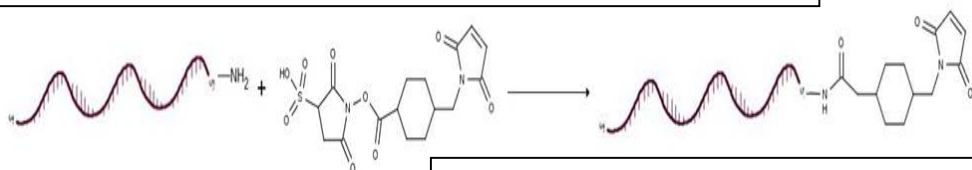
phosphate buffer, pH 6.8, the maleimide group of the newly formed DNA-linker complex was reacted with the free thiol groups of the dendrons. The reaction of maleimides is very specific to thiols at typical physiological pH 6.5 - 7.5, while the reaction of NHS-ester groups with primary amines is specific at pH 7.0 – 9.0.²⁰ Because of this, a more acidic phosphate buffer was used for the linking of DNA to dendrons than for the reaction linking the DNA and NHS-maleimide linker



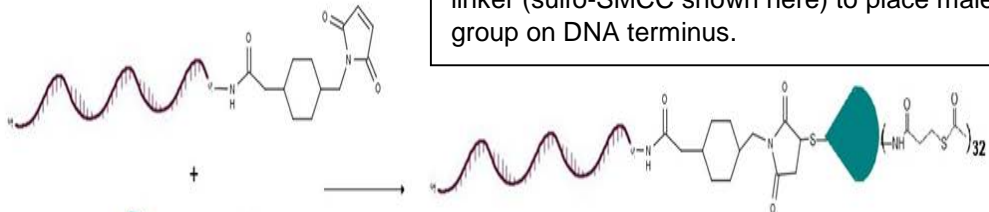
SATP functionalizes primary amines of dendrimers



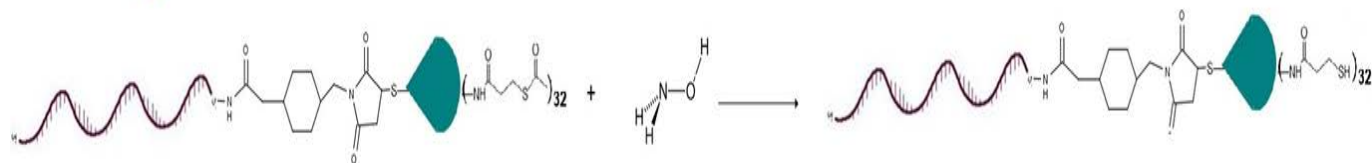
TCEP HCl reduces disulfide core of dendrimers, producing free thiol groups.



Terminal amino group on DNA will be reacted with NHS-maleimide linker (sulfo-SMCC shown here) to place maleimide functional group on DNA terminus.



DNA is reacted with dendrons via a Michael addition.



Protecting acetate groups are removed with hydroxylamine, allowing dendrimers to adsorb to gold.

Figure 3. Synthesis scheme by which conjugates were created.

Conjugate Purification

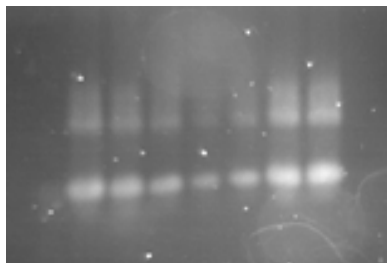


Figure 4. Gel image of conjugate synthesis product.

Agarose gel electrophoresis and extraction were used to purify and quantify the extent of the DNA-dendron conjugate reaction. DNA sequences coupled to dendrons displayed a mass shift relative to the free DNA strands, allowing the reacted bands to be identified, extracted and stored in a 1x Tris/Borate/EDTA (TBE) solution for several days at 4° C in order for the conjugate products to elute into the solution before concentration in 10 kDa MWCO amicon columns. In the gel image, the relative intensity in unreacted bands (bottom, Figure 4) and reacted bands (top, Figure 4) allowed the ratio of conjugates relative to free DNA to be quantified.²¹

Monolayer Preparation

Conjugates were reacted with a solution of hydroxylamine in order to remove protecting acetate groups and create free thiol groups that allowed the dendrimers to self-assemble onto the gold surface. The gold surfaces used for DNA immobilization were cleaned in a piranha solution (70/30 (v/v) mixture of concentrated H₂SO₄/ 35% H₂O₂) for at least one hour prior to use. Piranha solution is a powerful oxidizing solution that reacts strongly with organic materials, and therefore cleans residual organic molecules off of the slide. Gold slides removed from the piranha solution were thoroughly rinsed with deionized water and dried with a stream of nitrogen before being immediately submerged into a conjugate solution to act as substrates for SAMs.

Functional Analysis

Because surface plasmon resonance (SPR) reflectivity measurements can be used to detect molecular adsorption to surfaces, this technique was used to quantitate the surface densities and binding capacities of the SAMs. For each conjugate, 100 μL quantities of solutions of target analyte varying in concentration from 10 nM to 10 μM were injected over the monolayer surface at a flow rate of 10 μL/min. For each injection, the change in signal, or change in refractive index was measured. A larger change in signal indicates higher binding frequency. After each injection of analyte solution was bound to the SAM, an injection of 50 mM sodium hydroxide (NaOH) solution was injected over the surface to dehybridize the analyte from the DNA probes, allowing multiple trials to be performed on the same surface. A typical SPR measurement is represented in Figure 5.

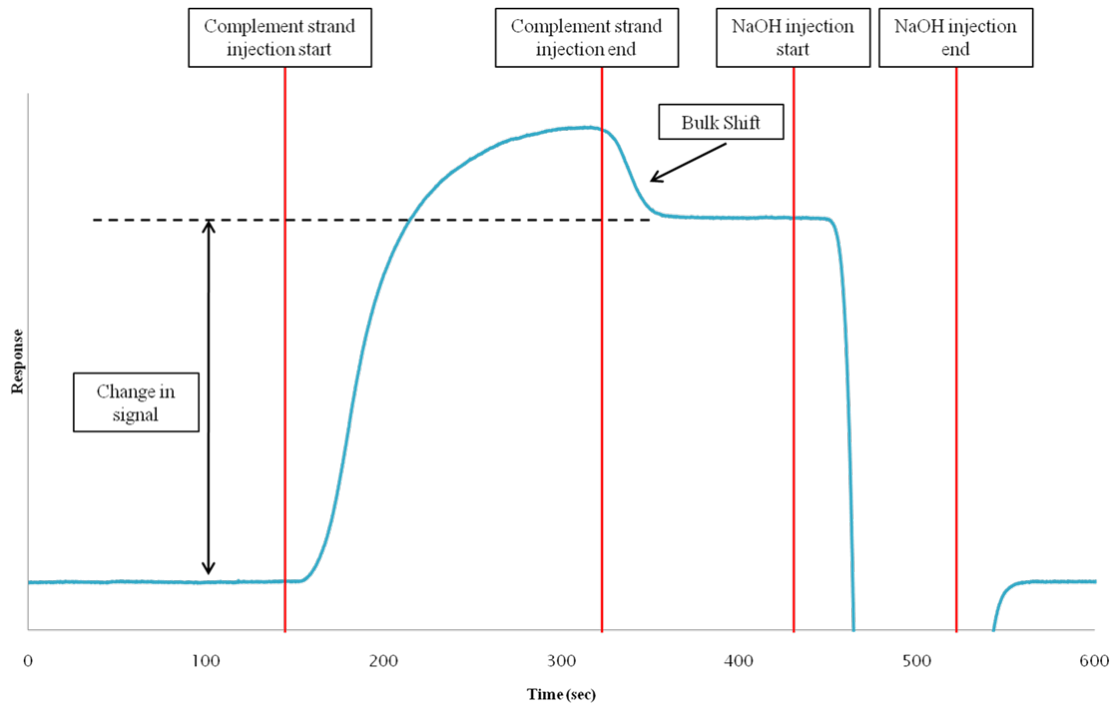


Figure 5. Representation of a typical hybridization trial. The baseline shift after the analyte is allowed to hybridize to the probe strands indicates the hybridization efficiency of the SAM.

RESULTS

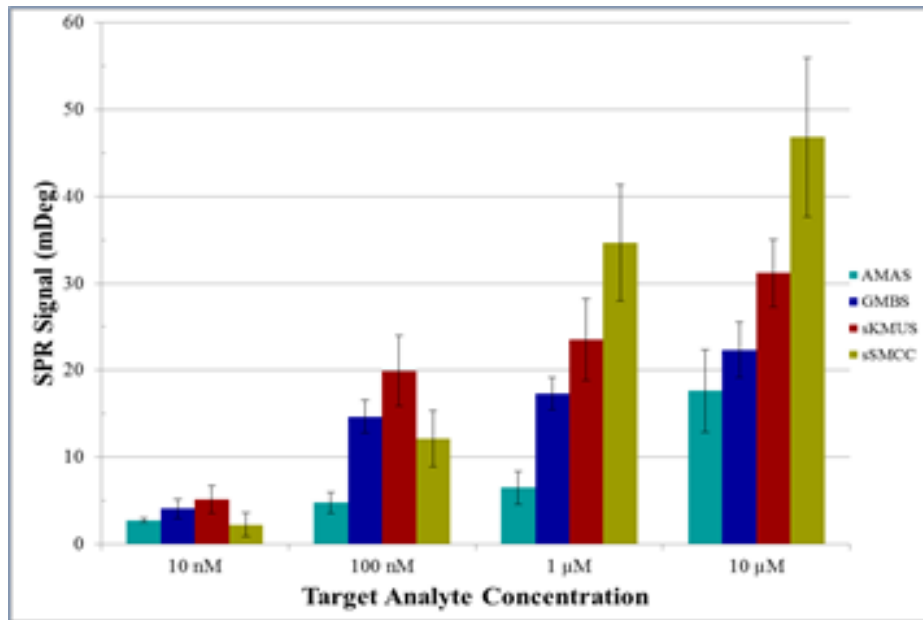


Figure 6. SPR shift (mDeg) produced by conjugates of all four linkers from the binding of probe strands to different concentrations of analytes.

DISCUSSION

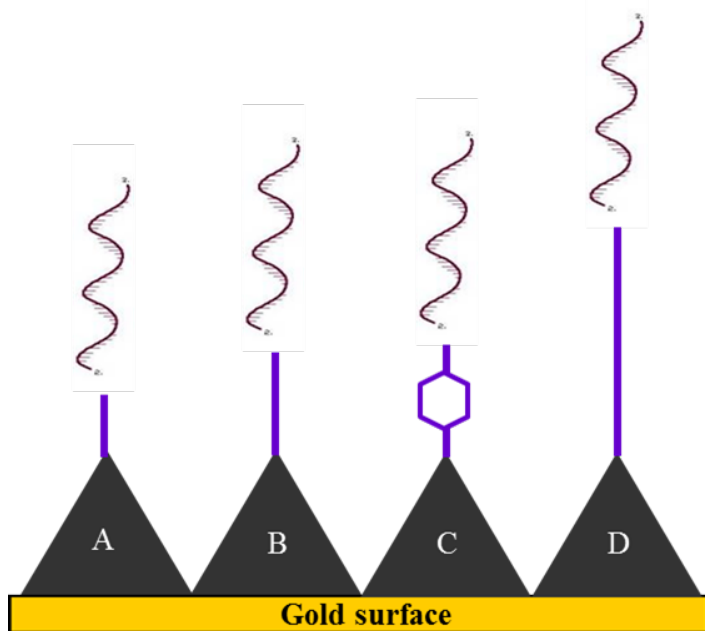


Figure 7. Representation of SAMs composed of examined linkers arranged in increasing length. Linkers scaled to relative length with one another.

A) AMAS B) GMBS C) sSMCC D) sKMUS

Effect of Linker Length

The effect of linker length on binding capacity was examined by comparing the binding capacity of SAMs composed of three linkers with comparable structures but different lengths: AMAS (4.4 Å), GMBS (7.3 Å), and sKMUS (16.3 Å) (Figure 7, “A,” “B,” and “D”). Over the course of repeated trials, longer linkers demonstrated significantly higher binding capacities than shorter linkers of similar structure (Figure 6), indicating that an increase in linker length improves binding capacity. This is likely due to the superior ability of longer linkers to extend probes from the surface, increasing their accessibility to the target analyte.

Effect of Linker Structure

The effect of linker structure on binding capacity was examined by comparing the binding capacity of two linkers similar in length, but different in structure: sSMCC and GMBS (Figure 7, “B” and “C”). Although similar in length, the measured binding capacity of GMBS (7.3 Å) was significantly less than the value measured for sSMCC (Figure 6). This difference was attributed to increased stability provided by existence of an internal hindered cyclohexane ring within the sSMCC linker. The lesser binding capacity of GMBS, which has only an internal aliphatic chain, may make it more prone to entanglement with neighboring probe strands, decreasing both the stability and the binding capacity.

Relative Effects of Linker Length and Structure

The results indicate that both hindered linker structure and longer linker length promote better binding capacity. However, they do not indicate the relative importance of each variable. To assess this, the binding capacity of sKMUS (16.3 Å) (Figure 7, “D”), an unhindered linker, was examined. Monolayers assembled with sKMUS exhibited a superior binding performance relative to monolayers assembled with GMBS and AMAS, but an inferior binding performance relative to monolayers assembled with sSMCC at target concentrations of 1 μM and 10 μM (Figure 6). Because the binding capacity of sKMUS fell between that of the hindered linkers, sSMCC and AMAS, a possible explanation is that the benefits of a longer, less hindered linker length eventually plateau due to entanglement.

For the two lowest target concentrations (10 and 100 nM), it appears that sSMCC has a lower binding capacity than the GMBS and sKMUS. Further examination of sSMCC would have to be undergone in order to determine whether this is accurate. Oftentimes, SPR graphs do not exactly resemble the one depicted in Figure 5. The baseline measurements are performed visually. Certain variables, such as temperature, and bubbles in the pH 7.20 phosphate buffer used in the SPR system can result in a baseline that is not completely flat, but instead has a curve that typically spans 0 - 5 mDeg. When this occurs, a visual estimate of the baseline is performed. Zach Hunter, a lab member who left the lab before this project began, collected the data for the binding capacities of SAMs composed of sSMCC. Because the baseline values are not always completely clear, it is possible that the baselines for SAMs composed of sSMCC were underestimated. For SAMs constructed with AMAS, GMBS and sKMUS, the middle of a curved baseline was used as an estimate. It is possible the bottom of a curved baseline was used as an estimate for SAMs composed of sSMCC. A several mDeg discrepancy would be more likely to affect the qualitative accuracy of the lower baseline shifts of the 10 and 100 nM target concentrations relative to the higher baseline shifts of the 1 and 10 μ M target concentrations.

FUTURE PLANS

Research

Because sSMCC is the only previously examined rigid linker, the effect of linker length on SAMs composed of rigid linkers is unclear. Future work will involve examining the binding capacities of SAMs composed of a greater variety of rigid linkers in order to further examine the effect of linker structure and length on the binding capacities of SAMs.

Dissemination

In addition to presenting at Marshall University's research symposiums during the summer of 2015 and Sigma Xi Research Day in May, 2016, I also plan to present my research at the 250th American Chemical Society National Meeting & Exposition at Boston, Massachusetts from August 16 – 20, 2015. Toward the end of the summer of 2015, I plan to begin the process of manuscript publication. I am open to any other opportunities in which I can present my research.

OUTCOMES

The financial support provided to me by NASA WV Space Grant Consortium has allowed me to spend considerably more time performing research than I would have been able to do otherwise. Because of this, I have made more progress in my research than I had originally anticipated upon starting undergraduate research.

I have been able to present my research at Marshall University's Summer Research Symposiums in addition to the 44th Central Regional American Chemical Society Meeting in Pittsburgh, Pennsylvania.

ACKNOWLEDGEMENTS

I would like to acknowledge Dr. Scott Day for allowing me to work in his research lab and for his support and guidance during the course of my undergraduate research, Chris Warner for teaching me laboratory techniques necessary for conjugate synthesis, Zach Hunter for preliminary data,

Tyler Skidmore for his assistance over the course of this project, Dr. Michael Norton for the use of his laboratory, the Marshall University Chemistry Department for supporting me throughout my undergraduate research with the Alumni-Sponsored Summer Undergraduate Fellowship and NASA for funding through the West Virginia Space Grant Consortium.

REFERENCES

News Medical. <http://www.news-medical.net/news/20090624/Protein-biochips.aspx>. (accessed October 2013).

Brandstetter, T. *IMTEK – Chemistry and Physics of Interfaces – CPI*. <http://www.cpi.uni-freiburg.de/teaching/lecture-biochip-technologies/2012-biochip-technologies-1-materials-in-the-life-sciences> (accessed November 2013).

Wang, J. From DNA Biosensors to Gene Chips. *Nucleic Acids Research*. 2000, 28 (16), 3011–3016.

Freeman, W. M.; Robertson, D. J.; Vrana, K. E. Fundamentals of DNA Hybridization Arrays for Gene Expression Analysis. *Biotechniques* 2000, 29 (5), 1042–1055.

Boozer, C.; Ladd, J.; Chen, S.; Jiang, S. DNA-Directed Protein Immobilization for Simultaneous Detection of Multiple Analytes by Surface Plasmon Resonance Biosensor. *Analytical Chemistry* 2006, 78 (5), 1515–1519.

Yin, X.-B.; Xin, Y.-Y.; Zhao, Y. Label-Free Electrochemiluminescent Aptasensor with Attomolar Mass Detection Limits Based on a Ru(phen)₃²⁺-Double-Strand DNA Composite Film Electrode. *Analytical Chemistry* 2009, 81 (22), 9299–9305.

Bodovitz, S.; Joos, T.; Bachmann, J., Protein Biochips: The Calm Before the Storm. *Drug Discovery Today* 2005, 10 (4), 283–287.

Vijayendran, R. A.; Leckband, D. E., A Quantitative Assessment of Heterogeneity for Surface-Immobilized Proteins. *Analytical Chemistry* 2001, 73 (3), 471-80.

Metzger, S. W.; Lochhead, M. J.; Grainger, D. W. Surface Technologies to Improve Performance in Protein Microarray Based Molecular Diagnostics. *In Vitro Diagnostic Technology*. 2002, 8, 39–45.

Haynes, C. A.; Norde, W., Globular Proteins at Solid/Liquid interfaces. *Colloids Surfaces B: Biointerfaces*. 1994, 2, 517-66.

Rusmini, F.; Zhong, Z.; Feijen, J., Protein Immobilization Strategies for Protein Biochips. *Biomacromolecules* 2007, 8 (6), 1775-1788.

Stadtherr, K.; Wolf, H.; Lindner, P., An Aptamer-Based Protein Biochip. *Analytical Chemistry*. 2005, 77 (11), 3437-3443.

Mark, S. S.; Sandhyarani, N.; Zhu, C.; Campagnono, C.; Batt, C. A., Dendrimer-Functionalized Self-Assembled Monolayers as a Surface Plasmon Resonance Sensor Surface. *Langmuir* 2004, 20 (16), 6808-6817.

Benters, R.; Niemeyer, C. M.; Drutschmann, D.; Blohm, D.; Wohrle, D., DNA Microarrays PAMAM Dendritic Linker Systems. *Nucleic Acids Research* 2002, 30 (2), 10.

Ajikumar, P. K.; Ng, J. K.; Tang, Y. C.; Lee., J. Y.; Stephanopoulos, G.; Too, H.-P, Carboxyl-Terminated Dendrimer Coated Bioactive Interface for Protein Microarray: High Sensitivity Detection of Antigen in Complex Biological Samples. *Langmuir* 2007, 23 (10), 5670-5677

Li, A.; Yang, F.; Ma, Y.; Yang, X., Electrochemical Impedance Detection of DNA Hybridization Based on Dendrimer Modified Electrode. *Biosensors and Bioelectronics* 2007, 22 (12), 1716-1722.

Day, B. Scott; Fiegland, Larry R.; Vint, Erik S.; Shen, Wanqiu; Morris, John R.; Norton, Michael L. Thiolated Dendrimers as Multi-Point Binding Headgroups for DNA Immobilization on Gold *Langmuir* 2011, 27 (20), 12434-12442.

Warner, C.; Hunter, Z.; Vint, E.; Jamieson, R.; Mickles, T.; Day, S., Characterization of DNA/Dendron SAMs on Gold. Poster presented at:

Pierce Protein Biology Products. <http://www.piercenet.com/cat/nhs-maleimide-crosslinkers> (accessed October 2013).

Smyth, D.G.; Blumenfeld, O.O.; Konigsberg, W., Reaction of N-ethylmaleimide with peptides and amino acids. *Biochemical Journal*. 1964, 91(3), 589.

Bell, S. A.; McLean, M. E.; Oh, S.-K.; Tichy, S. E.; Zhang, W.; Corn, R. M.; Crooks, R. M.; Simanek, E. E., Synthesis and Characterization of Covalently Linked Single-Stranded DNA Oligonucleotide-Dendron Conjugates. *Bioconjugate Chemistry*. 2003, 14 (2), 488-493.

MODULATING NEURAL CELL AND CENTRAL NERVOUS SYSTEM BIODEGRADATION OF IMPLANTABLE ENGINEERED MICROENVIRONMENTS USING APROTININ-STABILIZED FIBRIN

Arrin Carter
Department of Biology College of Science
Marshall University
Huntington, WV 25755

ABSTRACT

Experimental cell-based therapies for neurodegenerative disorders often involve implantation of bioengineered fibrin matrices into the region of interest. However, a major drawback to using fibrin is its rapid degradation by neural cell-derived proteases. The approach described here provides an efficient and broadly applicable method that produces aprotinin-stabilized fibrin matrices of predicted stability in either cultured neural cells or as implants into brain. In neural cell culture, fibrin containing no aprotinin, or with noncovalently incorporated aprotinin, was rapidly degraded. As predicted, when aprotinin was covalently crosslinked into the hydrogel, degradation was delayed and the extent of stability was directly proportional to the aprotinin concentration. To demonstrate whether these in vitro data reflect in vivo relevance, cylinders of fibrin/aprotinin were implanted into rat brain and the integrity of the implants assessed 3 weeks after surgery. Corroborating the cell culture data, cylinders were degraded in proportion to the concentration of crosslinked aprotinin. Efforts to stabilize fibrin have led to hydrogels of either limited stability or with such excessive stability that any regenerated cellular structures are likely to be impeded by the nondegraded matrix. Furthermore, current methods to immobilize aprotinin into biomaterials are complex, time-consuming or require engineered DNA constructs. Described here is a facile and tailorable method to prepare fibrin hydrogels with predictable stability in the brain environment. This provides a microenvironment upon which therapeutic neural cells can develop and differentiate that will eventually degrade to be replaced with the new cellular architecture.

INTRODUCTION

The basic premise underlying regenerative medicine is that diseases and disorders caused by dysfunctional or injured tissue can be treated with cell replacement therapy (Blelloch 2008; Chien 2008; Fox, Daley et al. 2014; Zupanc and Sirbulescu 2015). Regarding neurological diseases and disorders, many efforts are aimed at the restoration of function in non-neurogenic areas of the central nervous system (CNS). One approach involves implantation of therapeutic cells (Fricker, Carpenter et al. 1999) into the region of interest while a complementary method involves the direct delivery of recombinant proteins (Chen, Henry et al. 2007; Henry, Hughes et al. 2007) or other substances (Conway and Schaffer 2014) that themselves have therapeutic potential. The latter approach depends upon recruitment of neural stem cells from neurogenic niches into the non-neurogenic regions, or activation of a population of occult progenitor cells that may reside in these

areas (Maya-Espinosa, Collazo-Navarrete et al. 2014). Exogenous cells or factors often migrate or diffuse away from the area of the implant, thus lessening the therapeutic efficacy of the approach (Smith, Chen et al. 2007; Lorentz, Kontos et al. 2011). This problem has been addressed by imbedding cells or purified proteins into biological matrices which serve as implantable scaffolds that restrict the cells or proteins to the proper anatomical location (Jhaveri, Hynd et al. 2009; Hansen, Muller et al. 2010; Park, Lim et al. 2010; Kauer, Figueiredo et al. 2011; Zhang, Tokatlian et al. 2011; Stanwick, Baumann et al. 2012). Both synthetic and natural substances have been used as matrix material and these include acrylics (MartinezRamos, Valles-Lluch et al. 2012), Matrigel™ (Jin, Mao et al. 2010), chitosan (Bozkurt, Mothe et al. 2010; Kim, Tator et al. 2011), hyaluronic acid (Parajo, D'Angelo et al. 2010; Centola, Abbruzzese et al. 2013), gelatin (Havenith, Versnel et al. 2011; Fon, AlAbboodi et al. 2014) and fibrin (Lee, Polio et al. 2010; Wood, MacEwan et al. 2010; Yasuda, Kuroda et al. 2010; Anderson, Siegman et al. 2011; Han, Jin et al. 2011). Our laboratory is especially interested in fibrin as an implantable, biocompatible matrix because it has many desirable properties of a clinically acceptable therapeutic reagent.

Fibrin is an especially promising scaffold for therapies aimed at neurological disorders because of its viscoelastic properties (Zuidema, Rivet et al. 2014), versatility in bioconjugate reactions (Wood, MacEwan et al. 2010), similarity to extracellular matrix proteins found in the brain (Georges, Miller et al. 2006) and current use in numerous clinical applications (Chalmers, Darling Iii et al. 2010; Dhillon 2011; Hoyt, LaViolette et al. 2014; Tan, Takagi et al. 2014). However, neural tissues exhibit robust degradative proteolytic activity against extracellular matrices and many studies have shown that fibrin is rapidly degraded (fibrinolysis) by neural cells, both in vitro and in vivo (FaberElman, Miskin et al. 1995; Le, Besson et al. 2003; Lo, Broderick et al. 2004; Sun, Hu et al. 2006; Ethell and Ethell 2007; Gueye, Ferhat et al. 2011; Jeon, Kim et al. 2012). The enzymes thought to mediate this degradation include plasmin and matrix metalloproteases (Sashindranath, Sales et al. 2012; Hultman, Cortes-Canteli et al. 2014). This places significant limitations on fibrin's therapeutic use in neurological applications because implants must survive long enough to influence local cellular activity in the CNS prior to degradation. Conversely, we argue that a fibrin implant should eventually degrade in order to physically yield to the newly formed cellular structures. Aprotinin, a small polypeptide serine protease inhibitor of plasmin and matrix metalloproteases (Netzel-Arnett, Mitola et al. 2002; Collen, Hanemaaijer et al. 2003; Reichel, Lerchenberger et al. 2011; Lerchenberger, Uhl et al. 2013; Lu, Korotcova et al. 2014), has been incorporated into various preparations of fibrin to slow its degradation. However, unless aprotinin is covalently incorporated into the hydrogel it is apparent that the inhibitor will rapidly diffuse out of the matrix rendering it once again susceptible to degradation (Willerth, Arendas et al. 2006; Lorentz, Kontos et al. 2011; Conway and Schaffer 2014; Hyatt, Wang et al. 2014; Sacchi, Mittermayr et al. 2014; Thomson, Dupras et al. 2014). This led to the recent efforts to immobilize aprotinin into fibrin by crosslinking the small protein into the matrix.

One method to achieve covalent immobilization of aprotinin into fibrin involved the generation of a recombinant version of the inhibitor containing an additional eight amino acid sequence at its carboxy-terminus (Lorentz, Kontos et al. 2011). This octamer corresponds to the substrate sequence for transglutaminase which is involved in the thrombin/Factor XIIIa polymerization of fibrinogen. When the recombinant aprotinin is present during the fibrinogen to fibrin polymerization, the engineered octamer sequence facilitates the covalent incorporation of the inhibitor into the matrix. While increased fibrin stability was observed, such an approach requires making the engineered plasmid construct, expressing the recombinant protein in a heterologous

bacterial expression system and purifying the material prior to use. Also, it was not readily apparent that the recombinant aprotinin/fibrin product could be easily tuned to yield matrices with different stabilities; the lowest concentration of immobilized recombinant aprotinin gave extreme resistance to degradation. We suggest that the ideal matrix must eventually degrade in a matter of days or weeks, depending upon the application.

An alternative method has been described involving a complex multistep synthesis of conjugated fibrin-apolitinin whose *in vitro* degradation could be tuned by crosslinking various concentrations of aprotinin into fibrin using 4-(4-Nmaleimidophenyl) butyric acid hydrazide hydrochloride (Smith, Chen et al. 2007). These fibrin-apolitinin conjugates were of limited stability in a chick chorioallantoic membrane angiogenesis assay; while the matrix was indeed more stable compared to fibrin containing non-crosslinked aprotinin, by day four it had nevertheless experienced significant degradation. We suggest that in cases where biological stability is required for more than a few days, an alternative method is required.

Existing protocols are tedious, time-consuming, require unique, molecularly engineered aprotinin constructs, or exhibit limited control over matrix half-life. The existing methods described above tested *in vivo* stability via subcutaneous implants in mice or as angiogenic matrices on chick chorioallantoic membranes. Neither of these environments exhibit the significant proteolytic/fibrinolytic activities that are observed in the brain; importantly, this degradation is known to be mediated by aprotinin-inhibitable plasmin and matrix metalloproteinases which justifies the exploration of new methods to stabilize this particular peptide into fibrin. Furthermore, despite the widespread use of fibrin hydrogels in experimental and clinical neurobiology, there are scant reports which address the stabilization of fibrin in the CNS. We present an efficient and versatile method to covalently incorporate aprotinin into fibrin in a method that does not require specialized laboratory skills, reagents or equipment, and can be optimized to yield matrices of nearly any desired biological half-life in neural tissues, ranging from days to weeks.

MATERIALS AND METHODS

Subventricular Zone Neural Progenitor Cell (SVZ-NPC) Culture

All animal procedures were performed following an approved protocol from the Institutional Animal Care and Use Committee of Marshall University. Cell culture reagents were from Life Technologies and growth factors were from R&D Systems. SVZ-NPCs were isolated from 200-275 gm female Sprague-Dawley rats according to standard methodology (Wachs, Couillard-Despres et al. 2003). The cells were maintained in DMEM/F12 media supplemented with B27/N2 according to the manufacturer's recommendation, penicillin/streptomycin (100 U/ml), 2 µg/ml heparin, 20 ng/ml bFGF-2, and 20 ng/ml EGF. The cells were maintained on a constantly rocking (30 rpm) platform at 37°C, 5% CO₂ in 6 well non-tissue culture treated plates. Spheroids and aggregates were enzymatically dissociated into single-cell preparations using Accutase® approximately every 2 weeks for propagation or as needed for use in experiments. To accomplish this, spheroids were recovered from culture and allowed to settle at 1 x g for five minutes. The supernatant was removed and 1 ml of Accutase® was added to the sample which was incubated at 37°C for 10-15 minutes with frequent trituration. The homogenous cell suspension was centrifuged

for 5 minutes at 500 x g at ambient temperature. The pellet was either resuspended in the maintenance media described above, or used for seeding tissue culture wells containing fibrin domes (vide infra).

Preparation of fibrin matrices

All stock components were dissolved in PBS unless otherwise noted. Solutions containing fibrinogen (from bovine plasma, Sigma-Aldrich) and varying amounts of aprotinin (from bovine lung, Sigma-Aldrich) were prepared as 20 μ l (final volume) aliquots on Parafilm® in a humidified chamber. When crosslinker was used, disuccinimidyl suberate (Pierce Chemical Co.) was freshly dissolved in dry DMSO (dried over 4Å, 40 mesh molecular sieves) and added to the sample at a final concentration of 50 μ M. The final fibrinogen concentration 36 μ M and the fibrinogen-fibrin conversion was initiated by the addition of 0.1 U thrombin (1 μ l, from bovine plasma, SigmaAldrich). To prepare domes for cell culture experiments, the preparation was quickly transferred into individual wells of 24-well tissue culture plates and the sample allowed to polymerize for 20-30 minutes before the careful addition of media and cells. Fibrin cylinders for surgical implantation were prepared in a similar manner, except that fluorescent fibrinogen (Alexa 488 fibrinogen, Life Technologies) was admixed with the preparation at a final concentration of 0.15 mg/ml. Polymerization was initiated via thrombin and the sample was quickly drawn into quartz tubes (Fiber Optic Center, dimensions, 0.70 mm i.d. x 3.5 cm) such that a 6 mm long cylinder was generated.

In vitro assessment of fibrin stability with SVZ-NPCs

Approximately 1 x 10⁴ cells were seeded into wells containing fibrin domes with or without aprotinin and/or DSS, in 600 μ l aliquots of DMEM/F12, B27/N2, penicillin/streptomycin. Media was changed every 3-4 days. Mosaic photomicrographs were taken of each dome on specific days and select experiments were subject to time lapse microscopy over 3 days to directly visualize the time course of neural cellmediated degradation. Images were acquired using a Zeiss Axio Observer microscope (10x objective) outfitted with a Zeiss PM S1 live cell incubator, controlled by AxioVision software. Dome area was measured using this same software program. These in vitro experiments were repeated at least twice for each concentration of aprotinin. Since degradation rates varied slightly depending upon both the SVZ-NPC batch and passage number, the results of an individual series of experiments from the same cell batch and passage number are shown.

In vivo assessment of fibrin stability with brain implantation

Fibrin cylinders were made as described above and a small disc of PVDF (0.56 mm dia., Berkley) was inserted into the quartz tube and served as a plunger head. Anesthesia of female Sprague Dawley rats (250-300 gm) was induced via 5% isoflurane and maintained with 2.5% isoflurane (oxygen carrier flow rate maintained at 0.8 L/min). The animal's scalp was shaved and, after fitting the animal into a Kopf stereotaxic frame, the scalp was swabbed with Betadine®. An approximately 2 cm incision (anterior-posterior) was made in order to expose the skull bregma and lambda suture landmarks. The exposed skull was scrubbed with 3% H₂O₂ to clear away subcutaneous connective tissue. Two stereotaxic frame manipulator arms were used, one on each arm of the Kopf "U" frame, and both were angled 170° to the right of midline. To implant a cylinder

into the right hemisphere, the tip of the fibrin cylinder-containing quartz tube (on the first manipulator arm) was moved, relative to the bregma, 0.13 cm anterior and 0.30 cm right of midline. A small hole was drilled using a round dental bur at the location corresponding to these coordinates. The dura was gently pricked with a 25 gauge needle and the tube driven 0.73 cm down the dorsoventral axis on an angle 17° off midline to the right. A 0.5 mm stainless steel wire, affixed onto the second manipulator arm positioned directly above the first arm, served as a plunger and was lowered into the fibrin cylinder-containing tube. The plunger was lowered until the plunger head reached the top of the fibrin cylinder. The plunger was held immobile by the second manipulator arm while the quartz tube was slowly raised (1/4 turn/45 seconds) via the first manipulator. This maneuver results in the fibrin cylinder being placed in the brain along a predetermined path as the quartz tube is pulled out of the brain with the plunger holding the cylinder in place. After complete extraction of the quartz tube and a five minute incubation period, the plunger was slowly removed, the skull hole plugged with bone wax and the scalp closed with absorbable sutures plus Histoacryl®. Animals were injected with dexamethasone (0.4 mg/kg s.c. in 0.9% sterile saline) once at the time of anesthesia induction and then each day for four days postoperatively. For pain management, animals were injected with buprenorphine (0.15 mg/kg s.c.) immediately after surgery and then daily for two additional days.

Animals were sacrificed three weeks after surgery by bilateral pneumothoracotomy, fixed via transcardial perfusion with 0.9% NaCl with 2U/ml heparin followed by 4% PFA, and brains removed. Following overnight post-fixing in 4% PFA, brains were equilibrated in 30% sucrose until no longer buoyant and sectioned into 20 µm sections using a Leica cryostat. Sections were mounted on Superfrost™ Plus slides (Fisher Scientific) using Fluoro-Gel II with DAPI (Electron Microscopy Sciences) as a mountant, covered with #1 coverslips and sealed with clear nail polish. Sections were observed on a Zeiss Axio Observer fluorescence microscope using Zeiss filter cube 38HE (470/40 excitation; 525/50 emission; 495 split). The area of fluorescent fibrin remaining in the section was quantitated using AxioVision software (Zeiss).

RESULTS

Aprotinin-mediated in vitro stability

To establish a baseline for these studies, fibrin alone was cultured with SVZNPCs and the rate of degradation determined. The data indicate rapid degradation of the matrix, with only 20% of the dome remaining at Day 5 and no observable material remaining after seven days (Fig. 1A and Fig. 2). Very little additional stability was observed when 30 µM aprotinin was included, albeit non-covalently, into the fibrin dome (Fig. 1C and Fig. 2). This supports a number of reports indicating that the inhibitor

(M_w= 6500 dalton) rapidly diffuses out of fibrin or other matrices (Buchta, Hedrich et al. 2005; Smith, Chen et al. 2007; Lorentz, Kontos et al. 2011). Fig. 1B is the results observed when DSS alone was added to the fibrin. Interestingly, the crosslinker alone imparted slight resistance to SVZ-NPC mediated degradation (Fig. 1B and Fig. 2), suggesting that the DSS crosslinked structure of fibrin is itself somewhat more resistant to proteolytic degradation compared to native fibrin. Finally, aprotinin, at 30 µM and covalently crosslinked into fibrin, completely resisted degradation throughout the duration of this experiment (7 days; Fig. 1D and Fig. 2). Additional

experimentation (data not shown) revealed that fibrin domes crosslinked with 30 μM aprotinin were completely intact up to 3 weeks in culture.

An aprotinin dose-response experiment was performed over a 15 day experimental period to determine whether it would be possible to develop fibrin hydrogels of varying degrees of stability in the presence of SVZ-NPCs. It was observed that fibrin stability could indeed be readily controlled depending upon the concentration of DSS-crosslinked aprotinin that was incorporated into the hydrogels (Figure 3). At 7.5 μM , domes were essentially completely resistant to degradation for the entire duration of the experiment. At lower concentrations, the dome half-life varied in a dose-dependent manner, indicating that it is possible to fine-tune fibrin matrices to a particular stability.

Time lapse analysis of in vitro fibrin degradation

Live cell time lapse microscopy provides an opportunity to observe cellular behavior as the SVZ-NPC derived neural cells grow, differentiate, interact and degrade the matrix. Video 1 shows a dome seeded with cells over a 5 day period. As shown, cells exhibit dynamic migration around the border of the fibrin dome and on the bottom of the culture dish that is directly adjacent to the matrix. The entire dome is observed to degrade in essentially a symmetrical manner, indicative of the presence of secreted, diffusible proteases (Gueye, Ferhat et al. 2011). However, specific areas of the dome appear to degrade more rapidly than others and form lacunae. Clusters of cells and cellular projections are intimately coincident with these regions suggesting the presence of cell-surface proteolytic activity, in addition to cell-secreted proteases (Verrall and Seeds 1989; Dejouvencel, Doeuvre et al. 2010; Ferraro, Morrison et al. 2011). The media used in this study was serum-free defined media and it is reasonable to conclude that the neural cells themselves directly produced the fibrinolytic, aprotinin-inhibitable enzymes.

Aprotinin-mediated in vivo stability

Our long term goal is to develop therapeutic neural implants and since the environment within the CNS is quite different from that of cell culture, we evaluated the stability of fibrin/aprotinin/DSS matrices that were implanted into rat brain. We developed a cylindrical matrix whose three dimensional architecture was amenable to implantation and these were surgically placed into the striatum of rats along a predetermined path. All of the animals recovered fully after the procedure and there were no obvious behavioral sequelae. Three weeks postoperatively the animals were sacrificed and brains processed for fluorescent histology. There were no indications of tumors, aberrant cell growth or significant long term damage. The implants were readily visualized since the fibrin was prepared using fluorescently labeled fibrinogen (Fig. 4). Cylinders made with 7.5 μM aprotinin were largely intact after three weeks, while cylinders that were cast with 0.75 μM or 0.075 μM aprotinin were 80% and 95% degraded, respectively (Fig. 4 and Fig. 5).

DISCUSSION

Fibrin biodegradation or fibrinolysis is a natural process mediated by both secreted (e.g. plasmin) and cell-associated (e.g. MMPs) proteolytic enzymes. Aprotinin has been demonstrated to inhibit the activity of both classes of proteases, which are produced by many cell types including neural cells. Indeed, the brain exhibits robust fibrinolytic activity which is thought to be critical in the natural response to stroke (Lo, Broderick et al. 2004), but this presents a challenge for the

development of fibrin-based implants. In order to advance current thinking regarding CNS therapies based on injectable or implantable matrices, we undertook this study to develop a biocompatible, customizable and implantable matrix based on fibrin, an extensively characterized and widely used hydrogel.

Fibrin was rapidly degraded when seeded with SVZ-NPCs and non-covalently incorporated aprotinin had no impact on this degradation. This has been reported by a number of groups and is attributed to the rapid diffusion of the 6.5 kDa aprotinin out of the hydrogel. When aprotinin was covalently incorporated into fibrin, the resultant matrix was stabilized in the presence of neural cells and this was directly proportional upon the concentration of inhibitor used. It was possible to generate matrices whose degradation rate varied from less than one week (0.075 μM aprotinin) to more than one month (7.5 μM aprotinin). Indeed, the highest concentration of inhibitor generated essentially non-biodegradable fibrin.

Importantly, when fibrin cylinders prepared with crosslinked aprotinin were surgically implanted into rat brain, similar dose-dependent stability was observed. The highest dose of inhibitor (7.5 μM) provided nearly complete resistance to degradation over the time frame of the experiment (three weeks), while 10-fold and 100-fold less aprotinin gave concomitantly less resistance. We suggest that neural implants must be stable enough to provide a suitable time frame for a desired cellular response to cues provided by the implant, but must eventually degrade completely in order to yield to de novo complex cellular structures. Significantly, over the three week period between surgery and sacrifice, there were no obvious deleterious postoperative effects of the implants on the animals in terms of overt behavior, tumorigenesis or significant brain damage.

There are many synthetic and natural polymers that have been used as matrices for the therapeutic delivery of cells, proteins/peptides or other compounds into tissues. Our laboratory posits that fibrin is the ideal material for such procedures, especially those aimed at furthering our understanding of neurological disorders and the development of novel therapies thereof. Fibrin is moldable yet pliable, rendering it likely to be intimately absorbed and juxtaposed with soft neural tissue following implantation; it is readily modified via chemical crosslinking agents such as the amino-directed reagent described here; it is biocompatible and biodegradable and thus appropriate for implantation in clinical applications; matrices of various mechanical strengths can be prepared by varying the thrombin/fibrinogen ratio (Georges, Miller et al. 2006; Mooney, Tawil et al. 2010); it is cast and gelled under mild conditions enabling the incorporation of labile peptides, proteins and cells; fibrin is very similar in “softness” to brain tissue and cultured neurons grow much better (and astrocytes much worse) on this matrix than on more stiff material (Georges, Miller et al. 2006; Bektas, Nadalin et al. 2014); and fibrin-thrombin-aprotinin are currently used in clinical applications (Bektas, Nadalin et al. 2014). This report further strengthens the argument that fibrin holds potential as an implantable matrix into the CNS; we demonstrate that degradation rates can be customized by incorporating specific amounts of immobilized aprotinin. Applications such as the transient delivery of a neurotrophin may require a rapidly degraded matrix, while, on the other hand, providing a stable extracellular matrix for regeneration of a complex structure such as a neural migratory pathway may necessitate several weeks of stability.

Our goal was to develop a simple, reproducible and tunable means of making a fibrin-based matrix which incorporated aprotinin to guard against rapid proteolytic degradation. We accomplished this by using a chemical crosslinker directed at reactive amino groups which will covalently couple

peptides and proteins. Succinimide-based protein crosslinkers have been used to covalently incorporate a number of different factors into fibrin. These include keratinocyte growth factor (to study epithelial cells) (Geer, Swartz et al. 2005), VEGF and FGF-2 (to evaluate angiogenesis) (Arkudas, Tjiawi et al. 2007) and germane to our interests, FGF-2, VEGF, NGF, NT3 and RGD peptide to characterize neurogenesis (Schense and Hubbell 2000; Janmey, Winer et al. 2009). Disuccinimidyl suberate is an ideal crosslinking agent for the covalent modification of proteins. This agent reacts with amino groups (i.e., α amino group of protein amino termini and the ϵ amino group of lysines) under mild conditions at physiological pH (Cierniewski and Budzynski 1993) and will form irreversible covalent amide bonds, in the present case between aprotinin and fibrin.

Our laboratory is especially interested in the development of regeneration-based therapies for Parkinson's disease. Recent work from our lab and others suggest that exogenous neural stem cells do not efficiently integrate upon implantation into the brain (Bao, Wei et al. 2010; Chou, Greig et al. 2011; Spitzer, Sammons et al. 2011; Deng, Liang et al. 2013). Surprisingly, in animal models of Parkinson's disease such maneuvers were associated with improvements in Parkinsonian behavior despite little or no integration of exogenous cells. Subsequent analysis revealed that such benefits were likely due to endogenous neural responses to the implant, not to the implanted cells themselves. This supports our long term goal which is to use fibrin-based hydrogels to engineer implantable microenvironments that are conducive to the restoration of neural function in neurological disorders. This paper describes a major step toward that goal, namely, development of a facile means to generate stabilized implantable fibrin matrices of a unique cylindrical architecture that can be customized to specific rates of degradation. Such a tool may lead to novel therapies involving the implantation of these cylinders into damaged or diseased neural tissues in an effort to create new migratory pathways for therapeutic endogenous adult neural stem cells.

These findings should be reproducible for any investigator interested in using fibrin implants into rat striatum. However, should one be interested in implantation into other regions of the brain, or into other species (where the fibrinolytic environment may be different from that of the rat striatum), it may be necessary to use different concentrations of aprotinin to achieve a matrix of a particular lifespan. This same caveat holds for those interested in cell culture studies; the peculiarities inherent in different neural cell cultures will necessitate the generation of aprotinin dose-response data to optimize the inhibitor concentration required for a desired stability. Such experiments are relatively simple, inexpensive and, once in hand, the optimal concentration is dependably reproducible.

We suggest that the approach described here is novel based on the geometry of the matrix (cylinders) and the ease of precise surgical implantation into the brain. Compared to injectable, semi-solid fluid gels, the fibrin cylinders can be implanted in a manner that provides a bridge between two regions in the brain. For example, it seems obvious that providing a new migratory path between the neurogenic subventricular zone and a damaged or dysfunctional area of the brain has therapeutic potential.

CONCLUSION

In closing, we predict that this work will provide impetus to focus on fibrin as a readily-modified and implantable hydrogel for neurological disorders. The current study demonstrates the

feasibility of engineering fibrin to a predetermined degree of stability against biodegradation. Furthermore, when appropriate amounts of aprotinin are incorporated into cylindrical in vivo implants, over time the material degrades completely leaving little trace of damage or inflammation. Studies to bioengineer fibrin as an implantable customized microenvironment that contains aprotinin plus select neurotrophic factors to guide neurogenesis (including migration, neuritegenesis, maturation and integration) are on-going.

ACKNOWLEDGEMENTS

This work was supported by a grant from the National Science Foundation (Grant Award Number: 1003907). A.B.C. was supported by a NASA West Virginia SGC Fellowship. This paper is dedicated to the memory of the late Dr. Stephen J. Kopp, President of Marshall University, 2005-2014.

REFERENCES

- Anderson, S. M., S. N. Siegman, et al. (2011). "The effect of vascular endothelial growth factor (VEGF) presentation within fibrin matrices on endothelial cell branching." *Biomaterials* 32(30): 7432-43.
- Arkudas, A., J. Tjiawi, et al. (2007). "Fibrin gel-immobilized VEGF and bFGF efficiently stimulate angiogenesis in the AV loop model." *Mol Med* 13(9-10): 480-7.
- Bao, X., J. Wei, et al. (2010). "Transplantation of human bone marrow-derived mesenchymal stem cells promotes behavioral recovery and endogenous neurogenesis after cerebral ischemia in rats." *Brain Res* 1367: 103-13.
- Bektas, H., S. Nadalin, et al. (2014). "Hemostatic efficacy of latest-generation fibrin sealant after hepatic resection: a randomized controlled clinical study." *Langenbecks Arch Surg* 399(7): 837-47.
- Blelloch, R. (2008). "Regenerative medicine: short cut to cell replacement." *Nature* 455(7213): 604-5.
- Bozkurt, G., A. J. Mothe, et al. (2010). "Chitosan channels containing spinal cord-derived stem/progenitor cells for repair of subacute spinal cord injury in the rat." *Neurosurgery* 67(6): 1733-44.
- Buchta, C., H. C. Hedrich, et al. (2005). "Biochemical characterization of autologous fibrin sealants produced by CryoSeal and Vivostat in comparison to the homologous fibrin sealant product Tissucol/Tisseel." *Biomaterials* 26(31): 6233-41.
- Centola, M., F. Abbruzzese, et al. (2013). "Scaffold-based delivery of a clinically relevant anti-angiogenic drug promotes the formation of in vivo stable cartilage." *Tissue Eng Part A* 19(17-18): 1960-71.
- Chalmers, R. T., R. C. Darling III, et al. (2010). "Randomized clinical trial of tranexamic acid-free fibrin sealant during vascular surgical procedures." *Br J Surg* 97(12): 1784-9.

- Chen, K., R. A. Henry, et al. (2007). "Creating a neurogenic environment: the role of BDNF and FGF2." *Mol Cell Neurosci* 36(1): 108-20.
- Chien, K. R. (2008). "Regenerative medicine and human models of human disease." *Nature* 453(7193): 302-5.
- Chou, J., N. H. Greig, et al. (2011). "Enhanced survival of dopaminergic neuronal transplants in hemiparkinsonian rats by the p53 inactivator PFT- α ." *Cell Transplant* 20(9): 1351-9.
- Cierniewski, C. S. and A. Z. Budzynski (1993). "Localization of the cross-linking site of GPRVVERHK in the gamma-chain of human fibrinogen." *Eur J Biochem* 218(2): 321-5.
- Collen, A., R. Hanemaaijer, et al. (2003). "Membrane-type matrix metalloproteinase-mediated angiogenesis in a fibrin-collagen matrix." *Blood* 101(5): 1810-7.
- Conway, A. and D. V. Schaffer (2014). "Biomaterial microenvironments to support the generation of new neurons in the adult brain." *Stem Cells* 32(5): 1220-9.
- Dejouvencel, T., L. Doeuvre, et al. (2010). "Fibrinolytic cross-talk: a new mechanism for plasmin formation." *Blood* 115(10): 2048-56.
- Deng, X., Y. Liang, et al. (2013). "Co-transplantation of GDNF-overexpressing neural stem cells and fetal dopaminergic neurons mitigates motor symptoms in a rat model of Parkinson's disease." *PLoS One* 8(12): e80880.
- Dhillon, S. (2011). "Fibrin sealant (evicel(R) [quixil(R)/crosseal]): a review of its use as supportive treatment for haemostasis in surgery." *Drugs* 71(14): 1893-915.
- Ethell, I. M. and D. W. Ethell (2007). "Matrix metalloproteinases in brain development and remodeling: synaptic functions and targets." *J Neurosci Res* 85(13): 2813-23.
- Faber-Elman, A., R. Miskin, et al. (1995). "Components of the plasminogen activator system in astrocytes are modulated by tumor necrosis factor- α and interleukin-1 β through similar signal transduction pathways." *J Neurochem* 65(4): 1524-35.
- Ferraro, G. B., C. J. Morrison, et al. (2011). "Membrane-type matrix metalloproteinase-3 regulates neuronal responsiveness to myelin through Nogo-66 receptor 1 cleavage." *J Biol Chem* 286(36): 31418-24.
- Fon, D., A. Al-Abboodi, et al. (2014). "Effects of GDNF-loaded injectable gelatin-based hydrogels on endogenous neural progenitor cell migration." *Adv Healthc Mater* 3(5): 761-74.
- Fox, I. J., G. Q. Daley, et al. (2014). "Stem cell therapy. Use of differentiated pluripotent stem cells as replacement therapy for treating disease." *Science* 345(6199): 1247391.
- Fricke, R. A., M. K. Carpenter, et al. (1999). "Site-specific migration and neuronal differentiation of human neural progenitor cells after transplantation in the adult rat brain." *J Neurosci* 19(14): 5990-6005.

- Geer, D. J., D. D. Swartz, et al. (2005). "Biomimetic delivery of keratinocyte growth factor upon cellular demand for accelerated wound healing in vitro and in vivo." *Am J Pathol* 167(6): 1575-86.
- Georges, P. C., W. J. Miller, et al. (2006). "Matrices with compliance comparable to that of brain tissue select neuronal over glial growth in mixed cortical cultures." *Biophys J* 90(8): 3012-8.
- Gueye, Y., L. Ferhat, et al. (2011). "Trafficking and secretion of matrix metalloproteinase-2 in olfactory ensheathing glial cells: A role in cell migration?" *Glia* 59(5): 750-70.
- Han, Q. Q., W. Jin, et al. (2011). "The promotion of neurological recovery in an intracerebral hemorrhage model using fibrin-binding brain derived neurotrophic factor." *Biomaterials* 32(12): 3244-52.
- Hansen, K., F. J. Muller, et al. (2010). "A 3-dimensional extracellular matrix as a delivery system for the transplantation of glioma-targeting neural stem/progenitor cells." *Neuro Oncol* 12(7): 645-54.
- Havenith, S., H. Versnel, et al. (2011). "Spiral ganglion cell survival after round window membrane application of brain-derived neurotrophic factor using gelfoam as carrier." *Hear Res* 272(1-2): 168-77.
- Henry, R. A., S. M. Hughes, et al. (2007). "AAV-mediated delivery of BDNF augments neurogenesis in the normal and quinolinic acid-lesioned adult rat brain." *Eur J Neurosci* 25(12): 3513-25.
- Hoyt, A. T., P. S. LaViolette, et al. (2014). "Fibrin sealant to prevent subdural electrode migration during intracranial electroencephalographic monitoring in a patient with a large arachnoid cyst." *J Neurosurg Pediatr* 14(1): 115-9.
- Hultman, K., M. Cortes-Canteli, et al. (2014). "Plasmin deficiency leads to fibrin accumulation and a compromised inflammatory response in the mouse brain." *J Thromb Haemost* 12(5): 701-12.
- Hyatt, A. J., D. Wang, et al. (2014). "Mesenchymal stromal cells integrate and form longitudinally-aligned layers when delivered to injured spinal cord via a novel fibrin scaffold." *Neurosci Lett* 569: 12-7.
- Janmey, P. A., J. P. Winer, et al. (2009). "Fibrin gels and their clinical and bioengineering applications." *J R Soc Interface* 6(30): 1-10.
- Jeon, H., J. H. Kim, et al. (2012). "Plasminogen activator inhibitor type 1 regulates microglial motility and phagocytic activity." *J Neuroinflammation* 9: 149.
- Jhaveri, S. J., M. R. Hynd, et al. (2009). "Release of nerve growth factor from HEMA hydrogel-coated substrates and its effect on the differentiation of neural cells." *Biomacromolecules* 10(1): 174-83.

- Jin, K., X. Mao, et al. (2010). "Transplantation of human neural precursor cells in Matrigel scaffolding improves outcome from focal cerebral ischemia after delayed postischemic treatment in rats." *J Cereb Blood Flow Metab* 30(3): 534-44.
- Kauer, T. M., J. L. Figueiredo, et al. (2011). "Encapsulated therapeutic stem cells implanted in the tumor resection cavity induce cell death in gliomas." *Nat Neurosci* 15(2): 197-204.
- Kim, H., C. H. Tator, et al. (2011). "Chitosan implants in the rat spinal cord: biocompatibility and biodegradation." *J Biomed Mater Res A* 97(4): 395-404.
- Le, D. M., A. Besson, et al. (2003). "Exploitation of astrocytes by glioma cells to facilitate invasiveness: a mechanism involving matrix metalloproteinase-2 and the urokinase-type plasminogen activator-plasmin cascade." *J Neurosci* 23(10): 4034-43.
- Lee, Y. B., S. Polio, et al. (2010). "Bio-printing of collagen and VEGF-releasing fibrin gel scaffolds for neural stem cell culture." *Exp Neurol* 223(2): 645-52.
- Lerchenberger, M., B. Uhl, et al. (2013). "Matrix metalloproteinases modulate ameboidlike migration of neutrophils through inflamed interstitial tissue." *Blood* 122(5): 770-80.
- Lo, E. H., J. P. Broderick, et al. (2004). "tPA and proteolysis in the neurovascular unit." *Stroke* 35(2): 354-6.
- Lorentz, K. M., S. Kontos, et al. (2011). "Engineered aprotinin for improved stability of fibrin biomaterials." *Biomaterials* 32(2): 430-8.
- Lu, Z., L. Korotcova, et al. (2014). "Aprotinin, but not epsilon-aminocaproic acid and tranexamic acid, exerts neuroprotection against excitotoxic injury in an in vitro neuronal cell culture model." *J Thorac Cardiovasc Surg* 147(6): 1939-45.
- Martinez-Ramos, C., A. Valles-Lluch, et al. (2012). "Channeled scaffolds implanted in adult rat brain." *J Biomed Mater Res A* 100(12): 3276-86.
- Maya-Espinosa, G., O. Collazo-Navarrete, et al. (2014). "Mouse embryonic stem cell-derived cells reveal niches that support neuronal differentiation in the adult rat brain." *Stem Cells*.
- Mooney, R., B. Tawil, et al. (2010). "Specific fibrinogen and thrombin concentrations promote neuronal rather than glial growth when primary neural cells are seeded within plasma-derived fibrin gels." *Tissue Eng Part A* 16(5): 1607-19.
- Netzel-Arnett, S., D. J. Mitola, et al. (2002). "Collagen dissolution by keratinocytes requires cell surface plasminogen activation and matrix metalloproteinase activity." *J Biol Chem* 277(47): 45154-61.
- Parajo, Y., I. D'Angelo, et al. (2010). "Hyaluronic acid/Chitosan nanoparticles as delivery vehicles for VEGF and PDGF-BB." *Drug Deliv* 17(8): 596-604.

- Park, J., E. Lim, et al. (2010). "Nerve regeneration following spinal cord injury using matrix metalloproteinase-sensitive, hyaluronic acid-based biomimetic hydrogel scaffold containing brain-derived neurotrophic factor." *J Biomed Mater Res A* 93(3): 1091-9.
- Reichel, C. A., M. Lerchenberger, et al. (2011). "Plasmin inhibitors prevent leukocyte accumulation and remodeling events in the postischemic microvasculature." *PLoS One* 6(2): e17229.
- Sacchi, V., R. Mittermayr, et al. (2014). "Long-lasting fibrin matrices ensure stable and functional angiogenesis by highly tunable, sustained delivery of recombinant VEGF164." *Proc Natl Acad Sci U S A* 111(19): 6952-7.
- Sashindranath, M., E. Sales, et al. (2012). "The tissue-type plasminogen activator/plasminogen activator inhibitor 1 complex promotes neurovascular injury in brain trauma: evidence from mice and humans." *Brain* 135(Pt 11): 3251-64.
- Schense, J. C. and J. A. Hubbell (2000). "Three-dimensional migration of neurites is mediated by adhesion site density and affinity." *J Biol Chem* 275(10): 6813-8.
- Smith, J. D., A. Chen, et al. (2007). "Immobilization of aprotinin to fibrinogen as a novel method for controlling degradation of fibrin gels." *Bioconjug Chem* 18(3): 695701.
- Spitzer, N., G. S. Sammons, et al. (2011). "Autofluorescent cells in rat brain can be convincing impostors in green fluorescent reporter studies." *J Neurosci Methods* 197(1): 48-55.
- Stanwick, J. C., M. D. Baumann, et al. (2012). "Enhanced neurotrophin-3 bioactivity and release from a nanoparticle-loaded composite hydrogel." *J Control Release* 160(3): 666-75.
- Sun, C. Y., Y. Hu, et al. (2006). "Brain-derived neurotrophic factor inducing angiogenesis through modulation of matrix-degrading proteases." *Chin Med J (Engl)* 119(7): 589-95.
- Tan, L. A., I. Takagi, et al. (2014). "Management of intended durotomy in minimally invasive intradural spine surgery: clinical article." *J Neurosurg Spine* 21(2): 27985.
- Thomson, K. S., S. K. Dupras, et al. (2014). "Proangiogenic microtemplated fibrin scaffolds containing aprotinin promote improved wound healing responses." *Angiogenesis* 17(1): 195-205.
- Verrall, S. and N. W. Seeds (1989). "Characterization of 125I-tissue plasminogen activator binding to cerebellar granule neurons." *J Cell Biol* 109(1): 265-71.
- Wachs, F. P., S. Couillard-Despres, et al. (2003). "High efficacy of clonal growth and expansion of adult neural stem cells." *Lab Invest* 83(7): 949-62.
- Willerth, S. M., K. J. Arendas, et al. (2006). "Optimization of fibrin scaffolds for differentiation of murine embryonic stem cells into neural lineage cells." *Biomaterials* 27(36): 5990-6003.

Wood, M. D., M. R. MacEwan, et al. (2010). "Fibrin matrices with affinity-based delivery systems and neurotrophic factors promote functional nerve regeneration." *Biotechnol Bioeng* 106(6): 970-9.

Yasuda, H., S. Kuroda, et al. (2010). "Effect of biodegradable fibrin scaffold on survival, migration, and differentiation of transplanted bone marrow stromal cells after cortical injury in rats." *J Neurosurg* 112(2): 336-44.

Zhang, J., T. Tokatlian, et al. (2011). "Physically associated synthetic hydrogels with long-term covalent stabilization for cell culture and stem cell transplantation." *Adv Mater* 23(43): 5098-103.

Zuidema, J. M., C. J. Rivet, et al. (2014). "A protocol for rheological characterization of hydrogels for tissue engineering strategies." *J Biomed Mater Res B Appl Biomater* 102(5): 1063-73.

Zupanc, G. K. and R. F. Sirbulescu (2015). "Cell replacement therapy: Lessons from teleost fish." *Exp Neurol* 263: 272-6.

Fig. 1. Photomicrographs of fibrin domes in SVZ-NPC culture. Fibrin domes containing aprotinin and/or DSS were cast in 24 well tissue culture plates and seeded with SVZNPCs. On the indicated day a 12 x 15 mosaic photomicrograph of each dome was obtained. (A) Fibrin only. (B) Fibrin plus 50 μ M DSS. (C) Fibrin plus 30 μ M aprotinin. (D) Fibrin plus 50 μ M DSS and 30 μ M aprotinin. The dark structures seen in some of the images are aggregates of cells that are out of the focal plane. Scale bar, 500 μ m.

Fig. 4. Concentration dependence of crosslinked aprotinin on fibrin stability in brain implants. Fibrin cylinders made with Alexa 488-fibrinogen and containing increasing amounts of aprotinin crosslinked with 50 μ M DSS were implanted into rat brain striatum (right hemisphere). Animals were sacrificed three weeks following surgery and brain sections visualized for Alexa 488 fluorescence. (A) Implanted cylinder containing 0.075 μ M aprotinin. (B) Implanted cylinder containing 0.75 μ M aprotinin. (C) Implanted cylinder containing 7.5 μ M aprotinin. Scale bar, 2000 μ m.

STANDARDIZATION OF *E. COLI* COLIFORM COUNTING FOR THE DETERMINATION OF STREAM HEALTH FROM COMBINED SEWER OUTFLOWS ALONG WHEELING CREEK

Evan Collins
Biology/Chemistry
Wheeling Jesuit University
Wheeling, WV 26003

ABSTRACT

Five sites along Big Wheeling Creek in Wheeling, WV were chosen, which spanned from Elm Grove down to close the mouth of the creek at Tunnel Green Recreational Park. These sites were chosen based on their proximity to Combine Sewer Overflows (CSO) which discharge when approximately 2.5 mm of rain have fallen in a given area. A total of 230 samples were taken from the creek, 115 *E. coli* Fecal Coliforms (EFC) and 115 Non-*E. coli* Fecal Coliforms (NEFC), over a sampling period of 23 days. Once the EFC and NEFC were enumerated, a percentage was taken to determine a ratio of EFC vs. Total Coliform Counts (TCCs). The r^2 value from this analysis was 0.63 and an average EFC/TCC ratio of 36%. In an attempt to validate the use of EasyGel as a test medium, the experiment documented that the EasyGel medium used was not as accurate as the standard media currently recommended despite its simplicity. EFC levels in the creek were also shown to be independent of the CSOs opening after greater than 2.5mm of rainfall. As for acceptable levels of coliforms, the months of July and August had the most samples, and consequently both months exceeded the EPA's limit of 10% of EFCs greater than 400 Colony Forming Units (CFUs)/100 mL.

INTRODUCTION

There are many different pathogens which plague public water systems from *Cryptosporidium parvum* which leads to cryptosporidiosis to protozoans such as *Giardia intestinalis* which leads to intestinal diarrhea (Huang & White, 2006). This experiment utilizes the knowledge of waterborne pathogens, more specifically *Escherichia coli*, to form a hypothesis based on previous research in the field. It has been known for many years that fecal coliforms (which include *E. coli*, *Klebsiella*, and other Enterobacters) are a good measure of stream quality, especially when taking a recreational stream into account. However, total coliform counts (TCC) are being phased out in favor of EFC enumeration in its stead. According to Garcia-Armisen et al, a statistically significant ratio of 0.77 or better can be obtained through freshwater enumeration techniques which correlate EFC and NEFC (2007).

The mere presence of EFCs indicates indirectly that the stream may be contaminated with pathogens other than *E. coli* (CDC, 2015). *E. coli* itself may be harmful as well for it can incorporate the Shiga toxin, a very potent enteric toxin, which may lead to severe diarrhea. It has been found in patients diagnosed with dysentery; and may lead to other disorders such as pneumonia, hemorrhaging, and vomiting (CDC, 2015). This means that EFCs in this case could successfully be utilized as a predictor for stream health rather than TCCs; which is a good practice as it could help identify watersheds which are at risk for harboring waterborne pathogens.

Wheeling Creek has been under investigation in previous experiments at Wheeling Jesuit University by its biology department students, but nothing definitive has been ascertained from these studies so far. Since CSOs are considered a point source of pollution by the EPA, the sites were monitored between these point sources in an attempt to enumerate the EFC and NEFC populations in 100 mL aliquots per sample. In order to do this, the EPA Clean Water Act of 1972 was used as a guideline, and Wheeling Creek was studied over a 4 month period which included 23 total sampling dates. According to the United States Environmental Protection Agency (USEPA), CSOs are a way in which domestic waste may be discharged into streams after heavy rainfalls of 2.5 mm or greater, affecting 772 cities in the United States (Combined Sewer, 2013). For this reason it is necessary to make sure that the water in the stream does not exceed the legal limits of total coliform as well as *E. coli* coliform counts of 5.0 percent of samples per month (Basic Information, 2013). The Fecal Coliform (FC) count for West Virginia non-Ohio River streams must be maintained at or under 200 Colony Forming Units (CFU) per 100 mL of water, and no more than 10 percent can exceed 400 CFU per 100 mL over a sampling period of at least 5 samples per month (Bacterial Water, 2003).

MATERIALS AND METHODS

I. Materials

1 Yellow Springs Incorporated (YSI) 556 Multi Probe; 1 HACH Chemical Kit with nitrates, phosphates, and ammonia testers; 5 (per day) 100 mL Corning Lab[®] sampling containers with chlorine standard reagent (Thiosulfate); 5 (per day) Coliscan[®] EasyGel[®] petri plates with agar; 1 37°C incubator @ 5% CO₂; 1 cold room @ 2°C; 1 cooler with ice (per day), 2 field note books for observations.

II. Collection

Using 5 predetermined sites along the Wheeling Creek area, each was tested for total Fecal Coliforms (FC), focusing mainly on the amount of *E. coli* FC in each of the samples. Each site was chosen for its location at, near, or downstream from a CSO. Each site, upon arrival, was tested for pH, temperature, and dissolved oxygen was determined with the YSI 556 multi probe, while the stream conditions (such as storm drains, rainfall, etc.) were also noted. Once the stream conditions were taken and recorded, 100 mL of water was collected from each site in a pre-sterilized, Corning Lab container containing a thiosulfate tablet used for chlorine standardization, and placed in ice to prevent further bacterial growth, then taken back to the lab for further analysis.

III. Coliform Enumeration

The samples were then prepared for each of 5 Coliscan Easygel medium. Once the gels were ready, 0.5, 1.0, 1.5, 2.0, and 2.5 mL of sample water were pipetted from each sample into the pre-made medium. This was done to determine which FC count meets the criteria recommended by the manufacturer. After the first week, 1.5 mL had the best growth lawns on the medium, which simplified counting the CFUs after each 48 hour incubation cycle.

All 100 mL sampling containers were shaken vigorously for approximately 10 seconds to ensure an even colony distribution in the 1.5 mL sample taken from each one. The 1.5 mL was then pipetted from the 100 mL sample container into the Coliscan Easygel medium, next it was gently

inverted approximately 10 times to ensure a complete mixture of the sample into the gel. The gel was then poured into a plate designed specifically for the Coliscan EasyGel medium and allowed to set for up to 20 minutes. After setting, the gels were incubated at 37° C for 48 hours since the initial testing proved that the 24 hour incubation was not adequate for growth with a 1.5 mL dilution. Following incubation, the gels were removed and the number of EFC vs. NEFC counts were recorded.

IV. Other Stream Parameters

A HACH Chemical Kit containing the necessary reagents to test for nitrates, phosphates, and ammonia nitrogen was utilized in the laboratory for the beginning of the experiment, however the tests were not utilized in the end of the experiment because the kit’s limit of detection (LOD) was too high for any of the parameters to have been successfully determined. These were tested according to the manufacturer’s instructions which can be found at <http://hach.com> under product number 2712000.

V. Positive and Negative Controls

After the experiment was finished, it was necessary to conduct a set of both positive and negative controls on the Coliscan agar which was used. Since the agar tested as blue for *E. coli*- positive and pink for non-*E. coli* *Enterobacter*-positive gram-negative rods, it was necessary to do a positive and negative control for each one. Samples of *E. coli*, *Citrobacter*, *Klebsiella pneumoniae*, and *Enterobacter cloacae*. Following aseptic techniques, these were isolated from a monoculture of each in trypticase soy broth (TSB) for each of *Citrobacter*, *Klebsiella*, and *Enterobacter cloacae*, and then regrown in a new media to ensure viability of each culture. Each of the newly-inoculated TSB broths were then incubated at 37°C for 24 hours. Since only the *E. coli* and *K. pneumoniae* grew, these were the only two which were evaluated as positive and negative controls respectively. Following incubation, each was streaked individually on an EasyGel® plate agar and incubated for another 24 hours at 37°C. After incubation, the results were recorded and checked against the standard colony colors; that is the *E. coli* was checked against the blue color that is representative of an *E. coli* colony according to Coliscan’s procedures as well as the pink color for each of the non-*E. coli* enterobacter, *K. pneumoniae*. As per the manufacturer’s standard, the plates streaked with *E. coli* returned a lawn of blue colonies only, while the plate streaked with *Klebsiella pneumoniae* returned a lawn of pink colonies. These results conclude that the colonies identified in the experiment can be concluded as differing *Enterobacters*.

RESULTS

I. Tested Stream Parameters

Nitrates in mg/mL						
Date	Site	1	2	3	4	5
4/14/2014						

4/22/2014		0.00	0.00	0.00	0.00	0.00
4/28/2014		0.00	0.00	0.00	0.00	0.00
6/2/2014		0.00	0.00	0.00	0.00	0.00
6/5/2014		0.00	0.00	0.00	0.00	0.00
7/7/2014		0.00	0.00	0.00	0.00	0.00
7/9/2014		0.00	0.00	0.00	0.00	0.00
7/11/2014		0.00	0.00	0.00	0.00	0.00
7/14/2014		0.00	0.00	0.00	0.00	0.00
7/16/2014		0.00	0.00	0.00	0.00	0.00
7/18/2014		0.00	0.00	0.00	0.00	0.00
7/21/2014		0.00	0.00	0.00	0.00	0.00
7/22/2014		0.00	0.00	0.00	0.00	0.00
7/23/2014		0.00	0.00	0.00	0.00	0.00
7/28/2014		0.00	0.00	0.00	0.00	0.00
7/31/2014		0.00	0.00	0.00	0.00	0.00
8/1/2014		0.00	0.00	0.00	0.00	0.00
8/4/2014		0.00	0.00	0.00	0.00	0.00
8/5/2014		0.00	0.00	0.00	0.00	0.00
8/6/2014		0.00	0.00	0.00	0.00	0.00
8/28/2014		0.00	0.00	0.00	0.00	0.00
9/5/2014		0.00	0.00	0.00	0.00	0.00
9/12/2014		0.00	0.00	0.00	0.00	0.00

Table 1. One of the tested stream parameters, Nitrates, was the only one carried throughout the entire experiment as it was the only one that was not interfered with by the thiosulfate standard in

the 100 mL sampling bottles. No nitrates were detected in the stream since the concentration was less than the HACH Chemical Kit's LOD.

II. Stream Conditions

Water Temperature in °C	Site	1	2	3	4	5
	Date					
	4/14/2014	15.71	15.00	15.82	15.69	15.96
	4/22/2014	17.33	17.54	17.60	17.75	17.20
	4/28/2014	13.73	13.84	13.91	13.83	14.56
	6/2/2014	22.62	23.57	23.61	23.43	24.21
	6/5/2014	24.36	25.34	25.32	25.47	25.76
	7/7/2014	26.21	27.41	27.48	27.59	26.97
	7/9/2014	25.83	26.89	26.73	27.21	27.24
	7/11/2014	27.23	27.93	27.71	28.29	27.00
	7/14/2014	25.18	25.90	25.83	25.72	26.07
	7/16/2014	23.83	24.32	24.27	23.84	23.61
	7/18/2014	21.88	21.73	21.94	21.42	21.33
	7/21/2014	24.12	24.55	24.84	23.98	24.27
	7/22/2014	28.46	29.91	29.63	29.46	29.00
	7/23/2014	27.37	28.08	27.73	28.14	27.88
	7/28/2014	22.86	22.85	22.80	22.93	23.45
	7/31/2014	20.94	21.78	21.51	21.11	21.01

8/1/2014		20.56	21.69	22.57	22.61	21.62
8/4/2014		24.92	26.94	26.68	26.19	25.96
8/5/2014		25.59	27.17	26.97	27.25	26.61
8/6/2014		24.92	26.10	27.00	26.86	27.08
8/28/2014		25.12	25.39	25.08	25.19	25.30
9/5/2014		26.22	26.83	26.65	26.55	27.00
9/12/2014		19.60	19.56	19.56	19.54	19.77

Table 2. Water temperature measured in °C for each day samples were collected. The temperature was highest at the peak of the summer and lowest at the beginning of the experiment in April as is expected with the varying temperature range from mid-spring to late summer.

pH						
	Site	1	2	3	4	5
Date						
4/14/2014		8.48	8.68	8.61	8.65	8.66
4/22/2014		8.54	8.66	8.68	8.65	8.66
4/28/2014		8.45	8.52	8.54	8.53	8.59
6/2/2014		8.40	8.58	8.60	8.66	8.67
6/5/2014		8.39	8.44	8.41	8.41	8.41
7/7/2014		8.33	8.41	8.47	8.46	8.46
7/9/2014		8.34	8.25	8.31	8.15	7.95
7/11/2014		8.41	8.47	8.48	8.44	8.45
7/14/2014		7.89	8.10	8.19	8.08	8.20
7/16/2014		8.20	8.33	8.45	8.40	8.44
7/18/2014		8.05	8.29	8.35	8.23	8.31

7/21/2014		8.12	8.35	8.39	8.33	8.30
7/22/2014		8.44	8.48	8.46	8.54	8.45
7/23/2014		7.93	8.33	8.29	8.32	8.39
7/28/2014		8.31	8.24	8.28	8.41	7.64
7/31/2014		8.13	8.44	8.42	8.41	8.45
8/1/2014		8.06	6.92	8.35	8.31	8.18
8/4/2014		8.32	8.55	8.54	8.55	8.48
8/5/2014		7.97	8.54	8.57	8.55	8.53
8/6/2014		8.09	8.51	8.50	8.52	7.76
8/28/2014		8.13	8.48	8.48	8.45	8.44
9/5/2014		8.21	8.41	8.45	8.46	8.52
9/12/2014		8.20	8.19	8.24	8.31	8.25

Table 3. pH was also measured each day of testing; this, too remained relatively constant throughout the experiment.

DO in mg/L						
	Site	1	2	3	4	5
Date						
4/14/2014		16.30	12.53	12.72	11.99	11.51
4/22/2014		15.10	11.55	11.87	12.56	13.39
4/28/2014		12.62	11.90	10.85	13.24	11.48
6/2/2014		11.11	15.68	16.25	12.01	10.84
6/5/2014		2.84	3.50	3.72	3.16	3.52
7/7/2014		8.86	9.57	9.71	8.98	8.53

7/9/2014		8.61	7.64	7.58	8.13	7.58
7/11/2014		8.12	8.66	8.63	8.33	7.38
7/14/2014		5.41	7.05	6.97	6.64	6.68
7/16/2014		8.61	10.13	10.40	9.42	8.78
7/18/2014		6.75	8.91	9.09	8.12	8.48
7/21/2014		6.08	9.56	9.85	8.79	7.80
7/22/2014		8.29	8.27	8.82	9.00	7.55
7/23/2014		7.35	7.55	7.12	7.99	7.36
7/28/2014		7.14	7.30	7.16	7.13	6.59
7/31/2014		6.67	8.90	8.88	8.57	8.07
8/1/2014		5.00	5.20	6.62	6.05	5.12
8/4/2014		7.98	8.40	8.53	8.70	7.21
8/5/2014		6.75	8.67	8.52	8.06	7.02
8/6/2014		6.92	9.37	8.91	9.32	8.54
8/28/2014		8.92	6.35	6.18	6.30	6.06
9/5/2014		4.93	5.53	5.82	5.36	5.72
9/12/2014		5.85	5.98	6.00	6.07	5.41

Table 4. Dissolved oxygen measured in mg/L for each day of testing.

III. External Conditions

Weather for Wheeling, April 2014-Sept. 2014	
Day	Precip.
	(mm)
4/14/2014	0
4/22/2014	0
4/28/2014	0
6/2/2014	0
6/3/2014	1.5
7/7/2014	0
7/10/2014	0
7/11/2014	0
7/14/2014	8.4
7/16/2014	0
7/18/2014	0
7/21/2014	0
7/22/2014	0
7/23/2014	0
7/28/2014	2.3
7/31/2014	4.8
8/1/2014	0

8/4/2014	1.5
8/5/2014	0
8/6/2014	9.1
8/28/2014	6.1
9/5/2014	0
9/12/2014	2.8

Table 5. Precipitation data for Wheeling, WV showing the precipitation per day in mm. All information retrieved from the U.S. Climate data website (2014).

III. Fecal Colony Enumerations

Total <i>E. coli</i> Fecal Colonies per 100 mL						
	Site	1	2	3	4	5
Date						
4/14/2014		67	200	533	133	4267
4/22/2014		67	0	67	0	0
4/28/2014		0	3067	400	67	67
6/2/2014		67	0	67	67	67
6/5/2014		133	0	0	67	0
7/7/2014		133	133	67	133	267
7/9/2014		267	400	667	533	400
7/11/2014		400	133	267	133	133
7/14/2014		4067	3467	2800	2867	3267
7/16/2014		200	200	333	267	333
7/18/2014		467	200	133	400	800
7/21/2014		333	400	200	200	200

7/22/2014		0	133	867	1267	600
7/23/2014		400	267	2600	67	1200
7/28/2014		600	533	333	400	400
7/31/2014		733	333	533	200	867
8/1/2014		67	133	267	333	0
8/4/2014		400	533	333	67	400
8/5/2014		400	67	67	267	267
8/6/2014		867	400	400	733	1733
8/28/2014		733	333	667	333	800
9/5/2014		667	1533	1067	800	933
9/12/2014		933	400	133	533	667

Table 6 Total enumeration of all *E. coli* fecal colonies counted site⁻¹ day⁻¹ 100 mL⁻¹ of sampled water. These were originally counted as colony numbers, but were later transformed with the following equation so that the dilution factor of the original 100 mL sample represented the total number of colonies:

$$Total\ colonies = \frac{100}{1.5} * CFU$$

Total Non- <i>E. coli</i> Fecal Colonies per 100 mL						
	Site	1	2	3	4	5
Date						
4/14/2014		200	1200	5533	67	4533
4/22/2014		0	0	0	67	67
4/28/2014		200	800	1667	133	667
6/2/2014		733	1733	1133	1067	1400

6/5/2014		1000	1133	1000	1067	1200
7/7/2014		1467	1600	2467	1800	1600
7/9/2014		1133	1533	800	733	200
7/11/2014		333	267	1000	867	733
7/14/2014		1000	933	1200	733	1400
7/16/2014		800	1000	800	667	1933
7/18/2014		400	1200	933	733	733
7/21/2014		600	467	533	533	600
7/22/2014		1000	1333	600	400	400
7/23/2014		1200	600	200	867	467
7/28/2014		733	1467	533	600	333
7/31/2014		533	867	400	800	333
8/1/2014		533	400	467	800	467
8/4/2014		1067	667	1133	800	1067
8/5/2014		1000	2067	1933	2000	2067
8/6/2014		1667	1800	1933	1667	1067
8/28/2014		467	467	467	467	600
9/5/2014		800	2400	1200	1467	1600
9/12/2014		1933	2133	1200	800	1533

Table 7. Total enumeration of all non-*E. coli* fecal colonies counted site⁻¹ day⁻¹ 100 mL⁻¹ of sampled water. These were originally counted as colony numbers, but were later transformed with the following equation so that the dilution factor of the original 100 mL sample represented the total number of colonies:

$$\text{Total colonies} = \frac{100}{1.5} * CFU$$

IV. Predictive Data for the *E. coli* Fecal Coliforms in Wheeling Creek

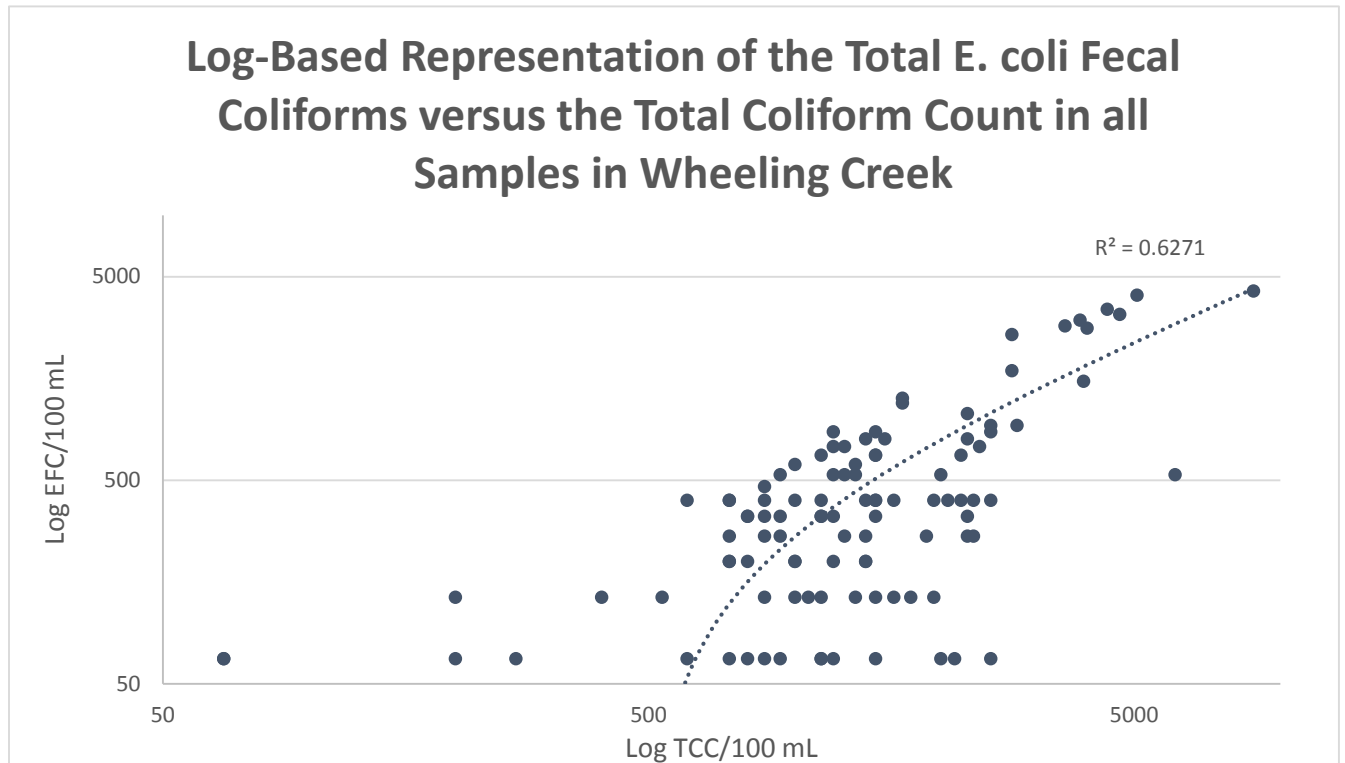


Figure 1. The total EFCs were plotted against the TCCs which include both EFC and NEFC in the 100 mL samples of water. The dependent EFCs are represented on the y-axis, while the independent Total Colony Counts are represented to the x-axis. The scale was readjusted to a log-log scale to better compress the data and to show the very little amount of correlation present.

V. CSOs and EFC Counts

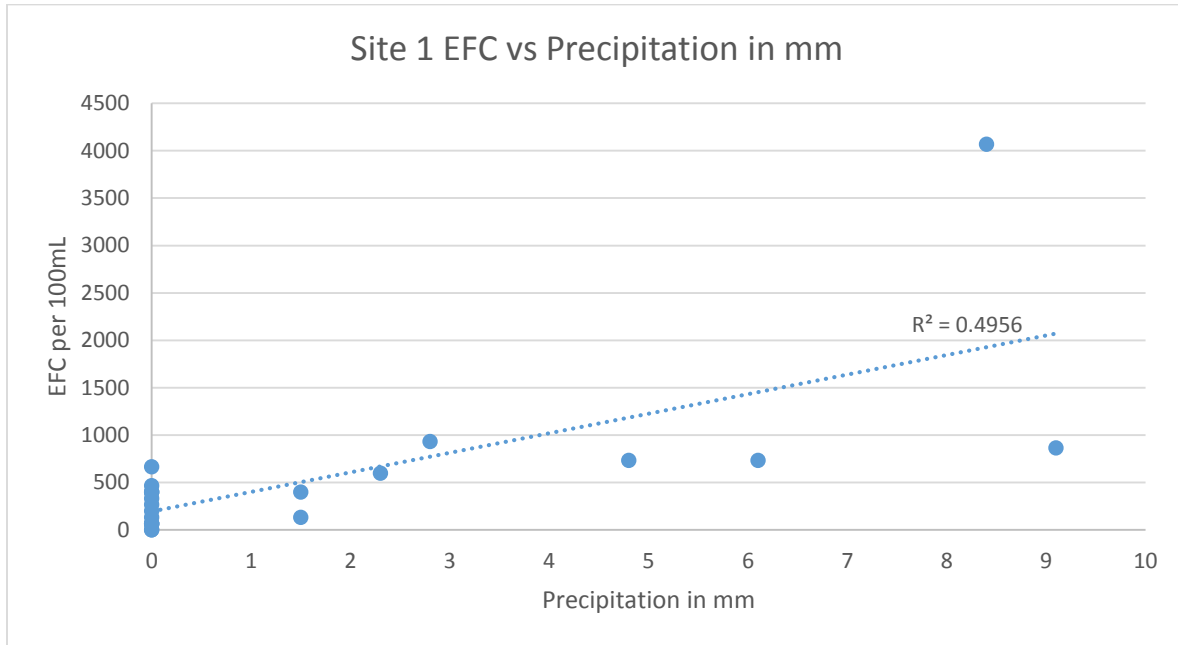


Figure 2. Site 1 EFCs plotted against the precipitation site⁻¹ day⁻¹.

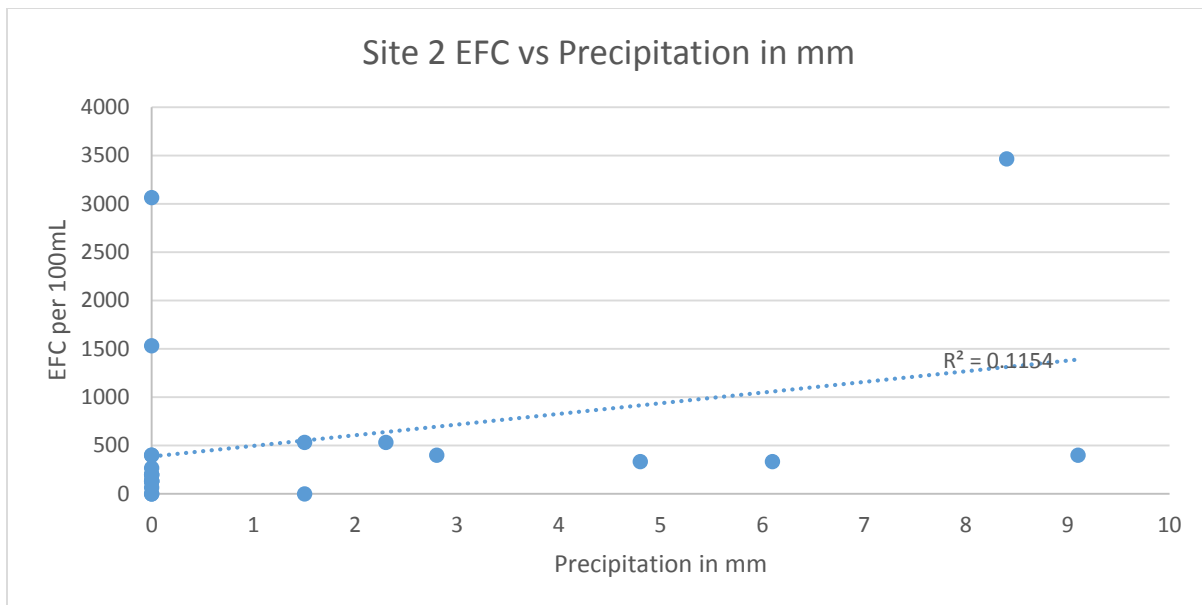


Figure 3. Site 2 EFCs plotted against the precipitation site⁻¹ day⁻¹.

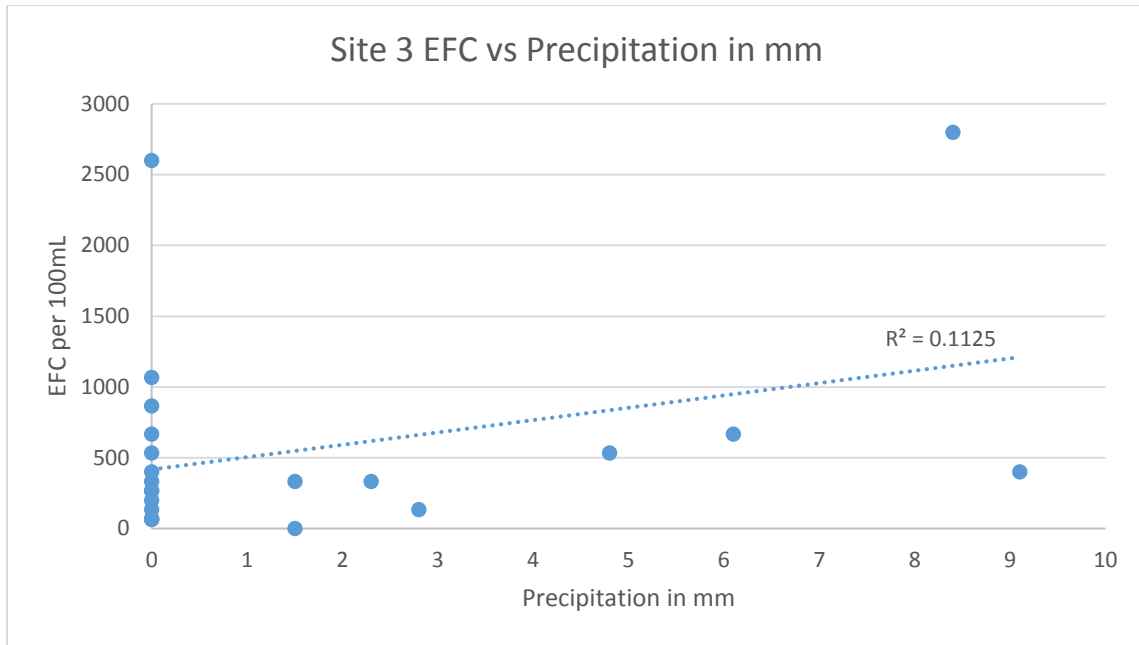


Figure 4. Site 3 EFCs plotted against the precipitation site⁻¹ day⁻¹.

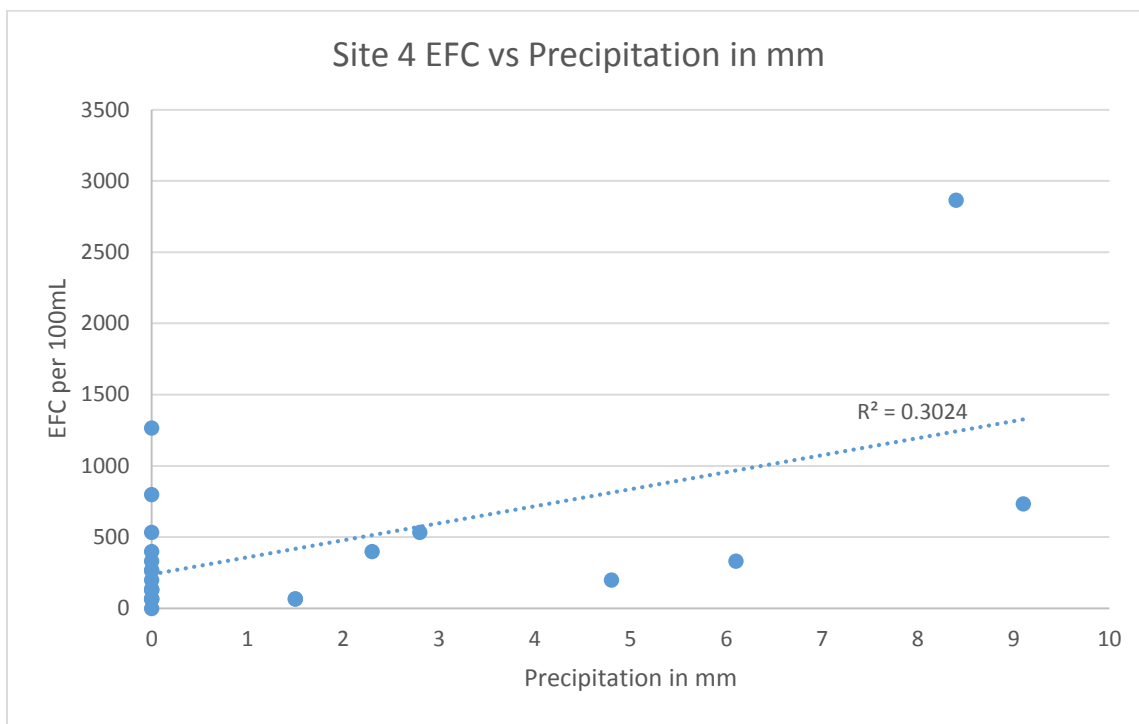


Figure 5. Site 4 EFCs plotted against the precipitation site⁻¹ day⁻¹.

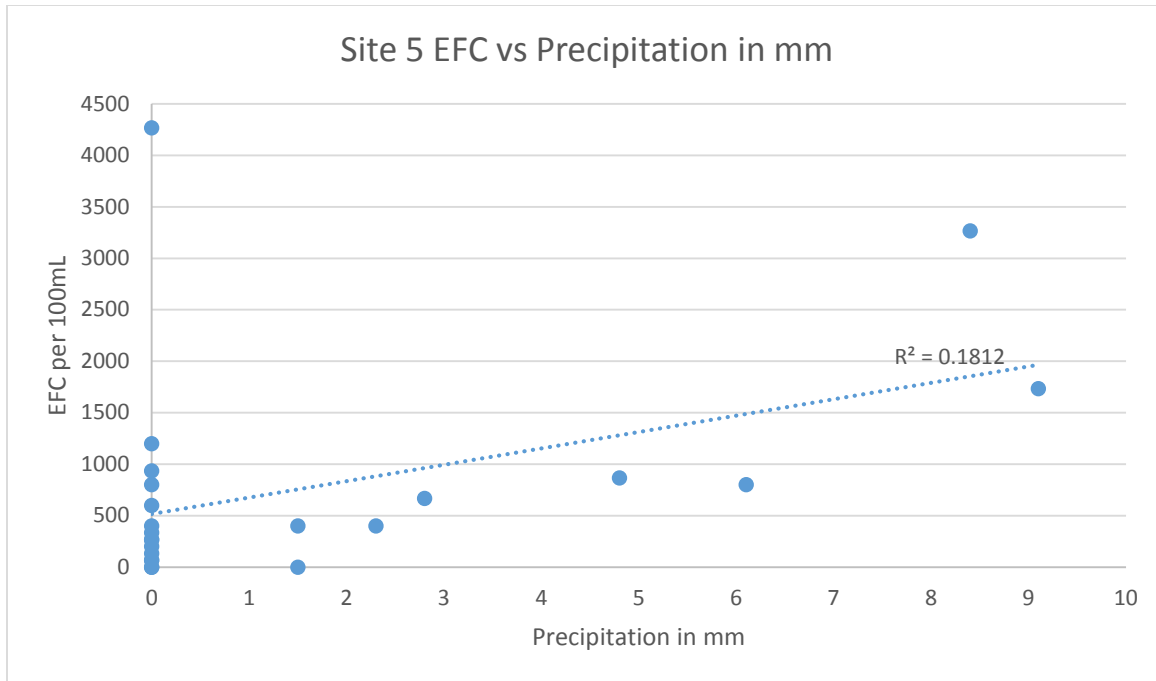


Figure 6. Site 5 EFCs plotted against the precipitation site⁻¹ day⁻¹.

DISCUSSION

I. Evaluation of EFC/TCC Ratios

According to Garcia-Armisen et al., there should have been a relatively high correlation of EFC to TCC as a result of stream sampling as the *E. coli* make up a large percentage of the total coliforms and a relatively high ratio of 0.77 EFC/TCC (2007). Due to a large gap between data points, the data was transformed into a log-log scale as to better represent what the data means and to condense the overall data set. For the data collected, a correlation of EFC/TCC was approximately equal to 0.63 as seen in Figure 1 in the results section, resulting that the data could be considered statistically sound. However, when the equation in Figure 2 is used to compare the Garcia-Armisen data to this experiment's data, a percent difference of 35.3% was obtained, meaning that the correlative values in this experiment are not nearly as strong as that in the experiment this was modeled after, the Garcia-Armisen data. As for the ratio of EFC/TCC, the expected value was around the Garcia-Armisen standard of 77%, but fell short of that mark, at only 36%, as seen in the equation provided in Figure 3. This is a 72% difference between the data values according to the percent difference equation. This is true for other experiments in which the EFC/TCC ratio was calculated. It appears that the ratio is above 60% such as that in experiments performed by the EPA in their publication, "Bacterial Water Quality Standards for Recreational Waters" (2013). This also includes the experiment utilizing the membrane filtration done by Hamilton et al. where the EFC/TCC ratio is much higher than the present experiment (2005). Hamilton et al. obtained a ratio of 80% or greater in their experiments, which nearly coincides with the results from the Garcia-Armisen et al. experiment of a 77% EFC/TCC ratio.

II. EFC Counts and CSO Openings

Each site was tested between of a CSO with the prediction that the CSOs would cause a dramatic increase in the amount of EFCs on the days that it rained throughout the experiment. Overall, it appears as if the presence of EFCs in the creek are non-correlative as seen in Figures 3-6 because of the large number of days where there was no rain. Yet on the peak days of interest where the CSOs opened up at 2.5 mm of rainfall, it appears as if they may have some impact on the total EFC for that day. This is especially pertinent on July 14, 2015 where the counts exceeded the total average of EFCs by twice as much and the NEFCs exceeded the total average by 1.9 times as many colonies counted. The rainfall on July 14 was a driving factor for this conclusion as it was 4 times the threshold for CSO overflow for this day. A possible relation between the rainfall, CSO, and colony counts could be made with this data point, however it is only an isolated point and may have no real bearing on future EFC counts.

There were marked increases in the amount of fecal coliforms on the days it did rain. A total of 5 days throughout the experiment where the rain exceeded 2.5 mm, meaning a successful opening of the CSOs along the creek during these days took place. On these days, the average number of EFCs per sample increased by 237% on the days a CSO opened. This could not be seen for the plots such as those in Figures 3-6 show. However, individual analysis documents there was a large average increase of EFCs enumerated on the 5 days it rained. These results were also compared to the Ohio River Valley Water Sanitation Commission (ORSANCO), as possible source dates for the levels in the Ohio River downstream from the mouth of Wheeling Creek (ORSANCO, 2014). Each week ORSANCO monitors the Ohio River for a very large array of parameters including fecal coliforms. However, none of the days in which greater than 400 EFC/100mL was observed preceding an exceedance in the normal EFC counts in the Ohio River. Because of this, Wheeling Creek is ruled out as a possible point source of EFC pollution in the Ohio River over the given period of time.

III. Tested Stream Parameters

Each of the parameters was checked for the majority of the experiment, however it was decided on July 28, 2014 that some of the tests being done were not needed. The phosphates were found to be producing false positives the entire duration of testing because of the phosphate reagent in the sampling bottles; which present to neutralize any chlorine in the sample. The standard reagent for the chlorine was thiosulfate and this gave a false positive for each of the ammonia and phosphates whenever tested with the same water as the 100 mL sampling containers. This also may have interfered with the testing of nitrates which is explained below.

Nitrate levels were also well- below the LOD of the nitrate kits which were provided. The testing of nitrates continued throughout the experiment since they were considered to be the most important of the tested parameters. However, it wasn't until September 5, 2014 that standards arrived in the lab to test the sensitivity of the kit. The standard test for the nitrates is a standard solution of nitric acid in water (44.3 mg/L nitric acid). A series of dilutions of the standard reagent were prepared that ranged from 0.443 mg/L, 4.43 mg/L, and 44.3 mg/L for a total of 3 standard reagents. The nitrate test was then run on each of the standard solutions following the HACH chemical kit's instructions provided in Part IV of the Materials and Methods section. It was found, at the conclusion of the standard tests, that the limit of detection for the HACH kit was well outside

the apparent stream conditions, where a colorimetric change did not occur until the 44.3 mg/L of nitrates was attained. This could mean that either the thiosulfate reagent in the sampling containers reacted with the nitrates in the stream samples, or that the stream had such a low amount of nitrates that the testing kit was not sensitive enough to show any change.

According to Mallin et al. (2000) it was expected that fecal colonies would have been directly related to, and dependent on, human interactions, especially the levels of nitrates in the watersheds with significant human interactions, such as Wheeling Creek. However, according to Table 1, there were no observable nitrates in the stream at any one point in the experiment. Since it was expected that the nitrates would have a positive correlation, it can be safely assumed that the absence of these nitrates was not a significant variable since EFCs still persisted throughout the entire experiment. The CSOs which were tested between never resulted in a single peak, meaning that the levels of nitrates were kept well below the permissible U.S. standard levels of 10.0 mg/L according to the point and non-point pollution standards set forth by Novotny and Chesters (1981), and has not changed according to the newest EPA guidelines (1992).

CONCLUSION

Since the EPA only allows for 10% of samples to be above 400 CFU/100mL in a one month period, it may be time to rethink the allowance of CSOs in future city plans. As for Wheeling Creek, the samples in the months of July and August (the months where 5 or more samples were taken) were over the allotted 10% by 25% and 18% respectively. Consequently, each of these months had days when the CSOs opened at 2.5mm of precipitation or greater, meaning that these months were affected considerably by the dramatic increase in EFCs. The CSOs along Wheeling Creek allow human runoff and refuse during times of heavy rainfall into the water, which increases the likelihood of finding other pathogens in the water. As stated earlier, the CDC published that the mere presence of EFCs in a water source increases the probability of finding other pathogens such as *Cryptosporidium parvum*, which may evade normal water filtration methods and cause cryptosporidiosis in a large percentage of a population (CDC, 2015). This means that of the 772 cities affected nationally, including Wheeling, WV, a CSO discharges that it must be taken into account when determining the safety of recreational stream waters, since there is a dramatic increase in EFCs during this time.

The high deviation from the previous experimenters' values indicates that the EasyGel medium may not be the best medium, nor the most accurate in determining stream health at a quantitative level. This is partially due to the EasyGel method being more of a qualitative rather than a quantitative measure for coliform counting as it does not pass the entire 100 mL through a membrane filtration system (MFS), or by a series of dilutions in the most probable number (MPN) method (Santiago-Mercado & Hazen, 1987). Instead the EasyGel method relies solely on the presence of a representative number of colonies in the sample from the experiment's 1.5 mL dilutions. Despite vigorous shaking, as described in the methods, before each site sample was plated onto a different EasyGel agar plate. It was hoped that in this experiment that these techniques (MFS and MPN) could be replaced by the EasyGel as a future technique since its preparation time is much shorter than that of either the MFS or MPN methods. However, the EasyGel method used in this experiment appears to not be as reliable due to the lack of the data with that of previously published data utilizing the standardized methods.

ACKNOWLEDGEMENTS

A special thanks to all those who were able to make this presentation possible, first and foremost my mentor, Dr. Andy Cook, the NASA Space Grant Consortium for all of the funding, and lastly Dr. Benjamin Stout for lending his tools and time to help with sampling in the field.

REFERENCES

Center for Disease Control and Prevention. (2015). *Escherichia coli general information*. Retrieved from <http://www.cdc.gov/ecoli/general/index.html>

Chin, D.A. (2010). *Linking Pathogen Sources to Water Quality in Small Urban Streams*. Journal of Environmental Engineering. 249-253.

Garcia-Armisen, T., Prats, J., Servais, P. (2007). *Comparison of culturable fecal coliforms and Escherichia coli enumeration in freshwaters*. Canadian Journal of Microbiology. Vol. 53: 798-801.

Hamilton, W.P., Kim, M., Thackston, E.L. (2005). *Comparison of commercially available Escherichia coli enumeration tests: Implications for attaining water quality standards*. Water Research. Vol. 39. Issue 20: 4869-4878.

Huang, D.B, White, A.C. (2006). *An updated review on Cryptosporidium and Giardia*. Gastroenterol Clinic of North America. Vol. 35: 291-314.

Mallin, M.A., Williams, K.E., Esham, E.C., Lowe, R.P. (2000). *EFFECT OF HUMAN Development on Bacteriological Water Quality in Coastal Watersheds*. Ecological Society of America. Vol. 10, No. 4: 1047-1056.

Novotny, V., Chesters, G. (1981). *Handbook of Nonpoint Pollution Sources and Management*. New York, NY: Van Nostrand Reinhold Company. 424-430.

Ohio River Valley Water Sanitation Commission. (2014). *2014 Bacterial Report*. Retrieved from <http://www.orsanco.org/bacteria>

Santiago-Mercado, J., and Hazen, T.C. 1987. Comparison of four membrane filter methods for fecal coliform enumeration in tropical water. Appl. Environ. Microbiol. Vol. 53: 2922–2928.

United States Climate Data. (2014). *Climate data for Wheeling, WV*. Retrieved from <http://www.usclimatedata.com/climate/wheeling/west-virginia/united-states/uswv0799/2014/1>

United States Environmental Protection Agency. (1992). *Water Monitoring and Assessment: 5.7 Nitrates*. Retrieved from <http://water.epa.gov/type/rsl/monitoring/vms57.cfm>

United States Environmental Protection Agency. (2003). *Bacterial Water Quality Standards for Recreational Waters (Freshwater and Marine Waters Status Report)*.

Washington, D.C. United States Environmental Protection Agency. (2013). *Basic Information about Pathogens and Indicators in Drinking Water*. Retrieved from <http://water.epa.gov/drink/contaminants/basicinformation/pathogens.cfm>

United States Environmental Protection Agency. (2013). *Clean Water Act Definition of "Waters of the United States"*. Retrieved from <http://water.epa.gov/lawsregs/guidance/wetlands/CWAwaters.cfm>

United States Environmental Protection Agency. (2013). *Combined Sewer Overflows*. Retrieved from <http://water.epa.gov/polwaste/npdes/cso/>

TEMPERATURE EFFECTS ON LIMB GROWTH AND IGF-I DELIVERY TO MOUSE BONES

Miles Gray
Biochemistry
Marshall University
Huntington, WV 25755

ABSTRACT

Limb length inequality is a potentially disabling condition that can occur in growing children naturally or after injury. Treatments are often limited to painful and expensive surgeries. A primary goal in our lab is to create cost effective methods for stimulating extremity growth with noninvasive techniques. Preliminary research using mice has shown bones that grow longer at warmer temperatures, with increased diffusion of molecules to limb bones at higher temperatures than at lower temperatures. Insulin-like growth factor (IGF)-I is the major circulating hormone required for growth. The focus of ongoing research in our lab is to determine whether warm temperature increases limb length by augmenting delivery of IGF-I to elongating bones. To address this problem, our lab established a protocol for adding a fluorescent tag to IGF-I so that it can be visualized in bones of a live mouse. **The objective of the current study is to determine the extent to which free dye has been removed from a sample of fluorescently labeled IGF-I protein using thin layer chromatography (TLC).** Removal of free (unbound) dye is important to confirm that fluorescence in the bone is only dye-conjugated protein. This work was done as part of my Capstone research. These experiments complement a unilateral (one-sided) limb heating study in which we compare right-left side differences in limb length after mice are exposed to daily IGF-I injections and limb heating. This paper presents our methods for fluorescent protein labeling and validation using TLC, as well as our results from a daily unilateral limb heating trial. Results from the TLC study demonstrated that all free dye was removed from the sample. These results are significant because they help validate methods for studying transport of IGF-I into growing limbs of mice at different temperatures and growth phases. My mentor then injected the labeled IGF-I protein into live mice and tracked its delivery into their growing bones. To examine long-term effects of the IGF-I injections, we planned to administer unlabeled IGF-I to mice and expose them to a daily unilateral heating regimen in an effort to quantify IGF-I effects on extremity lengthening. Unfortunately, due to a shipping error, we received mice that were older than we typically use for experiments. Our other experiments used mice that correspond to “toddler age” in humans. The mice we received last summer approximated “school age.” **We utilized the opportunity to determine whether heat effects on limb growth were age dependent.** We found that although growth diminishes with age, there was still a measurable heat-treatment effect. When older animals were compared to the younger group, the relative amount of growth (heat-treated side compared to non-treated side) was nearly the same. Results demonstrate that heat could still be an effective treatment to increase limb length at older age points. This research is relevant for developing approaches to treat limb length discrepancies in children using temperature to augment molecular delivery to growing bones without surgery.

INTRODUCTION

Differential bone lengthening is a serious condition in growing children or adolescents that can occur naturally or after a particular injury. The growth disorder can result in limb-length inequality, a condition in which one leg is longer than the other. Differences as small as 3-4% can hinder normal walking in humans [1]. These differences can lead to more complicated health conditions like scoliosis and osteoarthritis [3]. Treatment for such ailments often currently requires invasive surgery and a painful recovery. Observations from nature have stimulated a line of research that uses temperature as a noninvasive way to manipulate limb growth. In nature, “Allen’s rule” is a biological principal, which states that limb length varies with the environmental climate in which that species lives [6]. Limbs are shorter in cold climates and longer in warm climates. This rule is thought to be based on a surface-area to volume ratio. Animals in colder climates need to conserve heat and therefore have shorter limbs. In contrast animals in warmer climates are in danger of overheating and thus have a greater surface area to volume ratio (longer limbs) in order to disperse heat. Temperature acts as a catalyst in most chemical and biochemical reactions. The law of thermodynamics states that average kinetic energy of a molecule is directly proportional to temperature [2]. These properties can be roughly applied to the circulation of materials throughout a living system. It is known that cold temperatures trigger vasoconstriction, a process by which blood vessels tighten and shunt blood away from extremities and towards the animal’s center of mass. Shunting blood away from the limbs can result in lower blood flow rates and the impairment of growth. In contrast, warm temperatures permit vasodilation, which can increase blood flow and the rate of growth [4]. However, the mechanism by which temperature increases limb length is still unknown. In an effort to address this question, our lab created a unilateral heating model to induce differential extremity growth in mice. Results from these experiments showed that bone length and bone mass were greater on the heat-treated side of normal mice [5]. In this study we used mice as a model to examine whether temperature increases limb growth by augmenting the delivery of growth-essential nutrients to growing mouse bones. Insulin-like growth factor (IGF-I) is a hormone that plays a major role in childhood growth. It is produced in the liver and plays a major role in childhood growth. **We hypothesize that heat increases the delivery of IGF-I to growing mouse bones.** Fluorescent protein labeling methods were developed to track the rate at which IGF-I was delivered to the bones at varying temperatures. These experiments complement a unilateral (one-sided) limb heating study in which we compare right-left side differences in limb length after mice are exposed to daily IGF-I injections and limb heating. This research is relevant for developing approaches to treat limb length discrepancies in children using temperature instead of surgery.

METHODS

All procedures were carried out according to IACUC guidelines. The proper training for animal care and research methods had been completed prior to starting the study.

Protein Labeling

Our lab has established a protocol for adding a fluorescent tag to IGF-I so that it can be visualized in a live mouse. The methods use a reactive dye (Alexa-488) that non-specifically binds to proteins (Life Technologies A37570). Amine-reactive dye was added to the IGF-I protein sample and was incubated for one hour. Using a spin column, the labeled conjugate was passed through size-exclusion resin. The resin acts as a filter with pores that takes small particles more time to pass through than larger ones. The labeled protein conjugate is a larger molecule than the free dye, which allows the labeled protein conjugate to be collected, while leaving any unbound free dye in the resin. Spectrophotometry was implemented to determine the degree of conjugation.

Thin Layer Chromatography

Thin Layer Chromatography (TLC) is a technique that separates two or more substances from each other based on their relative polarities. Substances that move up the plate are considered less polar than those that travel smaller distances. TLC was implemented in order to determine whether free dye remained in a sample of IGF-1 labeled with Alexa-488 dye (Fig. 1). Samples of reactive dye and protein (2 μ L of each sample) were pipetted on a silica TLC plate. A 1:1 solvent mixture of ethanol and chloroform was used to initiate movement of the substances up the plate (approximately 15 minutes) The plate was viewed using a GFP (Green Fluorescent Protein) filter on a fluorescence stereomicroscope (Fig. 2) The use of thin layer chromatography is necessary for determining that all of the fluorescent dye present in the bones during *in vivo* imaging is bound to the protein. It is important that free (unbound) dye is removed so we can verify that the fluorescence in the bone is only dye-conjugated protein. Ideally the protein protein-dye conjugate should remain at the origin and not migrate up the plate.

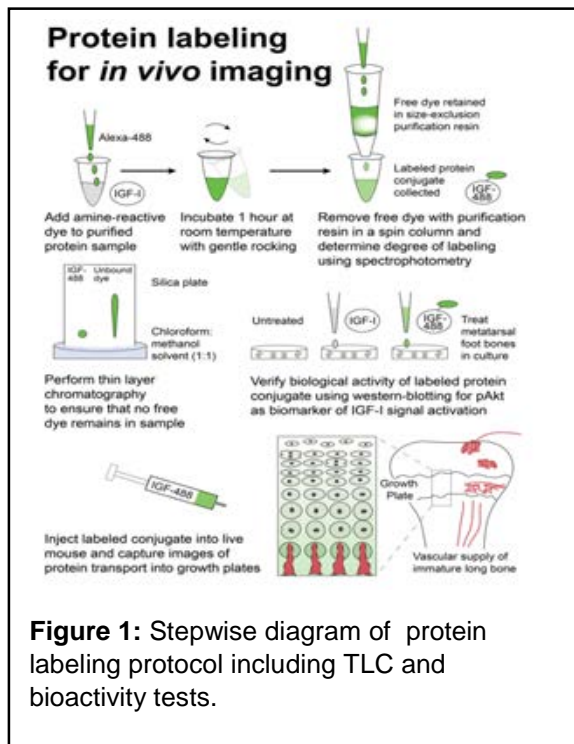


Figure 1: Stepwise diagram of protein labeling protocol including TLC and bioactivity tests.

Treatment and Groups

A sample N= 12 mice were separated into two groups containing 6 mice each: 1) wild-type mice that were injected with IGF-I and given daily unilateral heating; and 2) wild-type mice that are not treated and served as a control. The mice were older than we typically use due to a shipping error that occurred from the vendor. The estimated starting age of these mice was five weeks. The heat-treated mice were placed under an isoflurane anesthetic via a commercial vaporizer, while receiving unilateral (one-sided) application of 40C heat (using a heating pad) for 40 minutes per day, for a period of 14 days total. Whilst undergoing treatment, vitals such as respiration, core temperature were monitored closely to ensure their safety. Using an infrared thermometer the

limbs, tails, cool and cool ears, and heating pad were monitored and recorded in regulated intervals and as needed. My mentor used multiphoton imaging to quantify the distribution of IGF-I in the limbs of the wild-type mice. Multiphoton imaging is a technique that enables us to track the dispersion of fluorescently-labeled proteins and molecules in a live animal.

Halfway through the heating trial, the mice were injected with an oxytetracycline antibody that binds to ossifying bone and fluoresces under ultraviolet spectroscopy. This method allows us to track by how much the bone elongated during the time period from injection to endpoint.

Independent Role in the Project

The TLC and the heating trial is where I contributed the most towards this study. I performed the TLC experiments alongside Dr. Gabriela Ion (a Serrat lab member) for guidance in the beginning, and then moved toward a more independent role. During the trial, my role was to anesthetize mice, position them on the heating pad, measure temperatures and vitals, and monitor the pad temperature. When we harvested the mice at the end of heating trial, I captured photos, euthanized, measured organs and ears, dissected bones and aided in data collection.

Measurable Outcome Variables:

We predict that unilateral heating will increase bone length and dispersion of IGF-I into mouse limbs. The primary variables of interest are: quantitative analysis of the limb lengths, ear area, skeletal growth rate, and IGF-I measured in limb bones using multiphoton microscopy. We assessed right-left differences in these variables using paired t-tests in SPSS statistical software to determine whether they are increased on the heat-treated side of each mouse.

RESULTS AND DISCUSSION

Thin Layer Chromatography

Results from the TLC study demonstrated that all free dye was removed from the sample. Retention factor is measured as the distance the substance moves up the plate divided by the distance of the solvent. In this study, the retention factor of the protein-dye conjugate was zero. The TLC plate (Fig. 2) show that the majority of the Alexa-488 dye has been bound to the protein, and no free dye remains in the labeled protein sample. Based on the principals of chromatography, substances that move up the plate are considered less polar than those that travel smaller distances. Therefore, the less polar free dye appears as a streak on the plate. Absence of a streak on the protein sample means there is no free (unbound) dye in the protein conjugate. With this information, we can be confident that what we view under fluorescence microscopy is not free dye but actual protein. Had this not been the case, taking measurements of the growth plates would be difficult, because we would not know whether fluorescence was dye alone or dye conjugated protein. It is essential to verify that the dye is bound exclusively to protein when examining fluorescence in the growth plates of elongating bones. This method gives us the opportunity to confirm that the IGF-488 preparation was successful. Using TLC, we were able to demonstrate

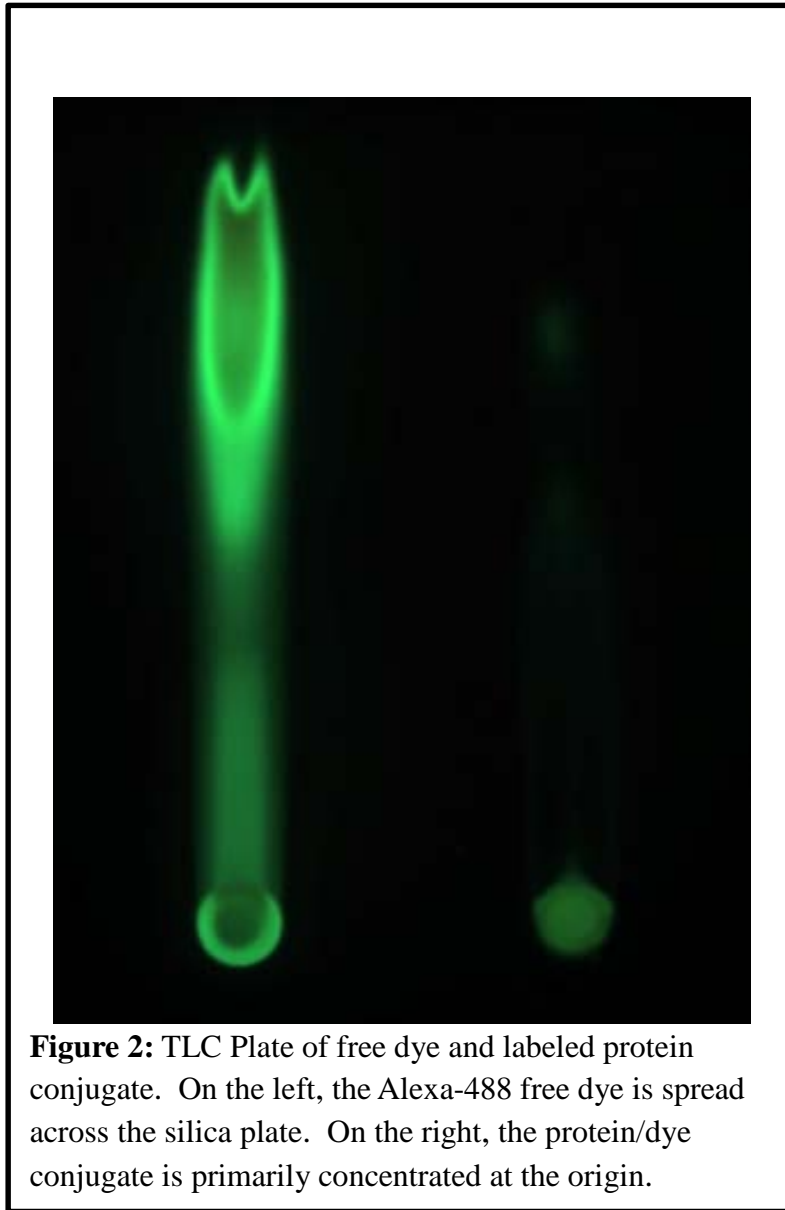


Figure 2: TLC Plate of free dye and labeled protein conjugate. On the left, the Alexa-488 free dye is spread across the silica plate. On the right, the protein/dye conjugate is primarily concentrated at the origin.

that all free dye was removed from the sample. Therefore, when the conjugate is injected into a live animal, to track IGF-I delivery, we can be confident that the fluorescence represents only dye conjugated protein.

A bioactivity test was also done separately in our lab by treating metatarsal bones in culture with the labeled protein conjugate. Western blotting for pAKT revealed that the IGF-I remained functional post-labeling. Together with the TLC results, these tests confirm that the labeling method was successful and is important because it provides a method to study temperature effect on IGF-1 delivery to mouse bones with confidence.

Unilateral Limb Heating

Analysis of the growth of the heat-treated mice led to interesting results. Both groups of mice (non-treated controls and experimental) exhibited small daily gains in mass as opposed to what we have seen in previous trials. The major difference was in the initial starting mass of these mice. A normal 3 week-old mouse weighs

approximately 8-9 grams; while these mice started around 16-17 grams. This matches the growth curve of a 5 week-old mouse (Fig. 3b). Thus, we believed there was a discrepancy in the shipment of mice. Instead of the 3 week-old mice that we requested, we instead received 5 week-old animals. Our lab was able to turn this dilemma into a valuable opportunity to study how age impacts the temperature effect on limb length.

We compared the daily mass gained by our 5 week-old mice to that of previous experiments using 3-week old mice by creating a plot of body mass versus age in days (Fig. 3).

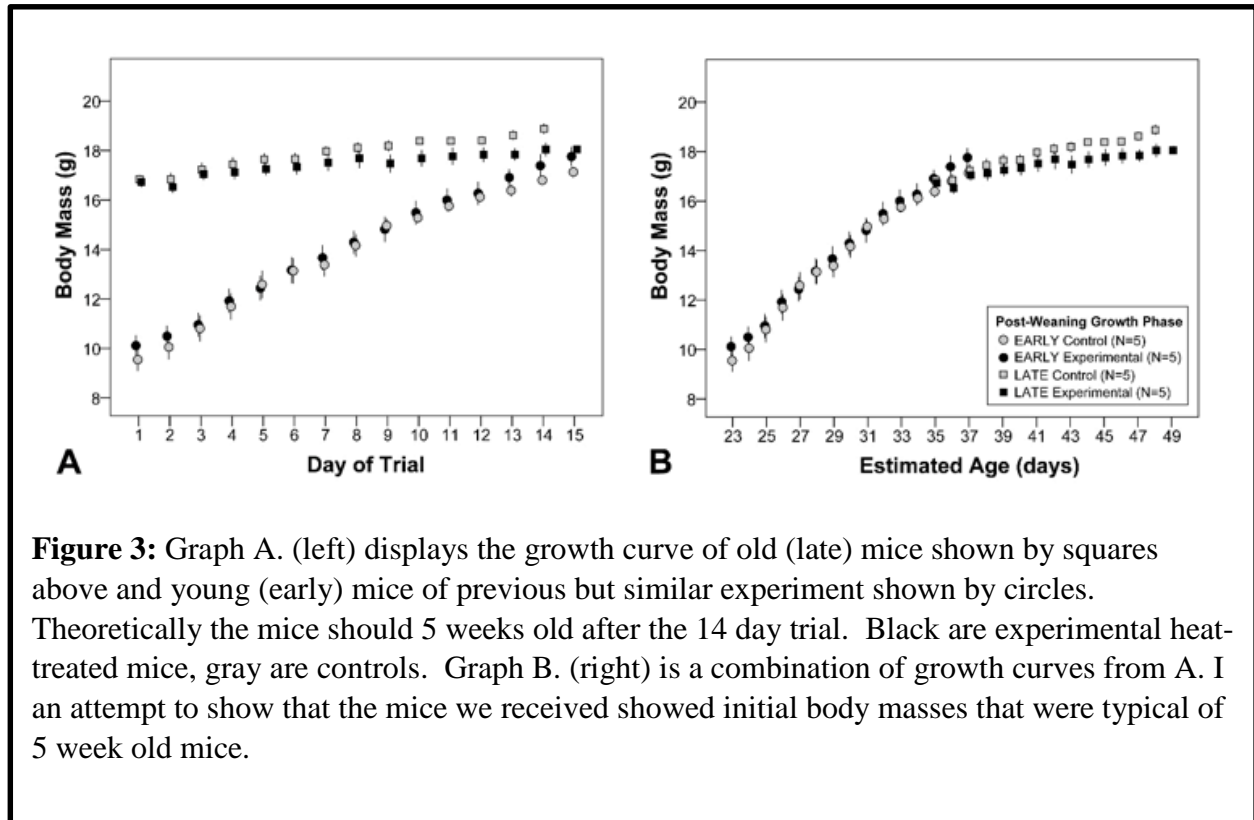


Figure 3: Graph A. (left) displays the growth curve of old (late) mice shown by squares above and young (early) mice of previous but similar experiment shown by circles. Theoretically the mice should be 5 weeks old after the 14 day trial. Black are experimental heat-treated mice, gray are controls. Graph B. (right) is a combination of growth curves from A. I attempted to show that the mice we received showed initial body masses that were typical of 5 week old mice.

In doing so we found that the young mice grew at a rate that was 5 times as fast as the older mice (Fig. 3a).

Aside from body mass, we tracked tibial elongation in the mice by means of oxytetracycline labeling. From this we discovered that the younger mice from our previous experiments had a tibial elongation rate that was more than twice that of the older mice. From these data, we were able to confirm our theory of the approximate age of the mice we received, and concluded that the age of the mice increases their growth rate decreases.

Although we saw a decrease in growth rate because of the age of the mice, we were still able to demonstrate a left-right differential between their extremities. The relative difference between the lengths of the heated and unheated side were similar. This suggests that a heat induced response to limb length inequality is still possible in later phases of postnatal growth.

Future Plans

Our lab plans to continue to study the mechanism by which heat facilitates bone elongation. This summer, the lab intends to perform another trial in which IGF-I will once again be tracked in vivo while we are still implementing the confirmation methods of TLC and bioactivity tests. I plan to continue working on this research project through this summer until I begin medical school in the fall. Graduate student Holly Tamski (PhD candidate and recipient of 2014-15 NASA fellowship), medical student Jenna Kerby (recipient of 2013-14 NASA fellowship), and soon to be Pharmacy student Kaitlynn Hughes will also be partaking in the experiments. Holly will continue the

research throughout the school year. This summer, I will be trained to perform ear area analysis and further dissection techniques to expand my knowledge and research abilities.

Valuable Aspects of the Program

This financial support has been essential to my research experience. The stipend has been used to fund my salary this past year. Without this funding, I might not have received any research training, which in turn would have hindered my whole undergraduate experience as Biochemistry major since this represented part of my Capstone project. This salary made research over the summer possible because I live out of state and would not have been able to afford living in West Virginia without the aid of government loans. Currently I am taking organic chemistry lab and found that many of the required experiments involved using TLC to confirm our results; because of this research I have been able to use the techniques I learned in the Serrat Lab in my chemistry course, and vice versa.

This fellowship has led to many opportunities for me including, but not limited to, presenting a poster at Undergraduate Research Day at the Capitol (URDC), fulfilling my Capstone graduation requirement for Marshall University, and the most significant to me was being able to present this research at the Experimental Biology (EB) conference in Boston as an undergraduate. Because of the NASA fellowship I have been able to understand the importance of research and communication between peers. I intend to present my research in the form of a poster one more time at Marshall University's College of Science Sigma Xi research day on May 1st. In the fall as I prepare for medical school, I will be thankful for the experience this fellowship has given me in the field of anatomy. I have not taken any physiology or anatomical course during my undergraduate career, so having a little background in skeletal structure will be of some use as it was on the Medical College Admittance Test. My experiences dissecting ears and bones will also be of great use. As my mentor is an anatomy professor for the first year medical students I look forward to seeing her the coming year and possibly working in this lab again.

CONCLUSION

We found that TLC is an effective way of determining whether there is free dye left that was not bound to the protein. The protein was found to still be biologically active as per the pAKT bioactivity test that Dr. Gabriela Ion ran and presented at the Experimental Biology meeting last month. With the limb heating study, we found that our young mice (3-5 weeks of age) had body mass and limb growth rates that were five and two times, respectively, greater than those of the older mice (5-7 weeks age). We saw that the unilateral limb heating increased the extremity size of both young and older groups, with the effect diminishing with increasing age. These results and those obtained in subsequent studies will be important because therapeutic heat treatments could prove to be a cost-effective, non-invasive way to treat limb-length discrepancies in the future.

ACKNOWLEDGEMENTS

We thank C. Farnum, R. Williams, A. Williams, G. Ion and the VA Medical Center and CEB staff for support. H. Tamski, J. Kerby, A. Heaberlin and N. Crow helped performed experiments and

helped collect data. We are grateful to Dr. Howard and the Marshall Animal Resource Facility for animal husbandry, assistance with equipment set up, and room temperature monitoring. Marcos Serrat helped design and assemble the anesthesia manifold. D. Neff provided valuable imaging aid. This research was supported, in part, by funding from NASA WV Space Grant Consortium, ASBMR Grants in Aid Program, National Science Foundation (MRI-R2 0959012), University of Kentucky CCTS Pilot Program (NIH UL1TR000117), and the National Institute of Arthritis and Musculoskeletal and Skin Diseases of the National Institutes of Health (1R15AR067451-01). This work was aided by the use of facilities at the Huntington VA Medical Center. I thank Marshall University's Chemistry department for approving this as my Capstone requirement. Lastly, I would like to thank Dr. Serrat for mentoring me before and during the fellowship.

REFERENCES

1. Brady et al., 2003. *Journal of Orthopedic & Sports Physical Therapy*. 33: 221-234.
2. Chang, Raymond. *The First Law of Thermodynamics. Physical Chemistry for the Biosciences*; University Science Books: United States, 2005; 59-60.
3. Serrat MA, Efaw ML, Williams RM. Hindlimb heating increases vascular access of large molecules to murine tibial growth plates measured by in vivo multiphoton imaging. *J Appl Physiol*. 2014. 116(4):425-38.
4. Serrat MA, King D, Lovejoy CO. Temperature regulates limb length in homeotherms by directly modulating cartilage growth. *Proc Natl Acad Sci U S A*. 2008. 105(49):19348-53.
5. Serrat MA, Schlierf TJ, Efaw ML, Shuler FD, Godby J, Stanko LM, Tamski HL. *J Orthop Res*. 2015 May;33(5):692-8. doi: 10.1002/jor.22812. Epub 2015 Mar 5.
6. Brooker RJ, Widamaier EP, Grahm LE, Stiling PD. *Animal Bodies and Homeostasis. Biology*; McGraw-Hill Companies Inc. 2011; 832-850.

EXPLORING THE TEMPERATURE DEPENDENCE OF PHOTOASSEMBLY

Shane Kagen
Biochemistry
Marshall University
Huntington, WV 25703

ABSTRACT

Deciphering the complexities of the oxygen-evolving complex is imperative to the advancement of renewable and cleaner energies. The oxidation of water into protons, electrons, and oxygen gas has its use in fuel cells as well as in increasing the efficiency of solar panels. By understanding the oxygen-evolving complex, it may become possible to increase its efficiency. As a result, crops can be bred or modified to be hardier and solar power could potentially become more efficiently harvested as an energy source. In order to determine the characteristics of the oxygen-evolving complex, its basic properties must first be defined on a fundamental level. In order to do this, oximetry has been used in order to evaluate the efficiency of the production of oxygen, a product of biological water oxidation. Using a Clark-type electrode attached to a temperature controlled water bath, the efficiency of oxygen production of an oxygen-evolving complex containing sample can be evaluated at varying temperatures. It has been determined that *in vitro*; *Spinacia oleracea*'s oxygen-evolving complex has a variable maximum of around either 28°C or 38°C. This may indicate some variation between crops from which the samples were prepared. Further, the efficiency of the complex has been found to increase in the presence of CaCl₂ redox mediator 2,6-dichloro-1,4-benzoquinone.

INTRODUCTION

Photosynthesis is the process by which photosynthetic organisms (plants, algae, and some bacteria) convert light energy of specific wavelengths into energy which is stored chemically in the bonds of monosaccharides. This process begins in photosystem II (PSII), which resides within the thylakoid membrane of chloroplasts. In PSII, photopigments capture light energy of specific wavelengths and excite electrons. These excited electrons will leave the photosystem as they are used in order to produce adenosine triphosphate (ATP) and other temporary energy storage molecules which will be used later in carbon fixation.

The oxygen-evolving complex (OEC) is a metal cluster in PSII of higher order photosynthesizing organisms that is composed of one calcium and four manganese atoms¹. The structure can be seen in Figure 1. The OEC oxidizes water in order to restore electrons to PSII. This process causes stepwise oxidation due to sequential extraction of electrons from a photooxidized chlorophyll a (chl a) pair¹. Once the OEC is sufficiently oxidized (four oxidation events), electrons are then stripped from water to generate oxygen and protons². These protons are used to form a gradient that is used in the aforementioned ATP synthesis. This is also the primary source of atmospheric oxygen.

The process of photosynthesis is an inefficient one. Moreover, PSII is not yet wholly understood. Understanding PSII may provide the key to increasing the efficiency of photosynthesis. Increasing

the efficiency of photosynthesis and PSII could open opportunities in agriculture and synthetic water oxidation and photosynthetic systems that could increase crop yields, reduce energy shortages, and provide a cleaner energy source³.

In order to effectively study these complexes in the lab, PSII-enriched membranes were isolated from spinach leaves through a detergent wash and differential centrifugation. This is known as the Bertholt, Babcock, and Yocum method named after the designers of the procedure⁴. These were tested in various conditions and rate of oxygen evolution was measured to determine the activity of the OEC.

The chemistry that the OEC catalyzes is temperature sensitive. This is due to the activation barrier of the rate-limiting step being dependent on temperature. The specific focus of this research was and is to determine at what temperatures the OEC reacts optimally in order to determine the activation energy and mechanisms of the assembly of the OEC. Conditions involving the presence of extrinsic proteins and introduction of salts that contain ions found within the complex were also introduced to further determine explore the temperature dependent properties of the OEC.

EXPERIMENTAL METHODS AND MATERIALS

The following procedures for extraction of PSII-enriched particles and oxygraph electrode description and set up were received directly from the thesis of Emilee Hope Cooke⁵. PSII-enriched particles were extracted from spinach according to the procedure outlined by Berthold, Babcock, and Yocum⁴, with modifications from Kolling, et.al². Spinach was chosen due the accessibility of the organism and it is already a well-studied model system. The absorbance values allow for easy determination of chl *a* concentration, which directly correlates to the concentration of PSII. This correlation allows for the calculation of oxygen production rates. The preparation has many light sensitive steps and is performed under dim green light to prevent damage to the photosystem in the preparation.

The following procedures for PSII-enriched particle isolation as well as the instrument setup were used with minor modifications from the thesis of Emilee Hope Cooke. “The process begins by removal of the petioles, or center vein of the leaf, which were removed because they hold a large amount of proteases. Due to human skin containing proteases as well, gloves were worn to prevent protein degradation in the leaves. The remaining portion of the leaves were then placed in a commercial juicing machine and mixed with K1 buffer (0.1 M sucrose, 0.2 M NaCl, 35 mM 4-(2-hydroxyethyl)-1-piperazineethanesulfonic acid (HEPES), at pH 7.4 with NaOH) and protease inhibitors (table 1). This mix is then ground in order to lyse the cells⁵. Lysed cells potentially release proteases as well. In order to reduce damage to important proteins, the procedure is performed as quickly as possible at low temperatures in the presence of protease inhibitors.

Table 1. Protease inhibitors of the PSII-enriched membrane preparation		
Protease Inhibitor	Inhibits	Reversible/ Irreversible
AEBSF hydrochloride	serine proteases	irreversible

aprotinin bovine lung	serine proteases	reversible
E-64	cysteine proteases	irreversible
leupeptin hemisulfate	serine/ cysteine proteases and trypsin like proteases	reversible

After cell lysis, in order to pellet and remove whole cells, organelles, cell walls, and DNA that persisted; the filtrate was strained and then placed into 250 mL centrifuge tubes and centrifuged at 3000 Xg for 2 min at 4 °C. The supernatant was then collected and centrifuged at 8600 Xg for 15 min at 4 °C. The pellet was then resuspended and a minimal volume of K2 buffer (0.4 M sucrose, 5 mM NaCl, 5 mM MgCl₂•6H₂O, 15 mM CaCl₂ (AN), 50 mM 2-(N-morpholino)ethanesulfonic acid•H₂O (MES•H₂O), at pH 6.5 with NaOH) with protease inhibitors using a brush and homogenizer⁵.

The chl *a* concentration was then calculated using a Shimadzu UV-1800 scanning UV-Vis: 5 µl of prep and 995 µl of 80% (v/v) acetone were mixed in a 1.5 mL snap cap tube and spun in a microfuge for 5 min. Then the absorbance at 652 and 750 were measured and used to calculate the concentration of chlorophyll using $([Chl\ a] \text{ (mg/mL)} = ((OD_{652} - OD_{750}) \times \text{optical path length (1cm)} \times 27.8 \text{ g}^{-1} \text{ cm}^{-1} \times \text{Dilution factor (200)} / 1000 \text{ mg/g} / 1 \text{ mL})^4$. This was done twice and the average of the two was used to calculate the amount of triton needed for the detergent treatment⁵.

Then the suspension was diluted to 2.5 mg/mL chlorophyll with K2 buffer with protease inhibitors. Next the suspension was placed in a beaker and stirred slowly at 4 °C for 12 min with a magnetic stirrer while 20 mg Triton X-100 (20% w/v) :1 mg Chl *a* was added slowly along the side of the beaker (the final Chl concentration should be about 2 mg/mL). This step is performed in order to partially degrade the thylakoid membranes. However, the Triton exposure time should not exceed 30 min so that the thylakoid membrane does not get degraded too much⁵.

The mixture was then transferred into 42 mL centrifuge tubes and centrifuged at 40,000 Xg for 18 min at 4 °C (total time in Triton X-100 should not exceed 30 min) in order to pellet sub thylakoidal membranes and mostly separate PSI from PSII. In order to determine if the separation of PSI from

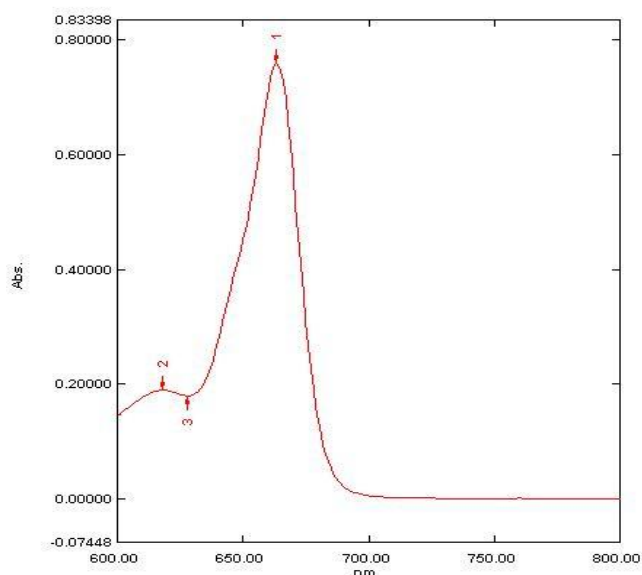


Figure 2. An example UV absorbance spectra for determining chlorophyll a concentration of PSII-enriched membranes

PSII was successful sodium dodecyl sulfate polyacrylamide gel⁶. Next the supernatant, which contained PSI, was decanted and the pellet was resuspended in minimal volume of K2 buffer with protease inhibitors, while avoiding the white part of the pellet, which is starch. The resuspended pellet was then put into four 42 mL centrifuge tubes, which were filled the rest of the way up with K2 buffer with protease inhibitors and centrifuged at 40,000 Xg for 18 min at 4 °C. Then the pellets were resuspended in a minimal volume of K3 buffer (50 mM MES, 35 mM NaCl, 0.3 M sucrose, at pH 6 with NaOH) with protease inhibitors and put into two 42 mL centrifuge tube and centrifuged at 40,000 Xg for 18 min at 4 °C (this step was repeated if the supernatant was not clear). If the supernatant was clear the pellet was resuspended in a minimal volume of K3 and frozen in liquid nitrogen and stored in liquid nitrogen (at -80 °C)⁵.

Measurements were made using a Hansatech Oxygen Electrode; this applies a small polarizing voltage between the platinum cathode and the silver anode of the electrode disc, and oxygen is consumed at the platinum cathode. The current that is generated when the oxygen is consumed is proportional to the oxygen activity in the sample. The electrode was setup according to the Hansatech Operations Manual. The electrode was cleaned using Hansatech rapid electrode disc polish and a cotton swab to remove oxide and chloride deposits on the silver anode, then rinsed with distilled water and dried with a paper towel. Next a 50% saturated solution of KCl was added to the electrode well and a drop was also put on the top. KCl is needed to serve as the electrolyte, in order to conduct the signal. Then a piece of cigarette paper is placed on top of the electrode and covered by an oxygen permeable membrane forming a wick. Next an O-ring was applied over the electrode dome to hold the wick in place using an applicator. After the electrode disc was prepared it was put into the oxygraph. The oxygraph was then calibrated by using 2 mL of oxygenated water, prepared by shaking a flask of distilled water for a few minutes, and then adding in nitrogen gas when prompted by the computer program. After use the electrode was disassembled and stored in a dessicator^{5,7}.

The PSII-enriched membranes were stored in liquid nitrogen. Before experiments were run, two to three pellets of the membranes were removed, placed in a snap-cap tube, and allowed to thaw in ice in a box closed off from light. While thawing the PSII-enriched membranes, the electrode was prepared and the water bath was set to a temperature ranging from 5-50°C; 500mM CaCl₂, 50mM K₃Fe(CN)₆, 10mM 2,6-dichloro-1,4-benzoquinone (DCBQ), and K3 buffer with a pH of 6.0 were also prepared. The K₃Fe(CN)₆ was wrapped in foil and placed in the closed ice box in order to prevent light exposure. DCBQ was also kept in foil due to light sensitivity. Once the membranes thawed, two sets of 5 μL were micropipetted into 1.5-mL snap-cap tubes. Next, 995 μL of 80% (v/v) acetone were added as a solvent. The sample was then placed in a centrifuge for 5 min or until the solution is homogenous. The solution was then transferred into a cuvette and placed in the Shimadzu UV-1800 scanning UV-Vis. The data obtained from the wavelengths 652 and 750 were used to determine the concentration of the solution of membranes that remains in the ice as was described in the PSII-enriched membrane preparation. This concentration was used to determine the amount of PSII-enriched membranes used in later solutions; it was generally determined that between 3 μL and 7 μL of PSII-enriched membranes were needed per mL of solution. The final concentrations of added solutions were 5 mM K₃Fe(CN)₆, 0.0125 mg/mL PSII-enriched membranes, and 0.15 mM DCBQ (dissolved in DMSO if it is added). These solutions were placed in the chamber of the oxygraph, which is removed from light. Data is collected for 5 min before light is introduced into the system. After the 5 min period, a projector is turned on and focused at the sample; data collection continues for approximately 3–5 min longer. The data

received can be manipulated to represent the oxygen evolution rate of the sample (using the equation $(\text{rate} = ((\text{slope nmol O}_2/\text{mL}/\text{min} * 60 \text{ min}/\text{hr})/1000 \mu\text{mol O}_2/\text{nmol O}_2)/ 0.0125 \text{ mg chl } a/\text{mL}))^{5,6}$; this was interpreted as a measure of efficiency and activity of PSII-enriched particles.

The addition of certain compounds – sucrose, NaCl, MES pH buffer, electron acceptor potassium ferricyanide – is necessary for the function of the PSII-enriched particles. Some other compounds, such as redox mediators DCBQ, increase the efficiency of electron movement through the photosystem and thus increase the efficiency the OEC. Interestingly, it was found that CaCl₂ causes a significant increase in oxygen evolution of the PSII-enriched particles as well when DCBQ is not present. The actual reason for this is still being explored.

RESULTS AND DISCUSSION

The maximum activity of the OEC was previously found to be at 28°C⁶, but has since been determined to be preparation dependent with an alternate maximum being found around 38°C. This was compared in figure 4. This has been shown to be consistent with maxima for whole cell plants and algae. The addition of DCBQ has been shown in multiple species to drop the maxima to 28°C while simultaneously increasing the rate of oxygen evolution up to eight fold, as seen in figure 3. This was consistently true for *Spinacia oleracea*. This was possibly caused by DCBQ being able to decouple some process within PSII, or DCBQ has some factor of temperature dependence itself that allows it to overcome some inefficiencies of the OEC at lower temperatures⁵. A possible cause of the previously mentioned shift from non-DCBQ maxima of 28°C to 38°C has been hypothesized to be related to the strain of *Spinacia oleracea*. It is believed that, due to location of purchase and growth, the preparations that have 38°C maxima are were derived from a heat resistant strain of spinach. Specifically, 28°C maxima spinach was purchased from an organic Amish farm while the 38°C organic spinach was purchased from large-scale retailers.

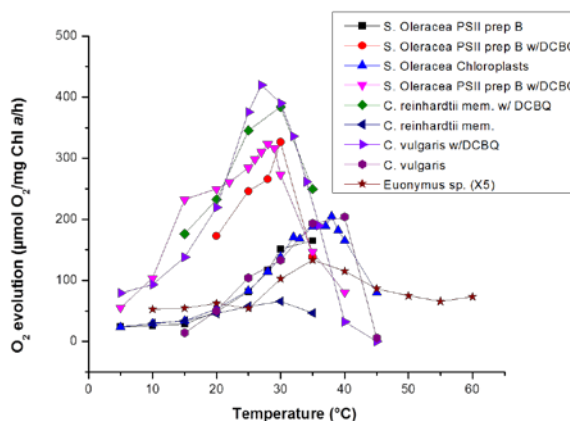


Figure 3. (above) Temperature titrations of multiple species in with and without redox mediator DCBQ

Additionally, it was found that CaCl_2 , in the absence of redox mediators, had a significant positive effect on the rate of oxygen evolution shown in figure 4. The reason for this increase is not fully understood, but may be possibly related to some divalent cation effect. Additionally, it was determined that the effect of a redox mediator completely or nearly completely overrides the effect of the CaCl_2 .

Figure 4. Temperature titrations of oxygen evolution rates with .01 mM DCBQ (red), 25 mM CaCl_2 (blue), both (purple), and neither (black) determined via oximetry

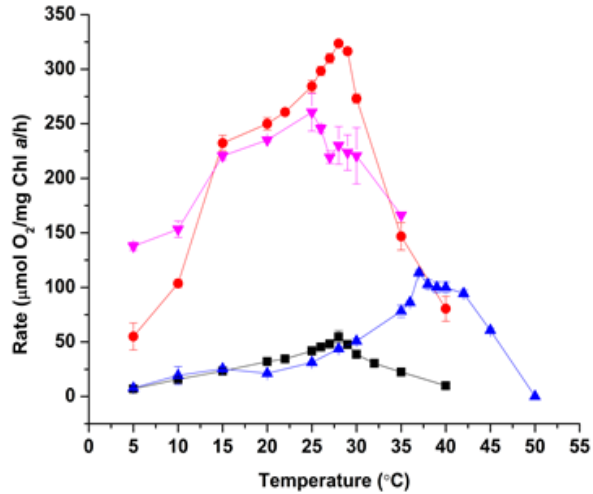


Figure 4. Temperature titrations of oxygen evolution rates with .01 mM DCBQ (red), 25 mM CaCl_2 (blue), both (purple), and neither (black) determined via oximetry

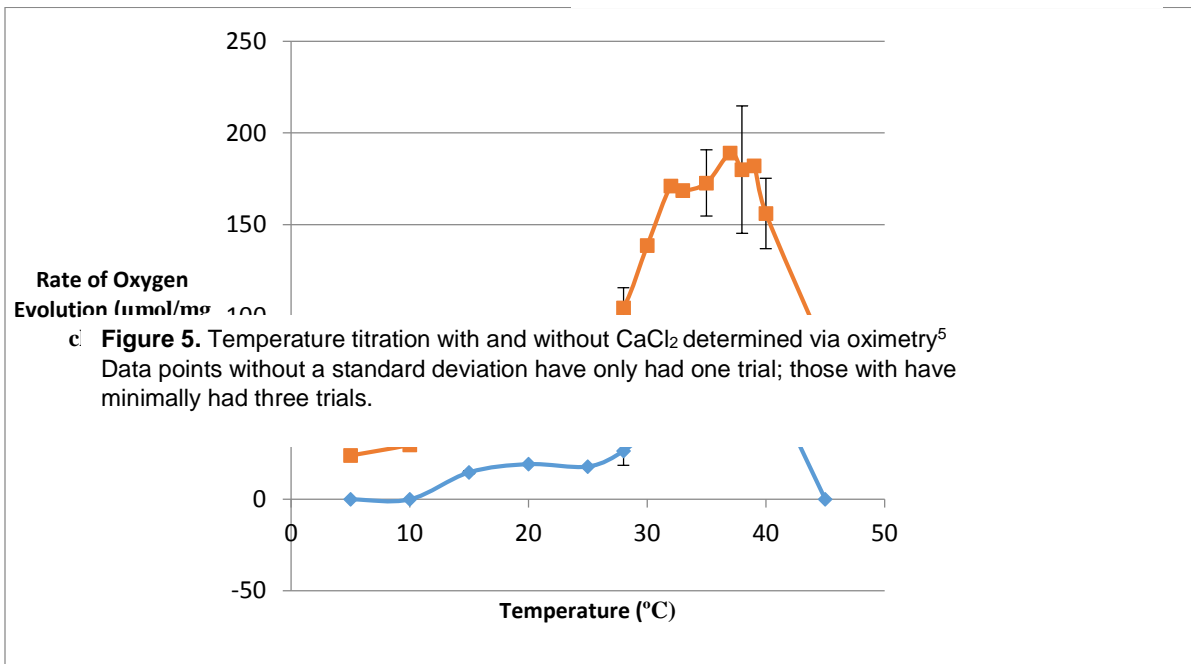


Figure 5. Temperature titration with and without CaCl_2 determined via oximetry⁵
Data points without a standard deviation have only had one trial; those with have minimally had three trials.

FUTURE WORK

The potential next steps in these experiments constitute the standardization of the spinach used in the lab. This boils down to the in-house growth of spinach from a known seed provider. This spinach will then be used in the same experiments performed previously in order to determine its temperature maxima and evaluate the consistency of previous results. Additionally, if the CaCl_2 seems to provide the same effect, the substitution of other divalent salts such as MnCl_2 would possibly confirm or deny the hypothesis that the effect is due to a divalent cation effect. Beyond that, an additional procedure known as photoassembly has a temperature dependence as well. Photoassembly is a process by which the OEC and surrounding extrinsic proteins are forcefully removed and the OEC is then rebuilt onto the PSII-enriched membranes. In doing photoassembly, the already poor efficiency of the OEC is reduced. Standard means of using DCBQ to improve the efficiency of the OEC and PSII are too strong and result in electron cycling from the OEC to itself which eliminates most water oxidation. In order to improve the efficiency, experimentation with short tailed quinones could be done with both standard PSII-enriched membranes and with photoassembled PSII.

EXPERIENCES

By performing research under a grant, I have been able to garner experience that will have value throughout the rest of my life. I have had opportunities to view both academic and industrial work in the field of chemistry and the chance to learn more about prominent instruments being used in the field today. By being funded in my research, I was able to maintain easy accessibility to my university in order to further my education in many other regards as well. It is due to these experiences that I have improved an already strong respect for working men and women in the many careers of chemistry and science, in general.

ACKNOWLEDGEMENTS

I would like to thank the NASA West Virginia Space Grant Consortium for funding my research. I would further like to thank Derrick Kolling, Ph.D. for being a helpful and instructive research advisor. Further, the Marshall Department of Chemistry furthered my opportunities through their summer research program. This program allowed me the opportunity to visit DOW chemical in South Charleston. Thus, I would further like to acknowledge DOW chemical for allowing me and others to attend their facilities and demonstrate an average day of work.

LITERATURE REFERENCES

1. Umena, Y.; Kawakami, K.; Shen, J.; Kamiya, N. Crystal structure of oxygen-evolving photosystem II at a resolution of 1.9 Å. *Nature*. May 2011, Vol. 473 Issue 7345, p55-60
2. Kolling, D.R.J., Cox, N., Ananyev, G.M., Pace, R.J., Dismukes, G.C. What Are the Oxidation States of Manganese Required To Catalyze Photosynthetic Water Oxidation? *Biophysical Journal*, 2012, 103:1-10.
3. Reece, S.Y., Hamel, J.A., Sung, K., Jarvi, T.D., Esswein, A.J., Pijpers, J.J.H., Nocera, D.G. Wireless Solar Water Splitting Using Silicon-Based Semiconductors and Earth-Abundant Catalysts. *Science*, 2011, 334:645-648.

4. Berthold, D. A., G. T. Babcock, and C. F. Yocum. 1981. A highly resolved, oxygen-evolving photosystem II preparation from spinach thylakoid membranes: EPR and electron-transport properties. *FEBS Lett.* 134:231-234.
5. Cooke, Emilee Hope. "The pH Dependence of Photosystem II Oxygen-Evolving Complex Assembly". 2014. Theses, Dissertations and Capstones. Paper 475. <http://mds.marshall.edu/etd/869/>
6. Board, James Scott II. "Toward a Comprehensive Model of Photosystem II Oxygen Evolving Complex Photoassembly". 2013. Theses, Dissertations and Capstones. Paper 475. <http://mds.marshall.edu/etd/475>
7. <http://www.hansatech-instruments.com>

Exploring the Temperature Dependence of Photoassembly

Shane Kagen
Biochemistry
Marshall University
Huntington, WV 25703

ABSTRACT

Deciphering the complexities of the oxygen-evolving complex is imperative to the advancement of renewable and cleaner energies. The oxidation of water into protons, electrons, and oxygen gas has its use in fuel cells as well as in increasing the efficiency of solar panels. By understanding the oxygen-evolving complex, it may become possible to increase its efficiency. As a result, crops can be bred or modified to be hardier and solar power could potentially become more efficiently harvested as an energy source. In order to determine the characteristics of the oxygen-evolving complex, its basic properties must first be defined on a fundamental level. In order to do this, oximetry has been used in order to evaluate the efficiency of the production of oxygen, a product of biological water oxidation. Using a Clark-type electrode attached to a temperature controlled water bath, the efficiency of oxygen production of an oxygen-evolving complex containing sample can be evaluated at varying temperatures. It has been determined that in vitro; *Spinacia oleracea*'s oxygen-evolving complex has a variable maximum of around either 28°C or 38°C. This may indicate some variation between crops from which the samples were prepared. Further, the efficiency of the complex has been found to increase in the presence of CaCl₂ redox mediator 2,6-dichloro-1,4-benzoquinone.

INTRODUCTION

Photosynthesis is the process by which photosynthetic organisms (plants, algae, and some bacteria) convert light energy of specific wavelengths into energy which is stored chemically in the bonds of monosaccharides. This process begins in photosystem II (PSII), which resides within the thylakoid membrane of chloroplasts. In PSII, photopigments capture light energy of specific wavelengths and excite electrons. These excited electrons will leave the photosystem as they are used in order to produce adenosine triphosphate (ATP) and other temporary energy storage molecules which will be used later in carbon fixation.

The oxygen-evolving complex (OEC) is a metal cluster in PSII of higher order photosynthesizing organisms that is composed of one calcium and four manganese atoms¹. The structure can be seen in Figure 1. The OEC oxidizes water in order to restore electrons to PSII. This process causes stepwise oxidation due to sequential extraction of electrons from a photooxidized chlorophyll a (chl a) pair¹. Once the OEC is sufficiently oxidized (four oxidation events), electrons are then stripped from water to generate oxygen and protons². These protons are used to form a gradient that is used in the aforementioned ATP synthesis. This is also the primary source of atmospheric oxygen.

The process of photosynthesis is an inefficient one. Moreover, PSII is not yet wholly understood. Understanding PSII may provide the key to increasing the efficiency of photosynthesis. Increasing the efficiency of photosynthesis and PSII could open opportunities in agriculture and synthetic

water oxidation and photosynthetic systems that could increase crop yields, reduce energy shortages, and provide a cleaner energy source³.

In order to effectively study these complexes in the lab, PSII-enriched membranes were isolated from spinach leaves through a detergent wash and differential centrifugation. This is known as the Bertholt, Babcock, and Yocum method named after the designers of the procedure⁴. These were tested in various conditions and rate of oxygen evolution was measured to determine the activity of the OEC.

The chemistry that the OEC catalyzes is temperature sensitive. This is due to the activation barrier of the rate-limiting step being dependent on temperature. The specific focus of this research was and is to determine at what temperatures the OEC reacts optimally in order to determine the activation energy and mechanisms of the assembly of the OEC. Conditions involving the presence of extrinsic proteins and introduction of salts that contain ions found within the complex were also introduced to further determine explore the temperature dependent properties of the OEC.

Experimental Methods and Materials:

The following procedures for extraction of PSII-enriched particles and oxygraph electrode description and set up were received directly from the thesis of Emilee Hope Cooke⁵. PSII-enriched particles were extracted from spinach according to the procedure outlined by Berthold, Babcock, and Yocum⁴, with modifications from Kolling, et.al². Spinach was chosen due the accessibility of the organism and it is already a well-studied model system. The absorbance values allow for easy determination of chl *a* concentration, which directly correlates to the concentration of PSII. This correlation allows for the calculation of oxygen production rates. The preparation has many light sensitive steps and is performed under dim green light to prevent damage to the photosystem in the preparation.

The following procedures for PSII-enriched particle isolation as well as the instrument setup were used with minor modifications from the thesis of Emilee Hope Cooke. “The process begins by removal of the petioles, or center vein of the leaf, which were removed because they hold a large amount of proteases. Due to human skin containing proteases as well, gloves were worn to prevent protein degradation in the leaves. The remaining portion of the leaves were then placed in a commercial juicing machine and mixed with K1 buffer (0.1 M sucrose, 0.2 M NaCl, 35 mM 4-(2-hydroxyethyl)-1-piperazineethanesulfonic acid (HEPES), at pH 7.4 with NaOH) and protease inhibitors (table 1). This mix is then ground in order to lyse the cells⁵. Lysed cells potentially release proteases as well. In order to reduce damage to important proteins, the procedure is performed as quickly as possible at low temperatures in the presence of protease inhibitors.

Table 1. Protease inhibitors of the PSII-enriched membrane preparation

Protease Inhibitor	Inhibits	Reversible/ Irreversible
AEBSF hydrochloride	serine proteases	irreversible
aprotinin bovine lung	serine proteases	reversible
E-64	cysteine proteases	irreversible

leupeptin hemisulfate

serine/

reversible

cysteine proteases
and trypsin like proteases

After cell lysis, in order to pellet and remove whole cells, organelles, cell walls, and DNA that persisted; the filtrate was strained and then placed into 250 mL centrifuge tubes and centrifuged at 3000 Xg for 2 min at 4 °C. The supernatant was then collected and centrifuged at 8600 Xg for 15 min at 4 °C. The pellet was then resuspended and a minimal volume of K2 buffer (0.4 M sucrose, 5 mM NaCl, 5 mM MgCl₂•6H₂O, 15 mM CaCl₂ (AN), 50 mM 2-(N-morpholino)ethanesulfonic acid•H₂O (MES•H₂O), at pH 6.5 with NaOH) with protease inhibitors using a brush and homogenizer⁵.

The chl *a* concentration was then calculated using a Shimadzu UV-1800 scanning UV-Vis: 5 µl of prep and 995 µl of 80% (v/v) acetone were mixed in a 1.5 mL snap cap tube and spun in a microfuge for 5 min. Then the absorbance at 652 and 750 were measured and used to calculate the concentration of chlorophyll using $[\text{Chl } a] \text{ (mg/mL)} = ((\text{OD}_{652} - \text{OD}_{750}) \times \text{optical path length (1cm)} \times 27.8 \text{ g}^{-1} \text{ cm}^{-1} \times \text{Dilution factor (200)} / 1000 \text{ mg/g/ 1 mL})^4$. This was done twice and the average of the two was used to calculate the amount of triton needed for the detergent treatment⁵.

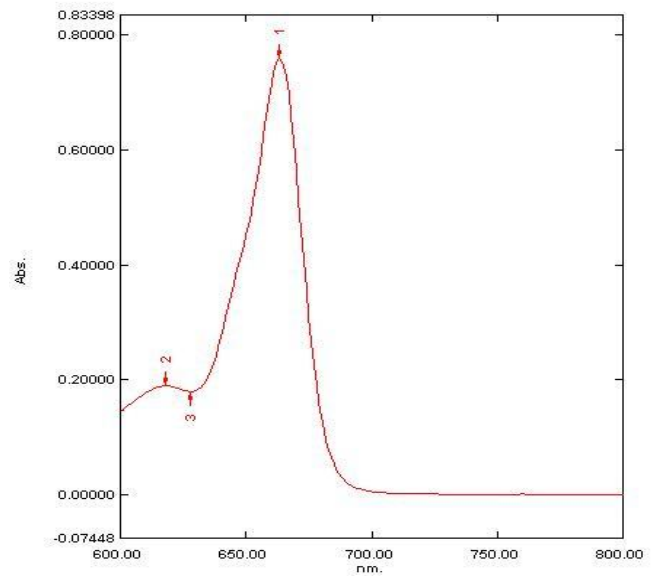


Figure 2. An example UV absorbance spectra for determining chlorophyll a concentration of PSII-enriched membranes

Then the suspension was diluted to 2.5 mg/mL chlorophyll with K2 buffer with protease inhibitors. Next the suspension was placed in a beaker and stirred slowly at 4 °C for 12 min with a magnetic stirrer while 20 mg Triton X-100 (20% w/v) : 1 mg Chl *a* was added slowly along the side of the beaker (the final Chl concentration should be about 2 mg/mL). This step is performed in order to partially degrade the thylakoid membranes. However, the Triton exposure time should not exceed 30 min so that the thylakoid membrane does not get degraded too much⁵.

The mixture was then transferred into 42 mL centrifuge tubes and centrifuged at 40,000 Xg for 18 min at 4 °C (total time in Triton X-100 should not exceed 30 min) in order to pellet sub thylakoidal membranes and mostly separate PSI from PSII. In order to determine if the separation of PSI from PSII was successful sodium dodecyl sulfate polyacrylamide gel⁶. Next the supernatant, which contained PSI, was decanted and the pellet was resuspended in minimal volume of K2 buffer with protease inhibitors, while avoiding the white part of the pellet, which is starch. The resuspended pellet was then put into four 42 mL centrifuge tubes, which were filled the rest of the way up with K2 buffer with protease inhibitors and centrifuged at 40,000 Xg for 18 min at 4 °C. Then the pellets

were resuspended in a minimal volume of K3 buffer (50 mM MES, 35 mM NaCl, 0.3 M sucrose, at pH 6 with NaOH) with protease inhibitors and put into two 42 mL centrifuge tube and centrifuged at 40,000 Xg for 18 min at 4 °C (this step was repeated if the supernatant was not clear). If the supernatant was clear the pellet was resuspended in a minimal volume of K3 and frozen in liquid nitrogen and stored in liquid nitrogen (at -80 °C)⁵.

Measurements were made using a Hansatech Oxygen Electrode; this applies a small polarizing voltage between the platinum cathode and the silver anode of the electrode disc, and oxygen is consumed at the platinum cathode. The current that is generated when the oxygen is consumed is proportional to the oxygen activity in the sample. The electrode was setup according to the Hansatech Operations Manual. The electrode was cleaned using Hansatech rapid electrode disc polish and a cotton swab to remove oxide and chloride deposits on the silver anode, then rinsed with distilled water and dried with a paper towel. Next a 50% saturated solution of KCl was added to the electrode well and a drop was also put on the top. KCl is needed to serve as the electrolyte, in order to conduct the signal. Then a piece of cigarette paper is placed on top of the electrode and covered by an oxygen permeable membrane forming a wick. Next an O-ring was applied over the electrode dome to hold the wick in place using an applicator. After the electrode disc was prepared it was put into the oxygraph. The oxygraph was then calibrated by using 2 mL of oxygenated water, prepared by shaking a flask of distilled water for a few minutes, and then adding in nitrogen gas when prompted by the computer program. After use the electrode was disassembled and stored in a dessicator^{5,7}.

The PSII-enriched membranes were stored in liquid nitrogen. Before experiments were run, two to three pellets of the membranes were removed, placed in a snap-cap tube, and allowed to thaw in ice in a box closed off from light. While thawing the PSII-enriched membranes, the electrode was prepared and the water bath was set to a temperature ranging from 5-50°C; 500mM CaCl₂, 50mM K₃Fe(CN)₆, 10mM 2,6-dichloro-1,4-benzoquinone (DCBQ), and K3 buffer with a pH of 6.0 were also prepared. The K₃Fe(CN)₆ was wrapped in foil and placed in the closed ice box in order to prevent light exposure. DCBQ was also kept in foil due to light sensitivity. Once the membranes thawed, two sets of 5 µL were micropipetted into 1.5-mL snap-cap tubes. Next, 995 µL of 80% (v/v) acetone were added as a solvent. The sample was then placed in a centrifuge for 5 min or until the solution is homogenous. The solution was then transferred into a cuvette and placed in the Shimadzu UV-1800 scanning UV-Vis. The data obtained from the wavelengths 652 and 750 were used to determine the concentration of the solution of membranes that remains in the ice as was described in the PSII-enriched membrane preparation. This concentration was used to determine the amount of PSII-enriched membranes used in later solutions; it was generally determined that between 3 µL and 7 µL of PSII-enriched membranes were needed per mL of solution. The final concentrations of added solutions were 5 mM K₃Fe(CN)₆, 0.0125 mg/mL PSII-enriched membranes, and 0.15 mM DCBQ (dissolved in DMSO if it is added). These solutions were placed in the chamber of the oxygraph, which is removed from light. Data is collected for 5 min before light is introduced into the system. After the 5 min period, a projector is turned on and focused at the sample; data collection continues for approximately 3–5 min longer. The data received can be manipulated to represent the oxygen evolution rate of the sample (using the equation $(\text{rate} = ((\text{slope nmol O}_2/\text{mL}/\text{min} * 60 \text{ min}/\text{hr})/1000 \text{ } \mu\text{mol O}_2/\text{nmol O}_2)/ 0.0125 \text{ mg chl } a/\text{mL}))$ ^{5,6}; this was interpreted as a measure of efficiency and activity of PSII-enriched particles.

The addition of certain compounds – sucrose, NaCl, MES pH buffer, electron acceptor potassium ferricyanide – is necessary for the function of the PSII-enriched particles. Some other compounds, such as redox mediators DCBQ, increase the efficiency of electron movement through the photosystem and thus increase the efficiency the OEC. Interestingly, it was found that CaCl₂ causes a significant increase in oxygen evolution of the PSII-enriched particles as well when DCBQ is not present. The actual reason for this is still being explored.

RESULTS AND DISCUSSION

The maximum activity of the OEC was previously found to be at 28°C⁶, but has since been determined to be preparation dependent with an alternate maximum being found around 38°C. This was compared in figure 4. This has been shown to be consistent with maxima for whole cell plants and algae. The addition of DCBQ has been shown in multiple species to drop the maxima to 28°C while simultaneously increasing the rate of oxygen evolution up to eight fold, as seen in figure 3. This was consistently true for *Spinacia oleracea*. This was possibly caused by DCBQ being able to decouple some process within PSII, or DCBQ has some factor of temperature dependence itself that allows it to overcome some inefficiencies of the OEC at lower temperatures⁵. A possible cause of the previously mentioned shift from non-DCBQ maxima of 28°C to 38°C has been hypothesized to be related to the strain of *Spinacia oleracea*. It is believed that, due to location of purchase and growth, the preparations that have 38°C maxima are were derived from a heat resistant strain of spinach. Specifically, 28°C maxima spinach was purchased from an organic Amish farm while the 38°C organic spinach was purchased from large-scale retailers.

Additionally, it was found that CaCl₂, in the absence of redox mediators, had a significant positive effect on the rate of oxygen evolution shown in figure 4. The reason for this increase is not fully understood, but may be possibly related to some divalent cation effect. Additionally, it was

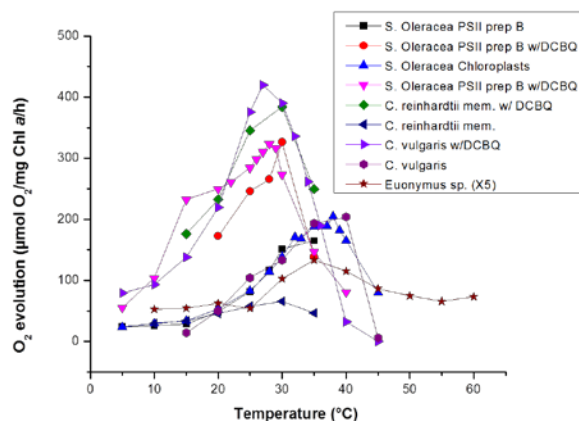


Figure 3. (above) Temperature titrations of multiple species in with and without redox mediator DCBQ

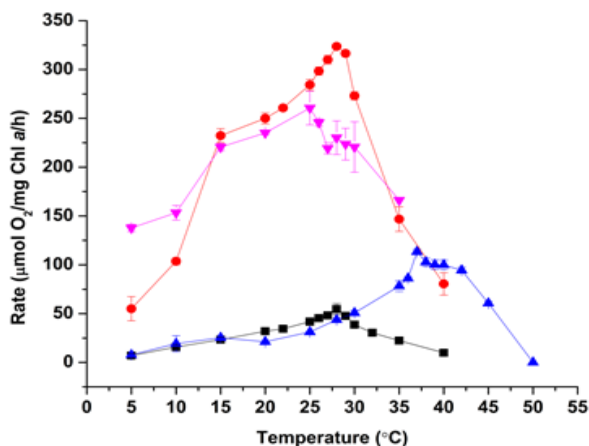


Figure 4. Temperature titrations of oxygen evolution rates with .01 mM DCBQ (red), 25 mM CaCl₂ (blue), both (purple), and neither (black) determined via oximetry

determined that the effect of a redox mediator completely or nearly completely overrides the effect of the CaCl_2 .

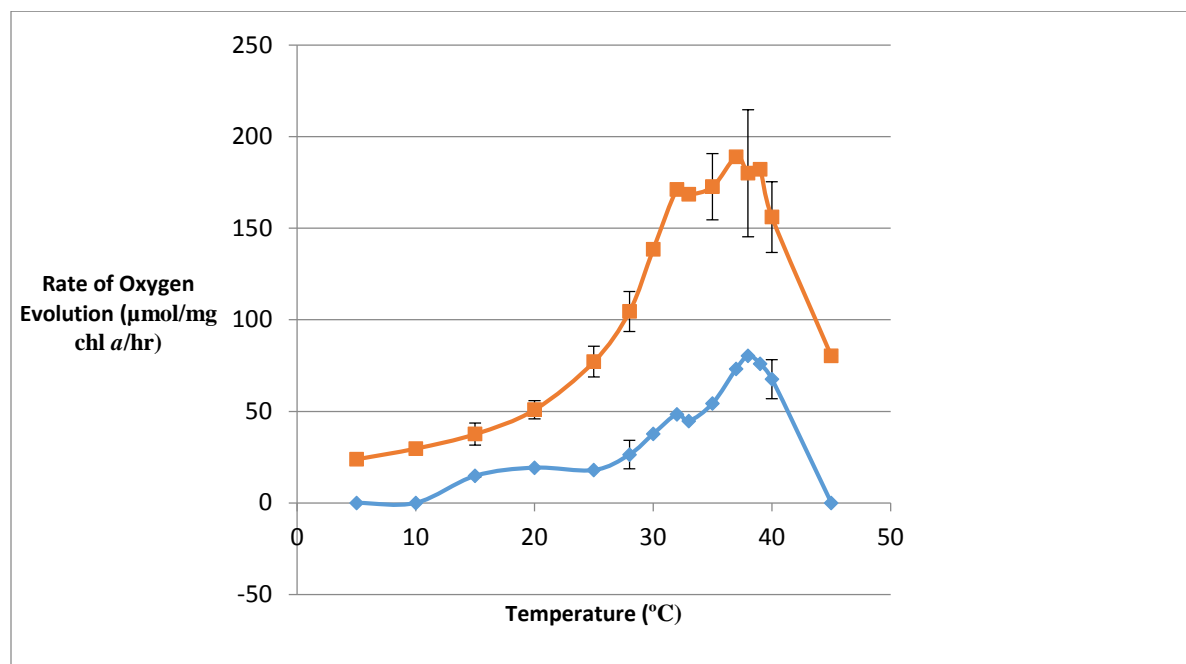


Figure 5. Temperature titration with and without CaCl_2 determined via oximetry⁵
Data points without a standard deviation have only had one trial; those with have minimally had three trials.

FUTURE WORK

The potential next steps in these experiments constitute the standardization of the spinach used in the lab. This boils down to the in-house growth of spinach from a known seed provider. This spinach will then be used in the same experiments performed previously in order to determine its temperature maxima and evaluate the consistency of previous results. Additionally, if the CaCl_2 seems to provide the same effect, the substitution of other divalent salts such as MnCl_2 would possibly confirm or deny the hypothesis that the effect is due to a divalent cation effect. Beyond that, an additional procedure known as photoassembly has a temperature dependence as well. Photoassembly is a process by which the OEC and surrounding extrinsic proteins are forcefully removed and the OEC is then rebuilt onto the PSII-enriched membranes. In doing photoassembly, the already poor efficiency of the OEC is reduced. Standard means of using DCBQ to improve the efficiency of the OEC and PSII are too strong and result in electron cycling from the OEC to itself which eliminates most water oxidation. In order to improve the efficiency, experimentation with short tailed quinones could be done with both standard PSII-enriched membranes and with photoassembled PSII.

EXPERIENCES

By performing research under a grant, I have been able to garner experience that will have value throughout the rest of my life. I have had opportunities to view both academic and industrial work in the field of chemistry and the chance to learn more about prominent instruments being used in the field today. By being funded in my research, I was able to maintain easy accessibility to my university in order to further my education in many other regards as well. It is due to these experiences that I have improved an already strong respect for working men and women in the many careers of chemistry and science, in general.

ACKNOWLEDGEMENTS

I would like to thank the NASA West Virginia Space Grant Consortium for funding my research. I would further like to thank Derrick Kolling, Ph.D. for being a helpful and instructive research advisor. Further, the Marshall Department of Chemistry furthered my opportunities through their summer research program. This program allowed me the opportunity to visit DOW chemical in South Charleston. Thus, I would further like to acknowledge DOW chemical for allowing me and others to attend their facilities and demonstrate an average day of work.

LITERATURE REFERENCES

1. Umena, Y.; Kawakami, K.; Shen, J.; Kamiya, N. Crystal structure of oxygen-evolving photosystem II at a resolution of 1.9 Å. *Nature*. May 2011, Vol. 473 Issue 7345, p55-60
2. Kolling, D.R.J., Cox, N., Ananyev, G.M., Pace, R.J., Dismukes, G.C. What Are the Oxidation States of Manganese Required To Catalyze Photosynthetic Water Oxidation? *Biophysical Journal*, 2012, 103:1-10.
3. Reece, S.Y., Hamel, J.A., Sung, K., Jarvi, T.D., Esswein, A.J., Pijpers, J.J.H., Nocera, D.G. Wireless Solar Water Splitting Using Silicon-Based Semiconductors and Earth-Abundant Catalysts. *Science*, 2011, 334:645-648.
4. Berthold, D. A., G. T. Babcock, and C. F. Yocum. 1981. A highly resolved, oxygen-evolving photosystem II preparation from spinach thylakoid membranes : EPR and electron-transport properties. *FEBS Lett.* 134:231-234.
5. Cooke, Emilee Hope. "The pH Dependence of Photosystem II Oxygen-Evolving Complex Assembly". 2014. Theses, Dissertations and Capstones. Paper 475. <http://mds.marshall.edu/etd/869/>
6. Board, James Scott II. "Toward a Comprehensive Model of Photosystem II Oxygen Evolving Complex Photoassembly". 2013. Theses, Dissertations and Capstones. Paper 475. <http://mds.marshall.edu/etd/475>
7. <http://www.hansatech-instruments.com>

ASSESSING RELIANCE AND PLANNING EXPANSIONS OF TRANSPORTATION INFRASTRUCTURE WHILE ACCOUNTING FOR FUTURE CLIMATE SCENARIOS

Elijah Meyer
Civil Engineering
West Virginia University
Morgantown, WV 26506

ABSTRACT

This research looks at the effects of future climate scenarios on the transportation infrastructure of Bangladesh. The goal of the research is to determine if future sea level rise in Bangladesh will affect the transportation infrastructure in a way that is detrimental to Bangladesh itself. This has been done by using four different flooding scenarios from the Intergovernmental Panel on Climate Change Report, 2007. These four scenarios are possible flooding scenarios caused by climate change over different periods of time. Using ESRI ArcMap, it was possible to simulate these flooding events and then estimate travel times and find how much more each flooding event increased the travel time of Bangladesh's infrastructure as a whole. The case study shows the need for further improvements of the transportation infrastructure in Bangladesh before these flooding scenarios happen in order to prevent a degradation of the system as a whole.

INTRODUCTION

The last decade has seen numerous examples of extreme climatic events affecting regions all over the world. The snowstorm in South in January 2014 caused 5000 flight cancellations and nearly 1500 accidents with costs expected to run into 100's of millions (Los Angeles Times, 2014). In the year 2013, there were seven climate related disasters costing more than 1 billion dollars in the United States with 41 totals all over the world (Kahn, 2014). The total cost of the damage of Hurricane Sandy in the United States was US \$ 65 billion (Smith and Katz, 2013). Flash floods have resulted in significant amount of deaths in areas like Bangladesh. A recent study shows that the cost of flood damage could be as high as \$1 trillion a year for coastal studies if appropriate action is not taken (Hallegatte et al., 2013).

One of the big issues in extreme flood events is that in densely populated areas like South Asia a significant section of the population can get stranded or cut off when all access infrastructures is affected. This significantly affects the ability of the population to recover from the floods as it is difficult to organize relief and recovery efforts. While developing disaster management plans, it is critical to assess the vulnerability of existing infrastructure to extreme weather events and take this into account while making investments for infrastructure planning and operations.

Bangladesh is a country in the Indian sub-continent with a population of more than 150 million. The population is expected to grow by another 100 million before stabilizing. The population density of Bangladesh is nearly five times any other country with a population of more than 100 million (Streatfield and Karar, 2008). Bangladesh experiences significant natural disasters and flooding events, the impact of which is magnified due to the high population and population

density coupled with poor infrastructure. The country experienced 68 floods between 1980 and 2010, an average of 2.19 per year. Every flood affects nearly 3.5 million people on an average and causes damages in the order of hundreds of millions of US dollars (Disaster Statistics). The focus of the case study is to study the impacts of future sea level raises from various climate change scenarios on the connectivity between major urban areas on affected infrastructure in the major counties in Bangladesh.

In order to study the impacts of flooding on the transportation system in Bangladesh, it first had to be research whether climate change would affect Bangladesh's coastal waters at all. It was determined after reading the Intergovernmental Panel on Climate Change (IPCC) Report, 2007, that there are four scenarios for coastal sea rise which were B1, A1T, A2, and A1F1 corresponding to sea level rises of 0.28m, 0.325m, 0.37m, and 0.425m respectively (IPCC, 2014). Since it was determined that these scenarios did in fact exist, the flooding in Bangladesh had to be simulated.

Using ESRI ArcMap, the four scenarios were able to be simulated. The transportation system in Bangladesh was placed into ArcMap and then turned into a network using the network analyst extension. First, ArcMap's raster calculator function was used in order to place a flooding event on the map. This function works by showing all areas of which a rise of water will effect. Once the flooding event was placed on the map, it was now possible to find all places where water would possibly flood regional, zilla, and national roads. Once these places were found, network analyst was used in order to determine the travel time from each major city in Bangladesh to every other major city.

Finally, all information was placed into tables and the percent change in travel time after flooding was found. The data could now be ordered by which cities were affected most to see determine what the overall effect on the system was. The percent change in road length was also found based off what roads were being flooded.

OBJECTIVE

The objective of this research is to develop a decision support framework: (i) to assess the vulnerability of existing transportation infrastructure to extreme flood events and (ii) identify critical infrastructure expansion/retrofitting plans which maximize the resilience of infrastructure to disruptions. This research adopts a multi-disciplinary approach as it combines methods from climate sciences, flood predictions, environmental engineering and transportation engineering so that accurate estimation of potential damage of future infrastructure disruptions from climate threats can be obtained. The methodology developed in this work will be applied to a case study in Bangladesh. However the framework developed is generalizable and applicable to all regions in the world provided sufficient data is collected.

METHODOLOGY

Ultimately there are four major tasks for this research. These four tasks can be generalized and expanded to other places of interest, not only just Bangladesh. This research will provide a framework to account for other future flooding events caused by climate change all around the world. The tasks are as follows:

Task 1: Identify if Coastal Flooding Events Exist in Bangladesh

This task involved finding real research which was already done to note that there were actual flooding events that could occur in Bangladesh. Without knowing whether or not there was research to support that future flooding could occur, there would not be a reason to do this research as future flooding scenarios would not be known. With the research done by the IPCC, we could see that future flooding events were in fact possible and that continuing the research would be useful.

Task 2: Identify Infrastructure Components Affected by Flooding

Using ESRI ArcMap, it is possible to determine what a rise in coastal waters will do to the transportation system in Bangladesh using the raster calculator function. After using the raster calculator function it will be possible to assess flooding damages to travel time by using the Network Analyst extension. The Network Analyst extension allows one to find roads which will be flooded and identify them. Once these roads are identified, the extension can be used to find new routes which are not affected by flooding. The extension will find the shortest possible route which avoids all flooding. These new found routes could range from very little change from original travel time all the way up to 10 times the original travel time.

Task 3: Evaluate connectivity and accessibility related issues associated with affected infrastructure

The performance of transportation infrastructure after a disaster is important for disaster relief. If the connectivity is affected during a disaster, entire cities and populations could be cut off from relief. In this tasks, stochastic shortest path algorithms will be used to identify the likelihood of a communities in Bangladesh being cut-off from the nearest urban center. Note that deterministic network algorithms are not applicable in this case as there is a different likelihood of infrastructure being disrupted for any different future flooding scenarios. In some cases a community may not be entirely cut-off. Depending on the flooding scenario, there can be cases were relief efforts to a community can be slowed down due to the poor state of the infrastructure post floods. The task will also characterize the accessibility of communities with respect to increase in travel times to the nearest urban center for all potential future flooding scenarios. Based on the analysis, a list of critical communities will be identified based on post disaster transportation infrastructure performance and the population of communities.

Task 4: Identify critical infrastructure segments to develop, retrofit to minimize the accessibility and connectivity related issues associated with network disruptions.

The final task of the research is to identify what infrastructure segments could use development in order to minimize connectivity and accessibility issues in the event of a major disaster. In this work we will develop a new integer programming model which allocates investment to maximize connectivity across all vulnerable communities in the network across all disaster scenarios. Note that the results of connectivity maximizing infrastructure enhancements maybe significantly different from travel time minimizing infrastructure enhancements. For example if there two routes connecting two cities, one takes an hour and the other two hours. If the objective is travel time minimization then it makes sense to add more lanes and invest in the one hour route. However, if the goal is connectivity maximization and if the one hour route is more vulnerable to floods, it would be more prudent to invest in the two hour routes. When you have number of vulnerable communities and the budget is limited, one has to optimally allocate the resources in an equitable manner.

RESULTS

Table 1 provides a list of the major urban areas in Bangladesh and their associated population. Dhaka is the most populated urban area with a population of more than 12 million. The average population in the 64 major centers identified was 2.5 million. Table 2 provides the total road lengths by classification in the seven major divisions of Bangladesh. Chittagong division has the largest zilla roads, Dhaka has the highest national roads, and Khulna district has the highest regional roads among the seven major divisions of Bangladesh.

TABLE 1: Major Urban Areas and Population (Source: <http://www.geohive.com/cntry/bangladesh.aspx>, Bangladesh population 2011)

URBAN AREAS	POPULATION	URBAN AREAS	POPULATION
Dhaka	12,043,977	Maulvibazar	1,919,062
Chittagong	7,616,352	Faridpur	1,912,969
Comilla	5,387,288	Nilphamari	1,834,231
Mymensingh	5,110,272	Bhola	1,776,795
Tangail	3,605,083	Jhenaidah	1,771,304
Sylhet	3,434,188	Lakshmipur	1,729,188
Gazipur	3,403,912	Natore	1,706,673
Bogra	3,400,874	Nawabganj	1,647,521
Noakhali	3,108,083	Patuakhali	1,535,854
Sirajganj	3,097,489	Bagerhat	1,476,090
Dinajpur	2,990,128	Munshiganj	1,445,660
Narayanganj	2,948,217	Feni	1,437,371
Kishoreganj	2,911,907	Manikganj	1,392,867
Rangpur	2,881,086	Thakurgaon	1,390,042
Brahmanbaria	2,840,498	Sherpur	1,358,325
Jessore	2,764,547	Lalmonirhat	1,256,099
Naogaon	2,600,157	Gopalganj	1,172,415
Rajshahi	2,595,197	Madaripur	1,165,952
Pabna	2,523,179	Shariatpur	1,155,824

Sunamganj	2,467,968	Chuadanga	1,129,015
Chandpur	2,416,018	Pirojpur	1,113,257
Gaibandha	2,379,255	Rajbari	1,049,778
Barisal	2,324,310	Panchagarh	987,644
Khulna	2,318,527	Magura	918,419
Jamalpur	2,292,674	Joypurhat	913,768
Cox's Bazar	2,289,990	Barguna	892,781
Netrakona	2,229,642	Narail	721,668
Narsingdi	2,224,944	Jhalokati	682,669
Habiganj	2,089,001	Meherpur	655,392
Kurigram	2,069,073	Khagrachhari	613,917
Satkhira	1,985,959	Rangamati	595,979
Kushtia	1,946,838	Bandarban	388,335

TABLE 2: Road Lengths in Bangladesh (Source:

<http://www.humanitarianresponse.info/operations/bangladesh/dataset/bangladesh-roads-0>)

Division	Zilla Road Length (m)	National Road Length (m)	Regional Road Length (m)
Barisal	772790	84046	101463
Chittagong	2561115	639425	225897
Dhaka	1937975	691485	345701
Khulna	1288690	333412	347322
Rajshahi	1238678	379992	300091
Rangpur	874325	434058	148314
Sylhet	839170	257014	79015

We simulated flooding resulting from four sea level rise scenarios from the Intergovernmental Panel on Climate Change Report, 2007. The four scenarios considered were B1, A1T, A2, and A1F1 corresponding to sea level rises of 0.28m, 0.325m, 0.37m, and 0.425m respectively (IPCC, 2014). The four scenarios were chosen as they corresponded to four distinct levels of sea level rise. First, we estimated the percentage of usable roadway infrastructure in each of the seven divisions belonging to the three roadway classes for each climate change flooding scenario.

TABLE 3: Percentage usable roadway segments

	Scenario B1				Scenario A1T		
	National	Regional	Zilla		National	Regional	Zilla
Barisal	98.32%	100.00%	100.00%	Barisal	98.31%	100.00%	99.67%
Chittagong	98.86%	99.64%	100.00%	Chittagong	98.79%	99.60%	99.87%
Dhaka	99.89%	99.82%	100.00%	Dhaka	99.89%	99.79%	99.80%
Khulna	99.98%	99.99%	100.00%	Khulna	99.95%	99.97%	99.36%
	Scenario A2				Scenario A1F1		
Barisal	98.31%	100.00%	99.67%	Barisal	98.31%	100.00%	99.67%
Chittagong	98.77%	99.56%	99.86%	Chittagong	98.77%	99.56%	99.86%
Dhaka	99.88%	99.79%	99.80%	Dhaka	99.88%	99.79%	99.80%
Khulna	99.95%	99.97%	99.36%	Khulna	99.95%	99.97%	99.36%

Table 3 shows the percentage usable roadway segments in all four climate change scenarios. Four of the seven divisions were affected by sea level rise. The roadway segments in the remaining three divisions are not affected and thus not shown in the table. In general, the national roadway segments were affected more than the local roads, which is a cause for concern. On the whole the percentage of usable roadway segments appears to be high. However in terms of roadway infrastructure, more than the length affected, significant loss of connectivity and accessibility can occur if critical roadway segments are affected. It is well known that transportation connectivity and accessibility has significant impact on market productivity and local economy (Wesibrod and Beckwith, 1991; Economic Development Research Group, 2011; Kalliski et al., 1999). The rest of the case study focuses on impact on climate change on travel times and connectivity between the major urban areas in Bangladesh. The travel times and distances between cities before and after flooding were estimated using the ArcGIS Network Analysis and map algebra tools.

The following metrics were calculated for each city:

$$TT^i = \sum_{j=1, j \neq i}^{64} \frac{(TT_{FLOOD}^{ij} - TT_{ORIG}^{ij})}{TT_{ORIG}^{ij}}$$

Where TT^i is the travel time index for urban area i

TT_{FLOOD}^{ij} is the travel time between urban areas i and j under flooded scenario

TT_{ORIG}^{ij} is the travel time between urban areas i and j under current scenario

The travel time index provides an estimate of how disconnected an urban area becomes in the event of flooding. The higher the value of the travel time index, the higher the chance of that urban area becoming isolated in the event of the flooding. This has significant implications for trade, commerce, and providing relief supplies. One major deficiency with this method is that it does not account for the importance of the origin and destination urban areas. To account for this issue we have developed a new metric

$$CP^i = \sum_{j=1, j \neq i}^{64} \frac{(C_{FLOOD}^{ij} - C_{ORIG}^{ij})}{C_{ORIG}^{ij}}$$

$$C_{FLOOD}^{ij} = P^i * P^j * f(TT_{FLOOD}^{ij})$$

$$C_{ORIG}^{ij} = P^i * P^j * f(TT_{ORIG}^{ij})$$

$$f(TT_{FLOOD}^{ij}) = \frac{1}{TT_{FLOOD}^{ij}}$$

$$f(TT_{ORIG}^{ij}) = \frac{1}{TT_{ORIG}^{ij}}$$

Where CP^i is the connectivity parameter for urban area i

C_{FLOOD}^{ij} is the connectivity between zone i and zone j under flood

C_{ORIG}^{ij} is the connectivity between zone i and zone j under current conditions

P^i is the population in zone i

P^j is the population in zone j

$f(TT_{FLOOD}^{ij})$ is the friction factor which is assumed to be inverse of the travel time.

The connectivity between two urban areas is assumed to be directly proportional to the population of the two urban areas and inversely proportional to the distance between them. This assumption is consistent with the Gravity Model which is a common assumption in transportation planning models (Garber and Hoel, 2014). Note that ideally we would use the future population. However since we do not have access to the estimated population growth in each urban area and the goal here is to find a metric which accounts for the “importance” of each urban area, we used the current population as the weight. In addition to calculating the travel time index and connectivity index for each city, we also identified the top 10 origin destination pairs in terms of travel time and connectivity indexes (TT^{ij} and CP^{ij}). This will give an idea of critical urban corridors where money should be invested in the future for climate proofing the infrastructure.

$$TT^{ij} = \frac{(TT_{FLOOD}^{ij} - TT_{ORIG}^{ij})}{TT_{ORIG}^{ij}}$$

$$CP^{ij} = \frac{(C_{FLOOD}^{ij} - C_{ORIG}^{ij})}{C_{ORIG}^{ij}}$$

The metrics presented above focused on travel times and connectivity between urban centers.

TABLE 4: Top five affected urban areas

	B1		A1T		A2		A1F1	
	Travel Time Index	Connectivity Parameter						
Patuakhali	8.28	-6.91	10.31	-8.31	14.11	-10.47	14.14	-10.49
Barisal	0.60	-0.37	0.98	-0.63	1.63	-0.85	3.15	-2.69
Jhalokati	0.50	-0.33	0.83	-0.60	1.18	-0.83	6.32	-4.52
Madaripur	0.34	-0.25	0.59	-0.45	0.97	-0.67	1.39	-0.94
Shariatpur	0.29	-0.23	0.52	-0.41	0.84	-0.58	1.17	-0.85

Table 4 shows the top 5 affected areas in terms of the travel time index and the connectivity parameters across all four climate change scenarios. We found that the results due to travel time indexes were perfectly correlated with the results due to connectivity parameter. Patuakhali is the most affected urban area in Bangladesh with the highest chance of getting disconnected due to future sea level rises. Note that the travel time increase from Patuakhali to other urban areas ranges from 828% in scenario B1 to 1414 % under scenario A1F1. This is a significant increase and efforts must be made to retrofit the roadway segments leading out of Patuakhali or build alternate roadways or modes of transportation at higher elevation as nearly 1.5 million people reside in that area. Cox’s Bazaar and Chittagong are not significantly affected under scenario B1. However when the sea level rise is more than 0.325(scenario A1T and higher) they are significantly affected with travel time increases of nearly 500% and 300% respectively.

Table 5: Top five affected corridors (Origin Destination Pairs)

From-To	Travel Time Index	Connectivity Parameter	From-To	Travel Time Index	Connectivity Parameter
Scenario B1			Scenario A1T		
Patukhali-Barisal	0.597	-0.374	Barisal-Patukhali	0.751	-0.429

Patukhali-Jhalokati	0.499	-0.333	Jhalokati-Patukhali	0.642	-0.391
Patukhali-Pirojpur	0.339	-0.253	Patukhali-Madaripur	0.428	-0.300
Patukhali-Madaripur	0.339	-0.253	Patukhali-Pirojpur	0.385	-0.278
Patukhali-Gopalganj	0.301	-0.231	Patukhali-Gopalganj	0.380	-0.276
Scenario A2			Scenario A1F1		
Barisal-Patukhali	0.751	-0.429	Jhalokhati-Barisal	1.485	-0.598
Jhalokati-Patukhali	0.642	-0.391	Patukhali-Barisal	1.289	-0.563
Patukhali-Madaripur	0.428	-0.300	Patukhali-Jhalokati	0.996	-0.499
Patukhali-Pirojpur	0.385	-0.278	Patukhali-Madaripur	0.738	-0.425
Patukhali-Gopalganj	0.380	-0.276	Dhaka-Narayanganj	0.672	-0.402

Table 5 shows the top 5 affected origin destination pairs. As expected the major affected corridors is between the top 5 affected urban areas identified in table 5. The Patuakhali-Barisal corridor is the worst affected with travel time increases ranging from nearly 60% to 1289 %. If budget is a significant constraint, then the focus of the roadway investments must be on developing a better corridor between Patuakhali and Barisal. One of the surprising aspects of this analysis is that Dhaka does not feature in the top 10 affected urban areas. One potential reason for this is the strategic central location of the capital city with good existing connectivity to all other major urban areas. The main insight from this case study is that while the percentage of roadway segments affected by future sea level rise based flooding scenarios is low, it can have significant impacts on connectivity and thus economic productivity of a region. Thus while making investments to climate proof future infrastructures it is critical to make strategic investments which improve connectivity rather than just focusing on volume of affected infrastructure.

CONCLUSION

It has been found that there is need for improvements of the transportation system. From the results, one can see that the coastal flooding most definitely had an effect on the transportation system as a whole. Some cities had an overall travel time increase of upwards of 10 times longer travel times. These longer travel times would cause devastating issues with regards to economics and overall traffic flow as whole. As most places use their interstates for interstate commerce, this effect on travel time would make it more difficult to deliver goods throughout Bangladesh from one city to another.

The percentage of roadways affected by the flooding is very low, but the actual travel times have increased by a significant amount. This shows that just a little flooding in the coastal regions could easily hurt travel time exponentially. The most affected cities were Patuakhali and Barisal and thus, the roadway between these two cities is the most affected overall.

Transportation updates must be made in order to curve the devastating effects of these floods or the entire economy could collapse as a whole in Bangladesh because it would be nearly impossible to get goods between major cities in a reasonable time period.

There is possibility for improvements of these roads. The roads could be made to be more elevated in order to put them above the flooding. There could also be some alternate routes made in order to stop the effects of the flooding on travel time. Since flooding causes travelers to completely go out of their way to get from one city to another, these alternate routes could be made to avoid the flooding and decrease travel time as whole. Bangladesh also relies on rail transportation to transport goods, and since most of these railways have depots in major cities, these railways would also be affected. With the railways affected along with the major interstate roads, one can see how bad of a situation there is if the climate change scenarios actually take place.

ACKNOWLEDGEMENTS

This research paper was made possible by many people and organizations. Below I would like to acknowledge those who made this paper possible:

First and foremost, the grant from the NASA West Virginia Space Grant Consortium is what made this research possible. Without the stipend, I would have been unable to complete this project as finances would not have allowed for that.

Second, I would like to thank my mentor, Dr. Avinash Unnikrishnan. Through his guidance, the project was given direction. His advice also helped to keep the project on track and made for an overall more quality project.

Finally, I would like to thank Dr. Antarpreet Jutla. His knowledge in ArcMap helped make this project possible as I had no previous experience with this program.

REFERENCES

P. K. Streatfield , Z. A. Karar, Population Challenges for Bangladesh in the coming decades, Journal of Health, Population, and Nutrition, Volume 26 (3), 261 – 272, 2008. Disaster Statistics, Available at: <http://www.preventionweb.net/english/countries/statistics/?cid=14>, Last Accessed February 2014.

Intergovernmental Panel on Climate Change (IPCC), Projected Climate Change and its Impacts, Available at: http://www.ipcc.ch/publications_and_data/ar4/syr/en/spms3.html#table-spm-1, Last Accessed February 2014.

N. J. Garber, L. A. Hoel, Traffic and Highway Engineering, Cengage Learning, 2014.

Economic Development Research Group. Interactions between Transportation Capacity, 30 Economic Systems, and Land Use: Final Report. Strategic Highway Research Program, 31 Project C03, National Academies Press, 2011.

G. Weisbrod, J. Beckwith. Measuring Economic Development Benefits for Highway

Decision-making: The Wisconsin Case. Transportation Research Record 1262. 1991.

J. Kaliski, S. Smith, G. Weisbrod. Major Corridor Investment - Benefit Analysis System. Proceedings of the 7th TRB Conference on Application of Transportation Planning Methods, 1999.

Hallegatte, S., Green, C., Nichols, R. J., and J. Corfee-Morlot (2013). Future flood losses in major coastal cities, Nature Climate Change, Volume 3, 802- 806.

Kahn, B., (2014). Record number of billion dollar disasters globally in 2013, Available at: <http://www.climatecentral.org/news/globe-saw-a-record-number-of-billion-dollar-disasters-in-2013-17037>

Los Angeles Times (2014), Across snow-struck Atlanta it's a case of Dude, where's my car?, Available at: <http://articles.latimes.com/2014/jan/30/nation/la-na-nn-atlanta-storm-traffic-abandoned-cars-20140130>

Smith, A., and R. Katz (2013). U.S. Billion-dollar Weather and Climate Disasters: Data Sources, Trends, Accuracy and Biases. Natural Hazards, Volume 67, 387- 410.

THE EFFECTS OF SOCCER BALL HEADING ON SCENT PERCEPTION: SEVERITY OF EFFECTS IN ADOLESCENCE DURING HIGH SCHOOL COMPETITION

Emily Robinson
Psychology
Wheeling Jesuit University
Wheeling, WV 26003

ABSTRACT

Past research shows that soccer ball heading has detrimental effects on memory, reaction time and impulse control, as well as scent identification ability and olfactory functioning. The current study examined the effects of heading frequency and intensity on scent identification of high school soccer players. Researchers predicted that the total correct scent identifications would be lower for those players who head the soccer ball with high frequency and intensity. Seventy high school soccer players (30 men and 40 women) completed a brief survey about their soccer-playing history. They were then asked to complete the Brief Smell Identification Test (BSIT). An independent samples t-test showed females correctly identified more scents than males. Two groups were formed from the data collected from the survey: a high and low group based on the number of times a ball was headed and high and low group based on the intensity with which the ball was headed. A two between ANOVA was completed on both the frequency group and the intensity group. Results showed that those who headed the ball more frequently had significantly fewer correct scent identifications. Also, those who headed the ball with greater intensity had significantly fewer correct scent identifications. A two between ANOVA was performed on these two groups and focused on males only, which resulted in males with higher heading intensity and higher heading frequency performing significantly worse in scent identification than females. A positive correlation was also found in males between age and heading the ball more frequently. Soccer players should consider this research in order to educate and prevent future damage to the nasal cavity.

INTRODUCTION

Previous research has found a relationship between “heading” a soccer ball and physiological functions. For instance, Fields (1989) found that incorrect “head-to-ball” contact had been the cause for many head injuries. With existing relationships between soccer ball heading and physical damages, it is possible to find other areas where physical functioning is weakened.

Webbe and Ochs (2003) increased evidence to support that soccer ball heading frequency caused some temporary cognitive impairment. Male soccer players completed several tests to determine cognitive ability, such as the Facial Recognition test and the California Verbal Learning Test. Players gave self-reports of their heading estimates. Those players with high heading frequencies and having experienced heading in the past seven days had significantly lower scores on the California Verbal Learning Test.

Capiola, Raudenbush and Dennis (2009) conducted a study in which they examined memory, reaction time, and impulse control as affected by soccer ball heading. College level soccer players completed soccer ball heading questionnaires and had their cognition measured with a neuro-cognitive computer-based assessment both pre and post seasons. Results showed that those participants with high soccer ball heading intensities had significantly lower levels of verbal memory, as well as higher levels of reaction times and impulse control.

Regarding soccer, Rutherford and Stephens (2007) determined that many injuries are considered to be head injuries and there is a significant amount of them that cause brain trauma. Heading is suggested to be the cause for this head trauma. "Angular head acceleration" is found to give the highest risk of head injury. Assessment of these soccer related head injuries extends from concussions to talk of dementia and amyotrophic lateral sclerosis. This study did evaluate heading as evidence for neuropsychological impairment; however, it was concluded that there is still no reliable evidence to definitively conclude this as a cause.

Kirdendall and Garrett (2001) reviewed publications regarding head injuries, specifically soccer ball heading, and the effects it has on cognitive dysfunction. The results of this questioned the exact cause for cognitive dysfunction in soccer players. Although, the study did conclude that concussions are a cause and often result from soccer related head injuries.

Past studies have also found a significant correlation between head trauma and olfactory dysfunction where there may even be potential for anosmia to develop (Haxel, Grant, & Mackay-Sim, 2008). In this study, patients with head trauma of different severities were given surveys by telephone and then screened for olfactory functions by way of the Brief Smell Identification Test. Those participants found to have olfactory dysfunction were then assessed using Sniffin' Sticks and olfactory-evoked potential recording. Some participants reported a weakened sense of smell after their injury. However, incidence of olfactory dysfunction after head trauma was found in more participants than the amount who actually reported that weakened sense of smell. The study also concluded that the site of trauma is more important than simply the probability of a decrease in olfactory functioning. The contact between a soccer ball and the head may then be considered as head trauma in terms of causing olfactory dysfunction.

Raudenbush and Capiola (2010) had soccer athletes complete soccer-heading surveys and have their olfactory functioning measured with a variety of scent identification tests. Heading intensity and frequency were found amongst those causes that were accountable for 75% of the weakened olfactory functioning and decreased scent identification ability. Overall, the study concluded that the greater the soccer ball heading frequency and intensity, the lower in ability to identify scents. From that research, the question could be posed as to why soccer ball heading causes a decrease in olfactory functioning and scent identification?

Cognitive abilities decreased from damage caused by head to soccer ball contact, so it is believed that olfactory functions may be decreased as a result of damage to receptors or nerves in the olfactory epithelium from soccer ball heading. Also, it is shown that with more head trauma, these damages are greater. Soccer ball heading is considered to be head trauma, so one could expect to see more damage with higher frequencies and intensities of soccer ball heading. To assess this possibility Custer, Moore, Robinson, Schlegel and Raudenbush (2014) examined the effects of heading frequency and intensity on nasal capacity. Undergraduate soccer players completed a

brief survey about their soccer-playing history and underwent inhalation and exhalation assessment. Results indicated that those athletes who headed the ball with greater frequency or intensity had significantly lower inhalation and exhalation performance than those athletes who headed the ball with lower frequency or intensity. Such performance is typically indicative of damage within the nasal airway.

Given the decreases noted above in scent identification ability, cognitive performance, and nasal structural damage, more research needs to be conducted to determine when these decreases begin. One possibility is the damage could begin during the high school years of soccer players. Thus, high school freshman scent identification ability should be normal and then should decrease as the players get older. Determining if this is true is an important next step in being able to educate soccer players about the potential dangers of frequent or intense heading. The present study will assess scent identification ability in high school soccer players. Participants will consist of soccer athletes who are both starting to play soccer as well as those who have been playing for several years. If the damage begins in high school adolescence, results should show that the greater the number of years of their team play, the worse their scent identification ability (while controlling for other factors, such as initial frequency of ball heading, intensity of ball heading, dizziness during play, and past concussions). If the damage does not begin in high school adolescence, results should show no relationship between number of years since team play and scent identification ability.

METHOD

Participants

Seventy high school soccer players (30 men and 40 women; mean age 15.84, std. 1.27, age range 13 to 19) from local high schools took part in the study. Participants came from both the men's and women's soccer teams. They were recruited by explaining the study to them prior to their practice. During these brief meetings, the soccer players were told the study would take place at the next practice. Participation required approximately 15 minutes, and all participants were treated in accordance with APA ethical standards.

Materials

After agreeing to participate, players were given the consent form to sign. Consent forms required a signature from a parent/guardian if the participant was a minor (See Appendix A). The forms were handed out during the meeting and returned with signatures at the next practice, where they were then collected and kept separate from the surveys and data sheets. Next, participants were given a brief survey asking them their age, sex, and about some of their soccer playing history (See Appendix B). The following five questions were asked in the survey: "For how many years have you played high school-level soccer?", "In the past soccer season, in a typical soccer game, how many times did you 'head' the ball?", "On a scale from 0 to 10, what is the average force intensity with which you typically 'head' the ball? A larger number indicates greater 'heading' force intensity", "In the past soccer season, how many times have you become dizzy or disoriented after you 'head' the ball?" "How many times have you been diagnosed with a concussion?" After completing the survey, participants were asked to fill out the Brief Smell Identification Test (BSIT). The BSIT is a rapid and effective 12 item-screening test for detecting smell loss. The test employs: banana, chocolate, cinnamon, gasoline, lemon, onion, paint thinner, pineapple, rose,

soap, smoke and turpentine, with the scents being presented via “scratch and sniff.” It is currently the only FDA-cleared “smell test” on the market.

Procedure

Participants were tested individually in a classroom. They were given a consent form to sign, and for their parent/guardian to sign if a minor, in order to agree to take part in the study. Next, participants filled out a survey that asked them about their soccer playing history. After completing the survey, the participants filled out the Brief Smell Identification Test (BSIT). The BSIT is a rapid and effective 12 item-screening test for detecting smell loss. The participants completed the study after finishing the BSIT. The researchers kept this with the participants’ surveys.

RESULTS

To assess sex differences, data were analyzed with an independent t-test on total correct scent identifications. Females correctly identified significantly more scents than males $t(68)=-2.098$, $p=0.04$. A correlation was then conducted on males’ intensity on heading versus males’ total correct scent identifications and a trend was found with $p=0.091$ and $r=0.314$. Data was then sorted into a low and high group for the number of times the ball was headed and into a low and high group for the intensity with which the ball was headed, low intensity being 0-5 and high intensity being 6-10. A two between ANOVA was performed on the number of times the ball was headed. Significance was found for frequency, $F(1,66)=10.501$, $p=0.002$. Also, significance was found for sex, $F(1,66)=10.396$, $p=0.002$. Those who headed the ball more frequently had significantly lower total correct scent identifications. Also, males who head the ball more intensely had significantly lower total correct scent identifications.

A two between ANOVA was conducted on the intensity with which participants headed the ball. Results were significant for intensity, $F(1,66)=4.336$, $p=0.041$. Significance was also found for sex, $F(1,66)=6.412$, $p=0.014$. Participants who headed the ball with more intensity had significantly lower total correct scent identifications. Also, males who headed the ball with more intensity had significantly lower total correct scent identifications than females.

A correlation was conducted on the total correct scent identifications and questions from the questionnaire. Significance was found for age of males and how many times they head the ball per game with $p=0.042$ and $r=0.373$. Also, a trend was found for age of males and how intensely they head the ball with $p=0.100$ and $r=0.306$. This means, as males grow older they are also heading the ball more frequently.

DISCUSSION

The present study found females were able to correctly identify more scents than men. Also, the study found soccer players with higher heading frequency had significantly lower correct scent identifications. Through isolating males, results showed males with higher heading frequency also had significantly lower correct scent identifications. The soccer players with higher heading intensity had significantly lower correct scent identifications. When focusing on males, results showed males with higher heading intensity also had significantly lower correct scent identifications. A correlation also showed that as males grow older they are heading the ball more

frequently. This means soccer players with higher heading frequency and intensity are unable to identify scents as well as other soccer players with low heading frequency and intensity.

These results could have occurred because heading a soccer ball has been found to decrease olfactory functioning of soccer players. This inhibits soccer players' ability to identify scent types, which was previously found in college soccer players (Raudenbush and Capiola, 2010). The results may have also occurred because soccer players are encouraged to head the ball as part of the game, so they head the ball frequently and with high intensity. This action of heading the soccer ball has been found to effect regions of the brain in the past that deal with sense of smell, verbal memory, reaction time, and impulse control (Capiola, Raudenbush and Dennis, 2009). A high frequency or intensity of heading the soccer ball could reduce a player's ability to identify scents from the constant contact on a player's head.

The present study provides vital information for current high school soccer players. The results show that heading a soccer ball could have detrimental effects on soccer players' sense of smell. According to this research, high school male soccer players appear to be the most susceptible to this damage. The current research demonstrates that harmful effects to olfactory functioning are capable of beginning at young ages, such as adolescence. This expands on the past research that found similar results on college soccer players.

Limitations may have been a small sample size, with only seventy participants. The local high schools studied did not have many soccer players available to participate in the study. Due to this, the results might not represent the majority of high school soccer players. Another limitation may have been that the participants filled out a self-report questionnaire on the frequency and intensity that they headed the soccer ball. The soccer players may not remember the exact amount they head the soccer ball, so the study did not measure their actual behavior, but instead their recall.

This study could lead to more significant findings in the future. One study that could be performed would be to determine if heading the soccer ball has permanent effects. For example, once the soccer players have completed playing organized soccer forever, a study could assess their scent identification increases. Future research should also identify specific areas of the brain that are affected by heading the soccer ball. This study encourages soccer players to wear protective headwear while playing soccer to decrease the chance of decreasing olfactory functioning from frequent heading and intense heading of the soccer ball.

ACKNOWLEDGEMENTS

Thank you for the grant by the NASA WV Space Grant Consortium as well as my mentor Dr. Raudenbush. This research was made possible through your support.

REFERENCES

Capiola, A., Raudenbush, B., & Dennis, D. (2009). *Effects of soccer ball heading intensity on memory, reaction time and impulse control*. Presented at the Eastern Psychological Association Conference, Boston, MA.

Custer, Moore, Robinson, Schlegel and Raudenbush (2014) *The Effects of Soccer Ball Heading Frequency and Intensity on Nasal Inspiratory and Expiratory Function as Measured by*

Rhinological Patency. Presented at the Eastern Psychological Association Conference, Boston, MA.

Fields, K. B. (1989). Head Injuries in Soccer. Physician And Sportsmedicine, 17(1), 69,72-73.

Haxel, B. R., Grant, L. & Mackay-Sim, A. (2008). Olfactory dysfunction after head injury. The Journal of Head Trauma Rehabilitation, 23, 407-413.

Kirdendall, D. T. & Garrett, W. E. (2001). Heading in soccer: Integral skill or grounds for cognitive dysfunction? Journal of Athletic Training, 36, 328-333.

Raudenbush, B., & Capiola, A. (2010). *Effects of soccer ball heading on scent identification and olfactory functioning*. Presented at the Eastern Psychological Association Conference, New York, NY.

Rutherford, A. & Stephens, R. (2007). Does football heading impair cognitive function? Source: Cognitive disorders research trends. Sentowski, H. C. (Ed.); pp. 7-50. Hauppauge, NY, US: Nova Science Publishers

Webbe, F. M. & Ochs, S. R. (2003). Recency and frequency of soccer heading interact to decrease neurocognitive performance. Applied Neuropsychology, 10, 31-41

FIGURE CAPTIONS

Figure 1: A figure representing the total correct scent identifications for males and females.

Figure 2: A figure representing the total correct scent identifications of high frequency and low frequency heading groups for males and females.

Figure 3: A figure representing the total correct scent identifications of high intensity and low intensity heading groups for males and females.

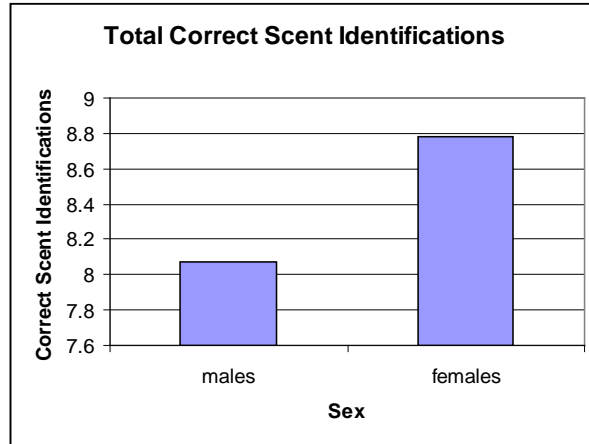


FIGURE 1

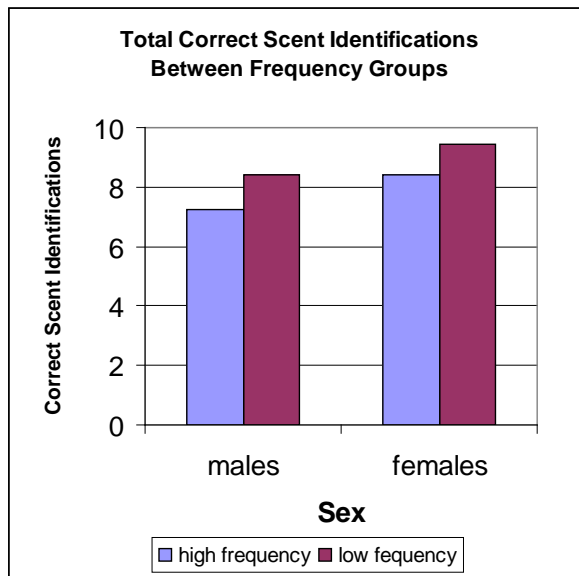


FIGURE 2

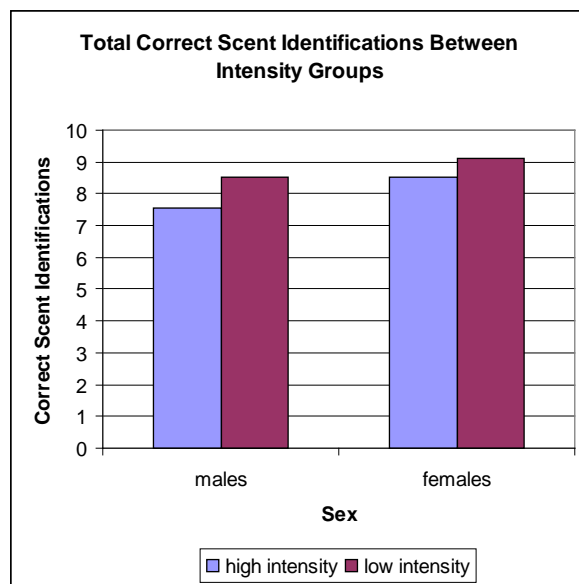


FIGURE 3

**APPENDIX A:
CONSENT FORM**

Soccer Study Consent Form

You are about to participate in a study that will examine your olfactory functioning. You will be asked to complete a brief survey and fill out a scratch and sniff booklet. You may not personally benefit from this study; however, your data will be combined with the data from other participants to better understand effects of soccer heading on olfactory functioning. This study will take approximately 30 minutes to complete. There are no known risks from participating in this study.

You will be asked to complete a short demographics sheet, but your responses will be anonymous and confidential. You will not put your name or any identifying information on the survey of the demographics sheet. Your responses will be coded with a number. The only place your name will appear is on this consent form. There is no way to connect your consent form to your data sheet because they will be kept in separate folders. All of our data and consent forms will be kept in a binder and stored in our secure laboratory.

If you have any questions about the nature of this study, please ask the experimenter. Your participation in this study is voluntary, and you may withdraw your consent and discontinue the study at anytime.

This research is being conducted by a member of Dr. Raudenbush's physiological psychology course. The project has been approved by the Institution Review Board. If you have any questions about the project now or in the future, you may contact Dr. Raudenbush at (304)-243-2330 or Alison Kreger, Chair of the Institutional Review Board at (304)-243-7201 x103.

I, _____, state that I volunteer to participate in this research project. I understand the purpose of the research, and I have had any questions answered by the researchers. Further, I understand that I do not have to complete the study, and that I can stop at anytime, without penalty. I know that my results are completely anonymous and confidential.

Signature of Participant

Date

Signature of Parent/Guardian if under 18

Date

**APPENDIX B:
SOCCER PLAYER SURVEY**

FOR HOW MANY YEARS HAVE YOU PLAYED HIGH SCHOOL-LEVEL SOCCER?

IN THE PAST SOCCER SEASON, IN A TYPICAL SOCCER GAME, HOW MANY TIMES DID YOU “HEAD” THE BALL?

ON A SCALE FROM 0 TO 10, WHAT IS THE AVERAGE FORCE INTENSITY WITH WHICH YOU TYPICALLY “HEAD” THE BALL? A LARGER NUMBER INDICATES GREATER “HEADING” FORCE INTENSITY

IN THE PAST SOCCER SEASON, HOW MANY TIMES HAVE YOU BECOME DIZZY OR DISORIENTED AFTER YOU “HEAD” THE BALL?

HOW MANY TIMES HAVE YOU BEEN DIAGNOSED WITH A CONCUSSION?

COMBINED METHODS FOR OBJECT RECOGNITION

Jared Strader
Mechanical Engineering
West Virginia University
Morgantown, West Virginia 26505

ABSTRACT

In this study, popular methods for object recognition were investigated for simple objects in partially unknown environments. By combining methods such as feature matching, image segmentation, texture analysis, and machine learning, an algorithm is developed for recognizing objects quickly and efficiently. The algorithms are developed in C++ using Robot Operating System (ROS) and OpenCV without a graphics processing unit using only the 1.8 GHz dual core Intel Atom processor on the Advantech PCM-9389. The report overviews the investigated methods, and the considerations for implementation with limited processing speed. The methods developed were proven to work during the 2014 NASA Centennial Sample Return Challenge by recognizing the desired object leading to the completion of the level one challenge.

INTRODUCTION

Object recognition is a necessary technology for intelligent vision applications such as surveillance systems, machine vision, localization and mapping, manipulation, or autonomous navigation. Due to the advances in machine learning and feature extraction techniques, object classification and recognition algorithms have progressed significantly in recent years. Despite the advancements in object recognition techniques, considerable progress is still required before having robots or vehicles reliably interacting with unknown or uncertain environments without human intervention. The purpose of object recognition is to locate a known object in an image or video. Humans recognize a multitude of objects in images with little effort. Despite the fact that the image of the object may vary in size, rotation, or viewpoint, humans can effortlessly recognize objects even when they are partially obstructed from view. Although the task of recognizing objects is trivial for humans, the task is surprisingly difficult for computer vision systems. In recent years, the topic of computer vision and object recognition has received considerable attention. Many approaches have been developed over multiple decades. Each approach attempts to find a solution for central issues common to object recognition problems such as object representation, feature extraction, feature-model matching, hypothesis formation, and object verification. Each issue presents a unique problem, and approaches attempt to solve these problems accurately and efficiently. As in any robotic application, computational power is limited and algorithmic efficiency is vital.

My research aimed to develop robust methods for object recognition in partially unknown environments. During the study, many different methods were analyzed and implemented to find a solution with adequate efficiency and accuracy. The first section describes the details of the objects and environment considered for the study. The various methods investigated will be described in detail in the second section, as well as the advantages and disadvantages of each technique. The third section investigates choosing an object, which is easily recognizable at a large

distance, and the final section includes the results and details of the final algorithms developed from the study.

BACKGROUND

Computer vision is essential for developing fully autonomous systems that are capable of interacting in dynamic or unknown environments. Computer vision is can be an extremely rich source of information if implemented properly. Current methods are far from matching the capabilities of humans, and although many object recognition algorithms exist, they are often require substantial tuning or modification to achieve adequate robustness, especially in unknown or dynamic environments. In the process of developing an algorithm for robust object recognition, many different existing algorithms were investigated, modified, and combined to obtain an efficient and robust technique. Although the focus of the project is object recognition, image segmentation is an important component of and effective object recognition algorithm and will be discussed in the following sections. The most popular categories of techniques for object recognition include machine learning and feature matching.

Feature Matching

The most popular or common methods for object recognition are feature-based methods such as Scale-Invariant Feature Transform (SIFT) and Speeded Up Robust Features (SURF). Additional feature based methods include Binary Robust Independent Elementary Features (BRIEF), oriented BRIEF (ORB), and Features from Accelerated Segment Test (FAST). Cascade classifiers are also popular feature based methods that achieve faster performance than SIFT and SURF. Cascade classifiers are most commonly used for face recognition. In general, feature based methods are more computationally demanding than appearance based methods, but this is not necessarily true for every case. Although some feature based methods are scale and rotation invariant, feature based methods perform poorly when the three dimensional pose of the object is unknown. This could lead to false positive or false negative. Feature matching using SURF, SIFT, BRIEF, and ORB were tested for this project. An example of a true positive is given in Figure 1 and an example of a false positive is given in Figure 2.



Figure 1 - Successfully detected object using Speeded Up Robust Features (SURF)

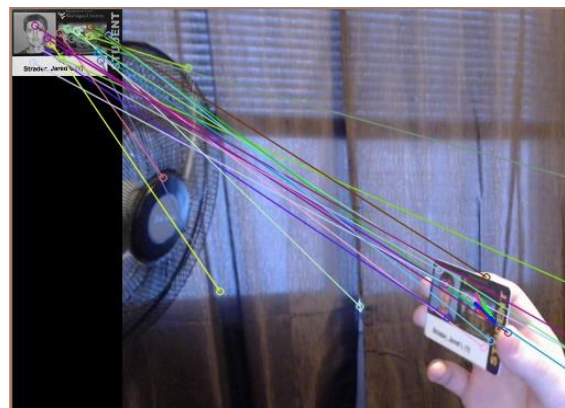


Figure 2 - False detection using Speeded Up Robust Features

Machine Learning

Another very popular method for object recognition is machine learning. The most popular machine learning methods for object recognition and computer vision include Support Vector Machines (SVM), AdaBoost, Neural Networks, Linear Discriminant Analysis (LDA), Clustering, and Naïve Bayes. Machine learning methods involve collecting large amounts of data for training and testing. This requires several steps such as pre-processing, feature extracting, training the classifier, and testing the classifier using new data or cross validation. To properly train a classifier, the data must contain a large variety of lighting condition and object orientations. Without adequate data, machine learning algorithms perform poorly. Due to the limited amount of data, machine learning algorithms were not tested for this project. In future experiments, machine learning algorithms will be implemented to test the performance on simple objects in partially unknown environments.

Image Segmentation

Image segmentation is the process of partitioning an image in multiple segments to simplify the representation of the image. The segments typically correspond to natural parts of the image, objects, or individual surfaces. In the case of object recognition, the image segmentation portion of the algorithm should segment the image in regions containing single objects, so each segment can be analyzed individually. The image segmentation algorithm must be fast and efficient, so the segments have sufficient time to be analyzed by the object recognition algorithm. The most popular segmentation algorithms include salient region segmentation, color segmentation, and texture segmentation. Salient region segmentation is most useful if the image is known to only contain a single object. Color segmentation separates the image into regions based on the pixels intensities, and texture segmentation separates the image into regions based on texture.

EXPERIMENT DESCRIPTION

Object Description

The majority of the algorithms were tested on the objects used for the NASA Centennial Sample Return Challenge, but the developed methods can be applied to different objects with similar characteristics. The main objects of interest are described below:

- Blue Rock: Rock painted blue with major dimension between 6cm and 10 cm.
- Pink Ball: Penn Pink Championship Extra Duty Tennis Ball
- Red Puck: Soft Shot Red Hock Puck
- Pre-Cached: Cylinder slightly under 8cm in diameter and 8cm in length with hook.
- Orange Pipe: Fluorescent orange 20cm long PVC Pipe with outside diameter of 2.67cm spray-painted fluorescent orange.

Images of the object are given in Figure-1. The last part of the study consists of determining an object (beacon), which can be accurately and efficiently recognized at a large distance. The only limitation for the beacon is that the largest dimension must be less than 2 meters.



Figure 1: From left to right the object are displayed as pre-cached, orange, pipe, pink tennis ball, blue rock, red hockey puck

ENVIRONMENT DESCRIPTION

The objects are assumed to be located on the ground, and only outdoor natural environments are considered, so the objects are assumed to be sitting on grassy or dirt surfaces. Multiple objects or objects sitting on concrete are not considered for this experiment.

EQUIPMENT DESCRIPTION

The algorithms were developed in C++ using OpenCV for image processing, and Robot Operating System (ROS) for implementing the software and algorithms. ROS is a computer framework for integrating multiple devices and programs, and OpenCV is an open source computer vision library in C, C++, and Python. The algorithms were implemented on the Advantech PCM-9389, which contains a 1.8 GHz dual core Intel Atom processor. The algorithm must be able to run in real-time, so the computer must be able to process each image as fast as possible. The images for the experiment were all captured using the Logitech C920 webcam.

METHODS

Image Segmentation

The designed algorithm required multiple steps to segment and recognize the desired object. The most efficient and computationally cheap method of segmentation is color segmentation. The first step involved segmenting the image using the pixel intensities in the image to detect color. To segment the image using the pixels intensities, thresholding is used to determine if the pixel is within range of the desired color. Using thresholding, a binary image is obtained where the pixels within range are assigned 1 and the pixels out of range are assigned 0. Each color requires different threshold values, so the image must be segmented once for each color. For blue, red, and white objects, the image is represented in the RGB color space where R is red, G is green, and B is blue. For white, the brightness and relative greyness are the most important characteristics. The brightness is determined by the maximum value between the red, blue, and green channels. The representation is shown in eq. (1).

$$\text{Brightness} = \max(R, G, B)/255 \quad (1)$$

The relative greyness is determined by calculating the variation between the red, blue, and green channels. The representation is given in eq. (2).

$$\text{Greyness} = 1 - (\max(R, G, B) - \min(R, G, B)) / 255 \quad (2)$$

The result of the greyness ranges from 0 to 1 where 1 is grey and 0 is not grey. The binary image for white objects is obtained using the brightness and the greyness with thresholding. For red and blue segmentation, the ratios between the red, blue, and green channels are thresholded for determining if a pixel is red, blue, or neither. The representation for the amount of redness of a pixel is shown in eq. (3).

$$\text{Redness} = (R - (B + G)) / 255 \quad (3)$$

The value for the redness ranges from 0 to 1 where 1 is red and 0 is not red. Since the data types are unsigned, $R - (B + G)$ will always be a non-negative integer between 0 and 255. The representation for the amount of blueness of a pixel is shown in eq. (4).

$$\text{Blueness} = (B - (R+G)) / 255 \quad (4)$$

The value for the blueness ranges from 0 to 1 where 1 is blue and 0 is not blue. Similar to the red, the quantity $B - (R + G)$ will always be a non-negative integer between 0 and 255 since the data types are unsigned. For the pink and orange objects, the image is represented in the HSV color space where H is hue, S is saturation, and V is value. The HSV color space is helpful because the color component is reduced in the hue channel, so only one channels is necessary for obtaining the binary image of pink and orange objects, but including the saturation and value will improve the segmentation accuracy because if pixels have too high or low saturation and value, the hue is sensitive. The threshold values for orange are given in eq. (5).

$$\begin{aligned} 0 &\leq H \leq 24 \\ 131 &\leq S \leq 197 \\ 164 &\leq V \leq 255 \end{aligned} \quad (5)$$

Where hue ranges from 0 to 180, and saturation and value range from 0 to 255. Since orange is similar to red, the orange segmentation may segment red pixels in addition to orange pixels, but if any pixel is identified as red, the pixel will not be considered for the orange segmentation. The threshold values for pink are given in eq. (6).

$$\begin{aligned}
140 \leq H \leq 180 \\
10 \leq S \leq 255 \\
127 \leq V \leq 255
\end{aligned}
\tag{6}$$

Similar to orange, pink segmentation may segment red pixels in addition to pink, but any pixel identified as red is no considered for the pink segmentation. The pixel segmentation is completed in a specific order, so each pixel is only assigned a single color. The order is given in the following diagram.

White → Red → Blue → Orange → Pink

Once a pixel is assigned a color, the algorithm moves to the next pixel, so each pixel is assigned only a single color. After each pixel is assigned a color, the binary images for each color are extracted, so a single binary image is obtained for each color. Next, morphological operation are completed to remove noise from the images, so the segments can be extracted for further processing and classification. The morphological operation implemented are erosion and dilation. The image is first eroded to remove noise and artifacts, then then the image is dilated to expand the remaining elements. The blobs in the resulting image are extracted as candidate objects. The results of the segmentation algorithm are given in the results section.

Smoothness

After extracting the candidate objects, features containing texture information and region information are extracted to determine if the candidate object is a sample or non-sample. The smoothness of an object is can be calculated using two different methods. The first methods involve edge detection. Intuitively, if an object looks visually smooth, there will be little or no edges in the object. On the other hand, if the object looks visually rough, there will be many edges inside the object. This is exactly how the smoothness is calculated using edges. First, the object candidate is extracted from the original image and converted to greyscale. Next, the edges are detected using the canny edge detector. The result image is a binary image where each 1 represents part of an edge. Next, the binary image is dilated to enlarge the edges. This is the roughness image. Using the roughness image, the smoothness is calculated using the formula in eq. (7).

$$\text{Smoothness} = 1 - \text{sum}(\text{Roughness}) / (\text{width} * \text{height})
\tag{7}$$

Where Roughness is the binary edge image of the candidate object after dilation and width and height are the width and height of the Roughness image. The smoothness for method 1 ranges from 0 to 1 where 1 is smooth and 0 is not smooth. For the second method for calculating smoothness, the local binary pattern (LBP) algorithm was slightly modified to obtain a smoothness value for each pixel in the image. The algorithm is completed as follows for an image A:

1. Calculate the LBP of image A , name this image B .
2. For each neighbor u of pixel $b \in B$, denoted $u \in N(b)$, check if $u < p$ where p is the pixel in image A corresponding to b .
3. The smoothness is the number of neighbors of p such that $u < p$.

The smoothness in method 2 ranges from 0 to 8 where 8 is smooth and 0 is not smooth. The first method distinguishes between samples and non-samples better than the second method, so the first method is implemented in the final algorithm. Examples of the resulting images for both methods are given in the results section.

Region Information

The region information necessary to determine if the object is sitting in the grass. Since the objects are known to be sitting on the ground and not on sidewalks, the objects will most likely have grass in the same region in addition to dirt. If there is no grass around the object, the object is most likely not sitting on the ground. To classify the objects correctly, the region confidence must be high. To determine if the region around the object contains grass, exactly 8 regions around the object (top left, top, top right, middle left, middle right, bottom left, bottom, bottom right) of equal size to the object are extracted from the original image. We will call this boundary segments. Each boundary segment is converted to the HSV color space, and a histogram for each boundary segment is calculated from the hue channel containing 180 bins. Next, the highest bin from each boundary segment is determined from the histogram. The hue value for grass was experimentally determined to be between 30 and 60. If the highest bin in a boundary region is between 30 and 60, the boundary region is considered to be a grassy region. Each region is given either a 1 or a 0 depending if the region is grassy or not. To determine the region confidence of the object region containing enough grass, the following calculation is given in eq. (8) is completed.

$$\text{Region} = (R_1 + R_2 + R_3 + R_4 + R_5 + R_6 + R_7 + R_8) / 8 \quad (8)$$

Where each R is either 0 or 1 depending if the boundary region is grassy or non-grassy. The resulting value is between 0 and 1 where 1 means the object is completely surrounded by grass, and 0 means the object region does not contain grass.

Classification

To classify the each candidate as a sample or non-sample, the smoothness and region confidence is calculated for each candidate and both criteria are weighted to determine an overall confidence. If the confidence is above the determined threshold, the candidate is classified as one of the five samples, if the confidence is below the determined threshold the object is classified as non-sample. The combined confidence is shown in eq. (9).

$$\text{confidence} = 1/3 * \text{region} + 2/3 * \text{smoothness} \quad (9)$$

The resulting value for confidence ranges from 0 to 1 where 1 is high probability the candidate is a sample and 0 is low probability the candidate is a sample. After classifying the object as sample, the color of the object is used to determine the type of sample since each object is a different color.

RESULTS

The segmentation result for the pre-cached sample is given in Figure 4. The object candidates after thresholding and morphological operations shown by the red circles.



Figure 2 - Resulting candidates from segmentation algorithms. Candidates are circled in red.

The binary image of the segmentation algorithm after morphological operations is given in Figure 5.

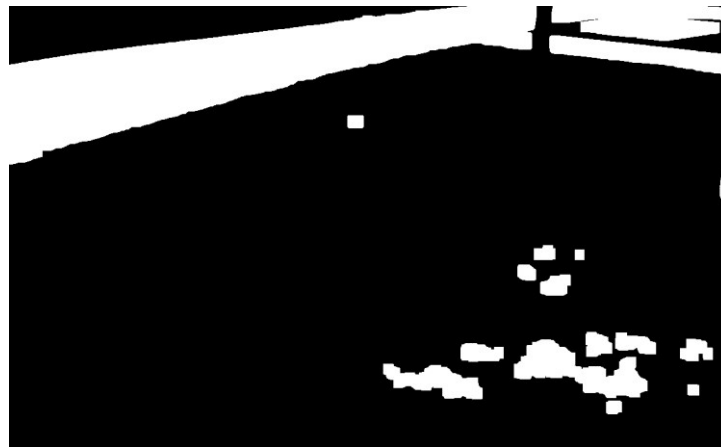


Figure 3 - Resulting binary image after the segmentation algorithm and morphological operations. The white blobs are the candidates.

Calculating the smoothness using edges is very useful for removing false positives. The smoothness image is the inverse of the roughness image described in the previous section. The extracted pre-cached sample candidate and the smoothness image using edges for the pre-cached sample are given in Figure 6.

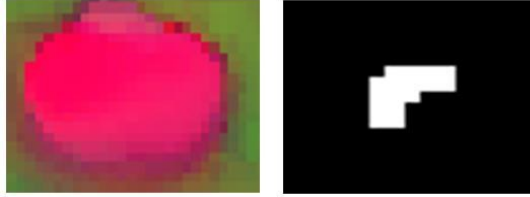


Figure 4 – From left to right, extracted pre-cached sample in HSV color space, smoothness binary image for extracted pre-cached sample.

Examples of false positives from the segmentation algorithm are given in Figure 7.

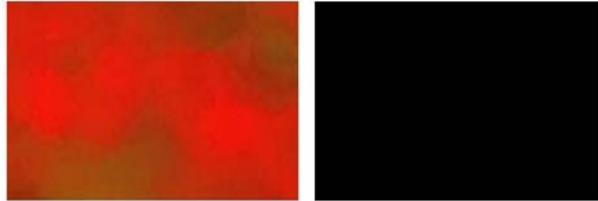


Figure 5 – From left to right, extracted false positive from the segmentation algorithm in HSV color space, smoothness image of the extracted false positive.

Notice the smoothness image for the pre-cached sample contains white pixels while the smoothness image for the false positive contains only black pixels. The majority of false positive or patches of dirt, which are very rough images. Since the segmentation algorithm extracts many false positives, the smoothness image is helpful in rejecting false positive. The smoothness calculated from local binary pattern (LBP) is not as effective as the edges, but the results algorithm are given in Figure 8.

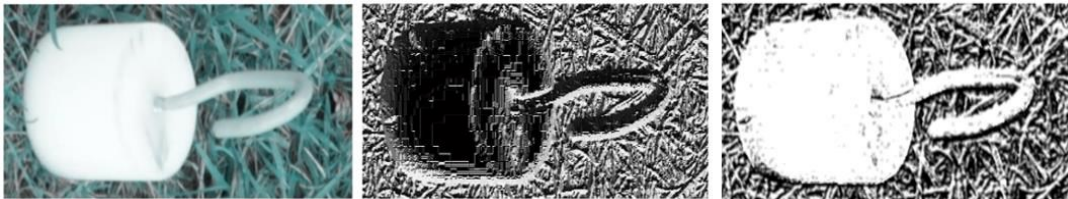


Figure 6 - From left to right, original image, LBP image, smoothness image from LBP

Notice the smoothness image calculated from LBP is much noisier than from the edges. Even though the pre-cached sample is clearer to human perception in LBP version, the edge version is more simple and robust to noise.

CONCLUSION

For the NASA Sample Return Challenge, the processing power is the primary constraint for computer vision. Since the environment is partially known, multiple constraints such as region information and smoothness can be applied to reject false positive. Overall, the smoothness is very robust on low resolution images (1280 x 720 pixels) when the object is no more than 5 meters from the camera. The method described in this paper was implemented on the Cataglyphis rover for 2014 NASA Centennial Sample Return Robot Challenge, and the method proved to be successful during the challenge and during the experiments. To further improve the method, additional constraints could be applied to detect the objects when they are not in the grass, or to more accurately segment the colored objects. In this method, shape information is not considered

due to the computational complexity of extracting shape features. Overall, the algorithm is effective and reasonably robust to changes in the environment.

ACKNOWLEDGEMENTS

This research is supported by the Undergraduate Research Fellowship program administered through the NASA WV Space Grant Consortium. The author would like to thank Dr. Yu Gu for his help and support throughout the project.

REFERENCES

- [1] Bay, Herbert, Andreas Ess, Tinne Tuytelaars, and Luc Van Gool. "Speeded-Up Robust Features (SURF)." *Computer Vision and Image Understanding* 110.3 (2008): 346-59. Print.
- [2] D. Jugessur, and G. Dudek. "Local appearance for robust object recognition." In *Proc. CVPR*, 2000
- [3] Corke, Peter I. *Robotics, Vision and Control: Fundamental Algorithms in MATLAB*. Berlin: Springer, 2011. Print.
- [4] Lowe, D. "Distinctive image features from scale invariant keypoints" *International Journal of Computer Vision*, 60, 2 (2004), pp. 91-110
- [5] Healey, Christopher G., and James T. Enns. A perceptual colour segmentation algorithm. Tech. Rep. TR-96-xx, Department of Computer Science, University of British Columbia, 1996.

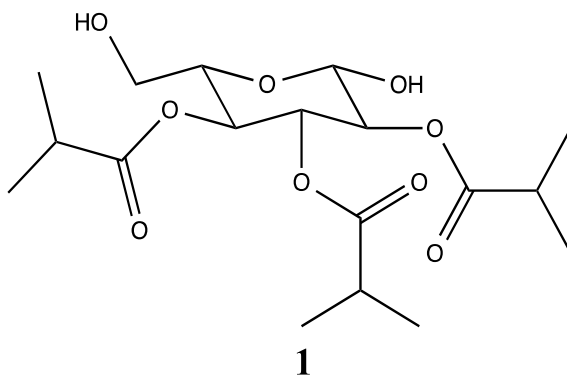
III. NASA Graduate Research Fellowship Reports

SYNTHESIZING AND TRIALING TRIESTERIFIED MONOSACCHARIDES ON THE BIOCONTROL GENERALIST PREDATOR, GREEN LACEWING, *CHRYSOPERIA RUFILABRIS*

Hannah Cavender
Biotechnology
West Virginia State University
Institute, WV 25112

ABSTRACT

Integrated pest management utilizes selective pesticides to combat pests while decreasing harmful effects on beneficial insects. Acylglucose, (2R,3S,4R,5S,6S)-2-hydroxy-6-(hydroxymethyl)tetrahydro-2H-pyran-3,4,5-triyl tris(2-methylpropanoate) **1**, was selected as a potential candidate for a natural pesticide. The target compound was investigated from a retrosynthetic perspective, which allowed for the development of a synthetic route. The five step synthesis begins with protection of the primary position with *tert*-butyldiphenyl(chloro)silane (95%). This protection is followed by a secondary one of the anomeric position with phenylthiol (92%). Esterification of positions 2, 3 and 4 yields the acylated diprotected glucose (90%). The final two steps are deprotections of the primary (80%) and anomeric position (75%). The development of a synthetic route allows for the production of acylglucoses, which can be trialed on the generalist predator, *Chrysoperia rufilabris*.



INTRODUCTION

Project Description

The overall goal of this research is to develop a synthetic route to generate triesterified monosaccharides (acylsugar) and assess the effect on the biocontrol generalist predator, green lacewing, *Chrysoperia rufilabris*.

Objective 1). Develop a synthetic route to generate triesterified monosaccharides (acylsugars).

Objective 2). Assess the effect of triesterified monosaccharides on the egg, larval and adult stages of the biocontrol generalist predator, *C. rufilabris*.

Project Summary

Protected culture production of most crops including tomatoes use biological controls, such as *Chrysoperia rufilabris*, as a part of their integrated pest management (IPM) program. Thus, it is important to assess any changes in the production system and how they will affect the IPM system being used before implementation. Breeding acylsugar mediated resistance into tomato varieties for the protected culture system offers the potential to control whiteflies and aphids, the two top insect pests. However, no research has assessed these compounds potential effects on biological control agents. Acylsugars could prove to be an environmentally friendlier alternative to harsh pesticides, so optimizing their natural production would be ideal.

Our first step was to develop a synthetic route for acylglucoses in order to quantify their effects on biological controls in the greenhouse. The target compound was investigated from a retrosynthetic perspective. The procedure follows a five-step synthesis beginning with an initial selective protection of the primary hydroxyl group with a silyl ether (95%). The anomeric carbon is then protected with a sulfide (Tanaka et al. 2009) and the remaining positions 2, 3 and 4 are then esterified with excess acid chlorides (92% and 90% respectively). The final two steps are deprotections of the primary hydroxyl position (80%) and the anomeric position (75%) (Holton et al. 1994; Waschke et al. 2012).

Purification of each compound was conducted utilizing silica gel chromatography. Full characterization of purified product at each step is also in progress for each intermediate utilizing infrared, ¹H and ¹³C nuclear magnetic resonance, and mass spectroscopy methods. These spectroscopy methods can be used in conjunction to determine unique properties of the compound. Infrared spectroscopy is utilized to determine functional groups, so the presence of the esters, and hydroxyl groups will be indicated in this step. ¹H and ¹³C nuclear magnetic resonance spectroscopy will determine the number and type of protons and carbons, as well as their orientation in the compound. Lastly, mass spectroscopy is used to determine the mass of the compound synthesized.

The method of trialing will be based off of a newer modified exposure assay that involves multiple routes of subjection including oral, direct, and residual (Amarasekare and Shearer 2013b). Following exposure, the larvae and adult stages will be monitored for examination of lethal and sub-lethal affects. Any changes in fecundity and fertility will also be investigated.

BACKGROUND

According to the USDA, the United States is in the lead in the worldwide production of tomatoes. California and Florida each produce fresh-market tomatoes on 30,000-40,000 acres, accounting for two-thirds of the total U.S. fresh market varieties (Thornsbury 2012). Tomatoes can be grown by one of two production systems: in open-field or in protected culture. Protected culture systems vary from being highly sophisticated with large scale greenhouses, to less advanced systems with high and micro tunnels (Welbaum 2015). Protected culture has the benefit of allowing the grower to have more control over elements that affect the crop year-round. In these systems, the ventilation, light intensity, and temperature are adjustable for optimization of plant growth (Welbaum 2015).

Having optimal condition for plant growth is ideal, especially in the case of tomatoes, since they are an integral part of the worldwide diet. There have been several studies conducted that establish a link between the consumption of tomatoes, and the reduced risk of chronic diseases. A diet rich in tomatoes (300g daily for one month) increases HDL-cholesterol by 15.2% (Blum et al. 2006). Tomatoes are a major source of carotenoid antioxidant lycopene. The lycopene content in various tomato products ranges from 42 ppm to 365 ppm, with the average daily consumption being estimated around 25.2 mg/day. The intake of fresh tomatoes actually accounts for 50% of the total lycopene intake (Rao, Waseem, and Agarwal 1998). There is also a suggestion in recent epidemiologic studies that there is potential benefit of this carotenoid against the risk of prostate cancer, with emphasis on the more lethal forms of this cancer (Giovannucci 2002). The consumption of two to four servings of tomato sauce per week was associated with about a 35% risk reduction of total prostate cancer and a 50% reduction of advanced (extraprostatic) prostate cancer (Giovannucci 2002).

Given the fact that tomatoes are essential to a healthy human diet, and that consumer demand is on the rise, the ability to grow tomatoes year round is crucial. Tomatoes are not only a dietary importance; they also have high economic value. The role of round field tomatoes is shrinking; in 2011 protected-culture tomatoes made up 40 percent of the U.S. tomato supply (Thornsbury 2012). Currently, tomatoes produced in protected culture are dominating the retail industry and becoming more common in food service (Thornsbury 2012).

However, as in field production, protected-culture is not without its complications. Humans are not the only ones with an appetite for this betacarotenoid-rich crop, insect pests are a limiting factor for quality production. Insect pests such as thrips, whitefly and aphid species can cause massive losses in tomatoes both directly (feeding on plant components), or indirectly (transmission of plant viruses) (Morales and Anderson 2005; Pappu, Jones, and Jain 2009; Polston and Anderson 1997). High densities of silverleaf whitefly (SLW) can induce an irregular ripening disorder in tomatoes as a result of their phloem feeding and toxic saliva (Schuster 2001). This damage results in an economic loss due to unmarketable fruits (Schuster 2001). In addition, SLW is a vector of multiple viruses in the Geminiviridae family, which includes the severe tomato yellow leaf curl virus (TYLCV) (Polston and Anderson 1997). Tomato production can come to a complete halt with the transmission of TYLCV, with losses reaching up to 100% (Saikia and Muniyappa 1989).

The primary aphid species of concern are the green peach aphid, *Myzus persicae* and the potato aphid, *Macrosiphum euphorbiae*. However, only the green peach aphid is known to transmit viruses to tomatoes, which include Alfalfa mosaic virus, Potato virus Y, and Tobacco etch virus (Davis, Pernezny, and Broome 2012). While the potato aphid does not serve as a vector of viruses, the damage induced by these pests when they are present in high volume is substantial (Davis, Pernezny, and Broome 2012). Potato aphids can distort leaves and stems, stunt plants, and cause necrotic spots on leaves (Davis, Pernezny, and Broome 2012). The green peach aphid and potato aphid can both result in the production of sooty mold on foliage and fruit due to their secretion of honeydew (Davis, Pernezny, and Broome 2012).

Solanum pennellii is a wild tomato that exhibits insect resistance and contains high densities of type IV glandular trichomes. (Goffreda et al. 1989, Hawthorne et al. 1992, Juvik et al. 1994, Liedl et al. 1995, Rodriguez et al. 1993). These glandular trichomes excrete a mixture of 2,3,4-tri-O-acylated glucose esters that function as a physical and chemical deterrent to small arthropod

pests (Walters and Steffens 1990). The acyl moieties can consist of iso-branched, ante-iso-branched, and straight chain fatty acid side chains ranging from 4 to 12 carbons in length (Burke et al. 1987; Sharpio et al. 1994). Acylsugars can consist of a variation of different acyl moiety acylglucoses and acylsucroses. Southern *S. pennellii* accessions exude acylglucoses consisting primarily of i4:0 and its extension products as the predominant fatty acid constituents (Leckie et al. 2014). Southern accessions tend to have higher acylsugar levels than do northern accessions (Shapiro et al. 1994). Cultivated tomato leaves also produce acylsugars, at very low levels, consisting of tri and tetra-O-acylsucrose esters with the esterified fatty acids ranging from 2 to 12 carbons in length (Schillmiller et al. 2010).

The non-toxicity and broad spectrum of the resistance are major advantages to the use of this in tomato production. Since acylsugars are non-toxic to the pests controlled, most of which feed on multiple hosts, the pressure for insects to become acylsugar resistant should be less than is commonly seen for pesticides and high antibiosis-mediated plant resistance mechanisms (Kennedy et al. 1987). Acylsucroses have been synthetically produced, where the sucrose is reacted with an aliphatic acid chloride in an aprotic polar solvent (Chortyk 1996). In this process, all of the hydroxyl groups are acylated. There is no such method for the synthesis of acylglucoses due to the more complex nature of the limited esterification of positions 2, 3, and 4. The application of purified *S. pennellii* LA716 acylglucoses to cultivated tomato leaves has shown that these compounds are effective, rate dependent feeding deterrents of potato aphids, green peach aphids, tomato fruitworm, beet armyworm, American serpentine leafminer, and silverleaf whitefly (Goffreda et al. 1988; Goffreda and Mutschler 1989; Juvik et al. 1994; Hawthorne et al. 1992; Liedl et al. 1995).

The cultivated tomato does not possess type IV glandular trichomes and therefore does not accumulate acylsugars on its surface (Fobes, Mudd, and Marsden 1985). Breeding of cultivated lines using *S. pennellii* LA716 as the donor parent has led to the development of the acylsugar-producing tomato breeding line CU071026 (Leckie, De Jong, and Mutschler 2012). However, the existence of synthetic acylglucoses will allow application to cultivars at times of vulnerability such as after wetting, and for heirloom varieties that lack the appropriate genes. Also, synthetic acylglucoses can be used for trialing on pest and biological control insects. Additionally, there is potential to use these acylglucoses on other crops if they prove to be non-toxic to biological controls. Before these acylglucoses can be synthesized, a blueprint for their construction must be taken under consideration via retrosynthesis. Examination of the final expected product, will allow for a stepwise determination of the precursor products. Once all of the precursor products are determined, the synthetic route can be delved into further.

Integrated pest management (IPM) systems incorporate the application of selective pesticides and biological controls. The pesticides are evaluated based on action threshold, level of pests and natural enemies, surveillance and monitoring systems, use of pheromones, traps, bio-pesticides, and narrow spectrum pesticides to minimize undesirable side-effects (Haskell and McEwen 1998). Biological control is defined as the use of living natural enemies to suppress pest populations (Heinz, Van Driesche, and Parella 2004). Natural enemies of insects and mites include parasitic wasps that use pests as hosts for their offspring, predators that consume their prey, and pathogens that cause disease (Heinz, Van Driesche, and Parella 2004). Since the efficient use of biological control involves maintaining a balance in the population levels of beneficial organisms and of

pests, it is necessary before the implementation of a pesticide to examine potential side-effects on beneficial organisms (Haskell and McEwen 1998).

Most commonly the greenhouse whitefly (*T. vaporariorum*) is controlled with the use of the parasitic wasp *E. formosa* (Heinz, Van Driesche, and Parella 2004). This program is successful unless the wasp is killed by pesticides applied against other pests, or if parasitized nymphs are removed via trimming before the emergence of adult wasps (Heinz, Van Driesche, and Parella 2004). The three species of aphids that are commonly a threat to tomato cultivars are green peach aphid (*Myzus persicae*), greenhouse potato aphid (*Aulacorthum solani*) and potato aphid (*Macrosiphum euphorbiae*) (Heinz, Van Driesche, and Parella 2004). These are most commonly controlled by localized applications of aphicide pirimicarb, or the anti-feedant chemical pymetrozine (Heinz, Van Driesche, and Parella 2004).

Green lacewings (*Chrysoperla rufilabris* and *Chrysoperla carnea*) can also be utilized in aphid and whitefly control (McEwen, New, and Whittington 2007). Larval lacewings fulfill many of the requirements of an effective biological control agent since they are avid predators with an efficient prey localizing capacity (Sundby 1966; Bond 1980). One *C. carnea* larva can consume an average of 487 aphids or 511 whitefly pupae before pupation (Afzal 1978). Lacewings are polyphagous, feeding on a wide range of pests including aphids, whitefly, mites, mealybugs, Colorado potato beetle, and various lepidopteran pests such as bollworms (Séméria and New 1984). Additional benefits of lacewings are their high resistance to common insecticides, as well as their high reproductive rate (McEwen, New, and Whittington 2007). Larval rearing has become economically viable, and when this stage is released it will stay in targeted area (McEwen, New, and Whittington 2007).

In 1974, the Working Group ‘Pesticides and Beneficial Organisms’ of the International Organization for Biological Control/West Palaearctic Regional Section (IOBC/WPRS) was established with a major aim to encourage development of standard methods for testing side-effects of pesticides on natural enemies that would be acceptable to all cooperating institutions (Hassan 1994). Parasites and predators of agricultural pests naturally work to reduce the population of their prey or host, therefore decreasing the damage caused by the pest (Haskell and McEwen 1998). Thus, the importance of selective pesticides that work in concert with the biological control is of high relevance. The IOBC developed standard laboratory, semi-field, and field methods to test the side-effects of pesticides on beneficial organisms (Hassan 1994). Guidelines to test the side effects of pesticides on natural enemies has been published in multi-author publications (Hassan 1998; Amarasekare and Shearer 2013b; Bigler 1988; Suter 1978; Vogt et al. 1998). Harmlessness of pesticides can be shown by laboratory experiments, however harmfulness can only be confirmed under practical conditions in the field (Hassan 1994). Pesticides found to be harmless to a particular beneficial organism in the laboratory test are most likely to be harmless to the same organism in the field and no further testing in semi-field or field experiments is therefore recommended (Haskell and McEwen 1998).

Vogt (1998) described a laboratory method for testing the side-effects of pesticides on *C. carnea*, which is the first tier within the sequential testing scheme. This method was based on the laboratory glass plate test developed by Suter (1978) and Bigler (1988). This test was designed to evaluate the acute residual toxicity of a pesticide as well as sub-lethal effects on reproductive performance

of the emerging adults. However, Amarasekare and Shearer (2013) proposed the use of a more robust assay that combines contact, residual, and oral routes of exposure.

Since, bio control agents and selective pesticides are used in concert to control pests in integrated pest management, multiple elements must be reviewed before introducing a new component into an IPM system. Currently, the knowledge of the mode of action of acylsugars is that they can terminate entrapped herbivores by suffocation (Puterka et al. 2003), starvation, or by ingestion of toxins (Simmons et al. 2004). However, there is no current information on the use of acylsugars in an integrated pest management system and their affect on the biological control agent, *C. rufilabris*.

Justification and Rationale

A straightforward synthesis of acylglucoses has not been developed. Use of purified compounds from crude plant extracts is problematic as they are difficult to obtain and separate due to the similar structures. Synthesizing acylglucoses would allow for the production of pure products for test and perhaps future use as an insecticide. Use of a single acylglucose will allow testing on *Chrysoperia rufilabris* to determine if plants expressing or having acylsugar sprayed will interfere with the existing IPM system in tomato production in protected culture and if breeding acylsugar resistance into tomato varieties for protected culture is feasible.

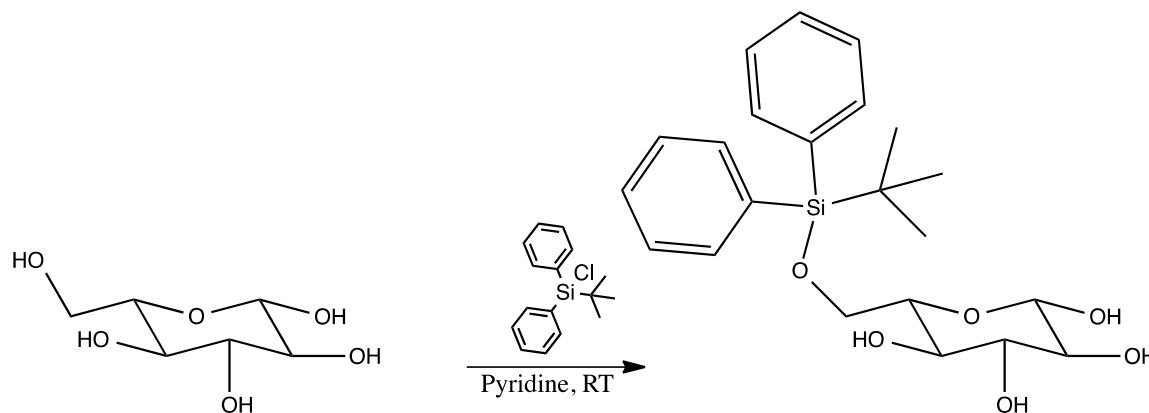
MATERIALS AND METHODS

Objective 1). Develop a synthetic route to generate triesterified monosaccharides and scale up the production.

The isobutyryl acid chloride was selected for the creation of the ester at positions 2, 3 and 4 because Southern *S. pennellii* accessions exude acylglucoses consisting primarily of i4:0 and its extension products as the predominant fatty acid constituents (Leckie et al. 2014).

Step 1:

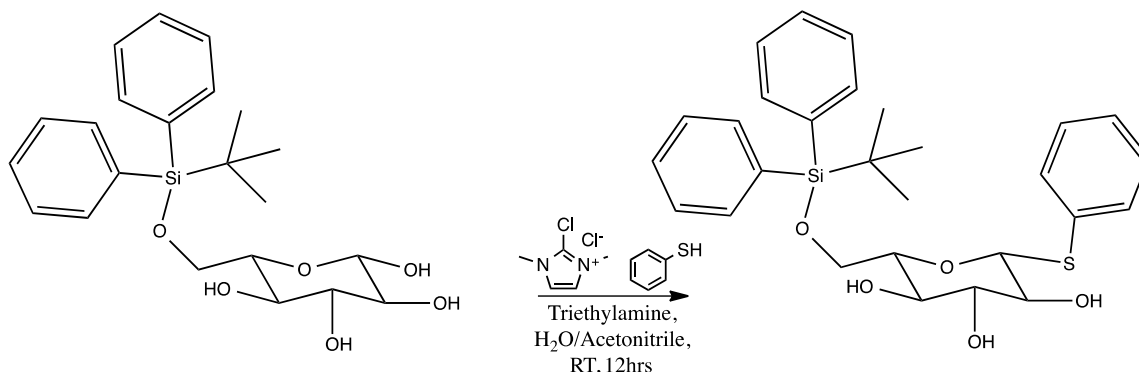
Protection of unhindered alcohol in D-glucose via regioselective addition of a TBDPS ether, using TBDPS-Cl in pyridine to give protected glycoside.



Scheme 1: Protection of primary alcohol with TBDPS

Step 2:

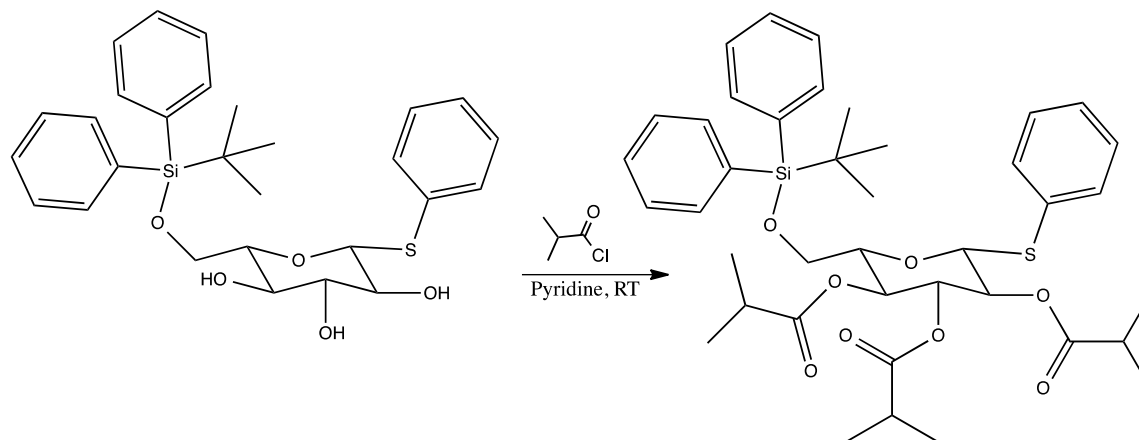
Protection of the anomeric carbon of monoprotected glucose via an intramolecular dehydration reaction in aqueous media using phenylthiol and 2-chloro-1,3-dimethylimidazolium to give diprotected glucose.



Scheme 2: Protection of anomeric position with phenylthiol

Step 3:

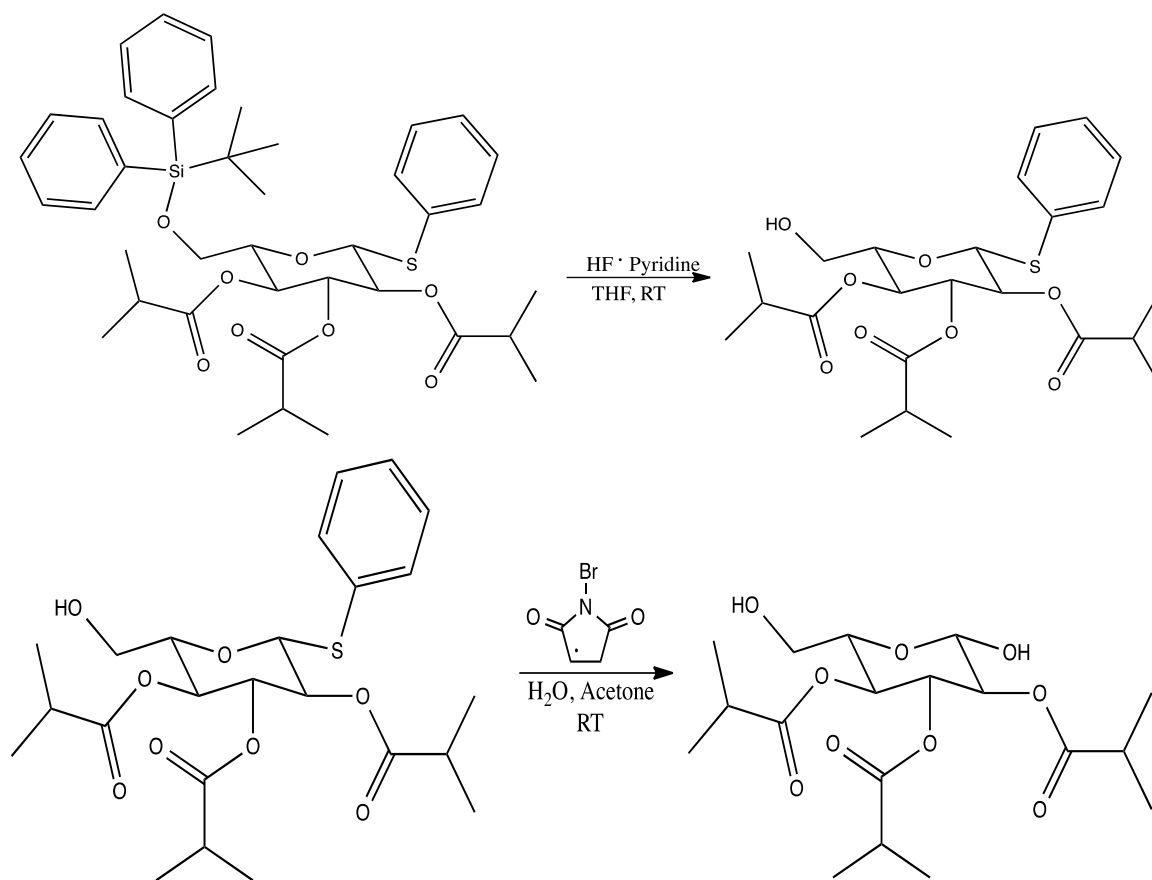
Esterification of protected glycoside using acid chloride provides to yield fully protected sugar.



Scheme 3: Esterification of positions 2, 3, and 4 of diprotected glucose.

Step 4 and 5:

Deprotection of protected glycoside occurs in two separate steps. First, the silyl protecting group is removed using HF•pyridine in THF. After this product is purified, then the anomeric carbon can be deprotected via an oxidative reaction using N-bromosuccinimide to yield the triesterified monosaccharide.



Scheme 4a and b: Deprotection of primary and anomeric positions utilizing HF• pyridine and n-bromosuccinimide, respectively.

RESULTS AND DISCUSSION

Retrosynthetic Analysis

Retrosynthesis involves the process of examining the final product and working backwards to construct the synthetic blueprint. Figure 1 is outline of the retrosynthetic approach. Investigation of the final product makes it apparent that in order to not subject the primary and anomeric positions to esterification, they must be protected. Protection of the primary position can be accomplished by tert-butyl(chloro)diphenylsilane. This protecting group is bulky, and therefore due to steric hindrance should add to the primary position. The anomeric position is unique, making the selective protection of this position proceed via an intramolecular dehydration reaction. The addition of acid chlorides, in this case isobutyryl chloride, to compounds containing hydroxyl groups results in the formation of an ester, which is what should result at positions 2, 3 and 4.

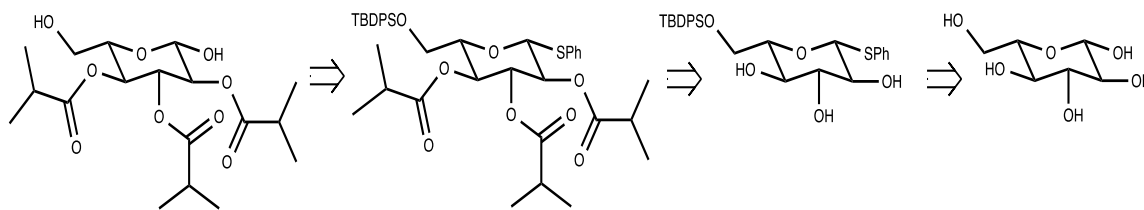


Figure 1: Retrosynthesis of (2R,3S,4R,5S,6S)-2-hydroxy-6-(hydroxymethyl)tetrahydro-2H-pyran-3,4,5-triyl tris(2-methylpropanoate).

Construction of (2R,3S,4R,5S,6S)-2-hydroxy-6-(hydroxymethyl)tetrahydro-2H-pyran-3,4,5-triyl tris(2-methylpropanoate)

The construction of (2R,3S,4R,5S,6S)-2-hydroxy-6-(hydroxymethyl)tetrahydro-2H-pyran-3,4,5-triyl tris(2-methylpropanoate) commenced with the starting protection of D-glucose with tert-butyl(chloro)diphenylsilane. This reaction resulted in a white crystal with a percent yield of 95%. The protection of the anomeric position followed, by reacting the monoprotected glucose with phenylthiol. This product was a yellow crystal (92%). This step tends to result in a higher percent yield if the formation of 1,3-dimethyl-1,3-dihydro-2H-imidazol-2-one is not completely separated from the product during purification. The separation is difficult due to the close r_F values of the products. Next, the diprotected glucose is reacted with a dilute solution of isobutyryl chloride, this reaction occurs quickly within forty-five minutes. This results in the esterification of the diprotected glucose, once purified, is also crystalline in nature (90%). The deprotection of the TBDPS group protecting the primary position occurs utilizing HF•pyridine. The small fluoride anion nucleophilically attacks the silicon center. This results in the formation of a strong Si-F bond, which allows for the cleavage. The product is a viscous liquid (80%). The last deprotection uses n-bromosuccinimide, in which the bromine is open for nucleophilic attack by the sulfur, the neighboring oxygen then donates electrons, which causes the removal of the sulfur group. Water can then add to the anomeric position, and after deprotonation, the final product is present as a white crystal (75%).

CONCLUSION

As mentioned previously, the overall goal of this research was to develop a synthetic route to generate triesterified monosaccharides (acylsugar) and assess the effect on the biocontrol generalist predator, green lacewing, *Chrysoperia rufilabris*. Retrosynthesis was utilized to construct a blueprint for the successful synthesis of acylglucose, (2R,3S,4R,5S,6S)-2-hydroxy-6-(hydroxymethyl)tetrahydro-2H-pyran-3,4,5-triyl tris(2-methylpropanoate). A five step synthesis was successfully carried out, and characterization is currently underway. The next objective should be completed during the Summer of 2015.

FUTURE PLANS

Following the complete characterization of the final product, the next objective will be carried out. The goal of objective two is to assess the effect of triesterified monosaccharides on the egg, larval and adult stages of the biocontrol generalist predator, *C. rufilabris*.

Experimental Design of Future Trials

Insect Rearing

Chrysoperla rufilabris eggs will be ordered from greenmethods.com. Eggs will be individually separated into 59-ml translucent plastic portion cups, due to the cannibalistic nature of the immature green lacewings. Eggs will be kept in a growth chamber (23°C, 60% RH, and photoperiod of 16:8 (L:D) h) (Amarasekare and Shearer 2013a). The emerging larvae will be fed a diet of *Ephestia kuehniella* eggs. Upon emergence of adults, gender will be determined (Vogt et al. 2000). Males and females will be separated until treatment.

Bioassay-Lethal Effects

Glass arenas will consist of 8.255 cm x 8.89 cm 8 oz square jars (peakcandle.com). This bioassay will use a worst-case cumulative exposure scenario, where adults and larvae will be exposed to the acylglucose through contact, residual, and ingestion exposure (Amarasekare and Shearer 2013a). The amount of acylglucose used will correlate to the threshold amount of the product necessary for deterring settling and oviposition of pests (50-70 μ g/cm²) (Liedl et al. 1995). For this investigation, 60 μ g/cm² will be used, which in terms of concentration is 0.0513 mol/L. Cheese cloth lids and *E. kuehniella* eggs will be saturated in 100 ml of the treatment for 30 s, and then air-dried. The glass arenas will be treated with 4.403 mg dissolved in 236 ml of acetone, and the solvent will be left to evaporate out in a desiccation chamber to allow for even distribution of compound on surface (60 μ g/cm²). The adult food (mixture of eggs, honey, wheat germ, brewer's yeast, condensed milk, and water) will be treated in a 9 cm petri-dish.

Larvae and adults will be treated in a 9 cm-dia glass petri dish as a group of three larvae or a single pair of adult male and female per replicate per treatment, respectively (larvae; n=15 [5 replicates] and adults; n=24 [12 replicates]) (Amarasekare and Shearer 2013a). Treated insects will be carefully transferred to glass arenas with a soft brush. Larvae will be reared individually, and provided with treated *E. kuehniella* eggs (0.2-0.3 g). Adults will be paired, one male and one female per arena, and transferred to glass arena covered with cheese cloth lids, secured with metal lids. The adults will be fed a diet of the treated artificial mix mentioned above. All adults will be provided distilled water using a small (38 mm dia) piece of water soaked cotton roll placed in clear capless disposable micro-centrifuge tube (1.7 ml) attached to bottom of arena with putty (Amarasekare and Shearer 2013a).

Arenas will be placed in environmental growth chamber at 23°C, 60% RH, and photoperiod of 16:8 (L:D) h. Adult and immature *C. rufilabris* will be assessed for mortality daily for 10 d after treatment (Amarasekare and Shearer 2013a). Untreated *E. kuehniella* eggs (0.2-0.3 g) and fresh adult food will be provided to surviving larvae and adults, 72 hours after treatment. Treated larvae will be reared until emergence of adults, and their development time will be determined. Gender will also be determined with emergence of adults using methods described by Vogt et al. (2000). The adult sex ratio will then be calculated as the percentage of females [females/(males+females)] *100 (Amarasekare and Shearer 2013a). The surviving treated adults will be assessed for sublethal effects (Amarasekare and Shearer 2013a).

Surviving adults will be reared and provided with food and water three times a week until their death. The cheese cloth lids from adult arenas will be collected every other day to evaluate the number of eggs each female laid and subsequent egg hatch for 20 d. The eggs will be counted under a microscope, and separated individually into petri-dishes (Amarasekare and Shearer 2013a). The eggs will be placed into the environmental growth chamber (23°C, 60% RH,

photoperiod of 16:8 (L:D) h) and monitored for emergence of larvae. Egg hatch and emergence of larvae will be counted.

One-way analysis of variance (ANOVA) will be performed for mortality, developmental time, survival, sex ratio, fecundity, fertility, and egg viability. Two-way ANOVA will be performed for adult longevity by gender (Amarasekare and Shearer 2013a). The means will be compared at $P \leq 0.05$ significance level.

ACKNOWLEDGEMENTS

I would once again like to acknowledge NASA West Virginia Space Grant Consortium for all of the funding that they have contributed to my project. I could not meet my objectives without the dedication of this program. A very special thank you is sent out to Dr. Majid Jaridi, he embodies the ideal scholar as well as having a charitable spirit. His approachability and dedication to students is inspiring, and I have benefitted greatly from knowing him. I would also like to express appreciation for my dedicated advisors, Dr. Barbara Liedl and Dr. Micheal Fultz for their unyielding patience. I have subjected both of them to hours worth of peer editing, and my professional growth has contributed greatly from their guidance. Last but not least, I show gratitude to WVSU for allowing me to make use of their facilities and for supporting my graduate career.

REFERENCES

- Afzal, M. & Khan, M.R. 1978. 'Life history and feeding behavior of green lacewing *Chrysopa carnea* Steph. (Neuroptera, Chrysopidae)', *Pakistan Journal of Zoology*: 83-90.
- Amarasekare, K. G., and P. W. Shearer. 2013a. 'Comparing Effects of Insecticides on Two Green Lacewings Species, *Chrysoperla johnsoni* and *Chrysoperla carnea* (Neuroptera: Chrysopidae)', *Journal of Economic Entomology*, 106: 1126-33.
- Bigler, F. 1988. 'A laboratory method for testing side-effects of pesticides on larvae of the green lacewing, *Chrysoperla carnea* Steph.(Neuroptera, Chrysopidae)', *Bulletin SROP (France)*.
- Blum, A., M. Merei, A. Karem, N. Blum, S. Ben-Arzi, I. Wirsansky, and K. Khazim. 2006. 'Effects of tomatoes on the lipid profile', *Clin Invest Med*, 29: 298-300.
- Bond, Alan B. 1980. 'Optimal foraging in a uniform habitat: The search mechanism of the green lacewing', *Animal Behaviour*, 28: 10-19.
- Chortyk, O.T. 1996. 'Chemically synthesized sugar esters for the control of soft-bodied arthropods.' In.: Google Patents.
- Davis, R.M., K. Pernezny, and J.C. Broome. 2012. *Tomato Health Management* (APS Press).
- Fobes, J. F., J. B. Mudd, and M. P. Marsden. 1985. 'Epicuticular Lipid Accumulation on the Leaves of *Lycopersicon pennellii* (Corr.) D'Arcy and *Lycopersicon esculentum* Mill', *Plant Physiol*, 77: 567-70.
- Giovannucci, Edward. 2002. 'A Review of Epidemiologic Studies of Tomatoes, Lycopene, and Prostate Cancer', *Experimental Biology and Medicine*, 227: 852-59.
- Haskell, P.T., and P.K. McEwen. 1998. *Ecotoxicology: pesticides and beneficial organisms* (Kluwer Academic Publishers).
- Hassan, Sherif A. 1994. 'Activities of the IOBC/WPRS working group" Pesticides and beneficial organisms"', *IOBC WPRS BULLETIN*, 17: 1-1.

- . 1998. 'The initiative of the IOBC/WPRS working group on pesticides and beneficial organisms.' in, *Ecotoxicology* (Springer).
- Heinz, Kevin M, Roy G Van Driesche, and MP Parella. 2004. *Biocontrol in protected culture* (Ball Publishing).
- Holton, Robert A., Hyeong Baik Kim, Carmen Somoza, Feng Liang, Ronald J. Biediger, P. Douglas Boatman, Mitsuru Shindo, Chase C. Smith, and Soekchan Kim. 1994. 'First total synthesis of taxol. 2. Completion of the C and D rings', *Journal of the American Chemical Society*, 116: 1599-600.
- Leckie, Brian M, Darlene M De Jong, and Martha A Mutschler. 2012. 'Quantitative trait loci increasing acylsugars in tomato breeding lines and their impacts on silverleaf whiteflies', *Molecular Breeding*, 30: 1621-34.
- Liedl, Barbara E, Darlene M Lawson, Kris K White, Joseph A Shapiro, David E Cohen, William G Carson, John T Trumble, and Martha A Mutschler. 1995. 'Acylsugars of wild tomato *Lycopersicon pennellii* alters settling and reduces oviposition of *Bemisia argentifolii* (Homoptera: Aleyrodidae)', *Journal of Economic Entomology*, 88: 742-48.
- McEwen, P.K., T.R. New, and A.E. Whittington. 2007. *Lacewings in the Crop Environment* (Cambridge University Press).
- Morales, Francisco José, and Pamela K Anderson. 2005. *Whitefly and whitefly-borne viruses in the tropics: building a knowledge base for global action* (CIAT).
- Pappu, HR, RAC Jones, and RK Jain. 2009. 'Global status of tospovirus epidemics in diverse cropping systems: successes achieved and challenges ahead', *Virus research*, 141: 219-36.
- Polston, Jane E, and Pamela K Anderson. 1997. 'The emergence of whitefly-transmitted geminiviruses in tomato in the western hemisphere', *Plant Disease*, 81: 1358-69.
- Puterka, Gary J, William Farone, Tracy Palmer, and Anthony Barrington. 2003. 'Structure-function relationships affecting the insecticidal and miticidal activity of sugar esters', *Journal of economic entomology*, 96: 636-44.
- Rao, A. V., Zeeshan Waseem, and Sanjiv Agarwal. 1998. 'Lycopene content of tomatoes and tomato products and their contribution to dietary lycopene', *Food Research International*, 31: 737-41.
- Saikia, AK, and V Muniyappa. 1989. 'Epidemiology and control of tomato leaf curl virus in Southern India', *Tropical Agriculture*, 66: 350-54.
- Schuster, David J. 2001. 'Relationship of silverleaf whitefly population density to severity of irregular ripening of tomato', *HortScience*, 36: 1089-90.
- Séméria, Y., and T.R. New. 1984. *Biology of Chrysopidae* (Springer Netherlands).
- Simmons, Aaron T, Geoff M Gurr, Des McGrath, Peter M Martin, and Helen I Nicol. 2004. 'Entrapment of *Helicoverpa armigera* (Hübner) (Lepidoptera: Noctuidae) on glandular trichomes of *Lycopersicon* species', *Australian Journal of Entomology*, 43: 196-200.
- Sundby, Ragnhild A. 1966. 'A comparative study of the efficiency of three predatory insects *Coccinella septempunctata* L. (Coleoptera, Coccinellidae), *Chrysopa carnea* St. (Neuroptera, Chrysopidae) and *Syrphus ribesii* L. (Diptera, Syrphidae) at two different temperatures', *Entomophaga Entomophaga*, 11: 395-404.
- Suter, H. 1978. 'Prüfung der Einwirkung von Pflanzenschutzmitteln auf die Nutzarthropodenart *Chrysopa carnea* Steph. (Neuroptera; Chrysopidae): Methodik und Ergebnisse', *Schweizerische landwirtschaftliche Forschung. La Recherche agronomique en Suisse*.

- Tanaka, Tomonari, Takeshi Matsumoto, Masato Noguchi, Atsushi Kobayashi, and Shin-ichiro Shoda. 2009. 'Direct Transformation of Unprotected Sugars to Aryl 1-Thio-. BETA.-glycosides in Aqueous Media Using 2-Chloro-1, 3-dimethylimidazolium Chloride', *Chemistry Letters*, 38: 458-59.
- Thornsbury, Suzanne. 2012. 'Low Prices Continue for Fresh-Market Vegetables ', *Vegetables and Pulses Outlook*, 350: 1-52.
- Vogt, H, F Bigler, K Brown, MP Candolfi, F Kemmeter, Ch Kühner, M Moll, A Travis, A Ufer, and E Viñuela. 2000. 'Laboratory method to test effects of plant protection products on larvae of *Chrysoperla carnea* (Neuroptera: Chrysopidae)', *Guidelines to evaluate side-effects of plant protection products to non-target arthropods*: 27-44.
- Vogt, Heidrun, P Degrande, J Just, S Klepka, C Kühner, A Nickless, A Ufer, M Waldburger, Anna Waltersdorfer, and F Bigler. 1998. 'Side-effects of pesticides on larvae of *Chrysoperla carnea* (Neuroptera, Chrysopidae): actual state of the laboratory method.' in, *Ecotoxicology* (Springer).
- Walters, D. S., and J. C. Steffens. 1990. 'Branched Chain Amino Acid Metabolism in the Biosynthesis of *Lycopersicon pennellii* Glucose Esters', *Plant Physiol*, 93: 1544-51.
- Waschke, Daniel, Yevgeniy Leshch, Julian Thimm, Uwe Himmelreich, and Joachim Thiem. 2012. 'Synthesis of fluorinated ketoheptoses as specific diagnostic agents', *European Journal of Organic Chemistry*, 2012: 948-59.
- Welbaum, G.E. 2015. *Vegetable Production and Practices* (CABI).

GRAPHENE-NANOPARTICLE COMPOSITE GAS SENSORS

Andrew Graves
Chemical Engineering
West Virginia University
Morgantown, WV 26502

ABSTRACT

The fundamental hypothesis being explored in this research is that chemoresistive sensor arrays based on graphene-nanoparticle composites can be used as the basis for an electronic nose for molecular gas phase species of interest in NASA manned and unmanned missions environments. To test these gas sensors, simple pulse tests between an inert gas (argon) and analyte gas (hydrogen or carbon monoxide). These tests were performed at temperatures ranging from $\sim 20^{\circ}\text{C}$ to over 700°C . It was found that undecorated sensors show a convoluted response to both temperature and gas composition. Additionally, it was found that the sensors showed excellent temperature sensitivity. A second test type, static tests, was employed to deconvolute the temperature response from the chemical response uncovered by the pulse tests. For these test, the sensor response were recorded as a function of temperature at a constant gas compositions. The results were then quantitatively compared at corresponding temperatures between gases. In this way, the temperature effects could be accounted for, leaving only the chemical effect. Under these static gas compositions conditions, a large sensitive to the analyte gasses were found. A new, high temperature test setup has been designed and constructed that will allow for a precise control of the temperature; this will allow for the chemical and thermal response of the device to be fully decoupled. Testing with this new system is ongoing. Most importantly, we have begun to develop a fundamental understand of the operation of these devices and the ground work has been laid for the eventual manufacturing of these sensors to serve as electronic noses and in other sensing capacities of interest to NASA.

INTRODUCTION

The excellent physical, mechanical and electrical properties of graphene are well known and over recent years many attempts to utilize these excellent properties have been met with varying degrees of success and the field of sensors is no exception. (1) (2) (3) (4) (5)

Applications of the sensors developed here are of interest to NASA. They range from room temperature applications, involving critical human factor to high temperature applications, such as gas detection nearer high temperature engine components or components that experience high temperatures on atmospheric reentry.

The research detailed here complements and extends past and ongoing efforts on the development and evaluation of graphene devices. Presented here are the initial results of these graphene devices as evaluated for their gas sensing abilities. The graphene synthesis process used was in part developed through a NASA research initiation grant. (6) The broader current research effort in our laboratory is funded in part by the Department of Energy (DOE Award Number: DE-FE0011300) and is focused on the synthesis of graphene-nanoparticle composites, fabrication of the basic sensor structures, and demonstration of overall utility of these sensors for energy related

applications environments. The main goals of the research detailed here are: validating the basic hypothesis (that the graphene-nanoparticle composites can function as an electronic nose for the sensing of a wide range of gasses across a wide range of temperatures) and secondly to develop an in-depth understanding of the fundamental sensor properties and their operation.

To test the hypothesis, a custom gas testing set up and sensor platform was designed and constructed, designated *Mark I*. The Mark I setup enabled testing in different gaseous environments over a wide range of temperatures. Argon, hydrogen and carbon monoxide are the three gasses tested to date and data has been collected from room temperature up to 800°C. A Keithley 4200 semiconductor characterization system (SCS) was used to collect electrical data from the devices as a function of both gas composition and temperature.

A second, high temperature test system, designated *Mark II*, has been constructed and initial testing is underway. The Mark II system allowed for the testing of the same gasses but with much better temperature control and a larger temperature range. The Mark II system more closely models high temperature gas environments.

Background

Two gasses species are currently undergoing testing; both of which are of interest to NASA. The first, carbon monoxide (CO), is a critical human factor important to all manned missions and the second, hydrogen (H₂) is a primary component in fuels used by many rocket engines. Specifically, Rocketdyne's older RS-25 and J-2X engines, but more importantly Rocketdyne's RL10, F1B engines and the Nuclear Thermal Rocket (NTR); all engines planned for use in the new Space Launch System (SLS), the successor to the space shuttle program. (7) This report will detail the results obtained thus far. Once through testing has been completed with these gasses, the obvious next test gas will be oxygen (O₂). Not only is oxygen a critical human factor but also one of the main components in the rocket fuel.

The proposed gas sensing mechanism is based on the adsorption of gas onto the graphene surface and the resulting charge transfer. Once gas molecules have adsorbed onto the sensing surface, a charge transfer will occur. This is driven by the differences in electronegativity between the surface and the gas molecules. This charge transfer will cause the electrical properties of the graphene to change, making it either more or less conductive, depending on the direction of the charge transfer. Adding nanoparticles to the surface of the graphene may modify the charge transfer as well as modify the adsorption rates of different gasses. This will enhance the sensitivity and provide a basis for selectivity of the devices. In this way the sensors can be tuned to a particular type of gas. From here, the typical fingerprinting methodology will begin: an array of sensors, made up of sensors sensitive to specific types of gasses, will be combined on a chip. Each sensor will be electrically monitored independently when the chip is exposed to a gas mixture. The larger the sensor array, the more specific the fingerprint. The sensor array may operate in a simple binary manor, where sensors either respond to a gas or do not. Additionally, once the behavior of each type of sensor is well characterized, the degree to which each sensor responds can be utilized to further add to the specificity of the gas fingerprinting. A simple cartoon illustrating the basic concept of gas fingerprint using a sensor array is shown in Figure 1. This illustration shows a sensors array acting in a simple resistance mode were the sensors respond in one of three different modes: increase, decreases or no change in resistance (trinary response mode) as compared to a

reference state. By simply monitoring the resistance of an array of nanoparticle-decorated sensors, the detection of a range of gases could be achieved.

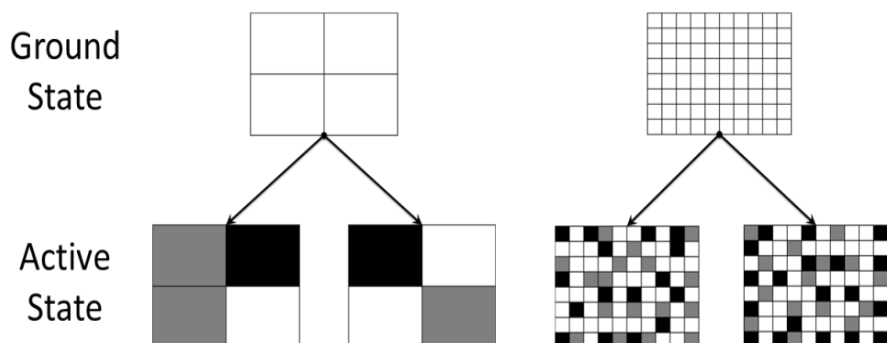


Figure 18: Cartoon depicting the fingerprinting of gasses using different sized arrays and operating in a simple ternary response mode (positive)

Device Assembly

Two to three layer graphene was grown onto a 10 X 10 mm² SiC substrate by Saurabh Chaudhari. (8) An interdigitated gold patterns were deposited onto the graphene surface to serve as electrical contact points for wire bonding and to ensure good electrical communication with the graphene. Individual 2.5 X 2.5 mm² sensors were diced from the larger substrates. A diagram of this pattern can be seen in Figure 2(A).

The Mark I device assembly consisted of four distinct components: the Resistance Temperature Device (RTD), Pt-100 heater, a 16 pin Transistor Out (TO) header and the graphen-SiC-Nanopartical composite. First, the Pt-100 heater leads were spot welded to two pins on the TO header. The RTD was then cemented (via Caramabond 890) to the Pt-100 heater and the RTD leads spot-welded to two additional pins. The graphene composite was then cemented (via Carabond 890) to the heater. Once the cement had cured, several redundant wire bonds were then made between the contact pads on the graphene sample to pins on the TO header. A close up picture of a completed device can be seen in Figure 2 (B, C).

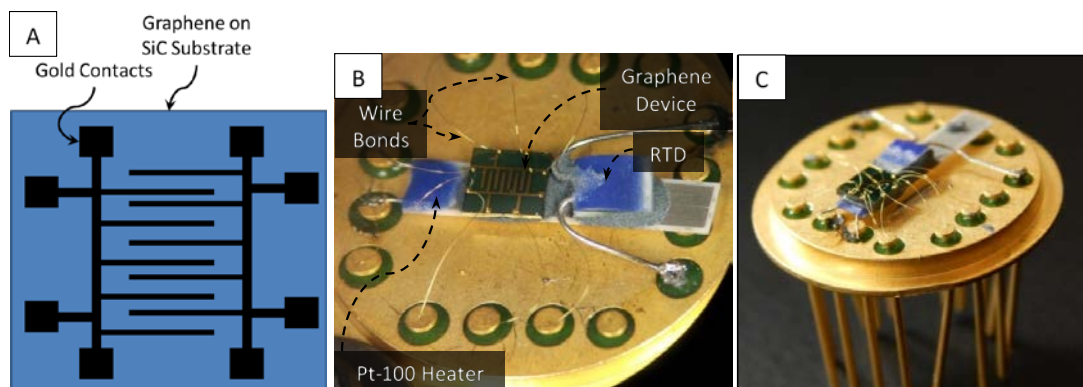


Figure 19: A) A schematic of the interdigitated sensor pattern. B) A picture of a complete device with the identified major components. C) A picture showing the entire TO header

EXPERIMENTAL SETUP

The Mark I custom test setup was designed so that temperature control of the gas sensor and the flow of three different gas streams (one inert carrier gas and two analyte gasses) could be achieved. The temperature of the test device was controlled with a Pt-100 platinum heater. This heater was driven by an operator controlled, variable DC power supply. The gas flows were controlled by a

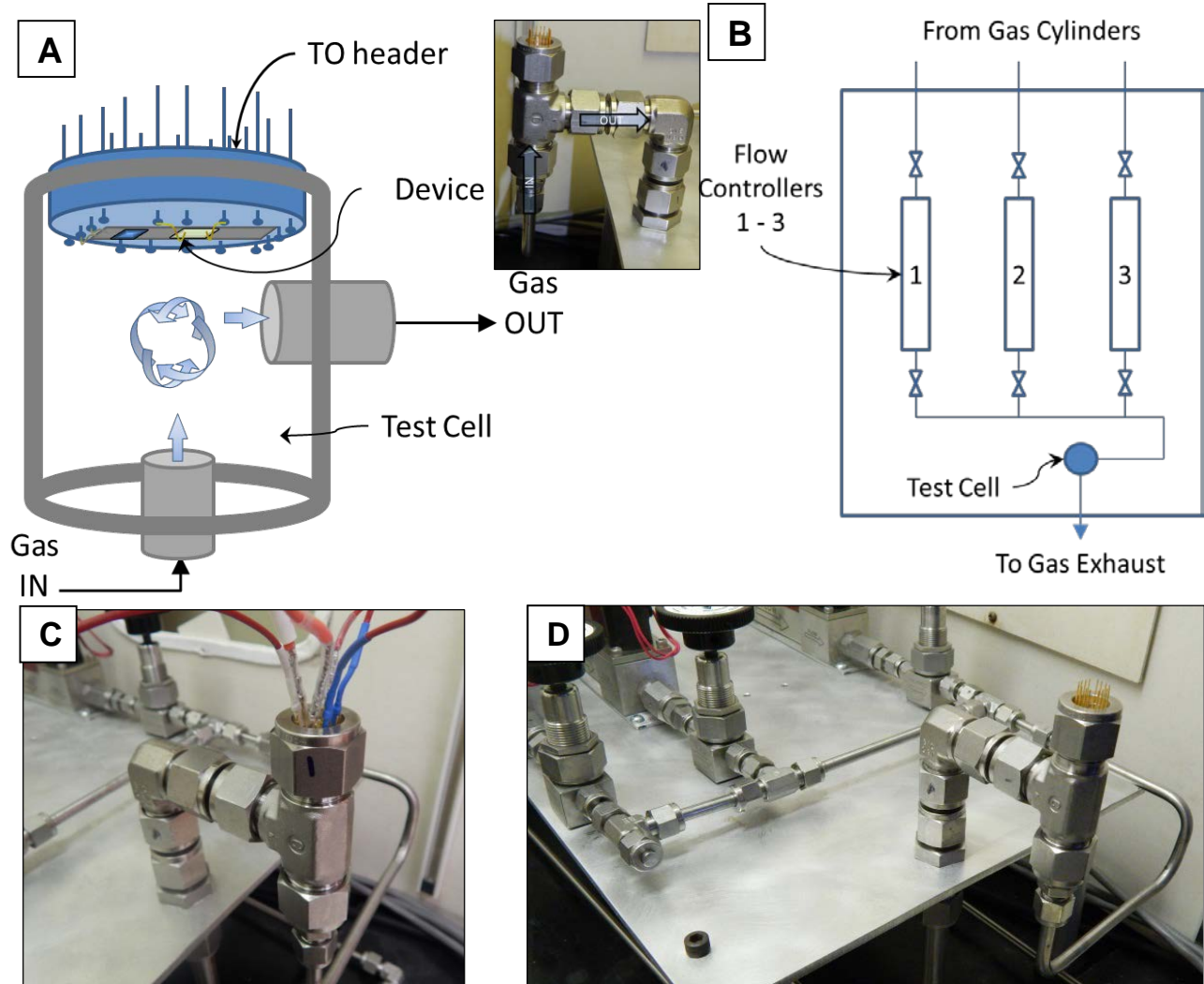


Figure 20: A) A simple schematic of the test cell. B) A simple schematic of the gas flow setup. Flow controller 1 carries Argon, 2 and 3 carries hydrogen and carbon monoxide respectively. The gas plumbing is designed such that tracer gasses are introduced into the main argon line via side injection lines. This ensures good mixing with the carrier gas. C) Electrical connection is made MKS model 247C digital flow controller, also operator control. Electrical readings from the sensor were monitored by a Keithley 4200 semiconductor characterization system (SCS). A rough schematic of the test setup can be seen in Figure 3.

The cell was designed such that good mixing occurs within the cell and the inlet gas mix impinges directly onto the gas sensor. The TO header seals via swage-lock with the test cell. Electrical

contact to the graphene device was made through wire bonds from the device to the output pins in the TO header.

Gas Sensing Methodology

This section describes the manner in which data from the tested sensors were collected and analyzed. Several testing schemes were used to elicit a response from the gas sensors. The first was a simple pulse test, abbreviated “*I-t tests*”. In these tests current readings from the device were recorded as a function of time as gas composition was changed. A temperature was set at the start of the test and a constant voltage bias was applied across the device. The current flow through the device was recorded throughout the duration of the experiment. A steady state background flow of argon was established in the system and then interrupted with pulses of CO or H₂ and the sensor response monitored. All testing was done at atmospheric pressure.

The second test method was abbreviated as “*I-V test*”: The test scheme was executed in the following manner. Starting at room temperature, measured current values were recorded across a voltage sweep while the device was kept at a constant temperature (excluding the Ohmic heating of the device) and constant gas composition. Once data was collected across the voltage sweep range, the temperature of the device was then stepped up and current values were again recorded over the same voltage sweep range but at the new temperature. This process was repeated in a step wise manner until the maximum temperature was reached. The device was allowed to cool, the gas composition was altered and starting at room temperature again, the process was repeated. In this way, the devices current carrying capacity was recorded as a function of both voltage and temperature. This allowed for a comparison to be made in different gaseous environments while accounting for temperature effects. All testing was done at atmospheric pressure.

RESULTS AND DISCUSSION

Initial Device Characterization

Initial stress testing of the device assembly was done in an open air environment. The devices performed very well; the wire bonds maintained electrical and mechanical integrity, the RTD and graphene wafer remained bound to the heater via the high temperature cement, even after several high temperature cycles and TO header did not experience excessive heating. The graphene showed excellent stability at high temperature ($> 600^{\circ}\text{C}$) in the oxidative environment of the open laboratory with no loss in functionality. The device was cycled to high temperature several times over the course of several hours. A picture of a device at high temperature can be seen in Figure 4.



Figure 21: A picture of the initial testing with a device at different stages of the high temperature tests in open air. The device showed excellent stability.

Temperature Sensing

During the initial testing it quickly became apparent that the sensor devices show excellent temperature sensitive. Figure 5 shows the results of IV tests as a function of temperature in an Ar gas flow. The negative voltage and current values indicate polarity of the applied voltage and resulting current.

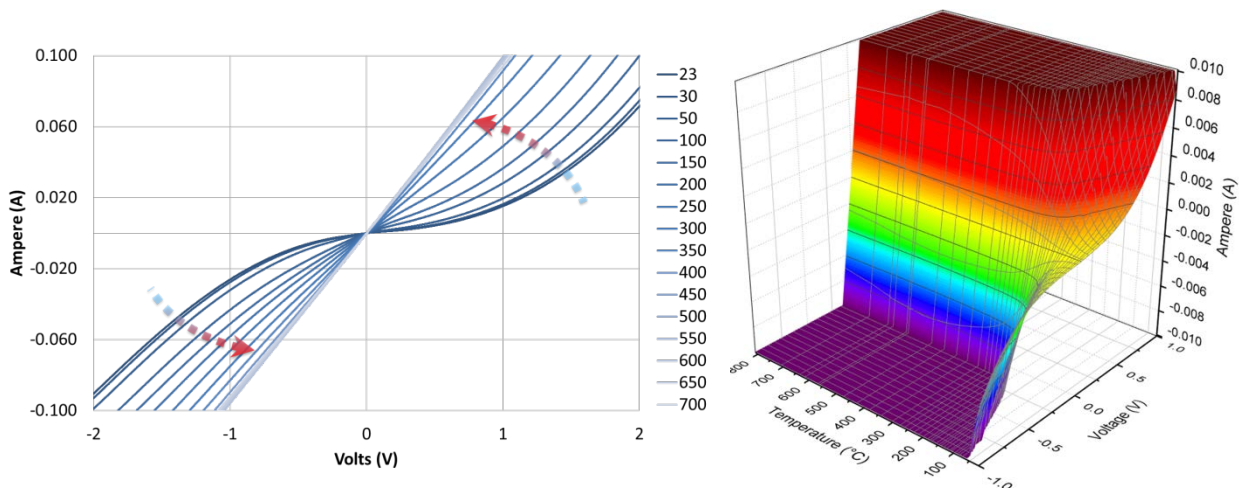


Figure 22: (A) The arrows indicating the shift in IV behavior with increasing temperature. Higher temperatures increase the conductivity of the device. (B) A 3-D plot taken from a similar

Figure 5 (A) shows that, with increasing temperature, the devices electrical properties change in the following two ways. The device become more conductive and exhibits an IV profile which transitions from one of semiconducting Schottky behavior to metallic Ohmic behavior. It can be seen that the resistance of the graphene decreases by a large amount when the temperature is increased through 600 °C and above. Data from a similar test are represented in 3-D from in Figure 5. The transition from Schottky to Ohmic behavior can more clearly be seen in Figure 5(B).

After closer evaluation of the device response on the high end of the temperature range, it was found that there was a temperature at which the devices experience a minimum resistance. Once this temperature was surpassed, the devices resistance began to increase. This temperature was found to vary among devices, but appears to be unaffected by Ar, H₂ or CO environments. To determine the temperature of least resistance (TOLR), a temperature study was conducted. A constant voltage bias was applied to the device and the current passing through the sensor was monitored as the temperature was ramped up. The results of these tests conducted in argon and hydrogen can be seen in Figure 6. While there are slight differences in the two curves, these differences are at present within the repeatability of the experiments (with respect to device consistency and RTD consistency). However, it is conceivable that this metric may become gas sensitive for nanoparticle decorated devices.

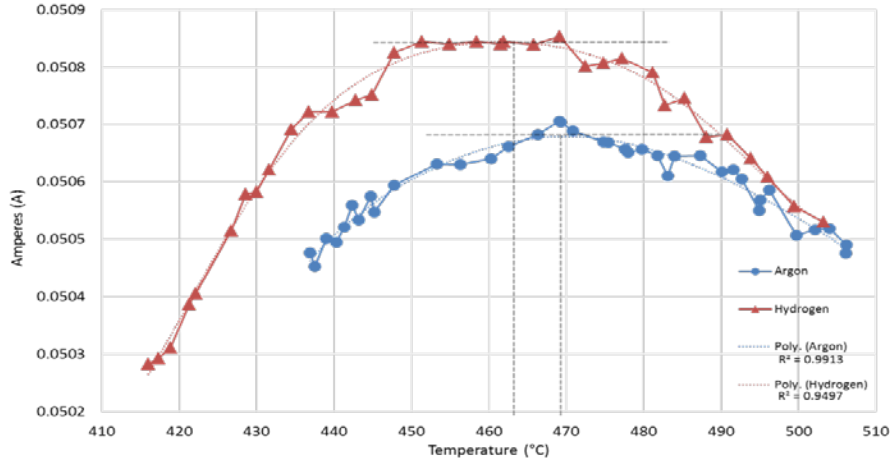


Figure 23: Current as a function of temperature. This plot shows the data from two trials; one is an argon environment and the other in a hydrogen environment. A curve was fitted to the data and the temperature corresponding to its global maxima was found. For this particular device the temperature for minimum resistance was found to be ~463 °C in argon and ~ 469 °C in hydrogen; within the repeatability of the experiment.

Additionally, it was found that the devices experience some level of inconsistent hysteresis when thermally cycled. Occasionally when a device underwent a thermal cycle, its room temperature I-V curve did not return to its pre-heated state. At times the heating cycle improved the devices electrical conductivity, while other times it decreased it. It is not known if this hysteresis is influenced by gas composition or not. At constant temperature, electrically cycling the devices appears to have no hysteresis effect. An example of this behavior can be seen in Figure 7.

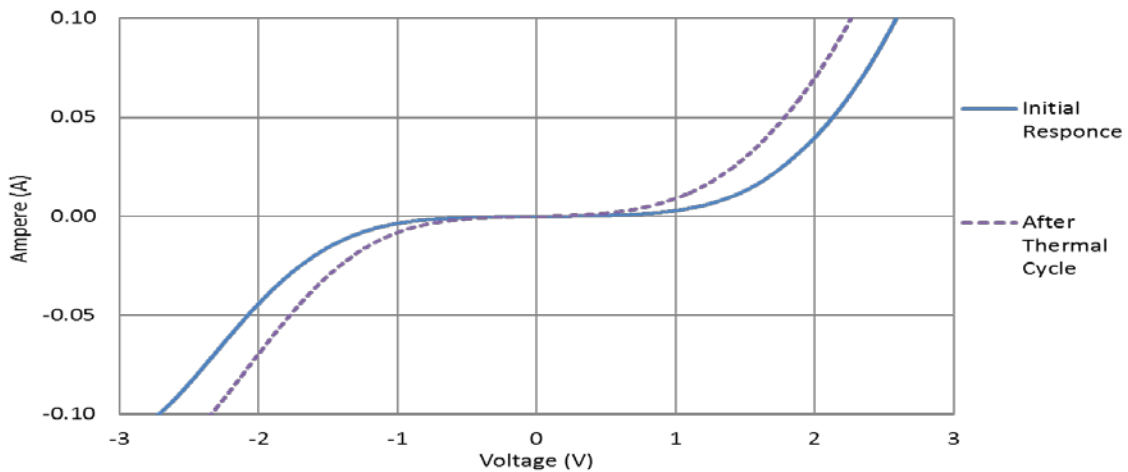


Figure 24: The change in I-V characteristics at room temperature after a thermal cycle to 600 °C.

Gas Sensing

As discussed in the *Background* subsection, one mode of operation for these devices relies on charge transfer between gas molecules and the graphene layers, potentially mediated or enhanced by metallic nanoparticles. It is proposed that this charge transfer could be detected by electrically monitoring the graphene. In order to determine if charge transfer events were occurring (and therefore a potential gas sensing mechanism) two methods of electrical analysis were used: *I-t* and *I-V* tests.

I-t Gas Pulse Results

For these tests a constant voltage was applied to the devices and the resulting current recorded over time. During the course of the experiment, the gas composition of the sensor environment was changed in an on-off stepped manner. Due to the different physical properties of the gasses (thermal conductivity and specific heat) and the low thermal mass of the test system, the temperature of the test setup varies as a function of gas composition. When switching from argon to hydrogen the higher thermal conductivity of hydrogen increases the amount of heat transferred to the cool walls of the test cell. This had an overall effect of cooling the test chamber. Therefore, these pulse results are a combination of both the chemical and thermal effects of the gas on the device. Initially an attempt was made to manually maintain the temperature of the system as the gases were switched, but in so doing the temperature fluctuations masked sensor response. Using an electronic feedback controller would cloud the data in the same way. Because this problem could not be covered in this iteration of the test platform, the Mark II setup was designed and will be discussed in the next section.

In Figure 8 the results of a low temperature, hydrogen pulse test in a background of argon gas can be seen. The starting temperature was 200 °C and the flow rate of both gasses was 20 SCCM. All testing was done at atmospheric pressure.

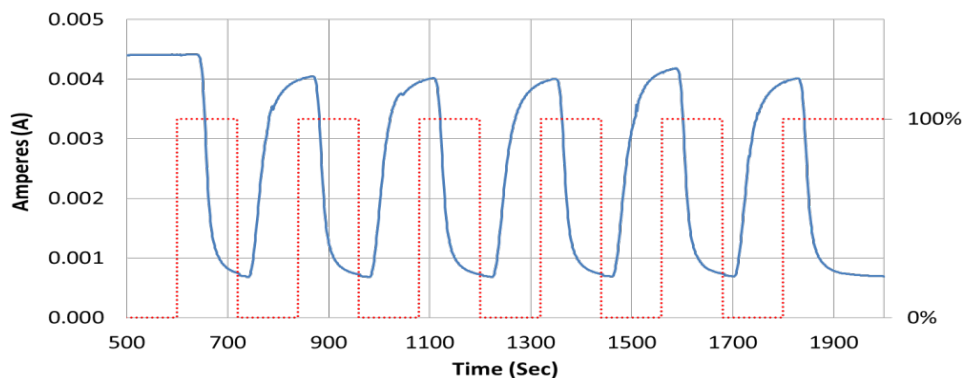


Figure 25: The results of a pulse test: gas composition was cycled every two minutes from Ar to H₂. The device was allowed to stabilize for 500 second in argon with a voltage of 200 mV and a starting temperature of 200 °C. The left axis displays current values which correspond to the solid line, the right axis showing percent hydrogen with the balance being argon.

The results of a high temperature, hydrogen pulse test in a background of argon gas can be seen in Figure 9. The flow rates of both gasses were 20 SCCM, the duration of each pulse was approximately two minutes and the starting temperature was 700 °C.

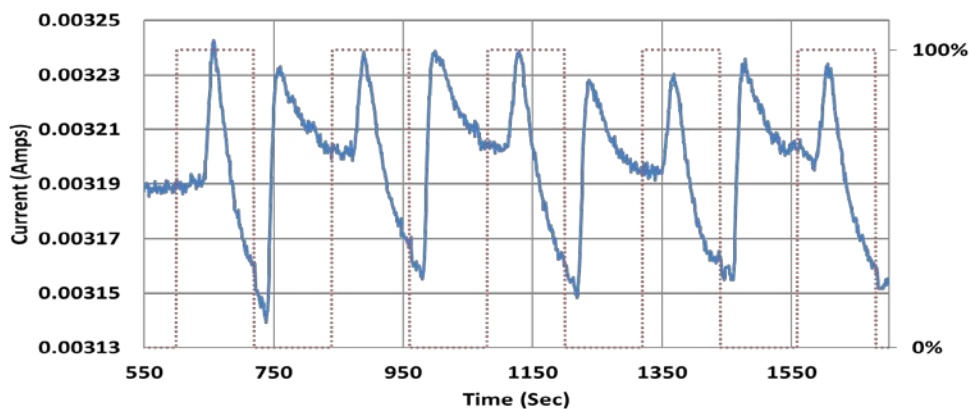


Figure 26: A high temperature pulse test. The background test was argon and the pulse gas was hydrogen. The starting temperature was 700°C. The left axis displays current values which correspond to the solid line, the right axis showing percent hydrogen with the balance being argon.

The sensor response appears to be bimodal with an initial increase in conductivity followed by a decrease in conductivity.

It is believed that the majority of the bimodal response is the result of the device passing through the temperature of minimum resistance (TOMR) (as discussed in *Temperature Sensing* subsection); the device starts out at a temperature above the TOMR then, as the gas composition in the test chamber changes from argon to hydrogen (a more thermally conductive gas) the system cools off, which lowers the temperature of the devices through the TOMR. Based on results presented in the following section, it is reasonable to conclude that there is indeed a chemical response to the gas; however the much larger thermal response masks this. The Mark II test setup will not have this temperature compensation issue as discussed in the *Future Plans* section.

Figure 10 shows the sensor response to both hydrogen and carbon monoxide performed over the course of the same experiment with a background gas of argon. The dotted line shows the hydrogen percentage and the solid line shows the carbon monoxide percentage. There is a marked difference in response to hydrogen versus carbon monoxide, though how much of this is due to the difference in thermal effect of the two gasses is unknown. This issue will be addressed in the *Future Plans* section. In this particular experiment there was a slight drift in the baseline response.

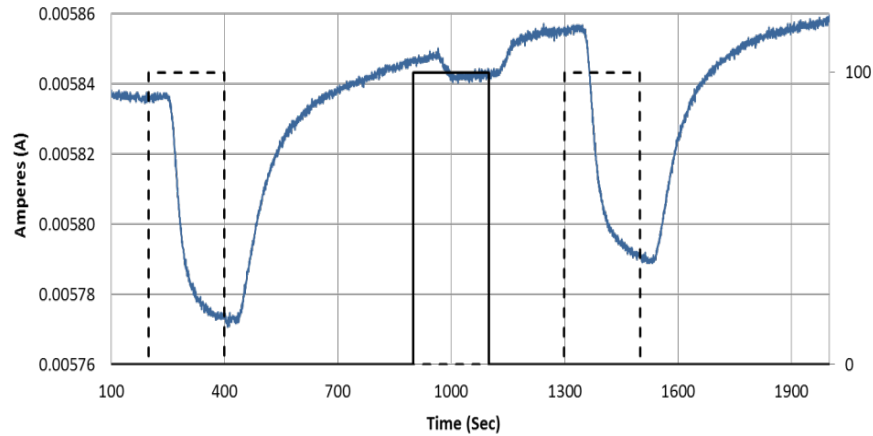


Figure 27: The left axis displays current values which correspond to the solid line, the right axis showing percent hydrogen and carbon monoxide with the balance being argon.

IV Results

As described in the Gas Sensing Methodology subsection, current data for the I-V tests were made as a function of temperature for a particular gas. The resulting data can then be used to construct a 3-dimensional plot of current, voltage and temperature for each gas, which illustrates the device behavior when exposed to the gas. By considering the response of the device in inert argon to be the devices ‘ground state’, the response of the device to hydrogen or carbon monoxide can be then referenced to the original response in argon. The resulting differences in these 3-D surfaces are a graphical representation of the gas response between the two different gases. An example of this analysis can be found in Figure 11. In Figure 11(A, B) the sensor response in argon and hydrogen as a function of voltage and temperature can be seen. In both cases, the apparent “floor” or “zero” in the response is artificially introduced due to the current limitation imposed by the Keithley 4200 semiconductor characterization system.

By taking these 3-D surfaces and subtracting the hydrogen surface from the argon surface, the plot in Figure 11(C) is generated. The plot in Figure 11(C) is the 3D surface generated when the difference between each corresponding data point from Figure 11(A) and Figure 11(B) are plotted. In order to determine how much the device changes for its base response (taken to be in inert argon) Equation 1 was used to construct the surface seen in Figure 11(D). The resulting surface is the percentage change between each corresponding point from Figure 11(A) and Figure 11(B).

$$\frac{(H_2 \text{ response} - Ar \text{ responses})}{Ar \text{ Resonse}} \times 100 \% = \% \text{ Change from Ar to } H_2 \quad (1)$$

The percentage difference from argon to hydrogen becomes large at very low voltages. This is because this is where the largest difference between Schottky and Ohmic behavior is seen; the device exhibits Schottky behavior at those points in argon (the device passes almost zero current at low voltages) but then at these same points in hydrogen, the device is Ohmic in nature and therefore drew an amount of current that is proportional to the voltage across it; a small amount but still many times more than when the device was showing Schottky behavior in the same regime.

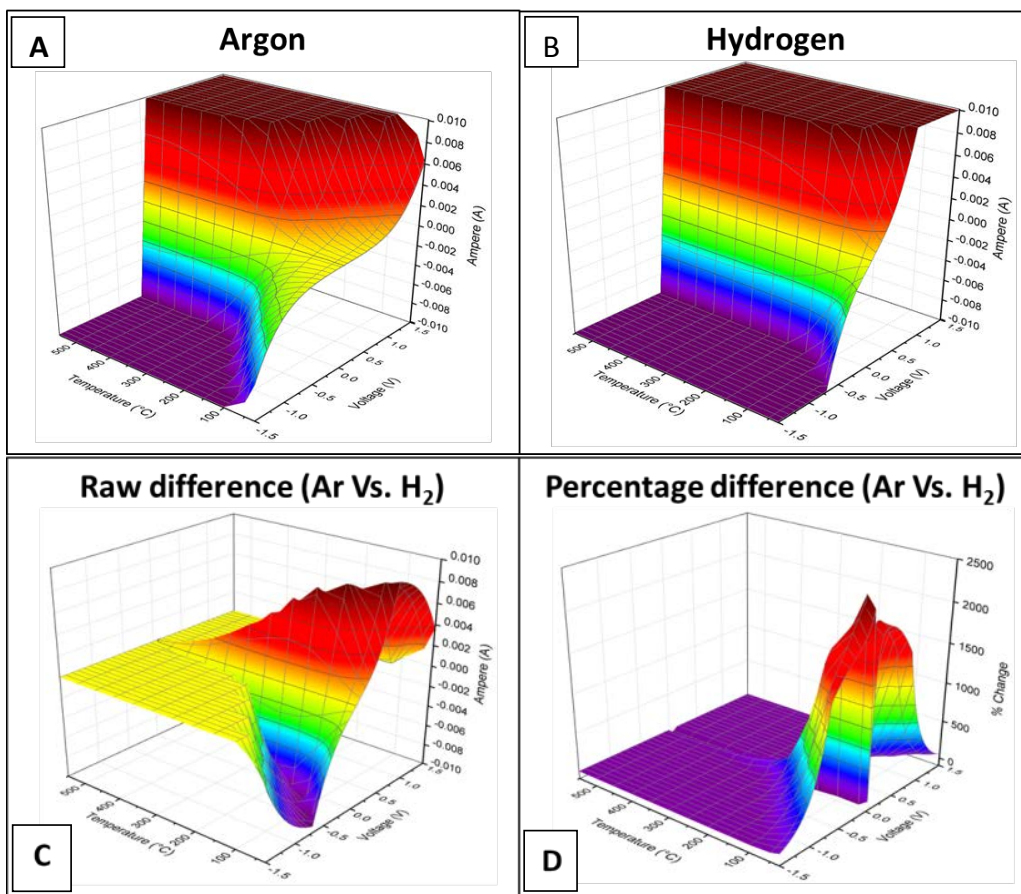


Figure 28: 3-D plot showing the response in argon (A) and hydrogen (B). The corresponding raw differences in current (C) and the resulting percentage change in current (D).

Similar tests were conducted with CO. However, it was found that at elevated temperatures a nickel film (confirmed via XPS) was deposited onto the surface of the device, which shorted out the electrical contacts on the device surface. It is suspected that the nickel was scavenged from the stainless steel test chamber walls by the carbon monoxide once the walls reached a critical temperature. This will not be a problem with the Mark II test setup, as detailed in the *Future Plans* section. It is unknown exactly at what temperature this occurs, though it is suspected it may occur around 400 °C. However, as seen in Figure 12, at low temperatures (before nickel deposition) there is a clear difference in response when compared with the same plot for hydrogen (Figure 10(D)). While the percentage change from the devices' ground state in argon is almost an order of

magnitude less for carbon monoxide than for hydrogen, the devices peak sensitivity point shifts up in the temperature range approximately 200 °C. This indicated that with future testing, it may be possible to differentiate between hydrogen and carbon monoxide.

Future Plans

As mentioned in the *Results and Discussion* section, testing with carbon monoxide at elevated temperatures is limited with the current test system. At temperatures above 400 °C a nickel film deposits onto the surface of the device which shorts the device out. This is believed to occur once the walls of the test chamber reach a critical temperature. Once this occurs, nickel is scavenged by the carbon monoxide gas from the stainless steel walls of the test chamber and then deposited onto the device surface. A before and after picture of a shorted out device can be seen in Figure 13. The design of the Mark II test system, discussed later in this section, will eliminate this problem.

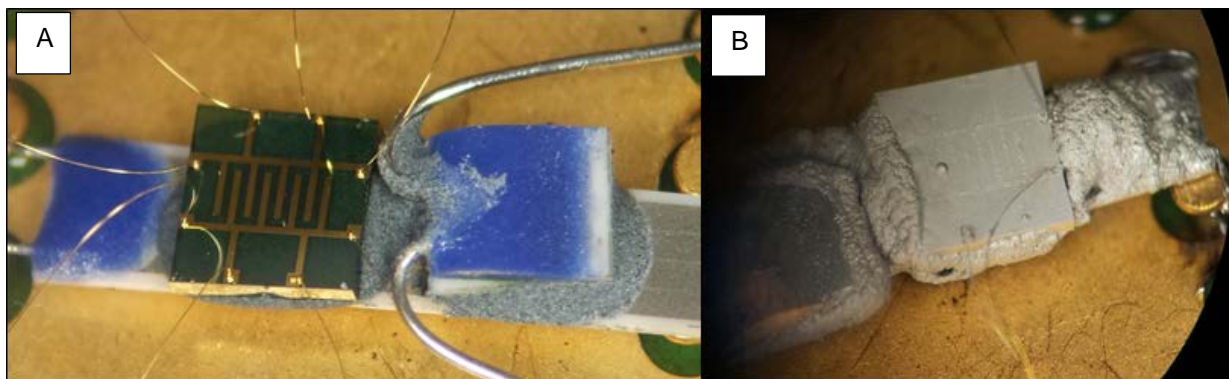


Figure 30: A device before (A) and after (B) high temperature testing with carbon monoxide. The light colored nickel film is clearly seen in (B). The composition of the film was confirmed via XPS.

The Mark I system has several advantages: simple operation, high testing throughput and has allowed us to show proof-of-concept data with regards to the gas sensing potential of the devices. Initially designed for a maximum temperature of only 500 °C, the current test setup has exceeded expectations. We have managed to collect meaningful data at temperatures as high as 800 °C. It will continue to be used to supplement the next generation testing setup. However, there are inherent limitations in this design including the localized heating of the sample and the temperature restrictions of the setup. The heater heats only the sensing wafer to the desired temperature while the test gasses enter the test cell several hundred degrees cooler and are then only partially heated when in close proximity to the device. The test gasses only reach the set temperature once they come into contact or near-contact with the sensing surface. Depending on the transport characteristics of the gasses and sensing mechanism of the device, this heating method can potentially affect the sensing performance. Because of these limitations, the Mark II test system was designed and constructed.

The Mark II Test System

The Mark II test system consists of a bench-top high-temperature furnace and a ceramic sample probe. A 1.5 inch OD quartz tube serves as the gas test chamber inside the furnace. The new sensor platform (discussed below) is mounted to the end of a 4-hole ceramic rod. The ceramic rod houses two platinum test leads that connect to the sensor platform on the furnace-side and on the lab-side connect to the electrical monitoring equipment. A simple schematic of the Mark II test system can be seen in Figure 14(A).

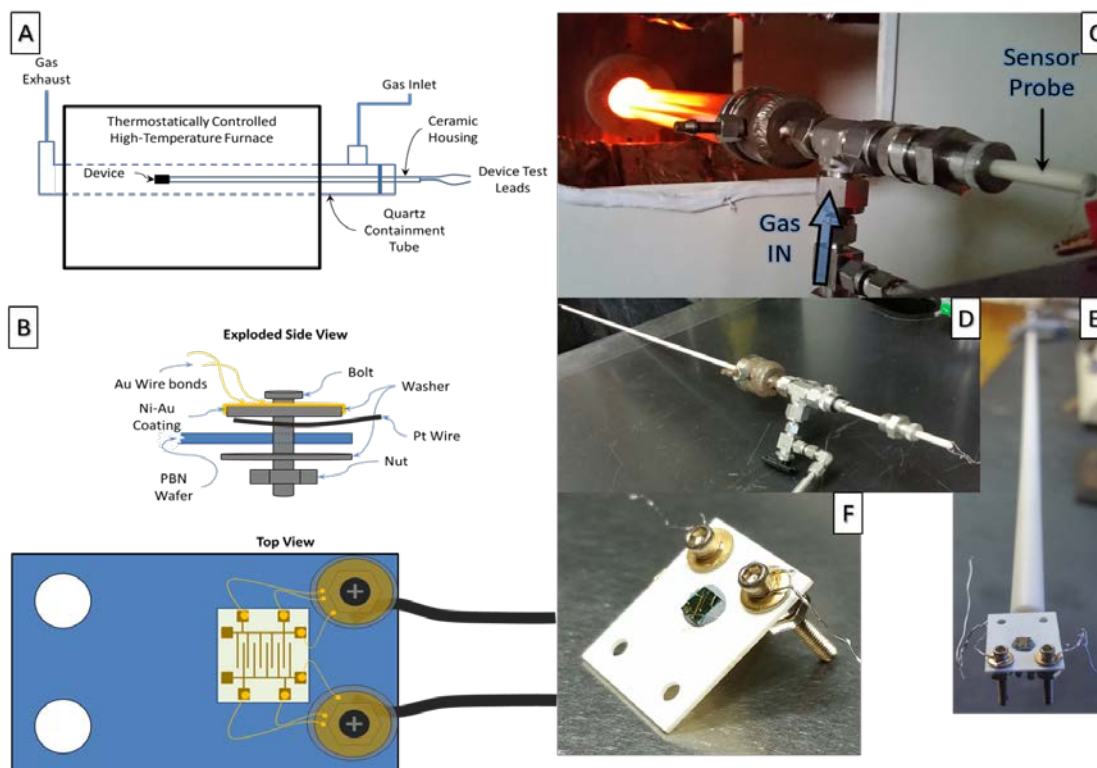


Figure 31: A) A simple schematic of the next generation testing setup. The new materials and new design will allow for much higher and more stable tests temperatures to be achieved. This new design will preheat the incoming gasses and maintain the entire test device at the desired temperatures. B) A simple schematic of the new sensor platform; TOP: an exploded view of the bolt assembly where the sample electrically interfaces with the Pt test leads, BOTTOM: top view of the PBN wafer-sensor assembly. C) The complete sensor probe assembly fully inserted into the furnace. D) The sensor probe and gas inlet assembly prior to insertion. E) The sensor mounted to the tip of the four-hole ceramic rod. F) A close-up of the new sensor platform.

This design allows for much higher temperatures to be reached (in excess of 1000 °C) and a more consistent temperature. Due to the method of heating and the combined thermal mass of the system, the temperature of the device will be unaffected by gas composition. This solves perhaps the biggest problem with the Mark I test setup.

The Mark II test system required a complete redesign of the sensor platform. Rather than an aluminum-gold TO header acting as the mounting scaffold for the sample (as was the case in the

Mark I design), an ultra-high temperature resistance ceramic was used: pyrolytic boron nitride (PBN). The PBN wafers dimensions were: 12.0 mm X 15.0 mm X 0.50 mm; the wafers had four 1.60 mm ID holes machined in each corner, 2.40 mm from the sides of wafer. A bolt/washer/nut assembly was mounted through two of the holes. A platinum wire was sandwich between the bolt head and the washer. The washers were coated with 200 nm of nickel and 600 nm of gold via e-beam evaporation. The sensors were cemented to the PBN. Gold wire bonds were made between the sensors contacts and the Ni-Au coated washers. The Pt wires from the sensor platform were braded with the Pt wires from the end of the ceramic rod. A rough schematic of this can be seen in Figure 13(B) and pictures of the sensor platform and ceramic rod assembly can be found in Figure 13(E - F).

Because the gasses are heated in a quartz tube, this eliminated the contamination issues associated with CO that we experienced with the Mark I design as well as allowing for a wider range of gasses to be tested, such as hydrazine (of particular interest due to its use in rocket fuels). Additionally, by externally heating the device, we can more closely simulate high temperature environments. Preliminary experiments and high quality electrical measurements have been taken with the Mark II test setup. All in all, the Mark II test setup is proving to be very promising based on initial experiments.

Fingerprinting

Testing with devices decorated with metallic nanoparticles is currently ongoing but incomplete. The primary focus of work to date has been the development of reproducible nucleation and growth methods and in qualitative characterization of the composite system. This includes particle size and high distribution along with surface coverage. Electrical and gas characterization studies of the composite devices have been initiated and the next step will be to test multiple devices at once. The Mark II sensing platform was designed with this in mind. The extra holes in the ceramic rod and PBN wafer allow for additional test leads to be connected to a second device. Testing two sensors, with different nanoparticles, is the first step towards developing fingerprints for specific gasses. Optimization and characterization of the nucleation of Au, Pt, Ag and Ir nanoparticles onto the graphene surfaces has been on-going. Analysis techniques have included AFM and SEM and show promising results. Figure 15 is an SEM image of a graphene surface which has had silver nanoparticles nucleated on the surface. Efforts will continue on the optimization and characterization of the nanoparticle systems.

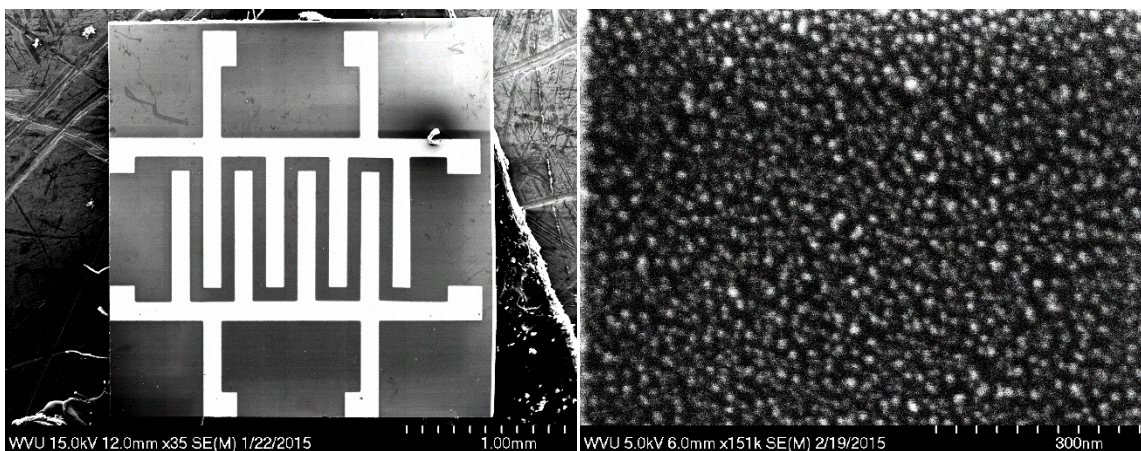


Figure 32: Initial characterization of metallic nanoparticles: A) SEM image of the sensor. Scale bar is 1.0 mm B) SEM image of Ag nanoparticles on the graphene surface. Scale bar is 300 nm.

ADDITIONAL BENEFITS OF THE RESEARCH MADE POSSIBLE BY THE NASA FELLOWSHIP

In addition to the scientific knowledge gained about these gas sensors, participation in the NASA fellowship program has yielded many additional benefits. The challenges of designing and constructing two different custom testing setups proved to be a great learning experience. Through this research I have had the opportunity to be exposed to areas outside my area of training; specifically with respect to the electrical engineering aspects of this project. This has turned into an incredible learning opportunity that I would have otherwise not been able to experience. In addition to the theoretical knowledge gained, over the course of this research I have had the opportunity to learn real world laboratory skills. I have been able to become proficient with SEM, AFM, wire-bonding, e-beam evaporation and electrical characterization techniques.

CONCLUSION

Over the past nine months we have refined the fabrication method of the sensor devices assemblies; additionally, we have designed and built two functioning testing platforms (the Mark I and the Mark II) for the evaluation of these sensors under different environments. We have begun to develop a fundamental understanding of the operation of these devices and the ground work has been laid for an electronic nose for molecular gas phase species of interest in NASA manned and unmanned missions environments. We have found the devices to be very temperature sensitive and sensitive to changes in gas composition. This sensitivity has expressed itself as a change in the resistivity of the few-layer graphene surface of the devices.

Upon exposure to hydrogen, the device's electrical conductivity increases as compared to conductivity in argon. A similar behavior is found with carbon monoxide; though approximately an order of magnitude less in response. Through trial and error we have discovered the limitations of the Mark I test setup and, having learned from that, designed and built the more capable Mark II setup.

The fact that graphene has both a thermal and a chemical response may at first seem a complicating factor but given the ability to independently measure temperature, this should not be a problem. In fact, it may turn out that the response of the graphene sensor array to a temperature ramp may form a basis for the gas characterization algorithm. In this case, the combined effects, which depend on gas identity, may prove useful. Additionally, a sensor array built from these sensors could prove to be all-in-one temperature and chemical sensing device. Finally, the fact that graphene is sensitive to changes in temperature suggests that, suitably passivated with respect to chemical interactions, graphene itself it could be used as a temperature sensor and possibly that one- and two-dimensional arrays of graphene could be used for thermal imaging among many other temperature applications.

ACKNOWLEDGEMENTS

First, I wish to thank NASA WV Space Grant Consortium for their funding and support without which this research would not have been possible. I would also wish to thank my research adviser, Dr. Charter Stinespring, whose guidance and assistance has extended well beyond what is required. I wish to thank the scientist who actually fabricates the graphene surfaces and pioneered the nanoparticle nucleation studies, Saurabh Chaudhari, without him there would be no devices; also, an undergraduate student, Megan Cain who has assisted greatly in the analysis of the nanoparticle component of this project.

REFERENCES

1. *Properties of graphene: a theoretical perspective*. **D.S.L. Abergel, V. Apalkov, J. Berashevich, K. Ziegler, Tapash Chakraborty**. 4, s.l. : Advances in Physics, 2010, Vol. 59, pp. 261-482.
2. *Intrinsic Response of Graphene Vapor*. **Yaping Dan, Ye Lu, Nicholas J. Kybert, Zhengtang Luo**,. 4, 2009, Nano Letters, Vol. 9, pp. 1472-1475.
3. *Adsorption of H₂O, NH₃, CO, NO₂, and NO on graphene: A first-principles study*. **Leenaerts, O, Partoens, B and Peeters, F.M.** 12, 2008, Physical Review B, Vol. 77.
4. *Practical Chemical Sensors from Chemically Derived Graphene*. **Fowler, JD, et al.** 2, 2009, ACS Nano, Vol. 3, pp. 301-306.
5. *Detection of individual gas molecules adsorbed on graphene*. **Schedin, F, et al.** 9, 2007, Nature Materials, Vol. 6, pp. 652-655.
6. *Novel Method for Producing Graphene Sensors and Electronics*. **Grant, NASA Space Grant Consortium Research Initiation**. 2008-2009.
7. **Rocketdyne, Aerojet**. <http://www.rocket.com/space-launch>. *www.rocket.com*. [Online] 2014. <http://www.rocket.com/space-launch>.
8. **Chaudhari, Saurabh**. *Graphene from SiO₂*. Chemical Engineering, WVU. s.l. : West Virginia University, To Be Published. PhD Dissertation.

AUTONOMOUS MINING OF LOOSE AGGREGATE

Alexander Hypes
Master of Science – Mechanical Engineering
West Virginia University
Morgantown, WV 26501

ABSTRACT

Getting objects to space is a high cost activity principally limited by the objects weight. One method of getting larger objects into space would be to create them there in the first place. Mining is the first step towards larger objects in space and unlocks the door leading to super space structures and long range space vessels. Autonomous mining provides the ability to mine in remote places found in space without necessitating human control. These same techniques have many terrestrial applications such improved mining safety, reduced mining costs, and autonomous transportation of materials. Pose estimation of mobile robots requires alternative methods when GPS and magnetic heading information are unavailable.

This paper presents a method to estimate the pose of a ground-based mobile robot in GPS-denied environments. The proposed navigation system has applications in extraterrestrial environments where GPS systems are not present and magnetic fields are absent or unknown. This work develops an algorithm utilizing ultra-wide band (UWB) ranging radio data coupled with an inertial-navigation system (INS) to estimate position and heading in an unknown outdoor environment. The proposed system requires a single base station from which a relative pose is estimated. The proposed method is verified through simulation. The results were presented at the American Institute of Aeronautics and Astronautics (AIAA) Region I Student Conference.

INTRODUCTION

One of NASA's primary goals is the advancement of STEM fields through space exploration and flight. One of the biggest barriers of space flight is the high cost of putting heavy objects into space. One proposed method of reducing cost would be to develop in-situ resource utilization (ISRU). Some of the most abundant resources available in space can be found in the rocks and loose aggregate found on the surface of Planets, moons and asteroids. The first step towards utilizing these resources is to mine and transport them to a location where further processing can be done. Autonomous mining would allow for both the mining and transportation of loose aggregate found on the surface of many planets and asteroids²³.

On Earth, the process of mining valuable minerals requires highly skilled equipment operators and often puts both operators and miners in or near dangerous situations. The labor required to operate these machines as well as the safety equipment necessary to protect workers in these environments is both costly and time consuming to setup and maintain²⁴. West Virginia has a long history of mining operations and research that can improve the mining process could strongly benefit the state.

Autonomous mining provides the ability to move loose aggregate from one location to another without human intervention. Autonomous mining can be safer than traditional mining in that it removes humans from dangerous environments and it also allows for mining in highly remote locations, such as asteroids or other planets. It is cost effective due to its ability to be both highly optimized and without highly skilled operators.

A major technical hurdle for autonomous mining is the problem of the robot knowing where it is within a given environment, known as localization or pose estimation. Localization is accomplished through the use of multiple sensors to accurately predict the robots current location given certain information. A Kalman filter is the de facto standard for this type of sensor fusion. A Kalman filter is a process that operates recursively on streams of noisy sensor data to produce a statistically optimal estimate of the system state. Less formally, Kalman filters can be used to merge data statistically from multiple sources (which might be unreliable in the short run) to form a more accurate estimate of the system state (in this case the position).

Pose estimation of robots in environments lacking GPS and magnetic fields can be challenging. Before the advent of GPS and other global navigation systems, inertial navigation systems (INS) were used for position sensing¹. INS provides dynamic information through direct measurements of instantaneous accelerations and gyroscopic angular rates. INS is attractive as it is self-contained, nonradiating, and nonjammable². INS based navigation methods require an external observable to overcome long-term integration drift^{2,4}. Common external observables used for navigation are the Earth's magnetic field, visual odometry, and navigation systems such as GPS¹⁵. Many harsh environments (indoor, urban canyon, extraterrestrial, etc.) lack or prevent the use of such observables⁴.

GPS-denied research to date has focused primarily on flight navigation (e.g. unmanned aerial vehicles (UAV), micro air vehicles (MAV), projectiles)^{6,21} and underwater navigation⁵ typically using machine vision as an relative positioning mechanism^{6,15,21}. Ground-based research typically focuses on Simultaneous Localization and Mapping (SLAM) techniques for use with autonomous vehicles^{18,19,20}. SLAM techniques, although having high accuracy, typically have high processing requirements due to the landmark extraction, multiple hypothesis tracking methods, and large maps frequently employed^{19,20}.

One method of obtaining an external positioning reference is through the use of Ultra-Wide Band (UWB) ranging radios. UWB radios have been in used in military applications for over 50 years⁷. UWB radios provide centimeter level geometric distance over kilometers of distance between pairs of radios⁸. Due to their high resolution and bandwidth, UWB radios are able to provide high ranging accuracy even in the environments typically found in GPS-denied areas⁴.

UWBs also find use in indoor motion capture systems which require very high accuracy¹⁶ as well as in outdoor systems seeking higher accuracy than GPS alone could provide¹⁷. Ranging accuracy is principally limited by positive bias due to multipath propagation and the increase of measurement variance with distance^{4,7}. An extended Kalman filter (EKF) is used in the proposed algorithm to combine navigation information efficiently. The EKF has a long history of use as a reliable navigation filter for state estimation^{10,11} and is an attractive due to its ability to compensate for measurement noise error^{10,12,14}.

The rest of this paper is organized as follows. The Nomenclature immediately follows this section and presents a list of terms and symbols used throughout the paper. The System Description section presents the description of the proposed navigation system and its overall configuration. System Modeling details the mathematical relationships used to model the robot kinematics, the navigation filter, and the measurement noise. Simulation and Results details the setup of the simulation environment, its initial conditions, and the results of the simulations. The Discussion section follows the conclusions based on the simulations. Dissemination follows the public display of the results at the AIAA Region I Student Conference in the form of a technical paper and a presentation. Conclusions details the conclusions from the overall project and the experiences gained.

NOMENCLATURE

a	= generic signal vector
a_m	= generic signal vector with noise added
A_x, A_y	= homing beacon ranging radio A components of position (m)
B_x, B_y	= homing beacon ranging radio B components of position (m)
f	= state transition function
F_k	= state transition Jacobian matrix at time-step k
h	= observation function
H_k	= observation Jacobian matrix at time-step k
I	= identity matrix
l	= distance between wheels (wheel track) (m)
L_{1k}, L_{2k}	= geometric distance between homing beacon radios and robot at time-step k (m)
$L_{1k,m}, L_{2k,m}$	= measured geometric distance between homing beacon radios and robot at time-step k (m)
O_r	= instantaneous center of rotation
P	= estimated covariance matrix
Q	= process noise covariance matrix
r	= radius of distance to O_r (m)
r_w	= wheel radius (m)
R	= observation noise covariance matrix
sn	= additive noise function
u_k	= control input vector
V_L, V_R	= components of tangential wheel velocity (m/s)
$V_{Lk,m}, V_{Rk,m}$	= measured components of tangential wheel velocity at time-step k (m/s)
V_x^B, V_y^B	= components of robot velocity in body frame coordinate system (m/s)
x, y	= components of robot position in local coordinate system (m)
X_k	= state vector at time-step k
\tilde{y}_k	= Kalman innovation residual at time-step k
Y_k	= output vector at time-step k
Z_k	= observation matrix at time-step k
Δt	= change in time since last time-step k (s)
θ	= robot heading (rad)
$\dot{\theta}, \omega$	= yaw angular rate of change (rad/s)
σ_a	= standard deviation of signal noise value
σ_L	= standard deviation of homing beacon ranging radio separation distance variation (m)
$\sigma_{L_1}, \sigma_{L_2}$	= standard deviation of ranging radio geometric distance measurement noise (m)
$\sigma_{V_L}, \sigma_{V_R}$	= standard deviation of wheel velocity measurement noise (m/s)

- σ_θ = standard deviation of yaw measurement noise (rad/s)
- φ = gyro drift random walk component
- $\omega_{k,m}$ = measured yaw angular rate of change at time-step k (rad/s)
- ω_L, ω_R = angular speed of each wheel (rad/s)

SYSTEM DESCRIPTION

The proposed navigation system consists of a homing beacon and a differentially driven mobile robot. The homing beacon is outfitted with two (2) UWB ranging radios separated by a known distance as shown in Fig. 1. The robot is equipped with a single UWB ranging radio, an IMU gyroscope configured to measure yaw rate, and the ability to measure the angular velocity of the left and right powered wheels.

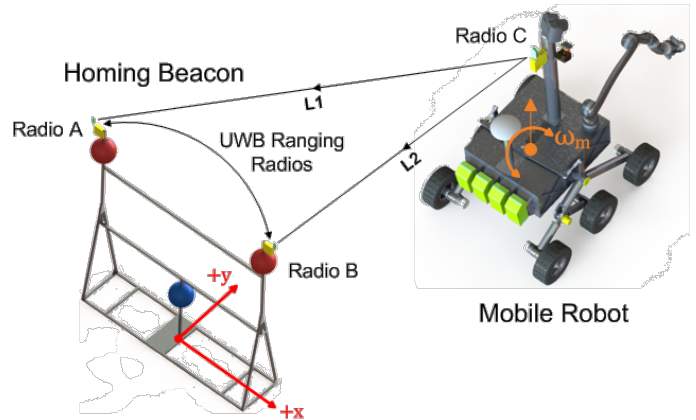


Figure 1. System Overview

SYSTEM MODELING

Robot Locomotion Model

The robot is modeled as a differential drive robot using input wheel velocities as shown in Fig. 2. First l is defined as the wheel track, r_w is defined as outside radius of the wheel. A key assumption of this model is that no slipping of the wheels occurs at any time. If both the right wheel velocity V_R and the left wheel velocity V_L are equal, the robot will translate in a straight line without a change in heading. If both inputs have the same magnitude but opposite directions, the robot will rotate without translating¹³. If the two velocities are different, the robot will translate along an arc of radius r about an instantaneous center of rotation O_r and its heading will change with a yaw rate of ω as follows:

$$O_r = \frac{l(V_R + V_L)}{2(V_R - V_L)} \quad (1)$$

$$\omega = \frac{V_R - V_L}{l} \quad (2)$$

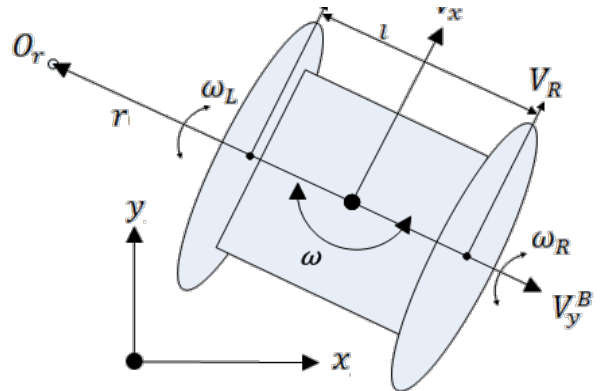


Figure 2. Robot Locomotion Diagram.

Using these equations yields the kinematic velocity model for the robot:

$$V = \omega O_R = \frac{V_R + V_L}{2} \quad (3)$$

The tangential wheel velocities (V_R, V_L) and the rotational rates of each wheel (ω_R, ω_L) are defined as follows:

$$V_R = r_w \omega_R \quad (4)$$

$$V_L = r_w \omega_L \quad (5)$$

Defining V_x^B and V_y^B as the respective x and y velocities in the body frame of the robot, the above equations can be rearranged into matrix form as follows:

$$\begin{bmatrix} V_x^B \\ V_y^B \\ \dot{\theta} \end{bmatrix} = \begin{bmatrix} r/2 & r/2 \\ 0 & 0 \\ r/l & -r/l \end{bmatrix} \begin{bmatrix} \omega_R \\ \omega_L \end{bmatrix} \quad (6)$$

Kalman Filter Equations

An Extended Kalman Filter (EKF) is used as the base localization and sensor fusion algorithm as derived in Ref. 14. The EKF has input vector u_k , which contains the wheel velocities (V_R and V_L), and output vector y_k , containing the geometric distance from each ranging radio to the robot (L_1 and L_2) and the yaw rate of the robot (ω). The filter also defines state vector X_k containing the robots position and heading (x_k, y_k, θ_k) at timestep k .

The continuous time body frame motion model Eq. 6 is discretized into finite time-steps with index k and the time since last time-step is defined by Δt . Eqs. 8, 9 and 10 represent the position and heading of the robot after conversion into the local coordinate system.

$$u_k = \begin{bmatrix} V_{Rk} \\ V_{Lk} \end{bmatrix}_{2 \times 1} \quad (7)$$

$$x_k = x_{k-1} + V_x^B \Delta t \cdot \cos(\theta_{k-1}) = x_{k-1} + \Delta t \frac{(V_{Rk-1} + V_{Lk-1})}{2} \cos(\theta_{k-1}) \quad (8)$$

$$y_k = y_{k-1} + V_y^B \Delta t \cdot \sin(\theta_{k-1}) = y_{k-1} + \Delta t \frac{(V_{Rk-1} + V_{Lk-1})}{2} \sin(\theta_{k-1}) \quad (9)$$

$$\theta_k = \theta_{k-1} + \omega \Delta t = \theta_{k-1} + \Delta t \frac{(V_{Rk-1} - V_{Lk-1})}{l} \quad (10)$$

The discrete equations are then formulated into state vector X_k which can be estimated using the state transition function f from the state vector X_{k-1} and inputs u_{k-1} for the previous time-step.

$$X_k = f(X_{k-1}, u_{k-1}) = \begin{bmatrix} X_k \\ y_k \\ \theta_k \end{bmatrix}_{3 \times 1} = \begin{bmatrix} x_{k-1} + \Delta t \frac{(V_{R_{k-1}} + V_{L_{k-1}})}{2} \cos(\theta_{k-1}) \\ y_{k-1} + \Delta t \frac{(V_{R_{k-1}} + V_{L_{k-1}})}{2} \sin(\theta_{k-1}) \\ \theta_{k-1} + \Delta t \frac{(V_{R_{k-1}} - V_{L_{k-1}})}{l} \end{bmatrix}_{3 \times 1} \quad (11)$$

The state transition Jacobian F_k is calculated by taking the Jacobian of f with respect to X_k as follows¹⁴:

$$F_k = \left. \frac{\partial f}{\partial X} \right|_{X_{k-1}, u_{k-1}} = \begin{bmatrix} 1 & 0 & -\Delta t \frac{(V_{R_{k-1}} + V_{L_{k-1}})}{2} \sin(\theta_{k-1}) \\ 0 & 1 & \Delta t \frac{(V_{R_{k-1}} + V_{L_{k-1}})}{2} \cos(\theta_{k-1}) \\ 0 & 0 & 1 \end{bmatrix}_{3 \times 3} \quad (12)$$

Defining the coordinates of the ranging radios on the homing beacon as A_x A_y for radio A and B_x B_y for radio B, the geometric distances L_1 and L_2 between robot radio and the respective homing beacon ranging radios can be calculated as follows:

$$L_{1k} = \sqrt{(A_x - x_k)^2 + (A_y - y_k)^2} \quad (13)$$

$$L_{2k} = \sqrt{(B_x - x_k)^2 + (B_y - y_k)^2} \quad (14)$$

The change in heading ω_k for the robot in the local coordinate frame is defined by:

$$\omega_k = \frac{(\theta_k - \theta_{k-1})}{\Delta t} \quad (15)$$

Eqs. 13, 14, and 15 are formulated into output vector Y_k which can be estimated using the observation function h from the state vector X_{k-1} for the previous time-step. Y_k is directly differenced with observation matrix Z_k when computing the innovation residual \tilde{y}_k .

$$Y_k = h(X_{k-1}) = \begin{bmatrix} L_{1k} \\ L_{2k} \\ \omega_k \end{bmatrix}_{3 \times 1} = \begin{bmatrix} \sqrt{(A_x - x_k)^2 + (A_y - y_k)^2} \\ \sqrt{(B_x - x_k)^2 + (B_y - y_k)^2} \\ \frac{(\theta_k - \theta_{k-1})}{\Delta t} \end{bmatrix}_{3 \times 1} \quad (16)$$

The observation Jacobian matrix H_k is calculated by taking the Jacobian of h with respect to X_k as follows¹⁴:

$$H_k = \frac{\partial h}{\partial X} \Big|_{X_k} = \begin{bmatrix} \frac{x_k - A_x}{\sqrt{(A_x - x_k)^2 + (A_y - y_k)^2}} & \frac{y_k - A_y}{\sqrt{(A_x - x_k)^2 + (A_y - y_k)^2}} & 0 \\ \frac{y_k - A_y}{\sqrt{(B_x - x_k)^2 + (B_y - y_k)^2}} & \frac{y_k - A_y}{\sqrt{(B_x - x_k)^2 + (B_y - y_k)^2}} & 0 \\ 0 & 0 & \frac{1}{\Delta t} \end{bmatrix}_{3 \times 3} \quad (17)$$

Measurement Noise Simulation

For the simulation the robot is given a list of wheel velocities at each point in time and the required measurement data is generated. Truth pose data is first generated using Eqs. 11, 13, and 14. Measurement data is then generated by adding noise to the truth data. If we define a truth signal as a and it's noisy measured signal as a_m then the calculation of a noisy signal using zero-mean Gaussian white noise with a variance of σ_a added using additive noise function sn is defined as follows:

$$a_m = a + sn(\sigma_a) \quad (18)$$

Measurements $V_{R_{k,m}}, V_{L_{k,m}}, L_{1_{k,m}}, L_{2_{k,m}}$ have noise added to their signals using the values shown in Table 1. Additionally, the yaw measurement $\omega_{k,m}$ includes a gyro drift component modeled as random walk variable φ as follows:

$$\omega_{k,m} = \omega_k + sn(\sigma_a) + rand(\varphi) \quad (19)$$

SIMULATION AND RESULTS

All simulations begin with the robot at global coordinates (0,0) with a velocity of zero and a heading of $\pi/2$ rad. The initial conditions need not be exact, although estimates further from truth impart a higher chance of filter divergence. The initial estimate for the covariance matrix P_0 is the identity matrix I . The process noise covariance matrix Q is set with an assumed wheel velocity variance of 0.1 m/s for each wheel and an assumed heading variance of 0.1 rad.

$$Q = \begin{bmatrix} \sigma_{V_R}^2 & 0 & 0 \\ 0 & \sigma_{V_L}^2 & 0 \\ 0 & 0 & \sigma_{\theta}^2 \end{bmatrix}_{3 \times 3} = \begin{bmatrix} 0.1 & 0 & 0 \\ 0 & 0.1 & 0 \\ 0 & 0 & 0.1 \end{bmatrix}_{3 \times 3} \quad (20)$$

The measurement noise covariance matrix R is set with an assumed ranging radio measurement variance of 0.25 m for each radio measurement and a yaw rate measurement variance of 0.1 rad/s.

$$R = \begin{bmatrix} \sigma_{L_1}^2 & 0 & 0 \\ 0 & \sigma_{L_2}^2 & 0 \\ 0 & 0 & \sigma_{\omega}^2 \end{bmatrix}_{3 \times 3} = \begin{bmatrix} 0.5 & 0 & 0 \\ 0 & 0.5 & 0 \\ 0 & 0 & 0.1 \end{bmatrix}_{3 \times 3} \quad (21)$$

Table 1 contains a list of the variances used to add white Gaussian noise to the truth data using Eq. 18. Additionally, the gyro drift term ϕ is modeled with a value of 0.001 (rad/s)².

Table 1. Additive Noise Table

	Variance	Units
ω	0.001	(rad/s) ²
L_1	0.250	m ²
L_2	0.250	m ²
V_R	0.100	(m/s) ²
V_L	0.100	(m/s) ²

The EKF solution was simulated for multiple sets of generated data. Each simulation represents approximately 5 min of real world time. Due to many parameters being random and calculated at run time, multiple runs with the same initial conditions and input velocity matrices may not produce the same results. Table 2 shows the absolute mean, standard deviation, and peak values for x, y, and two dimensional (2D) geometric position errors. Table 3 shows the absolute mean, standard deviation, and peak values of heading error associated with each run. Psuedocode for the EKF can be found in the Appendix.

Table 2. Position Error (m) Statistics

	X Mean	X Std.	X Max	Y Mean	Y Std.	Y Max	2D Mean	2D Std.	2D Max
Sim. 1	0.120	0.150	0.430	0.045	0.040	0.152	0.140	0.143	0.430
Sim. 2	0.052	0.039	0.142	0.046	0.044	0.141	0.075	0.052	0.171
Sim. 3	0.031	0.027	0.123	0.925	1.297	3.489	0.933	1.292	3.489
Sim. 4	0.074	0.060	0.186	0.075	0.088	0.424	0.120	0.090	0.434

Table 3. Heading Error Statistics

	Radians			Degrees		
	θ Mean	θ Std.	θ Max	θ Mean	θ Std.	θ Max
Sim. 1	0.187	0.127	0.582	10.7	7.3	33.3
Sim. 2	0.133	0.101	0.545	7.6	5.8	31.2
Sim. 3	0.404	0.257	1.195	23.1	14.8	68.5
Sim. 4	0.241	0.205	0.925	13.8	11.8	53.0

Figure 3 shows a 2D overview plot of the true path and the estimated paths found via odometry (Eq. 6) and the proposed EKF solution. The location of the homing beacon radii are shown as the black (A) and red stars (B). The homing beacon radii are separated by a distance of 2 m plus a small random component σ_L of 0.05 m.

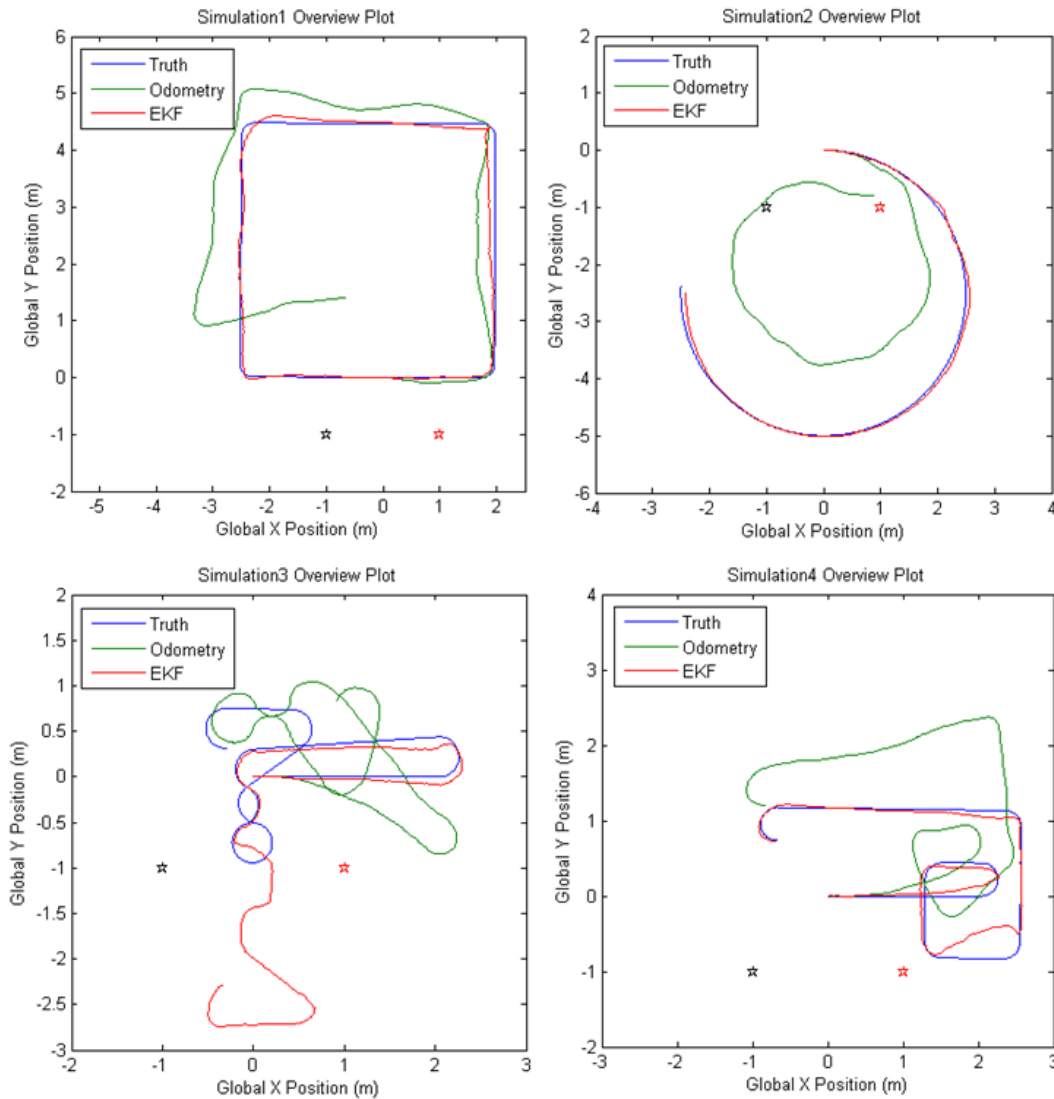


Figure 3. 2D Position Plot of Truth and Estimation Solutions

In Simulation 1 the robot travels in a loop approximately 4.5 meters square. EKF position remains close to the true position over the entire course of the run. The absolute 2D geometric error peaks at 0.430 m with a mean of 0.140 m and a standard deviation of 0.143 m. The maximum absolute heading error is 33.3 deg and the average heading error is 10.7 deg with a standard deviation of 7.3 deg. The y position error is generally smaller than the x position error for the majority of the simulation. The EKF solution follows the true path over the length of this simulation, showing the highest error when furthest from the homing beacon.

In Simulation 2 the robot travels in a circular loop approximately 5 m diameter. The EKF position remains close to the true position over the course of the run. The absolute 2D geometric error peaks at 0.171 m with a mean of 0.075 m and a standard deviation of 0.052 m. The maximum absolute heading error is 31.2 deg and the average heading error is 7.6 deg with a standard deviation of 5.8 deg. The EKF solution follows the truth path over the length of this simulation, showing the lowest 2D positioning and heading error of any simulation.

Simulation 3 shows the robot traveling over a self-intersecting path designed to test the limits of convergence for the EKF solution. The robot travels very close a position directly between the two ranging radios on the homing beacon, defined as a zero-angle position. This position combined with sharp turning results in the filter diverging. The position tracked after this point follows a mirrored general shape of the robots path on the opposite side of the homing beacon. This run exhibits the highest positional errors due to its divergence. The 2D geometric error peaks at 3.489 m with an average error of 0.933 m and a standard deviation error of 1.292 m. The absolute maximum heading error is 68.5 deg with a mean of 23.1 deg and a standard deviation of 14.8 deg.

Simulation 4 shows the robot traversing a self-intersecting path that travels very near the zero-angle position line and contains significantly less turning compared to Simulation 3. The EKF solution shows high 2D positional error when the three radios are close to forming a straight line. The max 2D positional error is 0.434 m with an average error is 0.120 m and a positional standard deviation error of 0.090 m. The absolute maximum heading error is 53.0 deg with an average error of 13.8 deg and a standard deviation of 11.8 deg.

DISCUSSION

A method of localization for ground-based robots in environments lacking GPS and magnetic heading information with applications for ISRU was presented. A key feature of the proposed method is that the system provides coarse localization in GPS-denied environments requiring only a small homing beacon, UWB ranging radios, and sensors commonly found on mobile robots.

As demonstrated in Simulations 3 and 4, heading and y positional error greatly increases as the robot approaches a zero-angle position. Simulation 3 shows that hard turning when at or near this position can cause filter divergence. This divergence did not occur in Simulation 2 despite the robot passing over the zero-angle position line. This continued convergence is due to the filter not being overwhelmed with the heading error associated with turning during this time. The mirrored divergence shown in Simulation 3 is a phenomenon that results due to the non-uniqueness of solutions found by trilateration of the ranging radio distances. For every solution located in the +y direction from the homing beacon, there exists a mirrored solution in the -y direction from the homing beacon.

Measurement noise, and by extension position error, increases as the robot moves further from the beacon. Loss of y-axis measurement fidelity increases as the angle formed by the homing beacon radios and the robots ranging radio approaches zero. The addition of another radio either to the homing beacon or on the robot itself, provided it not in a zero-angle position configuration, would guarantee uniqueness of the measurement solution and possibly avoid divergent filter solutions.

DISSEMINATION

A technical paper featuring the above research was submitted and accepted to the AIAA Region I Student Conference hosted by Virginia Tech in Blacksburg, VA. The conference, which ran from March 27th to March 28th, 2015, was attended and a presentation titled “Mobile Robot Localization with Ultra-wide Band Radios in GPS-Denied Environments” was exhibited. Additionally the research above will form the basis of the author’s thesis. The conference provided valuable experience in regards to technical paper creation and submissions as well as technical presentations.



Figure 4. AIAA Conference Presentation

APPENDIX

Extended Kalman Filter Psuedocode

1.	define $\mathbf{f}, \mathbf{F}, \mathbf{h}, \mathbf{H}, \mathbf{Q}, \mathbf{R}$	// system model
2.	define \mathbf{P} and \mathbf{X}	// initialize state and error covariance
3.	begin loop	
4.	$\mathbf{X}_k = \mathbf{f}(\mathbf{X}_{k-1}, \mathbf{u}_{k-1})$	// predict state estimate
5.	$\mathbf{P}_k = \mathbf{F}_{k-1}\mathbf{P}_{k-1}\mathbf{F}_{k-1}^T + \mathbf{Q}_{k-1}$	// predict error covariance estimate
6.	$\tilde{\mathbf{y}}_k = \mathbf{Z}_k - \mathbf{h}(\mathbf{X}_k)$	// update innovation residual
7.	$\mathbf{S}_k = \mathbf{H}_k\mathbf{P}_k\mathbf{H}_k^T + \mathbf{R}_k$	// update innovation covariance estimate
8.	$\mathbf{K}_k = \mathbf{P}_k\mathbf{H}_k^T\mathbf{S}_k^{-1}$	// calculate Kalman gain
9.	$\bar{\mathbf{X}}_k = \mathbf{X}_k + \mathbf{K}_k\tilde{\mathbf{y}}_k$	// update state estimate
10.	$\bar{\mathbf{P}}_k = (\mathbf{I} - \mathbf{K}_k\mathbf{H}_k)\mathbf{P}_k$	// update covariance estimate
11.	end loop	

CONCLUSION

The objectives of the project were to develop a localization method for ground based robots and the control software necessary to facilitate autonomous mining. A method of localization for ground-based robots in environments lacking GPS and magnetic heading information was presented. A key feature of the proposed method is that the system provides coarse localization in GPS-denied environments requiring only a small homing beacon, UWB ranging radios, and sensors commonly found on mobile robots. Due to the long development timeline for the localization algorithm, the control software has not yet been written.

Further research into ground based localization is needed with a recommended focus on the localization synergy that is present when multiple ground robots can use UWB radios between each other. These extra links could greatly improve location accuracy as well as the maximum distance from the homing beacon before signal quality degrades to unacceptable levels.

ACKNOWLEDGEMENTS

This research was partially supported by the NASA WV Space Grant Consortium Graduate Research Fellowship Program and the Department of Mechanical and Aerospace Engineering at WVU. Special recognition is needed for Dr. Yu Gu for his unending guidance and support as well as Kyle Lassak for his implementation specific help.

The author would like also like to expand on the enormous amount of personal experience and knowledge that was gained due to the direct support from the West Virginia Space Grant Consortium. Research experience was gained over the course of the project as well as invaluable technical writing skills that were developed during the writing of the technical paper. Additionally, the student conference provided valuable insights into the requirements to present at a technical conference as well as a visible display of the work and support being provided by the WV Space Grant Consortium.

REFERENCES

- ¹Britting, Kenneth R. Inertial navigation systems analysis. 2010.
- ²Barshan, Billur, and Hugh F. Durrant-Whyte. "Inertial navigation systems for mobile robots." *Robotics and Automation, IEEE Transactions on* 11.3 (1995): 328-342.
- ³Bortz, Jonh E. "A new mathematical formulation for strapdown inertial navigation." *Aerospace and Electronic Systems, IEEE Transactions on* 1 (1971): 61-66.
- ⁴Jourdan, Damien. Wireless sensor network planning with application to UWB localization in GPS-denied environments. Diss. Massachusetts Institute of Technology, 2006.
- ⁵Bachrach, Abraham, et al. "RANGE–Robust autonomous navigation in GPS -denied environments." *Journal of Field Robotics* 28.5 (2011): 644-666.
- ⁶Weiss, Stephan, Davide Scaramuzza, and Roland Siegwart. "Monocular-SLAM–based navigation for autonomous micro helicopters in GPS-denied environments." *Journal of Field Robotics* 28.6 (2011): 854-874.
- ⁷Segura, M., V. Mut, and C. Sisterna. "Ultra wideband indoor navigation system." *IET Radar, Sonar & Navigation* 6.5 (2012): 402-411.
- ⁸Adams, John Carl, et al. "Ultra-wideband for navigation and communications." *Aerospace Conference, 2001, IEEE Proceedings.. Vol. 2. IEEE, 2001.*
- ⁹Badino, Hernán, Daniel Huber, and Takeo Kanade. "Real-time topometric localization." *Robotics and Automation (ICRA), 2012 IEEE International Conference on. IEEE, 2012.*
- ¹⁰Crassidis, John L. "Sigma-point Kalman filtering for integrated GPS and inertial navigation." *Aerospace and Electronic Systems, IEEE Transactions on* 42.2 (2006): 750-756.

- ¹¹Misra, Pratap, and Per Enge. *Global Positioning System: Signals, Measurements and Performance* Second Edition. Lincoln, MA: Ganga-Jamuna Press, 2006.
- ¹²Bird, Jeff, and Dale Arden. "Indoor navigation with foot-mounted strapdown inertial navigation and magnetic sensors [emerging opportunities for localization and tracking]." *Wireless Communications, IEEE* 18.2 (2011): 28-35.
- ¹³Tzafestas, Spyros G. *Introduction to Mobile Robot Control*. 2013.
- ¹⁴Haykin, Simon. "Kalman filters." *Kalman Filtering and Neural Networks* (2001).
- ¹⁵Ojeda, Lauro, and Johann Borenstein. "Personal dead-reckoning system for GPS-denied environments." *Safety, Security and Rescue Robotics, 2007. SSRR 2007. IEEE International Workshop on. IEEE*, 2007.
- ¹⁶Corrales, Juan Antonio, F. A. Candelas, and Fernando Torres. "Hybrid tracking of human operators using IMU/UWB data fusion by a Kalman filter." *Human-Robot Interaction (HRI), 2008 3rd ACM/IEEE International Conference on. IEEE*, 2008.
- ¹⁷Opshaug, Guttorm R., and Per Enge. "Integrated GPS and UWB navigation system:(motivates the necessity of non-interference)." *IEEE UWBST*. 2002.
- ¹⁸Levinson, Jesse, Michael Montemerlo, and Sebastian Thrun. "Map-Based Precision Vehicle Localization in Urban Environments." *Robotics: Science and Systems. Vol. 4*. 2007.
- ¹⁹Thrun, Sebastian, et al. "Stanley: The robot that won the DARPA Grand Challenge." *Journal of field Robotics* 23.9 (2006): 661-692.
- ²⁰Montemerlo, Michael, et al. "FastSLAM: A factored solution to the simultaneous localization and mapping problem." *AAAI/IAAI*. 2002.
- ²¹Achtelik, Markus, et al. "Stereo vision and laser odometry for autonomous helicopters in GPS-denied indoor environments." *SPIE Defense, Security, and Sensing. International Society for Optics and Photonics*, 2009.
- ²²Kubrak, Damien, et al. "Multi—sensor fusion for localization. Concept and simulation results." *Proceedings of the 2009 ION Conference on Global Navigation Satellite Systems, Savannah 2009*. 2009.
- ²³O’Leary, Brian, Michael J Gaffey, David J. Ross, Rober. “Retrieval of Asteroidal Materials”. *SPACE RESOURCES and SPACE SETTLEMENTS,1977 Summer Study at NASA Ames Research Center, Moffett Field, California. NASA*, 1979.
- ²⁴“Coal Market Module.” *National Energy Modeling System 2013, U.S. Energy Information Administration*, 2013.

THE NATURE OF MAGNETIC RECONNECTION AT THE DAYSIDE MAGNETOPAUSE

Colin Komar
Physics
West Virginia University
Morgantown, WV 26506
Mentor: Dr. Paul Cassak

ABSTRACT

Magnetic reconnection is a phenomenon that occurs in hot ionized gases, also known as plasmas, whereby oppositely directed magnetic field components break and cross-connect, converting energy stored in the magnetic fields to plasma motion and heat. Reconnection occurs between Earth's magnetic field and the interplanetary magnetic field (IMF) carried by the solar wind, plasma emanating from the sun. Reconnection occurs at the sunward boundary of Earth's magnetosphere, the region of space that is dominated by Earth's magnetic field. However, predicting the properties of reconnection at this boundary, including basic considerations such as where reconnection occurs and how efficiently, remain an unsolved problem. We identify possible sites of reconnection by locating magnetic separators, magnetic field lines that separate regions of different magnetic topologies at the dayside magnetopause. Magnetic separators are found in distinct global resistive magnetohydrodynamic (MHD) simulations performed using the three-dimensional Block Adaptive Tree Solar wind Roe-type Upwind Scheme (BATS-R-US) code with a uniform resistivity with IMF orientations ranging from perpendicular to anti-parallel to Earth's magnetic field. We analyze reconnection local to the magnetic separator by measuring reconnection parameters in planes perpendicular to the magnetic separator and comparing the results to local models of reconnection.

INTRODUCTION

There is ongoing debate whether dayside reconnection is entirely controlled by the conditions imposed by the magnetosphere's external driver, the solar wind, or whether the plasma parameters local to the magnetopause have an effect. While observations and simulations have shown the relative importance of local physics determining the local reconnection dynamics (Borovsky et al., 2008; Walsh et al., 2014), it is not presently understood how the local reconnection dynamics affect the larger magnetospheric dynamics.

From our point of view, in order to systematically study this issue, one must first carefully analyze the reconnection physics local to the magnetic separator. This approach has been used in the solar context before (Parnell et al., 2010), in which the authors analyzed reconnection local to self-consistently generated separators in a resistive MHD code. The authors demonstrated that X-point magnetic field geometries typical of reconnection and reconnection outflows appear in planes perpendicular to the magnetic separator.

We have located the magnetic separators in our global magnetospheric resistive MHD simulations in previous studies (Komar et al., 2013, 2014), so we therefore employ a similar methodology in

order to quantify reconnection local to the dayside portions of the magnetic separators. We go beyond previous work by systematically measuring local parameters in each separator plane and comparing the results to local reconnection theory predictions of the reconnection rate. As reconnection at the dayside magnetopause is inherently asymmetric, it is natural to test the predictions of asymmetric reconnection theory to assess this theory's capability of predicting the separator's reconnection rate. Previous studies have presented scaling studies of anti-parallel asymmetric reconnection in 2D slab geometries in resistive MHD (Cassak and Shay, 2007), two-fluid Hall MHD (Cassak and Shay, 2008, 2009), and in particle-in-cell (Malakit et al., 2010) simulations; the asymmetric reconnection predictions were shown to perform well in 2D. However, the theory is manifestly 2D, having been derived in 2D and tested in 2D simulations. Therefore, it is not fully understood if it can be applicable to the fully 3D magnetosphere (J. Dorelli, GEM Summer Workshop, 2014). While attempts have been made to determine the applicability to the fully 3D magnetopause for due southward IMF (Borovsky et al., 2008; Ouellette et al., 2014), we are not aware of any studies applying these relations to IMF oriented obliquely with the geomagnetic dipole.

We perform a series of distinct simulations with with base solar wind parameters: velocity $\mathbf{v}_{\text{SW}} = -400 \text{ km/s } \mathbf{x}$, density $n_{\text{SW}} = 20 \text{ cm}^{-3}$, temperature $T_{\text{SW}} = 232,100 \text{ K}$, IMF strength $|\mathbf{B}_{\text{IMF}}| = 20 \text{ nT}$, at orientations $\theta_{\text{IMF}} \geq 90^\circ$, where θ_{IMF} is the angle the IMF makes with the Earth's dipole axis. For these simulation parameters, we find that local Sweet-Parker asymmetric reconnection theory does surprisingly well at predicting the scaling of the rate of reconnection at the separator and holds for simulations with or without a dipole tilt. Agreement between the two breaks down once the IMF strength is lowered from our base simulation parameters. We argue that the breakdown in agreement is numerical in nature and not a failure of the local reconnection theory.

METHODOLOGY

The Determination of the Magnetic Separators

We employ the separator mapping algorithm of Komar et al. (2013) which has been shown to reliably trace the magnetic separators connecting the magnetic nulls in global magnetosphere simulations for any IMF direction. In the separator tracing algorithm, a hemisphere is initially centered around a magnetic null. The hemisphere's surface, with size of 1 Earth radius (R_E) for our purposes, is discretized into a grid. The magnetic field lines piercing the hemisphere at each grid point are traced to determine their magnetic topology: closed terrestrial, solar wind, and open either connected to the north or south magnetic poles. The approximate location of the separator is determined by finding where these four magnetic topologies meet on a hemisphere's surface. Then, another hemisphere is centered at the determined separator location, and the procedure is iterated to trace the separator. The dayside separator is traced from northern to southern null in this fashion.

The Determination of Planes Normal to the Separator

We develop a procedure to construct planes normal to the separator by defining an orthonormal basis at every point along the separator from the known points on the separator and their positions relative to Earth. As a motivation for the procedure, consider the separator in our $\theta_{\text{IMF}} = 90^\circ$ base simulation, plotted in Fig. 1(a). The plane centered normal to the separator at the subsolar point $\mathbf{r}_{\text{Sep}} = (8.4, 0.0, 0.0)$ is sketched as the dashed line. We define a coordinate system (x', y', z') for this plane. The out-of-plane unit vector \mathbf{z}' points along the separator, i.e., along the magnetic field

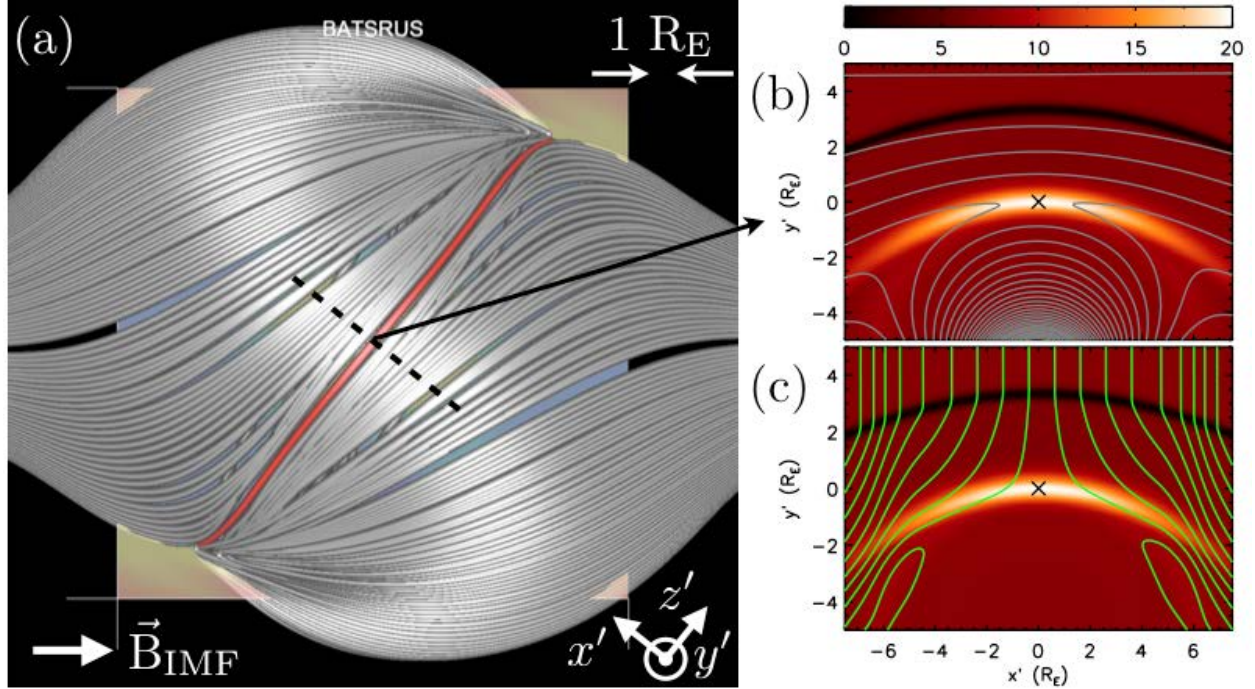


Figure 1: Results of determining the plane normal to the separator at the subsolar magnetopause in a simulation with $\theta_{\text{IMF}} = 90^\circ$. Panel (a) depicts the orientation of the separator plane centered at $\mathbf{r}_{\text{Sep}} = (8.4, 0.0, 0.0) R_E$ in GSM coordinates (dashed black line). Panels (b) and (c) display the out-of-plane current density J_z as the color background in nA/m^2 and displays contours of (b) the flux function Ψ in gray and (c) contours of the stream function Φ in green. The separator is located at $(0, 0)$ in the x' - y' plane and marked with an X.

with $\mathbf{z}' = 0.62 \mathbf{y} + 0.78 \mathbf{z}$. Note, unprimed coordinates are given in the Geocentric Solar Magnetic (GSM) system, with \mathbf{x} pointing from Earth to the sun, \mathbf{y} is perpendicular to Earth's magnetic dipole axis and points from dawn to dusk, and \mathbf{z} completes the right-handed triplet. We define the y' direction as the inflow direction and x' as the outflow direction. For the case study, the inflow direction at the subsolar point is aligned with the solar wind flow, so $\mathbf{y}' = \mathbf{x}$. Finally, the in-plane unit vector completing the orthonormal triplet is defined by $\mathbf{x}' = \mathbf{y}' \times \mathbf{z}'$.

With this coordinate system in mind, we now describe the method by which we determine this coordinate system at an arbitrary point on the separator. For the k -th location along the separator, the out-of-plane unit vector \mathbf{z}'_k is tangent to the separator. Using a second order finite difference, this gives

$$\mathbf{z}'_k = \frac{\mathbf{r}_{k-1} - \mathbf{r}_{k+1}}{|\mathbf{r}_{k-1} - \mathbf{r}_{k+1}|}, \quad (1)$$

where \mathbf{r}_{k-1} and \mathbf{r}_{k+1} are the previous and subsequent separator locations, respectively. We note that one could think of defining \mathbf{z}'_k by the magnetic field direction \mathbf{b} at the separator location, but this definition fails when the magnetic field parallel to the separator is small, such as for due southward IMF ($\theta_{\text{IMF}} = 180^\circ$). The formulation of Eq. (1) guarantees a meaningful \mathbf{z}' for any IMF orientation and magnetospheric dipole tilt.

The unit vector \mathbf{y}'_k in the direction of the inflow is given by the normal to the magnetopause at \mathbf{r}_k . This is calculated by finding the projection of \mathbf{r}_k normal to \mathbf{z}'_k . Mathematically, this is represented as

$$\mathbf{y}'_k \propto \mathbf{r}_k - (\mathbf{r}_k \cdot \mathbf{z}'_k) \mathbf{z}'_k. \quad (2)$$

Finally, \mathbf{x}'_k completes the right-handed triplet by taking the cross product

$$\mathbf{x}'_k = \mathbf{y}'_k \times \mathbf{z}'_k. \quad (3)$$

With this orthonormal basis, the x' - y' plane is expected to be the reconnection plane. Coordinates of locations in this plane are translated back to GSM coordinates, and NASA's Community Coordinated Modeling Center's Kameleon software suite is used to sample the plasma number density n , thermal pressure p , magnetic field \mathbf{B} , plasma flow \mathbf{u} , and current density \mathbf{J} from each simulation onto this plane. Each plane spans $-7.5 \leq x' \leq 7.5$ and $-5 \leq y' \leq 5$ in Earth radii (R_E) and each direction is sampled in $\Delta x' = \Delta y' = 0.0625 R_E$ increments; the separator is centered at $(0, 0)$ in each x' - y' plane. Finally, the magnetic field \mathbf{B} , plasma flow \mathbf{u} , and current density \mathbf{J} vectors are transformed from GSM coordinates to the primed coordinates of the separator plane, e.g., $B_{x'} = \mathbf{B} \cdot \mathbf{x}'$.

We return to the separator in our simulation with $\theta_{\text{IMF}} = 90^\circ$ in Fig. 1 where panel (a) sketches the plane through the subsolar point with a dashed black line. Panels (b) and (c) display the out-of-plane current density component J_z' as the color background in nA/m². The separator's location in the x' - y' plane is marked with an X at $(0,0)$ in panels (b) and (c).

In order to gain insight into what reconnection might look like in this plane, we employ a method used in 2D geometries to determine the structure of the magnetic field that is not formally generalizable to 3D. (No conclusions are drawn from this; it is merely presented for perspective.) Consider a system that in 2D is independent of z' . We define the flux function $\Psi(x', y')$ as

$$\mathbf{B} = -\mathbf{z}' \times \nabla' \Psi, \quad (4)$$

where the magnetic field \mathbf{B} and derivatives ∇' are only considered in the x_2 - y_2 plane. We note that the flux function Ψ is the z_2 component of the vector potential \mathbf{A} . Since $\mathbf{B} \cdot \nabla' \Psi = 0$, lines of constant Ψ represent magnetic field lines. By taking the vector product between \mathbf{z}' and Eq. (4), one obtains $\nabla' \Psi = \mathbf{z}' \times \mathbf{B}$, where $\mathbf{z}' \cdot \nabla' \Psi = 0$ since we are in 2D. Finally, as with determining an electrostatic potential from an electric field, Ψ can be determined from the integral

$$\Psi = \int d\mathbf{l} \cdot (\mathbf{z}' \times \mathbf{B}) = \int d\mathbf{l} \cdot (B_{y'} \mathbf{x}' - B_{x'} \mathbf{y}'), \quad (5)$$

where $d\mathbf{l}$ is the path taken in evaluating the integral. Just as in electrostatics, Ψ is independent of the path of integration in 2D. We calculate Ψ by integrating from the lower, left corner of the x' - y' plane, first along x' , and then along y' . Contours of constant Ψ , representing magnetic field lines, are the gray lines depicted in Fig. 1(b).

One can similarly define a 2D stream function Φ to obtain the streamlines (field lines of the velocity vector) in the x' - y' plane with the simple substitution of Φ for Ψ , and velocity components $u_{x'}$ and $u_{y'}$ for $B_{x'}$ and $B_{y'}$ in Eq. 4. Figure 1(c) displays contours of constant Φ in green which give the in-plane streamlines.

Figure 1 displays several features that are qualitatively consistent with the local picture of 2D Sweet-Parker collisional reconnection (Parker, 1957; Sweet, 1958), albeit occurring in a dipolar magnetic field instead of straight magnetic field lines. First, the out-of-plane current layer is thin and elongated. The reconnecting magnetic field components are also oppositely directed with the IMF pointing along $-\mathbf{x}'$ and is carried along $-\mathbf{y}'$ in the magnetosheath; the dipolar magnetic field points along $+\mathbf{x}'$ and slowly convects towards the magnetopause along $+\mathbf{y}'$. These magnetic fields undergo reconnection at the separator and with newly reconnected magnetic flux located downstream of the separator, displaying a curved X-point reconnection geometry. Lastly, the plasma convects horizontally outward from the separator along \mathbf{y}' with speeds $|\mathbf{u}| \approx 205$ km/s, higher than the vertically directed magnetosheath flow speed $|\mathbf{u}| \approx 150$ km/s. This suggests reconnection has a role in accelerating the outflowing plasma. Thus the plane normal to the separator at the subsolar magnetopause qualitatively resembles the 2D pictures of reconnection.

We note that the technique for determining the in-plane magnetic field and streamlines works remarkably well for the subsolar magnetopause, and most likely results from the high degree of symmetry in this simulation since it does not include a dipole tilt and that the IMF has reflection symmetry about $y = -z$.

Measuring Plasma Parameters in Reconnection Planes

Having described the procedure to obtain planes normal to the separator and the plasma parameters in these planes, we wish to analyze the reconnection in each plane. To do so, we need the plasma parameters just upstream of the dissipation region since this plasma and the magnetic field it carries serves as the free energy for reconnection.

We start by sampling the out-of-plane current density J_z' along y' at $x' = 0$ to determine the location of maximum current density J_{\max} . Note

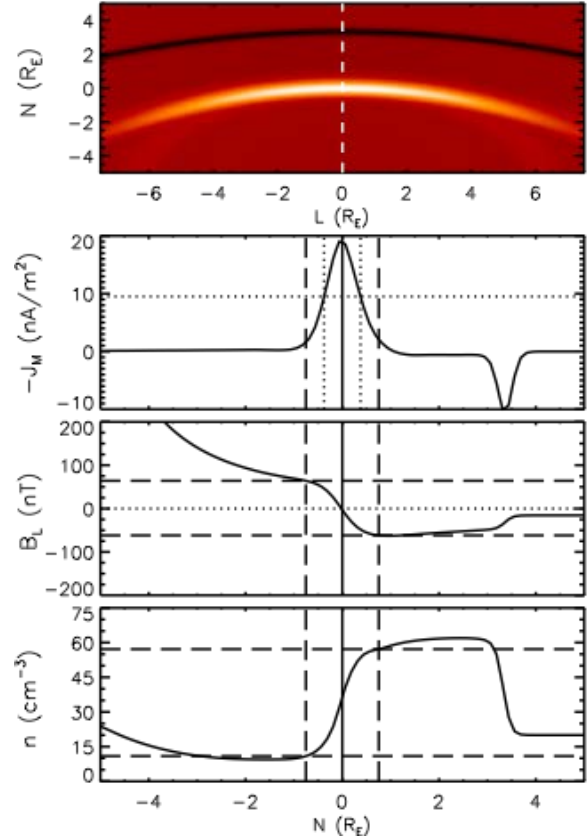


Figure 2: Determination of the upstream plasma parameters in a simulation with $\theta_{\text{IMF}} = 90^\circ$ for the separator plane located at the subsolar point. Panel (a) displays the out-of-plane current density J_z' and the white dashed line at $x' = 0$ displays the line along which plasma parameters are sampled. Panel (b) displays the out-of-plane current density along $x' = 0$ with the separator's location depicted by the solid line and locations where $J_z' = 0.5 J_{\max}$ displayed with vertical dotted lines. The value of $0.5 J_{\max}$ is marked by the horizontal dotted line. The vertical dashed lines in panels (b)-(d) indicate the locations where the magnetospheric and magnetosheath parameters are measured. Panel (c) displays the reconnecting magnetic field component $B_{x'}$ in nT, whereas panel (d) displays the plasma number density n in cm^{-3} ; the horizontal lines in these plots mark the respective magnetospheric and magnetosheath values of these parameters.

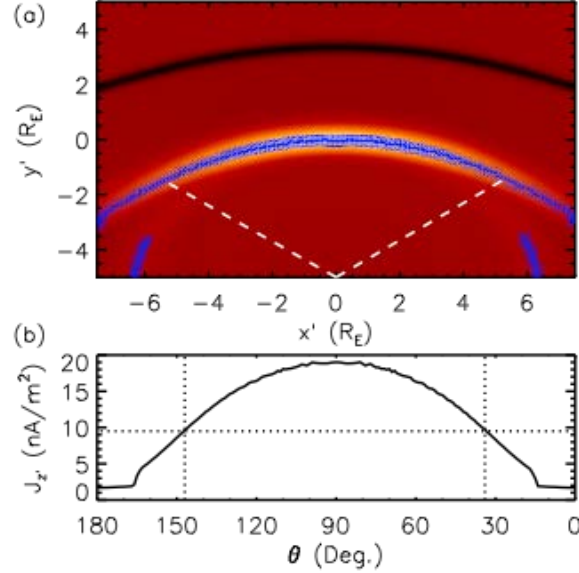


Figure 3: Results of determining the dissipation region half-length L with maxima of the out-of-plane current density J_z' for the plane normal to the separator at the subsolar point in a simulation with $\theta_{\text{IMF}} = 90^\circ$. (a) The locations of current maxima are displayed as blue asterisks and (b) the current density values in nA/m^2 at each of these points as a function of sampling angle θ as measured from the $+x'$ axis. The left and right edges θ_{Left} and θ_{Right} of the dissipation region are displayed as dotted vertical lines and are determined by where the current density falls to $0.5 J_{\text{max}}$ as indicated by the horizontal dotted line.

that J_{max} may not be located at the separator, as it would be for symmetric reconnection; it can be offset during asymmetric reconnection (Cassak and Shay, 2007). We define the full-width, half-max (FWHM) of the out-of-plane current density profile as the dissipation region's thickness 2δ . We define y'_{SH} and y'_{MS} as the locations corresponding to the magnetosheath and magnetospheric edges of the out-of-plane current profile, respectively. The number densities n and reconnecting magnetic field components $B_{x'}$ of the magnetosheath and magnetosphere are measured at $(0, y'_{\text{SH}} + \delta)$ and $(0, y'_{\text{MS}} - \delta)$, respectively, in the x' - y' plane.

We return to the separator plane displayed in Fig. 1 in order to demonstrate the procedure for measuring the upstream plasma parameters; the results are displayed in Fig. 2. Panel (a) displays the out-of-plane current density J_z' as the color background with a dashed white line at $x' = 0$ displaying the line along which the plasma parameters are sampled. Panel (b) shows the out-of-plane current density along $x' = 0$, with vertical dotted lines at the locations y'_{MS} and y'_{SH} where the current density has the value $0.5 J_{\text{max}}$ and is marked with a horizontal dotted line. The separator's location is marked with a solid vertical line at $y' = 0$. The left dashed vertical lines mark $y'_{\text{MS}} - \delta$ where the magnetospheric plasma parameters are measured and the magnetosheath's plasma parameters are measured at $y'_{\text{SH}} + \delta$ marked by the right vertical dashed line. Panel (c) displays the reconnecting magnetic field components $B_{x'}$ in nT and panel (d) displays the plasma number density n in cm^{-3} , respectively. The locations where the upstream parameters are sampled are again displayed with vertical dashed lines; dashed horizontal lines in panels (c) and (d) display the sampled values. One can see that each determined parameter is representative of the asymptotic regions upstream of the dissipation region as desired. The upstream values for this plane on the

magnetospheric side are $B_{x',MS} = 64$ nT and $n_{MS} = 11$ cm⁻³ and for the magnetosheath plasma are $B_{x',SH} = -61$ nT, and $n_{SH} = 57$ cm⁻³; the dissipation region has half-width $\delta = 0.38$ R_E.

In order to check the validity of the asymmetric reconnection scaling relations, we must determine the half-length L of the dissipation region. Care must be taken in determining the dissipation region length as it is curved due to the structure of Earth's magnetosphere. We therefore start by identifying the reconnection dissipation region by sampling the out-of-plane current density $J_{z'}$ along cuts oriented at an angle θ from the $+x'$ axis in the x' - y' plane as displayed in Fig. 3; the cuts start at $(0, -5)$ R_E and the current density is sampled in $1/16$ R_E increments, with θ discretized into 1° increments from $[0^\circ, 180^\circ]$. The first current density maximum along each cut is retained. The right and left edges of the dissipation region are defined as θ_{Right} and θ_{Left} where the first current density maximum achieves a value of $J_{z'} = 0.5 J_{\text{max}}$, where J_{max} is the maximum current density value along $x' = 0$, as described earlier in this section. L is directly calculated from the arc length of the measured current maxima locations as

$$2L = \int_{\theta_{\text{Right}}}^{\theta_{\text{Left}}} dS \simeq \sum_{k=\theta_{\text{Right}}}^{\theta_{\text{Left}}} \Delta S_k, \quad (6)$$

where ΔS_k is the distance between the k -th current maximum at \mathbf{S}_k and its neighbor at \mathbf{S}_{k+1} given by

$$\Delta S_k = |\mathbf{S}_{k+1} - \mathbf{S}_k|. \quad (7)$$

Figure 3 displays the results of this current sampling method for the separator plane at the subsolar point for the $\theta_{\text{MF}} = 90^\circ$ simulation. Panel (a) displays the out-of-plane current density $J_{z'}$ as the color background and current density maxima are displayed with blue asterisks. Panel (b) plots the values of current density maxima in nA/m² as a function of the sampling angle θ . Vertical dotted lines display the determined locations of θ_{Left} and θ_{Right} , with the horizontal dotted line displaying $0.5 J_{\text{max}}$. The dissipation region's half-length $L = 5.84$ R_E for this plane.

We have now measured all of the relevant parameters in order to make a meaningful comparison with the theoretical asymmetric reconnection scaling relations presented in Cassak and Shay (2007), and compare these prediction with the reconnection rate measured in our global simulations. From the upstream reconnecting magnetic fields $B_{x'}$ and densities n , the dissipation region's half-width δ and half-length L , we can calculate the generalized asymmetric reconnection rate E_{asym} as

$$E_{\text{asym}} \sim \frac{B_{x',MS} B_{x',SH}}{B_{x',MS} + B_{x',SH}} c_{A,\text{asym}} \frac{2\delta}{L}, \quad (10)$$

and the asymmetric Sweet-Parker reconnection rate as

$$E_{\eta,\text{asym}} \sim \sqrt{\frac{\eta c_{A,\text{asym}}}{\mu_0 L} B_{x',MS} B_{x',SH}}, \quad (11)$$

with the asymmetric reconnection outflow speed $c_{A,\text{asym}}$ is given by

$$c_{A,\text{asym}}^2 \sim \frac{B_{x',MS} B_{x',SH}}{\mu_0 m_i} \frac{B_{x',MS} + B_{x',SH}}{n_{MS} B_{x',SH} + n_{SH} B_{x',MS}}, \quad (12)$$

where m_i is the proton mass and μ_0 is the permeability of free space. Equations (10) and (11) are compared with the reconnection rate at the separator $E_{z'} = \eta J_{z'}$. The procedure outlined here is repeated for all planes normal to the separator for all simulations in this study.

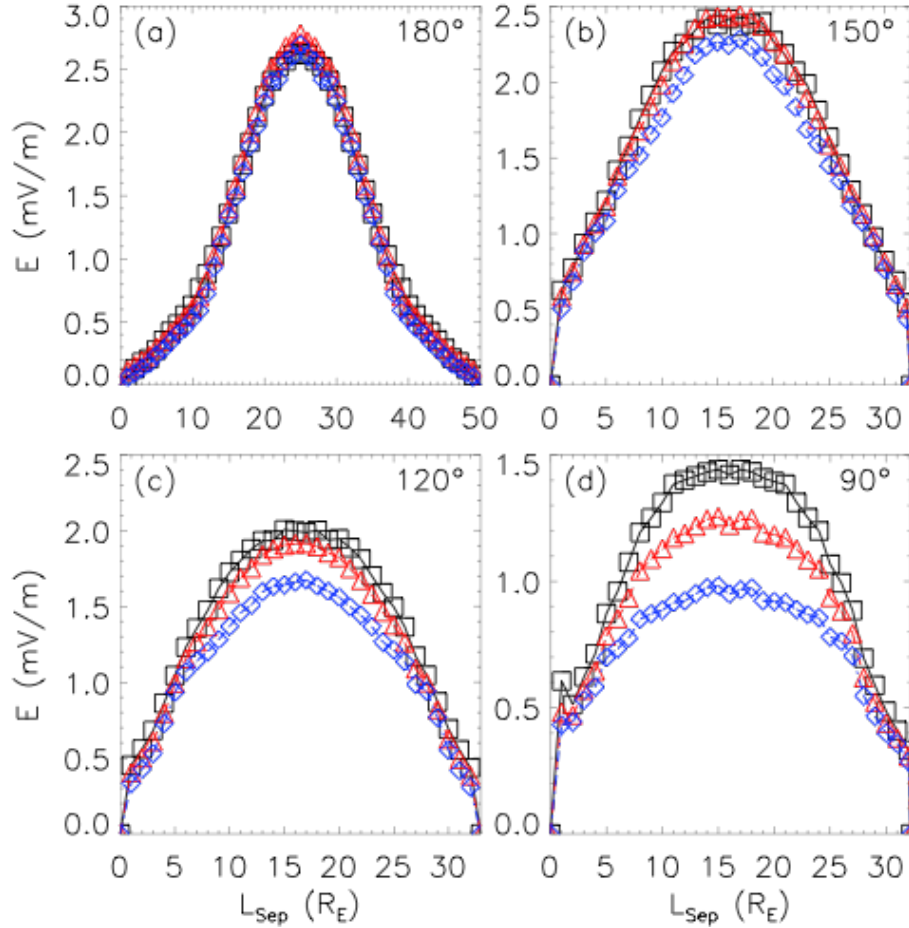


Figure 4: Results comparing the measured reconnection rate $E_{z'}$ (black squares) at the separator with the theoretical E_{asym} (blue diamonds) and the Sweet-Parker $E_{\text{asym},\eta}$ (red triangles) asymmetric reconnection rates in distinct simulations with (a) $\theta_{\text{IMF}} = 180^\circ$, (b) 150° , (c) 120° , and (d) 90° . All simulations use our base simulation parameters. Electric fields are plotted as a function of L_{Sep} , the distance along the separator from the northern magnetic null.

RESULTS

Figure 4 displays the measured reconnection rate $E_{z'}$ (black squares) along the separator in distinct simulations with (a) $\theta_{\text{IMF}} = 180^\circ$, (b) 150° , (c) 120° , and (d) 90° employing our base simulation parameters. The measured reconnection rate in mV/m is compared with the theoretical asymmetric reconnection rates E_{asym} (blue diamonds) and $E_{\eta,\text{asym}}$ (red triangles) given by Eqs. (10) and (11), respectively. The reconnection rates are plotted as a function of L_{Sep} , the distance along the separator from the northern magnetic null measured in R_E . Note the vertical scale is different for different θ_{IMF} , consistent with reconnection being faster for larger θ_{IMF} .

The results for $\theta_{\text{IMF}} = 180^\circ$ in panel (a) are exceedingly good, as the theoretical and measured values are almost indistinguishable. This is consistent with the results of Borovsky et al. (2008) and Ouellette et al. (2014), who tested the theoretical predictions for due southward IMF. The other clock angle simulations in panel (b)-(d) reveal good agreement in the scaling sense, meaning that all parameters differ by some coefficient that is approximately constant along the entire separator. While the scaling is strong for all simulations with a southward component of the IMF,

a comparison of absolute quantities shows that the quantitative agreement becomes progressively worse as the clock angle decreases.

As a way of quantifying the discrepancy between the measured reconnection rate and the predictions, the percent difference between the measured reconnection rate $E_{z'}$ and the generalized asymmetric reconnection rate E_{asym} is calculated as a function of the distance along the separator as

$$\% \text{ Error} = \frac{E_{\text{asym}} - E_{z'}}{E_{z'}} \times 100, \quad (13)$$

$E_{z'}$ and for the asymmetric Sweet-Parker reconnection rate $E_{\eta,\text{asym}}$ as

$$(\% \text{ Error})_{\eta} = \frac{E_{\eta,\text{asym}} - E_{z'}}{E_{z'}} \times 100. \quad (14)$$

Using these equations, we calculate the average percent difference along the middle third of the separator, those locations between $10 \leq L_{\text{Sep}} \leq 20 R_E$ for $\theta_{\text{IMF}} = 90^\circ, 120^\circ,$ and 150° , and $16 \leq L_{\text{Sep}} \leq 33 R_E$ for $\theta_{\text{IMF}} = 180^\circ$ for which E is significantly different from zero and the percent error is relatively constant with distance along the separator. The average percent errors are $[-33\%, -18\%, -8\%, -1\%]$ for E_{asym} and $[-14\%, -5\%, -0\%, +3\%]$ for $E_{\eta,\text{asym}}$ for $\theta_{\text{IMF}} = [90^\circ, 120^\circ, 150^\circ, 180^\circ]$, respectively. For both comparisons, there is a trend that the percent error gets larger for smaller θ_{IMF} ; the dependence is described fairly well as the percent error being proportional to $-\cos \theta_{\text{IMF}}$. This suggests that there is a systematic effect causing an offset that increases with decreasing θ_{IMF} , such as our algorithm to find δ or L , but the relatively flat percent error with separator location suggests the scaling result is accurately predicting the dependence on plasma parameters local to the reconnection site for these simulations.

We note that the two curves for $E_{\eta,\text{asym}}$ and E_{asym} should ideally lie on top of each other. However, in these cases there is some offset between the two. The percent difference between the two, using a form similar to Eq. (13), gives $[-22\%, -13\%, -8\%, -8\%]$ for the average percent error between the two theoretical predictions. Thus, E_{asym} is systematically 10–20% less than $E_{\eta,\text{asym}}$ for these simulations.

We perform a similar comparison for a simulation that includes a positive dipole tilt $\psi = 15^\circ$ (northern geomagnetic pole oriented sunward), with $\theta_{\text{IMF}} = 120^\circ$ and all solar wind parameters the same as our base simulations. Figure 5 displays the results from the dipole tilt simulation as before. We again see very good agreement in the scaling sense for both theoretical reconnection rates. As we did previously, we calculate the average percent differences for the middle third of the separator, for which the percent error is relatively constant. One finds the errors in E_{asym} and $E_{\eta,\text{asym}}$ to be -21% and -7% , respectively; these average percent differences are comparable to those seen in our base simulations for the same IMF clock angle. This suggests that the prediction is equally successful with or without a dipole tilt.

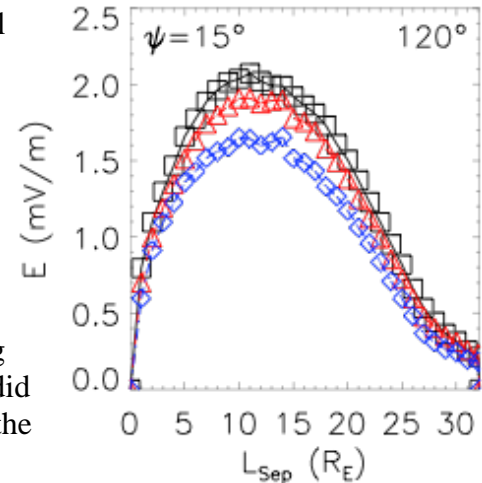


Figure 5: Comparison between the measured reconnection rate at the separator with the theoretical asymmetric reconnection rates in a simulation with $\theta_{\text{IMF}} = 120^\circ$ and positive dipole tilt of $\psi = 15^\circ$. See caption of Fig. 4 for definitions.

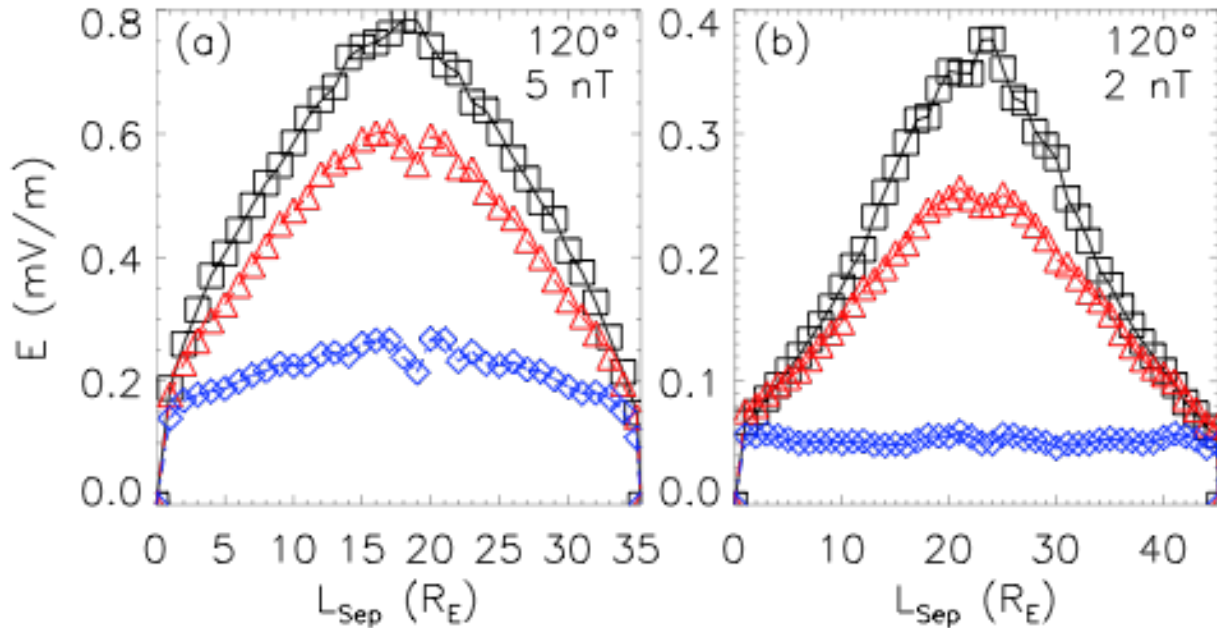


Figure 6: Comparison between the measured reconnection rate at the separator with theoretical asymmetric reconnection rates in distinct simulations with $\theta_{\text{IMF}} = 120^\circ$ and IMF strength of (a) 5 and (b) 2 nT. See the caption of Fig. 4 for definitions.

The results of this test are particularly important because our base simulations employ a high degree of symmetry given the solar wind's Earthward flow, and the IMF is further confined to the y-z GSM plane. The inclusion of the dipole tilt breaks this symmetry and causes the separator to move southward of the subsolar point and to be located in a region where the draping of the magnetosheath magnetic field across the magnetopause is noticeable. We find the magnetosheath's reconnecting magnetic field component near the subsolar magnetopause decreases by 7% in the dipole tilt simulation, suggesting draping is playing a role.

Finally, we perform an additional parametric test of the theory: we lower the IMF strength to 5 and 2 nT in two separate simulations, each with $\theta_{\text{IMF}} = 120^\circ$ and all other solar wind parameters equal to those of our base simulations. Figure 6 displays the results from these simulations with the reconnection rates displayed as before for the simulation with (a) $B_{\text{IMF}} = 5$ and (b) 2 nT.

Before discussing the reconnection rates, we note one important difference among our $\theta_{\text{IMF}} = 120^\circ$ simulations without a dipole tilt. The total length of the dayside separator $L_{\text{Sep,tot}}$ increases as IMF strength is lowered: $L_{\text{Sep,tot}} \approx 33 R_E$ for our base simulation with $B_{\text{IMF}} = 20$ nT as seen in Fig. 4(b), whereas $L_{\text{Sep,tot}} \approx 35 R_E$ and $L_{\text{Sep,tot}} \approx 45 R_E$ for $B_{\text{IMF}} = 5$ and 2 nT, respectively, as seen in Fig. 6(a) and (b). The difference in separator lengths among these simulations results from pressure balance at the magnetopause. The magnetic pressure of the IMF has a small contribution to the solar wind's total pressure so a decrease in the IMF strength lowers the solar wind's total pressure. The magnetopause correspondingly balloons outward resulting in a lengthening of the dayside separator.

As clearly seen in Fig. 6, the scaling arguments of asymmetric reconnection theory do much worse at predicting the reconnection rate measured at the separator. For the simulation with $B_{\text{IMF}} = 5$ nT simulation, the average percent errors of the middle third of the dayside separator in E_{asym} and

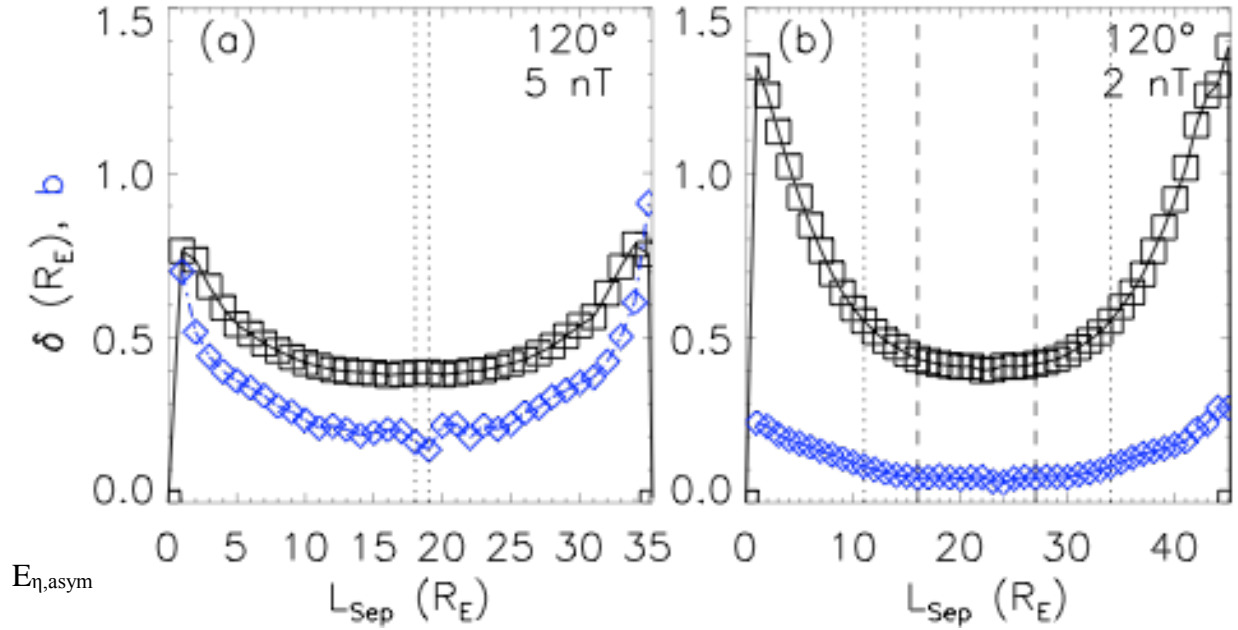


Figure 7: Plot of the dissipation region's half-width δ (R_E ; black squares) and the magnetic field ratio b (unitless; blue diamonds) as a function of distance along the separator measured from the northern null in R_E in simulations with $\theta_{IMF} = 120^\circ$ and (a) $B_{IMF} = 5$ and (b) 2 nT. The resolution threshold condition of Eq. (15) is plot with vertical for simulation grid sizes of $\Delta = 1/8$ (dotted) and $1/16$ R_E (dashed); reconnection is sufficiently resolved for locations on the separator external to these vertical lines.

are -65% and -21% ; likewise for the $B_{IMF} = 2$ nT simulation, the errors in E_{asym} and $E_{\eta,asym}$ are -84% and -28% , respectively. Secondly, $E_{\eta,asym}$ appears to have the best scaling with E_z' , whereas E_{asym} shows limited scaling agreement in the 5 nT simulation and no scaling agreement is present for the 2 nT simulation.

We argue that the reason for the lack of agreement in these cases results not from a failure in the theory, but rather from a numerical limitation of the present simulation grid, as previously noted in Cassak and Shay (2008). To demonstrate this, Fig. 7 plots the dissipation region's half-width δ in R_E as black squares and the magnetic field ratio $b \equiv B_{X',SH}/B_{X',MS}$ as blue diamonds as a function of the distance along the separator measured from the northern null in the simulations with IMF strength (a) 5 and (b) 2 nT.

One feature stands out in this figure: the magnetic field ratio b is not constant along the magnetic separator. This has significant implications for the location of the separator within the magnetopause current layer across the dayside magnetopause. The location of the X-line within the dissipation region in the separator plane's coordinate system is given by

$$\frac{\delta_{X,SH}}{\delta_{X,MS}} \sim \frac{B_{X',SH}}{B_{X',MS}} \equiv b, \quad (15)$$

where $\delta_{X,SH}$ and $\delta_{X,MS}$ are the distances from the dissipation region's magnetosheath and magnetospheric edges to the separator, respectively. Specifically, the separator is located towards the

magnetosheath for these simulations since $b < 1$. For the reconnection dynamics to be properly resolved in the simulations, the distance from the dissipation region's magnetosheath edge to the separator $\delta_{X,SH}$ must be resolved with one simulation grid cell of size Δ so that

$$\delta_{X,SH} > \Delta. \quad (16)$$

The dissipation region's full-width 2δ is defined as

$$2\delta = \delta_{X,SH} + \delta_{X,MS}. \quad (17)$$

Using these two equations, one can solve for $\delta_{X,SH}$ which is

$$\delta_{X,SH} = 2\delta \frac{b}{b+1}. \quad (18)$$

Using this result in Eq. (16) gives the minimum resolution required to resolve the separator's distance from the magnetosheath with one grid cell and is given by

$$2\delta \frac{b}{b+1} > \Delta. \quad (19)$$

Figure 7 displays the threshold condition given by Eq. (16) as vertical lines for grid cell sizes $\Delta = 1/8$ (dotted), which is the grid size we use to resolve the dayside magnetopause and $1/16 R_E$ (dashed); locations along the separator which satisfy Eq. (19) lie exterior to these vertical lines. This implies that we are sufficiently resolving the reconnection dynamics only at locations (a) $L_{Sep} < 18$ and $L_{Sep} > 19 R_E$ and (b) $L_{Sep} < 11$ and $L_{Sep} > 34 R_E$. The region between the vertical lines displayed in Fig. 7 is consistent with the regions where we see the largest discrepancies between the measured reconnection rate and the theoretical predictions, as displayed in Fig. 6.

These tests therefore suggest that we are not properly resolving reconnection for portions of the separator at the dayside magnetopause for our lower B_{IMF} simulations and therefore these simulations are not appropriate for testing the theory. For future work, this can be further tested by doubling the simulation resolution to $\Delta = 1/16 R_E$ in the simulation with $B_{IMF} = 5$ nT. Another way of testing this hypothesis is to increase the explicit resistivity, since this causes the magnetopause current layer to broaden from magnetic diffusion. Another option is to perform a simulation with an IMF strength around 10 nT, which may be enough to sufficiently resolve reconnection along the entire separator. Nonetheless, some combination of these approaches is required to test the effect of grid resolution. If the resolution proves to be the cause of the disagreement, this has important implications for other researchers studying dayside reconnection as many authors use numerical dissipation, so their dissipation region is under-resolved.

CONCLUSIONS

The analysis presented here suggests that, up to a scaling factor, the 2D asymmetric reconnection theory predicts the reconnection rate at the dayside magnetopause as a function of the upstream parameters local to the magnetic separator for southward IMF orientations. The theory has also been confirmed in previous scaling analyses of asymmetric reconnection in: laboratory experiments (Yoo et al., 2014; Rosenberg et al., 2015); observations of reconnection at Earth's dayside magnetopause (Mozer and Hull, 2010); anti-parallel reconnection in 2D slab geometries in resistive MHD (Cassak and Shay, 2007), two fluid (Hall-MHD with electron inertia) (Cassak and Shay, 2009), and particle-in-cell (Malakit et al., 2010; Hesse et al., 2013) simulations; and at the subsolar magnetopause for southward IMF in global simulations (Borovsky et al., 2008; Ouellette et al., 2014).

To the best of our knowledge, the present study is the only one of its kind to analyze reconnection local to the separator for oblique IMF orientations and including a dipole tilt. The present results suggest that the approach taken is appropriate for analyzing reconnection local to the magnetic separators. This suggests that we are uniquely poised to bridge the gap between reconnection physics local to the separator and reconnection's consequences for global magnetospheric dynamics.

ACKNOWLEDGMENTS

Support from the NASA WV Space Grant Consortium is gratefully acknowledged. I would additionally like to thank my advisor, Dr. Paul Cassak, for his unconditional support and advice as I have completed my Ph. D. in Physics at West Virginia University. Simulations were performed at the Community Coordinated Modeling Center at Goddard Space Flight Center through their public Runs on Request system (<http://ccmc.gsfc.nasa.gov>). The CCMC is a multi-agency partnership between NASA, AFMC, AFOSR, AFRL, AFWA, NOAA, NSF and ONR. The BATS-R-US Model was developed by the Center for Space Environment Modeling at the University of Michigan. The analysis presented here was made possible via the Kameleon and Space Weather Explorer software packages provided by the CCMC. The Kameleon software has been provided by the Community Coordinated Modeling Center at NASA Goddard Space Flight Center (<http://ccmc.gsfc.nasa.gov>). Software Developers: Marlo M. Maddox, David H. Berrios, Lutz Rastaetter. Additional thanks to J. C. Dorelli, A. Glocer, and R. Lopez for their insight and interesting discussions.

Value of NASA Graduate Research Fellowship Program

I have found the NASA Graduate Research Fellowship Program to be extremely valuable in my Ph. D. training. The \$12,000 stipend provided enough financial support for a semester in the Department of Physics and Astronomy at West Virginia University. This financial support supplemented my advisor's research funds and enabled me to succeed academically in a highly competitive funding environment.

As a direct result of this program, I have authored a paper with my advisor and our group's former postdoc, Ray Fermo. I presented a poster at the 2014 Geospace Environment Modeling (GEM) Summer Workshop, and was awarded a student prize in the 2014 GEM Student Poster Contest. I presented a poster at the 2014 American Geophysical Union (AGU) Fall Meeting on the study briefly presented in this report. We are in the process of drafting a paper on these results, which we intend to submit to *Geophysical Research Letters* in the coming months. Finally, with support from the West Virginia Space Grant Consortium, I was able to attend the Science Working Team meeting of NASA's Magnetospheric Multiscale (MMS) mission at Kennedy Space Center.

In closing, NASA's Graduate Research Fellowship Program through the West Virginia Space Grant Consortium has been an extremely rewarding experience. The financial support has allowed me to complete my Ph. D. at West Virginia University. I will be leaving WVU on April 30, 2015 to start a postdoctoral research scientist position at NASA Goddard Space Flight Center under the direction of Dr. Alex Glocer. The generous support of WVSGC has presented numerous opportunities to network with colleagues and complete my Ph. D. studies.

AWARDS, PUBLICATIONS AND PRESENTATIONS

Honors and Awards

Student Poster Prize, for the poster entitled “Comparative Analysis of Dayside Reconnection Models in Global Magnetospheric Simulations” awarded at the Geospace Environment Modeling Summer Workshop, June 2014

Dr. Mohindar S. Sehra Research Award, awarded annually by the West Virginia University Department of Physics and Astronomy ‘recognizing doctoral students advancing research in Physics by publishing research in high-quality, peer-reviewed Physics Journals, May 2014

Contributed Talks and Posters at Conferences

1. “Measures of Magnetic Reconnection at the Dayside Magnetopause”
2014 AGU Fall Meeting, Contributed Poster
San Francisco, CA, December 15, 2014
2. “Comparative Analysis of Dayside Reconnection Models in Global Magnetospheric Simulations”
2014 GEM Summer Workshop, Contributed Poster
Portsmouth, VA, June 17, 2014

Invited Talks

1. “Magnetohydrodynamic models: What are they? What can they be used for?”
2014 GEM Student Workshop
Portsmouth, VA, June 15, 2014
2. “On the Location of Magnetic Reconnection at the Dayside Magnetopause” □ Heliophysics Science Seminar □ NASA Goddard Space Flight Center, Greenbelt, MD April 24, 2014

Publications

1. Komar, C. M., R. L. Fermo, and P. A. Cassak (2015), “Comparative analysis of dayside magnetic reconnection models in global magnetosphere simulations,” *J. Geophys. Res.*, **120**, 276-294.

REFERENCES

- Borovsky, J. E., M. Hesse, J. Birn, and M. M. Kuznetsova (2008), What determines the reconnection rate at the dayside magnetosphere?, *J. Geophys. Res.*, **113**, A07210.
- Cassak, P. A., and M. A. Shay (2007), Scaling of asymmetric magnetic reconnection: General theory and collisional simulations, *Phys. Plasmas*, **14**, 102114.
- Cassak, P. A., and M. A. Shay (2008), Scaling of asymmetric Hall reconnection, *Geophys. Res. Lett.*, **35**, L19102.

- Cassak, P. A., and M. A. Shay (2009), Structure of the dissipation region in fluid simulations of asymmetric magnetic reconnection, *Phys. Plasmas*, **16**, 055704.
- Hesse, M., N. Aunai, S. Zenitani, M. Kuznetsova, and J. Birn (2013), Aspects of collisionless magnetic reconnection in asymmetric systems, *Phys. Plasmas*, **20** (6), 061210.
- Komar, C. M., P. A. Cassak, J. C. Dorelli, A. Gloer, and M. M. Kuznetsova (2013), Tracing magnetic separators and their dependence on IMF clock angle in global magnetospheric simulations, *J. Geophys. Res.*, **118**(8), 4998–5007.
- Komar, C. M., R. L. Fermo, and P. A. Cassak (2015), “Comparative analysis of dayside magnetic reconnection models in global magnetosphere simulations,” *J. Geophys. Res.*, **120**, 276-294.
- Malakit, K., M. A. Shay, P. A. Cassak, and C. Bard (2010), Scaling of asymmetric magnetic reconnection: Kinetic particle-in-cell simulations, *J. Geophys. Res.*, **115**, A10223.
- Mozer, F. S., and A. Hull (2010), Scaling the energy conversion rate from magnetic field reconnection to different bodies, *Phys. Plasmas*, **17** (10), 102906.
- Ouellette, J. E., J. G. Lyon, and B. N. Rogers (2014), A study of asymmetric reconnection scaling in the lyon-fedder-mobarry code, *J. Geophys. Res.*, **119**(3), 1673–1682.
- Parker, E. N. (1957), Sweet’s mechanism for merging magnetic fields in conducting fluids, *J. Geophys. Res.*, **62**, 509.
- Parnell, C. E., A. L. Haynes, and K. Galsgaard (2010), Structure of magnetic separators and separator reconnection, *J. Geophys. Res.*, **115**(A2), A02102.
- Rosenberg, M. J., C. K. Li, W. Fox, I. Igumenshchev, F. H. Séguin, R. P. J. Town, J. A. Frenje, C. Stoeckl, V. Glebov, and R. D. Petrasso (2015), A laboratory study of asymmetric magnetic reconnection in strongly driven plasmas, *Nat. Comm.*, **6**.
- Sweet, P. A. (1958), The Neutral Point Theory of Solar Flares, in *Electromagnetic Phenomena in Cosmical Physics, IAU Symposium*, vol. 6, edited by B. Lehnert, p. 123.
- Walsh, B. M., J. C. Foster, P. J. Erickson, and D. G. Sibeck (2014), Simultaneous ground- and space- based observations of the plasmaspheric plume and reconnection, *Science*, **343** (6175), 1122–1125.
- Yoo, J., M. Yamada, H. Ji, J. Jara-Almonte, C. E. Myers, and L.-J. Chen (2014), Laboratory study of magnetic reconnection with a density asymmetry across the current sheet, *Phys. Rev. Lett.*, **113**, 095002.

ULTRASOUND MEDIATED GENE DELIVERY IN IMMUNE-COMPETENT C57BL/6 MICE

Rounak Nande
PhD Candidate, M.Sc., Biomedical Sciences
Marshall University
Huntington, WV, 25701
Research Mentor: Dr. Pier Paolo Claudio

ABSTRACT

The use of human adenoviruses (hu-Ads) in gene transfer studies is limited because of their immunogenic nature. To circumvent this limitation we have developed a novel approach constituted of hu-Ads encapsulated inside microbubbles (MBs). The melanoma-differentiation-associated-gene-7 or interleukin-24 (mda-7/IL24) is a tumor suppressor with pro-apoptotic activity against several cancers. However, to translate the site-specific gene transfer of Ad.mda7 complexes by ultrasound-targeted microbubble destruction (UTMD) from the bench to the bedside, studies involving the use of immune-deficient animal and immune-competent mice models are required.

It has been shown that transfer of genes to mouse cells using hu-Ads is dependent on the expression of Coxsackie and Adenovirus Receptor (CAR) and certain integrins, which mediate hu-Ad attachment and internalization. Our hypotheses are that the murine derived prostate cancer cells will express CAR and/or α , β integrins and will be transduced by hu-Ads. Microbubbles will protect the viruses from inactivating substances such as complement. UTMD will enhance gene transfer in both DU145 and murine PC cells regardless of complement rich FBS media. We investigated the expression of CAR and α , β integrins in murine and control human DU145 PC cells by flow cytometry analysis.

We tested the infectivity of Ad.GFP (green fluorescent protein) and Ad.mda-7/IL24 on both murine and DU145 prostate cancer cells. Viral burst assay was carried out on murine and DU145 PC cells with the CTV.Mda7 oncolytic adenovirus to measure viral replication. We also tested the microbubble delivery of Ads with ultrasound in cell culture. Western blot analysis confirmed mda-7 protein expression following Ad-transduction. Annexin-V studies assessed the pro-apoptotic effect of the Ad.mda-7/IL24.

Our studies showed that cells express CAR receptor, α , β integrins and that Ad.GFP and Ad.mda-7/IL24 transferred their transgene in the murine and human DU145 prostate carcinoma cells. Murine PC cells were unable to replicate the CTV oncolytic virus. Additionally, mda-7/IL24 significantly increased the apoptotic rate of the murine and DU145 transduced cells. Microbubble delivery of Ads with ultrasound in cell culture enhances gene transfer into the cells regardless of the complement rich FBS media.

Our study demonstrated the feasibility of using human DU145 prostate adenocarcinoma cells and TRAMP-C2 cells derived from a murine model of prostate cancer to translate the ultrasound-mediated microbubble Adenovirus delivery system that we have developed.

INTRODUCTION

The primary objective of this grant was to test the effective means of mda-7/IL-24 gene delivery by ultrasound (US) and US contrast agents/microbubbles. The therapeutic potential of conditionally replication competent adenovirus (CRCAs) also known as cancer terminator virus (CTV (Ad.PEG-E1A-mda-7)) and non-replicating E1A deleted adenovirus carrying the mda-7/IL-24 gene (Ad.mda-7) was tested in both TRAMP-C2 and DU145 prostate cancer cell lines. As the project involves the uses of recombinant DNA and an infectious agent, an IBC (Institutional Biosafety Committee) approval was established before the study was started. Adenoviruses were amplified, purified, titrated, infected, disposed and stored according to the procedures and biosafety standards outlined in the established IBC protocol. These studies were completed and the results are outlined in this final report.

Additionally, the grant was also written to conduct an animal study. IACUC (Institutional Animal Care and Use Committee) approval has been established to develop a safe and effective means of gene delivery in vivo (immune-competent mice) that realizes the therapeutic potential of mda-7/IL-24 induction to combat human advanced Prostate Cancer malignancy. The protocol aims at targeting the primary prostate lesion in a TRAMP immune-competent mouse model of advanced prostate cancer along with the presence of a metastatic disease. These studies will take several more months before we get results as it takes sufficient time to cultivate a large colony from breeder mice.

BACKGROUND

For more than four decades, human adenoviruses have served as an excellent model system to study molecular mechanisms controlling cell cycle progression and cell death. More than 60 types of HAdV have currently been identified and divided into eight species, designated A, B1, B2, C, D, E, F and G. Members of the different species use different receptors for virus–host interactions and some are currently characterized as potential viral vectors in cancer gene therapy. HAdV show strict host specificity. Murine cells lack some of the receptors needed for HAdV infection such as the Coxsackie-and-Adenovirus Receptor (CAR), thus, murine cells are generally refractory (non-permissive) for HAdV infection and replication, although a very low level of HAdV infection and replication has been described in some mouse cells [1, 2].

Melanoma differentiation associated gene-7 also called interleukin-24 (mda-7/IL24) is well-known for its pro-apoptotic, anti-angiogenic, radio-sensitizing, immune-stimulatory properties and bystander activity on distant tumors [3-10]. Mda-7/IL-24 is a multifunctional suppressor gene belonging to the IL-10 family of cytokines [11, 12]. When delivered by HAdV vector, mda-7/IL-24 induces apoptosis selectively in almost all cancer cells while leaving normal cells unharmed [8]. Mda-7/IL-24 can be expressed and secreted from naïve normal and cancer cells thereby enhancing its apoptotic activity against primary and metastatic cancer [7]. Thus, HAdV expressing mda-7 should provide both tumor selectivity and adequate induction of newly synthesized MDA-7/IL-24 [3].

Gene therapy by adenoviral vectors has shown promising results in treating locally advanced cancers, however due to their immunogenicity they trigger both adaptive and innate immune responses. The antigenic nature of Ads leads to their rapid inactivation by neutralization antibodies and clearance by the immune system. Ad vectors elicit an innate immune response through the

myeloid differentiating factor 88 (MyD88)/Toll-like receptor (TLR)-9 resulting in the production of type I interferons (IFNs), interleukin (IL)-6 and IL-12 inflammatory cytokines [13, 14]. Additionally, unmodified viruses are generally non-specific in their action and this limits their use to direct target tumor or organ injection [3]. To circumvent these limitations we developed a novel approach wherein Ads are encapsulated inside the shell of acoustically active, lyophilized, lipid-encapsulated, perfluorocarbon microbubbles (MBs) (ultrasound (US) contrast agents), which act as delivery vehicles for a site-specific gene transfer system. MBs protect the viral payload from detection and rapid degradation by the hosts' immune system allowing for an intravenous (IV) injection rather than intratumoral (IT) injection [3, 15]. US breaks open the MB/Ads complexes by inducing cavitation, which allows Ads to transfer their transgene only to the sonoporated region. Cavitation of the MBs creates small shockwaves that increase cell permeability by forming temporary micropores on the cell surface bypassing the receptor-mediated dependence of HAdV. Our novel viral delivery technique mediated by MB and US brings new hope to the frontier of gene therapy and its use in clinical settings.

In order to facilitate the translation of this technology into human application, we envision testing an adenovirus carrying mda-7 (INGN 241) that is already in phase-I and -II clinical trials in patients with multiple solid tumors (none of which is of prostate origin) in treating prostate cancer cells [16]. *In vivo* studies involving the use of immune-deficient and immune-competent prostate cancer mice models are required. Thus, we studied the capacity of human Ad.mda-7/IL24 to infect mouse prostate cancer cells (Tramp-C2) derived from immune-competent mice and compared it to human prostate cancer (DU145). We also studied the effect of Ad.mda-7/IL24 to increase the apoptotic rate of TRAMP-C2 and DU145 prostate cancer cells following mda-7 gene transfer. Lastly, we tested US guided MB assisted gene delivery of reporter Ad.GFP in both murine and human prostate cancer cells.

MATERIALS AND METHODS

Cell Culture

The DU-145 (human prostate adenocarcinoma), TRAMP-C2 (mice prostate adenocarcinoma) and human kidney embryonic 293 cell lines were obtained from the American Type Culture Collection (ATCC, Rockville, MD). DU-145 cells were grown in RPMI 1640 (Hyclone, Waltham, MA) supplemented with 10% fetal bovine serum (FBS) (Hyclone, Waltham, MA), and 100 units/mL penicillin supplemented with 1 mg/mL streptomycin (both from Hyclone, Waltham, MA). The 293 cells were grown with Dulbecco's modified Eagle's medium (Hyclone, Waltham, MA) supplemented with 10% FBS (Hyclone, Waltham, MA). TRAMP-C2 cells were grown with Dulbecco's modified Eagle's medium (Hyclone, Waltham, MA) supplemented with 5% FBS (Hyclone, Waltham, MA), and 100 units/mL penicillin supplemented with 1 mg/mL streptomycin (both from Hyclone, Waltham, MA). All cells were grown at 37°C, in a 5% CO₂/95% atmosphere incubator.

Cytological Observations

The cells were examined under an inverted Olympus IX70 microscope (Olympus America, Inc. Melville, NY). Fluorescence images were captured with Sensicam QE camera (Cooke Co., Auburn

Hills, MI) and managed with the SlideBook 3.0 software (Intelligent Imaging Innovations Inc., Denver, CO).

Adenoviral production and purification

Ad-GFP, which expresses the green fluorescence protein gene under the strong cytomegalovirus (CMV) constitutive promoter was generated using the AdEasy system (Carlsbad, CA); the conditionally replication competent cancer terminator virus CTV-Mda7 (Ad.PEG-E1A-mda-7) [17-19] and Ad.mda-7 [20] were amplified and purified with the BD Adeno-X virus purification kit (BD Biosciences, Mountain View, CA) following manufacturer's directions. Viral titers were determined by a plaque assay and the titer was adjusted to 1.2×10^{12} plaque-forming units (pfu)/mL as described [20]. CTV-Mda7 (Ad.PEG-E1A-mda-7) and Ad.mda-7/IL-24 were provided by Dr. Paul Fisher (Virginia Commonwealth University, Richmond VA). Each viral stock was propagated and purified from 293 cell cultures. Cells were harvested 24-36 hours after infection, pelleted and re-suspended in heat-inactivated media. 293 cells were lysed by a three-freeze/thaw cycle method. Cell debris was removed. Viruses were purified by chromatography followed by dialysis. Viruses are aliquoted and stored at -80°C . Viral titers were determined by a plaque assay. Ad transductions were performed using 10, 25, 50 MOI Ads, in RPMI-1640 media with 2% Fetaclone-III heat-inactivated FBS (Hyclone, Thermo Scientific, Waltham, MA) and in with DMEM media with 2% Fetaclone-III heat-inactivated FBS (Hyclone, Thermo Scientific, Waltham, MA). Cells were collected after 24- or 48-hours.

Viral Burst assay

HEK 293 cells were used as control. HEK 293 cells, DU145 cells, TRAMP-C2 cells were infected with replicative HAdV (CTV.mda7) at 100 pfu/mL and 1,000 pfu/mL. Filtered transfection supernatants and viral particles present in the cells were collected at both 24 and 48 hours post-transfection. Cells were harvested 24- and 48- hours after infection, pelleted and re-suspended in heat-inactivated media. 293 cells were lysed by a three-freeze/thaw cycle method. Cell debris was removed. Viruses are aliquoted and stored at -80°C . The collective viral particles were tittered and determined by a plaque assay.

Antibodies

The following primary antibodies were used in Western Blot studies: mouse monoclonal anti-Mda-7/IL-24 k101 (GenHunter Corporation) (1:2,000 incubation for overnight), GFP cat#632377 (1:500) (BD Bioscience) and β -actin cat#A3853 (1:1,500) (Sigma Aldrich) as a control. The following are used in the flow cytometry studies: Rabbit Anti-Coxsackie Adenovirus Receptor Polyclonal Antibody, Alexa Fluor® 488 Conjugated bs-2389R-A488, Rabbit Anti-Integrin Alpha V + Beta 5 Polyclonal Antibody, Alexa Fluor® 647 Conjugated bs-1356R-A647 and Rabbit Anti-Integrin Alpha V + Beta 3 (CD51+CD61) Polyclonal Antibody, Alexa Fluor® 488 Conjugated bs-1310R-A488 from Bioss Inc.

Western blot analysis

DU-145 and TRAMP-C2 cells were transduced with 10, 25, 50 multiplicity of infection (MOI) of Ad.GFP and Ad.mda-7. Western blot analysis was conducted as previously described [3]. Cells were lysed on ice for 1hr with lysis buffer. Fifty μg of total protein plus loading buffer were loaded in each well for western blot analyses. SDS-PAGE was run using 8-12% bis-acrylamide gel at room temperature. Samples were blotted onto a nitrocellulose membrane. To detect proteins the membranes was blocked with 5% Milk-TBST overnight at 4°C and reacted to primary antibodies

for 2hr at room temperature with constant motion on a an orbital shaker. The membranes were washed with TBST to remove excess primary antibodies. Incubation for 45 minutes with appropriate secondary antibodies followed. Immunodetection was performed using the enhanced chemiluminescence (ECL) system (Amersham, IL) according to the manufacturer's instructions. Western blot analyses with antibodies against the targeted proteins were performed to validate successful viral transfection of the cells.

Flow Cytometry Assay

DU145 and TRAMP-C2 cells were checked for different surface Ad receptors such as CAR (coxsackie adenovirus receptor) and integrins $\alpha V\beta 3/5$. Each was compared against IgG control. 10 μ L of Boss primary conjugated antibody was added for 30 mins at 4°C. Washed several times with 2mL 1X PBS. Resuspended in 100 μ L of 1X PBS. Samples were analyzed on BD Accuri C6 Flow Cytometry.

Adenoviral transduced DU145 and TRAMP-C2 cells were trypsinized and collected. Cells were centrifuged at 5000 rpm, washed and suspended in 1% FCS-PBS. This step was repeated three times. Samples were prepared, run by a BD Accuri C6 Flow Cytometer (BD Bioscience, San Jose, CA). Single cells population was gated and an FL1 & FL4 area histogram was drawn and formatted to show only the events inside the single cell region.

Annexin-V assay

Apoptotic cells were analyzed with fluorescein isothiocyanate (FITC) conjugated to Annexin-V antibody and Propidium Iodide (PI) from the Annexin-V/FITC Kit (Bender MedSystems, Burlingame, CA) following manufacturer's instructions. Cells were trypsinized and washed with PBS. Cells were centrifuge and re-suspended in binding buffer. The samples were analyzed with BD Accuri C6 Flow Cytometer (BD Bioscience, San Jose, CA). Annexin-V assay experiment was repeated three times and was run as triplicate of technical repeats. Statistical analysis was performed with GraphPad Prism 6 statistical software.

UTMD for prostate cancer cells.

Human DU145 and murine TRAMP-C2 prostate cancer cells were grown in both Fetal Bovine Serum (FBS) rich media and Heat-inactivated FBS media. Targeson (Targeson, Inc. San Diego, CA) custom synthesis US contrast agent (perfluorocarbon microbubbles, encapsulated by a lipid monolayer and poly(ethyleneglycol) stabilizer) were prepared following manufacturer's instructions [3]. Cells were infected with Ad.GFP with 10MOI or with Ad.GFP complexed with microbubbles (Targeson) at 10MOI. US exposure was achieved with a Micro-Maxx SonoSite (SonoSite, Bothell, WA) US machine equipped with the transducer L25 set at 0.7 Mechanical Index (MI), 1.8 MPa for 1 min [3].

Statistical analysis

Statistical analysis was performed using the GraphPad Prism 6 statistical software. Comparison of cell death by Annexin-V on adenoviral transduced groups was conducted using an ANOVA test with post hoc test Tukey's multiple comparison test. p-values of less than 0.05 were considered statistically significant.

RESULTS

Cytological Observations after Adenoviral Gene Transfer

The murine TRAMP-C2 and human DU145 prostate cancer cells were transduced with an Ad carrying the green fluorescence protein (GFP) (Ad.GFP) (Figure 1) with increasing doses of 10, 25 and 50 MOI (multiplicity of infection). TRAMP-C2 cells and DU145 cells infected with various doses of Ad.GFP showed a dose dependent increase of fluorescence. However, DU145 cells showed a higher transduction of GFP in comparison to TRAMP-C2 cells at each multiplicity of infection.

Quantification of the Ad.GFP viral uptake

Ad.GFP uptake was determined for murine TRAMP-C2 and human DU145 prostate cancer cells by using FACS analysis after infecting the cells with 10, 25 and 50 MOI. A discrepancy is observed for TRAMP-C2 cells when infected with 10MOI, showing only a 90% uptake of Ad.GFP. A dose dependent increase in uptake of Ad.GFP is observed in TRAMP-C2 cells as the MOI is increased. DU145 cells on the contrary showed a 100% uptake regardless of MOI (Figure 2).

Quantification of Ad receptors present on the surface of the cells

Surface Ad receptors were determined by Accuri C6 flow cytometry for the percentage of expression of Coxsackie Adenovirus Receptor (CAR), integrin $\alpha V\beta 5$ and $\alpha V\beta 3$ that are known to be responsible for the attachment of Ad5 to mammalian cells (Table 1). Both human DU145 and murine prostate cancer cells showed a similar expression profile for CAR and integrin $\alpha V\beta 3/5$.

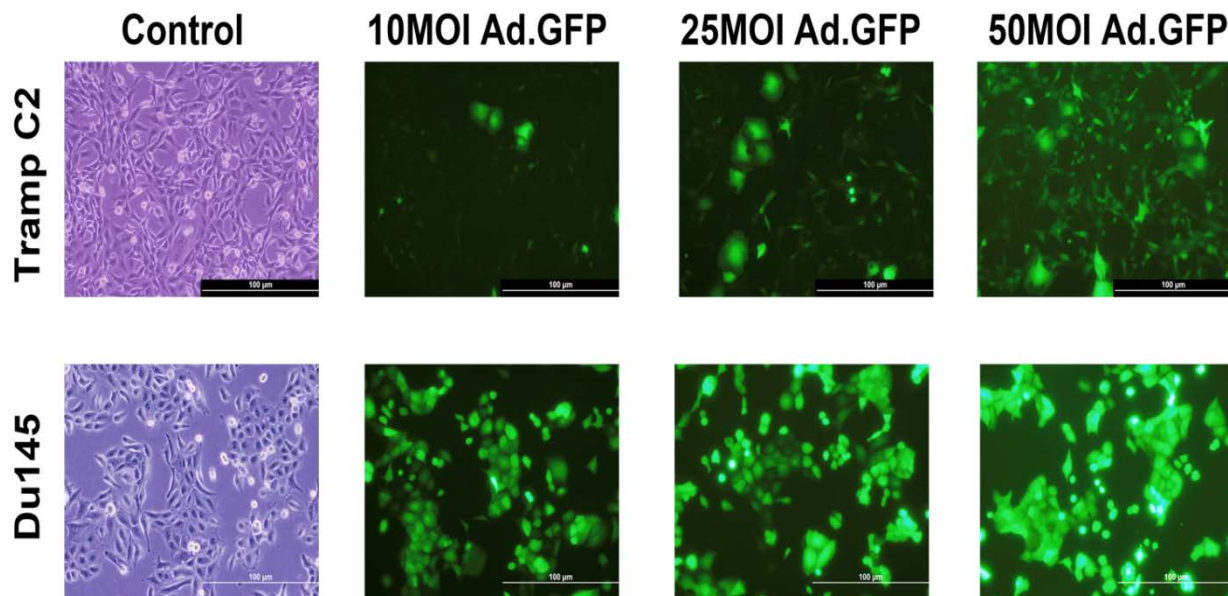


Figure 1. Fluorescence microscopy images of Ad.GFP (10, 25, 50 MOI) transduced TRAMP-C2 and DU145 cells. We effectively infected TRAMP-C2 cells with Ad.GFP and observed a dose-dependent expression of GFP, which was correlated to the increasing amount of Adenoviral MOI used.

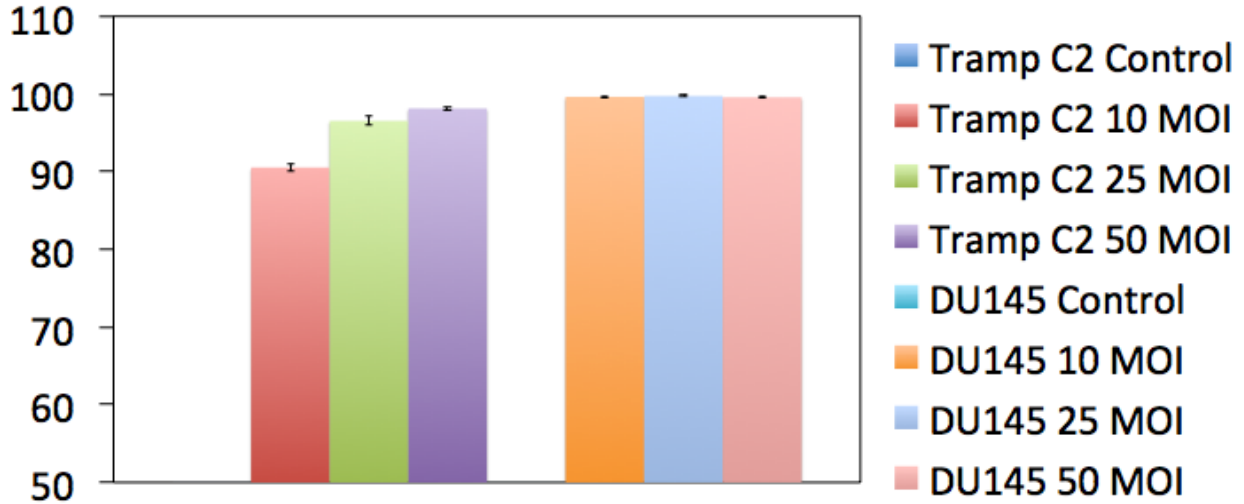


Figure 2. In vitro assessment of Ad.GFP uptake in murine and human carcinoma cell lines. Cells were infected at 10, 25 and 50 particles/cells (ppc) of Ad.GFP and harvested at 24 hours post-infection to determine the infectivity by FACS analysis.

Table 1. Determination of the expression of surface Adenoviral receptors by flow cytometry.

Cells	CAR	$\alpha V\beta 5$	$\alpha V\beta 3$
DU145	90.08±1.71	95.98±0.17	28.58±1.13
TRAMP-C2	96.60±0.22	93.9±1.38	32.70±1.97

Verification of protein expression by western blots

The TRAMP-C2 cell line is generated from prostate tumors harvested from a 32-week TRAMP mouse. We carried out infection studies with Ad5 carrying mda7 or GFP at different multiplicities of infection (MOI). Figure 3 shows dose dependent expression of GFP and mda-7 protein by western blot analysis (Figure 3). The results show that we effectively transferred to murine PC cells a transgene (GFP or mda-7) with Ad5 viruses.

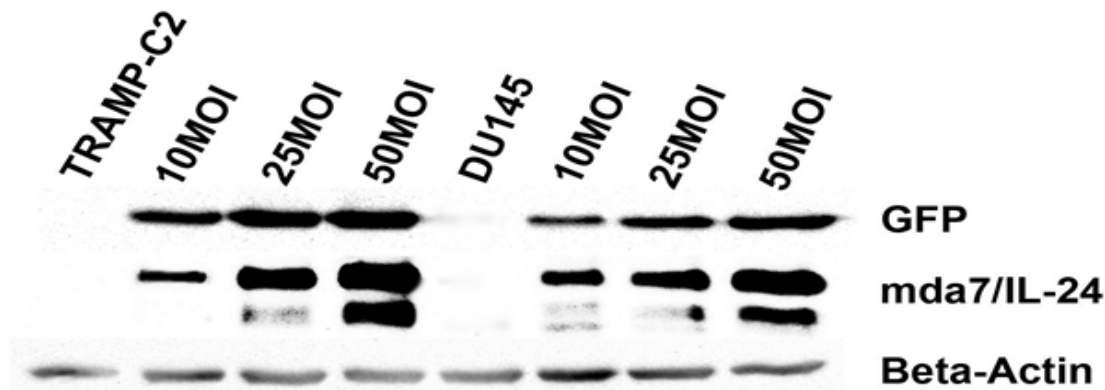


Figure 3. Western blot analysis of TRAMP-C2 and DU145 cells infected with different MOIs of Ad.GFP or Ad.mda-7/IL24. Cell lysates were run on SDS-PAGE and reacted with appropriate

specific primary and secondary HRP-conjugated antibodies. Beta actin was used as a loading control.

Viral burst assay to assess the capacity of replicative HAd5 to produce viral particles

The control HEK 293 embryonic kidney cells and human DU145 prostate cancer cells showed an increase in viral count at both 24 and 48 hours post infection of 100 pfu/mL and 1,000 pfu/mL replicative competent HAd5 (CTV). Thus, DU145 and HEK 293 are permissive for the replication of HAd5 and would make good animal models for testing the replicative and transfection ability of HAd5. However, TRAMP-C2 cells showed a decrease in viral count from 24 to 48 hours for both pfu of HAd5 indicating a lack of viral replication. Thus TRAMP-C2 cells are non-permissive for replication of HAd5 and would make a good animal model only for the transfection ability of HAd5 (Figure 4).

Annexin V staining for cell death

The apoptotic rate of the transduced cells was quantified by assessing Annexin-V expression. The analyzed cells were allocated in a quadrant diagram according to their DNA content and the presence of Annexin-V on the extracellular cell membrane during apoptosis. Statistical analysis was run on Annexin-V triplicates using Graphpad Prism 6 software for an ANOVA on dead cells with a post hoc test of Tukey's multiple comparison test (Figure 5 and Table 2). TRAMP-C2 and DU145 cells were undergoing apoptosis and necrosis, collectively called as dead cells. Non-transduced cells were compared to Ad.mda7/IL24 transduced cells. Mean and standard deviation from Annexin-V experiment was calculated for each adenoviral treated groups. There was an increase in the significance and percentage of cell death that was concentration dependent compared to the control. A significant percentage of cell death for TRAMP-C2 cells infected with 50MOI was observed in comparison to 10MOI of Ads (Figure 5 and Table 2). Cell death observed for TRAMP-C2 cells infected with 10MOI and 25MOI did not show any significant difference in comparison to DU145 cells infected with 10MOI. However, overall DU145 cells showed more cell death with Ad.mda7 at 25MOI and 50MOI in comparison to TRAMP-C2 cells infected with the same MOI.

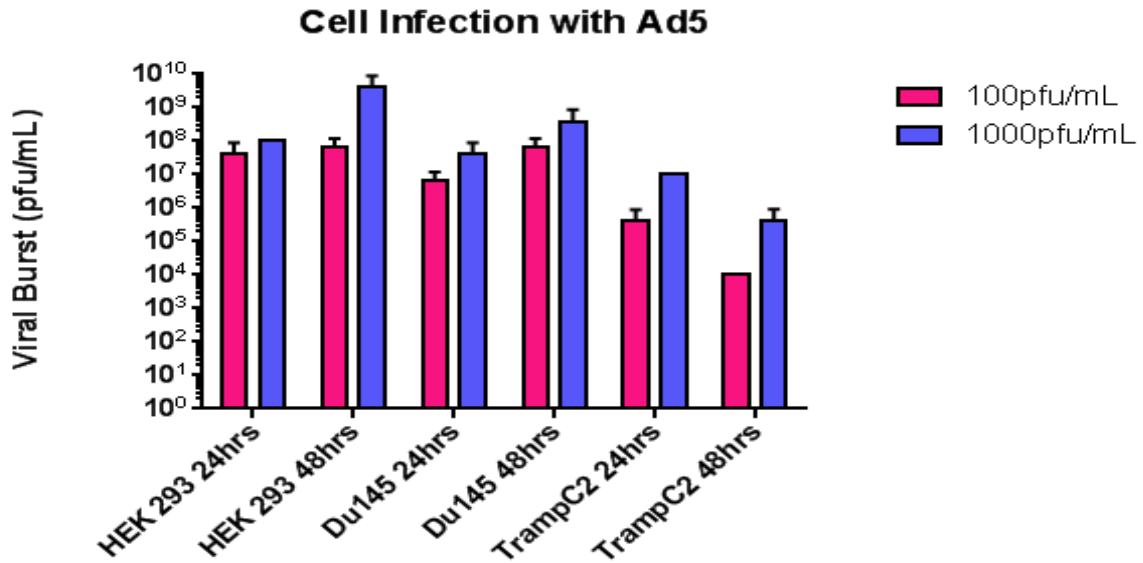


Figure 4. Subconfluent murine and human cell lines were infected with replicative competent HAdV at 100 pfu/mL and 1,000 pfu/mL and harvested 24- and 48-hours later.

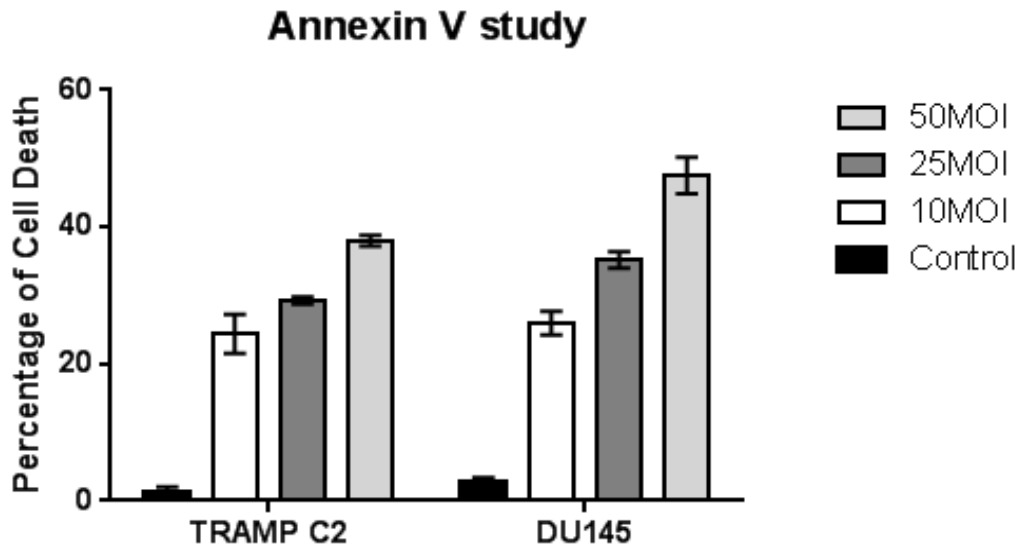


Figure 5. Annexin-V/PI staining of TRAMP-C2 and DU145 cells infected with Ad.mda-7/IL24. TRAMP-C2 cells were transduced with Ad.mda-7/IL24 at 10, 25 & 50 multiplicity of infection (MOI) and harvested at 96 hours post infection and determined by FACS analysis. Bar graph represent sum of apoptotic and necrotic cells.

Table 2. ANOVA (Analysis of Variance) significance table with a Post Hoc Tukey’s multiple comparison test for Annexin-V assay between TRAMP-C2 and DU145 cells transduced with Ad.mda7/IL-24. * The mean difference is significant at the 0.05 level.

Comparison between groups		Significant?
TRAMP-C2:Control	TRAMP-C2:10MOI	Yes
TRAMP-C2:Control	TRAMP-C2:25MOI	Yes
TRAMP-C2:Control	TRAMP-C2:50MOI	Yes
TRAMP-C2:Control	DU145:Control	No
TRAMP-C2:Control	DU145:10MOI	Yes
TRAMP-C2:Control	DU145:25MOI	Yes
TRAMP-C2:Control	DU145:50MOI	Yes
TRAMP-C2:10MOI	TRAMP-C2:25MOI	Yes
TRAMP-C2:10MOI	TRAMP-C2:50MOI	Yes
TRAMP-C2:10MOI	DU145:Control	Yes
TRAMP-C2:10MOI	DU145:10MOI	No
TRAMP-C2:10MOI	DU145:25MOI	Yes
TRAMP-C2:10MOI	DU145:50MOI	Yes
TRAMP-C2:25MOI	TRAMP-C2:50MOI	Yes
TRAMP-C2:25MOI	DU145:Control	Yes
TRAMP-C2:25MOI	DU145:10MOI	No
TRAMP-C2:25MOI	DU145:25MOI	Yes
TRAMP-C2:25MOI	DU145:50MOI	Yes
TRAMP-C2:50MOI	DU145:Control	Yes
TRAMP-C2:50MOI	DU145:10MOI	Yes
TRAMP-C2:50MOI	DU145:25MOI	No
TRAMP-C2:50MOI	DU145:50MOI	Yes
DU145:Control	DU145:10MOI	Yes
DU145:Control	DU145:25MOI	Yes
DU145:Control	DU145:50MOI	Yes

DU145:10MOI	DU145:25MOI	Yes
DU145:10MOI	DU145:50MOI	Yes
DU145:25MOI	DU145:50MOI	Yes

UTMD for prostate cancer cells.

Human DU145 and murine prostate cancer cells were infected either with Ad.GFP or complexed Ad.GFP/MB at 10MOI and after 24hours images were taken with fluorescent microscopy. US application increased the expression of GFP in comparison to the control or Ad.GFP alone group for both DU145 and TRAMP-C2 cells (Figures 6 and 8). US also allowed for the transfection of Ad.GFP in complement rich FBS media for both DU145 and TRAMP-C2 cells (Figures 6 and 8).

MBs also facilitated the transfection of Ad.GFP in both FBS rich and Heat Inactivated-complement depleted FBS media (Figures 7 and 9). Transfection increased further when Ad.GFP was complexed with a MB (Ad.GFP/MBs) and US was applied to the both DU145 and TRAMP-C2 cells (Figures 7 and 9). Similar GFP expression was observed for DU145 when complexed Ad.GFP/MBs were incubated with FBS and US was applied regardless for media being used (Figure 7) because FBS contains a complement, which binds to the free Ads on the surface of the bubble thereby inactivating the Ads. Similar observation was also recorded for TRAMP-C2 cells (Figure 9). Lastly, unclean complexed Ad.GFP/MBs showed similar GFP expression compared to cleaned (FBS incubated) complexed Ad.GFP/MBs in complement rich FBS media (Regular media). Highest transfection was observed for DU145 cells that received the unclean (FBS untreated) Ad.GFP/MBs and US (Figure 7).

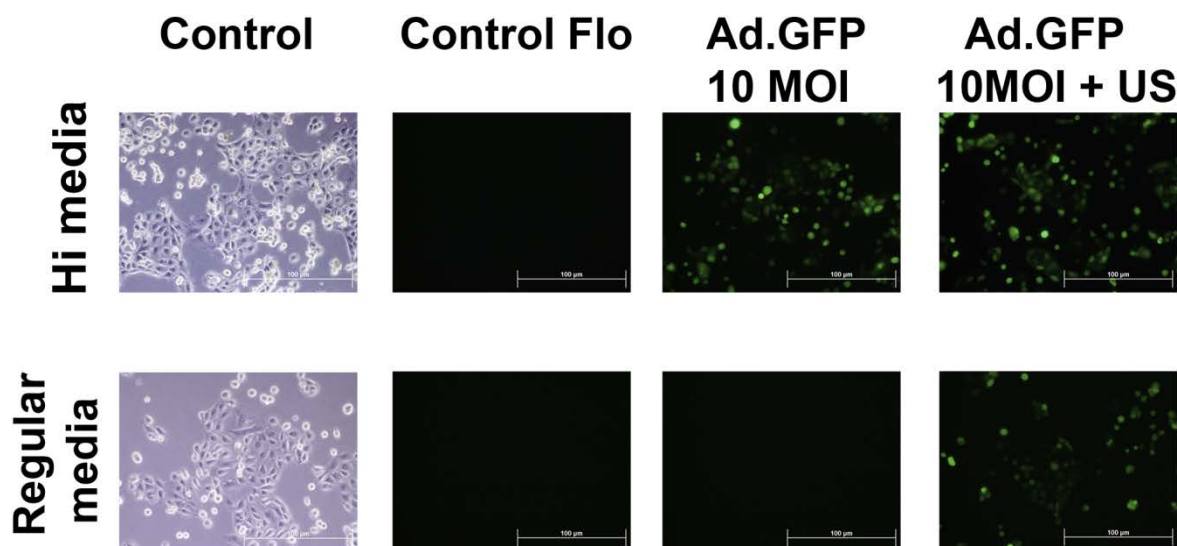


Figure 6. DU145 cells infected with Ad.GFP at 10MOI and Ultrasound application.

*Flo:Florescence, HI:heat inactivated, US: Ultrasound, Regular media: contains fetal bovine serum (FBS).

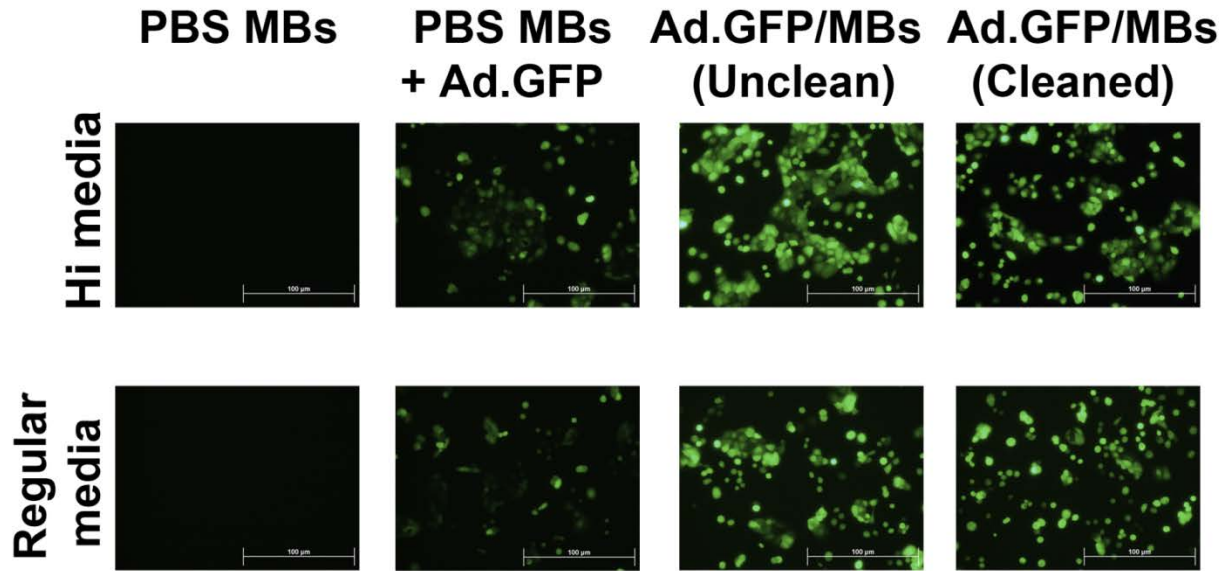


Figure 7. DU145 Cells infected with Ad.GFP/MBs at 10MOI and Ultrasound application. In second column MBs rehydrated with PBS was added separately with Ad.GFP at 10MOI. In the third column Ad.GFP/MBs were complexed but not cleaned with FBS before adding it to the cells. In the fourth column Ad.GFP/MBs were complexed and cleaned with FBS before adding it to the cells. *Flo:Florescence, HI:heat inactivated, US:Ultrasound, Regular media: contains fetal bovine serum (FBS).

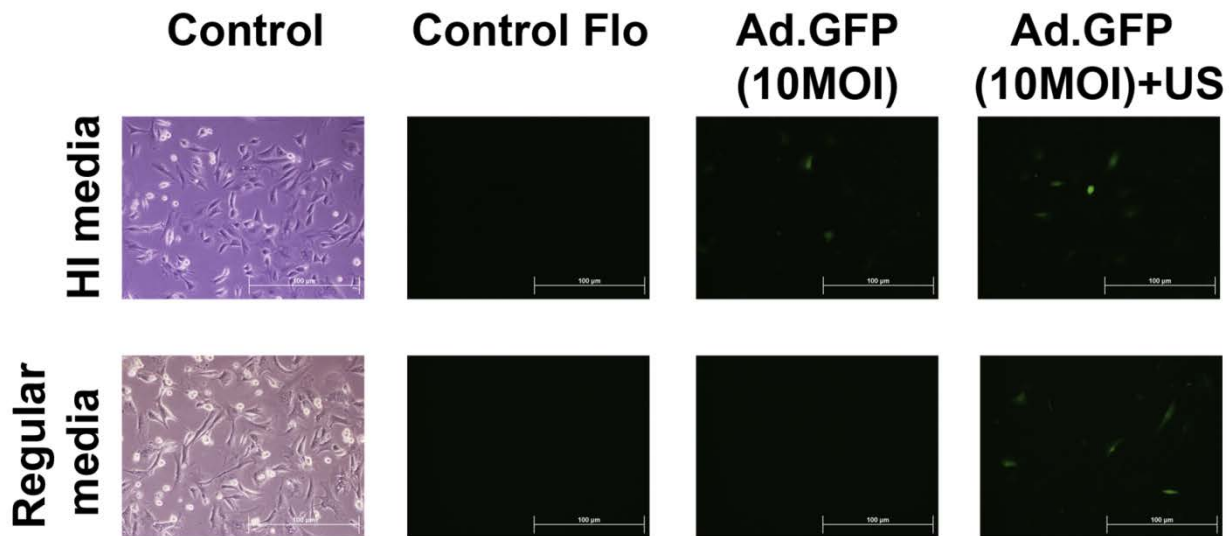


Figure 8. Tramp-C2 cells infected with Ad.GFP at 10MOI and Ultrasound application. *Flo:Florescence, HI:heat inactivated, US: Ultrasound, , Regular media: contains fetal bovine serum (FBS).

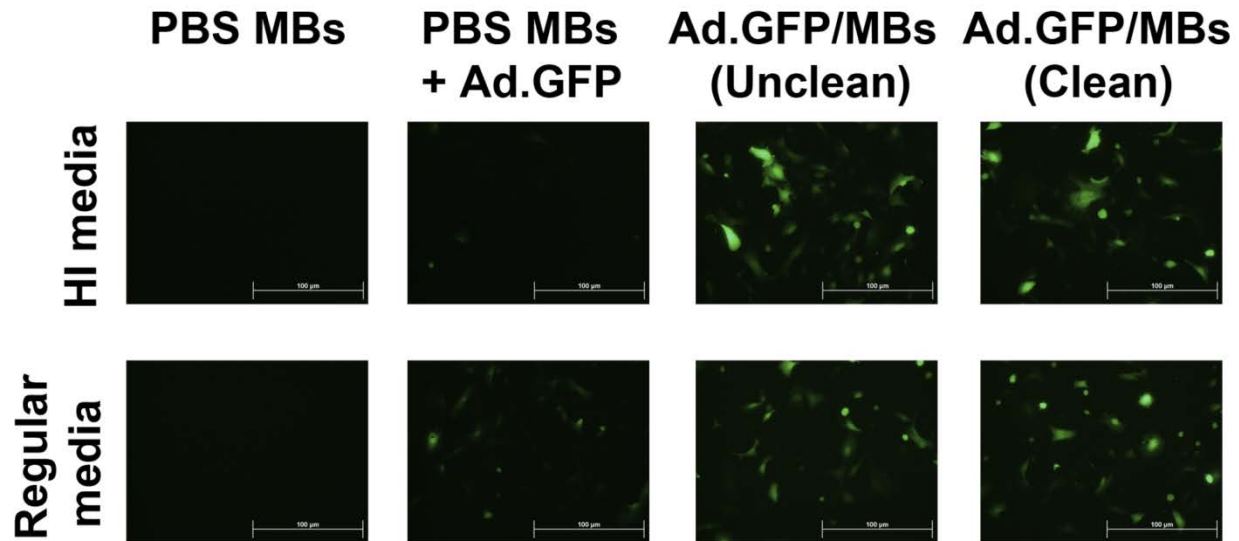


Figure 9. Tramp-C2 cells infected with Ad.GFP/MBs at 10MOI and Ultrasound application. In second column MBs rehydrated with PBS was added separately with Ad.GFP at 10MOI. In the third column Ad.GFP/MBs were complexed but not cleaned with FBS before adding it to the cells. In the fourth column Ad.GFP/MBs were complexed and cleaned with FBS before adding it to the cells. *Flo:Florescence, HI:heat inactivated, US: Ultrasound, , Regular media: contains fetal bovine serum (FBS).

DISCUSSION

There are many obstacles to successful virotherapy that have become apparent from clinical studies. This includes problems associated with the use of replicating human Ads that are species-specific as the non-human (animal) model systems rarely predicts the outcome seen in humans. For example, human tumor xenografts in nude mice can provide a ‘permissive’ preclinical model for Ads but nude mice are by definition immune-compromised [2]. Thus the immune responses due to Ads cannot be fully studied in this pre-clinical model. Additionally, due to species specificity, Ads do not replicate in normal mouse tissues thereby preventing any relevant off-target effects in such systems. Lastly, immune-compromised mice have a deficient immune system thus making it difficult to observe the effects of immune modulatory viruses [21]. Thus more suitable animal models need to be selected for the desired effect to be observed.

In this study, the ability of both replicating (CTV.mda7) and non-replicating (Ad.GFP and Ad.mda7/IL-24) human Ad5 was tested by infecting human DU145 and murine prostate cancer cells. The goal of this study was to test if human DU145 PC cells that are radio-resistant, androgen receptor ablated, p53 mutated cells and isolated from a brain metastasis would make a good pre-clinical model for the use of microbubble assisted gene delivery with US. This delivery system has several components that needed to be test to ensure successful translation from bench to bedside. The infection studies on DU145 cells with Ad.GFP, Ad.mda7 and CTV.mda7 showed successful transduction with different MOI of replication permissive HAd5 and demonstrated a therapeutic response to gene therapy with mda7. Lastly, US greatly enhanced the transgene expression of GFP when delivered with complexed Ad.GFP/MBs regardless of the presence of FBS, thus ensuring a proper penetration of the encapsulated Ads into the cell. FBS acted as a complement protein system inactivating the Ads from infecting DU145 cells. US and MBs cause temporary pore formation on

the plasma membranes and increase the permeability of the membrane to allow an increased Ad uptake. These factors make DU145 xenograts an attractive immune-compromised animal model to test the delivery of microbubble assisted gene delivery with US.

Similarly, TRAMP-C2 PC cells that are radio-resistant, possessing wild-type (wt) p53, isolated from 32-week old C57BL6 immune-competent mice with poorly differentiated prostate carcinoma were tested whether for the delivery of MB assisted gene therapy with US to verify if they would make a good pre-clinical immune-competent model. Similar results to DU145 studies were observed using TRAMP-C2 cells except that infection studies using TRAMP-C2 cells showed a reduced GFP expression in comparison to the transfected DU145 cells. However, a dose dependent increase in transgene expression was observed as the MOI were increased. This could not be explained by the Ads surface receptor expression in TRAMP-C2 cells, as they are similar to DU145. Also, a reduced therapeutic response was observed for Ad.mda7 transfected cells in comparison to DU145 cells, however still statistically significant in comparison to the control. Thus, murine immune-competent TRAMP-C2 prostate cells that can be syngeneically implanted into immune-competent C57BL6 would make an attractive model to study the immune-modulating, immune-responses due to the Ads and the therapeutic benefit of microbubble assisted US guided gene transfer. Additionally, the TRAMP mouse model of prostate cancer can be used to demonstrate the validity of UTMD mda-7 gene delivery approach in immune competent animals.

Successful completion of the immune competent animal studies will open the possibility to translate from the bench to the bedside the targeted mda-7 gene delivery method by performing clinical studies on metastatic prostate cancer patients.

ACKNOWLEDGEMENTS

I acknowledge the grant by the NASA WV Space Grant Consortium as well as my Research Mentor, Dr. Pier Paolo Claudio.

REFERENCES

1. Ganly, I., V. Mautner, and A. Balmain, *Productive replication of human adenoviruses in mouse epidermal cells*. J Virol, 2000. **74**(6): p. 2895-9.
2. Hallden, G., et al., *Novel immunocompetent murine tumor models for the assessment of replication-competent oncolytic adenovirus efficacy*. Mol Ther, 2003. **8**(3): p. 412-24.
3. Greco, A., et al., *Eradication of therapy-resistant human prostate tumors using an ultrasound-guided site-specific cancer terminator virus delivery approach*. Mol Ther, 2010. **18**(2): p. 295-306.
4. Caudell, E.G., et al., *The protein product of the tumor suppressor gene, melanoma differentiation-associated gene 7, exhibits immunostimulatory activity and is designated IL-24*. J Immunol, 2002. **168**(12): p. 6041-6.

5. Ramesh, R., et al., *Melanoma differentiation-associated gene 7/interleukin (IL)-24 is a novel ligand that regulates angiogenesis via the IL-22 receptor*. *Cancer Res*, 2003. **63**(16): p. 5105-13.
6. Yacoub, A., et al., *mda-7 (IL-24) Inhibits growth and enhances radiosensitivity of glioma cells in vitro via JNK signaling*. *Cancer Biol Ther*, 2003. **2**(4): p. 347-53.
7. Su, Z., et al., *Unique aspects of mda-7/IL-24 antitumor bystander activity: establishing a role for secretion of MDA-7/IL-24 protein by normal cells*. *Oncogene*, 2005. **24**(51): p. 7552-66.
8. Fisher, P.B., *Is mda-7/IL-24 a "magic bullet" for cancer?* *Cancer Res*, 2005. **65**(22): p. 10128-38.
9. Fisher, P.B., et al., *mda-7/IL-24, a novel cancer selective apoptosis inducing cytokine gene: from the laboratory into the clinic*. *Cancer Biol Ther*, 2003. **2**(4 Suppl 1): p. S23-37.
10. Sarkar, D., et al., *Melanoma differentiation associated gene-7 (mda-7)/IL-24: a 'magic bullet' for cancer therapy?* *Expert Opin Biol Ther*, 2007. **7**(5): p. 577-86.
11. Pestka, S., et al., *Interleukin-10 and related cytokines and receptors*. *Annu Rev Immunol*, 2004. **22**: p. 929-79.
12. Huang, E.Y., et al., *Genomic structure, chromosomal localization and expression profile of a novel melanoma differentiation associated (mda-7) gene with cancer specific growth suppressing and apoptosis inducing properties*. *Oncogene*, 2001. **20**(48): p. 7051-63.
13. Zhu, J., X. Huang, and Y. Yang, *Innate immune response to adenoviral vectors is mediated by both Toll-like receptor-dependent and -independent pathways*. *J Virol*, 2007. **81**(7): p. 3170-80.
14. Zhu, J., et al., *Innate immunity against vaccinia virus is mediated by TLR2 and requires TLR-independent production of IFN-beta*. *Blood*, 2007. **109**(2): p. 619-25.
15. Dash, R., et al., *Developing an effective gene therapy for prostate cancer: New technologies with potential to translate from the laboratory into the clinic*. *Discov Med*, 2011. **11**(56): p. 46-56.
16. Cunningham, C.C., et al., *Clinical and local biological effects of an intratumoral injection of mda-7 (IL24; INGN 241) in patients with advanced carcinoma: a phase I study*. *Mol Ther*, 2005. **11**(1): p. 149-59.
17. Sarkar, D., et al., *A cancer terminator virus eradicates both primary and distant human melanomas*. *Cancer Gene Ther*, 2008. **15**(5): p. 293-302.
18. Sarkar, D., et al., *Dual cancer-specific targeting strategy cures primary and distant breast carcinomas in nude mice*. *Proc Natl Acad Sci U S A*, 2005. **102**(39): p. 14034-9.

19. Sarkar, D., et al., *Eradication of therapy-resistant human prostate tumors using a cancer terminator virus*. *Cancer Res*, 2007. **67**(11): p. 5434-42.
20. Su, Z.Z., et al., *The cancer growth suppressor gene mda-7 selectively induces apoptosis in human breast cancer cells and inhibits tumor growth in nude mice*. *Proc Natl Acad Sci U S A*, 1998. **95**(24): p. 14400-5.
21. Tedcastle, A., et al., *Virotherapy--cancer targeted pharmacology*. *Drug Discov Today*, 2012. **17**(5-6): p. 215-20.

UNILATERAL HEATING TO INCREASE IGF1 UPTAKE AND BONE LENGTH IN MICE

Holly Tamski
Biomedical Sciences, PhD
Marshall University
Huntington, WV 25701

ABSTRACT

The prevalence of limb length inequality is about 90% in the general population. A limb length inequality of greater than 20 mm can significantly impair walking and ultimately cause conditions such as scoliosis, back pain, and osteoarthritis (Knutson 2005). The primary obstacle for treatment of limb length inequality is a limited ability to deliver therapeutic drugs to intact cartilage growth plates, which are the sites of bone elongation. Insulin-like growth factor 1 (IGF1) is the major circulating hormone of growth and is one of the treatments used for children with stunted linear growth. Research has established that exposure to warm ambient temperatures during growth can increase bone length in laboratory experiments. Previous work has also shown that warm temperature promotes transport of small soluble molecules that can enter the cartilage growth plate and potentially enhance extremity growth. **The purpose of this project was to test the hypothesis that exposure to warm temperature augments the actions of IGF1 in the growth plate to enhance length of the extremities.** The long-term goal is to use heat as a noninvasive clinical strategy to increase bone growth rate by enhancing activity of bone-lengthening drugs in the growth plate. The rationale for determining the relationship between temperature-enhanced bone growth and increased IGF1 action is to discover a way to use a heat-based therapy in combination with drug administration to improve the treatment of growth impairment in children. This project involved treating young growth hormone receptor knockout (GHRKO) mice, which are IGF1 deficient, to a daily 40-minute unilateral (one-sided) heating regimen for 14 days after the mice were weaned. The rationale was to test the effect of heat in a model that lacked this important hormone of growth. Wild-type C57BL/6 mice served as controls to demonstrate a heat effect. Growth plate height increased 8.3% on the heat-treated side of the wild type mice when compared to their non-treated side. There was no significant increase in growth plate height in the GHRKO mice, indicating that heat does not have an effect in the absence of IGF1. In order to determine the extent to which heat is retained in the extremities after the treatments, thermal imaging methods were developed during this funding period. Preliminary studies show that heat-treated limbs remained 3.3% warmer (0.8C) than the non-treated limb at 30 minutes, and 1.5% warmer (0.6C) at 60 minutes after the daily treatments had ended. These results are significant because they provide a first step toward developing therapies using a combination of heat and mild drug administration to enhance bone elongation noninvasively. Successful continuation of this work is expected to lead to future developments of clinical studies in the treatment of bone growth disorders using inexpensive, nonsurgical methods.

INTRODUCTION

Research has established that exposure to warm ambient temperature during growth increases bone length. The mechanism for the linear relationship between temperature and limb length is not yet

known. However, it is suspected that the relationship between temperature and limb length can be explained by the mechanism of heat increased insulin-like growth factor 1 (IGF1) activity in the growth plate (Serrat, Efaw, and Williams 2014). IGF1 is the major circulating hormone of growth (Mohan and Kesavan 2012; Yakar et al. 2005; Yakar, Rosen, and Beamer 2002). It is known that limb elongation is IGF1 dependent (Mohan and Kesavan 2012). Increased temperatures may have the ability to increase transport of small soluble molecules, such as IGF1, into the growth plate and enhance extremity growth (Serrat et al. 2014). We predict that heat therapy, in conjunction with routine administration of IGF1, will increase bone growth more than either heat or drug treatment alone. The *objective* of our research was to validate a unilateral heating model to increase length of specific long bones without surgical intervention. The *rationale* for determining the relationship between temperature-enhanced bone growth and increased IGF1 action was to discover a way to use a heat-based therapy in combination with drug administration to improve the treatment of growth impairment in children. Applying a comfortable heating device to the lower limb of a child is a more suitable solution to the alternative invasive procedures, which include external fixators to physically lengthen the limbs. We *hypothesize* that exposure to warm temperature augments the actions of IGF1 in the growth plate to enhance length of the extremities. To test this hypothesis, a unilateral (one-sided) heating model was established under two different conditions (1) unilateral heating of GH receptor knockout (GHRKO) mouse limbs; (2) unilateral heating of the limbs of wild-type (WT) C57BL/6 mice injected with saline and IGF1 (sc. 2.5 µg/g body weight). In both experimental groups, mice were unilaterally treated with heat (40C) for 40-minutes daily, for 2 weeks. GHRKO mice were chosen as a relevant model for this study because they have low levels of circulating IGF1 (List et al. 2011; Sims et al. 2000). The intent was to start the treatment when the mice were 3 weeks old because the mice are growing most rapidly between 3-5 weeks of age (Serrat, Efaw, and Williams 2014) Under the experimental condition (1) GHRKO mice and the wild-type controls were 3 weeks old at the start of unilateral heat treatment. However, due to an advantageous shipping error, the wild-type mice under experimental condition (2) were older (approximately 5 weeks of age) at the start of heat treatment. These older mice injected with IGF1 were therefore not included in this study. However, the older mice injected with the saline control functioned to answer a question about effects of heat on older animals. At the end of the 2-week heating period, mice were sacrificed and relevant tissues were harvested.

We were able to evaluate the success of our model by analyzing the effects of heat treatment on outcome variables such as tibial elongation rate, femoral length, and morphological differences in the tibial growth plate. Preliminary studies have already shown that femoral length of heat-treated limbs (40C) increased 1.3% and the tibial elongation rate was >12% greater than the non-treated side (30C) (Serrat, Schlierf, et al. 2014). This study evaluated the effects of heat-treatment in GHRKO mice, in which the animals are deficient in IGF1, the major hormone required for growth. Without functional growth hormone receptors, the mice are resistant to the actions of GH and therefore have elevated levels of GH and depressed levels of serum IGF1 (Kopchick et al. 2014; List et al. 2011). These mice mimic many of the conditions seen of human GH-insensitive Laron Syndrome and therefore are an efficient disease model for these experiments.

Bone elongation occurs at the cartilaginous growth plate (Fig. 1) when chondrocytes divide, differentiate, become enlarged and then gradually are replaced by mineralized tissue (Farnum, Tinsley, and Hermanson 2007; Hunziker 1994; Mohan and Kesavan 2012; Wilsman et al. 2008). The growth plate is therefore a focal area of interest when determining the effects of temperature on bone growth. Histological analysis of the growth plate in the proximal tibia was accomplished

using a Safranin O stain, which binds proteoglycans in cartilage and was used to quantitatively assess morphological differences between the non-treated and heat-treated limbs (Poole, Pidoux, and Rosenberg 1982). The proximal growth plate of the tibia is considered widely as a representative of long bone development (Lupu et al. 2001). There are three main zones of chondrocytes in the growth plate, the resting zone, proliferative zone, and hypertrophic zone (Farnum et al. 2007; Karimian, Chagin, and Sävendahl 2012; Lupu et al. 2001). In mammals, the enlargement of the hypertrophic zone in the growth plate contributes greatly to longitudinal growth (Cooper et al. 2013; Farnum et al. 2007; Lupu et al. 2001). This evidence suggests that, since warm temperature increases growth rate in mice, then the hypertrophic zone should be extended in the growth plates of the heat-treated limbs. IGF1 is expressed in both proliferating and pre-hypertrophic chondrocytes (Lupu et al. 2001; Yakar et al. 2002). If heat enhances IGF1 action in the growth plate, it is anticipated that the height of the cellular regions expressing high levels of IGF1 will increase with increasing longitudinal growth. In IGF1-deficient GHRKO mice, both the proliferative and hypertrophic zones are significantly reduced in size (Wang et al. 2004). These regions in heat-treated limbs of GHRKO mice are not expected to differ from their non-treated equivalents.

The main principle underlying this research is that warm temperature can act as a fundamental regulator for enhancing bone growth. In addition to exploring the impact of heat on IGF1 activity in the growth plate, we were also interested in the long-term effects of unilateral heat treatment on temperature retention in the limbs. We *hypothesize* that limb temperature on the heat-treated side will remain elevated between treatments. The technique used to investigate this hypothesis was infrared thermal imaging. Infrared thermography is used to quantify the period of heat retention after daily treatments and determine whether temperatures remain permanently elevated after multiple days of heating. We obtained a FLIR E6/E8 thermal imager to test in two pilot studies to determine the best methods for imaging. In the first pilot study, images of female WT mice (N=3) on the second day of unilateral heating were captured 30- and 60-minutes post-heating. Hindlimb temperature was measured at each time point to calculate the percent difference between the non-heated and heat-treated limb surface temperature. In the second pilot study, images of wild-type mice kept at ambient temperature (21C) were taken over a period of 4 days at three consecutive 30-minute time intervals. On day 4 of the study, mice were moved from a 21C room to an 18C room and allowed to acclimate for 30 minutes. Images were captured after 30 minutes at 18C and mice were then moved back to 21C, where images were captured 30 minutes later. This experiment was conducted to demonstrate changes in surface limb temperature after a short 30 minute acclimation period in rooms varying a slight 3C temperature difference.

CLINICAL BACKGROUND

The prevalence of leg length inequality is about 90% in the general population (Knutson 2005). Limb length inequality can impair walking and ultimately cause conditions such as scoliosis, back pain, and osteoarthritis. Treatment can range from a simple shoe lift (for differences of less than 2 cm) to various surgical techniques, such as invasive bone lengthening or shortening to equalize limb lengths (Hasler and Krieg 2012; Zhang and Yokota 2011; Zhang et al. 2009). The main obstacle for treatment is a limited ability to deliver therapeutic drugs to intact growth plates. Research has established that exposure to warm ambient temperatures during growth can increase bone length in laboratory experiments. Our lab has shown that temperature affects transport of small soluble molecules that can enter the cartilage growth plate and potentially enhance extremity

growth (Williams et al. 2007). Insulin-like growth factor 1 (IGF1) is the major circulating hormone of growth. It is unknown whether temperature influences activity of IGF1 in the growth plate. Temperature modulation using a unilateral heating model could be used to study the impact of mild heat on IGF1 signaling in the growth plate. Mice lacking function of the growth hormone receptor have low levels of circulating IGF1 and are therefore a good disease model to study temperature effects of IGF1 in the growth plate. The growth plate is an important focal area of interest when determining the effects of temperature on bone growth, since this is where bone elongation occurs.

METHODS

Experimental Unilateral Limb-Heating Model

Wild-type C57BL/6 mice (N=10), obtained from a commercial vendor, and growth hormone receptor knockout (GHRKO) mice (N=5), obtained from a colony at Ohio University (List et al. 2011), were treated once daily under isoflurane anesthesia to a 40-minute unilateral heating regimen for 14 days following our published methods (Serrat, Schlierf, et al. 2014). Treatments were done between 3-5 weeks of age because this is when mice are growing rapidly (Eisen 1976; Serrat 2013; Serrat, et al. 2014). The unilateral heating regimen began daily at the start of the light cycle because this is when growth rate is naturally the highest (Stevenson et al. 1990). Body temperatures and respiratory rates were taken throughout the 40-minute heating to ensure stable physiology. Following the same methods, another group of wild-type C57BL/6 mice were administered a subcutaneous injection of saline (2.5 ug/g body weight). Treatments were done between ~5-7 weeks of age.

Measurement of Femoral Length

Femora were removed from the right (heat-treated) and left (non-treated) sides of mice to determine whether there was an increase in length on the heat-treated side. The femur was dissected, dried overnight, and scanned on a flatbed scanner. Lengths were measured using ImageJ software. The femur was measured in both wild-type and the GHRKO mice and differences were compared between non-treated and heat-treated limbs using paired t-tests (described below). Comparing non-treated to heat-treated limbs to the standard growth curves established by wild-type control mice that were not exposed to heat determines the average difference in growth on the heat-treated side.

Histological Analysis of Tibial Growth Plate Using a Safranin O Stain to Quantitatively Assess Morphological Differences

Wild-type C57BL/6 mice and GHRKO mice followed the heating model outlined above. Tibias were harvested and processed for histological analysis following routine protocols. The tibias used for histology were embedded in paraffin wax and sectioned (6 μ m thick sections) using a microtome then mounted onto slides for staining. Safranin-O stain binds proteoglycans in cartilage (Poole et al. 1982). Images were analyzed using Image J software to demonstrate morphological changes in tibial growth plates from the heat-treated and non-treated limbs, using parameters such as chondrocytes size and height of each growth plate zone, which are strong predictors of bone elongation rate (Cooper et al. 2013). The total height of the growth plate was measured as the distance between the epiphyseal bone and the metaphyseal chondro-osseous junction. The

hypertrophic zone (HZ) was measured from the point of chondrocyte enlargement to the edge of the metaphyseal chondro-osseous junction (Lupu et al. 2001).

Infrared Thermography (Thermal Imaging) to Collect Quantitative Body Temperature

Thermal images were taken to collect surface temperature measurements during the mouse light cycle in two different pilot studies. In both studies, mice were conscious and lightly restrained while images were captured of each side of the mouse. During the first pilot study thermal images were captured using a FLIR E6 thermal imager. Images were taken on the second day of unilateral heat treatment of 24-day-old female C57BL/6 mice at 30- and 60-minute intervals following treatment (N=3). The FLIR E8 thermal imager was used to capture images during the second pilot study. Images of C57BL/6 mice kept at ambient temperature (21C) were taken over a period of 4 days at three consecutive 30-minute time intervals (N=3). On day 4 of the study, mice were moved from 21C ambient temperature to an 18C room and allowed to acclimate for 30 minutes. Images were captured after 30 minutes at 18C and mice were then moved back to 21C, where images were captured 30 minutes later. Limb temperatures were quantitatively measured using the FLIR software program. Right-left side differences in limb temperature will determine the long-lasting effects of the treatment. This is important to understand the impact of heat therapy by observing the extended period for which the limbs maintain warmer temperatures.

Statistical Analysis

Statistical analyses were performed using GraphPad Prism 6.0 (La Jolla, California, USA) software. Paired t-tests were used to compare absolute values from non-treated limbs to heat-treated limbs, since the non-treated limbs serve as an internal control in each individual animal. All values are reported as mean +/- SEM, and statistical significance was accepted at $p < 0.05$ (one-tailed). Multiple day comparisons of surface limb temperature data (infrared thermography) were analyzed using a two-way ANOVA. All values are reported as mean temperature difference +/- SEM, and statistical significance was accepted at $p < 0.05$.

RESULTS

Femoral Length Increased in Heat-Treated Limbs of Wild-Type Mice

When comparing the femoral length of heat-treated limbs to non-treated limbs, wild-type mice show a 1.13% increase in length on the heat-treated side. By comparison, GHRKO mice had only a non-significant (0.065%) increase in length of the heat-treated side.

Histological Analysis of the GHRKO Mouse Tibial Growth Plate

Preliminary histological analysis of the proximal tibial growth plate from a wild-type mouse post unilateral heat-treatment, revealed an enlargement in the size of the hypertrophic zone exposed to heat, suggesting heat may have an impact on bone turnover rate at the chondro-osseous junction. The size of the hypertrophic zone of the growth plate could be an indication of bone growth rate. Therefore, it was of interest to determine the effects of heat on both total growth plate height as well as hypertrophic zone height. Paraffin sections were stained with Safranin-O/Fast Green (cartilage is red, bone is green) to visualize and quantify growth plate morphology (Fig. 1). In the wild-type mice, there was a significant difference between the total height of the growth plate in

non-treated compared to heat-treated tibias ($p < 0.001$), as well as in the height of the hypertrophic zone (Fig. 1C). The total tibial growth plate height on the heat-treated side of the wild-type mouse was 8.3% larger than the non-treated side (Fig. 1C). The hypertrophic zone was 10.28% larger on the heat-treated side, which was significant compared to non-treated tibias ($p = 0.033$) (Fig. 1C). In GHRKO mice, the total growth plate height was only 1.82% larger in the heat-treated tibial growth plate (Fig. 1D). The difference was not statistically significant ($p = 0.818$). A similar trend was seen when comparing the height of the hypertrophic zone. In GHRKO mice, there was only a 0.04% increase in hypertrophic zone height on the heat-treated side. This was not a significant difference ($p = 0.998$).

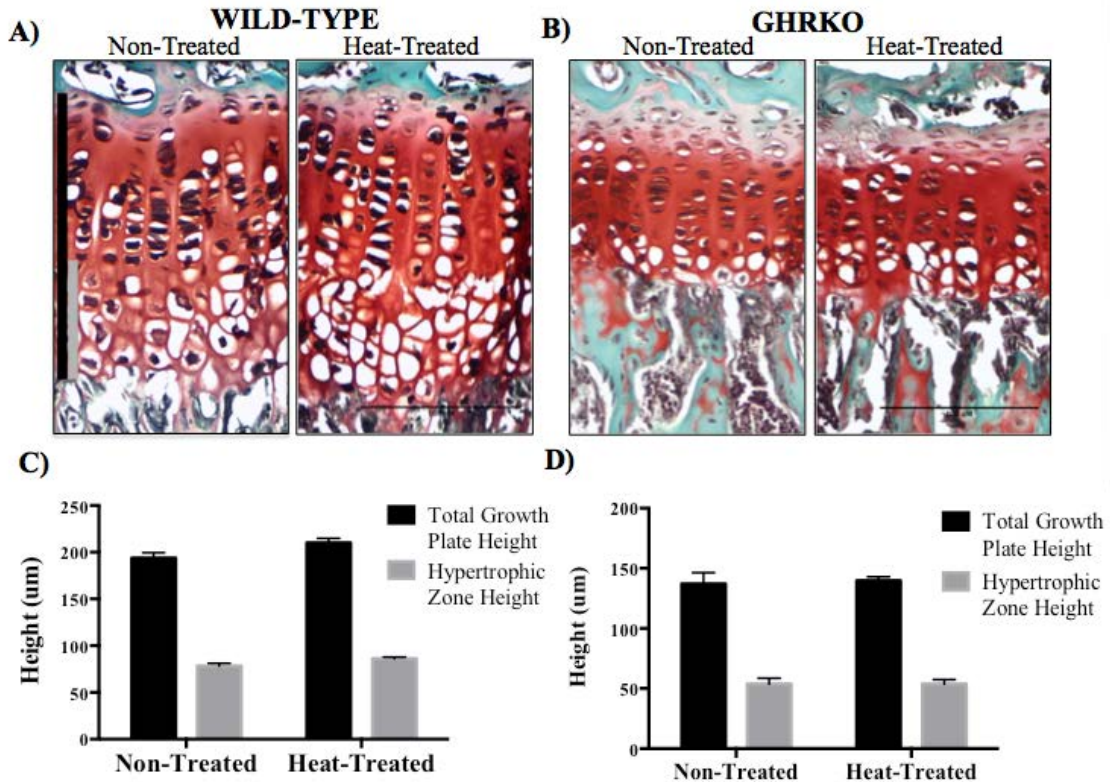


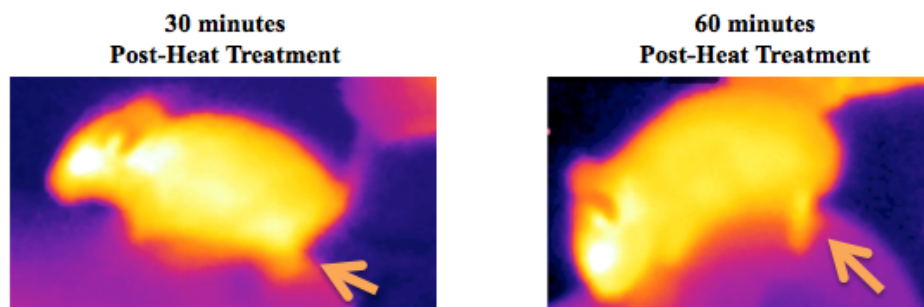
Figure 1. Effects of unilateral heating on proximal tibial growth plate height in 5-week old mice. Representative paraffin sections were stained with Safranin-O/Fast Green to visualize and quantify growth plate morphology in non-treated versus heat-treated tibias from wild-type (A) and GHRKO (B) mice (cartilage is red, bone is green). Growth plate height was quantified as shown by the vertical lines in (A). The vertical black line indicates total growth plate height and the gray line marks the height of the hypertrophic zone. Proximal tibial growth plates (total height and hypertrophic zone) are elongated on the heat-treated of the wild-type mice (C) ($N = 10$), while there was no statistically significant difference in growth plate height in the GHRKO mice (D) ($N = 5$). Scale bar = 100 μm . Asterisk indicates a statistically significant increase at $p < 0.05$ (paired t-test) on the heat-treated side when compared to the non-treated side.

Histological Analysis of the 7-Week-Old Mouse Tibial Growth Plate

Wild-type C57BL/6 mice ~5 weeks old were injected with saline and treated as explained in the methods (N=4). Paraffin sections were stained with Safranin-O/Fast Green (cartilage is red, bone is green) to visualize and quantify growth plate morphology. The younger heat-treated mice were harvested at 5 weeks of age but had not been injected (N=10). The older heat-treated mice were harvested at ~7 weeks of age. The total growth plate height in the 5-week-old mouse proximal tibia was 8.3% larger on the heat-treated side than on the non-treated side. This was a significant difference between heat-treated and non-treated tibias ($p < 0.001$). The 7-week-old mouse had the same 8.3% increase in total growth plate height in heat-treated tibias, which was not significant ($p = 0.063$). When comparing the increase of the hypertrophic zone size in heat-treated limbs to non-treated limbs, there was a 10.28% increase in 5-week-old mice ($p = 0.033$), but only a 7.12% increase in the 7-week-old mice ($p = 0.428$).

Thermal Imaging of Heat Retention in Mice Limbs

Pilot studies showed that the heat retained in the limbs of 24-day-old female C57BL/6 mice post-heat treatment on the second day of treatment, decreased over 30-minute time increments (N=3). The preliminary thermography data showed the heat-treated limb remained 3.3% warmer (0.8C) than the non-treated limb at 30 minutes, and 1.5% warmer (0.6C) at 60 minutes (Figure 2). Another group of C57BL/6 mice kept at 21C without treatment showed a negligible change in limb temperature over a period of 4 days (forelimb, $p = 0.285$; hindlimb, $p = 0.522$). There was no significant difference between left and right limbs (forelimb, $p = 0.142$; hindlimb, $p = 0.892$). On day 4, when these mice were acclimated to ambient room temperature (21C), and then moved to colder room (18C) and allowed to adjust for 30 minutes, there was a decrease in surface limb temperature (mean temperature difference +/- SEM: forelimb, 2.46 +/- 1.0; hindlimb, 2.54 +/- 1.0). After the same mice were moved back to 21C and allowed an additional 30 minutes to acclimate, an upward trend in surface limb temperature was observed (mean temperature difference +/- SEM: forelimb, 2.98 +/- 1.0; hindlimb, 1.50 +/- 1.0)(Figure 3).



	During Treatment	30 minutes Post-Treatment	60 minutes Post-Treatment
Non-Treated Hindlimb Temperature (C)	29.8	27.9	29.3
Heat-Treated Hindlimb Temperature (C)	40.7	28.8	29.7
% Difference in Hindlimb Temperature	36.7%	3.3%	1.5%

Figure 2. Thermal images captured on the second day of treatment show temperature gradients at 30- and 60-minute intervals following unilateral limb heating in 24-day-old female C57BL/6 mice. Arrows indicate the hindlimb. The table shows average surface temperatures of the heat-treated and non-treated sides (N=3). During this single experiment, heat-treated limbs remained 3.3% warmer than the non-treated limbs at 30 minutes, and 1.5% warmer at 60 minutes post-treatment.

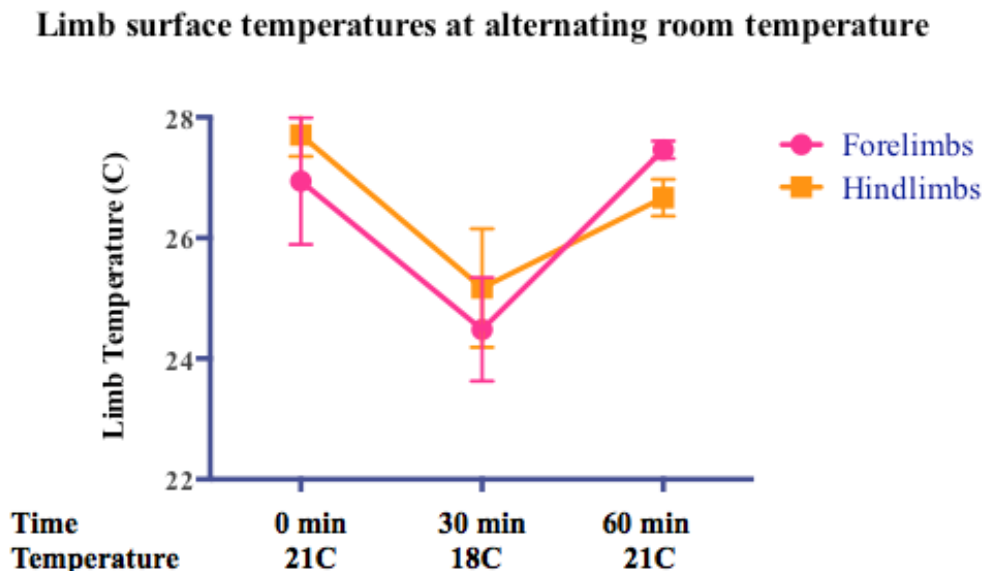


Figure 3. Line graph depicting surface temperatures of C57BL/6 mice acclimated to alternating room temperatures. Mice in this experiment were not subjected to any heat-treatment. Limb temperatures were recorded using a thermal imaging camera at baseline (Time=0 min) when mice were at 21C ambient temperature. Mice were then moved to an 18C room and allowed to acclimate for 30 minutes. Images were captured at the 30 minute time point at 18C and mice were then moved back to 21C, where images were captured 30 minutes later (Time=60 min). Measurements indicate that surface temperatures follow a general trend with changes in room temperature, and that this trend was similar in both fore- and hindlimbs. Data were analyzed using a two-way ANOVA followed by a Tukey’s multiple comparison test. Results indicated no significant differences between temperatures or limbs. Means +/- SEM are shown (N=3).

DISCUSSION

During postnatal life, bone elongation involves a combination of chondrocytic proliferation, differentiation, and deposition of extracellular matrix components. The size of the zone of the growth plate such as the hypertrophic zone correlates positively with the rate of elongation (Farnum et al. 2007). Our lab has shown that therapy using heat alone is a useful method for elongating limbs after a 2-week treatment (Serrat, Schlierf, et al. 2014). By studying the morphology of the growth plate, results demonstrate effects of heat on bone growth at the cellular level. Comparison of the histological sections of the proximal tibial growth plate revealed that both total height and hypertrophic zone height were lengthened in 3-week-old wild-type mice when treated with heat. However, this increase in growth plate size was not seen in GHRKO mice. Comparison of femoral length also showed an increase in length on the heat-treated side of wild-type mice that was not seen in GHRKO mice. Since GHRKO mice are known to be IGF1 deficient, it is suspected that there is an interaction between IGF1 and heat that is responsible for increasing bone elongation during treatment. The changes in morphology in the hypertrophic zone of the

heat-treated tibial growth plates suggest that heat is enhancing the rate of chondrocyte hypertrophy initiating an increased bone turnover rate.

Heat-treatment is typically done at 3-5 weeks of age because this is when the mice are growing rapidly (Eisen 1976; Serrat 2013; Serrat, Schlierf, et al. 2014). However, bone growth does continue but eventually slows with age and eventually ceases (Lui, Nilsson, and Baron 2011). It is expected that the rate of bone growth at 5 weeks of age would be continuing at a slower rate than when the mice are a younger 3 weeks of age. Results show that heat still had a positive impact on increasing total height of the tibial growth plate in the older mice compared to those that started treatment at a younger age. The effect, although present, was shown to be on a smaller scale than those that were younger. Further support could be provided with a larger sample size. Since the intention of the experiments was to inject mice with IGF1, only those that were injected with the saline control were compared to the younger wild-type mice and those that were injected with IGF1 were eliminated.

Thermal imaging provides a noninvasive procedure for collecting surface temperature measurements. Our pilot study suggests that limb temperatures remain elevated for up to 60 minutes post-heating. Preliminary data indicate that a slight 3C decrease in room temperature can elicit parallel changes in mouse surface temperature. We anticipate to reveal a more substantial change in surface temperature following multiple days of unilateral heating. Infrared thermography is a promising technique demonstrating diminutive variability between data. This was indicated by no significant difference observed in limb temperature of mice, regardless of side, when kept at 21C over a period of 4 days with no heat-treatment. These results will be important for understanding the impact of heat therapy by quantifying the extended period in which the limbs maintain warmer temperatures after daily treatments.

FUTURE PLANS

One of the main objectives of this project was to determine the effects of heat on bone growth when combined with the growth stimulating hormone IGF1. We demonstrated that heat does not have an impact on bone length in growth hormone receptor knockout mice that are deficient in IGF1. The next step is to inject wild-type mice with both IGF1 (to increase IGF1 levels) and an IGF1 blocking drug (to decrease IGF1 levels) to examine their respective impacts on bone elongation. This will be done to test whether heat will augment IGF1 activity in the growth plate by comparing left-right growth differences between injected groups. Saline injections will be administered as a control. We hypothesize that heat will have a greater lengthening effect when combined with IGF1, and that this effect will be blocked using the IGF1 inhibitor.

Other parameters for quantifying bone elongation rate include fluorochrome bone labeling. Tibial elongation rate will be quantified using an injection of oxytetracycline (OTC, 7.5 mg/kg dose) given to mice at the study midpoint. OTC binds to newly formed calcium at the chondro-osseous junction and acts as a “time-stamp” and allowing growth of long bones to be measuring during the period between injection and tissue collection (Hansson, Stenström, and Thorngren 1974; Serrat, Williams, and Farnum 2010). Growth rate will be quantified by measuring the vertical distance between the metaphyseal chondro-osseous junction and the position of the OTC band in metaphyseal bone (Farnum et al. 2007). Since there is a relationship between changes in cellular size at the site of the growth plate and bone elongation rate, future studies should show a positive correlation between histological analysis and fluorochrome labeling data. This ongoing research

is important for determining the cellular changes that underlie the differences in elongation rate of the heat-treated growth plates.

The results obtained from the thermal imaging pilot studies support the further continuation of imaging studies. Future studies that I have planned in my dissertation will allow the use of larger sample sizes to validate preliminary results. The next step involves a time-course experiment to determine period of heat retention following daily limb heating. To determine the most optimal time points, a time-course experiment will be conducted on a pilot group of animals (N=6) every hour during the 12-hour light cycle to establish realistic time points to image mice in a full study (see diagram below). The time points will be determined by temperature trends measured throughout the light cycle. We expect to identify 3 to 4 time points that show the most robust temperature trends. The purpose of this study is to determine the period of time in which heat is retained in the limbs following each daily heat treatment.



CONCLUSION

This study has shown that heat significantly increases the size of the proximal tibial growth plate in wild-type mice. In a disease model using mice that lacked the major growth hormone IGF1, there was no significant growth response to heat-treatment. It is also apparent that heat predominantly impacts the hypertrophic zone of the growth plate since this region of the growth plate was enlarged in heat-treated limbs of wild-type mice. This effect was not seen in the IGF1 deficient GHRKO mice. An explanation for the heat dependent growth effects seen in wild-type mice that are absent in the GHRKO mice is because of the decreased levels of circulating IGF1 in the knockout model. Heat may be augmenting the effects of IGF1 on the growth plate causing an increase in growth rate, which does not occur when IGF1 levels are diminished. This analysis of the growth plate provides a plausible explanation for the mechanism of heat-enhanced growth in young mice. Preliminary thermography data also support the ability of heat-treatment to have long-term effects on the treated limbs post-heating. These results will be supported in future studies with longer periods of imaging.

MOST VALUABLE ASPECTS OF PROGRAM

I would like to take the special opportunity to thank the NASA WV Space Grant Consortium for the opportunity to conduct this research. Without their financial support I would not have been able to continue with this project. This funding enabled me to continue my doctoral studies with 100% stipend and salary without have to take on an additional job for income as many other students do. This was my first opportunity to write a grant proposal and therefore was a great learning experience for me. The proposal in this grant formed the basis of my dissertation prospectus, which I defended during the funding period so this experience signified a huge milestone in my professional development. This project allowed me to collect preliminary data for my dissertation and helped me think critically while designing testable hypotheses and experiments, which taught me how to be a better scientist. While working on this study I was able to work alongside an expert from FLIR and had training on equipment that I had not previously

worked with in my current studies. I also had the opportunity to present my research at the Experimental Biology meeting in Boston, Massachusetts in March. All together I found this opportunity that was granted to me by the NASA WV Space Grant Consortium very rewarding and appreciate them for allowing me to make so many advancements as a research student in a small graduate program in West Virginia.

ACKNOWLEDGEMENTS

We thank the VA Medical Center and CEB staff for their support throughout this project. We are also thankful to Brian Lang with FLIR for providing us the Infrared Thermal imaging camera to demo during our pilot studies. We are grateful to Dr. Howard and the Marshall Animal Resource Facility for animal husbandry, assistance with equipment set up, and room temperature monitoring. This work was aided by the use of the facilities at the Huntington, West Virginia VA medical center. This research was made possible by generous funding from the NASA WV Space Grant Consortium, ASMBR Grants in Aid Program, and the National Institute of Arthritis and Musculoskeletal and Skin Diseases of the National Institutes of Health (1R15AR067451-01). I am so thankful to my research advisor and mentor Dr. Maria Serrat for her contribution to the development of this project.

REFERENCES

Cooper, Kimberly et al. 2013. "Multiple phases of chondrocyte enlargement underlie differences in skeletal proportions." *Nature* 495(7441):375–378.

Eisen, E. 1976. "Results of growth curve analyses in mice and rats." *Journal of animal science* 42(4):1008–23.

Farnum, Cornelia, M. Tinsley, and J.W. Hermanson. 2007. "Postnatal Bone Elongation of the Manus versus Pes: Analysis of the Chondrocytic Differentiation Cascade in *Mus musculus* and *Eptesicus fuscus*." *Cells Tissues Organs* 187(1):48–58.

Hansson, LI, A Stenström, and -G Thorngren. 1974. "Diurnal Variation of Longitudinal Bone Growth in the Rabbit." *Acta Orthopaedica* 45(4):499–507.

Hasler, Carol, and Andreas Krieg. 2012. "Current concepts of leg lengthening." *Journal of children's orthopaedics* 6(2):89104.

Hunziker, E B. 1994. "Mechanism of longitudinal bone growth and its regulation by growth plate chondrocytes." *Microscopy research and technique* 28(6):505–19.

Karimian, Elham, Andrei Chagin, and Lars Sävendahl. 2012. "Genetic Regulation of the Growth Plate." *Frontiers in Endocrinology* 2.

Knutson, Gary. 2005. "Anatomic and functional leg-length inequality: A review and recommendation for clinical decision-making. Part I, anatomic leg-length inequality: prevalence, magnitude, effects and clinical significance." *Chiropractic & Osteopathy* 13(1):11.

List, Edward et al. 2011. "Endocrine parameters and phenotypes of the growth hormone receptor gene disrupted (GHR-/-) mouse." *Endocrine reviews* 32(3):356–86.

- Lui, J.C., O. Nilsson, and J. Baron. 2011. "Growth Plate Senescence and Catch-Up Growth." *Cartilage and Bone Development and Its Disorders* 21:23–9.
- Lupu, Floria, Joseph Terwilliger, Kaechoong Lee, Gino Segre, and Argiris Efstratiadis. 2001. "Roles of Growth Hormone and Insulin-like Growth Factor 1 in Mouse Postnatal Growth." *Developmental Biology* 229(1).
- Mohan, Subburaman, and Chandrasekhar Kesavan. 2012. "Role of insulin-like growth factor-1 in the regulation of skeletal growth." *Current osteoporosis reports* 10(2):178–86.
- Poole, AR, I Pidoux, and L Rosenberg. 1982. "Role of proteoglycans in endochondral ossification: immunofluorescent localization of link protein and proteoglycan monomer in bovine fetal epiphyseal growth plate."
- Serrat, Maria. 2013. "Allen's rule revisited: temperature influences bone elongation during a critical period of postnatal development." *Anatomical record (Hoboken, N.J. : 2007)* 296(10):1534–45.
- Serrat, Maria, Thomas Schlierf, et al. 2014. "Unilateral Heat Accelerates Bone Elongation and Lengthens Extremities of Growing Mice." *Journal of Orthopaedic Research*.
- Serrat, Maria, Morgan Efaw, and Rebecca Williams. 2014. "Hindlimb heating increases vascular access of large molecules to murine tibial growth plates measured by in vivo multiphoton imaging." *Journal of applied physiology (Bethesda, Md. : 1985)* 116(4):425–38.
- Serrat, Maria, Rebecca Williams, and Cornelia Farnum. 2010. "Exercise mitigates the stunting effect of cold temperature on limb elongation in mice by increasing solute delivery to the growth plate." *Journal of Applied Physiology* 109(6):1869.
- Sims, Natalie et al. 2000. "Bone homeostasis in growth hormone receptor–null mice is restored by IGF-I but independent of Stat5." *Journal of Clinical Investigation* 106(9):1095.
- Stevenson, Sharon, Ernst Hunziker, Wolfgang Herrmann, and Robert Schenk. 1990. "Is longitudinal bone growth influenced by diurnal variation in the mitotic activity of chondrocytes of the growth plate?" *Journal of Orthopaedic Research* 8(1):132–135.
- Wang, J, J Zhou, C M Cheng, J J Kopchick, and C A Bondy. 2004. "Evidence supporting dual, IGF-I-independent and IGF-I-dependent, roles for GH in promoting longitudinal bone growth." *The Journal of endocrinology* 180(2):247–55.
- Williams, Rebecca, Warren Zipfel, Michelle Tinsley, and Cornelia Farnum. 2007. "Solute transport in growth plate cartilage: in vitro and in vivo." *Biophysical journal* 93(3):1039–50.
- Wilsman, Norman, Elizabeth Bernardini, Ellen Leiferman, Ken Noonan, and Cornelia Farnum. 2008. "Age and pattern of the onset of differential growth among growth plates in rats." *Journal of Orthopaedic Research* 26(11):1457–1465.

Yakar, S, CJ Rosen, and WG Beamer. 2002. "Circulating levels of IGF-1 directly regulate bone growth and density."

Yakar, Shoshana et al. 2005. "The growth hormone-insulin like growth factor axis revisited: lessons from IGF-1 and IGF-1 receptor gene targeting." *Pediatric Nephrology* 20(3):251254.

Zhang, Ping, Kazunori Hamamura, Charles Turner, and Hiroki Yokota. 2009. "Lengthening of mouse hindlimbs with joint loading." *Journal of Bone and Mineral Metabolism* 28(3):268–275.

Zhang, Ping, and Hiroki Yokota. 2011. "Elbow loading promotes longitudinal bone growth of the ulna and the humerus." *Journal of Bone and Mineral Metabolism* 30(1):31–39.

THE SUBLETHAL EFFECTS OF STREAM LIMING ON LIFE HISTORY SHIFTS IN *GYRINOPHILUS PORPHYRITICUS*

Shelby Timm
MS Biological Sciences
Marshall University
Huntington, WV 25755

ABSTRACT

Anthropogenic stream acidification is a global concern due to negative impacts on aquatic ecosystems. Direct application liming (DAL) has been used to neutralize acidified streams to restore aquatic biota; however, fine sediments associated with this mitigation practice fill interstitial spaces within the stream, changing the physical structure of the stream substrate and likely stressing biota. This mitigation technique has been used globally for decades, yet little data exist on its effects on amphibian populations. Life history theory predicts that stress will be ameliorated by life history tradeoffs. A potential tradeoff for amphibians is earlier metamorphosis, which would allow the species to leave unfavorable stream conditions, reducing exposure to stress induced by mitigation. My study investigates the effects of liming on amphibians by measuring variability in life histories, including differences in age structure, growth, body condition, and gape size of larval *Gyrinophilus porphyriticus*. From April 25, 2014 to August 23, 2014, I collected larvae from six streams in the Monongahela National Forest, West Virginia, which included three treatment streams and three control streams. I used skeletochronology to examine lines of arrested growth (LAGs), which are produced annually, in cross-sections of larval femurs. I failed to detect a treatment effect on age structure. I used ANCOVAs to examine differences in body condition, body size, and gape size. I observed that larvae located directly below DAL reached significantly larger body sizes at younger ages and appeared to have higher body conditions. Larvae below DAL had significantly smaller gape sizes than larvae in the treatment reference. The results of this study will increase our understanding of how large-scale mitigation practices can alter amphibian life histories, which could potentially result in unexpected emergent effects.

INTRODUCTION

Anthropogenic stream acidification, from industrial SO₂ emissions or acid mine drainage, is a global concern due to the negative impacts it has on aquatic ecosystems (Driscoll et al. 2003). To mitigate acidification, liming, i.e., the addition of calcium carbonate into aquatic systems, has been used in many industrialized nations to neutralize pH levels and improve water chemistry, with a majority of attention on game fisheries restoration (Eggleton et al. 1996; Mckie et al. 2006). Multiple liming methods have been used to mitigate acidic conditions, including dosers, full catchment, and direct application liming (Menendez et al. 1996; Menendez et al. 2000; Clair & Hindar 2005). Although liming has successfully increased pH and improved overall water chemistry (Clayton et al. 1998; Menendez et al. 1996; Clair & Hindar 2005), the mitigation practice itself acts as an ecosystem-level perturbation and could have broad ecological impacts and unexpected emergent effects.

Emergent effects are often scale dependent and arise when simple mechanisms interact at broad spatial scales (Harfoot et al. 2014) and can result when there are alterations to community structure (Carey & Wahl 2010; Reynolds & Elliott 2012). Fine sediments associated with liming can fill interstitial spaces within the stream, changing the physical structure of the stream substrate and likely stressing biota (Keener & Sharpe 2005). Liming also has the potential to alter trophic structure by changing species and predator composition, which may result in shifts in optimal life history strategies for biota. The interaction of these changes may produce unexpected emergent effects (Carey & Wahl 2010; Reynolds & Elliott 2012). These unexpected consequences, such as alterations in habitat and trophic structure, are important considerations given that economies of scale often encourage large-scale mitigation practices, such as liming (Carey & Wahl 2010; Reynolds & Elliott 2012).

Previous research has demonstrated that liming can have mixed effects on stream biota, particularly directly downstream of lime application, although results vary by stream (Clayton & Menendez 1996; Lefevre & Sharpe 2002; Clair & Hindar 2005; Keener & Sharpe 2005; McClurg et al. 2007). In general, liming increases fish abundance and survival and increases the presence of acid-sensitive macroinvertebrates (Clair & Hindar 2005; Mant et al. 2013); however, numerous studies have observed a decrease in overall macroinvertebrate abundance and diversity below lime application sites, which was often the direct result of increased sedimentation (LeFevre & Sharpe 2002; Keener & Sharpe 2005; Simmons et al. 2006; McClurg et al. 2007). Such variation in population-level responses to direct and indirect effects of liming indicates the need for further investigation on the possible impacts of this mitigation practice on aquatic biota. It is prudent to examine the utility of this mitigation practice with emergent effects in mind to ensure that there are no unintentional negative impacts on non-target wildlife to protect overall diversity. Specifically, there is a lack of information on how liming affects amphibians, which is necessary to understand broader impacts, such as ecological integrity (Welsh & Droege 2001).

Amphibians are often considered indicators of ecosystem health and integrity (Corn & Bury 1989; Welsh & Olliver 1998; Welsh & Droege 2001). Sedimentation is a major perturbation in many streams, leading to the loss of microhabitat (Waters 1995), and has been shown to negatively affect stream salamander abundance and survival (Welsh & Olliver 1998; Bonin 1999; Lowe and Bulger 2002). In addition to their sensitivity to sedimentation, salamander larvae have permeable skin, limited dispersal, and cannot escape aquatic conditions until metamorphosis, which make them good models for my study (Petranka 1998; Lowe 2003). Specifically, *Gyrinophilus porphyriticus*, the Spring Salamander, is an ideal study species because it relies on interstitial habitats, which can be greatly reduced below lime application (Bishop 1941; Bruce 1980; Keener & Sharpe 2005). *Gyrinophilus porphyriticus* is a fitting biological indicator due to its highly plastic life history with an aquatic larval stage ranging from three to six years, which varies depending on a number of environmental conditions (Bruce 1980; Resetarits 1995). In its larval stage, *G. porphyriticus* serves as a gape-limited, intermediate-to-apex predator in aquatic systems and can operate as a bellwether to trophic perturbations (Bruce 1980; Maret & Collins 1996; Welsh & Ollivier 1998).

Phenotypic divergence is typically low in *G. porphyriticus* from populations in close proximity along the stream corridor (Lowe et al. 2012); therefore, if environmental and trophic conditions are similar throughout the stream, then life history strategies should not differ. In *G. porphyriticus*, phenotypic divergence can be induced in novel or stressful environments and apparent shifts in life history strategies can be quantified to detect environmental changes, such that could be

manifested after liming (Stearns 1992; DeWitt et al. 1998). Therefore, optimal life history strategies vary in different environments; however, optimal strategies under stressors from environmental perturbations, such as liming, may not be equivalent with respect to fitness (Welsh & Olliver 1998).

Direct application liming (DAL) is the instream bulk application of sand-sized limestone and has become a widely-used method (Odom & Downey 1994; Keener & Sharpe 2005) for increasing stream pH. It is the primary method used in West Virginia and throughout Appalachia due to its affordability, ease, and its effectiveness compared to other methods (Ivahnenko et. al 1988; Clayton et al. 1998). Stream flow continuously distributes limestone particles downstream until the limestone pile is eroded away, at which time more lime is added (2-3 times per year). Limestone dissolution rates vary depending on particle size and initial pH (Sverdrup et al. 1986; Menendez et al. 2000). Undissolved particles can embed the natural substrate, reducing interstitial space, which is the primary habitat for many biota, including salamander larvae (Ivahnenko et. al 1988; Lowe & Bolger 2002). Reduction of microhabitat from sedimentation can increase stress in larvae and limit predator avoidance, potentially leading to life history shifts (Welsh & Olliver 1998; Resetarits 1995).

Little data exist on the effects of liming on amphibian populations; therefore, my study will examine variations in size and age of *G. porphyriticus* from limed and un-limed streams. Direct application liming has the potential to either promote longer larval periods due to improved conditions and decreased stress levels, or could lead to selection for early metamorphosis if stress levels increase, shifting optimal life history strategies (Stearns 1992; Arendt 1997). I used active DAL streams and un-limed control streams to examine the effects of liming on larval *G. porphyriticus* life history strategies, specifically population age structure, and individual body condition, growth, and gape size. I hypothesized that I would detect a tradeoff between life history parameters resulting from increased sedimentation from DAL. Specifically, I expected larvae downstream of the DAL sites to have younger populations, indicating selection for earlier metamorphosis, and lower individual body conditions, growth rates, and gape size from increased stress and alterations in trophic structure. By identifying the impacts of liming on amphibians, biologists can better manage aquatic habitats and determine if liming is beneficial to overall stream diversity. Understanding how liming affects non-target species will aid with improvements to methodology or bring into question the efficacy of this mitigation practice to achieve conservation and management objectives. My research will promote future studies on various mitigation practices in efforts to reduce unexpected emergent effects.

METHODS

Study Sites

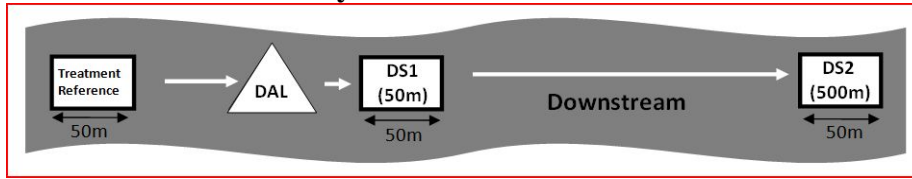
I collected *G. porphyriticus* larvae from multiple populations in the Gauley River watershed near Richwood, WV, in the southern portion of the Monongahela National Forest. I sampled six first- and second-order streams, which included three treatment streams and three control streams. I sampled two first-order streams within Sugar Creek of the Williams River, two first-order streams within Bear Run of the North Fork Cherry River, and two streams within Dogway Fork of the Cranberry River (treatment stream=second-order; control stream= first-order). Streams were characterized by rocky substrates, shallow stream depth (<1 m), and forested riparian zones. Direct application liming was applied to treatment streams several times yearly. Each lime application was applied by the West Virginia Division of Natural Resources directly into the stream to mitigate

for acid precipitation. The rate and volume of lime applications varied among sites. Sugar Creek was treated twice yearly in the spring and fall, totalling 45 tons of limestone fines. Bear Run was treated three times yearly in the spring, summer, and fall with a target limestone fines of 66 tons and Dogway Fork is limed throughout the spring, summer, and fall with nearly 250 tons of limestone fines. The rates and amount of application was dependent on drainage size and original pH and was designed to bring each stream up to a neutral pH. The West Virginia Division of Natural Resources used limestone fines that are 90% calcium carbonate or higher. Control streams were not treated with lime and had similar stream characteristics as treatment streams. Each treatment stream had a paired control stream to control for intra-study variability and to increase power to detect treatment effects (Sokal & Rohlf 1981). Of the available limed streams in the area, I selected streams that included large *G. porphyriticus* populations, had a paired control stream, and had a sufficiently long stream channel (~0.8 km) to incorporate three independent sampling sites.

Data Collection

Within each stream, I collected *G. porphyriticus* larvae from three independent sites (N=18 sites). Sample locations within treatment stream included a treatment reference located 100 m upstream of the DAL application site (Figure 1A). The first treatment site was located 50 m downstream of the DAL site (DS1) and the second treatment site was located 500 m downstream of the DAL site (DS2). Control streams were designed with the same site layout, but because there was no DAL site, the control sites were measured from a random reference point (Figure 1B). Control streams had one site located 100 m upstream of the reference point (UPC) and two sites located downstream of the reference point at 50 m below (DSC1) and 500 m below (DSC2). For treatment and control streams, each sampling site was 50 m long and at least 100 m from any other collection site to maintain independent larval populations (Lowe 2003). I collected larvae on multiple sampling occasions from April 25, 2014 to August 23, 2014 until at least eight individuals were collected from each site. I collected larvae using a flip and search method during diurnal surveys. All cover objects were flipped throughout the site until eight individuals were captured. *Gyrinophilus porphyriticus* larvae were most often found in the interstitial spaces under cobble sized rocks (between 64 mm and 256 mm diameter; Lane 1947) that were not embedded in the substrate and were generally located in riffles or pools (Lowe 2005). After I collected larvae, they were euthanized in MS-222 and transferred to 70% ethyl alcohol. I recorded pH on each sampling occasion, and fish and crayfish presence. The pH of each site was measured on at least two occasions with a pHTest ® Series, pH Testr30 meter, measured to the nearest tenth.

Treatment stream site layout



A) Control stream site layout

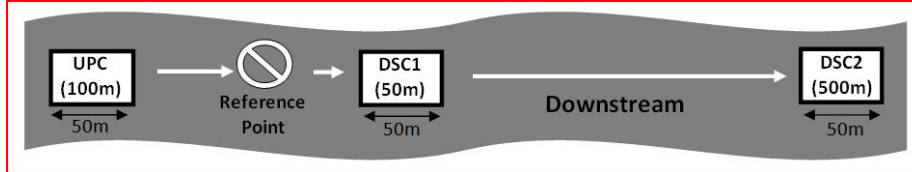


Figure 1: A) Treatment stream site layout. Sites relative to the direct application lime site (DAL). DS1= first downstream site; DS2= second downstream site. The treatment reference site was located 100 m above lime application and was not impacted by lime. Downstream site 1 (DS1) was located 50 m below the DAL site and DS2 was located 500 m below the DAL site. Each site was 50 m in length. B) Control stream site layout. Sites relative to random reference point. UPC=upstream control site; DSC1= first downstream control site; DSC2= second downstream control site. Upstream control site (UPC) was located 100 m above the reference point. Downstream control site 1 (DSC1) was located 50 m below the reference point and DSC2 was located 500 m below the reference point. Each site was 50 m in length.

Size and Age Determination

I measured snout-vent length (SVL) of preserved larva using calipers to the nearest 0.05 mm from the snout to the posterior edge of the cloacal slit. Wet mass was measured using a digital scale to the nearest milligram. Body condition was calculated using a ratio index of body mass divided by SVL so that the values could be compared across populations (Jakob et al. 1996). Gape size for each larva using calipers to the nearest 0.05 mm. Gape was measured across the width of the head from the edges of the mouth (Ohdachi 1994).

I used skeletochronological analysis of femurs for larval age determination. Age can be determined in amphibians by counting the number of lines of arrested growth (LAGs) in the cross-sections of the diaphysis of long bones or phalanges (Castanet et al. 1993; Smirina 1994). Lines of arrested growth are deposited annually in temperate regions during winter when growth slows and individuals are less active. The areas of bone between LAGs are laid during periods of active osteogenesis and are distinguishable from the darker staining LAGs (Castanet et al. 1993). Because LAGs are generally laid annually during the winter, they provide a reliable means of determining age (Castanet et al. 1993; Smirina 1994). This method has been verified using amphibians of known age and is most reliable in young, rapidly growing individuals, such as larvae (Smirina 1994). Age estimation in older individuals can be less accurate because early LAGs can be resorbed and slowed growth rates after sexual maturity result in LAGs that are very close together and difficult to distinguish. Thus, in this study, we limited our analysis to larval *G. porphyriticus* (Smirina 1994).

After preservation, the right hind limb of each individual was removed and placed directly into 5% nitric acid for decalcification (Bruce & Castanet 2006). Typically, the femur is separated from the

surrounding tissue and muscle before it is placed into nitric acid (Leclair & Castanet 1987; Socha & Ogielska 2010; Ashkavandi et al. 2012); however, after trying both methods, removing the tissue was deemed unnecessary. Leaving the surrounding tissue intact made the bones easier to handle and prevented them from being damaged during processing. Bones were decalcified for three hours then rinsed three times in deionised water and placed in 30% sucrose. If bones were not immediately cut, they were refrigerated at 4°C. To prepare the bone for cross-sectioning, I placed the leg upright in Tissue-Tek OCT Compound freezing medium. I then made 15 um cross-sections (Bruce & Castanet 2006) using a Leica CM 1950 cryostat (freezing microtome) at -15° C. I placed cross-sections from the diaphysis of the femur directly onto Superfrost Plus microscope slides (Wake & Castanet 1995; Bruce & Castanet 2006; Socha & Ogielska 2010). The slides were stained in Ehrlich's Hematoxylin for 10 minutes and then rinsed in deionised water for five minutes and permanently mounted with Clear-Mount, an aqueous mounting medium. Ehrlich's Hematoxylin was used because LAGs are most chromophilic with hematoxylin dyes (Castanet et al. 1993). Once stained, I examined the slides under a light microscope and counted the number of LAGs for each individual. Because each LAG was laid annually (Castanet et al. 1993; Smirina 1994), LAGs were translated directly to age. Larvae that lacked LAGs were considered young of the year and were assigned to the zero age class. If the sections were unclear the other femur was used to determine age.

Analysis

I determined each individual's age and did not have to exclude any individuals from analysis due to unclear LAGs or regenerated limbs. I aged each individual on three separate occasions using blind analysis to prevent bias (Castanet et al. 1993). In the event that more than one age was estimated for an individual, I retained the most recurring age for analysis. Any age discrepancies for an individual were within one year of other estimates, and no individual was estimated to be three different ages; therefore individual age estimates were consistent.

All statistical analyses were performed in SAS 9.4. I used an ANOVA to compare variation in pH across sampling sites in both reference and treatment streams. I used Fisher's exact tests to examine whether age frequency distributions differed among sites and streams (i.e., DAL treatment). Because young individuals (0-2) were underrepresented in my sample due to their secretive nature and greater use of interstitial spaces (Resetarits 1995), and because my goal was to examine differences in metamorphic age (Bishop 1941; Bruce 1980), I excluded age classes 0-2 in the age structure analysis. I used analysis of covariance (ANCOVA) to examine differences in body condition in treatment and control stream sites, while controlling for variation caused by age. I also used ANCOVAs to examine differences in SVL in treatment and control stream sites, while controlling variation caused by age. Differences in gape size in treatment and control stream sites, while controlling for variation caused by SVL, were also tested using ANCOVAs. I ran each ANCOVA with only two factors (i.e. treatment), to increase power since my sample size was small (McDonald 2014). I tested for homogeneity of slopes ($\alpha=0.05$) prior to running each ANCOVA. If slopes were homogenous, then the interaction statement was removed from the final ANCOVA (Engqvist 2005). If slopes were heterogeneous, then further analyses were not conducted. Significant covariates ($\alpha=0.05$) were determined using Type III of sum of squares. I used ANCOVAs to test for differences in body condition between the treatment reference and DS1 and the treatment reference and DS2 to determine if there was a treatment effect and if the effect persisted farther downstream at the DS2 site. I also used ANCOVA to examine differences between control stream sites, including for UPC and DSC1 and UPC and DSC2 to determine if

longitudinal stream differences affected body condition. I tested for differences in body size between the treatment reference and DS1 and the treatment reference and DS2 using ANCOVA. I conducted ANCOVAs for control streams and tested for differences in body size between UPC and DSC1 and UPC and DSC2. Snout-vent lengths from control streams were squared to meet the normality assumption. I used the body size ANCOVAs as a proxy for larval growth rate, since the analysis showed the increase in size relative to age. I analyzed gape size with ANCOVAs to test for differences between the treatment reference and DS1 and the treatment reference and DS2 and also for control stream sites, including analyses between UPC and DSC1 and UPC and DSC2.

I mirrored the distribution of sample sites within control streams to those in the treatment streams. While redundant, my analysis depended heavily on multiple ANCOVAs and this approach allowed me to use comparisons among sampled sites to test specific hypotheses and control for potential longitudinal effects. For example, by comparing treatment reference to DS1, I examined direct effects of DAL. By examining treatment reference to DS2, I assessed the effects of distance from DAL. Similar analyses were performed on the control stream with the expectation that we would not detect longitudinal differences and thus provide further support for treatment effects.

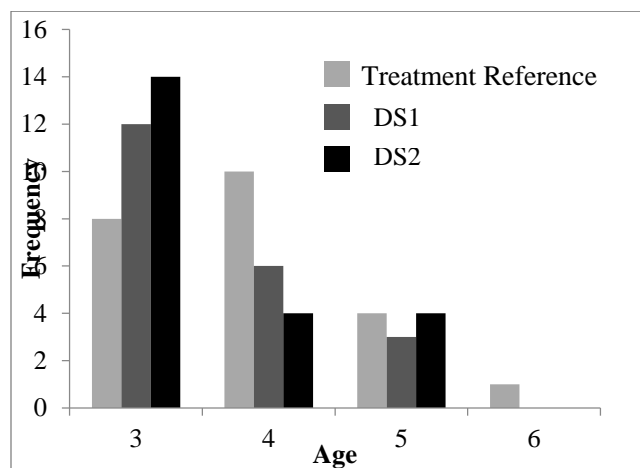
RESULTS

I collected 158 *G. porphyriticus* larvae. Individuals that were collected at the beginning of the sampling season had LAGs located at the periphery of the bone section, whereas larvae collected later in the summer had growth behind the most recent LAG, so the LAG was not at the periphery of the bone. Larvae ranged from zero (young of the year) to six years in treatment and control streams; however, I failed to detect 6-year individuals below DAL sites (Table 1). Average age was lowest at the DS1 site (Table 1). Younger age classes (0-2) were rarely encountered during sampling, likely because younger larvae inhabit interstices, the space between substrate particles, and are more secretive (Resetarits 1995). I detected a difference in pH between treatment and control streams, with a significantly higher pH below the DAL site ($F_{5,12} = 8.30$; $p = 0.0014$). The average pH in control streams and in the treatment reference was 4.8 and the average pH below lime was 7.0. I failed to detect a significant shift in age structure between sites in treatment ($p = 0.3534$) and control streams ($p = 0.2018$) using the Fisher's exact test (Figure 2). Although I failed to detect a significant treatment effect on age structure, the predominant age class for larvae below the DAL site was three years (57.1% in the DS1 and 63.6% in the DS2; Figure 2A) compared to larvae in the treatment reference, which were predominantly four years old (52.2%; Figure 2B).

Table 1: Descriptive statistics for snout-vent length (SVL) and age for treatment and control streams.

Treatment	SVL (mm)			Age (years)	
	n	Range	Mean \pm SD	Range	Mean \pm SD
Treatment Reference	27	26.50-61.67	47.13 \pm 9.25	0-6	3.56 \pm 1.22
DS1	27	25.70-67.20	47.85 \pm 12.16	0-5	2.96 \pm 1.37
DS2	26	28.10-67.75	49.08 \pm 10.41	1-5	3.27 \pm 1.00
Control	n	Range	Mean \pm SD	Range	Mean \pm SD
UPC	24	31.05-59.85	47.23 \pm 8.08	1-6	3.25 \pm 1.03
DSC1	27	35.20-58.75	48.83 \pm 7.00	2-6	3.67 \pm 1.21
DSC2	27	29.30-59.00	48.40 \pm 7.11	1-5	3.70 \pm 1.02

A) Treatment Streams



B) Control Streams

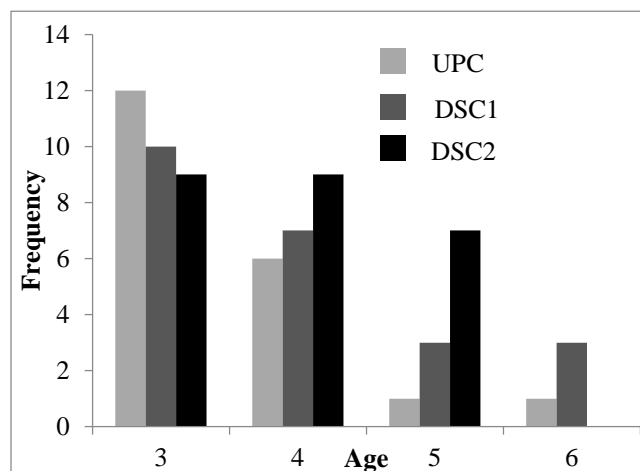


Figure 2: Age frequency distributions for 3-6 year larvae for treatment and control streams. I failed to detect a difference in treatment or control stream age structures.

I failed to detect significant differences in larval body conditions between sites in treatment and control streams. However, the analysis for the treatment reference and DS1 approached significance with ($F_{1,51}=3.31$; $p=0.0747$; Figure 3). Although not significant, larvae from DS1 in treatment streams appeared to reach higher body conditions than larvae in the treatment reference, compared to control stream larvae from UPC and DSC1, which did not differ ($F_{1,48}=0.32$; $p=0.5751$). I also failed to detect a longitudinal effect in body conditions between the treatment reference and DS2 sites ($F_{1,49}=2.04$; $p=0.1600$) and between the UPC and DSC2 sites ($F_{1,48}=0.61$; $p=0.4376$).

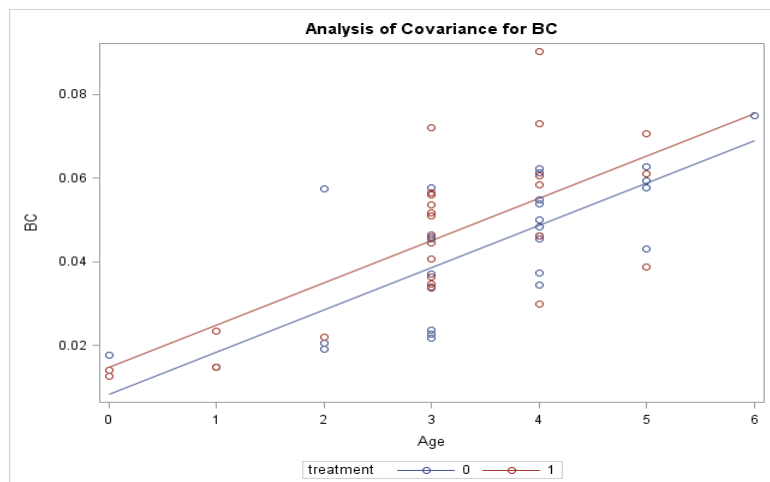


Figure 3: Body condition ANCOVA for treatment stream. Includes downstream site one (DS1; red), which is located 50 m below the lime application, and the treatment reference (blue), which is located 100 m upstream of the lime application.

I detected a significant treatment effect on body size. Specifically, body size differed between the treatment reference and DS1 (ANCOVA; $F_{1,51}=5.75$; $p=0.0202$; Figure 4). Larvae from DS1 in treatment streams reached larger body sizes (SVL) at younger ages than individuals that were located above the DAL site in the treatment reference. In the ANCOVA analysis for UPC and DSC1 in the control streams, I failed to detect a difference in body size ($F_{1,48}=0.03$; $p=0.8553$; Figure 5). In the treatment streams, larval body size from DS2 did not significantly differ from larvae in the treatment reference, however a similar trend to the DS1 site was present with larvae from DS2 reaching larger body sizes at younger ages than individuals from the treatment reference (ANCOVA; $F_{1,50}=2.74$; $p=0.1040$). In the ANCOVA analysis for UPC and DSC2 in the control streams, I failed to detect a difference in larval body sizes ($F_{1,48}=0.42$; $p=0.5224$).

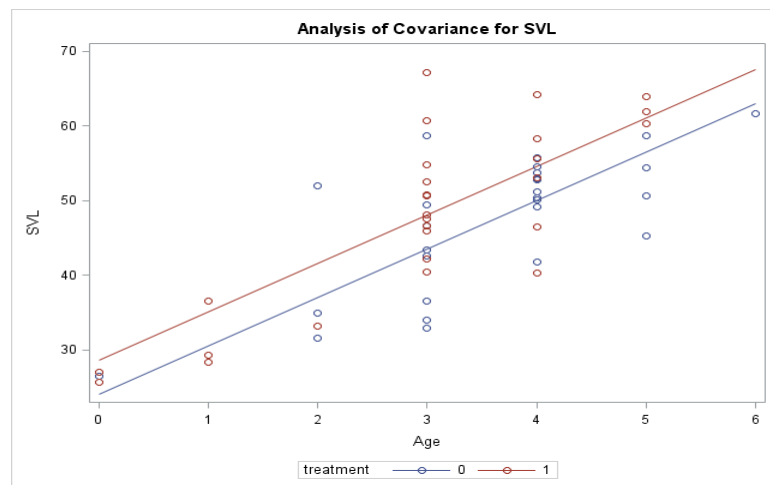


Figure 4: Treatment stream ANCOVA for snout-vent-length. Includes downstream site one (DS1; red), which is located 50 m below the lime application, and the treatment reference (blue), which is located 100 m upstream of the lime application.

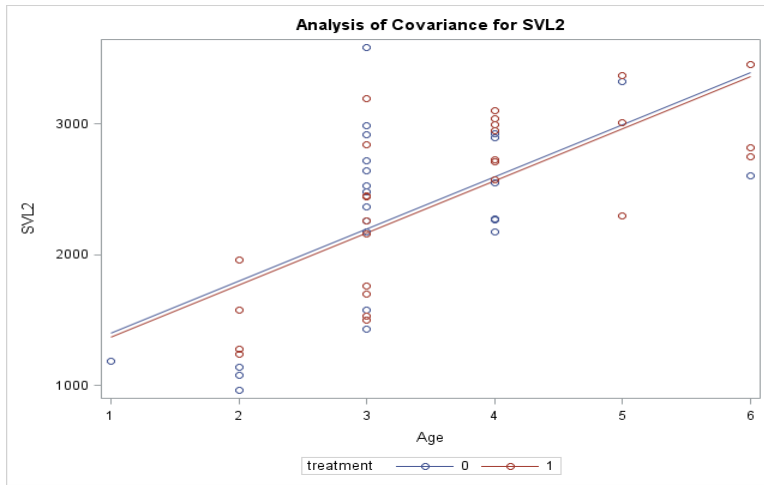


Figure 5: Control stream ANCOVA for snout-vent-length squared. Includes downstream control site one (DSC1; red), which is located 50 m below the reference point, and the upstream control site (blue), which is located 100 m upstream of the reference point.

I detected a significant treatment effect on gape size. Specifically, gape size differed between the treatment reference and DS1 (ANCOVA; $F_{1, 51}=9.48$; $p=0.0033$; Figure 6) and between the treatment reference and DS2 (ANCOVA; $F_{1, 50}=5.01$; $p=0.0296$). Larvae from the treatment reference had larger gape size at shorter SVLs than individuals from DS1 and DS2. In the ANCOVA analysis for UPC and DSC1 ($F_{1,47}=2.57$; $p=0.1159$; Figure 7) and for UPC and DSC2 ($F_{1,48}=1.85$; $p=0.1804$) in the control streams, I failed to detect a difference in gape size.

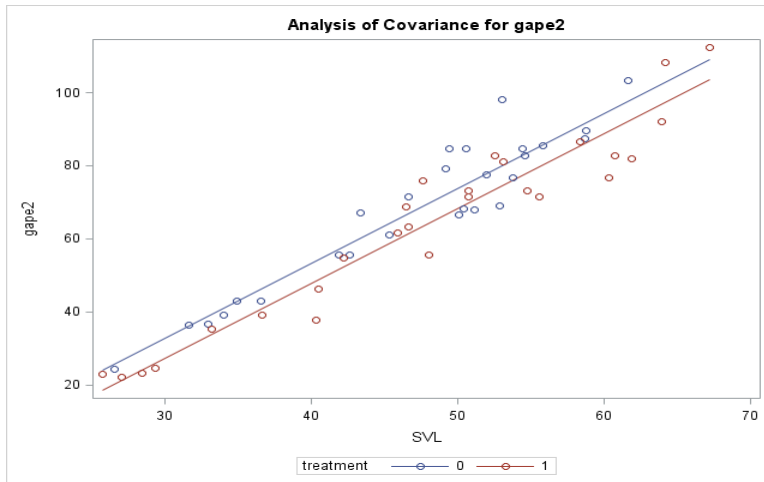


Figure 6: Treatment stream ANCOVA for gape size squared. Includes treatment reference (blue), which is located 100 m upstream of DAL, and the first downstream treatment site (DS1; red), which is located 50 m downstream of DAL.

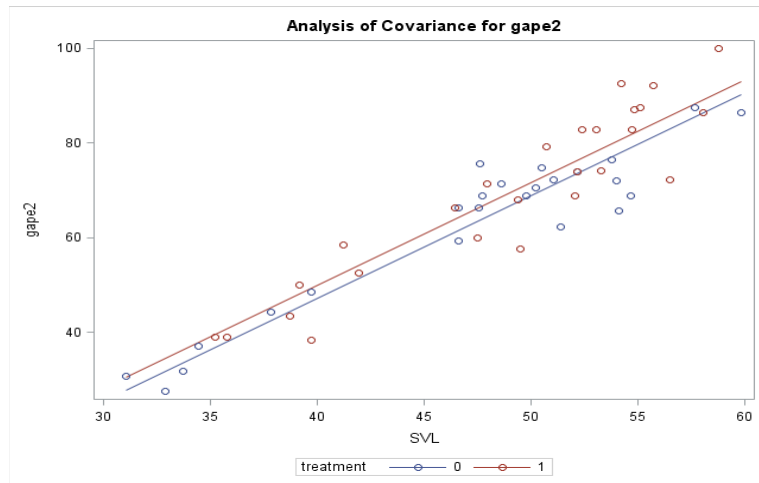


Figure 7: Control stream ANCOVA for gape size. Includes upstream control (UPC; blue), which is located 100 m upstream of the reference point, and the first downstream control site (DSC1; red), which is located 50 m downstream of the reference point.

DISCUSSION

The effects of DAL are complex and may have positive and negative effects on aquatic biota. In this study, I failed to detect an effect of DAL on larval *G. porphyriticus* age structure and body condition. However, liming significantly increased body size and decreased gape size in larval *G. porphyriticus* at the DS1 site, indicating population-level effects that potentially reflect life history shifts (Stearns 1992). Optimal life history strategies should maximize survival and fitness. Larvae from DS1 reached larger body sizes at younger ages compared to the treatment reference larvae; therefore larval growth rates were increased downstream of DAL sites. I failed to detect significant effects in control streams, suggesting that changes in body size were not the result of longitudinal differences in the stream.

Fish, which have been shown to decrease growth rates in *G. porphyriticus* through interference competition (Resetarits 1991, 1995; Lowe et al. 2004), were encountered in both treatment and control streams, and thus it is unlikely that observed differences in growth reflected fish presence below DAL sites, especially since the effect was not present at the DS2 site. Furthermore, faster growth rates, suggest that effects were not result of fish presence since predators typically decrease growth rates in *G. porphyriticus* (Resetarits 1991, 1995; Sih et al. 1988; Lowe et al. 2004). However, there is the potential for increased interactions with predators directly downstream of DAL due to decreased habitat availability from sedimentation (Sih & Kats 1991). Increased interactions with gape limited predators could select for increased growth rates until a size refugia is met, which is when larvae become less susceptible to predation (Wilbur 1980; Abrams & Rowe 1996; Urban 2008). The effect of liming on body size decreased at sites located farther downstream, likely because the habitat is less physically altered by sedimentation due to dissolution of the lime, providing greater habitat availability than sites located closer to lime application. The failure to detect a significant treatment effect on growth rates at DS2 supports that increased nutrient availability from improved water quality was not the selective factor and that reduced refugia from sedimentation directly below the DAL may increase predation risk.

Previous research has demonstrated that amphibians with varying phenotypes and growth rates exhibited tradeoffs that did not affect survival or reproduction (Clobert et al 2000). In this study, *G. porphyriticus* larvae exhibited plastic growth rates, which in theory, should be a mechanism to maximize overall fitness in the given environment and may or may not have negative tradeoffs (Hereford 2009).

Metamorphic size in *G. porphyriticus* occurs within a narrow range, with little plasticity in this trait (Wilbur & Collins 1973; Bruce 1980), suggesting that metamorphosis is size dependent. Rapid growth in *G. porphyriticus* larvae directly below the DAL site may indicate a life history tradeoff for earlier metamorphosis, since larvae are reaching minimum metamorphic size quickly. By quickly morphing into adults, which are less reliant on aquatic habitats than larvae, individuals can potentially become less susceptible to aquatic stressors (Wilbur & Collins 1973; Rohr et al. 2004). For many amphibians the timing of metamorphosis can vary by both age and size depending on a number of factors (Wilbur 1980; Arendt 1997; Bruce 2005). Some of the factors affecting metamorphic timing are temperature, resources, predator density, and habitat stability, such as water permanence or the absence of perturbations (Bruce 2005). The optimal life history strategy for an individual should therefore maximize growth, survival, and reproduction for a specific environment within the species range of plasticity (Arendt 1997; Bruce 2005).

Disturbed habitats, such as DAL sites, can induce rapid growth rates and can reduce time spent in stressful conditions (Wilbur & Collins 1973; Arendt 1997; Hereford 2009). Since growth appeared constant across sites in control streams, it is likely that favorable stream conditions contributed to delayed metamorphosis, increasing overall time that growth occurred prior to reproductive age (Bruce 1980; Arendt 1997; Rowe & Ludwig 2001). However, acidic conditions, like those in control stream and the treatment reference, can reduce amphibian growth rates, indicating that it too may act as a stressor (Freda & Dunson 1985; Pierce 1985).

Gape size was also impacted by lime treatment. Larvae below DAL sites, from both DS1 and DS2, had smaller gape sizes relative to SVL than larvae in the treatment reference. This effect was not seen in control streams. *Gyrinophilus porphyriticus*, like other salamanders, are gape-limited predators, which effects the type of prey they can ingest (Zaret 1980). Larvae with narrower gape sizes have a smaller range of available prey items (Maret & Collins 1996). Since gape size is positively correlated with body size large larvae have the largest range for prey selection, however according to my results larvae downstream of DAL had smaller gape sizes at relative sizes and were therefore more limited in their prey selection. The differences in gape size could indicate a change in prey composition below DAL, although this was not measured.

I failed to detect a significant effect of DAL on age structure or body condition. Although there was not a significant treatment effect on age structure, the predominant age class for larvae downstream of the DAL site was three years compared to larvae in the treatment reference, which were predominantly four years old. Below DAL sites, a majority of individuals could be completing metamorphosis at three years, versus four years upstream of the DAL site. I failed to locate six year larvae below DAL sites and average larval age was lowest at the DS1 site (Table 1). The failure to detect the oldest age class below DAL sites does not equate to absence; however, if larvae downstream of DAL completed metamorphosis at younger ages, I would expect to find fewer larvae in the older age classes. Although not significant, larval *G. porphyriticus* populations

tended to have higher body conditions at the DS1 site, but this effect was not present at the DS2 site, suggesting that the effect of liming on body condition decreased.

Because there was no difference in body condition in control stream sites, we assume that any effects detected below DAL sites were not the result of longitudinal stream differences. Higher body conditions are positively correlated with growth rates (Lowe et al. 2006) and generally indicate higher energy reserves and habitat quality (Pope & Matthews 2002; Schulte-Hostedde et al. 2005); however, higher body condition may be confounded with the increased growth rates of larvae from the same site. Higher body conditions could also be the result of increased prey densities (Beachy 1994, 1995) or decreased larval densities below DAL sites (Wilber & Collins 1973; Edwards 2014), limiting intraspecific competition. Although increased body condition generally indicates increased prey availability (Beachy 1994; Pope & Matthews 2002), sites located downstream of the DAL appeared to have fewer macroinvertebrates and previous research has shown that liming generally decreases the total biomass of macroinvertebrates (Okland & Okland 1986; Keener & Sharpe 2005). Since increased growth rates and body condition require higher energy reserves, the assumption would be that gape size would be large to facilitate a greater range of prey capture. By capturing large high energy prey, less time would be required for foraging (Walls et al. 1993; Forsman 1996). However, my results show that larvae with increased growth rate and body conditions have smaller relative gape sizes, which would greatly increase the time needed for foraging. By increasing foraging time, activity levels, and therefore mortality rates due to predation risks, are also increased; however, mortality was not measured (Stearns 1992; Werner and Anholt 1993; Arendt 1997; Roff 2000). Previous research on the effects of liming on *G. porphyriticus* abundance, although not significant, indicated that distance from lime and liming frequency were the most important covariates for abundance estimates, with lower abundance in sites closer to DAL sites and in sites with greater liming frequencies (Edwards 2014). The trend for lower abundance downstream of DAL suggests lower densities that could have resulted from increased mortality through predation. Decreased abundance would lower intraspecific competition and increase resource availability.

My results may indicate that selection is occurring, and larvae with the plasticity to grow faster and leave the stream at younger ages are the individuals able to survive directly below lime application, which would explain lower abundance downstream of the treatment. Plasticity is maintained in a species, such as *G. porphyriticus*, when individuals experience a range of environmental conditions and plasticity increases their overall survival and fitness (Stearns 1989; DeWitt et al. 1998). My research demonstrates that *G. porphyriticus* exhibits population-level responses to DAL mitigation, which may cause life history shifts in larvae. Further research is needed to identify specific mechanisms to understand if our observations are the direct effects of liming, such as increased sedimentation and changes in water chemistry, or caused by indirect effects, such as alterations in trophic structure, and how these changes contribute to emergent effects. It is important to further investigate the tradeoffs that are occurring within individuals with increased growth rates and smaller gape sizes, as well as differences in diet using gut content analysis to determine if trophic structure has been altered.

VALUABLE ASPECTS

The most valuable aspect of this program was the financial support, allowing me to gain a variety of research experiences. Without the Graduate Fellowship I would not have been able to afford

multiple trips to my study sites or have been able to spend a majority of my summer working in the lab conducting skeletochronology. This funding enabled me to make the most out of my thesis research and for that I will always be thankful.

ACKNOWLEDGEMENTS

I would like to thank my advisor, Dr. Jayme Waldron for her continued support throughout my research, my committee members, as well as all of my field and lab assistants. I would especially like to thank the NASA WV Space Grant Consortium for funding this research. This research would not have been possible without all of your support.

REFERENCES

- Abrams, P. and Rowe, L. 1996. The effects of predation on the age and size of maturity of prey. *Evolution* 50: 1052-1061.
- Arendt, J.D. 1997. Adaptive intrinsic growth rates: An integration across taxa. *The Quarterly Review of Biology* 72: 149-177.
- Ashkavandi, S., Gharzi, A., & Abbassi, G.M. 2012. Age determination by skeletochronology in *Rana ridibunda* (Anuran:Amphibia). *Asian Journal of Experimental Biological Sciences* 3(1):156-162.
- Bancilla, R., Hartel, T., Plaiasu, R., Smetes, J., and Cogalniceanu, D. 2010. Comparing three body condition indices in amphibians: A case study of yellow-bellied toad *Bombina variegata*. *Amphibia-Reptilia* 31: 558-562.
- Beachy, C. K. 1994. Community ecology in streams: Effects of two species of predatory salamanders on a prey species of salamander. *Herpetologica* 50: 129-136.
- Beachy, C.K. 1995. Effects of larval growth history on metamorphosis in a stream-dwelling salamander (*Desmognathus ochrophaeus*). *Journal of Herpetology* 29: 375-382.
- Bervin, K. and Gill, D. 1983. Interpreting geographic variation in life-history traits. *American Zoologist* 23: 85-97.
- Bishop, S. C. 1941. The salamanders of New York. *New York State Museum Bulletin*. 324:1-365.
- Bonin, J. 1999. COSEWIC status report on the spring salamander *Gyrinophilus porphyriticus* in Canada in COSEWIC assessment and status report on the spring salamander *Gyrinophilus porphyriticus* in Canada. Committee on the Status of Endangered Wildlife in Canada. Ottawa. 1-16 pp.
- Bruce, R.C. 1980. A model of the larval period of the Spring Salamander, *Gyrinophilus porphyriticus*, based on size-frequency distributions. *Herpetologica* 36:78-86.
- Bruce, R. C. 2005. Theory of complex life cycles: Application in Plethodontid salamanders. *Herpetological Monographs* 19: 180-207.

- Bruce, R.C. & Castanet, J. 2006. Application of skeletochronology in aging larvae of the salamanders *Gyrinophilus porphyriticus* and *Pseudotriton ruber*. *Journal of Herpetology* 40: 85-90.
- Carey, M.P. and Wahl, D.H. 2010. Interactions of multiple predators with different foraging modes in an aquatic food web. *Oecologia* 162: 443-452.
- Castanet, J., Francillon-Vieillot, H., Meunier, F. J., and Ricqles, A. DE. 1993. Bone and individual aging. *Bone* 7: 245-283.
- Clair, T.A. and Hindar, A. 2005. Liming for the mitigation of acid rain effects in freshwaters: A review of recent results. *Environmental Review* 13: 91-128.
- Clayton, J. and Menendez, R. 1996. Macroinvertebrate responses to mitigative liming of Dogway Fork, West Virginia. *Restoration Ecology* 4: 234-246.
- Clayton, J., Dannaway, E., Menendez, R., Rauch, H., Renton, J., Sherlock, S., and Zurbuch, P. 1998. Application of limestone to restore fish communities in acidified streams. *North American Journal of Fisheries Management* 18: 347-360.
- Clobert, J., Oppliger, A., Sorci, G., Ernande, B., Swallow, J., and Garland, T. 2000. Trade-offs in phenotypic traits: endurance at birth, growth, survival, predation and susceptibility to parasitism in a lizard, *Lacerta vivipara*. *Functional Ecology* 14: 675-684.
- Corn, P. and Bury, B. 1989. Logging in Western Oregon: Responses of headwater habitats and streams amphibians. *Forest Ecology and Management* 29: 39-57.
- DeWitt, T., Sih, A. and Wilson, D. 1998. Costs and limits of phenotypic plasticity. *Tree* 13:77-81.
- Driscoll, C., Driscoll, K., Mitchell, M., and Raynal, D. 2003. Effects of acidic deposition on forest and aquatic ecosystems in New York State. *Environmental Pollution* 123: 327-336.
- Downey, D., French, C., and Odom, M. 1994. Low cost limestone treatment of acid sensitive trout streams in the Appalachian mountains of Virginia. *Water, Air, and Soil Pollution* 77: 49-77.
- Edwards, E. 2014. Examining the effects of liming on *Gyrinophilus porphyriticus* with a comparison of multiple sampling methods. Theses, Dissertations, and Capstones. Paper 865.
- Eggleton, M.A., Morgan, E.L., and Pennington, W.L. 1996. Effects of Liming on an Acid-Sensitive Southern Appalachian Stream. *Restoration Ecology* 4: 247-263.
- Engqvist, L. 2005. The mistreatment of covariate interaction terms in linear model analyses of behavioural and evolutionary ecology studies. *Animal Behaviour* 70:967-971.
- Finlay, J. and Vanderburg, V. 2007. Introduced trout sever trophic connections in watersheds: Consequences for a declining amphibian. *Ecology* 88: 2187-2198.

- Forsman, A. 1994. Growth rate and survival in relation to relative head size in *Vipera berus*. *Journal of Herpetology* 28: 231-238.
- Forsman, A. 1996. Body size and net energy gain in gape-limited predators: A model. *Journal of Herpetology* 30: 307-319.
- Freda, J. and Dunson, W. 1985. Field and laboratory studies of ion balance and growth rates of Ranid tadpoles chronically exposed to low pH. *Copeia* 1985: 415-423.
- Harfoot, M., Newbold, T., Tittensor, D., Emmott, S., Hutton, J., Lyutsarev, V., Smith, M., Scharlemann, J., and Purves, D. 2014. Emergent global patterns of ecosystem structure and function from a mechanistic general ecosystem model. *PLOS Biology* 12(4): e1001841.
- Hartel, T., Nemes, S., Cogalniceanu, D., Ollerer, K., Schweiger, O., Moga, C., and Demeter, L. 2007. The effect of fish and aquatic habitat complexity on amphibians. *Hydrobiologia* 583: 173-182.
- Hereford, J. 2009. A quantitative survey of local adaptation and fitness trade-offs. *The American Naturalist* 173: 579-588.
- Ivahnenko, T., Renton, D., & Rauch, H. 1988. Effects of liming on water quality of two streams in West Virginia. *Water, Air and Soil Pollution* 41: 311-357.
- Jakob, E.M., Marshall, S.D., & Uetz, G.W. 1996. Estimating fitness: A comparison of body condition indices. *Oikos* 77:61-67.
- Keener, A. and Sharpe, W. 2005. The effects of doubling limestone sand applications in two acidic Southwestern Pennsylvania streams. *Restoration Ecology* 13: 108-119.
- Lane, E. W. 1947. Report of the Subcommittee on Sediment Terminology. *Transactions American Geophysical Union* 28(6): 936-938.
- Leclair, R. & Castanet, J. 1987. A skeletochronological assessment of age and growth in the frog *Rana pipiens* Schreber (Amphibia, Anura) from Southwestern Quebec. *Copeia* 1987:361-369.
- LeFevre, S. and Sharpe, W. 2002. Acid stream water remediation using limestone sand on Bear Run in Southwestern Pennsylvania. *Restoration Ecology* 10: 223-236.
- Lowe, W. and Bolger, D. 2002. Local and landscape-scale predictors of salamander abundance in New Hampshire headwater streams. *Conservation Biology* 16: 183-193.
- Lowe, W. 2003. Linking dispersal to local population dynamics: A case study using a headwater salamander system. *Ecology* 84(8): 2145-2154.
- Lowe, W., Nislow, K., and Bolger, D. 2004. Stage-specific and interactive effects of sedimentation and trout on a headwater stream salamander. *Ecological applications* 14: 164-172.

- Lowe, W. 2005. Factors affecting stage-specific distribution in the stream salamander *Gyrinophilus porphyriticus*. *Herpetologica* 61(2): 135-144.
- Lowe, W., Likens, G., and Cosentino, B. 2006. Self-organisation in streams: the relationship between movement behavior and body condition in a headwater salamander. *Freshwater Biology* 51: 2052-2062.
- Lowe, W., McPeck, M., Likens, G., and Cosentinos, B. 2012. Decoupling of genetic and phenotypic divergence in a headwater landscape. *Molecular Ecology* 21: 2399-2409.
- Luquet, E., Lena, J-P., Miaud, C., and Plenet, S. 2015. Phenotypic divergence of the common toad (*Bufo bufo*) along an altitudinal gradient: Evidence for local adaptation. *Heredity* 114: 69-79.
- Mant, R., Jones, D., Reynolds, B., Ormerod, S., and Pullin, A. 2013. A systematic review of the effectiveness of liming to mitigate impacts of river acidification on fish and macroinvertebrates. *Environmental Pollution* 179: 285-293.
- Maret, T. and Collins, J. 1996. Effect of prey vulnerability on population size structure of a gape-limited predator. *Ecology* 77: 320-324.
- McCahon, P. and Poulton, M. 1991. Lethal and sub-lethal effects of acid, aluminum and lime on *Gammarus pulex* during repeated simulated episodes in a Welsh stream. *Freshwater Biology* 25: 169-178.
- McClurg, S., Petty, J.T., Mazik, P., and Clayton, J. 2007. Stream ecosystem response to limestone treatment in acid impacted watersheds of the Allegheny Plateau. *Ecological Applications* 17: 1087-1104.
- McDonald, J.H. 2014. *Handbook of Biological Statistics* (3rd ed.). Sparky House Publishing, Baltimore, Maryland. This web page contains the content of pages 77-85 in the printed version.
- Mckie, B.G., Petrin, Z., and Malmqvist, B. 2006. Mitigation or disturbance? Effects of liming on macroinvertebrate assemblage structure and leaf-litter decomposition in the humic streams of Northern Sweden. *Journal of Applied Ecology* 43: 780-791.
- Menendez, R., Clayton, J., and Zurbuch, P. 1996. Chemical and fishery responses to mitigative liming of an acidic stream, Dogway Fork, West Virginia. *Restoration Ecology* 4: 220-233.
- Menendez, R., Clayton, J., Zurbuch, P., Sherlock, S., Rauch, H., and Renton, J. 2000. Sand-sized limestone treatment of streams impacted by acid mine drainage. *Water, Air, and Soil Pollution* 124: 411-428.
- Ohdachi, S. Growth, metamorphosis, and gape-limited cannibalism and predation on tadpoles in larvae of salamanders *Hynobius retardatus*. *Zoological Science* 11: 127-131.
- Okland, J. and Okland, K. 1986. The effects of acid deposition on benthic animals in lakes and streams. *Experientia* 42: 471-486.

- Pease, C. and Bull, J. 1988. A critique of methods for measuring life history trade-offs. *Journal of Evolutionary Biology* 1: 293-303.
- Petranka, J.W. 1998. *Salamanders of the United States and Canada*. Smithsonian Institution Press, Washington, D.C.
- Pierce, B. 1985. Acid tolerance in amphibians. *Bioscience* 35: 239-243.
- Pope, K. and Matthews, K. 2002. Influence of anuran prey on the condition and distribution of *Rana mucosa* in the Sierra Nevada. *Herpetologica* 58: 354-363.
- Resetarits, W. 1991. Ecological interactions among predators in experimental stream communities. *Ecology* 72: 1782-1793.
- Resetarits, W. 1995. Competitive asymmetry and coexistence in size-structured populations of Brook Trout and Spring Salamanders. *Oikos* 73: 188-198.
- Reynolds, C.S. and Elliott, J.A. 2012. Complexity and emergence in aquatic ecosystems: predictability in aquatic ecosystem responses. *Freshwater Biology* 57: 74-90.
- Roff, D. 2000. Trade-offs between growth and reproduction: An analysis of the quantitative genetic evidence. *Journal of Evolutionary Biology* 13: 434-445.
- Rohr, J., Elskus, A., Shepherd, B., Crowley, P., McCarthy, T., Niedzwiecki, J., Sager, T., Sih, A., and Palmer, B. 2004. *Ecological Applications* 14: 1028-1040.
- Rowe, L. and Ludwig, D. 1991. Size and timing of metamorphosis in complex life cycles: Time constraints and variation. *Ecology* 72: 413-427.
- Schulte-Hostedde, A., Zinner, B., Millar, J., and Hickling, G. 2005. Restitution of mass-size residuals: Validating body condition indices. *Ecology* 86: 155-163.
- Sih, A., Petranka, J., and Kats, L. 1988. The dynamics of prey refuge use: A model and tests with sunfish and salamander larvae. *American Naturalist* 132: 463-483.
- Sih, A. and Kats, L. 1991. Effects of refuge availability on the responses of salamander larvae to chemical cues from predatory green sunfish. *Animal Behavior* 42: 330-332.
- Simmons, J., Andrew, T., Arnold, A., Bee, N., Bennett, J., Grundman, M., Johnson, K., and Shepherd, R. 2006. Small-scale chemical changes by in-stream limestone sand additions to streams. *Mine Water and the Environment* 25: 241-245.
- Smirina, E.M. 1994. Age determination and longevity in amphibians. *Gerontology* 40:133-146.
- Smith-Gill, S. 1983. Developmental plasticity: Developmental conversion versus phenotypic modulation. *American Zoologist* 23: 47-55.

- Socha, M. & Ogielska, M. 2010. Age structure, size and growth rate of water frogs from central European natural *Pelophylax ridibundus*-*Pelophylax esculentus* mixed populations estimated by skeletochronology. *Amphibia-Reptilia* 31:239-250.
- Sokal, R. R., and F. J. Rohlf. 1981. *Biometry*. 2nd edition. W. H. Freeman. San Francisco, CA.
- Stearns, S. C. 1989. The evolutionary significance of phenotypic plasticity. *Bioscience* 39: 436-445.
- Stearns, S. C. 1992. *The Evolution of Life Histories*. Oxford University Press, Oxford, U.K.
- Sverdrup, H. 1986. The dissolution efficiency for different stream liming methods. *Water, Air and Soil Pollution* 31: 827-837.
- Urban, M. 2008. Salamander evolution across a latitudinal cline in gape-limited predation risk. *Oikos* 117: 1037-1049.
- Wake, D.B. & Castanet, J. 1995. A skeletochronological study of growth and age in relation to adult size in *Batrachoseps attenuates*. *Journal of Herpetology* 29(1):60-65.
- Walls, S., Belanger, S., and Blaustein, A. 1993. Morphological variation in a larval salamander: Dietary induction of plasticity in head shape. *Oecologia* 96: 162-168.
- Welsh, H. and Droege, S. 2001. A case for using Plethodontid Salamanders for monitoring biodiversity and ecosystem integrity of North American forests. *Conservation Biology*. 15: 558-569.
- Welsh, H.H. and Ollivier, L.M. 1998. Stream amphibians as indicators of ecosystem stress: a case study from California's redwoods. *Ecological Applications* 8: 1118-1132.
- Werner, E. and Anholt, B. 1993. Ecological consequences of the trade-off between growth and mortality rates mediated by foraging activity. *The American Naturalist* 142: 242-272.
- Wilbur, H. and Collins, J. 1973. Ecological aspects of amphibian metamorphosis. *Science* 182: 1305-1314.
- Wilbur, H. 1980. Complex life cycles. *Annual Review of Ecological Systems* 11: 67-93.
- Zaret, T. 1980. *Predation and freshwater communities*. Yale University Press, New Haven, Connecticut, USA.